



UNIL | Université de Lausanne

Unicentre

CH-1015 Lausanne

<http://serval.unil.ch>

Year : 2016

FROM REGIONAL LANDSLIDE DETECTION TO SITE-SPECIFIC SLOPE DEFORMATION MONITORING AND MODELLING BASED ON ACTIVE REMOTE SENSORS

Michoud Clément

Michoud Clément, 2016, FROM REGIONAL LANDSLIDE DETECTION TO SITE-SPECIFIC
SLOPE DEFORMATION MONITORING AND MODELLING BASED ON ACTIVE REMOTE
SENSORS

Originally published at : Thesis, University of Lausanne

Posted at the University of Lausanne Open Archive <http://serval.unil.ch>

Document URN : urn:nbn:ch:serval-BIB_C78D602246D92

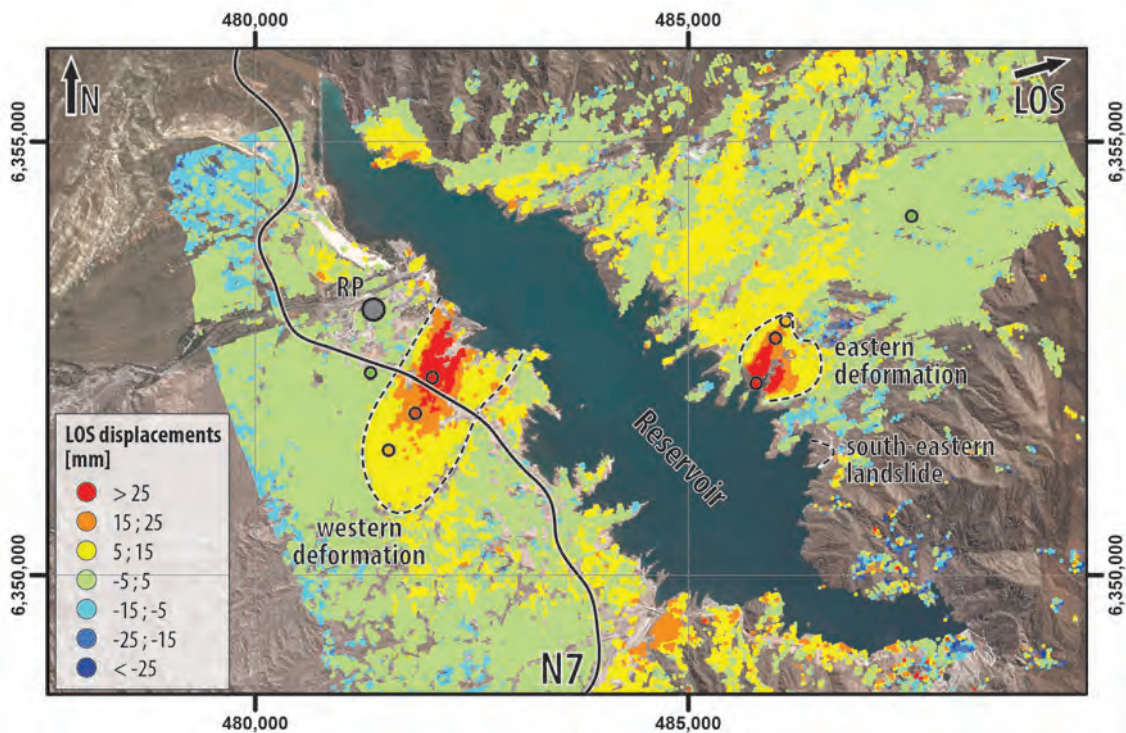
Droits d'auteur

L'Université de Lausanne attire expressément l'attention des utilisateurs sur le fait que tous les documents publiés dans l'Archive SERVAL sont protégés par le droit d'auteur, conformément à la loi fédérale sur le droit d'auteur et les droits voisins (LDA). A ce titre, il est indispensable d'obtenir le consentement préalable de l'auteur et/ou de l'éditeur avant toute utilisation d'une oeuvre ou d'une partie d'une oeuvre ne relevant pas d'une utilisation à des fins personnelles au sens de la LDA (art. 19, al. 1 lettre a). A défaut, tout contrevenant s'expose aux sanctions prévues par cette loi. Nous déclinons toute responsabilité en la matière.

Copyright

The University of Lausanne expressly draws the attention of users to the fact that all documents published in the SERVAL Archive are protected by copyright in accordance with federal law on copyright and similar rights (LDA). Accordingly it is indispensable to obtain prior consent from the author and/or publisher before any use of a work or part of a work for purposes other than personal use within the meaning of LDA (art. 19, para. 1 letter a). Failure to do so will expose offenders to the sanctions laid down by this law. We accept no liability in this respect.

FROM REGIONAL LANDSLIDE DETECTION TO SITE-SPECIFIC SLOPE DEFORMATION MONITORING AND MODELLING BASED ON ACTIVE REMOTE SENSORS



Thèse de doctorat

présentée à la faculté des géosciences et de l'environnement par

Clément Michoud

ingénieur géologue diplômé de l'université de Lausanne

Devant le Jury composé de
Monsieur le professeur Michel Jaboyedoff, directeur
Monsieur le docteur Marc-Henri Derron, co-directeur
Monsieur le docteur François Joseph Baillifard, expert
Monsieur le professeur Lars Harald Blikra, expert
Monsieur le professeur Jacques Locat, expert
Sous la présidence de monsieur le doyen François Bussy

Lausanne, 2016

IMPRIMATUR

Vu le rapport présenté par le jury d'examen, composé de

Président de la séance publique :	M. le Professeur François Bussy
Président du colloque :	M. le Professeur François Bussy
Directeur de thèse :	M. le Professeur Michel Jaboyedoff
Co-directeur de thèse :	M. le Docteur Marc-Henri Derron
Expert externe :	M. le Professeur Lars Harald Blikra
Expert externe :	M. le Professeur Jacques Locat
Expert externe :	M. le Docteur François Baillifard

Le Doyen de la Faculté des géosciences et de l'environnement autorise l'impression de la thèse de

Monsieur Clément MICHOU

Titulaire d'une
Maîtrise universitaire ès Sciences d'ingénieur géologue
Université de Lausanne

intitulée

FROM REGIONAL LANDSLIDE DETECTION TO SITE-SPECIFIC SLOPE DEFORMATION MONITORING AND MODELLING BASED ON ACTIVE REMOTE SENSORS

Lausanne, le 15 janvier 2016

Faculté des géosciences et de l'environnement



Professeur François Bussy, Doyen

“Write what you know. That should leave you with a lot of free time.”

Howard Nemerov

Résumé

De la détection régionale de glissements de terrain au suivi et à la modélisation de déformations à l'échelle du versant à l'aide de la télédétection active

Les glissements de terrain peuvent avoir des conséquences directes et indirectes sur les activités humaines et sur les individus. Afin d'améliorer la gestion des risques naturels, cette thèse de doctorat étudie les aptitudes des capteurs LiDAR (lasers optiques) et RaDAR (émetteurs micro-ondes) à la détection, la caractérisation et la quantification du risque de glissements à échelles régionales, ainsi que le suivi et la modélisation d'instabilités de pentes à l'échelle du versant.

A l'échelle régionale, nous démontrons tout d'abord la capacité des récents systèmes de LiDAR embarqués sur bateau à modéliser la topographie de falaises côtières en Normandie. Nous avons validé cette approche qui peut ainsi être généralisée pour cartographier et quantifier les chutes de blocs et glissements de terrain affectant un littoral. Ensuite, nous avons testé la méthode d'interférométrie RaDAR satellitaire pour recenser les glissements de terrain profonds dans les Andes argentines. Nous démontrons ici que la détection, la caractérisation et le suivi de glissements très lents, ainsi que la mesure de variation du niveau d'eau du lac de barrage voisin, sont possibles en utilisant les mesures de phases et d'amplitudes des images RaDAR satellitaires. Enfin, une étude sur l'estimation spatiale du risque de chutes de blocs le long de routes de montagnes est conduite dans le Val de Bagnes. Nous avons pour cela amélioré la méthode de la distribution de pentes et le logiciel de propagation FlowR. Ainsi, la susceptibilité de rupture de blocs détachés d'une paroi rocheuse et les fréquences relatives de leur propagation ont été estimées, permettant de quantifier et cartographier relativement simplement les dangers et risques associés à l'échelle de la vallée.

A l'échelle du versant, nous démontrons l'intérêt original de la fusion des données RaDAR et LiDAR terrestres pour pouvoir suivre et modéliser le glissement rocheux alpin de la Perraire ; nous avons pu cartographier ses limites d'extension et ses volumes, ainsi que mettre en évidence des déplacements translationnels non-homogènes se propageant le long d'une surface de rupture dièdre. Enfin, nous avons évalué les exigences spécifiques et les problèmes classiques des systèmes d'alertes de certains des glissements les plus étudiés dans le monde. Nous avons ainsi pu déterminer une liste de recommandations concrètes pour la conception de nouveaux systèmes fiables, ainsi que répertorier les limites conceptuelles actuelles qu'il faudrait améliorer.

En conclusion, la diversité des sites et contextes d'études forgea une expérience solide exposant les avantages et inconvénients des méthodes LiDAR et RaDAR, et souligna la nécessité grandissante de leurs utilisations de manières complémentaires et intégrées.

Summary

From Regional Landslide Detection to Site-Specific Slope Deformation Monitoring and Modelling Based on Active Remote Sensors

Landslide processes can have direct and indirect consequences affecting human lives and activities. In order to improve landslide risk management procedures, this PhD thesis aims to investigate capabilities of active LiDAR and RaDAR sensors for landslides detection and characterization at regional scales, spatial risk assessment over large areas and slope instabilities monitoring and modelling at site-specific scales.

At regional scales, we first demonstrated recent boat-based mobile LiDAR capabilities to model topography of the Normand coastal cliffs. By comparing annual acquisitions, we validated as well our approach to detect surface changes and thus map rock collapses, landslides and toe erosions affecting the shoreline at a county scale. Then, we applied a spaceborne InSAR approach to detect large slope instabilities in Argentina. Based on both phase and amplitude RaDAR signals, we extracted decisive information to detect, characterize and monitor two unknown extremely slow landslides, and to quantify water level variations of an involved close dam reservoir. Finally, advanced investigations on fragmental rockfall risk assessment were conducted along roads of the Val de Bagnes, by improving approaches of the Slope Angle Distribution and the FlowR software. Therefore, both rock-mass-failure susceptibilities and relative frequencies of block propagations were assessed and rockfall hazard and risk maps could be established at the valley scale.

At slope-specific scales, in the Swiss Alps, we first integrated ground-based InSAR and terrestrial LiDAR acquisitions to map, monitor and model the Perraire rock slope deformation. By interpreting both methods individually and originally integrated as well, we therefore delimited the rockslide borders, computed volumes and highlighted non-uniform translational displacements along a wedge failure surface. Finally, we studied specific requirements and practical issues experimented on early warning systems of some of the most studied landslides worldwide. As a result, we highlighted valuable key recommendations to design new reliable systems; in addition, we also underlined conceptual issues that must be solved to improve current procedures.

To sum up, the diversity of experimented situations brought an extensive experience that revealed the potential and limitations of both methods and highlighted as well the necessity of their complementary and integrated uses.

Acknowledgements

As the tradition wants, I have first to thank i miei maestri, Michel Jaboyedoff and Marc-Henri Derron. Michel's Science, but above all, his enthusiasm, team spirit, trust and taste for action were an amazing source of motivation! On another hand, Marc-Henri has the great ability to always keep a peaceful and reassuring calm, even facing up to strong scientific and technical issues, that does not hide his remarkable culture!

Moreover, I am feeling very grateful to the thesis jury, Lars Hard Blikra, François-Joseph Baillifard and Jacques Locat, supervised by François Bussy, who made a tremendous job by reviewing and discussing my manuscript; I acknowledge them for their time and for being here in Lausanne the 9th of December 2015 for the oral exam. It has been really valuable and appreciated!

I have to thank the Bagnes municipality where I spent so much time on the field, up in the air and in the basement. I am grateful to the Security service and Louis Ernest Sidoli for its financial support, their archives and for allowing us to publish maps and results. In addition, I would like to thank Marc Maret and again François Joseph Baillifard for their warm welcome, motivation to work with me and their great field experience!

I spent really good times in Dieppe for the MLS campaigns. This research was partly supported by (1) the FNS project "Characterizing and analysing 3D temporal slope evolution" and (2) the ICoD/CERG coordinated programme "Coupling terrestrial and marine datasets for coastal hazard assessment and risk reduction in changing environments". Surprisingly, here I discovered a great county and some splendid colleagues; indeed, it has been a real pleasure to work with Stéphane Costa, Robert Davidson, Pauline Letortu and Olivier Maquaire of the Caen University, as well as Christophe Delacourt of Brest University and Alban Legardien, the Aillot's Captain. Let's hope it lasts!

Regarding the Argentinian study, the used Envisat data have been acquired with the support of the ESA (Category-1 Project "Slope instabilities mapping using GIS, Differential SAR Interferometry methodologies and field investigations along the National Road N7, Mendoza Province, Argentina"). In addition, I really want to thank Valérie Baumann, formerly at the Argentina Geological Survey, and Tom Rune Lauknes, from the Norut, for their stimulating collaboration, patience and great experience on the Argentinian and InSAR fields.

I also have to fully acknowledge Carlo Rivolta and Davide Leva (Ellegi), Richard Metzger (Terranum) as well as Lene Kristensen and Lars Harald Blikra (Åknes/Tafjord Beredskap) since they fully contributed to the development of the LiSAmobile - Coltop3D integration tools introduced in Section 6.

The first three years were achieved within the framework of the FP7 European project "SafeLand". Sections 4, 5 and 7 have been partially supported by this project that is gratefully acknowledged. In addition, here I met a dynamic scientific community and I am grateful to have worked mainly with Audrey Baills, Ivo Baroň, Sara Bazin, Jordi Corominas, Josep Gili, Javier Hervás, Bjørn Kalsnes, Norman Kerle, Mario Lovisolo, Jean-Philippe Malet, Olga Mavrouli, Farrock Nadim, Alexandre Remaitre, Andre Stumpf and Veronica Tofani.

As stated in the Preamble, I also spent a lot of time on the Pont Bourquin earthflow, where I really appreciated the successful and friendly collaboration with Eric Larose and Denis Jongmans of the Grenoble University.

Now it's time to thank my legendary officemates: Antonio "el Señor tío" Abellán, Dariou "el tíou" Carreou, Marc "Citrus" Choffet, Pierrick "the buddy" Nicolet, Pascal "Monsieur" Horton and Richard "Captain" Metzger! Thanks for having been here, for the appreciated and constructive discussions about geology, science and above all, way of life, in the office, outside the office, days and nights, in Switzerland, outside Switzerland, in pubs, outside pubs, etc. Moreover, padawan Martin, Line, Battista, Benjamin, Céline, Florian, Gionna, Ivanna, Lucie, Marie, Mitch and Simon, together with first Michel's exemplary assistants (Thierry, Andrea and Papi Alex), significantly buttressed me those last seven years. I do not forget also current Michel's assistant Agnès, Jérémie, Antoine, Liliane, Emmanuel W. and C^{ie} for their help and renewed motivation. Thank you 'mates!

Finally, I have no word to express how much I am grateful to my family and best friends for their long-term continuous monitoring: Maman, Papa, Mamie, Papi, frangine, frangins, les copainings, merci pour tout l'enthousiasme avec lequel vous m'avez soutenu ; et surtout, merci de m'avoir toujours poussé « vers l'infini et au-delà ! ».

Last but not least, to my terrific wife: "I love you princess, you're so radiant!"

Preamble

From May 2009 to 2012, the first three years of this PhD thesis were achieved within the framework of the European project “SafeLand: Living with landslide risk in Europe: Assessment, effects of global change, and risk management strategies”. This project, involving 27 European institutions dealing with natural hazards, aimed to review current landslide risk assessments and associated management tools at different scales and to develop new common procedures supporting these existing strategies. With Prof Jaboyedoff, Dr Derron and Abellán, we mainly worked for the SafeLand area 4, focused on sensors capabilities and issues for landslide detection, monitoring and early warning. We indeed acted as Editors and main contributors of the SafeLand deliverable 4.1 widely summarizing scientific and technical aspects of landslide-related sensors (Michoud et al. 2012b). Moreover, we were also actively involved in deliverables about sensor selection guidelines (deliverable 4.4, Stumpf et al. 2011), research trends (deliverable 4.5, Tofani et al. 2012), early warning system settings (deliverable 4.8, Bazin et al. 2012) and remediation works (deliverable 5.1, Vaciago et al. 2011). In addition, we also investigated specific landslide failure mechanism types, working on the influences of anthropogenic activities on slope stabilities (deliverable 1.6, Nadim et al. 2010; in Annex B5, after Michoud et al. 2011).

To complete these theoretical studies, a practical experience of wide types of monitoring sensors has been acquired on different slope instabilities in the Swiss Alps. First, during my Master thesis, I learnt and applied spaceborne InSAR algorithms to monitor the La Frasse landslide. Later, on the Pont Bourquin earthflow (Jaboyedoff 2006; Jaboyedoff et al. 2009b) in Les Diablerets, I was in charge to plan, acquire and interpret data on surface displacements, sub-surface water level and meteorological conditions, based on rope extensometers, terrestrial LiDAR, electronic distance meters, global navigation satellite systems, inclinometers, piezometers and rain gauges (Michoud et al. 2012c). In collaboration with the University of Grenoble and the EPF Lausanne, the kinematic model established on our monitoring investigations even supported a pioneering research on earthflow failure forecasting from seismic noise monitoring (Mainsant et al 2012a, in annex A1). Later on, a second study conducted on the Barmasse rockslide in the Val de Bagnes focused on the practice of LiDAR and global navigation satellite systems. Here the integration of both techniques was required to emphasise non-homogeneous displacements, accumulating stresses in the scree deposits, which could thus fail (Michoud et al. 2013b).

Therefore this experience acquired via SafeLand and the first three landslides monitoring projects supported research developed hereafter in this thesis, being aware of current advantages and limits of active remote sensors.

Note

All chapters of this manuscript were written by the PhD candidate. Extracted from submitted and published scientific papers, chapter 2.1 and sections 3 to 7 were in addition refined with corrections and suggestions of the candidate's co-authors and reviewers. Only chapters 4.2 (on the natural context of the Potrerillos area), 5.2.1.a (on the original slope angle distribution method) and 5.2.2 (on the FlowR routine theory) were first written by the associated co-authors under the guidance of the PhD candidate.

Table of Content

Résumé	7
Summary.....	9
Acknowledgements	11
Preamble	13
Table of Content	15
Table of Annexes.....	19
Table of Acronyms	21
INTRODUCTION	23
1 Thesis context.....	25
1.1 Landslide processes.....	25
1.1.1 Slope movement description	25
1.1.2 Destabilization and triggering processes.....	28
1.2 Landslide risk management.....	30
1.2.1 Susceptibility mapping	30
1.2.2 Hazard characterization	32
1.2.3 Failure forecasting.....	34
1.3 Remote sensors and related stakes.....	35
1.4 Outline.....	38
1.4.1 Governing principles	38
1.4.2 Research sections into details	38
2 Active remote sensors.....	41
2.1 History of LiDAR developments.....	42
2.2 History of InSAR developments	48
LANDSLIDE REGIONAL HAZARD AND RISK MAPPING.....	53
3 Landslides detection and monitoring capability of boat-based Mobile Laser Scanning along Dieppe coastal cliffs, Normandy.....	55
3.1 Introduction.....	55
3.2 Mobile Laser Scanning principles	57
3.3 Point cloud processing	61
3.3.1 Devices technical specifications	61
3.3.2 Acquisitions on the vessel	61
3.3.3 Post-processing	65
3.3.4 Terrestrial Laser Scanning point clouds.....	66
3.4 MLS point clouds capability assessment	68
3.4.1 Methodology.....	68
3.4.2 Results	71
3.5 Discussion and conclusions	78
3.6 Supplementary material: Post processing captions	81
3.7 Updates from the 2014 acquisition campaign.....	82

4 Large slope deformations detection and monitoring along shores of the Potrerillos dam reservoir, Argentina, based on a Small-Baseline InSAR approach	85
4.1 Introduction	85
4.2 General setting.....	88
4.2.1 Morphotectonic context.....	88
4.2.2 Landscape and active surface processes	89
4.3 SAR data processing.....	91
4.3.1 Available SAR data	91
4.3.2 Landslides detection at regional scale	92
4.3.3 Landslides monitoring along shores of the Potrerillos' dam reservoir	96
4.3.4 Water level fluctuations of the reservoir.....	98
4.4 Discussions.....	99
4.4.1 Influences of the Andean orogen	99
4.4.2 Limitations to large landslides detection.....	101
4.4.3 SBAS-derived geometry	102
4.4.4 Reservoir-slope deformation interactions.....	102
4.5 Conclusions.....	104
4.6 Supplementary material: South-eastern landslide	105
5 Rockfall hazard and risk assessments along roads at a regional scale: example in Swiss Alps	109
5.1 Introduction	109
5.2 Methodology	113
5.2.1 Detection of sources areas	113
5.2.2 Runout assessment.....	117
5.2.3 Rockfall quantitative hazard mapping along roads.....	119
5.2.4 Rockfall quantitative risk assessment along roads	120
5.3 Case study: the Val de Bagnes	121
5.3.1 Settings	121
5.3.2 Rockfall hazard assessments.....	122
5.3.3 Rockfall risk assessment along the main roads of the valley	126
5.4 Discussions.....	127
5.4.1 Results within the study area	127
5.4.2 Recent rockfall event	128
5.4.3 Advantages and limitations of the presented approach.....	128
5.4.4 Influences of the cell size DEM	130
5.4.5 Hazard calibration.....	131
5.5 Conclusions	131
SITE-SPECIFIC LANDSLIDE MONITORING AND MODELLING.....	133
6 La Perraire rock slope deformation monitoring and modelling by Ground-based InSAR and terrestrial LiDAR integration.....	135
6.1 Introduction	135
6.2 Data acquisitions and processing methods.....	140
6.2.1 GB-InSAR monitoring campaigns	140
6.2.2 TLS monitoring campaign	143
6.2.3 TLS-based geometry modelling	146
6.3 Processing results	147
6.3.1 Short term continuous monitoring.....	147
6.3.2 Long term sequential monitoring	150
6.3.3 Geometry modelling	156
6.4 Synthesis and discussion.....	157

6.5	Conclusions.....	160
7	Experiences from site-specific landslide Early Warning Systems.....	163
7.1	Introduction.....	163
7.2	Design of the questionnaire	165
7.3	Results and interpretations.....	165
7.3.1	Units in charge of the EWSs	166
7.3.2	Landslides Settings	167
7.3.3	Monitoring systems.....	171
7.3.4	Dealing with populations	178
7.3.5	Practical challenges.....	182
7.4	Discussions and conclusions.....	182
7.5	Supplementary material.....	184
	CONCLUSIONS.....	191
8	Synthesis	193
8.1	Summary of specific conclusions.....	193
8.2	Current sensors capabilities	194
8.3	Research perspectives.....	197
9	Epilogue.....	201
	REFERENCES.....	203

Table of Annexes

Foreword

Curriculum Vitae and Publication List

Annexes A: publications in peer-reviewed journals, as co-author

- A1: Mainsant G, Larose E, Brönnimann C, Jongmans D, Michoud C and Jaboyedoff M: Ambient seismic noise monitoring of a clay landslide: toward failure prediction. *Journal of Geophysical Researches Earth Surface* 117, 12 p., 2012
- A2: Cloutier C, Agliardi F, Crosta G, Frattini P, Froese C, Jaboyedoff M, Locat J, Michoud C and Marui H: The First International Workshop on Warning Criteria for Active Slides: technical issues, problems and solutions for managing early warning systems. *Landslides* 12, 205-2012, 2015
- A3: Rouyet L, Kristensen L, Derron MH, Michoud C, Blikra LH, Jaboyedoff M and Lauknes TR: Evidence of rock slope breathing using GB-InSAR. Submitted to *Geomorphology*, 27 p, May 2015

Annexes B: selection of other relevant publications

- B1: Michoud C, Derron MH, Abellán A, Jaboyedoff M and Fornaro G: Radar Wave Principles, Interferometric Radar Distance-Meter and Differential SAR Interferometry. Deliverable 4.1 of the European project SAFELAND: Review of Techniques for Landslide Detection, Fast Characterization, Rapid Mapping and Long-Term Monitoring. Edited in 2010 by Michoud C, Abellán A, Derron MH and Jaboyedoff M, 105-125, 2010
- B2: Jaboyedoff M, Abellán A, Carrea D, Derron MH, Matasci B and Michoud C: LiDAR use for Mapping and Monitoring of Landslides, Accepted in *Encyclopedia Natural Hazards*, Taylor & Francis
- B3: Jaboyedoff M, Choffet M, Derron MH, Horton P, Loye A, Longchamp C, Mazotti B, Michoud C and Pedrazzini A: Preliminary slope mass movements susceptibility mapping using DEM and LiDAR DEM. In: *Terrigenous Mass Movements*, Pradhan and Buchroithner (Eds.), Springer-Verlag Berlin Heidelberg, 109-170, 2012
- B4: Jaboyedoff M, Horton P, Derron MH, Longchamp C and Michoud C: Monitoring Natural Hazards. In: *Encyclopedia of Natural Hazards*, Bobrowsky P.T. (Ed.), Springer Science+Business Media B.V., 12 pp., 2012
- B5: After Michoud C, Jaboyedoff M, Derron MH, Nadim F and Leroi E: Classification of landslide-inducing anthropogenic activities. 5th Canadian Conference on Geotechnique and Natural Hazards, Kelowna, Canada, 10 p., 2011

Table of Acronyms

3D	3 Dimensions
ADInSAR	Advanced DInSAR
ALS	Aerial Laser Scanning
ALS-DEM	Digital Elevation Model obtained by Aerial Laser Scanning
DEM	Digital Elevation Model
DInSAR	Differential InSAR
DSGSD	Deep Seated Gravitational Slope Deformation
ESA	European Space Agency
EWS	Early Warning System
GB-InSAR	Ground-Based InSAR
GIS	Geographic Information System
GNSS	Global Navigation Satellite System
GPS	Global Positioning System
HR	High Resolution
IMU	Inertial Measurement Unit
INS	Inertial Navigation System
InSAR	SAR Interferometry
LASER	Light Amplification by Stimulated Emission of Radiation
LiDAR	Light Detection And Ranging
LoS	Line Of Sight
MLS	Mobile Laser Scanning
NIR	Near InfraRed
PSI	Persistent Scatterers Interferometry
RaDAR	RAdio Detection And Ranging
RoI	Region of Interest
SAR	Synthetic Aperture Radar
SBAS	Small Baseline Subset
SNR	Signal to Noise Ratio
SRTM	Shuttle Radar Topography Mission
TLS	Terrestrial Laser Scanning
ToF	Time-Of-Flight
UAV	Unmanned Aerial Vehicles
XYZ	3D coordinates

INTRODUCTION

1 Thesis context

1.1 Landslide processes

1.1.1 Slope movement description

Landslides are often defined as the downhill displacement of a mass of debris, earth or rock by Cruden and Varnes (1996). But this common description does not highlight the wide variety of landslide types. For decades, scientists have attempted to disseminate and update landslide classifications to objectively describe all types of gravitational process with common concepts. Therefore, according to the leading successive classifications of Terzaghi (1950), Varnes (1978), Cruden and Varnes (1996) and Hungr et al. (2014), slope instabilities can be characterized by the following points:

1. Processes and materials

Slopes can evolve according to different types of landslide processes and motions. Indeed, instable masses can *fall*, *topple*, *slide*, *spread* and *flows* (Figure 1.1, Varnes 1978). Recently, Hungr et al. (2014) added the specific type of *slope deformation*, labelling extremely slow very large deep-seated landslides (Figure 1.2), also called *sackung* or *sagging* (Zischinsky 1969; Hutchinson 1988; Agliardi et al. 2001). Moreover, some landslide processes may have complex behaviours, combining several types of processes.

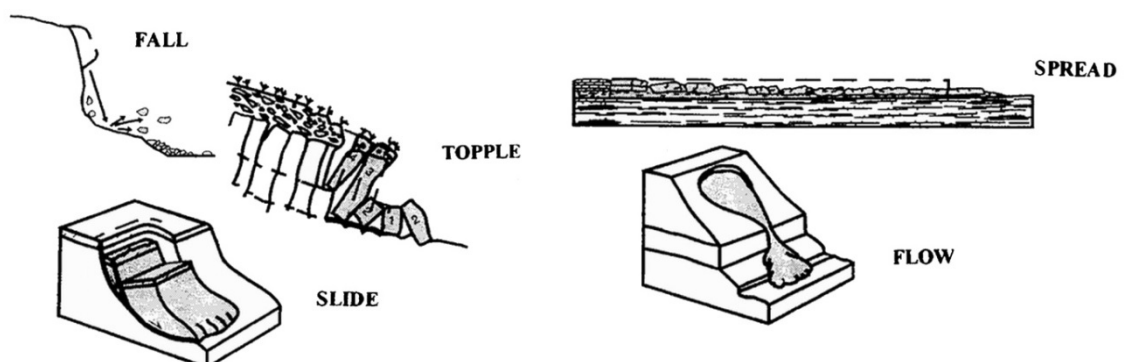


Figure 1.1: Scheme of the five singular types of landslide processes. Note that instability extents may considerably vary and no scale is assigned on these plots (modified after Varnes 1978).

Furthermore, it is also important to describe slope material-forming instabilities, usually based on the geotechnical-oriented classes of *rock*, *clay*, *mud*, *silt-sand-gravel-boulders*, *debris*, *peat* and *ice*.

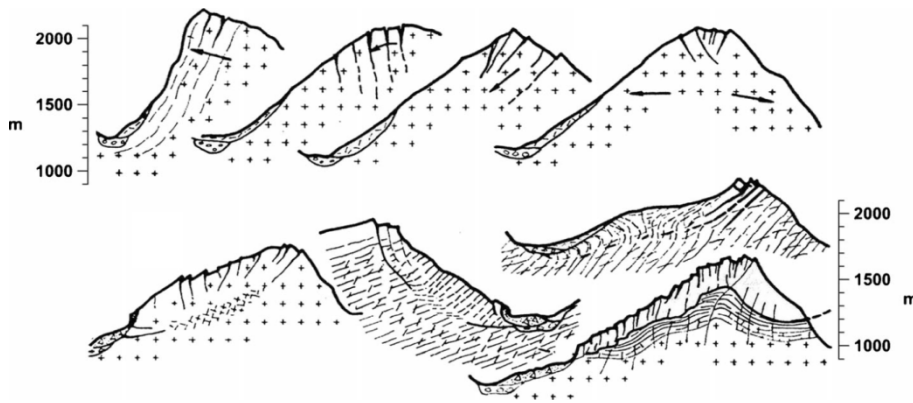


Figure 1.2: Examples of cross-section of Carpathian mountain slope deformations (Nemčok 1982, in Hungr et al. 2014).

These terms refer to specific geotechnical settings, such as mass strength, plasticity or grain size distribution, which strongly influence landslide behaviours and failure conditions (e.g Antoine et al. 1988; Sassa 1988). The Table 1.1 summarize the most recent updated landslide classification (Hungr et al., 2014) according to movement types and geotechnical slope-forming materials.

Table 1.1: Summary of the Hungr et al.’s landslide nomenclature (2014). Words in italic font are placeholders.

Type of movement	Rock	Soil
Fall	<i>Rock/ice</i> fall	<i>Boulder/debris/silt</i> fall
Topple	Rock block topple	<i>Gravel/sand/silt</i> topple
	Rock flexural topple	
Slide	Rock rotational slide	<i>Clay/silt</i> rotational slide
	Rock planar slide	<i>Clay/silt</i> planar slide
	Rock wedge slide	<i>Gravel/sand/debris</i> slide
	Rock compound slide	Clay/silt compound slide
	Rock irregular slide	
Spread	Rock slope spread	<i>Sand/silt</i> liquefaction spread
		Sensitive clay spread
Flow	<i>Rock/ice</i> avalanche	<i>Sand/silt/debris</i> dry flow
		<i>Sand/silt/debris</i> flowslide
		Sensitive clay flowslide
		Debris flow
		Mud flow
		Debris avalanches
		Earthflow
Peat flow		
Slope deformation	Mountain slope deformation	Soil slope deformation
	Rock slope deformation	Soil creep
		Solifluction

Other geological terms such as *granitic*, *volcanic* or *sediments*, may complete the slope-forming material description, but never should replace the geotechnical characterization (Hungr et al. 2014).

Indeed, some geological terms are not enough consistent and precise to point out landslide behaviours, as for example *alluvial deposits* that can refer to both different *clay* and *gravel* materials.

2. Extents and volumes

Slope instabilities can affect a wide range of slope thickness and surface (Figure 1.3). As an example, mountain slope deformations may affect hundreds of meter deep materials over entire slope scales larger than 1 km². On the contrary, earthflows can be confined to very superficial soil layers (typically less than 5 m) over small surfaces.



Figure 1.3: (Left) Large deep-seated landslide burying an entire Taiwan highway section (source: Metronews journal). (Right) Shallow planar slide affecting the first 30 cm thick layer of the morainic soil, in the Upper Bagnes valley.

Adjectives describing and quantifying involved extents and volumes can therefore be added to the classification system in order to complete the landslide description. Nevertheless, extents and volumes can already be implicit with the landslide nomenclature: for example, the difference between *mountain-* and *rock- slope deformations* is scale, the former being larger and deeper than the latter.

3. Activity and velocity

As described by Cruden and Varnes (1996), the activity of slope instabilities is not consistent over time and may have different states according to displacement rates and post-failure elapsed time. Therefore, landslide activity can be defined as *active*, *reactivated*, *suspended*, *dormant*, and *stabilized* states (Figure 1.4).

On the other hand, the successive slope movement stages can as well be classified as *pre-failure*, *onset of failure*, *post-failure* and *reactivation* states (Vaunat et al. 1994; Leroueil et al. 1996). In this case, the introduced concept of *mass failure* is defined as the most significant movement episode of in the landslide history, mainly involving the formation of a fully developed discrete or diffuse rupture surface (Leroueil et al. 1996; Hungr et al. 2014).

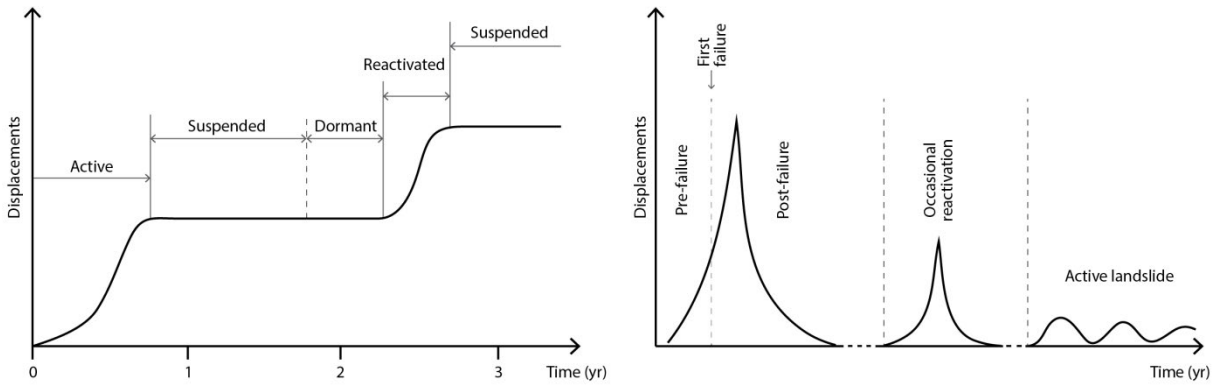


Figure 1.4: (Left) Landslide activity states according to Cruden and Varnes (1996). (Right) Slope movement stages according to Leroueil et al. (1996).

Moreover, typical landslide velocities can extremely vary for most cases. However, slope displacement rates can be implicit for some landslide types, such as rock/ice falls that are extremely rapid or solifluxions extremely slow (Hungr et al. 2014). Nevertheless, they can be defined according to the following velocity classes (Cruden and Varnes 1996): *extremely slow, very slow, slow, moderate, rapid, very rapid* and *extremely rapid* (Table 1.2).

Table 1.2: Landslide velocity classes according to Cruden and Varnes (1996).

	Extremely slow	Very slow	Slow	Moderate	Rapid	Very rapid	Extremely rapid
Velocity thresholds (mm/s)	$5 \cdot 10^{-7}$	$5 \cdot 10^{-5}$	$5 \cdot 10^{-3}$	$5 \cdot 10^{-1}$	$5 \cdot 10^1$	$5 \cdot 10^3$	
Typical velocities	1 mm/yr	16 mm/yr	1.6 m/yr	13 m/month	1.8 m/hour	3 m/min	5 m/sec
Human responses	Nil	Maintenance	Maintenance	Evacuation	Evacuation	Nil	Nil

1.1.2 Destabilization and triggering processes

Slope stability conditions are function of a sum of *inherent predisposing factors*, or *internal parameters*, as well as *external aggravating and triggering factors* (Terzaghi 1950; Varnes 1978; Selbi 1982; Záruba and Mencl 1982; Vaunat et al. 1994; Jaboyedoff and Derron 2005a; Corominas et al. 2014). All these factors have influences on at least one these four instability-leading physical processes identified by Terzaghi (1950): *weight of slope-forming material*, the *transported material*, *water conditions* and *high frequency vibration occurrences*.

1. Predisposing internal parameters

As an example, rock-mass stability conditions are controlled by the following inter-dependant internal parameters (Figure 1.5):

- *Topography*: slope height, angle, aspect, etc.
- *Geology*: lithology, grain-size distribution, strength, cohesion, plasticity, weathering, etc.
- *Rock-mass fracturing*: joint orientations, persistence, spacing, roughness, schistosity, etc.
- *Hydrogeology*: water table levels, material permeability, joints conductivity, etc.

According to landslide types, other internal parameters may affect slope stabilities as well, such as soil thickness for shallow planar soil slides (Nicolet et al. 2013) or minimum contributing area for debris flows (Rickenmann and Zimmermann 1993; Heinimann 1998; Horton et al. 2013).

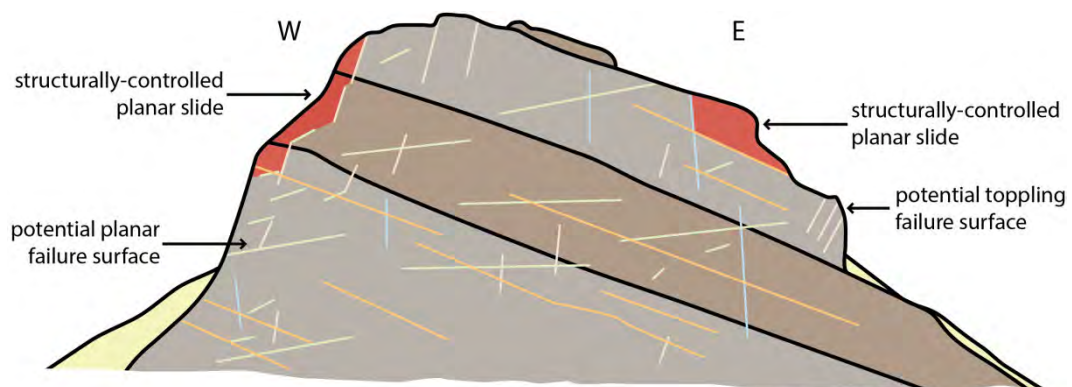


Figure 1.5: Illustration of rock-mass fracturing influences on rock-mass stability. Westside slopes: potential translational planar slides along light green joints. Eastside slopes: potential rock topple developed on light yellow joints and translational planar slides along yellow bedding planes (modified after Eisbacher and Clague 1984).

2. External destabilizing and triggering factors

In addition, the following external factors can also aggravate stability condition and trigger rock-mass failure, such as:

- *Gravity*
- *Meteorological conditions*: rainfall rates and soil saturation, freeze-thaw cycles, etc.
- *Seismicity and active tectonics*: close active faults, earthquakes, etc.
- *Anthropogenic activities* (as developed later in Section 1).

3. Destabilization vs triggering

Finally, the temporal limit between destabilization and triggering can sometime be hazy. Nevertheless, a distinction can be done to discriminate both processes (Michoud et al. 2011a). On the one hand, slope destabilization processes act on a relatively long period of time with a progressive decrease of the safety factors and during which local confined movements are possible. On the other hand, slope triggering occurs in a very short period of time during which the whole instable area fails.

1.2 Landslide risk management

Landslides, involving a wide range of processes, extents and velocities worldwide (Korup 2012), directly and indirectly affect human lives and activities (Schuster 1996; Kjekstad and Highland 2009; Geertseman et al. 2009). As an example, about 3.5 million people in Europe are nowadays threatened by slope instabilities (Jaedicke et al. 2010). Moreover, anthropogenic activities can degrade slope stability conditions (cf. Section 1), increasing by definition risks where infrastructures and people are present (Figure 1.6).



Figure 1.6: In Namsos, May 2009, a huge soft soil slide occurred just after blasting operations for road. Ten houses were destroyed but fortunately without making any fatality (pictures: courtesy of NGU and NGI).

Therefore, authorities in charge of landslide management have to handle procedures for quantitative risk assessments (Einstein 1988; Wu et al. 1996; Corominas et al. 2005a and 2014; Fell et al. 2005; Bründl et al. 2009; Clague and Roberts 2012; Jakob and Holm 2012). But all these procedures usually require as complete information as possible about spatial coverage, activity stages and velocities of considered instability processes.

1.2.1 Susceptibility mapping

From country to county scales, landslide inventory mapping aims to detect existing active and dormant instabilities. Inventories are classically based on visual recognition of mean landslide

morpho-structural features on aerial photos and topographic maps (Rib and Liang 1978; Záruba and Mencil 1982; Varnes 1984; Hutchinson 1995), such as non-vegetated scree deposits for active rockfall areas or clear fracture patterns in rotational slide crones (Figure 1.7).

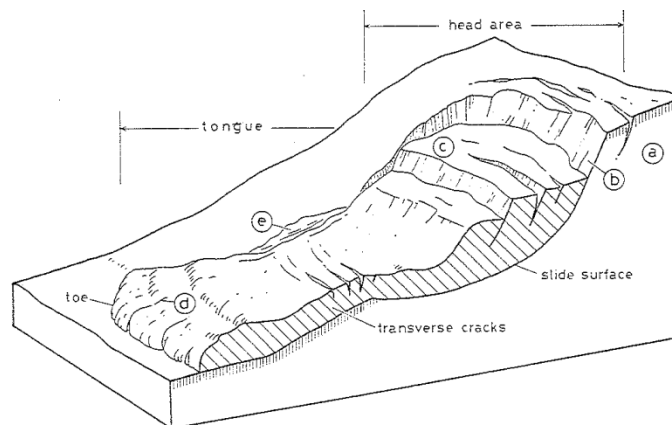


Figure 1.7: rotational slide morpho-structural features: a- lunar cracks, b- head scarp, c- transverse cracks, d- radial cracks, e- lateral ridges (in Záruba and Mencil 1982, modified after Varnes 1978).

Inventories can also be completed by landslides susceptibility mapping, as developed in Section 5. It indeed aims to detect the areas potentially or really exposed to natural hazards, without quantifying their intensities and frequencies (Lateltin et al. 1997; Guzzetti et al. 2012; Jaboyedoff et al. 2012b).

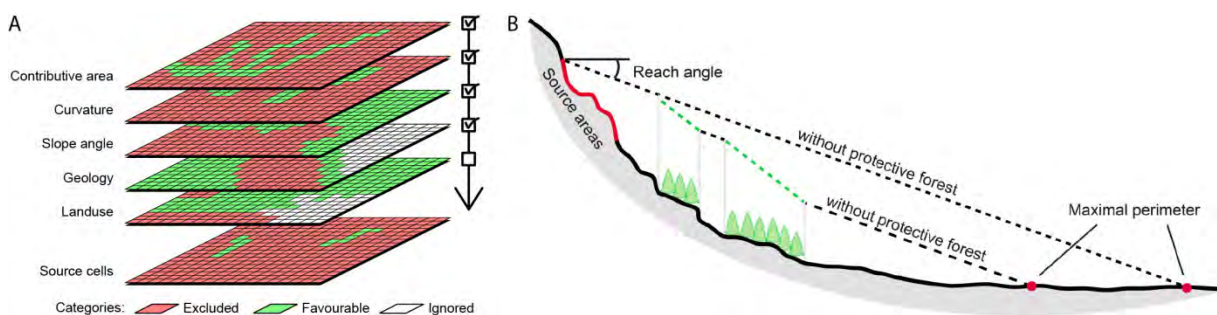


Figure 1.8: (A) Multi-criteria intersection approach, illustrated for debris flow source areas (after Horton et al. 2013). (B) Reach angle approach, illustrated for rockfalls with and without protective forests.

First, potential landslide source areas can be identified by spatial intersections of multi failure criteria. As examples, structural settings, slope angles, lithologies or range to faults criteria can be considered for rock fall susceptibilities (e.g. Hoek and Bray, 1981; Keefer 1984; Pierson et al. 1990; Jaboyedoff et al. 1999; Baillifard et al. 2003), while debris-flows would mainly investigate lands-uses, watershed extents or slope curvatures and angles (Figure 1.8A, after Takahashi 1981; Rickenmann and Zimmermann 1993; Delmaco et al. 2003; Horton et al. 2013). Then, potential maximal runout areas can be assessed thanks to pure mechanical process-based models (Dorren 2003a; Rickenmann 2005; Mangeney et al. 2007; Hungr and McDougall 2009). But such models require numerous input parameters describing natural settings (e.g. Crosta et al. 2004; Iovine et al. 2005) that should be

mapped; they would thus be difficult and time consuming to apply at regional scales. On the contrary, other empiric relations, such as the reach angle (Heim 1932), are optimized for wide assessments with few calibrations; they are frequently applied to rockfalls (Figure 1.8C after Heim 1932; Scheidegger 1973; Evans and Hungr 1993; Corominas et al. 1996; Dorren et al. 2005), snow avalanches (Voellmy 1955; Perla et al. 1980; Bakkehøi et al. 1983) or debris flows (Iverson et al. 1998; Horton et al. 2013).

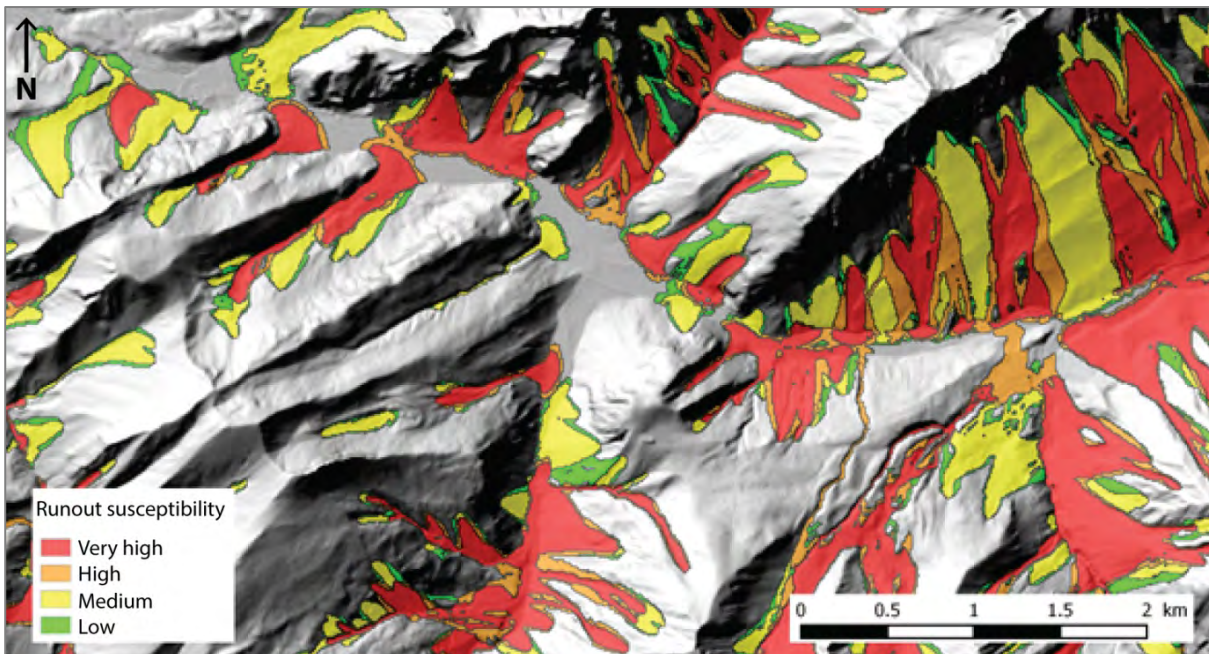


Figure 1.9: Example of debris flow susceptibility maps in the Swiss Alps (Horton and Michoud, unpublished results).

Both landslide susceptibility and inventory mapping are therefore an essential requirement for hazard and risk assessment at territory scales (Corominas et al. 2005a and 2014; Fell et al. 2008), in order to affordably prioritize areas on which detailed investigations will be the most necessary.

1.2.2 Hazard characterization

In some situations, landslides require detailed investigation to evaluate their hazard level; quantitative hazard assessments indeed aim to state on occurrence frequencies of slope failures and phenomena intensities of both existing and potential landslides (Varnes 1984; Wu et al. 1996; Wyllie and Mah 2004; Cornforth 2005; Fell et al. 2008; Corominas et al. 2011 and 2014). At slope-specific scales, specific analyses are thus focused on retrieving information on types of failure mechanisms, involved volumes and areas potentially affected by the landslide path (Crosta et al. 2006).

On the one hand, landslide intensities, such as slope deformations, can be estimated based on involved movement types, extents and volumes assessments (Figure 1.10), as detailed in Hutchinson (1995); it usually requires detailed field mapping of morpho-structural landslide features (Varnes

1984; Hutchinson 1995), and reliable geometrical or physical models that estimate depth and mechanisms of the main failure surfaces (Jaboyedoff and Derron 2015).

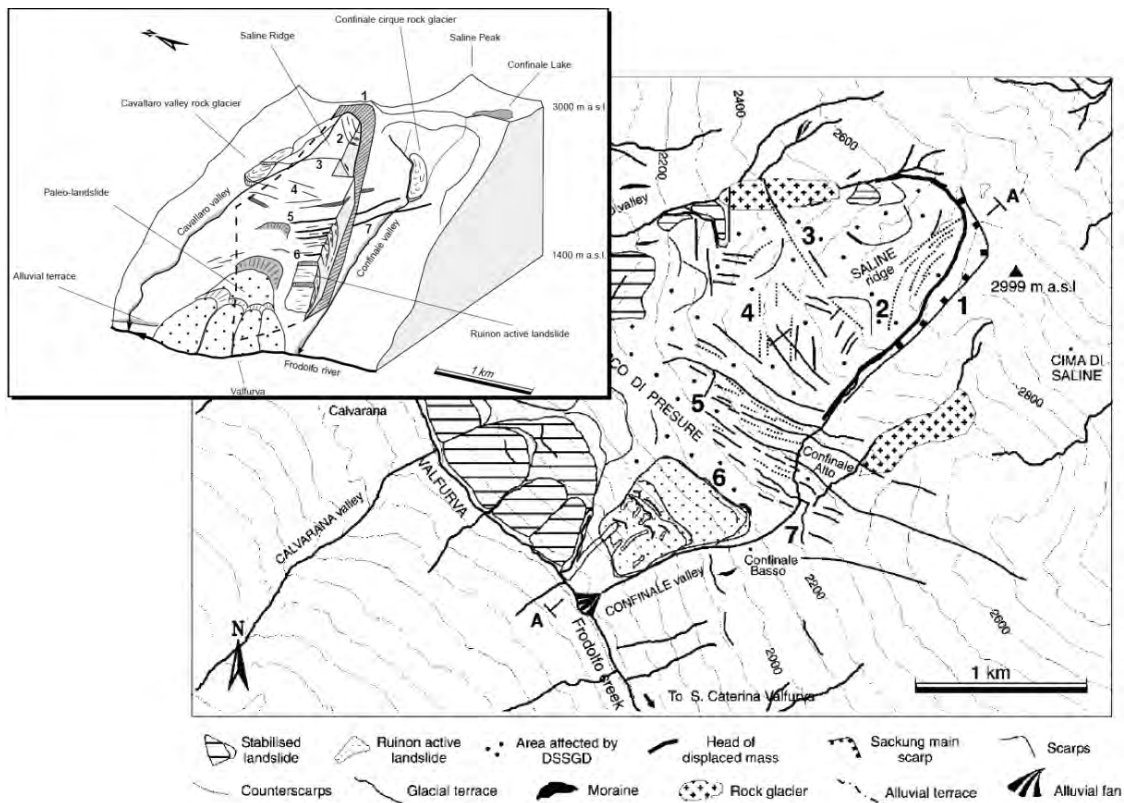


Figure 1.10: Example of detailed field mapping and resulting conceptual model of the Ruinon rock slope deformation (modified after Agliardi et al. 2001).

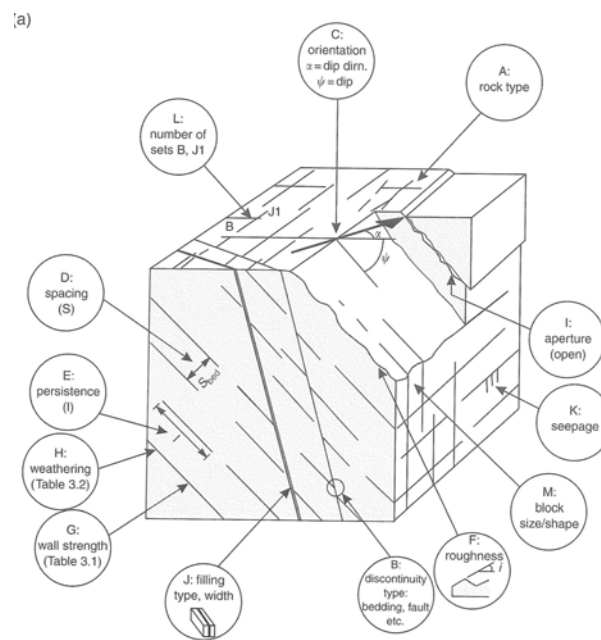


Figure 1.11: List of parameters that have to be estimated on outcropping rocks for rock fall hazard characterization (modified after Wyllie and Mah 2004). At outcrops: rock lithology, strength, weathering, etc. At joints: origin (bedding, schistosity, fold fracturing, etc.), dip, dip direction, spacing, persistence, filling material, water seepage, etc.

On the other hand, landslide occurrence frequency assessments require a consistent geotechnical understanding of involved slope destabilization and triggering factors (Figure 1.11), as well as slope movement rates of active instabilities (Baroň et al. 2012; Eberhardt 2012). In addition, these investigations can be completed by empirical statistic models linking landslide intensities and failure frequencies (Figure 1.12), based on extensive historical records (Hungri et al. 1999; Dussauge et al. 2002, 2003; Guzzetti et al. 2002; Guthries and Evans 2004; Brunetti et al. 2009; Matasci et al. 2015).

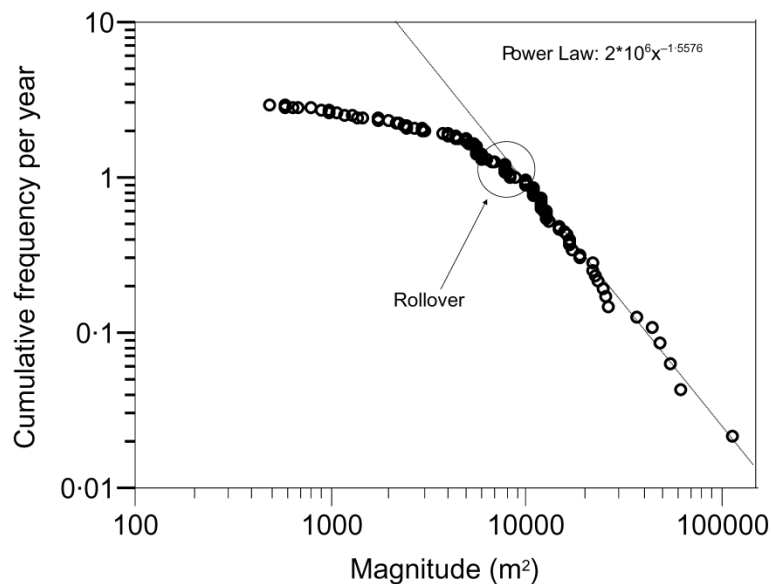


Figure 1.12: Magnitude–frequency and related power law curves for 136 debris flows and slides recorded in a Canadian county (Guthries and Evans 2004). Rollover causes (i.e. small events censoring or physical explanations) are still discussed (Hungri et al. 1999; Hovius et al. 2000; Guzzetti et al. 2002).

1.2.3 Failure forecasting

In order to manage risk imposed by identified slope instabilities, landslide hazards and exposures can be reduced or eliminated by structural countermeasures, as embankments, protective nets, anchors, superficial drainages or even check dams (Piteau and Peckover 1978; Holtz and Schuster 1996; Wyllie and Mah 2004; Cornforth 2005; Vaciago et al. 2011; Volkwein et al. 2011; Lambert and Bourrier 2013). However, these structural remediation works are usually not adapted to landslides involving large volumes and/or complex movement types (Crosta and Agliardi 2003b; Blikra 2012), even if they can seriously threaten people and infrastructures.

As a consequence, non-structural countermeasures have to be planned in order to reduce expositions, especially in term of human lives. It can be achieved thanks to consistent early warning systems in order to alert and evacuate endangered populations in case of imminent active large and complex instability failures (Angeli et al. 2000; Lacasse and Nadim 2009; Baum and Godt 2010; Froese and Moreno 2011; Blikra 2012; Jakob et al. 2012; Michoud et al. 2013; Cloutier et al. 2015).

Therefore, site-specific landslide early warning systems (developed in Section 7) require pertinent models to forecast imminent mass failures and flow initiations. They are based on extensive characterization works related to understanding of involved instability mechanisms: it is indeed necessary to setup pertinent systems that monitor the most significant failure initiation indicators at the most relevant locations (Eberhardt 2012; Michoud et al. 2013; Cloutier et al. 2015). As detailed in Baroň et al. (2012), these indicators are mainly related to mass movements, hydrogeological settings, geophysical properties or external triggers, such as tides or neo-tectonic activities.

Especially adapted to active rock and soil slides, short term forecasting methods of time to slope failure are nowadays mainly based on surface displacement monitoring data (Michoud et al. 2013) and the inverse velocity method (Saito 1969; Voight 1989; Fukuzono 1990; Crosta and Agliardi 2003b; Petley et al. 2005a and b; Rose and Hungr 2007; Federico 2012; Meyer et al. 2012). This empirical method states that time to slope failures is inversely proportional to current strain or displacement rate (Figure 1.13A). Most particularly, it provides steadily realistic predictions during last acceleration phases preceding mass failures (Figure 1.13B, Petley et al. 2005b; Rose and Hungr 2007).

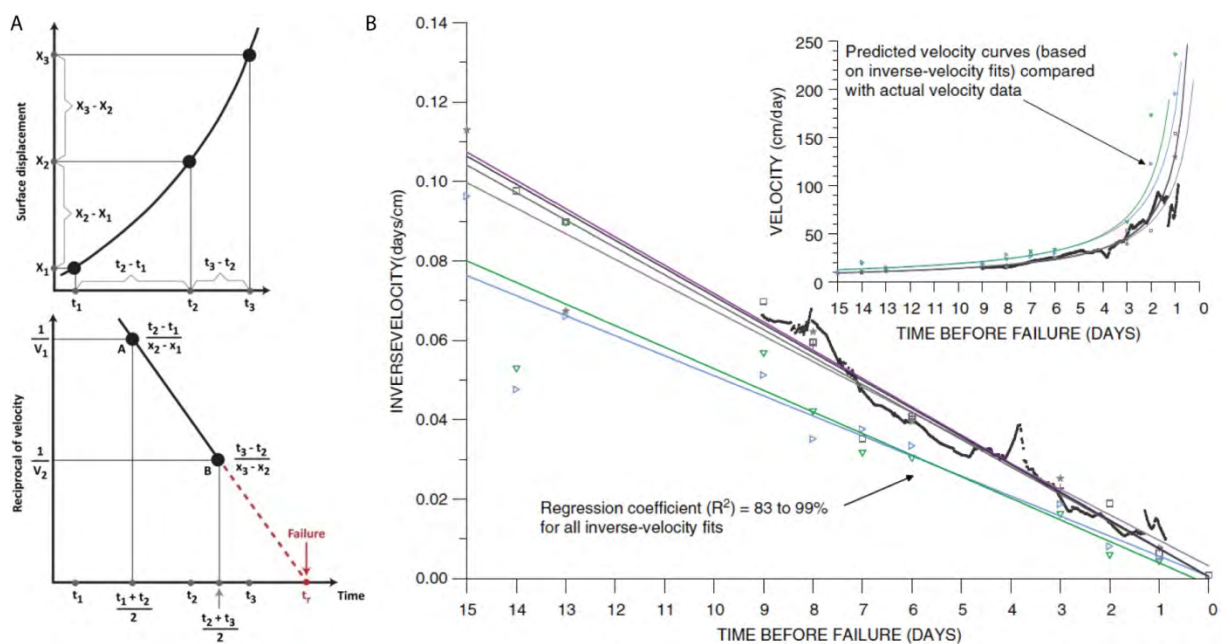


Figure 1.13: (A) Graphical reconstruction of the inverse velocity approach (in Rouyet 2013, modified after Fukuzono 1990). (B) Velocity and inverse velocity plots for five prisms and one wireline extensometer (black line) of a deep-seated toppling deformation monitored in an open mine (Rose and Hungr 2007).

1.3 Remote sensors and related stakes

Facing to the wide variety of studied gravitational processes and related destabilization factors, landslide hazard investigations are supported by an extensive set of remote-sensing and geotechnical methods, as synthetized in Figure 1.14 and illustrated in Figure 1.15.

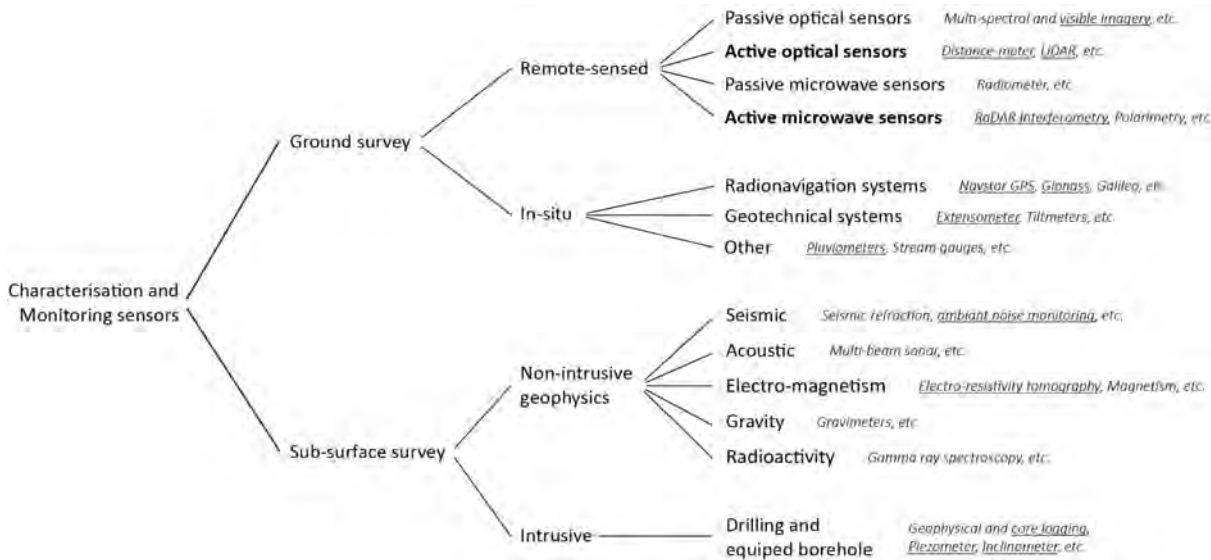


Figure 1.14: Synthesis of currently used landslide characterisation and monitoring sensors. During this PhD thesis and as assistant, all underlined techniques have been deployed and/or interpreted on earthflows and rockslides. (Modified after Michoud et al. 2012a and Rouyet et al. 2013)

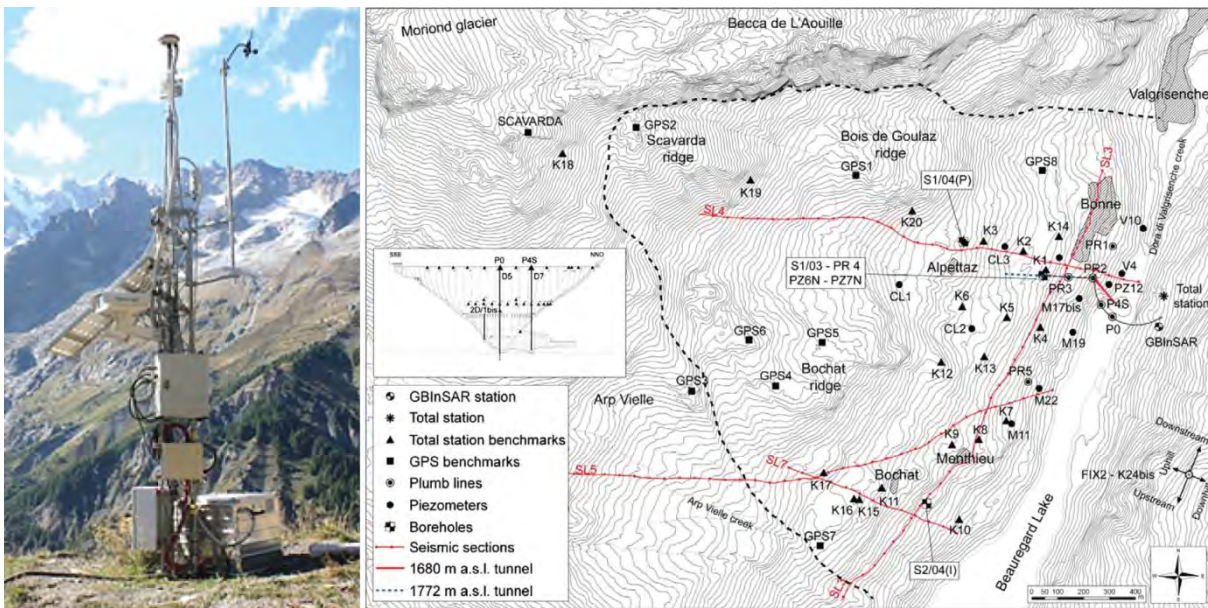


Figure 1.15: (Left) Monitoring station equipped by GNSS antenna, digital camera and weather gauges, implemented at the Mont de la Saxe rockslide. (Right) Monitoring network setup for a dam reservoir-affecting rock slope deformation, based on multiple complementary techniques (Barla et al. 2010).

As a complement to widespread aerial photos covering European countries for decades (Rib and Liang 1978; Záruba and Mencl 1982; Delacourt et al. 2007) and conventional geotechnical monitoring systems (Wilson and Mikkelsen 1978; Dunnicliff 1988; Kovári 1988), advanced remote sensors and performant processing algorithms are indeed under fast development and democratization for the last twenty years (Mantovani et al. 1996; Delacourt et al. 2007; Andrew et al. 2012; Michoud et al. 2012a; Tofani et al. 2013). Therefore, our capabilities to detect, survey and interpret active slope

deformations are particularly improved (cf. Section 2). Furthermore, these remote surveying sensors are nowadays usually integrated in early warning systems as reliable complementary techniques in addition to robust geotechnical instruments (Baroň and Supper 2013; Michoud et al. 2013a; Cloutier et al. 2015).

All sensors have singular capabilities according to different spatio-temporal resolutions, precisions, accuracies, field deployments and costs (Stumpf et al. 2011). Clear purposes must then initially be fixed, in term of landslide types and velocities, extents, stakes and budgets, in order to select the most appropriate and complementary methods according to their specific capabilities (Figure 1.16).

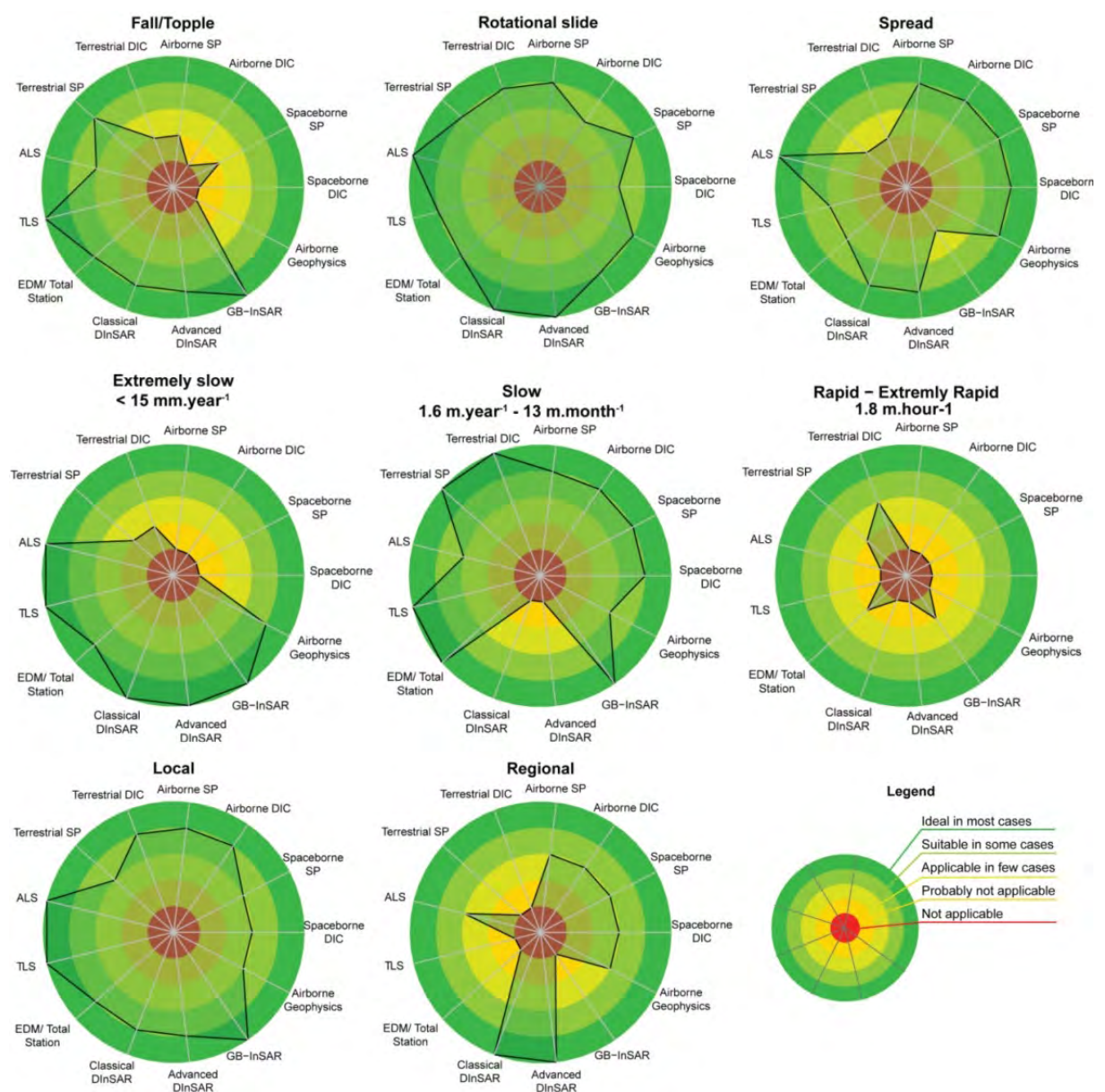


Figure 1.16: Suitability of remote sensing techniques for the monitoring of different landslide mechanisms and velocities at different scales (modified after Stumpf et al. submitted).

Within this context, the thesis aims to investigate current capabilities of active optical and microwave sensors in order to support:

- landslide detection and characterization at regional scales;
- spatial landslide risk assessment over large areas;
- slope instabilities monitoring and modelling at site-specific scales.

1.4 Outline

1.4.1 Governing principles

The first section introduces landslide processes and risk management tools to expose motivations and stakes of this PhD thesis to active remote sensing. The chapter 2 completes the scientific context setting of this research, with the literature review of the major development steps of LiDAR and SAR devices and their related applications in Earth Sciences.

Then Sections 3 to 7 compose the core of the manuscript. This research therefore wants to experiment current active remote sensors capabilities and limitations in various situations and contexts. Indeed, it aims to assess how recent LiDAR and InSAR developments and products can support many successive steps of reliable landslide risk management strategies, as described in Section 1.2:

- First of all, Chapters 3 to 5 are dedicated to landslide managements at regional scales, using mobile LiDAR and spaceborne InSAR acquisitions to first detect and characterize slope instabilities, and then to map rockfall hazard and risk mapping.

Therefore, these three sections aim to identify landslide hotspots over a large territory in order to prioritize sectors on which detailed investigation and mitigation measures will be the most efficient.

- Consequently, Chapters 6 to 7 are dedicated to slope-specific investigations, first illustrating into details an example of rockslide hazard characterization and modelling, and then finally assessing current practices to set pertinent early warning systems when required.

Finally, the last chapters expose the conclusions that sum up the original researches achieved in the thesis and that suggest perspectives for related future studies.

1.4.2 Research sections into details

Section 3 (*Landslides detection and monitoring capability of boat-based Mobile Laser Scanning along Dieppe coastal cliffs, Normandy*) aims to test boat-based mobile LiDAR capabilities in the Channel Sea for landslide detection and monitoring along Dieppe's unstable coastal cliffs, in High Normandy.

Ongoing developments were regularly shared by oral presentations at the 2011 *Optech's Innovative LiDAR Solutions Conference* in Toronto, at the 2013 *EGU General Assembly* in Vienna and the 2014 *Vertical Geology Conference* in Lausanne. Final results were afterwards published in the peer-reviewed journal *Landslides* as a technical note.

Section 4 (*Large slope deformations detection and monitoring along shores of the Potrerillos dam reservoir, Argentina, based on a Small-Baseline InSAR approach*) describes the detection and monitoring from spaceborne Radar interferometry of two deep-seated slope deformations along the Argentina Potrerillos dam reservoir. Outcomes were shared by oral presentation at the 2014 *IAEG Congress* in Torino and were published in the peer-reviewed journal *Landslides* as a research paper.

Section 5 (*Rockfall hazard and risk assessments along roads at a regional scale: example in Swiss Alps*) addresses to rock-mass-failure and runout susceptibilities assessments at regional scale adapting the Slope Angle Distribution and the empirical Fahrböschung in order to quantify rockfall risk along roads. This study was presented at the 2011 *EGU General Assembly* in Vienna and was published in the peer-reviewed journal *Natural Hazards and Earth System Sciences* as a research paper.

Section 6 (*La Perraire rock slope deformation monitoring and modelling by Ground-based InSAR and terrestrial LiDAR integration*) illustrates the necessity to integrate both terrestrial LiDAR and InSAR techniques to map limits, model geometry and kinematic and monitor displacements and strain rates of the 8 to 10 million m³ La Perraire rockslide. Intermediary results were shared by an oral presentation at the 2014 *EGU General Assembly* in Vienna.

Section 7 (*Experiences from site-specific landslide Early Warning Systems*) aims to share practices of existing early warning systems setup for some of the most studied landslides worldwide, in order to gather their valuable experiences and extract recommendations for future systems. Results were shown in the 2012 *EGU General Assembly* in Vienna and were published in the SafeLand deliverable 4.8, as well as in the peer-reviewed journal *Natural Hazards and Earth System Sciences* as a research paper.

2 Active remote sensors

As exposed in Section 1, this PhD thesis is focused on acquisitions, processing and interpretation of active optical and microwave sensors data at regional and local scales.

Optical devices are designed to record electromagnetic radiations with wavelengths ranging from near ultraviolet (from 10^2 nm) to near infrared (to 10^4 nm) while microwave devices are designed to record radiations of the microwave spectrum (wavelengths from about 5 mm to 30 cm). Contrary to passive sensors that record electromagnetic signals naturally reflected or emitted by the observed scene (as for standard photos or thermic infra-red imageries), active sensors record electromagnetic waves emitted by them. Therefore, the initial state of the emitted signals in term of amplitude, phase and wavelength is known and can therefore be compared to back scattered recorded wave state.

More specifically, researches developed hereafter are related to acquisitions and applications of LiDAR and InSAR data (cf. annexes B1 and B2). Derron et al. (2011) reviewed the capabilities of such techniques to detect different types of instabilities, to characterize their geometry and structures, to detect and monitor involved yearly extremely slow to slow movements (Figure 1.16), and to contribute to real-time warning systems (Tables 2.1 and 2.2).

Table 2.1: Indicative LiDAR and InSAR sensor specifications (modified after Derron et al. 2011).

	Aerial LiDAR	Terrestrial LiDAR	Spaceborne InSAR	Ground-based InSAR
Spatial data type	XYZ point cloud	XYZ point cloud	Uneven, discontinuous point distribution	Continuous raster
Range	Tens of m to km	3 km max on rock	Up to 800 km	4 km max on rock
Accuracy	Tens of cm in XYZ (30 cm at 1 km range)	cm in XYZ (1 cm at 100 m)	1 mm (line of sight displacement)	1 mm (line of sight displacement)
Spatial resolution or point density	1 – 100 pt / m ²	10 – 10'000 pt / m ²	Pixel size of 1-30 m	Pixel size of dm - m
Time resolution	Days – years	Hours – years	Weeks - months	Minutes – years

In addition, as developed in Sections 6 and 7, these methods can be complementary (Derron et al. 2011; Michoud et al. 2012). Indeed, in one hand, LiDAR sensors are particularly adapted to model infrastructures and topographies with very high point density, even in steep and inaccessible areas, and then to extract to sub-centimetric 3D displacements and volume changes of rock slope deformations over small and large blocks by comparing sequential acquisitions. On the other hand,

InSAR sensors are especially developed to detect and monitor, even continuously for ground-based devices, millimetric ground displacements over entire slopes or very large blocks.

Table 2.2: Indicative LiDAR and InSAR sensor capabilities for landslide investigations (modified after Derron et al. 2011 and Michoud et al. 2012).

	Aerial LiDAR	Terrestrial LiDAR	Spaceborne InSAR	Ground-based InSAR
Main advantage	Topography modelling at large scale with dm resolution in gentle surfaces	Topography modelling with cm resolution in steep slopes	Detection of very large slope instabilities in dry conditions	Continuous monitoring over large blocs at mm precision
Main limitation	Very low point density in forest and steep slopes	Fastidious manual post-processing	Quick loss of coherence and then sparse data	Atmospheric effects along weeks
Instability Detection	Excellent for geomorphologic analysis	--	Good on urban areas; moderate on natural surfaces	--
Geometry and Structure characterization	Good for contouring and structural analysis	Excellent for structural analysis	Contouring of large active instabilities only	Poor because of too low spatial resolution
Movement detection and characterization	Only when archives are available	Very good for some specific conditions	Very good in space and time when data available	High resolution imaging of displacement along LOS (line of sight)
Movement Monitoring	--	Limited to highly risky and accessible location such as mines, quarries and specific instabilities	A posteriori only	Very good when logistically feasible
Real-time warning	--	Under developments, nowadays limited to specific locations such as mines and quarries	--	Good when logistically feasible

2.1 History of LiDAR developments

LiDAR, an acronym of Light Detection And Ranging, is an active optical sensor which allows providing xyz points clouds of the topography with a centimetric to decimetric resolution. The history of LiDAR technologies is linked by definition to LASER developments. Since the mid Fifties, the physicists Charles Townes and Arthur Shawlow were investigating the feasibility and the development of optical MASER (Microwave Amplification by Stimulated Emission of Radiation). Its usual acronym LASER (for Light Amplification by Stimulated Emission of Radiation) was introduced in 1959 (Brooker 2009). Then, Theodore Maiman designed the first instrument which successfully produced in May 1960 a series of pulsed LASER (Hecht 1994). In less than one year, the first LiDAR was created, mainly for military purposes (Brooker 2009). However, those devices were built with semi-conductors that required an environment cooled to 77°K with liquid Nitrogen to operate. After

1970 and Hayashi's, Panish's and Alferov's researches, LASER can be operated at ambient temperatures (Brooker 2009).

Then in the Seventies, LASER technologies became democratized to civilian applications using LASER-based electronic distance-meters (Dallaire 1974), widely used for surveying application in cities, quarries and even tunnels environments (Petrie 1990; Petrie and Toth 2009). At the same time, first aerial LiDAR systems were able to measure the range between the plane and the target (i.e. the Earth surface) calculating the time of flight of the emitted pulse with a precision of 1 m (Miller 1965; Krabill et al. 1984), for altimetry (Sheperd 1965) and bathymetry purposes (Hoge et al. 1980). Indeed, for acquisition ranges longer than 100 m, all LiDAR devices (mobile or terrestrial) are basically based on the time of flight principle (Figure 2.1).

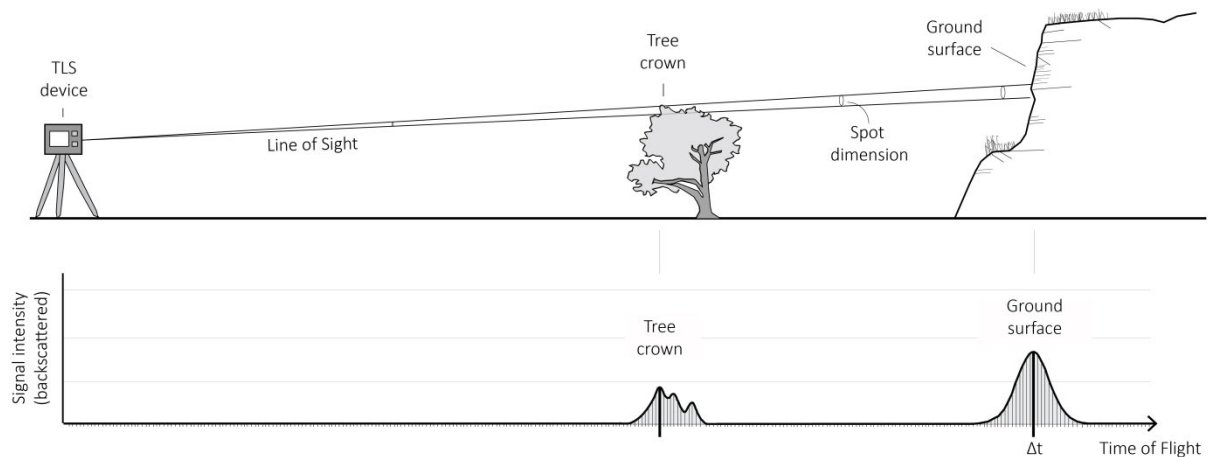


Figure 2.1: Scheme of Time-of-Flight principle applied to a terrestrial LiDAR device (modified after Abellán et al. 2014 and Jaboyedoff et al. accepted).

The sensor emits near-infrared laser pulses (wavelengths of 1'000 - 1'500 nm) on a line of sight perfectly known; this signal is then reflected by the terrain surface, biosphere, infrastructures or air dust. The device records times-of-flight that pulses take to go forth and back are recorded, being transformed into range, according to:

$$r = \frac{1}{2} \cdot c \cdot \Delta t + \varepsilon$$

where r is the range from the sensor to the target in [m], c is the light velocity in air in [m/s], Δt is the ToF in [s] and ε is the sum of environmental and instrumental noises in [m].

By scanning a region of interest with the emission of millions of laser pulses in different directions, a 3D image of the topography can thus be created from the recorded LOS and TOF with decimetric resolutions for aerial devices down to centimetric ones for terrestrial models. But aerial technologies were limited by the poor accuracy of inertial navigation systems (INS) which measure position of planes and direction of the LASER beam. Afterwards, following the general trend in all micro-

electronic domains, LASER devices became eye-safe, lighter, better and cheaper. In addition, in the early Nineties, the deployments of the navigation satellites constellations GPS-NAVSTAR (USA) and GLONASS (URSS) allowed to overcome the limits of former INS. These developments contributed then in late Nineties to considerably improve accuracy and accessibility of ALS data to universities (Wehr and Lohr 1999; Baltsavias 1999a).

By comparing topographies of sequential acquisitions, surface changes can be computed and 3D displacements extracted with a good precision, nowadays down to a sub-centimetric level for meticulous acquisitions. Indeed, first published applications of ALS showed the possibility to map topographical changes of the Greenland ice sheet (Krabill et al. 1995 and 1999), to produce DEM (Digital Elevation Model) (Baltsavias 1999b; Carter et al. 2001) or to create a 3D model of an urban environment (Haala and Brenner 1999). Then mapping and modelling landslide susceptibilities from HRDEM at regional scales became more frequent during the last decade (Chigira et al. 2004; Mc Kean and Roering 2004; Schulz 2004 and 2007; Ardizzone et al. 2007; Van den Eeckhaut et al. 2007; Haneberg et al. 2009; Jaboyedoff et al. 2012b; Michoud et al. 2012b).

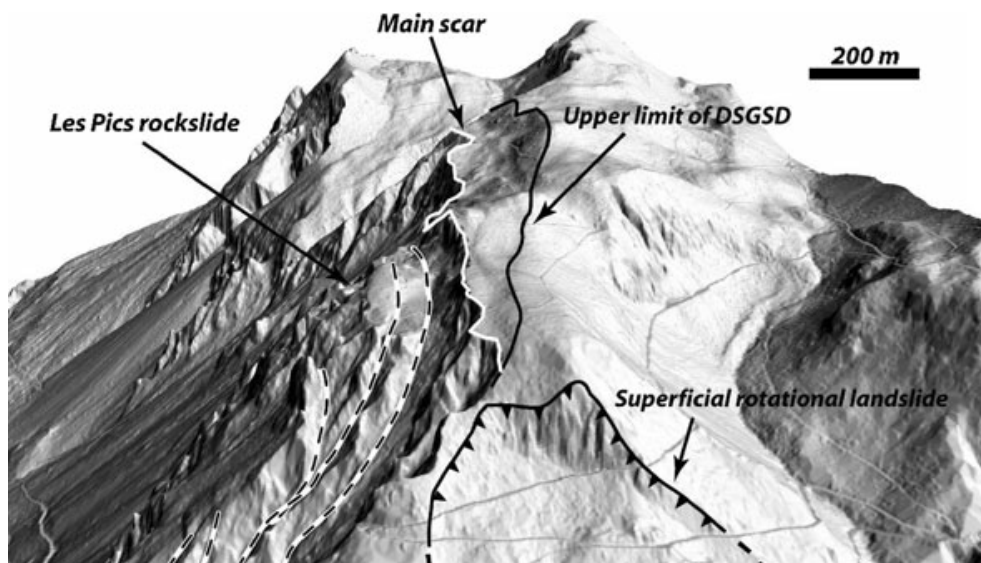


Figure 2.2: Example of Aerial LiDAR –based high resolution digital elevation model hillshading of les Pics instability in the Swiss Alps (in Jaboyedoff et al. 2012b; © DEM swisstopo).

During the last decades, spaceborne applications were deployed as well. As an example, the spaceborne MOLA (Mars Orbiter Laser Altimeter) sensor stayed on the Mars orbit from 1999 to 2001 in order to survey its topography (cf. Figure 2.3) and atmosphere (Smith et al. 2001; Neumann et al. 2003). Thus MOLA modelled the Mars surface with a square kilometre resolution and a vertical accuracy of 1 m (Smith et al. 2001). Regarding the Earth, the GLAS (Geoscience Laser Altimeter System) sensor setup on ICESat satellite was a LASER combination especially designed to monitor different environmental variables, such as polar ice sheet mass balances, vegetation canopy and land elevation with a vertical accuracy of 3 cm (Zwally et al. 2002; Abshire et al. 2005; Schutz et al. 2005).

One of the most relevant topographic products derived from the ICESat mission was the 500 m pixel resolution DEM of Antarctica (DiMarzio 2007). The acquisition of Earth surface topography by a new generation of satellite-based LiDAR, such as ICESat-2, is even planned for 2017 (Moussavi et al. 2014).

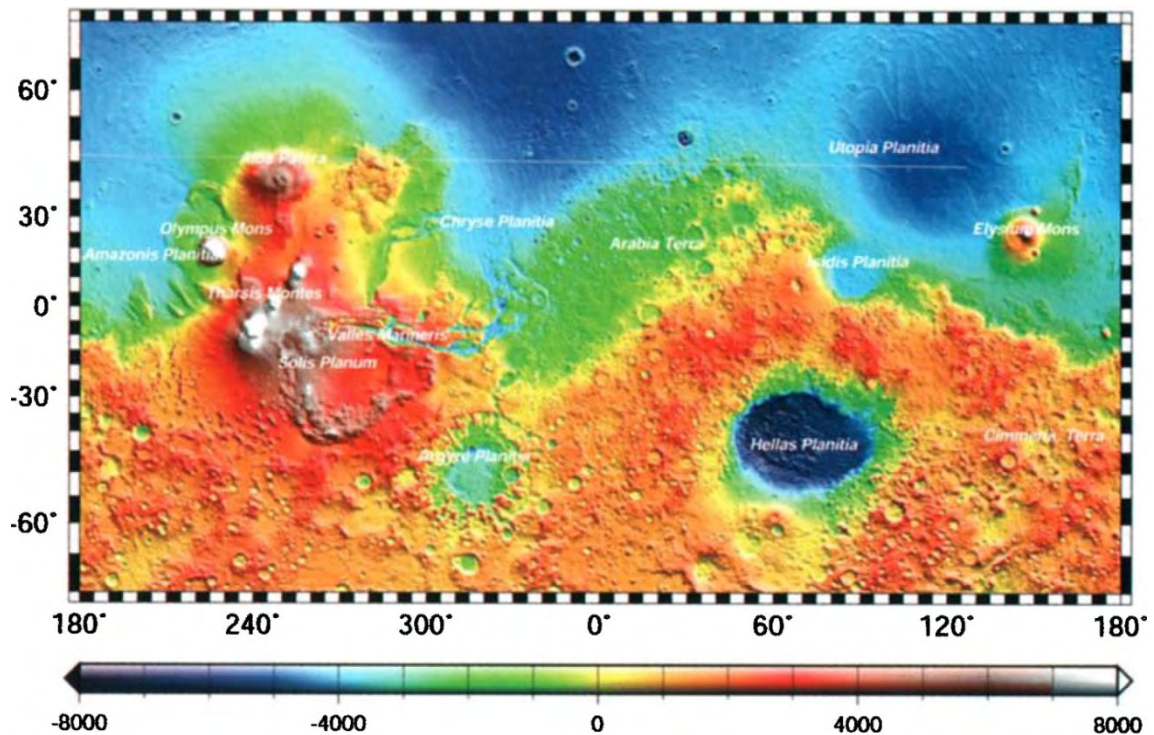


Figure 2.3: Mars topography extracted from the MOLA mission, ranging from -8'000 m to +8'000 m. Pixel size is about $1 \times 2 \text{ km}^2$ at the equator and 1° on Mars is about 59 km. (Modified after Smith et al. 2001)

In the meantime, first terrestrial LiDAR were designed and used for archaeological purposes (Beraldin 2000) and forensic applications (Selander 1998). Then, Gordon, Lichti and Stewart succeeded in surveying and modelling urban structures and even in monitoring their deformations using a terrestrial LiDAR (Gordon et al. 2001; Lichti et al. 2002). Since 2002, geological applications of TLS data are under fast developments, with e.g. (a) the extraction of rock face discontinuity orientation and roughness (Slob et al. 2002; Fardin et al. 2004; Feng and Röschoff 2004; Jaboyedoff et al. 2007; Sturzenegger et al. 2007; Lato et al. 2009; Gigli and Casagli 2011; Figure 2.5), (b) the monitoring of volcanic activities (Hunter et al. 2003), (c) the litho-stratigraphic modelling (Bellian et al. 2005; Buckley et al. 2008; Kurz et al. 2008), (d) the rockfall detection (Rosser et al. 2005 and 2007; Abellán et al. 2006 and 2010; Figure 2.4), (e) or the landslide monitoring (Teza et al. 2007; Oppikofer et al. 2008).

Nowadays, according to general trends in micro-electronic domains, better lenses and image capture chipsets, lighter electronic components and efficient stabilization processes are continuously released, still improving LiDAR capabilities in terms of maximal acquisition ranges, point density and accuracy (Jaboyedoff et al. 2009a). In addition, algorithms and processing methods are always under

developments. As an example, recent researches aim to semi-automatically classify and map geological units from back-scattered signal amplitudes or hyperspectral image integration (Kurtz et al. 2011; Buckley et al. 2013; Matasci et al. 2014; Figure 2.5), and aim as well to sequentially characterize in space and time of surface changes, displacements and strain rates within complex landslide masses (Aryal et al. 2012 and 2015; Carrea et al. 2012; Nissen et al. 2012 and 2014; Travelletti et al. 2014; Royán et al. 2015).

To go into details, a description of LiDAR principles written for the Encyclopedia Natural Hazards (Taylor & Francis editions) is available in annex B2. In addition, Jaboyedoff et al. (2012a) and Abellán et al. (2014) provide a complete review of LiDAR applications in Earth sciences and natural hazards.

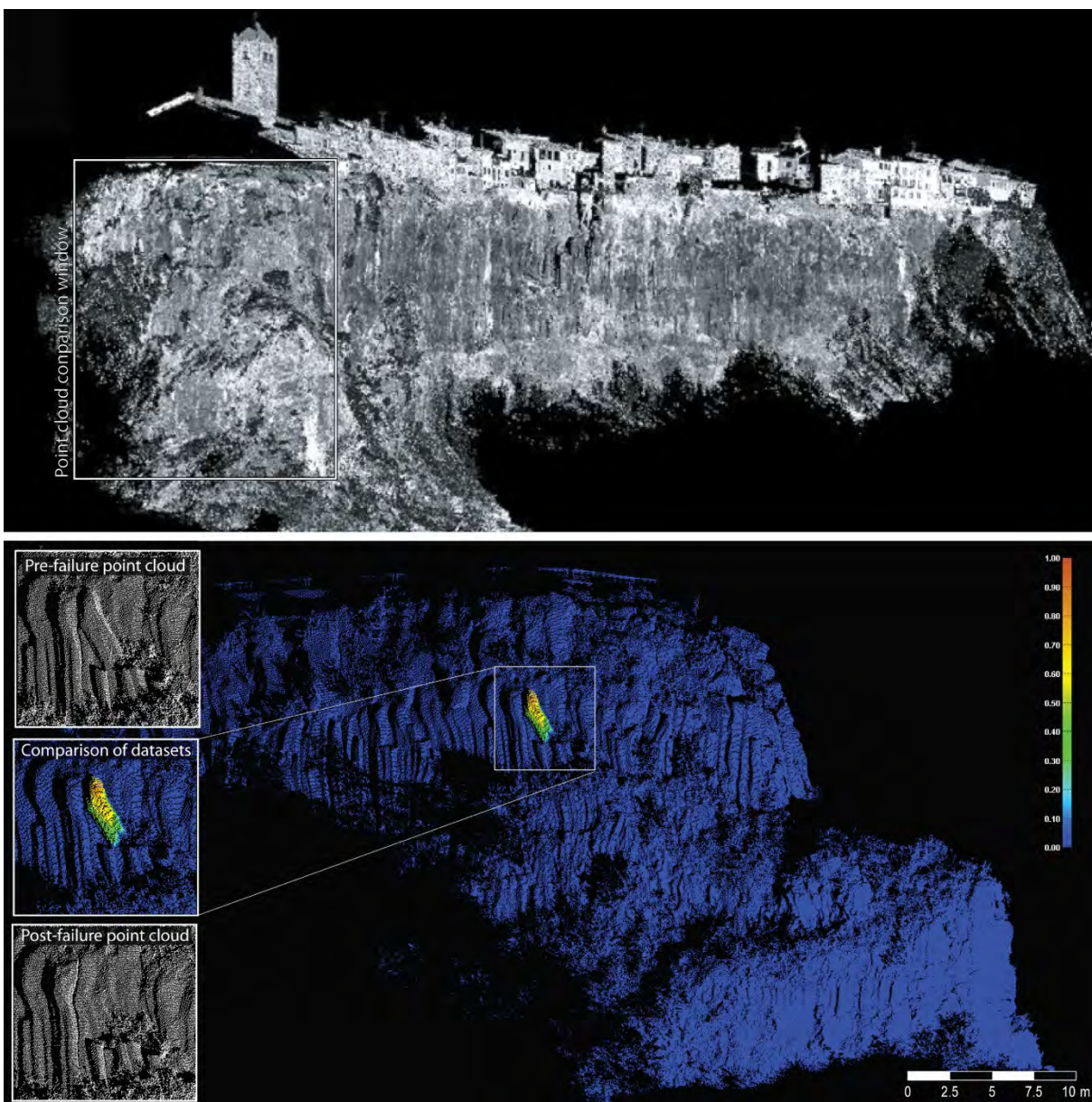


Figure 2.4: Rockfall detection by sequential dataset comparison, highlighting a collapse of a single basaltic column; pre- and post-failure point clouds are visible on the left (modified after Abellán et al. 2011).

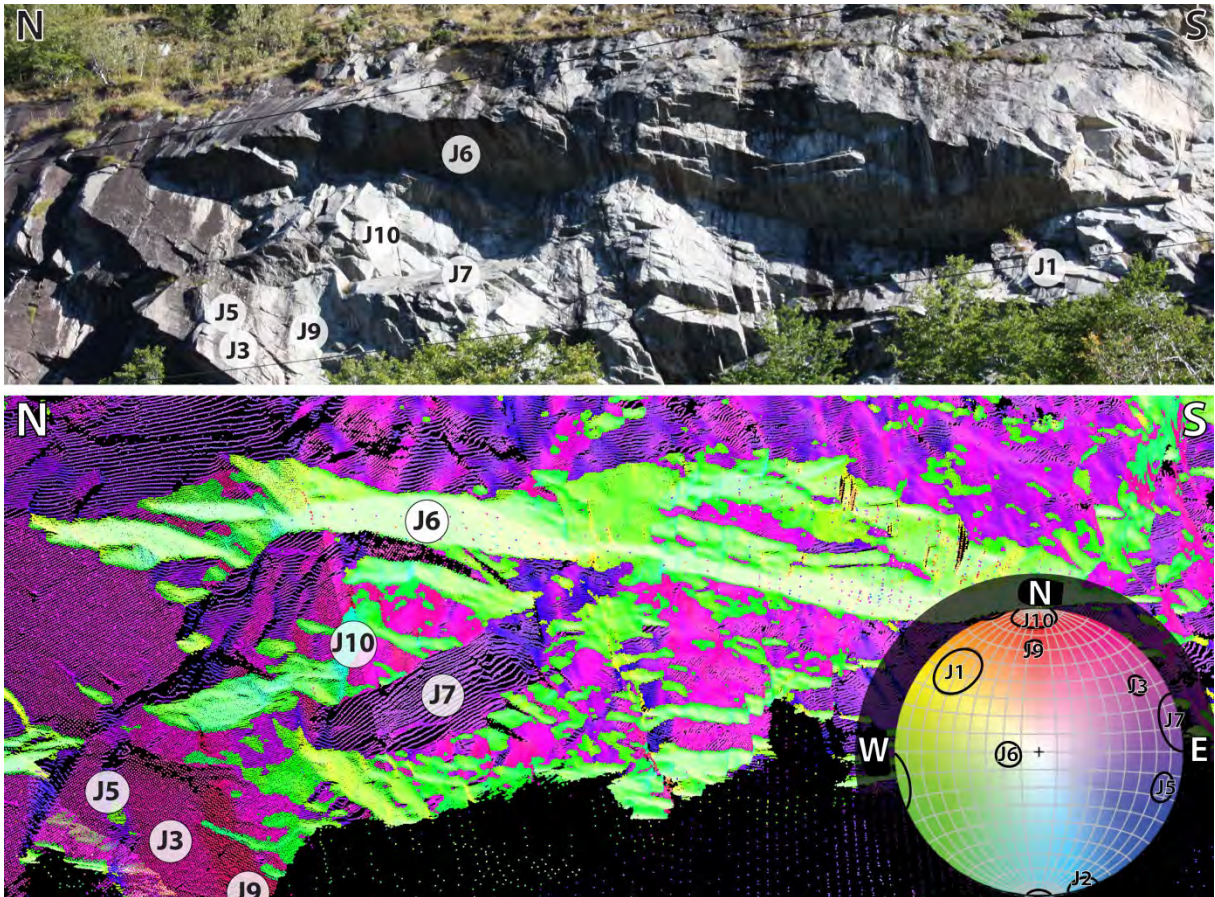


Figure 2.5: Remote structural analysis identifying on terrestrial LiDAR points cloud the orientations of outcropping planar discontinuities (after Michoud et al. 2011b).

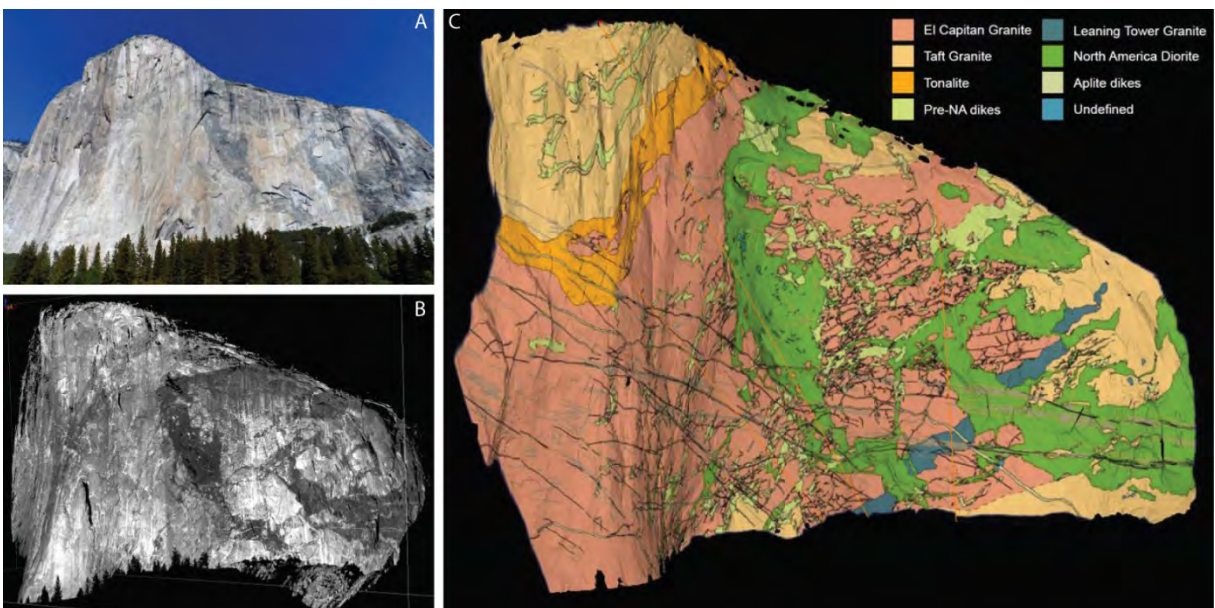


Figure 2.6: (A) El Capitan south-eastern face, 900 m high, Yosemite National Park. (B) Related terrestrial LiDAR point cloud with return signal intensity strength. (C) Vertical geological mapping based on high resolution photo (A) draped on TLS points cloud (B). (Modified after Matasci et al. 2014).

2.2 History of InSAR developments

InSAR is the acronym of Interferometric Synthetic Aperture RaDAR, RaDAR stating for Radio Detection And Ranging. Investigated since the beginning of the 20th century, active microwave (RaDAR) sensors have been developed during the 1940's and the World War II to remotely detect moving military targets. As explained in details in Woodhouse (2006), the main principle settles on the fact that a transmitting antenna emits an electromagnetic wave with fixed millimetric to decimetric wavelength, amplitude and phase. Then, the receiving antenna records the two-way travel time, the amplitude and the phase of the backscattered pulsed wave. Because the Radio wave has interacted with its environment and with the surface that reflected it, the recorded data can be processed to extract physical properties of the target (moisture, roughness, lithology, etc.) and to estimate its range. Compared to other optical or near infrared sensors, Radar sensors can be used night or day and are much less influenced by atmospheric conditions than optical sensors (Preissner 1978; Woodhouse 2006).

The development of Synthetic Aperture Radar (SAR) techniques (Wiley 1954) allowed to simulate large antennas, drastically increasing image resolutions. As an example, spaceborne SAR sensors nowadays acquire Earth images with a ground resolution of 30 m (e.g. Envisat platform) down to 1 m for the last generation of devices (e.g. TerraSAR-X platform). But the first civilian Radar imaging project at large scale was setup in 1967 to map from airplane a 20'000 km² Panama's province that has never been photographed before due to a perpetual and dense fog (Lillesand et al. 2008). Afterward, Shapiro published in 1972 the first application of the interferometric SAR (InSAR) techniques, mapping the Moon's topography using Radar sensors setup on the Earth's surface. Indeed, the topography of the region can be extracted by comparing the phase decay of back-scattered signals of two SAR images of a same area acquired from two different points of view and/or at a different time.

Later, Massonnet published in 1985 a technical note on the possibility to map temporal changes of the Earth's surface, "removing the signal of the topography" inside interferometric scenes. He established the concept of Differential InSAR (DInSAR) to detect and quantify millimetric ground displacements on decametric pixels at regional scales, since mathematically:

$$\Delta d_p = \frac{\lambda}{4\pi} \times (\varphi_t - \varphi_{t_{topo}} - \varphi_\varepsilon)$$

where Δd_p is the projection on the sensor line of sight of the ground surface displacements between two sequential acquisitions (cf. Figure 2.7), λ the sensor wavelength, φ_t the total interferometry between these acquisitions (back-scattered wave phase shift Φ_2 recorded at times t_2 minus t_1 's one Φ_1), $\varphi_{t_{topo}}$ the theoretical interferometric response imputed to the topography at time t_1 according to sensors configuration and φ_ε the other environmental and instrumental contributions that are

filtered (such as atmospheric layers, Earth flattening, etc.). In addition, small baselines and short time interval between SAR acquisitions enhance DInSAR movement detection capabilities.

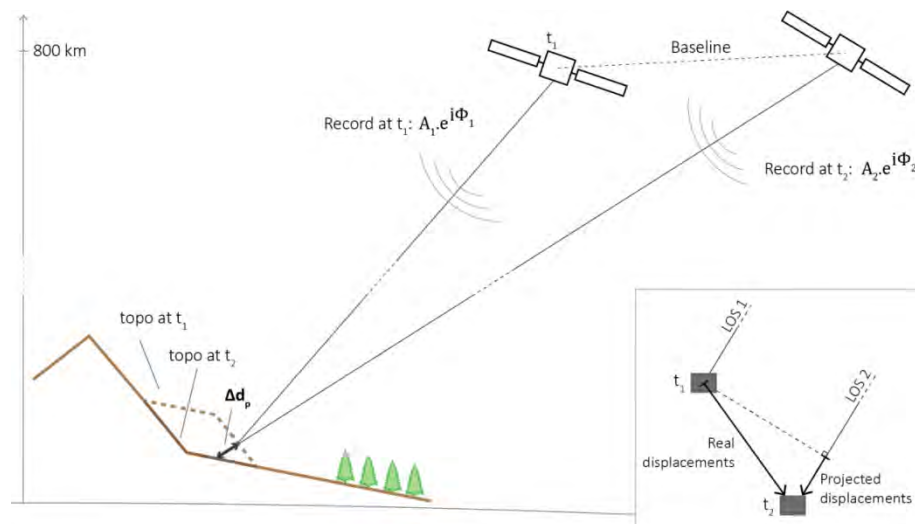


Figure 2.7: Unscaled scheme of differential SAR interferometry geometry applied to spaceborne acquisitions. Signals are recorded in a complex number where A is the back scattered amplitude and Φ the phase shift. In the lower right corner is illustrated how records of real displacements are actually projected on the LOS.

DInSAR has first been used in California to monitor swelling clays subsidence (Gabriel et al. 1989) and to get co- and post-seismic field displacements induced by the 1992 Lander's earthquake (Massonnet et al. 1993 and 1996; Zebker et al. 1994). Other natural applications of ground surface monitoring were then developed in parallel, such as in glaciology to survey ice sheet motion in Antarctica (Goldstein et al. 1993) and in volcanology to monitor deflations and inflations corresponding to the magma chamber's changes (Massonnet et al. 1995; Sigmundsson et al. 1997; Lanari et al. 1998; Lu et al. 1998; Francis and Rothery 2000).

Regarding specifically natural hazards and gravitational deformations, two studies surveying temporal displacements of the La Clapière landslide were published in 1996 (Fruneau and Apache 1996; Carnec et al. 1996), soon followed by other worldwide studies (e.g. Kimura and Yamagushi 2000). Afterwards, Squarzoni et al. (2003) were able to monitor the movements of the La Valette mudslide during nine years and Singhroy and Molch (2004) used DInSAR techniques to survey potential precursory deformations prior to a major rock slope collapse.

Since the beginning of the 2000's, new post-processing methods have been developed to overcome DInSAR limitations and noises (Zebker et al. 1997; Massonnet and Feigl 1998; Hanssen 2001) induced by comparing only two Radar images. In fact, the multi-temporal repeat-pass Radar interferometry (Advanced DInSAR) techniques, such as the Permanent Scatterers™ (Ferretti et al. 2000 and 2001), the Small Baseline Algorithm Subset (Berardino et al. 2002) or the SqueeSAR™ (Ferretti et al. 2011), use now a large multi-stack of SAR images in order to increase the signal-to-noise ratio, providing

much more accurate and reliable results to map (Figure 2.8) and monitor natural hazards (Berardino et al. 2003; Colesanti and Wasowski 2006; Herrera et al. 2010 and 2011; Lauknes et al. 2011).

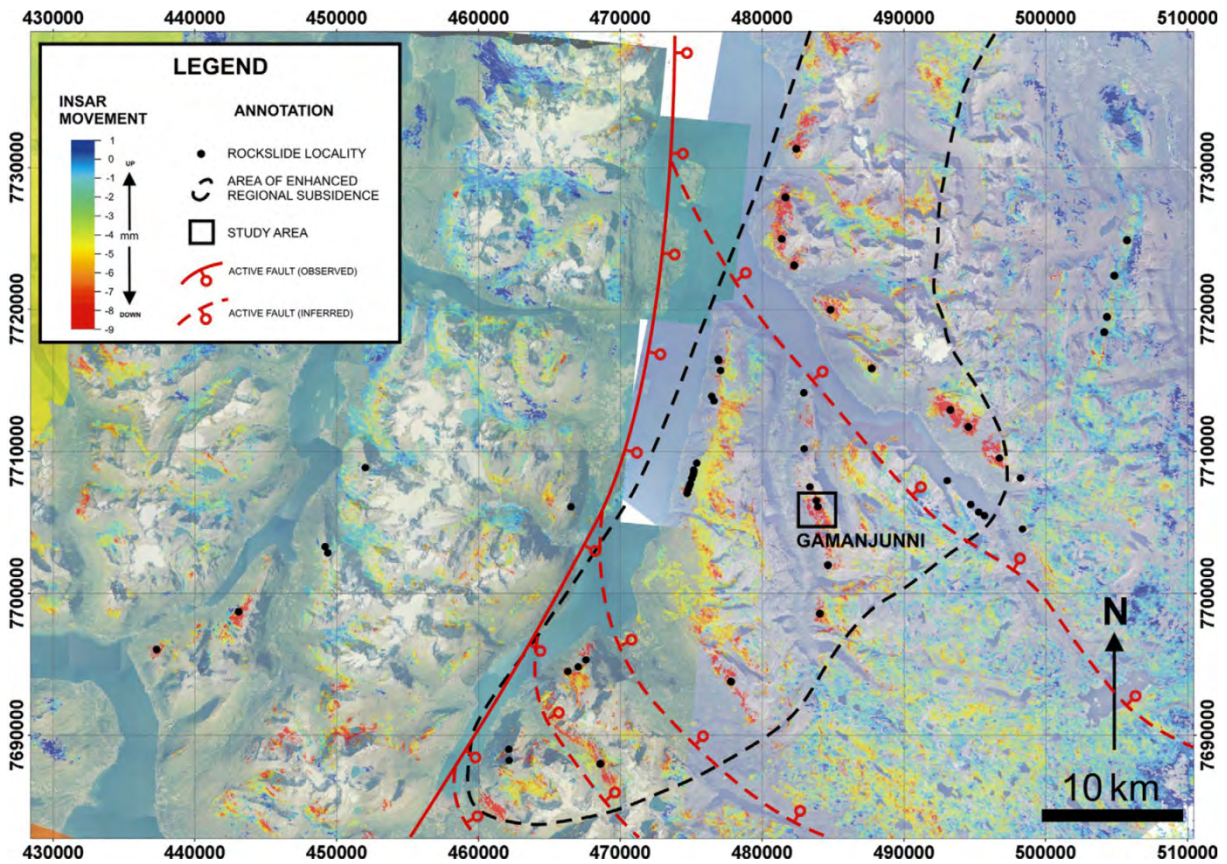


Figure 2.8: Regional detection of rock slope displacements over the last ten years in the Troms county, Northern Norway, based on the advanced Radar interferometry algorithm SBAS (in Henderson et al. 2011).

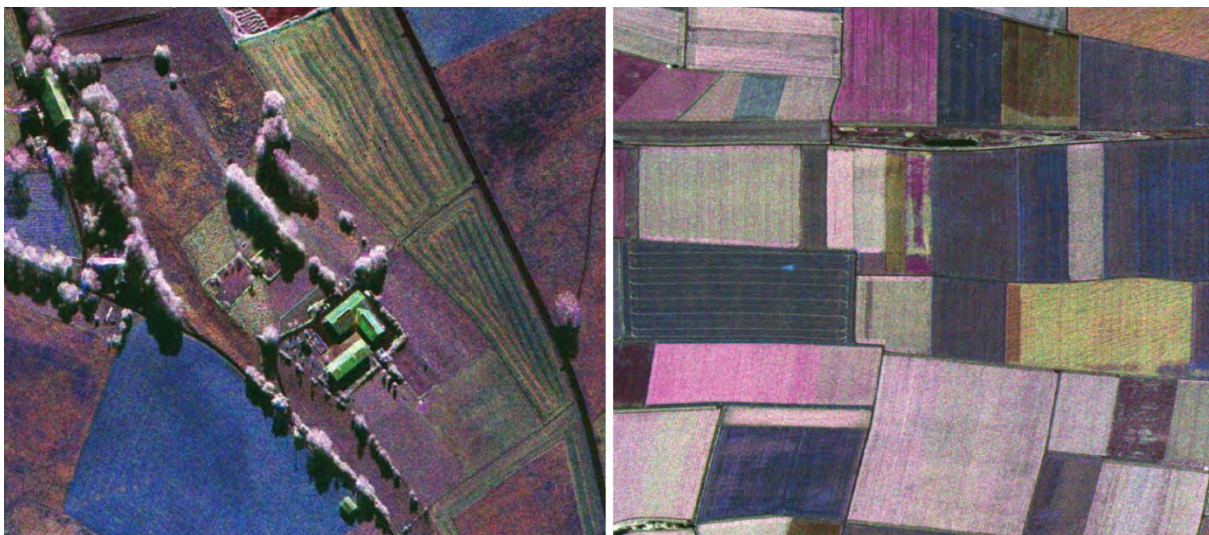


Figure 2.9: Amplitude images of the aerial F-SAR sensor, with a spatial resolution of 0.4 m (modified after Horn et al. 2011).

During the last decade, some marginal researches are achieved in order to design SAR sensors for airplanes platforms (Horn et al. 2009; Pfitzner et al. 2011), normally limited by too instable

trajectories to ensure reliable acquisitions. Since repeat-pass acquisitions with small baselines at low altitudes will drastically improve pixel resolutions (Figure 2.9) and decrease temporal and geometrical decorrelations (Bamler and Harlt 1998), perspectives are thus promising for high resolution topography modelling and active landslide inventory regional mapping.

Finally, new ground-based portable sensors (GB-InSAR) have been also developed to monitor millimetric ground displacements directly from the Earth's surface, with a very high temporal and spatial resolution (Figure 2.10). Thus, Tarchi et al. (1997, 2003a and 2003b) and then Antonello et al. (2004) demonstrated that the GB-InSAR is well optimized for the continuous monitoring of single suspected mass movements. This technique is currently becoming popular to measure very small displacements on volcanoes (Casagli et al. 2003 and 2008) and landslides (Herrera et al. 2009; Barla et al. 2010; Luzi 2010).

To go further, a valuable description of InSAR principles written for the SafeLand European project (FP7 2009-2012) is available in annex B1, as well as review papers from Massonnet and Feigl (1998), Woodhouse (2006), Ferretti et al. (2007), Caduff et al. (2014) or Monserrat et al. (2014).

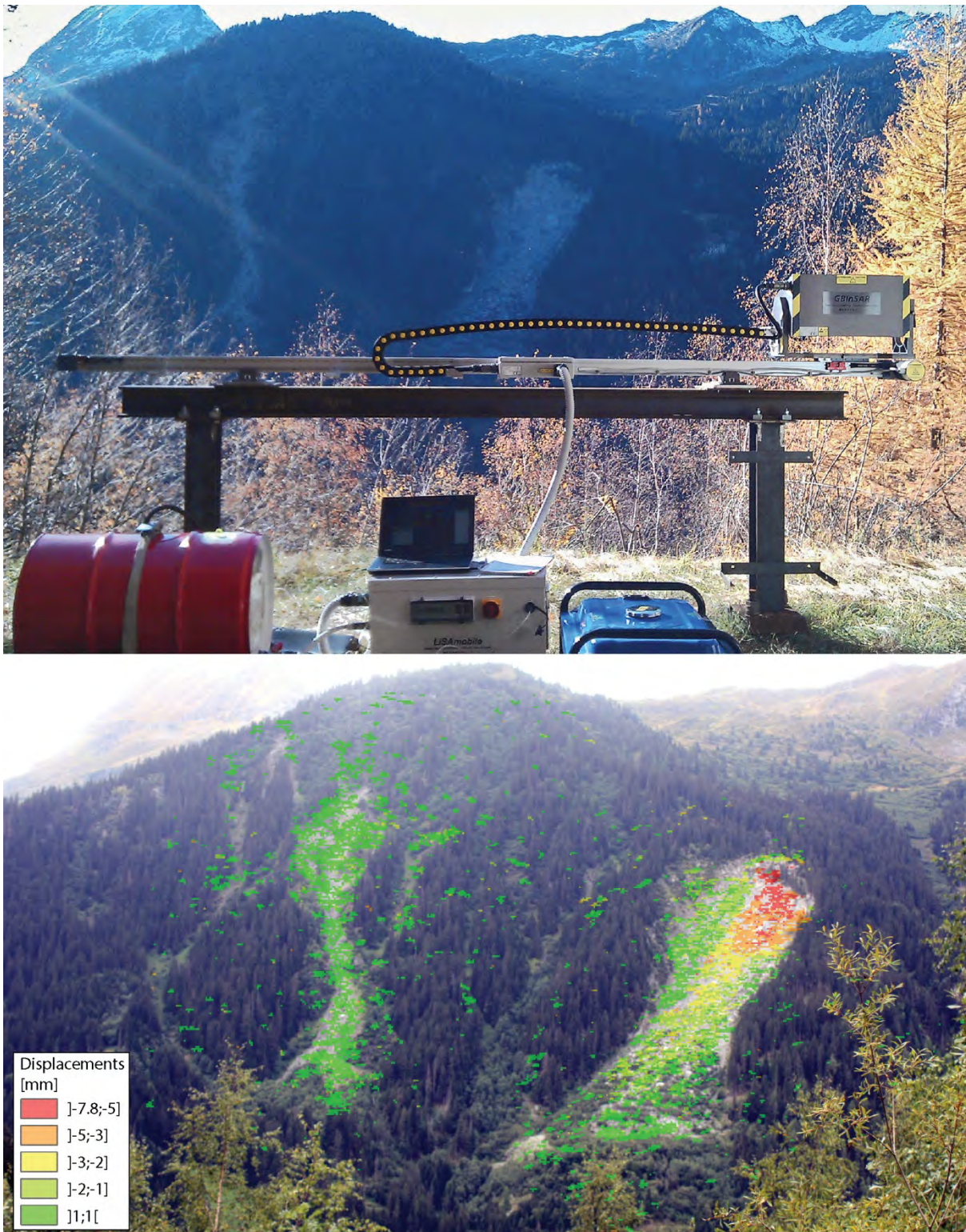


Figure 2.10: GB-InSAR setup and cumulated displacement monitoring at La Barmasse rockslide, measuring movements in the upper scarp up to 7.7 mm in 12 h recorded the 16 September 2011 (modified after Michoud et al. 2013b).

LANDSLIDE REGIONAL HAZARD AND RISK MAPPING

3 Landslides detection and monitoring capability of boat-based Mobile Laser Scanning along Dieppe coastal cliffs, Normandy

After Michoud C, Carrea D, Costa S, Derron MH, Jaboyedoff M, Delacourt C, Maquaire O, Letortu P and Davidson R: Landslide detection and monitoring capability of boat-based mobile laser scanning along Dieppe coastal cliffs, Normandy. *Landslides*, 12, 403–418, 2015.

Abstract

Integrated in a wide research assessing destabilizing and triggering factors to model cliff dynamic along the Dieppe's shoreline in High Normandy, this study aims at testing boat-based mobile LiDAR capabilities by scanning 3D point clouds of the unstable coastal cliffs. Two acquisition campaigns were performed in September 2012 and 2013, scanning (1) 30 km long shoreline and (2) the same test cliffs in different environmental conditions and device settings. The potentials of collected data for 3D modelling, change detection and landslide monitoring were afterward assessed. By scanning during favourable meteorological and marine conditions and close to the coast, mobile LiDAR devices are able to quickly scan long shoreline with median point spacing up to 10 cm. The acquired data are then sufficiently detailed to map geomorphological features smaller than 0.5 m². Furthermore, our capability to detect rockfalls and erosion deposits (> m³) is confirmed, since using the classical approach of computing differences between sequential acquisitions reveals many cliff collapses between Pourville and Quiberville and only sparse changes between Dieppe and Belleville-sur-Mer. These different change rates result from different rockfall susceptibilities. Finally, we also confirmed the capability of the boat-based mobile LiDAR technique to monitor single large changes, characterising the Dieppe landslide geometry with 2 main active scarps, retrogression up to 40 m and about 100'000 m³ of eroded materials.

Keywords: Mobile Laser Scanning, Coastline change detection, Rockfall, Landslide monitoring, High Normandy coastal cliffs.

3.1 Introduction

Laser Scanning and 3D point clouds have changed our perception and interpretation of slope deformations for the last 15 years and are nowadays widely used for landslide monitoring and warning systems (as reviewed by Jaboyedoff et al. 2012a; Baroň and Supper 2013; Michoud et al. 2013a; Stumpf et al. submitted). Terrestrial LiDAR (TLS) allows indeed measuring topography with

very high point density, including inaccessible steep slopes. Three dimensional displacements of rock masses can also be extracted by detecting topographic changes on sequential TLS acquisitions, as reviewed by Abellán et al. (2014); TLS-based rockfall detections were also carried out for detailed investigations on confined coastal cliffs (e.g. in Lim et al. 2005; Rosser et al. 2005 and 2007; Collins and Sitar 2008; Young et al. 2013; Letortu et al. 2014). However, this technique turned out not to be optimized for stability assessments over km long shoreline: accurate (and therefore time consuming) acquisitions along large areas are indeed not likely during short low tide periods and require in addition tedious post-processing to align the numerous scans. Despite being able to scan very large areas in short time, Aerial Laser Scanning devices (ALS) are also not indicated to detect rockfalls on the front of vertical coastal cliffs (Young et al. 2013), since they would not record dense and accurate back-scattered pulses on cliffs due to the high incidence angle between the latter and the laser beam (Baltsavias 1999a; Lichti et al. 2005). Alternatively, Mobile Laser Scanning (MLS) devices (Jaakkola et al. 2008; Kukko et al. 2012; Glennie et al. 2013) can be mounted on boats, setting up the scanner horizontally with a frontal view on shores (Figure 3.1); they have indeed recently demonstrated their capability to map topographic changes along fluvial banks (Alho et al. 2009; Vaaja et al. 2011 and 2013).

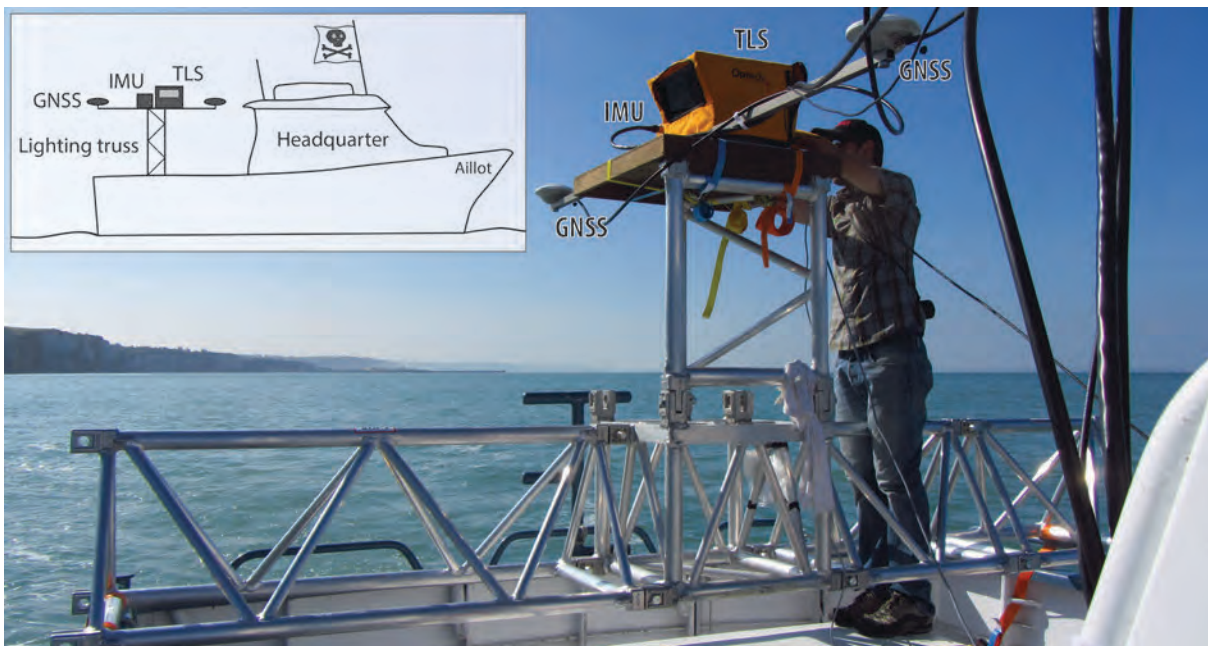


Figure 3.1: MLS setup on the boat L'Aillot. The system is tied up on the lighting truss at the same elevation than the cabin, in order to ensure a good GNSS horizon for the antennas and to avoid splash on the MLS.

A wide research plan intends to assess landslide destabilizing and triggering factors and to model cliff dynamic of the French High-Normandy coasts (Letortu 2013; Letortu et al. 2014). Total length of the High-Normandy cliffs is around 110 km with an average height of 60 m. Within this framework, this detailed study aims at testing MLS capabilities in tossing water of the Channel Sea. The Dieppe cliffs

are mainly formed by sub-horizontal deposits of soft Cretaceous chalk interlayered by thin bands of biogenic flint (Figure 3.2) corresponding to the Western termination of the Paris Basin. Due to their particularly low mechanical strength and being directly hit by oceanic storms (Costa et al. 2004 and 2014; Letortu et al. 2012 and 2014a), the high cliffs are thus destabilized by an intense weathering and sea erosion. Processes involved in rock falls and collapses are therefore regularly observed (e.g. in Costa 1997 and 2014; Duperret et al. 2002; Dewez et al. 2013) and contribute to quick retrogressive cliff processes of about 20 cm/year on average (Costa et al. 2004).



Figure 3.2: Location and illustration of classic morphology of vertical coastal cliffs close to Dieppe, French Normandy.

By acquiring dense 3D point clouds along vertical coastal cliffs and intertidal areas in September 2012, we want indeed to assess (a) the median point spacing for different acquisition conditions and (b) the repeatability of point clouds of the same area acquired several times. In addition, after a second acquisition campaign held in September 2013, we also aim at estimating the MLS capability to assess retreat rates over km long coastal cliffs, based on rockfall events and cliff foot erosion detection and quantification using classic shortest distance comparison approaches. All acronyms used in this note are summarized in Table 1.

3.2 Mobile Laser Scanning principles

A Terrestrial Laser Scanning (TLS) is an active optical sensor which allows providing xyz points clouds of the topography with a high resolution (Beraldin et al. 2000; Gordon et al. 2001). All long range TLS devices use laser pulses and are based on the Time of Flight principle (Vosselman and Maas 2010).

Table 3.1: Table of main acronyms used in chapter 3.

Acronym	Definition
$\alpha \beta \gamma$	Yaw, pitch and roll of the Cardan angles
ALS	Aerial Laser Scanning
Bft	Beaufort scale, describing marine conditions (wind, swell height, etc.)
GAMS	GPS Azimuth Measurement Subsystem™
GIS	Geographic Information System
GNSS	Global Navigation Satellite System
ICP	Iterative Closest Point
IGN	Institut national de l'information géographique et forestière
IMU	Inertial Measurement Unit
INS	Inertial Navigation System
J_n	Point clouds acquired the 20 September 2012
J_n'	Point clouds acquired the 26 September 2013
LiDAR	Light Detection And Ranging
LOS	Line Of Sight
MLS	Mobile Laser Scanning
M_n'	Point clouds acquired the 25 September 2013
SBET	Smoothed Best Estimate of Trajectory
TLS	Terrestrial Laser Scanning
TOF	Time Of Flight
UTM	Universal Transverse Mercator
WGS	World Geodetic System
<i>xyzi</i> file	ASCII text file structured in 4 columns: x, y, z coordinates and signal intensity
<i>xyzid</i> file	ASCII text file structured in 5 columns: as <i>xyzi</i> , plus point to surface difference

The sensor indeed emits a laser pulses on a Line Of Sight (LOS) perfectly known relatively to the device; the direction of the laser is controlled by one or two internal mirrors reflecting the signal and/or motors orienting the device itself. Emitted pulses are back-scattered by the terrain, vegetation, particles as sea spray and air dust, etc.

The Time Of Flight (TOF) that the pulses takes to go forth and back is recorded and is then converted into the range, knowing the light velocity (Eq. 3.1):

$$r = \frac{1}{2} \cdot c \cdot \Delta t \tag{Eq. 3.1}$$

where r is the range from the sensor to the target in [m], c is the light velocity in air in [m/s], and Δt is the ToF in [s].

A 3D image of the topography can thus be created from the recorded LOS and TOF. Now when performing scans from moving platforms such as boats, the directions of emitted pulses is only known relatively to the device, but the position and orientation of the device are changing during the acquisitions, which prevent from having all the points in the same local reference system.

However, by adding to the LiDAR an Inertial Navigation System (INS), composed of 2 Global Navigation Satellite System (GNSS) antennas and an Inertial Measurement Unit (IMU), it is then possible to achieve surveys from a vessel. The IMU indeed records the attitude of the platform on the boat by continuously measuring the Cardan angles (Figure 3.3), i.e. (α) yaw (or heading, azimuth of direction of motion), (β) pitch (back and forth shake) and (γ) roll (left to right shake). The GNSS antennas furthermore localize the instrument and enhance the yaw measurement.

In order to reconstruct the 3D topography, the entire point cloud is then post-processed performing for each single point a rigid body transformation; we can indeed apply to each point a roto-translation matrix to transform coordinates from its LiDAR internal system to a georeferenced system (Tupling and Pierrynowski 1987; Lichti et al. 2002; Oppikofer et al. 2009), according to Eq. 3.2:

$$\begin{pmatrix} p_x \\ p_y \\ p_z \\ 1 \end{pmatrix} = (R + T) \times \begin{pmatrix} l_x \\ l_y \\ l_L \\ 1 \end{pmatrix} \quad \text{Eq. 3.2}$$

with

$$R = R_z(\alpha) \times R_y(\beta) \times R_x(\gamma) \\ = \begin{pmatrix} \cos(\alpha) & -\sin(\alpha) & 0 & 0 \\ \sin(\alpha) & \cos(\alpha) & 0 & 0 \\ 0 & 0 & 1 & 0 \\ 0 & 0 & 0 & 0 \end{pmatrix} \times \begin{pmatrix} \cos(\beta) & 0 & \sin(\beta) & 0 \\ 0 & 1 & 0 & 0 \\ -\sin(\beta) & 0 & \cos(\beta) & 0 \\ 0 & 0 & 0 & 0 \end{pmatrix} \times \begin{pmatrix} 1 & 0 & 0 & 0 \\ 0 & \cos(\gamma) & -\sin(\gamma) & 0 \\ 0 & \sin(\gamma) & \cos(\gamma) & 0 \\ 0 & 0 & 0 & 0 \end{pmatrix}$$

$$\text{And } T = \begin{pmatrix} 0 & 0 & 0 & t_x \\ 0 & 0 & 0 & t_y \\ 0 & 0 & 0 & t_z \\ 0 & 0 & 0 & 1 \end{pmatrix}$$

$$\Rightarrow R + T = \begin{pmatrix} \cos(\alpha) \cdot \cos(\beta) & \cos(\alpha) \cdot \sin(\beta) \cdot \sin(\gamma) - \sin(\alpha) \cdot \cos(\gamma) & \cos(\alpha) \cdot \sin(\beta) \cdot \cos(\gamma) + \sin(\alpha) \cdot \sin(\gamma) & t_x \\ \sin(\alpha) \cdot \cos(\beta) & \sin(\alpha) \cdot \sin(\beta) \cdot \sin(\gamma) + \cos(\alpha) \cdot \cos(\gamma) & \sin(\alpha) \cdot \sin(\beta) \cdot \cos(\gamma) - \cos(\alpha) \cdot \sin(\gamma) & t_y \\ -\sin(\beta) & \cos(\beta) \cdot \sin(\gamma) & \cos(\beta) \cdot \cos(\gamma) & t_z \\ 0 & 0 & 0 & 1 \end{pmatrix}$$

where:

- R is the total rotation matrix; R_x , R_y and R_z are the fundamental rotation matrix about resp. axes x , y and z ;
- T is the translation matrix;
- α , β and γ are resp. the yaw, pitch and roll of the Cardan angles in [$^\circ$], measured by the IMU;
- (p_x, p_y, p_z) the point coordinates in [m] georeferenced in the UTM system;
- (t_x, t_y, t_z) the LiDAR location coordinates in [m] in the UTM system, measured by the GNSS;
- (l_x, l_y, l_z) the point coordinates in [m] in the LiDAR internal system, measured by the laser sensor.

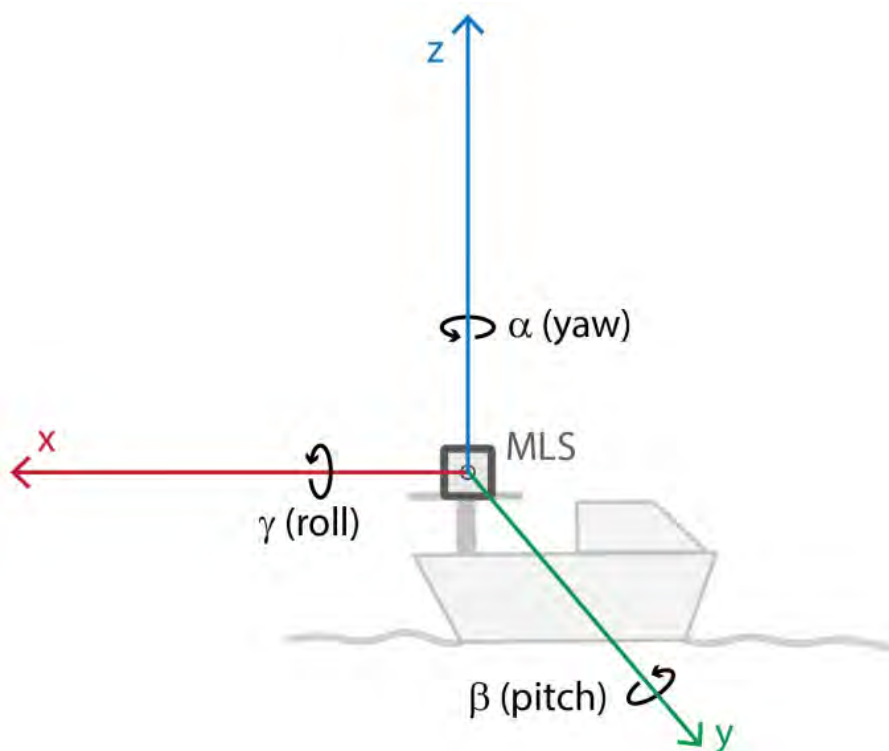


Figure 3.3: Illustration of the Cardan angles, i.e. yaw, pitch and roll.

MLS and ALS techniques are based on the same principles (Vosselman and Mass 2010). Nevertheless, MLS devices are smaller, lighter and cheaper than ALS ones; they are furthermore able to scan the coastline from a direct and horizontal point of view, ensuring a high point cloud density even on sub-vertical cliffs (cf. Section 3.3.3).

Exhaustive reviews of Mobile and Terrestrial LiDAR principles and applications are available in Vosselman and Mass (2010), Jaboyedoff et al. (2012a and in press), Kukko et al. (2012), Williams et al. (2013) and Abellán et al. (2014).

3.3 Point cloud processing

3.3.1 Devices technical specifications

The INS used for this study is an *Applanix™ POS-MV 320-V4*, having the following features according to its manufacturer:

- Acquisition frequency: 1 Hz
- Angular accuracy: 0.020°, up to 0.010° with a GNSS base station
- Positioning accuracy: up to 0.02 m, corrected with a GNSS base station

In addition to the INS, we used a Laser Scanner *Optech™ Ilris Long Range*, having the following features according to its manufacturer:

- Laser wavelength: 1'064 nm
- Pulse rate: 10 kHz
- Maximum range: about 2'000 m at 20% reflectivity
- Mean precision of range estimation: 4 mm at 100 m
- Angular accuracy: 8 mm at 100 m
- Beam diameter: 125 mm at 500 m (according to Baltsavias (1999), beam diameter is approx. equal to beam divergence, here 250 μ rad, times range)

For this study, an internal mirror of the LiDAR device is set up to move the laser beam only along vertical predefined LOS; the vessel attitude, and especially its velocity, is therefore mainly controlling the distance between successive scanned lines. The influence of the LiDAR device setup and the boat attitude is hereafter considered in Section 3.4.

3.3.2 Acquisitions on the vessel

a. Set up and calibration on the vessel

As illustrated in Figure 3.1, the IMU and the TLS of the mobile system are first screwed on an aluminium plate and the GNSS antennas are fixed on 2 arms of about 2 m long at each side of the plate. The xyz vector components from the IMU to the master GNSS antennas and to the laser scanner are then measured with a subcentimetric precision, according to target located on the top of the IMU box (Table 3.2 and Figures 3.4 and 3.5). These measures are valid as long as we set up the MLS system on the same plate.

Table 3.2: Parameters defined for the aluminium plate designed for the Ilris Long Range Scanner used for both campaigns.

	x (mm)	y (mm)	z (mm)	L (mm)
From IMU to Master GNSS antenna	+235	+810	+61	-
From IMU to the scanner	0	-270	+168	-
GAMS of the 20.09.2012	-5	-1'994	-3	1'994
GAMS of the 25.09.2013	5	-1'997	9	1'997
GAMS of the 26.09.2013	4	-1'995	-4	1'995

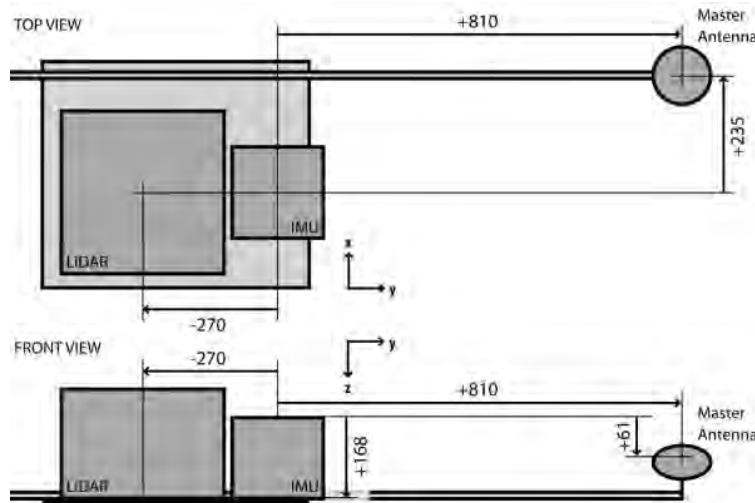


Figure 3.4: Measures of xyz vector components from the IMU to the master GNSS antenna and to the LiDAR base.



Figure 3.5: Setup of the Optech IlrisER TLS (yellow box with control screen) close to the Applanix IMU (orange box) and of the 2 GNSS antennas fixed at each side of the central plate on rigid arms.

For both campaigns, the MLS plate is then firmly tied up on lighting truss on the back deck of the fishing boat L’Aillot. The system is setup as high as possible to avoid splash on the LiDAR device, since it is not waterproof, and to ensure a consistent GNSS horizon for the antenna close to the cabin (usually signals from 7 and 9 GNSS satellites are caught, cf. Tables 3.3 and 3.4).

The GPS Azimuth Measurement Subsystem™ (GAMS) has afterward to be calibrated in order to enhance yaw and location measurements. By doing loops or 8-shaped trajectories during about 10

minutes, the INS is able to fix the phase ambiguity of GNSS signals recorded by the 2 antennas, and to calculate with a millimetric precision the vector between the 2 GNSS antennas (Applanix Corporation 2011). This calibration is performed every day.

b. Description of acquisitions

Table 3.3: Conditions and LiDAR acquisition parameters of the 4 scans realized on 20 September 2012.

	J1	J2	J3	J4
Sector	Ailly	Ailly > Dieppe	Ailly	Puys
Scan beginning time	11h28	12h28	15h21	16h16
Scan end time	11h48	13h13	15h36	16h55
Acquisition length	2'500 m	5'700 m	1'000 m	3'400 m
Range to cliffs	~650 m	~350-500 m	~200 m	~300 m
Tide	Low	Low	High	High
Boat velocity	~4 kn	~4 kn	~2,2 kn	~3,3 kn
Sea conditions (Beaufort)	2 Bft	2 Bft	2 Bft	2 Bft
Sun	From the side	From the side	In front	From the side
LiDAR vertical aperture	14°	14°	23°	18°
Angular resolution index	40	40	50	55
GNSS satellites caught	6-8	6-8	6-9	8-11

Table 3.4: Conditions and LiDAR parameters of acquisitions of the 5 scans realized on 25-26 September 2013.

	M1'	M2'	J1'	J2'	J3'
Sector	St-Aubin > Dieppe	St-Aubin > Dieppe	Dieppe > Penly	Penly > Criel	Dieppe landslide
Scan beginning time	9h18	13h55	10h00	12h07	14h35
Scan end time	12h10	16h17	11h30	13h25	14h45
Acquisition length	15'700 m	16'900 m	9'200 m	9'450 m	600 m
Range to cliffs	600-800 m	~300 m	~600-800 m	~600-800 m	~300 m
Tide	Low	High	Low	Low	High
Boat velocity	~3.5-4.5 kn	~4 kn	~3.4 kn	~3,6 kn	~3.7 kn
Sea conditions (Beaufort)	1 Bft	1 Bft	2 Bft	3 Bft	2.5 Bft
Sun	From the side	Cloudy	From the side	Cloudy	Cloudy
LiDAR vertical aperture	20°	36°	22°	22°	36°
Angular resolution index ¹	45	55	45	45	55
GNSS satellites caught	6-8	9-12	6	8-10	9

The angular resolution index is a spacing between laser shots on an artificial numeric scale designed by *Optech*TM: the lower the value is, the higher the point cloud resolution will be.

After several tests realized the days before, 4 operational acquisitions, named *J_n*, have been performed on 20 September 2012 on the Ailly and Puys sites, during a sunny day with a calm sea (2

Bft). Puy's cliffs have been scanned once, whereas the Cap d'Ailly shoreline has been acquired three times with large overlaps, to test point spacing and repeatability under different conditions, mainly changing the boat speed, range to the cliffs and LiDAR angular apertures and resolutions.

Encouraged by the 2012 experience, 4 acquisitions of about 10 km each, named *Mn'* and *Jn'*, have been achieved on 25 and 26 September 2013 in similar conditions from Saint-Aubin-sur-Mer to Criel-Plage. A smaller point cloud focused on the active retrogressive Dieppe landslide (cf. Section 3.4.2) has also been performed. Trajectories and conditions of acquisitions are illustrated in Figure 3.6 and summarized in Tables 3.3 and 3.4.

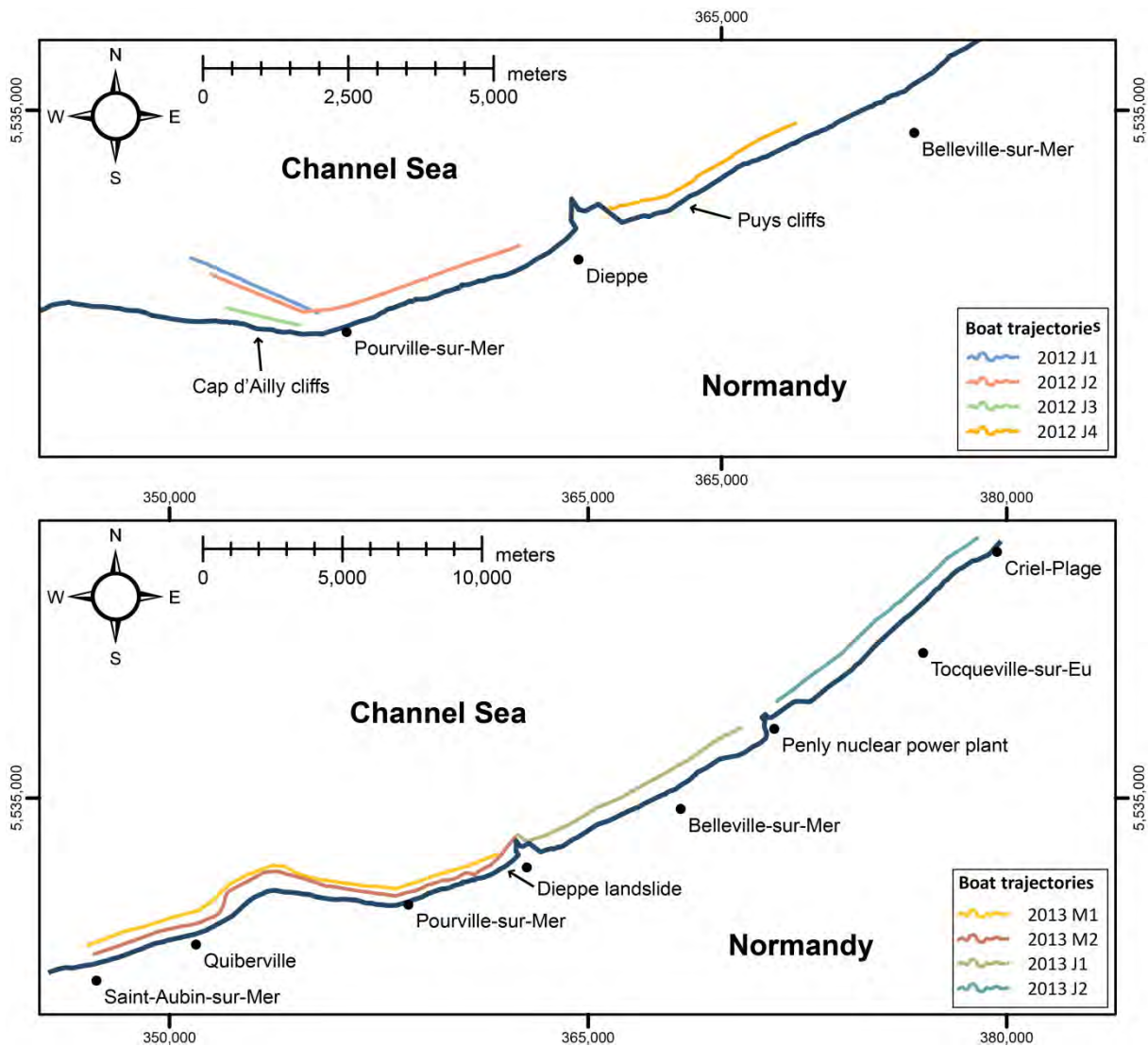


Figure 3.6: Boat trajectories during (up) acquisitions of the 20 September 2012 of Cap d'Ailly and Puy's cliffs and (down) of the 25-26 September 2013 between Saint-Aubin-sur-Mer and Criel-Plage.

3.3.3 Post-processing

a. Inertial Navigation System data

INS-recorded data are first filtered by computing the smoothed best estimated trajectories using the raw inertial and GNSS measurements. This correction, realized within the software *Applanix POSPac™ MMS 5.3*, indeed deletes outliers and artefacts from atmospheric perturbations and potential micro-losses of the GNSS signal.

Similarly to classic static GNSS studies (Gili et al. 2000), we then used close permanent GNSS antennas of the French Geographic Institute (IGN) as base stations to post-process and correct our GNSS signal. For the 2012 campaign, confined close to Dieppe, data from the Ambrumesnil permanent antenna has been used as base station. Regarding the 2013 campaign, for which acquisitions are covering 38 km of coast, GNSS data from several permanent antennas distributed along the coast were necessary for the post-processing: Ambrumesnil, Fécamp, Le Touquet, Cap Seine, Morgny, Houville-en-Vexin, Foucarmont and Herstmonceux permanent antennas. The final accuracy of post-processed positioning (trajectory and LiDAR LOS) is of about 3 cm.

The INS navigation data are then projected in the UTM 31°N WGS 84 coordinate system and exported in the SBET and polyline shapefile formats, in order to be coupled with LiDAR data or imported within GIS software.

b. Mobile Laser Scanning data

In order to get the final geometry of the LiDAR data, they have been processed according to the following procedure:

1. Raw LiDAR data, which are related to the LiDAR referential system, are coupled with positioning and orientation information of SBET files, synchronized together with GNSS time logs recorded on both files (the Raw and SBET ones).
2. Roto-translation matrix are then automatically computed and applied to each point using the software *Optech™ Parser 5.0.3.1* in order to georeference the acquisition (in UTM 31°N WGS 84). Point clouds are exported in ASCII text files structured in 4 columns: coordinates x, y, z and intensity of the back-scattered signal (named hereafter xyzi).
3. Point clouds are then manually and iteratively cleaned, as for common post-processing of TLS data (Jaboyedoff et al. in press): non ground points, i.e. outliers from reflected pulses on sea spray and air dust, as well as direct sunshine misinterpreted as LiDAR signal, are manually selected based on a visual interpretation and are then deleted, within the software *Polyworks™ PIFedit 10.1*.

4. After having carried out empirical and statistical analysis on signal intensities on representative populations of points reflected by sea spray, cliffs or sunshine, all points with signal intensity lower than 12 (on a scale [0;255]) have been considered as sea spray and foam and therefore deleted, within the software Polyworks™ ImInspect 10.1.
5. All cleaned point clouds are then re-exported in xyzi files.
6. Subset areas containing only cliffs areas and no vegetation or constructions are selected within 2012 and 2013 point clouds and are also exported in xyzi files.

The repeatability of MLS data is then assessed with only the 2012 acquisitions at the Cap d'Ailly (i.e. *J1*, *J2* and *J3*, all acquired in an interval of 4 hours):

1. The *J1* and *J3* point clouds are aligned on the *J2* one, used as reference, by progressively minimizing the distances between points to the *J2* meshed reference surface with an Iterative Closest Point -based (ICP, in Besl and McKey 1992) algorithm implemented in Polyworks™ ImInspect 10.1.
2. The realigned point clouds are exported in xyzi files.

In order to assess the MLS capability to detect and monitor topographic changes due to rockfall events, erosions of former deposits and retrogressive landslides on the 2012 and 2013 sequential acquisitions:

3. The 2013 *M2'* and *J1'* point clouds are aligned on respectively the 2012 *J2* and *J4* ones, used as references, following the process described in step 6.
4. The realigned point clouds are exported in xyzi files.

As explained in Section 3.4.2, these alignments, which might seem useless since the point clouds are already georeferenced, actually enhance the comparison of sequential acquisitions by reducing errors from the navigation inaccuracies.

3.3.4 Terrestrial Laser Scanning point clouds

As a part of the wide researches conducted on the Dieppe coastline stability (Letortu 2013; Letortu et al. 2014), a long-term TLS monitoring is carried out on cliffs in Ailly and Puys. On 18-19 September 2012, TLS-based point clouds of both sites have been acquired with a *Riegl LMS Z390i*; the dataset, georeferenced in the UTM 31°N coordinate system using 16 ground control points (GCP), has a median point spacing of about 1 cm (cf. section 3.4.2). In order to compare scans from both techniques, the following procedure has thus been applied:

1. As a decametric vertical translation has been observed between TLS and MLS acquisitions, which may stems from different geoids used between French and Swiss

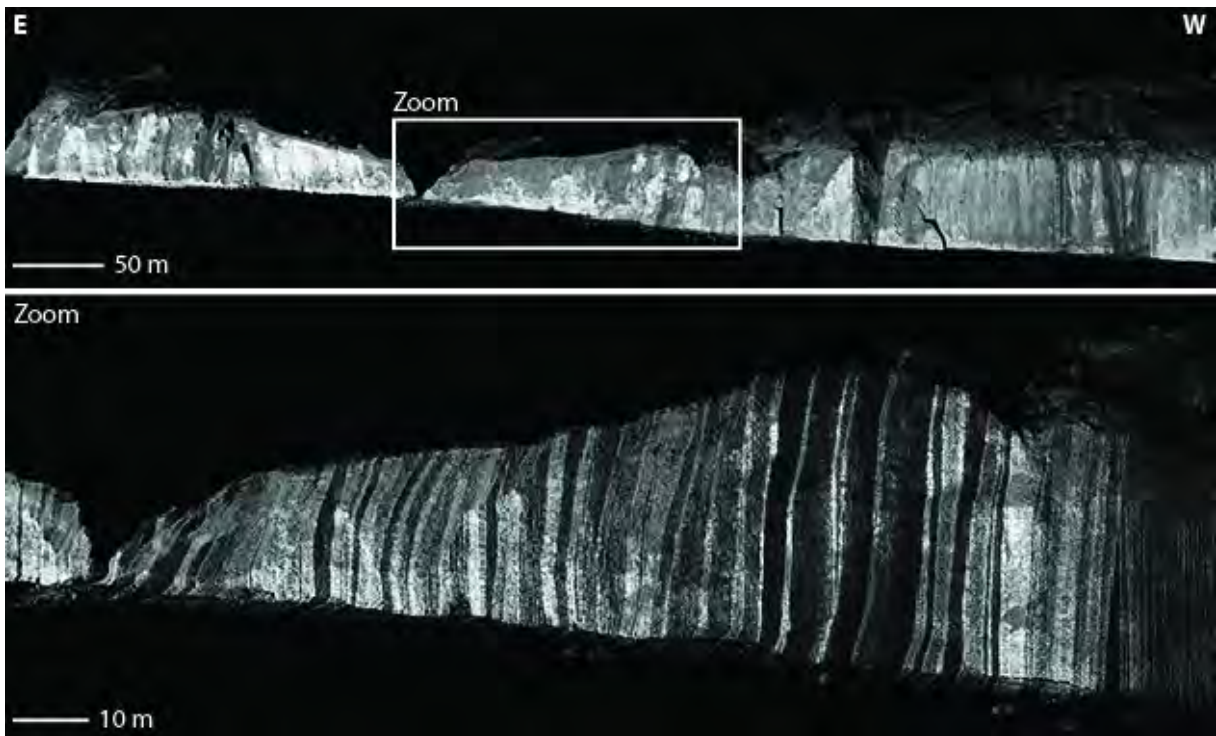


Figure 3.7: (Up) Final J3 point cloud of the Ailly site, manually and automatically cleaned, ready for the xyz exportation; the cleaned scan has 3'118'836 points, instead of 3'234'761 initially (only 3.6% of the points were deleted). (Down) Zoom in the cliff sector that is long-term monitored with TLS acquisitions. Spacing between vertical lines is mainly varying with boat velocities when it is tossed by wave or it is surfing on them (cf. Figure 3.9).

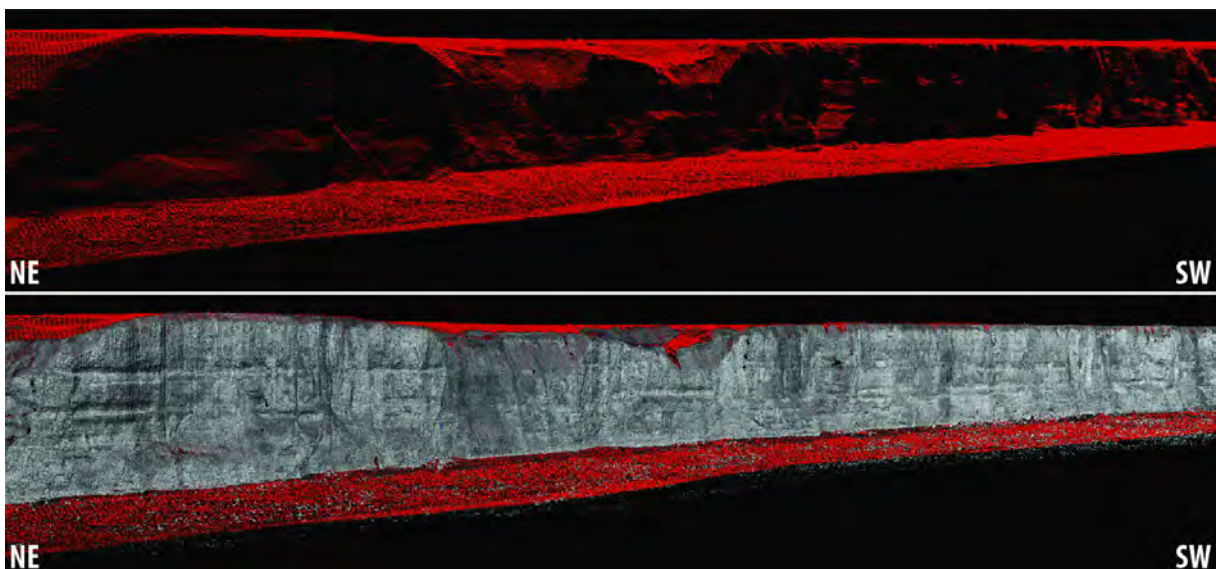


Figure 3.8: Illustration of point density difference between (up) the ALS point cloud (in red), and (down) the MLS point cloud (in grey) close to Puys (ALS data: © IGN).

partners, the Ailly and Puy TLS point cloud are aligned on resp. the J2 and J4 ones, used as references following the method described in step 6;

2. The TLS point cloud is exported in a xyzi file.

3.4 MLS point clouds capability assessment

3.4.1 Methodology

a. Median point spacing

The assessment of the resolution of each point cloud according to navigation conditions and device setup is described in this section. First, Euclidean distances of each point to its nearest neighbour have to be extracted. Then, statistics are achieved to describe the Euclidean distances distribution of each scan. For this purpose, the distribution median is first calculated; then the 68% and 95% quantiles of the difference to this median are computed to characterize the dispersion of the population. The median is preferred to the mean in order to minimize influences of outliers (Höhle and Höhle 2009). The process, implemented within a *Matlab*[™] routine, follows these steps:

1. The cleaned xyzi point cloud is imported;
2. The *knnsearch* function (Friedman et al. 1977) is computed to search the nearest neighbour of each point and to then to extract the Euclidean distance x between them;
3. The median \bar{x} of all distances x is calculated;
4. For each point, the difference in absolute value $|x - \bar{x}|$ between the distance to its nearest neighbour and the median value is calculated;
5. The 68% and 95% quantiles of the differences to the median are calculated.

In addition, we aim at discriminating the influences on the cliff's point spacing of (a) the LiDAR device setup (especially its vertical aperture and angular resolution), which should have a strong vertical component since its internal mirror is set up in order to move the beam vertically only, and (b) to the vessel attitude and its velocity, which should influence mostly the horizontal spacing (Figure 3.9). For this purpose, we apply to the *J1*, *J3* and *M1'* subset point clouds additional steps to sort nearest neighbours in 2 classes, the nearest vertical and nearest horizontal ones:

1. Now, the 25 nearest neighbours to each point are identified, again based on the *knnsearch* function (Friedman et al. 1977);
2. The angles between a vertical vector and the point to neighbour vector are extracted from the dot products for each point to their 25 nearest neighbours:
 - a. If the angles with the vertical are included within $[0^\circ ; 30^\circ[$ (threshold arbitrary set to deal with small ledges and tilted LOS, cf. Figure 3.9), neighbours are

considered belonging to the same LiDAR LOS and are therefore sorted with the nearest vertical neighbours class;

- b. If the angles with the vertical are included within $[30^\circ ; 90^\circ]$, neighbours are considered as not vertical and are therefore sorted with the nearest horizontal neighbours class (i.e. distances between LiDAR vertical LOS);
3. Again, statistics are achieved for the 2 classes, following the same procedure than before.

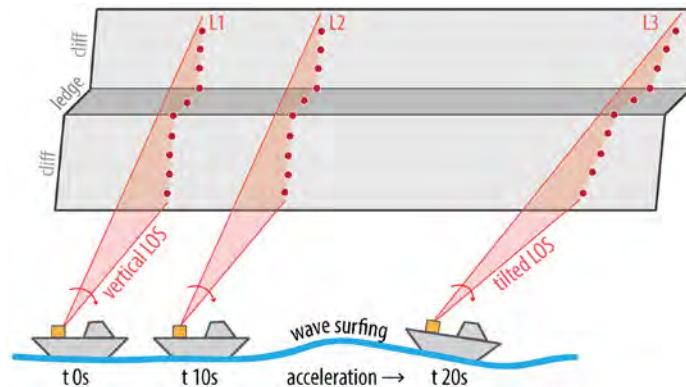


Figure 3.9: Illustration of the influence of LiDAR setup and vessel attitude on the vertical and horizontal spacing. The horizontal spacing between L1 and L2 is lower than between L2 and L3, since the boat accelerated when it surfed on a wave.

b. Acquisitions repeatability

According to technical specifications of devices (cf. section 3.3.1), the vessel attitude and trajectories are acquired with precisions up to 0.01° and 2 cm respectively. In addition, the LiDAR device records range measurements with a mean accuracy of 4 mm at 100 m. But in order to assess in real conditions the MLS repeatability capability, the *J1*, *J2* and *J3* point clouds are compared. As the Ailly cliffs are acquired the same day in 4 hours, we assume that the scanned topography is the same for the 3 point clouds; differences between them stem hence from devices measurement errors. The repeatability can then be quantified assessing the point clouds differences. *J2* is thus used as a reference surface, having the best overlapping ratio between scans, and its comparison to *J1* and *J3* subsets is then assessed with the following procedure:

1. The xyz *J2* and *J4* point clouds are imported in Polyworks™ ImInspect 10.1 and the reference surfaces are built according to a triangular mesh with an horizontal viewing vector (i.e. corresponding to a mean offshore position of the boat);
2. The aligned and not-aligned xyz *J1* and *J3* subset point clouds (cf. section 3.3.3) are imported, as well as the realigned Ailly and Puys TLS point clouds (cf. section 3.3.4);
3. Based on the nearest-neighbour algorithm, the Euclidean shortest distances d from *J1* and *J3* points to the meshed reference surface *J2* are computed; in the same way, the

Euclidean shortest distances d from the TLS points of Ailly and respectively Puys to their meshed reference surfaces, J2 and J4 resp., are computed;

4. These distances d are also computed from J2 and J4 points to their own meshed surface, as tests to identify errors coming exclusively from the surface meshing step and not from instrumental ones;
5. All comparisons are exported in *xyzi* and d files.

Statistics on computed differences d are then carried out according to the same method than for point spacing characterisation, i.e. following a routine implemented in *Matlab*TM:

6. The *xyzid* comparison files are imported;
7. The median \bar{d} of all distances d is calculated;
8. The median $|\bar{d}|$ of all absolute distances $|d|$ is calculated;
9. For each point, the difference in absolute value $|d - \bar{d}|$ between the distance to its nearest neighbour is calculated;
10. The 68% and 95% quantiles of the differences to the median \bar{d} are calculated.

c. Change detection and monitoring

In order to detect topographic changes between the 2012 to 2013 acquisition campaigns due to rock slope failures, erosion of former deposits or retrogressive landslides, ICP-based distance comparisons between sequential dataset can be assessed in *Polyworks*TM *ImInspect 10.1*. Indeed, after having refined the alignment of new point clouds on old ones:

- rockfall events are usually identified by computing shortest distances between the 2 topographies (Abellán et al 2014);
- retrogressive processes can easily be quantified by computing the horizontal distances parallel to the sliding direction (Jaboyedoff et al. 2009a).

In addition, volumes of detected rockfall events can be estimated using an alpha-shape concave hull method (Edelsbrunner and Mücke 1994), following a semi-automatic routine shown in Carrea et al. (2014):

1. Each rockfall or erosion deposit identified with the shortest distance comparison has first to be delimited on both old and new surfaces;
2. Point clouds of rockfalls or deposits shapes are meshed with tetrahedrons in *Matlab*TM and:
 - a. each tetrahedron basis contains no other point than the 3 ones of its edges;
 - b. tetrahedron heights have to be big enough to allow the filling of the form, but in the meantime, small enough to avoid the filling of the block surface concavities;

3. For each identified block, the volume of the mesh is computed by summing the volume of all the tetrahedrons.

3.4.2 Results

a. Decimetric median point spacing

As summarized in Tables 3.5 and 3.6, median point spacing of scans ranges from 20 cm for far scans to about 8 cm for the closest ones. Acquired in low tide conditions from 500-600 m range and with a 4 kn stream (7.4 km/h), *J1* and *J2* have median point spacing of about 22 and 12 cm with 68% quantiles of 16 and 9 cm. Acquired from 200 m and with a 2.2 kn stream (4.1 km/h), *J3* has a median point spacing of 8 cm with a 68% quantile of 5 cm (Figure 3.10). In addition, statistics on point spacing on subset clouds, focused on cliffs (our areas of interest), are almost equal to those of the complete scans, because the majority of the points are located on these cliffs. As a comparison, the Ailly and Puys TLS-based point clouds have median point spacing of about 1 cm (Table 3.7).

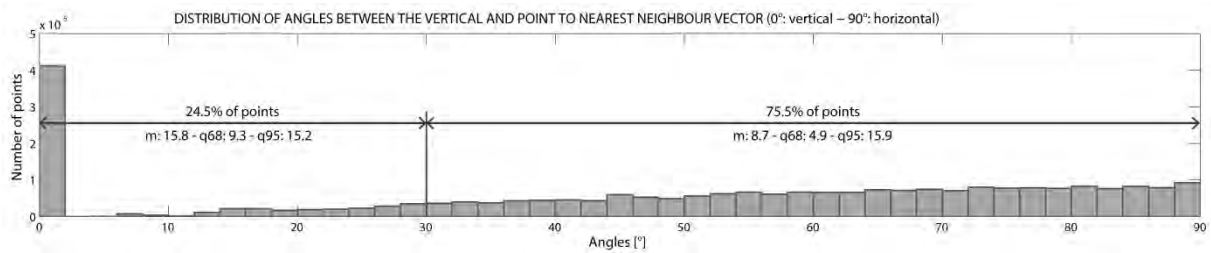


Figure 3.10: Angles distribution between the vertical and point to nearest neighbour vectors for the *J3* subset point cloud: 24.5% of the nearest neighbours are located on a vertical more or less 30° direction from points. Medians (m), 68% (q68) and 95% (q95) quantiles are in cm.

Regarding the vertical and horizontal component of the *J3* subset point spacing illustrated in Figures 3.7 and 3.8, 24.5% of points have their nearest neighbour close to the vertical, while 75.5% of the points have it uniformly distributed on their side. In addition, when we compare distances to nearest vertical and horizontal neighbours, we notice that horizontal point spacing is usually lower than the vertical one (Figure 3.11). It means that the vessel attitude, largely influenced by the boat velocity and marine conditions, is hence mainly controlling the general point spacing. Indeed, by navigating during a calm sea, the median horizontal point spacing is about 9 cm, while the median vertical one is about 16 cm (Figure 3.11, frame A). On the contrary, when the boat is tossed and surfs on swells, the median horizontal and vertical point spacing can reach up to 58 cm and 24 cm (resp.) (Figure 3.11, frame B).

Finally, point cloud resolutions can be also improved independently of the navigation conditions, adapting *Optech*™ device setup; for example, by setting in 2013 the LiDAR vertical aperture at 20°

and the angular resolution index at 45 (cf. Tables 3.3 and 3.4), instead of 14° and 40, the *M1'* median vertical and horizontal point spacing (20 and 12 cm) are indeed much lower than the *J1* ones (46 and 23 cm), although both were acquired in the same conditions (2 Bft), i.e. from 600-700 m with a 4 km stream.

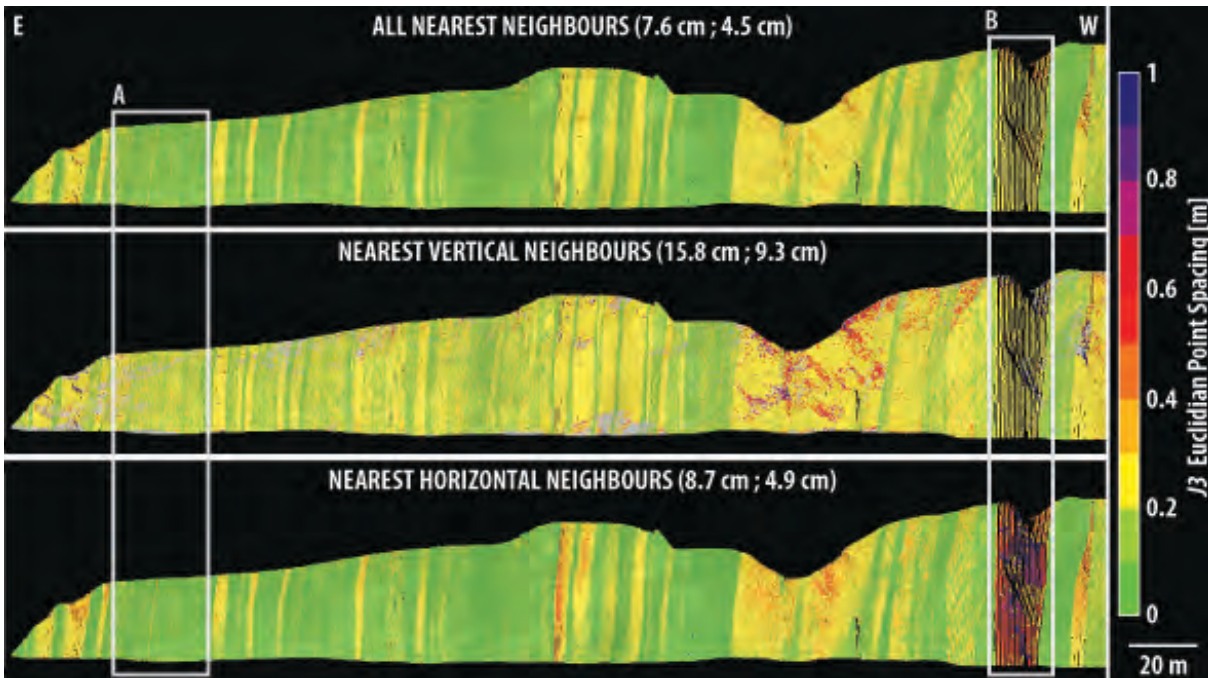


Figure 3.11: Euclidean point spacing of the *J3* subset point cloud considering (up) all nearest neighbours, (middle) nearest vertical neighbours and (down) nearest horizontal neighbours. Frames A and B match with examples developed in the text. Numbers in parenthesis correspond to median and 68% quantiles of point spacing distributions.

a. Decimetric repeatability after point cloud realignment

Now, regarding the MLS repeatability capability, comparisons results between *J1*, *J2* and *J3* point clouds acquired in an interval of 4 hours are summarized in Table 3.8. First, median absolute distances between points of the reference point clouds (*J2*) and its own triangulated mesh are lower than 1 cm, as expected, but with 68% and 95% quantiles of about 3 and 9 cm; errors introduced during the surface meshing step, especially in vegetated areas, are likely to explain the observed differences of similar magnitude in the test.

Then, median of absolute distances between *J1* and *J3* points and the *J2* reference surface are about 11 and 17 cm with 68% quantiles of 25 and 38 cm. Nevertheless, once *J1* and *J3* are realigned on *J2* (cf. section 3.3.3), both point clouds have smaller differences with the reference surface, median of absolute distances decreasing to about 9 and 7 cm with 68% quantiles of 17 and 12 cm. As a comparison, TLS acquisitions of Ailly and Puy sites are also realigned on *J2* and *J4* point clouds resp. and compared with them (Table 3.9): median of absolute distances are close to 4 cm, with 68% of 9 and 7 cm (resp.).

Differences between points clouds can therefore be drastically reduced by simply refining the alignment of all point clouds (Figures 3.12 and 3.13), reinforcing the repeatability capability of the boat-based mobile scanning technique.

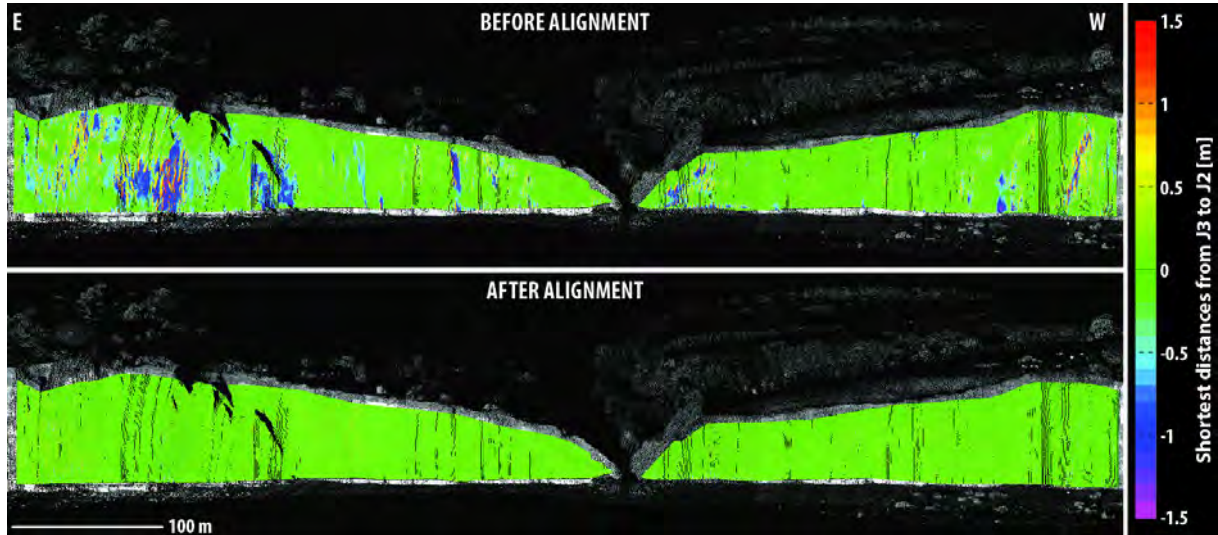


Figure 3.12: J3 points to J2 meshed surface Euclidean distances, before and after alignment (Positive values: points in front of the reference surface; Negative values: points behind the reference surface; scale in meters).

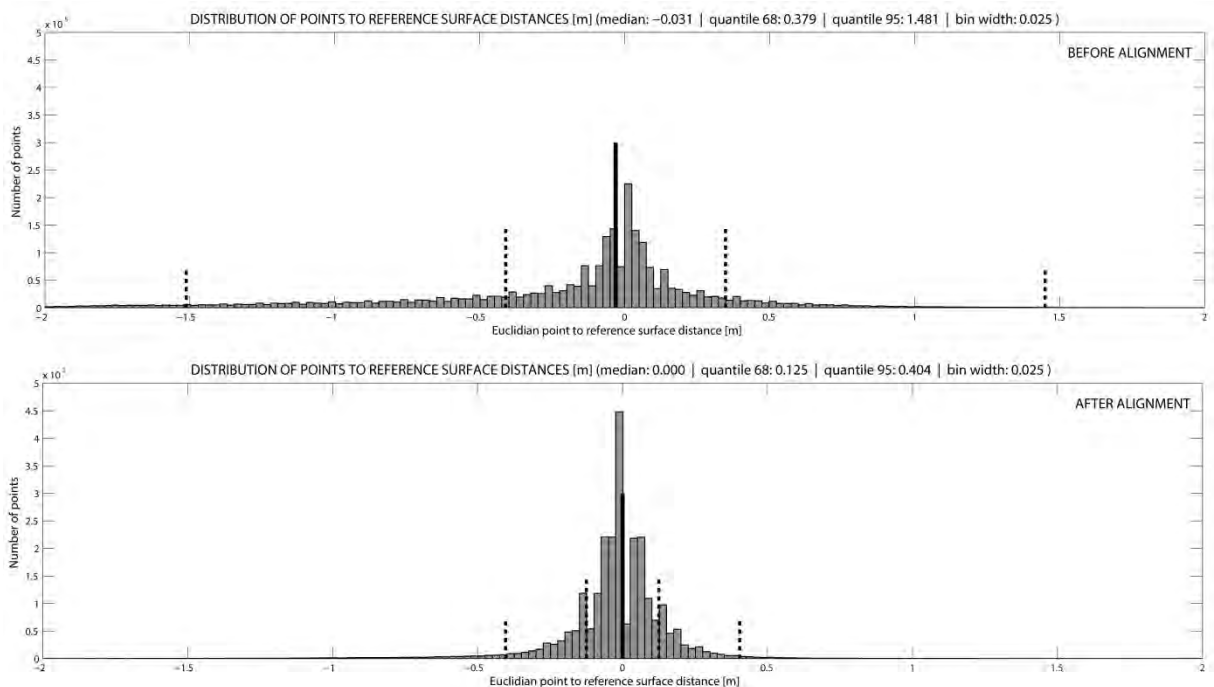


Figure 3.13: Shortest distances distributions from J3 points to J2 meshed reference surface, before (up) and after (down) J3 alignment on J2 (dark lines: median; dot lines: 68% and 95% quantiles).

Table 3.5: Median and dispersion values of point spacing for each 2012 MLS acquisitions.

		J1	J2	J3	J4
<i>Mean range and velocity</i>		650 m / 4 kn	450 m / 4 kn	200 m / 2.2 kn	300 m / 3.3 kn
<i>Aperture and resolution index</i>		14°/40	14°/40	23°/50	18°/55
All points	Number of points	2'173'560	8'500'660	3'118'836	7'700'024
	Median spacing	22.7 cm	12.2 cm	8.0 cm	8.4 cm
	Quantile 68	15.5 cm	8.8 cm	4.9 cm	5.2 cm
	Quantile 95	42.9 cm	30.8 cm	16.6 cm	17.5 cm
Cliff subsets	Number of points	1'427'830	6'062'001	2'539'891	6'816'492
	Median spacing	20.5 cm	10.7 cm	7.6 cm	8.1 cm
	Quantile 68	13.8 cm	7.5 cm	4.5 cm	4.9 cm
	Quantile 95	33.7 cm	24.8 cm	15.1 cm	16.5 cm

Table 3.6: Median and dispersion values of point spacing for each 2013 MLS acquisitions.

	M1'	M2'	J1'	J2'	J3'
<i>Mean range and velocity</i>	700 m / 4 kn	300 m / 4 kn	700 m / 3.4 kn	700 m / 3.6 kn	300 m / 3.7 kn
<i>Aperture and resolution index</i>	20°/45	36°/55	22°/45	22°/45	36°/55
Number of points	10'910'356	11'824'517	12'253'010	11'553'180	1'257'959
Median spacing	15.6 cm	14.0 cm	12.2 cm	14.2 cm	15.6 cm
Quantile 68	11.4 cm	10.5 cm	7.8 cm	8.0 cm	9.8 cm
Quantile 95	45.5 cm	36.2 cm	33.4 cm	33.0 cm	28.9 cm

Table 3.7: Median and dispersion values of point spacing for the two 2012 TLS acquisitions.

	TLS Ailly	TLS Puys
Number of points	4'678'910	8'332'012
Median spacing	1.1 cm	0.6 cm
Quantile 68	4.6 cm	0.6 cm
Quantile 95	11.3 cm	10.8 cm

Table 3.8: Median and dispersion values of shortest distances from J1 and J3 points to J2 meshed surface.

	J2 (test)	Subset J1		Subset J3	
		Not aligned	Aligned	Not aligned	Aligned
<i>Median spacing [cm]</i>	12.2	20.5		8.1	
Median distance [cm]	0.0	0.0	0.0	-3.1	0.0
Median absolute distance [cm]	0.6	11.4	9.0	17.0	7.0
Quantile 68 [cm]	3.1	25.0	17.2	37.9	12.5
Quantile 95 [cm]	8.9	95.6	75.2	148.1	40.3

Table 3.9: Median and dispersion values of shortest distances from TLS points to J2 and J4 meshed surfaces.

	Test J2	Test J4	TLS Ailly	TLS Puys
Aligned on	J2 (itself)	J4 (itself)	J2	J4
<i>MLS median spacing [cm]</i>	12.2	8.4	12.2	8.4
<i>TLS median spacing [cm]</i>	-	-	1.1	0.6
Median distance [cm]	0.0	0.0	0.0	0.0
Median absolute distance [cm]	0.6	1.1	4.7	4.2
Quantile 68 [cm]	3.1	0.1	7.8	7.1
Quantile 95 [cm]	8.9	6.3	27.7	31.9

b. Rockfall detection and rock spread monitoring

Regarding the change detection capability, it is nowadays possible to quickly assess retreat rates over *km* long coastal cliffs. Our capability to detect, map and quantify in details rockfall events and cliff foot erosion between Septembers 2012 and 2013, is indeed confirmed with classic nearest neighbours comparison approaches, as illustrated in Figures 3.14 to 3.16.

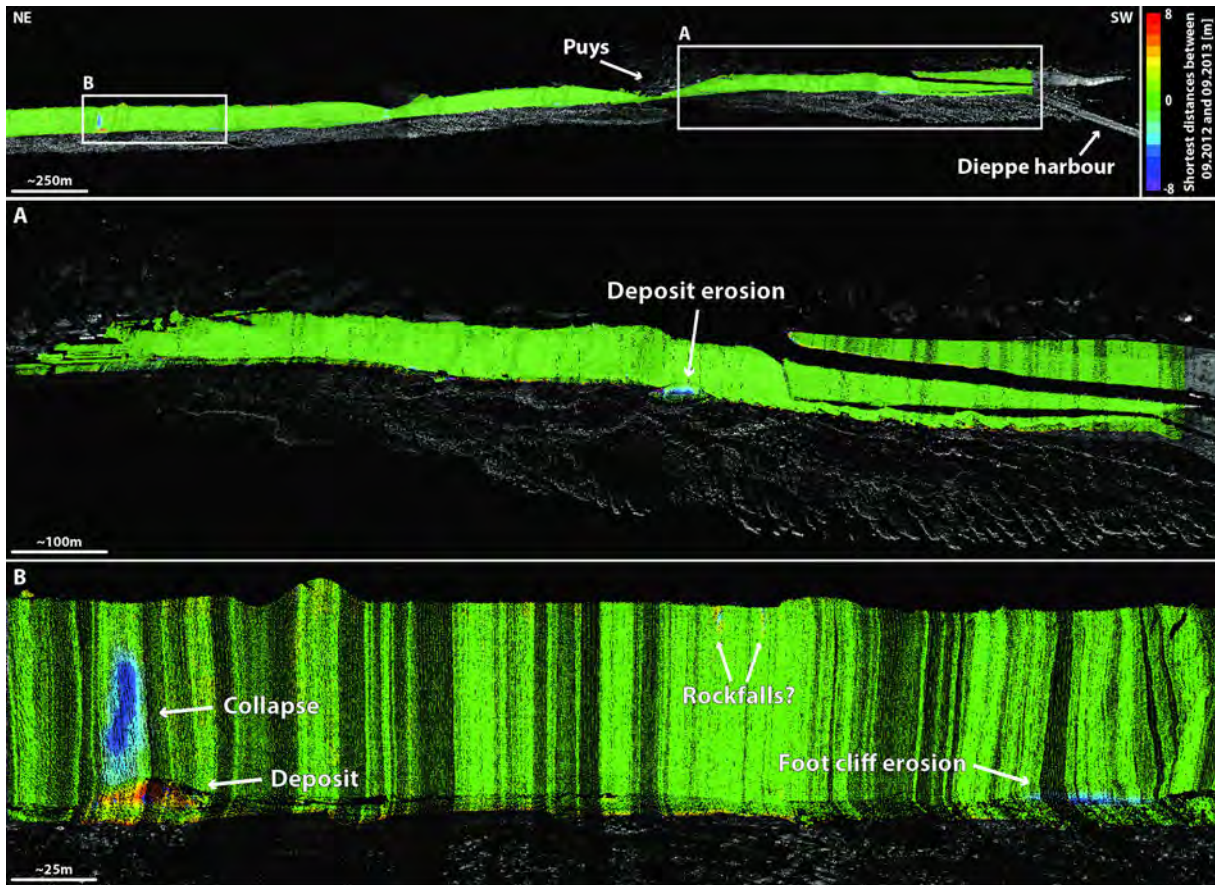


Figure 3.14: Shortest J2' points to J4 surface distances comparison between 2012 and 2013 point clouds wrapped on the intensities of the 2nd scan. Only few collapses and deposit erosions are detected along the Puys shoreline, and are detailed in the next caption. (Negative values: eroded material; Positives values: accumulated material)

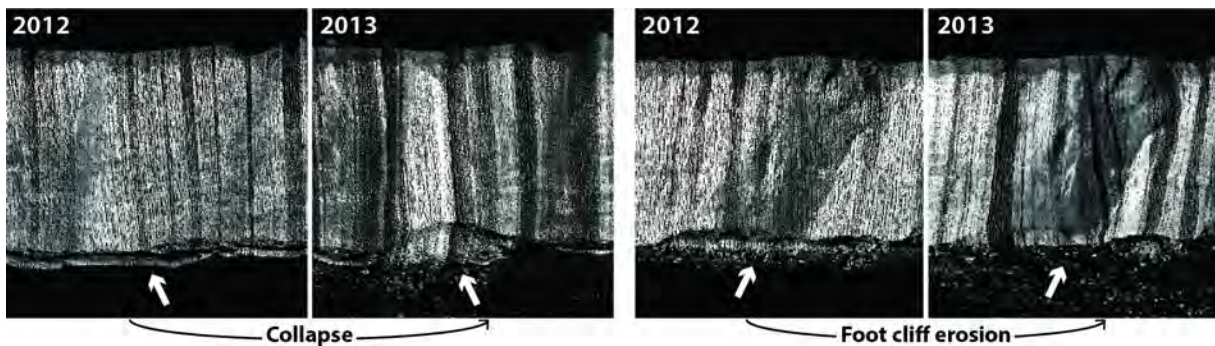


Figure 3.15: Point cloud comparisons of the collapse and the foot cliff erosion highlighted in the previous figure.

We can furthermore notice a greater number of collapses along the Cap d'Ailly shoreline than the Puy one, as confirmed by geological and hydrogeological settings very prone to failure in complex cliffs of Ailly (Costa 2014).

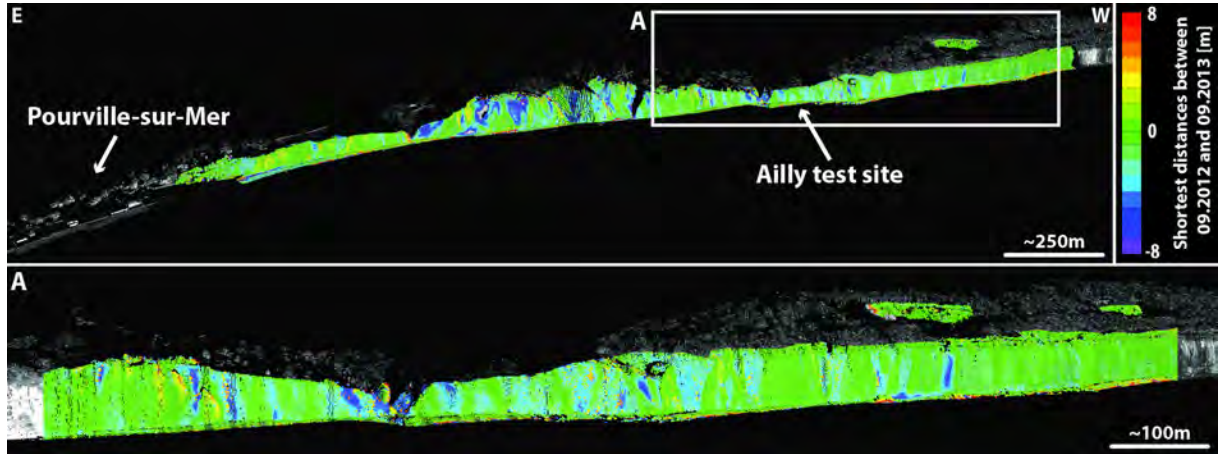


Figure 3.16: Shortest M2' points to J2 surface distances comparison between 2012 and 2013 point clouds wrapped on the intensities of the 2nd scan. Multiple rockfall events can be easily identified and quantified close to the Cap d'Ailly. (Negative values: eroded material; Positives values: accumulated material).

We afterward estimated cliff retreat of the “Dieppe landslide”: this large active sandy-clay earth and soft rock spread was activated the 17-18 December 2012 by the heavy autumnal and wintry rainfalls and destroyed several constructions (Figure 3.17). By extracting horizontal differences approximately parallel to the sliding azimuth between the 2012 J2 and the 2013 J4' point clouds, we measure a cliff retreat up to 40 m along 2 active scarps over 70 m wide (Figures 3.18 and 3.19). Then using the alpha-shape concave hull method (Edelsbrunner and Mücke 1994; Carrea et al. 2014), loss material volumes are estimated close to 100'000 m³, although the scree deposit volume is close to 35'000 m³, its major part being already eroded by the Channel waves and tidal currents.



Figure 3.17: Picture of the Dieppe landslide in September 2013; the mass movement destroyed several constructions close to the shoreline after its activation in December 2012.

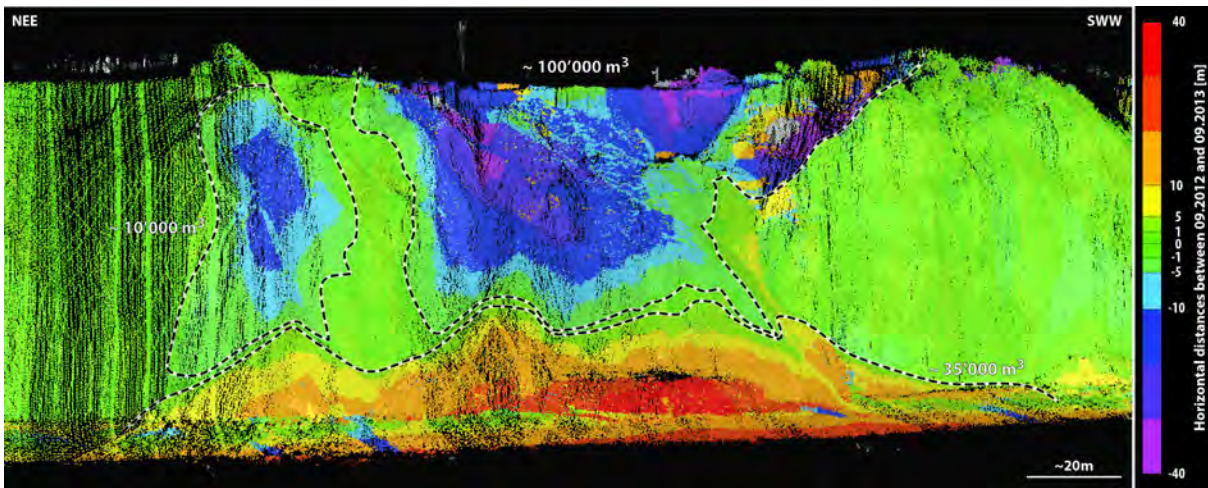


Figure 3.18: Fine horizontal distances comparison parallel to the sliding direction between 2012 J22 and 2013 J4' point clouds wrapped on the intensities of the 2nd scan, on the Dieppe landslide (Negative values: eroded material; Positives values: accumulated material).

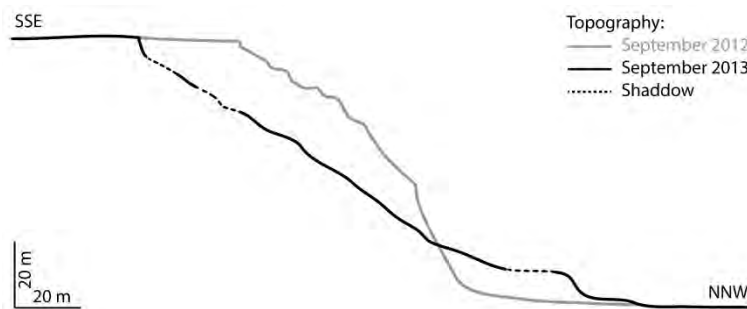


Figure 3.19: Topography prior and after the “Dieppe” landslide, extracted from the Septembers 2012 and 2013 MLS acquisition coupled with the ALS data at the flat top.

3.5 Discussion and conclusions

ALS devices have been widely used for coastal topography and shallow bathymetry modelling, especially with the SHOALS and derived systems (e.g. in Irish and Lillycrop 1999; Adams and Chandler 2002; Brock and Purkis 2009; Young et al. 2013; Earlie et al. 2014). But the incidence angle is a key factor for point cloud density and accuracy (Baltsavias 1999a; Lichti et al. 2005). For coastal shore topography such as cliffs, ALS data have then high inaccuracy and lack of information on vertical areas due to unfavourable high incident angles (Adams and Chandler 2002; Young et al. 2013; Earlie et al. 2014).

Meanwhile, boat-based MLS is a recent laser sensor development of that is able to scan *km* long sub-vertical coastline from a direct and horizontal point of view, improving point cloud densities and accuracies, and acquiring even overhangs. We here demonstrated along Dieppe coastal cliffs, High Normandy, France, that our MLS system (an Applanix POS-MV INS coupled with an Optech Ilirs LR

LiDAR), is indeed a promising technique supporting rockfall assessments and large landslide monitoring along vertical sea shores.

The navigation conditions, i.e. boat velocity and range to the cliffs largely controlling by Channel stream and tide, are mainly influencing the general point spacing; nevertheless, it can also be optimized with appropriate LiDAR device setup, in order to keep as coherent as possible vertical and horizontal spacing. First, by scanning during favourable meteorological and marine conditions (i.e. 2 Bft, very small swell and almost no stream, and no rain) and close to the coast (~200 m during high tide period), MLS devices are indeed able to quickly scan long shoreline with a median point spacing up to 10 cm. For example, it took 1.5 hours to scan 9 km of coastal cliffs at ~3.5 kn (6.5 km/h). Moreover, other tests performed during harsher conditions, with 1.5 m high swell and strong stream (4.5 Bft), also allowed us to extract 3D data with point spacing of about 30 cm. Nevertheless, scanning during quiet days is a better guarantee for a dense and uniform cover of areas of interest, since the LiDAR LOS is more easily controlled when the boat is not continuously tossed by waves.

Then, by increasing the laser pulse repetition frequency of newer LiDAR devices, point cloud resolution can also be enhanced. Indeed, previous acquisitions performed in Norwegian fjords and carried out with equivalent navigation conditions, but with an Ilris TLS of older generation with a pulse rate 4 times lower of 2.5 kHz, produced point clouds with median spacing of about 50 cm (Michoud et al. 2010b).

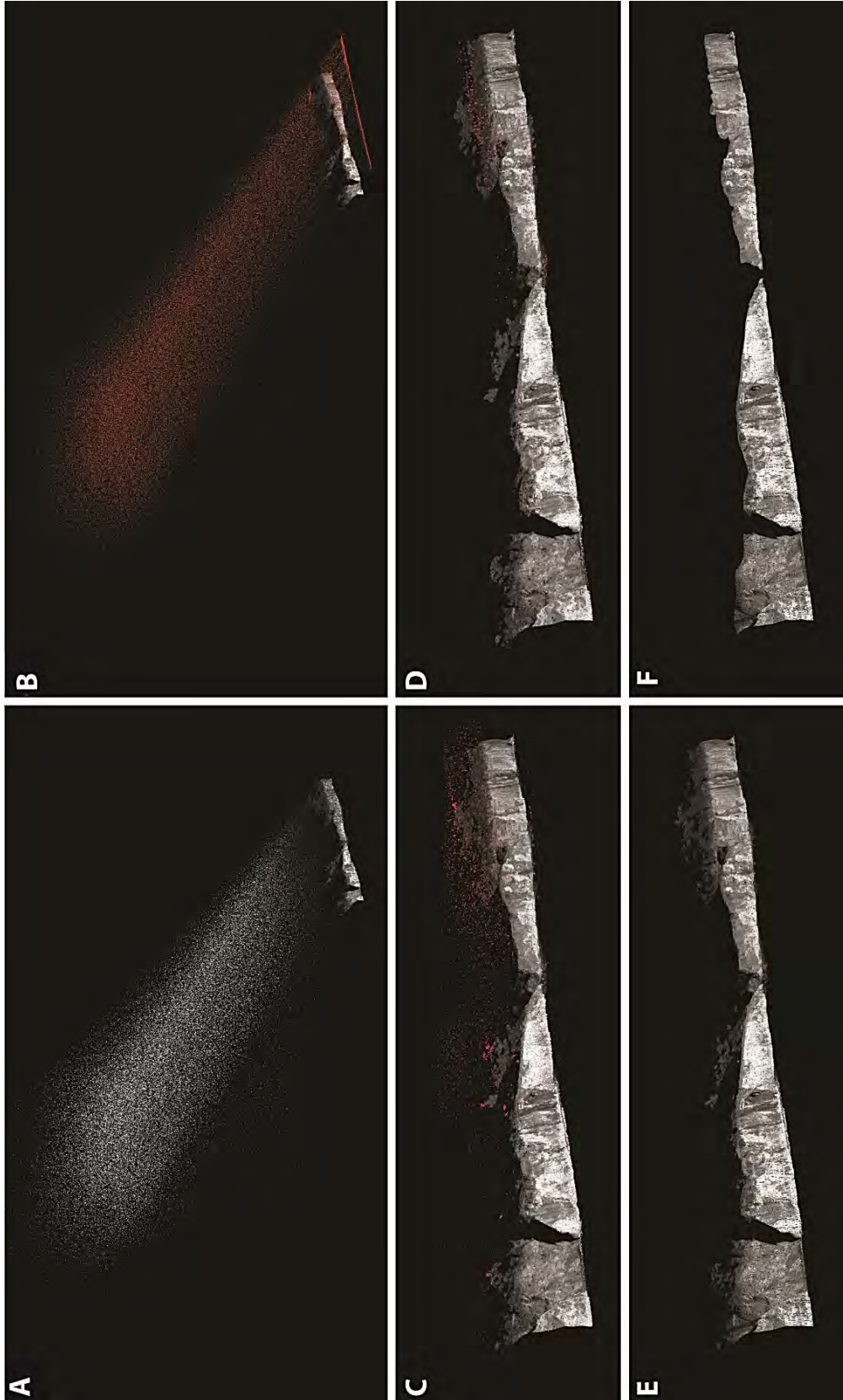
In addition, the monitoring with MLS of the constant erosion with *mm* and *cm* rates seems up to now not realistic, with measured repeatability close to 10 cm. Nevertheless, more accurate LiDAR, based on phase-shift between emitted and received signal instead of ToF principles (Vosselman and Maas 2010), can have repeatability of about 1 cm (e.g. in Vaaja et al. 2013). However these devices cannot perform scan from ranges longer than 150 m, strongly limiting their capabilities in areas with long intertidal zones, where boats don't navigate, such as in Dieppe. Nevertheless, precisions of our data are sufficient to map geomorphological features smaller than 0.5 m² along coastal cliffs.

At the same time, our capability to detect rockfalls and erosion deposits (> m³) is confirmed with classic approaches computing shortest distances between sequential acquisitions. Sectors with different rockfall susceptibilities have indeed been underlined, clearly detecting many cliff collapses between Pourville and Quiberville and only sparse changes between Dieppe and Belleville-sur-Mer. In addition, the Dieppe large landslide geometry has also been described, emphasizing 2 main active scarps with retrogression up to 40 m and about 100'000 m³ of eroded materials. In order to enhance detection mapping, we suggest dividing the point clouds in shoreline sections of constant aspect to refine alignments of piecewise data on the interpolated mesh of the reference point cloud; this alignment step actually minimize uncertainties from the INS measures.

Finally at larger scales, ALS and MLS might thus be used as complementary techniques along long coastlines with successions of gentler (optimized for ALS devices) and steeper (optimized for MLS devices) topographies. Additional acquisitions should be performed in the North of the study area along gentler slopes to experiment the potential inputs of using both techniques. Meanwhile, MLS capabilities for accurate change detection and mass balance monitoring along sub-vertical coastlines at low costs (compared to ALS devices and flights) could really support:

- Cliff retreat rates assessments for different sectors, by automatically extracting surfaces affected by rockfalls, compared to the entire surface of km long scanned cliffs. The routine developed by Carrea et al. (2014), that computes volumes, is indeed already able to individualize each collapsed block and could hence be adapted to also assess their surfaces;
- Landslide modelling and forecasting (Fukuzono 1990; Leroueil 2001; Rosser et al. 2007; Abellán et al. 2010; Royán et al. 2014) to manage risks dealing with affected infrastructures and inhabitants.

3.6 Supplementary material: Post processing captions



Post-processing of MLS point cloud: (A) J3 point cloud, after step 1; the initial scan has 3'234'761 points. (B) 1st manual selection of points due to outliers and sunshine and Channel reflexion artefacts, as explained in step 2. (C) Second manual selection of noisy points. The cleaning step is an iterative process. (D) Automatic selection of points with signal intensity lower than 12 (on a scale [0;255]), as explained in step 3. (E) Final J3 point cloud of the Ailly test site, manually and automatically cleaned, ready for the xyz exportation of step 4; the cleaned scan has 3'118'836 points. (F) Selection of the subset point cloud, including only points on cliffs, as detailed in step 5; the subset point cloud has finally 2'539'891 points.

3.7 Updates from the 2014 acquisition campaign

Conditions and LiDAR parameters of acquisitions of the 22 and 23 September 2014

	L1	L2	Ma1	Ma2
Sector	Veules > Quiberville	Quiberville > Dieppe	Fécamp > StPierre	StPierre > Veulettes
Scan beginning time	15h07	16h29	11h09	12h33
Scan end time	16h25	18h00	12h30	13h46
Range to cliffs	600-800 m	600-800 m	600 m	600 m
Tide	Low	Low	> Up	> Low
Boat velocity	~4-4.5 kn	~4-4.5 kn	5 kn	5 kn
Sea conditions	3 Bft	3 Bft	1 Bft	1 Bft
Sun	Cloudy sun	From the side	Sun	Sun
LiDAR vertical aperture	18°	18°	20°	20°
Angular resolution index	47	47	40	40

Conditions and LiDAR parameters of acquisitions of the 24 and 25 September 2014

	Ma3	Ma4	Me1	Me2	J1
Sector	Veulettes > Veules	Dieppe > Penly	Penly > Criel	Criel > Ault	Dieppe
Scan beginning time	13h50	16h41	9h08	10h29	Morning
Scan end time	15h29	17h50	10h24	11h50	
Range to cliffs	600 m	600 m	600 m	600 m	Close
Tide	> low	> low			
Boat velocity	4.5 kn	4.8 kn	~4.5-5 kn	5 kn	~2-3 kn
Sea conditions	1 Bft	1 Bft	3.5 Bft	4 Bft	1.5 Bft
Sun			Cloudy	Cloudy	From the side
LiDAR vertical aperture	20°	20°	20°	20°	20°
Angular resolution index	40	40	40	40	30



Figure 3.20: Photo of the Dieppe Landslide the 22 September 2014 (cf. Section 3.4.2b and Figures 3.17).

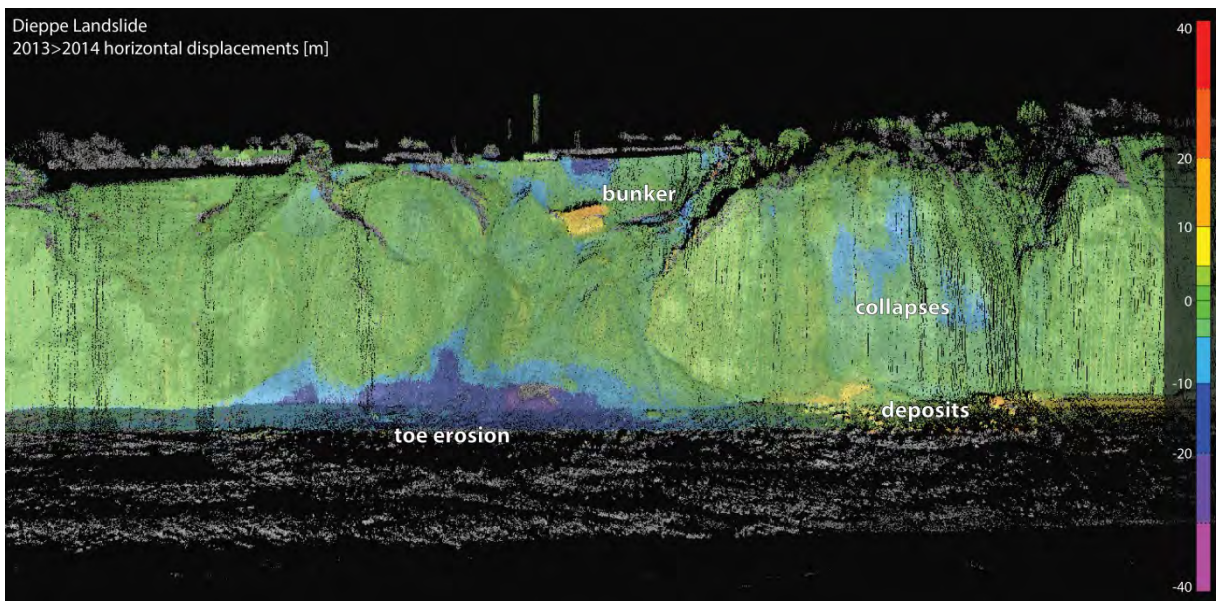


Figure 3.21: Fine horizontal comparison of the Dieppe landslide (cf. Section 3.4.2b and Figures 3.17 to 3.19) between Septembers 2014 and 2015. (Negative values: eroded material; Positives values: accumulated material)

4 Large slope deformations detection and monitoring along shores of the Potrerillos dam reservoir, Argentina, based on a Small-Baseline InSAR approach

After Michoud C, Baumann V, Lauknes TR, Penna I, Derron MH and Jaboyedoff M: Large Slope Deformations Detection and Monitoring along Shores of the Potrerillos Dam Reservoir, Argentina, based on a Small-Baseline InSAR Approach. *Landslides*, 24 p., published online 30 April 2015, in press.

Abstract

The Argentina National Road 7 that crosses the Andes Cordillera within the Mendoza province to connect Santiago de Chile and Buenos Aires is particularly affected by natural hazards requiring risk management. Integrated in a research plan that intends to produce landslide susceptibility maps, we aimed in this study to detect large slope movements by applying a satellite radar interferometric analysis using Envisat data, acquired between 2005 and 2010. We were finally able to identify two large slope deformations in sandstone and clay deposits along gentle shores of the Potrerillos dam reservoir, with cumulated displacements higher than 25 mm in 5 years and towards the reservoir. There is also a body of evidences that these large slope deformations are actually influenced by the seasonal reservoir level variations. This study shows that very detailed information, such as surface displacements and above all water level variation, can be extracted from spaceborne remote sensing techniques; nevertheless, the limitations of InSAR for the present dataset are discussed here. Such analysis can then lead to further field investigations to understand more precisely the destabilizing processes responsible for these slope deformations.

Keywords: Slope deformations, Detection, Monitoring, InSAR, Small baseline, Dam reservoir, Argentina.

4.1 Introduction

Landslide susceptibility mapping at regional scale is the starting point to detect areas exposed or potentially exposed to natural hazards and it is an essential support for hazard and risk assessment. In particular, the detection of active and large instabilities is decisive since these deformations can turn into rapid movements such as spreads, rockfalls or even rock avalanches (Crosta et al. 2013) that may affect infrastructures and/or population.

Landslides inventories constitute thus key baseline information during hazard assessments (Fell et al. 2008; Guzzetti et al. 2012). A classic approach to perform inventories is to use aerial photos, as these pictures provide an overall point of view of a large area (Rib and Liang 1978; Záruba and Mencl 1982). Nowadays, Aerial Laser Scanning (ALS) is widely used to produce High Resolution Digital Elevation Models (HRDEM) at regional scales; HRDEM have then become an essential input data of regional landslides inventory maps (Chigira et al. 2004; McKean and Roering 2004; Ardizzone et al. 2007; Jaboyedoff et al. 2012b; Pedrazzini et al. 2012). Their high level of detail allows indeed to identify main morpho-structural features developed as a result of slope deformations, such as crowns, counterscarps, double ridges or trenches being created by deep-seated slope deformations (DSGSD, e.g. Chigira 1992; Agliardi et al. 2001; Braathen et al. 2004; Crosta et al. 2013; Hungr et al. 2014).

In addition to aerial imaging and HRDEM, satellite Interferometric Synthetic Aperture Radar (InSAR) can also be used to update inventories and state of activities of slow slope deformations, as the method has proven suitable to detect and monitor extremely slow rotational slides, topples and spreads at regional scales (Massonnet and Feigl 1998; Lauknes et al. 2010; Henderson et al. 2011). The main principle of radar interferometry is based on studying the phase difference between two different synthetic aperture radar (SAR) images (Massonnet and Feigl 1998; Bamler and Hartl 1998). The main applications of InSAR are generation of topographic models (Shapiro et al. 1972) and studies of surface deformations (Massonnet et al. 1985; Gabriel et al. 1989), applied to crustal deformations (Massonnet et al. 1993; Massonnet et al. 1995; Sigmundsson et al. 1997) or even to landslides (Fruneau and Apache 1996; Carnerc et al. 1996; Kimura and Yamaguchi 2000; Squarzoni et al. 2003; Berardino et al. 2003; Saroli et al. 2005; Yin et al. 2010; García-Davalillo et al. 2014).

However, single interferograms are often difficult to interpret due to phase propagation delays related to different atmospheric conditions (Tarayre and Massonnet 1996; Zebker et al. 1997; Hanssen 2001; Doin et al. 2009). The last decade, new algorithms have been developed, such as persistent scatterer interferometry (PSI) (Ferretti et al. 2001), small baselines (SBAS) (Berardino et al. 2002) or SqueeSAR (Ferretti et al. 2011). They aim to improve the reliability of measures by separating movement signals from typical noise sources, and to provide temporal evolution of deformation behaviours. For example, the SBAS technique stacks and filters multi-temporal interferograms with small spatial baselines, increasing the signal to noise ratio (SNR) allowing tracking of temporally coherent distributed scattering.

These advanced algorithms are then frequently used for accurate landslide mapping and monitoring (e.g. Colesanti and Wasowski 2006; Fornaro et al. 2009; Herrera et al. 2011 and 2013; Lauknes et al. 2010; Bianchini et al. 2012; Cigna et al. 2013; Crosta et al. 2013; Bardi et al. 2014). Nevertheless, they are still often used as a complementary material to support pre-existing inventories updating state of activities of detected landslides (Guzzetti et al. 2012), since advanced InSAR techniques do not

usually detect more than 50% (e.g. in Bianchini et al. 2012; Herrera et al. 2013) of instabilities in rough relief terrains. It is mainly explained by (1) undetectable areas on westward and eastward slopes that are invisible by the SAR sensor stemming from geometric and radiometric distortions and (2) undetectable deformations on northward and southward slopes since they are easily perpendicular to the sensor line of sight (LOS) in both ascending and descending acquisition orbits (Hanssen 2001; Woodhouse 2006; Cascini et al. 2009). In addition, the ratio of detected landslides by such techniques can even be lower in densely vegetated areas, affected by strong decorrelations.

Following these statements, we carried out large slope deformation detections along the Argentinian National Road 7 (N7) within the Mendoza province, Argentina. The N7 is indeed an essential corridor of Southern America, linking Buenos Aires to Santiago de Chile by crossing the Andes Cordillera at the Cristo Redenor international pass up to 3'200 m a.s.l. At least 2'200 cars and trucks use the road every day (Dirección Nacional de Vialidad 2013). At the same time, this road section along the Mendoza River is exposed to numerous natural hazards, such as snow avalanches and landslides, and remains therefore frequently closed (Baumann et al. 2005). It represents an hazard for road users that must be considered and it also implies regional economic losses in case of prolonged road closure. Furthermore, the N7 follows the south-western reservoir shores of the Potrerillos hydropower dam (fully operational since the mid-2000s), which is a main source of drinking water and energy for the Mendoza city, as well as a touristic site. As reservoir-landslides interactions were reported in many investigations worldwide (Terzaghi 1950; Müller 1964; Riemer 1995; Wang et al. 2008; Schuster 2006; Bell 2007; Pinyol et al. 2012; Xia et al. 2013) slope deformation may also affect the N7 close to the reservoir. In addition, it has been regularly monitored with SAR techniques (Fu et al. 2010; Singleton et al. 2014; Tomás et al. 2014).

In this context, a long-term project, initiated by the Argentinian Geological Survey and the University of Lausanne, plans to produce inventory and susceptibility maps for snow avalanches, debris flows, rockfalls and slides (Wick et al. 2010a and b; Baumann et al. 2011) along the N7, between Potrerillos and Las Cuevas near the Chilean border (Figure 4.1), by means of remote sensing and regional numerical modelling approaches coupled with classical field survey (Jaboyedoff et al. 2012b). Within this framework, this study aims at making an inventory of large slope deformations. But without available HRDEM and orthophoto, a small baseline (SBAS) approach (Berardino et al. 2002) has hence been selected to detect as much large mass movements as possible, since the main landscapes with low and sparse vegetation and many outcrops (Figure 4.1) constitute relevant distributed scatterers (Lauknes et al. 2010).

In this paper, we therefore present results based on active mass movement detection by SBAS processing of ESA's Envisat satellite SAR images between Potrerillos and Uspallata, with a specific focus along shores of the Potrerillos dam reservoir where large slope deformations are detected and monitored.

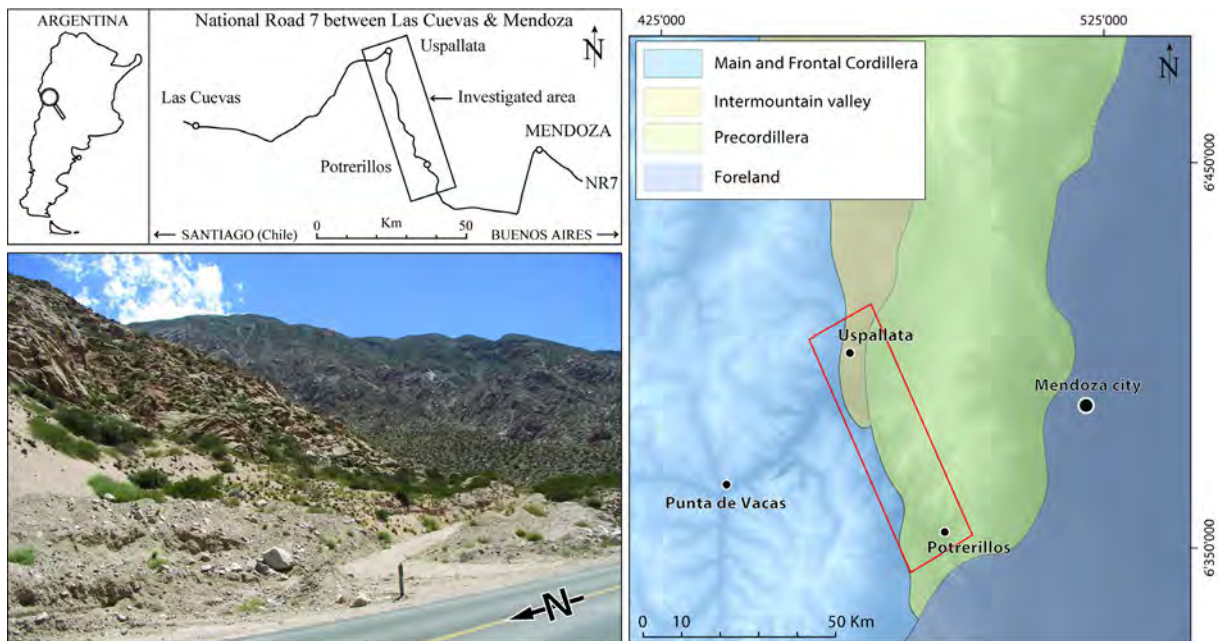


Figure 4.1: (Upper left) Location of the study area within the Mendoza Province. (Lower left) Illustration of the dominant landscape along the N7 corridor, where a rocky landscape with low and sparse vegetation is observed. (Right) Main morphotectonic units comprised in the study area.

4.2 General setting

4.2.1 Morphotectonic context

The study area extends along two main morphotectonic units named from west to east: Cordillera Frontal and Precordillera; both are separated by an intermountain valley (Figure 4.1). Here the tectonic style of the eastern Andes is strongly influenced by morphological and tectonic features related to Triassic and Paleozoic structures, reactivated during the Cenozoic (Kozłowski et al. 1993). In this region, oblique thrust fault structures with NW and NNW directions are widespread. In the following paragraphs, we describe main characteristics of these units:

- The Frontal Cordillera was uplifted during the Neogene by high-angle east-vergent reverse faults (Ramos 1997). Main outcrops correspond to the Permian-Triassic Choiyoi Group, composed of extrusive and intrusive igneous rocks. The relief of the Cordillera Frontal results from high rate uplift since the Neogene, and glacial and fluvial incision. Landscape was shaped by glaciers during Quaternary times, whereas current glaciers are constrained to a reduced area at high altitudes (3800 m a.s.l.; Trombotto and Borzotta 2009). Glacial retreat and seismic activity were proposed as conditioning factors of large slope collapses that have taken place in Holocene times (Hermanns et al. 2014).
- The Precordillera corresponds to a fold and thrust belt structured by east and west-vergent basement faults deforming Proterozoic to Neogene metamorphic and sedimentary rocks

(Giambiagi and Martinez 2008). In the Potrerillos area, Triassic conglomerates, sandstones, mudstones and volcanoclastic rocks uncomfortably overlay the Permian-Triassic volcanoclastic rocks from Choiyoi Group (Stipanovic 1979). On South and East of Potrerillos lake, outcrops are Neogene sedimentary rocks (Folguera et al. 2003). Here it is observed a dense drainage networks composed of slightly permanent or ephemeral colluvial creeks and gullies that give place to a rough landscape. The slopes are characterized by low gradients, where an erosive surface developed on Triassic to Tertiary sedimentary rocks. The eastern foothills show wide alluvial deposits belonging to different aggrading levels (Polansky 1963).

Between Uspallata and Potrerillos, the Mendoza River crosses the Frontal Cordillera and Precordillera with NW-SE direction. The Mendoza River here has an anastomotic pattern in addition to three main levels of terraces. At both sides of the valley, alluvial and colluvial fans are observed at the mouth of tributary rivers, as well as talus at the toe of rockslopes. Pediment surfaces with at least three different levels are well developed in the Potrerillos area (Figure 4.2).

4.2.2 Landscape and active surface processes

The landscape presents maximum elevations of 5400 m a.s.l. and lowest at around 1500 m a.s.l. Weather is characterized by arid and semi-arid conditions, with mean annual rainfall of 140-360 mm (Subsecretaría de Recursos Hídricos 2013). Most of the storms take place during October-March, and from June to August is the period of high snow fall. Mean temperature varies with altitude, between 1200 m a.s.l. and 3800 m a.s.l., namely 20°C and 4°C in summer and 5°C and -7°C in winter respectively (Fernández García and Polimeni 2003). The vegetation is sparse and mainly composed of thorny thickets, grass family and cactuses.

U shaped valleys are observed at high altitude, and in some places rock glaciers remain. At lower altitudes, landscape is dominated by fluvial action (Folguera et al. 2003). At Uspallata, the Mendoza River runs in a NE-SW direction, and then turns to the SE up to Potrerillos area, where a hydropower dam was built, creating a permanent water body extending around 9 km along the Mendoza valley (Figure 4.2).

Due to its tectonic and geomorphic history, the area has been active in terms of hillslope processes. Several large magnitude slope collapses have taken place during Holocene times. Eight rock avalanches with volumes of several million m³ were indeed mapped near Uspallata. Their detachment was located along the Carrera fault system and involved Permo-Triassic volcanic rocks of the Choiyoi Group (Fauqué et al. 2000). In addition, a large landslide was also recognized near the northern shore of the Mendoza river, 22 km upstream the Potrerillos reservoir (Fauqué et al. 2005). While these mass movements are proposed to be conditioned by active tectonic conditions, those located to the west of Uspallata, near Punta de Vacas in the Frontal Cordillera, have been proposed

to be linked to debuttressing of valley flanks after the glacial retreat (Fauqué et al. 2000 and 2005; Cortés et al. 2006; Hermanns et al. 2014).

Current active surface processes involve mainly snow avalanches, debris flows and rockfalls. Every year, the N7 is affected by several events from Potrerillos to Chile (Baumann et al. 2005 and 2011; Moreiras 2005 and 2006; Wick et al. 2010a and b). For example, in 2005, a $7 \times 10^4 \text{ m}^3$ debris flow covered the N7 at the Guido's curve along 300 m, hitting a car and stopping 3'000 vehicles during 12 hours (Wick et al. 2010b). Moreover, a large rock fall ($< 100 \text{ m}^3$) occurred in 2011 near the Guido's curve from an anthropic road cut slope in volcanic rocks reached the way and caused one fatality. In addition, in the Potrerillos area, rockfalls are widely recorded along cut over dip slopes on soft Triassic and Neogene sandstones and conglomerates. Morphology conditions, degree of rocks fracturing, amounts of sediments stored on watersheds and also unstabled cut-slope design are the main conditioning factors of these active processes. They are mostly triggered by rainfall and snow melting, but earthquake have also generated rock falls in the area (Wick et al. 2010a).

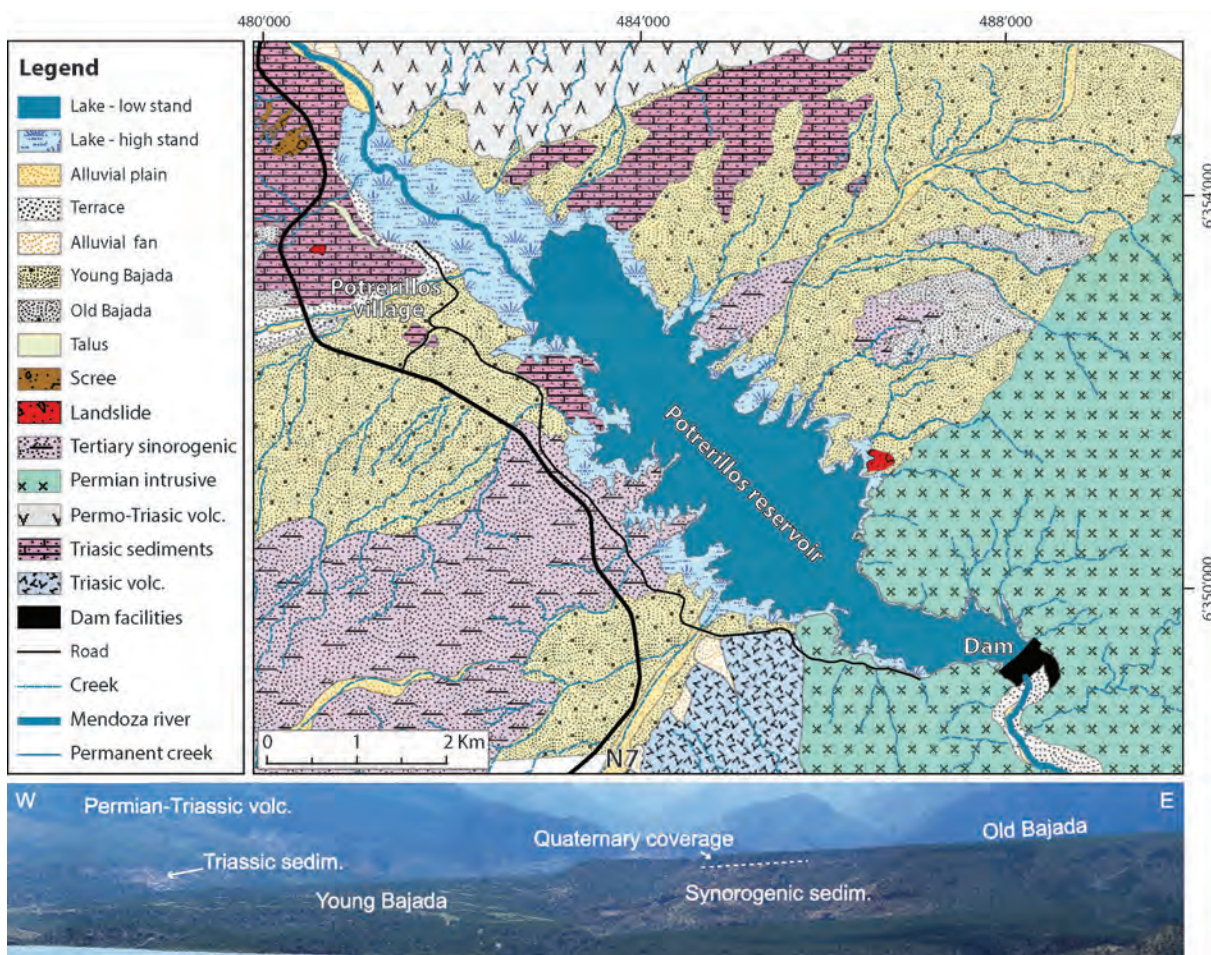


Figure 4.2: Geomorphologic map of the Potrerillos area (ages of units taken from Giambiagi et al. 2011), and Panorama picture of the north-eastern margin of the lake showing main geomorphologic and geologic units. The mapped landslide refers to the one described in the supplementary material.

4.3 SAR data processing

4.3.1 Available SAR data

Our analysis is based on 47 SAR images acquired by the European Space Agency (ESA) Envisat ASAR instrument. The scenes cover the road section Mendoza-Uspallata during the 2005–2010 period from both ascending and descending orbits (Figure 4.3).

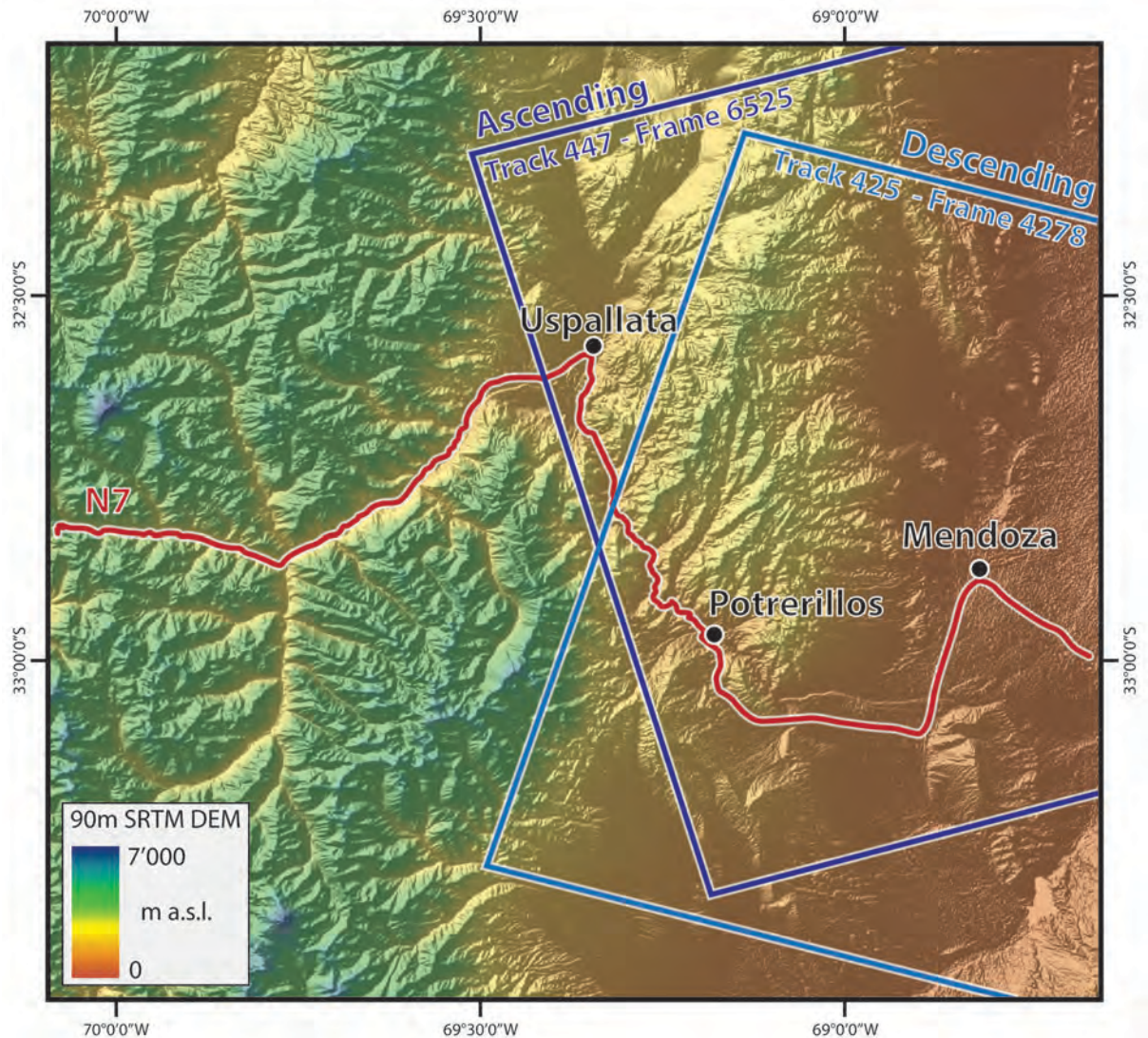


Figure 4.3: Frames of the Envisat ASAR ascending and descending scenes of the study area, wrapped on the 90m SRTM DEM used for the SBAS processing. (Raw Envisat data: ©ESA 2010; raw DEM data: ©SRTM NASA).

The 27 ascending scenes (track 447, frame 6525) were acquired from January 2005 to November 2006 and June 2009 to February 2010, whereas the 20 descending scenes (track 425, frame 4278) are from September 2007 to January 2010 (Table 4.1). Finally, the 90 m DEM acquired by the SRTM mission in 2000 (Jarvis et al. 2008) will be used to filter unwanted topographic- and atmospheric-related contributions.

Table 4.1: Envisat's tracks/frames 447/4278 and 425/6525 of SAR scenes provided by the ESA for this study (ESA Category-1 Project 7154).

Dates for ascending scenes [yyyy.mm.dd]	Dates for descending scenes [yyyy.mm.dd]
2005.01.11	2007.09.19
2005.02.18	2007.11.28
2005.03.25	2008.01.02
2005.04.29	2008.02.06
2005.06.03	2008.03.12
2005.07.08	2008.04.16
2005.08.12	2008.06.25
2005.09.16	2008.07.30
2005.10.21	2008.09.03
2005.11.25	2008.10.08
2006.02.03	2008.11.12
2006.03.10	2009.02.25
2006.04.14	2009.04.01
2006.05.19	2009.05.06
2006.06.23	2009.06.10
2006.07.28	2009.07.15
2006.09.01	2009.08.19
2006.10.06	2009.09.23
2006.11.11	2009.10.28
2008.04.18	2010.01.06
2009.06.12	
2009.07.17	
2009.08.21	
2009.09.25	
2009.12.04	
2010.01.08	
2010.02.12	

4.3.2 Landslides detection at regional scale

a. Regional SBAS processing

The Norut *GSAR* software (Larsen et al. 2005; Lauknes et al. 2010) has been used for all InSAR processing, following the principal steps described hereafter. Main settings are summarized in Table 4.2. For each dataset, raw SAR images are first focused to single-look-complex and then co-registered to ensure a perfect overlap between pixels from the different scenes in SAR geometry.

Regarding the ascending scenes, 107 interferograms with temporal and normal baselines (respectively time and distance intervals) lower than 1200 days and 400 m are computed (Figure 4.4A). In addition, 58 interferograms are calculated comparing the descending scenes having temporal and normal baselines lower than 400 days and 230 m (Figure 4.4B); smaller baselines were optimized for this second dataset since the descending acquisitions had shorter spatial and temporal baselines. For each interferogram, the topography-related phase was removed from the external

SRTM DEM using mathematical developments defining InSAR signal construction and simulating the DEM signal response (more details available in e.g. Massonnet and Feigl 1998; Hanssen 2001; Woodhouse 2006).

However, phase propagation delays created by temporal changes in atmospheric conditions within the troposphere between SAR acquisitions and orbital correction errors can still introduce artefacts and hamper interpretation (Zebker et al. 1997; Hanssen 2001). Interferograms too much affected by these artefacts were removed from the study using manual inspection; all interferograms having large areas with incoherent noise and no well-defined fringe patterns were deleted. Finally, 57 ascending and 36 descending interferograms were selected for processing.

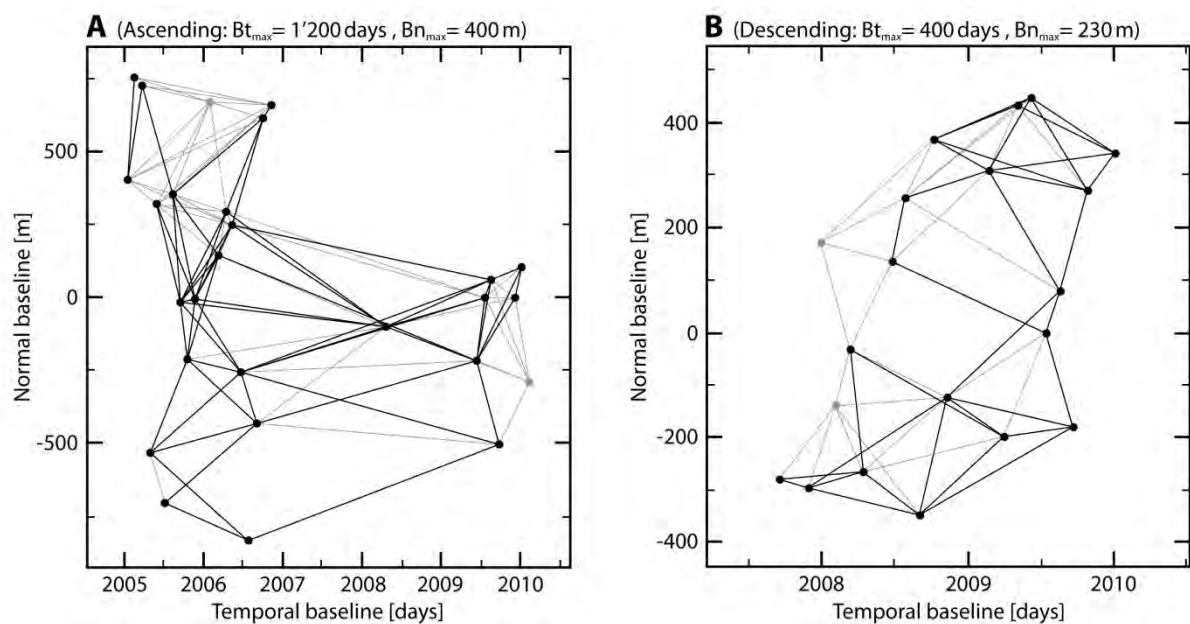


Figure 4.4: Normal baselines vs. temporal baselines plot (A) of the 107 interferometric ascending pairs using thresholds of 1'200 days and 400 m, and (B) of the 58 interferometric descending pairs using thresholds of 400 days and 230 m. Every line corresponds to a computed interferogram between 2 acquisitions; black lines correspond to interferograms kept after selection, while the grey lines are the non-selected ones.

The phase unwrapping step, which converts each ambiguous 2π cycle to absolute value of interferometric phase, is performed with the *SNAPHU* software (Chen and Zebker 2001). Prior to this step, noisy areas have been masked out in order to ensure a suitable continuity of values with a good enough coherence to be interpreted. Pixels with coherence lower than 0.35 on 50% of interferograms were thus masked out, which are about 66% of pixels of ascending interferograms and 50% of pixels of descending ones.

InSAR-based results are relative displacements between scatterers that need to be calibrated to get absolute ground movements. To do that, a common reference area (for which we assume no movements) is used for both ascending and descending processing. Ideally, this pixel must be in a

stable place, close to the study area and inside a cluster of several very coherent pixels; the pixel should also be in an area that remain stable when fixing the reference in different places during prior test processing. For these reasons, we selected a coherent point within an assumed stable area in the northern-western part of the Potrerillos reservoir and close to the N7 (Figure 4.5 and Figure 4.6). Finally, the stacks of unwrapped interferograms were inverted to extract time-series displacements and mean velocity for each pixel by applying the SBAS method.

Table 4.2: Main set parameters for SBAS processing with the *GSAR* software.

	Ascending scenes		Descending scenes	
	Regional	Local	Regional	Local
Size of scenes	47x140 km	10x8 km	46x92 km	37x32 km
Number of scenes	27		20	
Look azimuth-angle	074°27°		286°30°	
Max. temporal baseline	1'200 d		400 d	
Max. normal baseline	400 m		230 m	
Number of total interferograms	107		58	
Number of selected interferograms	57	75	36	23
Coherence thresholds	0.35 on 50% of interferograms			
Reference point (UTM19°S)	481'386 6'353'063	481'360 6'353'051	479'424 6'356'660	479'452 6'356'672
Number of reflectors	2'300'000	38'000	2'400'000	340'000

b. Results of the regional approach

Figure 4.5 displays the mean displacement velocities measured in the satellite line of sight direction (LOS), extracted from the ascending SBAS processing. We assume here that the largest part of the whole processed study area, mainly composed of Triassic to Neogene sedimentary rocks in the Foreland plains (Folguera et al. 2003), is not affected by large slope instabilities and that no regional tectonic deformations affect SBAS results (cf. Section 4.4.1); pixels from stable areas should thus constitute the highest majority of the coherent reflectors. Furthermore, we notice that both processed mean LOS velocities can be fitted by normal distributions; velocities of stable pixels, theoretically close 0 mm/yr, thus fix the mean of the normal distribution. As a result, by highlighting reflector clusters having velocities within high standard deviation ranges ($>2\sigma$), we detect either areas affected by strong artefacts or large slope displacements (Figure 4.5).

We also note that ascending results are less noisy than the descending ones (Figure 4.6), since the mean LOS velocity of all scatterers has a median and standard deviations of -1.2 and 2 mm/yr for ascending scenes, instead of -7 and 11 mm/yr for descending ones. Then regarding the spatial distribution of the about 2.4 million coherent points of ascending and descending processing, we can

state that point density is relatively high on the eastward and northward plains. It corresponds to areas with good coherence. On the contrary, elevated and steeply sloping regions have only sparse reflectors; the majority of them were indeed masked out since their coherence was lower than 0.35. This is probably due to steepness of terrain introducing radar geometrical effects such as foreshortening and shadowing, and also due to low coherence because of snow cover.

Regarding our region of interest, between Potrerillos and Uspallata, no cluster with significant velocity deviations imputed to slope instabilities can be thus detected, since pixels on steep slopes along the N7 corridor are indeed masked out (cf. Section 4.4.2). But, in the meantime, although no clear evidences of large landslides can be noticed on noisy descending results (Figure 4.6), we observe on ascending ones several distinct downward mass movements along gentle shores of the Potrerillos earth dam reservoir (Figure 4.5). Since these deformations may affect the N7, focused investigations are then achieved.

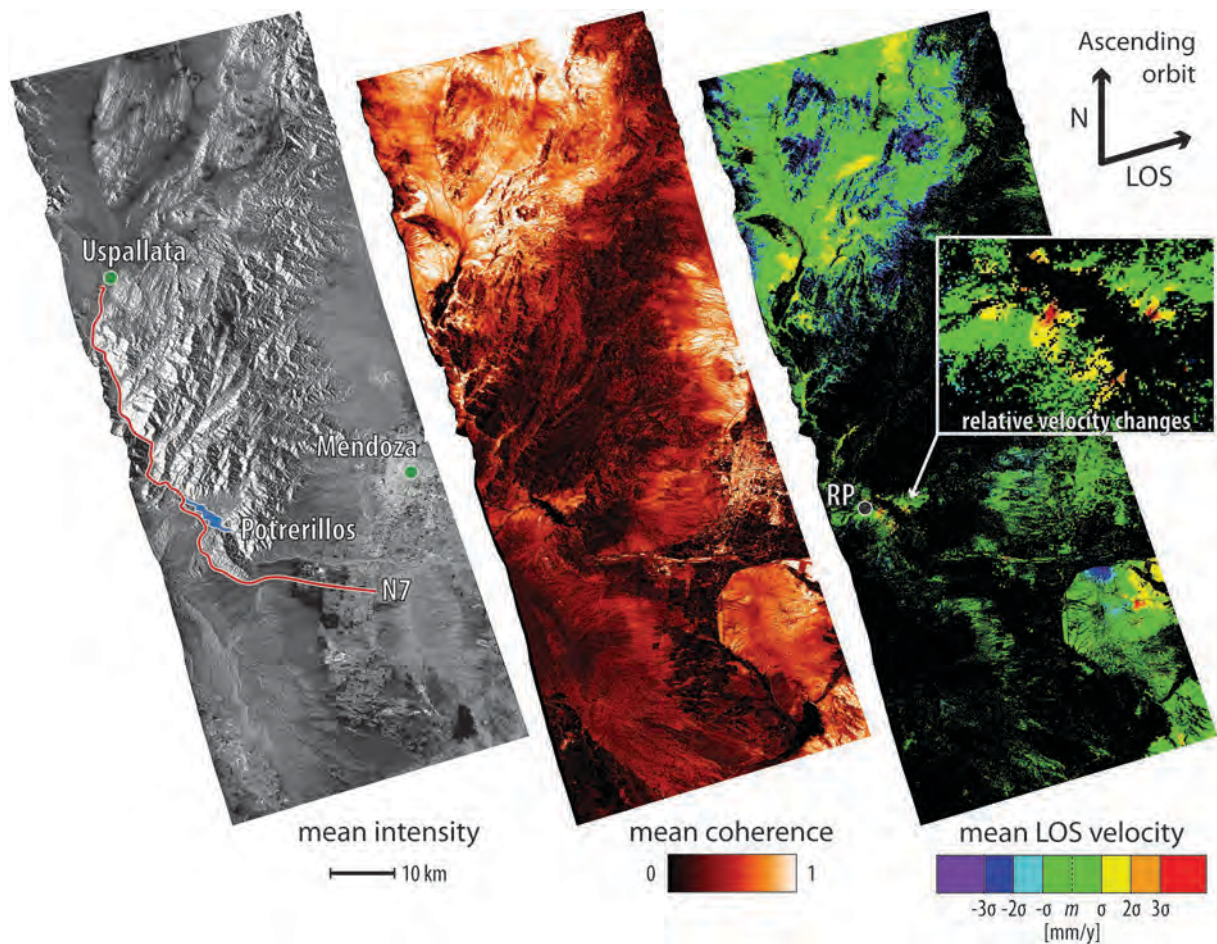


Figure 4.5: (Left) mean intensity of the 27 ascending scenes, (middle) mean coherences and (right) mean LOS velocities extracted from the SBAS processing of the 57 selected interferograms, with a median movement (m) of -1.4 mm/yr and a standard deviation (σ) of 2 mm/yr. Several downward mass movements along shore of the Potrerillos dam reservoir are noticed. In addition, other ground deformations are detected south of Mendoza close to oil extraction facilities. (Positive values: downward displacements, away from the sensor. Negative values: upward displacements, toward the sensor. Raw Envisat data: ©ESA 2010).

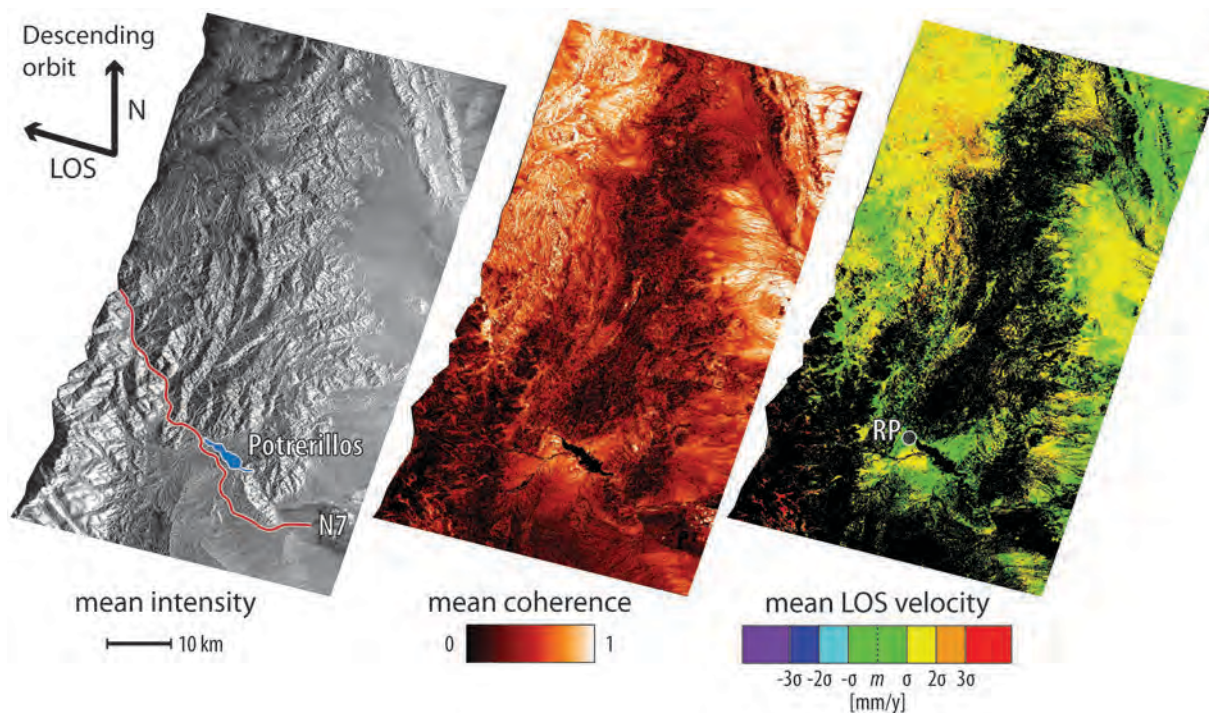


Figure 4.6: (Left) mean intensity of the 20 descending scenes, (middle) mean coherences and (right) mean LOS velocities extracted from the SBAS processing of the 36 selected interferograms, with a median (m) of -7 mm/y and a standard deviation (σ) of 11 mm/y. (Positive values: downward displacements, away from the sensor. Negative values: upward displacements, toward the sensor. Raw Envisat data: ©ESA 2010).

4.3.3 Landslides monitoring along shores of the Potrerillos' dam reservoir

a. Local SBAS processing

A focused SBAS processing is now carried out on this Potrerillos reservoir area. Main settings described in section 0 and Table 4.2 (such as maximal temporal and spatial baselines and coherence thresholds) are again applied. Nevertheless, the selection of interferometric pairs showing coherent signal within this smaller region of interest was optimized for this local study in order to extract displacement time series as reliable as possible. We indeed select 75 ascending and 57 descending interferograms; in addition, the reference point of the ascending processing was set in the new Potrerillos village in a cluster of very coherent pixels where no significant displacement was identified on regional results. For the same reasons, the reference point of the descending processing was set 2.5 km westwards from the Potrerillos village.

b. Detection and monitoring results

On the ascending results, two large mass movements with areas above the water level of about 2.5 and 0.7 km² are detected on the western and eastern shores of the lake. Both have cumulated

displacements higher than 30 mm in 5 years (Figure 4.7) and their velocity gradients suggest a general dip direction toward the reservoir.

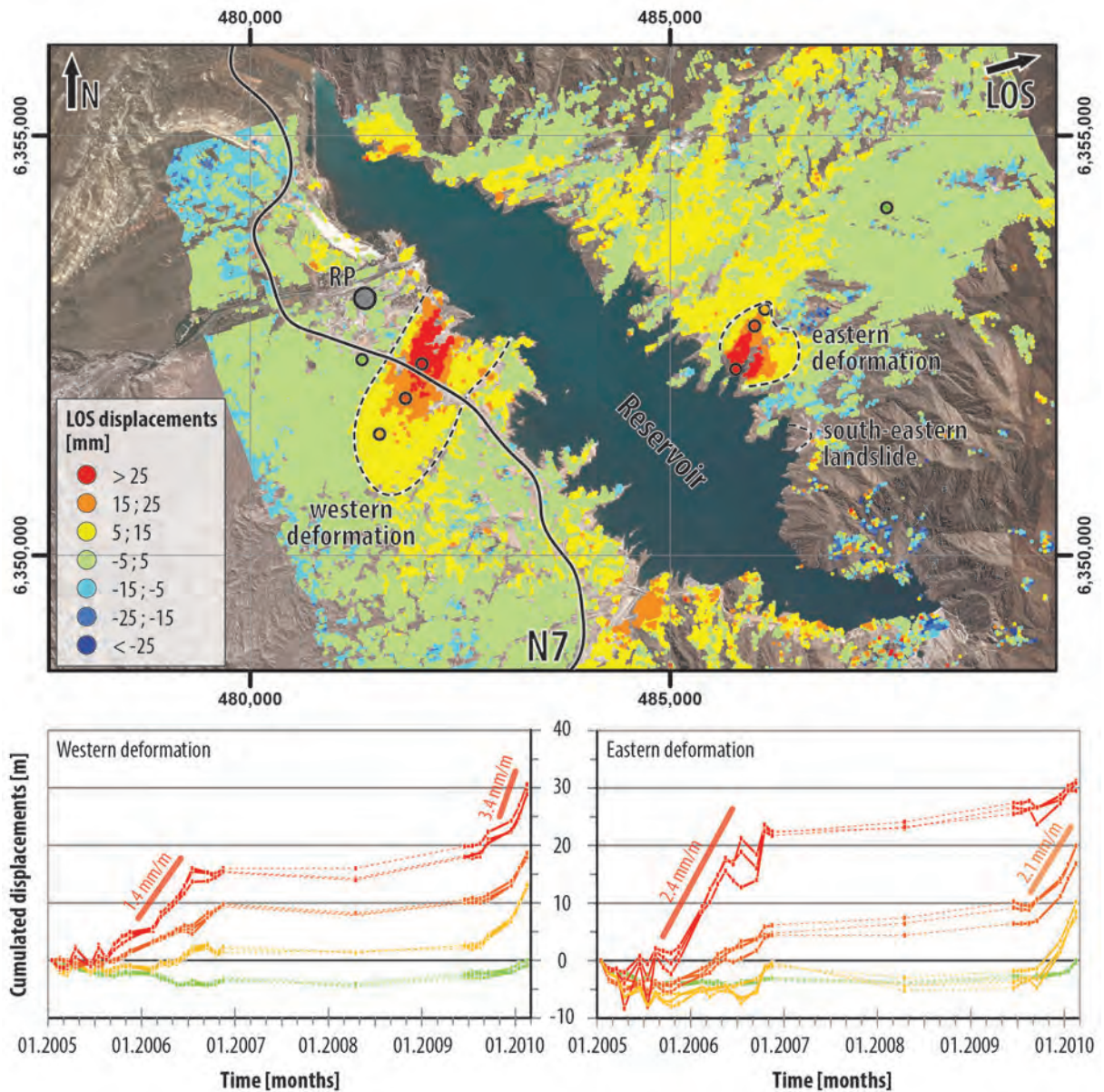


Figure 4.7: (Up) $LOS_{ascending}$ cumulated displacements and location of the 3 major surface displacements detected along the Potrerillos reservoir shoreline. (Down) Displacement time-series from January 2005 to February 2010 ($LOS_{ascending}$ projection) of several reflectors (coloured dots on map) within the western and eastern deformations and mean velocities. The dot lines underline potential fringe unwrapping ambiguity issues. The south-eastern landslide refers to the one described in the supplementary material. (Positive values: downward displacements, away from the sensor. Negative values: upward displacements, toward the sensor. Satellite image from ©GoogleEarth).

Smaller and slower movements are also noticed on the north-eastern and southern shores. Displacement time series furthermore confirm reliable patterns with constant and progressive movements during periods 2005-2006 and 2009 (when we got one acquisition each month), with mean velocities of about 8 mm/yr and up to 20 mm/yr respectively (Figure 4.7). On the contrary,

almost no displacements are extracted in 2007-2008, since having only one acquisition in 2 years increases significantly the fringe ambiguity potential issues (Woodhouse 2006). The total cumulated displacement measured on the ascending data, up to 30 mm in both large mass movements, is thus probably underestimated.

However, results from descending scenes (Figure 4.8) seem to be noisier with cumulated errors inside areas assumed as stable varying between about $[-7;7]$ mm in 2.5 years, instead of $[-5;5]$ mm in 5 years for the ascending interferograms. Moreover, the eastern deformation mapped in Figure 4.7 is not detected on this processing, and the western one is only detected on its upper part within a larger and slower mass movement.

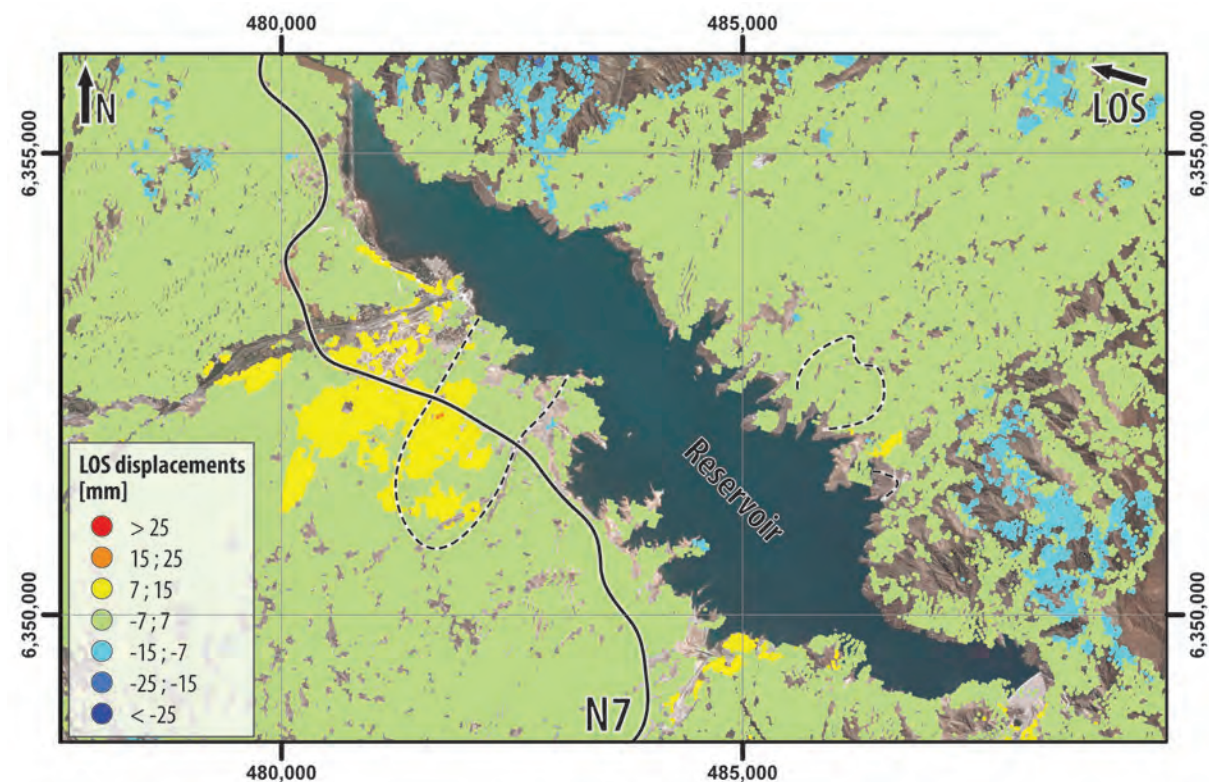


Figure 4.8: LOS descending cumulated displacements and location of the 3 major surface displacements detected along the Potrerillos reservoir shoreline. (Positive values: downward displacements, away from the sensor. Negative values: upward displacements, toward the sensor. Satellite image from ©GoogleEarth).

Their mechanisms and geometries (identified as deep extremely slow soft rock rotational and also translational slides), are afterward discussed in the Section 4.4.3.

4.3.4 Water level fluctuations of the reservoir

In order to study potential reservoir-landslides interactions, as it has been reported in many investigations worldwide since Terzaghi in 1950, the water level variation along time of the Potrerillos reservoir has been surveyed and extracted from SAR return amplitude images (Figure 4.9).

These variations are first qualitatively assessed by comparing the reservoir surface changes along time. Indeed the larger the reservoir area is, the higher is the water level (López et al. 2011). Afterwards we select on each of the 47 amplitudes images 16 pixels well distributed along the reservoir shoreline and we estimate their elevation by overlapping these images on the SRTM DEM. We compute for all scenes the median (attenuating extreme value effects; Höhle and Höhle 2009) and the standard deviation of the 16 values; we then delete outliers and compute again filtered standard deviation, in order to decrease errors introduced by the SRTM model and sometimes unclear limits between water and land at a pixel scale. The water level variation of the reservoir along time is finally assessed by connecting all median elevations while first qualitative observations must be respected.

As a result, we notice that the water level is varying along time between -25 m and +15 m around a mean level that makes a range of elevation of about 40 m, actually close to the 44 m (minimum and maximum levels are respectively at 1'342 and 1'386 m a.s.l.) stated in López et al. (2011). The reservoir level, artificially regulated, is usually high from February to August. It quickly draws down afterwards till December, and is then filled till the beginning of February, fed by usual high discharge peaks of the Río Mendoza in December and January due to the snow melting in the high river watershed (Subsecretaría de Recursos Hídricos 2013).

4.4 Discussions

4.4.1 Influences of the Andean orogen

Mendoza regions is subjected to tectonic uplift resulting from the compressive strains formed because of the subduction of the Nazca plate beneath the Sudamerican plate, which forms the Andean Mountains. The southern section of the central Andes is hence affected by significant Eastward shortening rates caused by episodic release of transient elastic deformations during large earthquakes and by permanent displacements due to the Pampean flat-slab and the mountain uplift (Gansser 1973; Ramos 1999). GNSS measurements are showing north-eastward displacement rates between about 7.3 mm/yr at San Juan and 19.4 mm/yr at Santiago de Chile (Kendrick et al. 1999).

These deformations are supposed to be uniform within our study area, since its extent is relatively small compared to the continental scale of the Andean orogen. This subduction component is therefore implicitly deleted at the beginning of the SBAS processing by focusing and co-registering the successive SAR scenes that might be translated by continuous mm displacements (cf. section 4.3.2.a) and is de facto not considered.

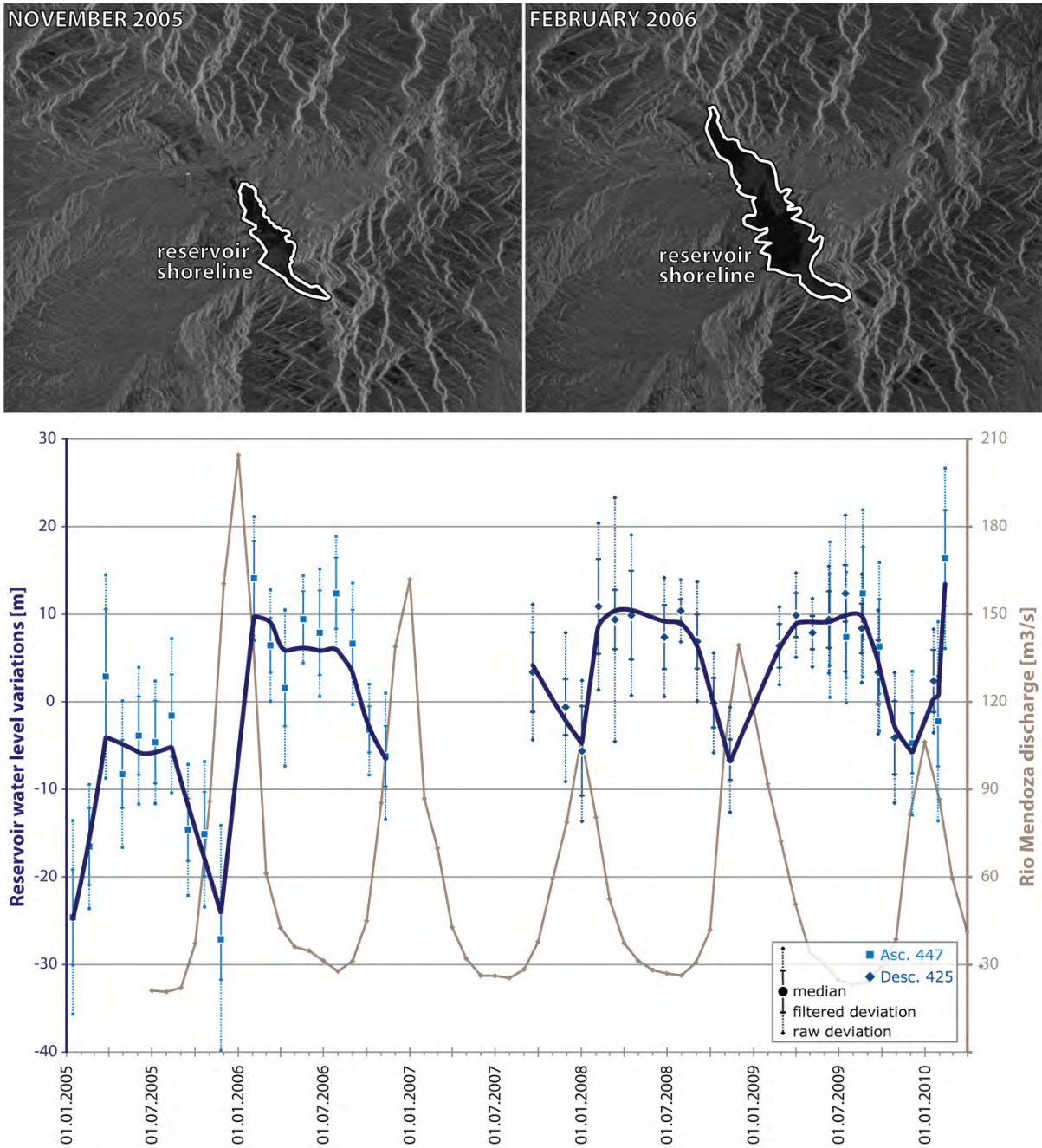


Figure 4.9: (Up) Delimitations on SAR return amplitudes images of the Potrerillos reservoir shorelines during low and high water level periods (November 2005 and February 2006 respectively). (Down) Potrerillos reservoir level fluctuations extracted from SAR return amplitude images compared to Río Mendoza discharge. (Raw Envisat data: ©ESA 2010; Río Mendoza discharge data at the Guido station: ©Subsecretaría de Recursos Hídricos).

4.4.2 Limitations to large landslides detection

Regional mean LOS velocities are correlated with the scatters' azimuth (in SAR geometry) and elevation on both regional processing. As illustrated in Figure 4.10, quadratic polynomial trends can indeed be fitted.

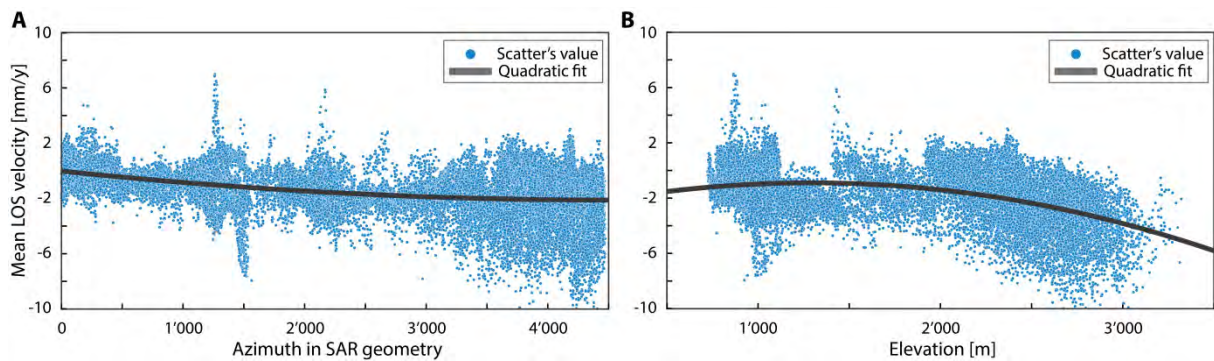


Figure 4.10: (A) Mean LOS velocities vs. azimuth plot, as well as (B) mean LOS velocities vs. elevation plot, and their quadratic trends. Data are extracted from the ascending SBAS processing, displaying 1/75 of points.

As we assume no influence of the Andean tectonic (cf. section 4.4.1), these correlations result from two main uncertainty sources in the input data. Firstly, the correlation of mean LOS velocities and azimuthal pixel coordinates may be misinterpreted as a regional N-S displacement trend, but it should actually be attributed to orbital errors. Inaccurate Envisat trajectories estimations with errors higher than 3 meters are indeed a common source of residual fringes on interferograms (Hanssen 2001) unrelated to any real ground movements. Secondly, the refractivity index of the atmosphere varies vertically, mainly because the successive horizontal layers of the stratified troposphere have specific water vapour pressures (Hanssen 2001). Differential vertical phase delays are thus recorded during SAR acquisition, according to the air column thickness (which is correlated with the topography) crossed by the radio wave. Hanssen (2001) even shows that the related interferometric phase errors can reach more than 35 mm for 2 points 2'500 m vertically apart.

The general trend, related to the orbital errors and the tropospheric delay, is hence estimated by fitting a quadratic polynomial function on mean LOS velocities according to azimuths and elevations and is then removed (performed in a *MATLAB*[™] environment). Nevertheless it did not improve our ability to detect large slope instabilities along the N7 corridor between Potrerillos and Uspallata, also as many points were masked out before this correction to unwrap the interferograms. More complex corrections included within the whole SBAS processing chain are indeed required and are under development (Lauknes 2011 and current research).

Moreover, a higher resolution DEM (other than the 30 m ASTER one that has too much artefact on those elevated areas) and some ground control points with 3D displacement time series would have

been also necessary to better estimate these topography-related delays and to ensure reliable reference point locations. Completed with additional Envisat data, especially for 2007 and 2008, it would considerably improve the SBAS processing by reducing the temporal and normal baselines, as well as fringe unwrapping ambiguity issues. Unfortunately these data, as well as ERS and ALOS ones, are not available for the study area.

4.4.3 SBAS-derived geometry

According to the Cruden and Varnes classification of landslides types (Cruden and Varnes, 1996), both deformations can be identified as deep extremely slow soft rock slides. Both deformations indeed involve weak sandstones and plastic clays of hundreds of meters deep (Folguera et al. 2003); they are moreover both extended over large areas, which let us assume that the main sliding surface is deep seated (Carter and Bentley 1985; Jaboyedoff and Derron 2015). In addition, the geometry of the sliding surface can be derived from the SBAS results. Differences of displacement ranges of the eastern and western deformations observed on the ascending and descending processing can indeed be explained with simple geometrical considerations. A same true displacement vector indeed produces 2 distinct responses once projected on the 2 different ascending and descending LOS vectors that have look azimuth-angle of $074^{\circ}27'$ and $286^{\circ}30'$, respectively, according to Envisat orbits.

Regarding the western deformation, assuming a north-eastward movement (i.e. 025° , toward the reservoir) as suggested by its displacement gradient, a plunge of 34° is necessary on its upper part to reproduce the 2 measured the ascending and descending SBAS responses. Moreover, a plunge of 05° in its lower part of this instability would be orthogonal to the descending LOS, explaining why no displacements are here detected on descending interferograms. The variation of the azimuth-plunge from $025^{\circ}34'$ in the upper part to $025^{\circ}05'$ to its toe seems to indicate a general rotation of the mass movement.

In the meantime, regarding the eastern deformation, a horizontal south-westwards displacement (i.e. $200^{\circ}00'$) would also be almost orthogonal to the descending LOS. The detection of this mass movement would here again be hampered in that geometry, explaining why the displacement is detected on the ascending results but not on the descending ones. A near horizontal translational displacement would in this case suggest a slope spread behaviour (Hung et al. 2014), which might be controlled by plastic clay deposits noticed here (cf. section 4.4.4; Folguera et al. 2003).

4.4.4 Reservoir-slope deformation interactions

We now compare the Potrerillos water level variations with displacements patterns of both monitored mass movements (Figure 4.11). In 2007 and 2008, no correlations between displacement

rates and the reservoir level can be observed, due to severe fringe unwrapping ambiguity issues that misrepresent SBAS measurements. But, we can nevertheless notice two periods of high displacement rates from February 2005 to July 2006 and September 2009 to February 2010, which actually correspond to reservoir drawdown and filling periods. It therefore seems that deformation behaviours are actually modified in case of drawdown or filling. In comparison to the relatively stable periods from June to August 2009, velocities indeed increase up to about 0.8 mm/month during the reservoir drawdown from October to December; later, from end of August to beginning of October and from December to February 2010, during filling periods, velocities increase up to about 2.7 mm/month. The same pattern can also be noticed between August 2005 and July 2006. Moreover, we observe that high displacement rates continue from mid-April to July 2006, i.e. during 2.5 months after the stabilization of the water level to its highest level reached for the first time. In addition, all displacements are measured downwards and no up and down fluctuations due soil swelling and drying associated to cyclic water level variations are observed.

According to the geological local map (Folguera et al. 2003), the western and eastern slope deformations are both developed on tertiary rocks, i.e. hundreds meters thick fine sandstones layers regularly interlayered with thin clay deposits and coarse conglomerates, and are locally covered by superficial Quaternary sedimentary breccia deposits. Destabilizing effects of reservoir drawdown have been reported in such lithologies, e.g. by Terzaghi (1950) or in Canelles (Pinyol et al. 2012) where the drawdown-induced landslide is mainly controlled by the low permeability and high plasticity of interlayered clay deposits. In addition, as reported in Riemer (1995) and Bell (2007) in such lithological contexts, sliding surfaces are frequently activated since water tables that significantly rise with reservoir filling may saturate bank materials, reducing the residual strength of shale surfaces and developing severe hydrostatic uplift pressure at the shale-sandstone contacts. Moreover some delay between filling and displacements might also be observed and explained by usual low permeability and high capillarity of the fine sandstones (Bell 2007) that slow down the water table rising in these unsaturated materials.

In the meantime, the semi-arid conditions at Potrerillos are characterized by low annual cumulated rainfalls of about 200 mm/yr between 2004 and 2012 (Subsecretaría de Recursos Hídricos 2013). Summer periods, when most of the rain is recorded (Figure 4.11), correlate with reservoir filling periods due to the Río Mendoza high discharge from snow melting in the high river watershed (cf. Section 4.3.4); no conclusions on rainfall-landslide interactions can then be extracted from displacements time-series. Moreover, there is no pre-dam construction reliable SAR data (cf. Section 4.4.2) to really investigate rainfall effects on both landslides excluding the reservoir fluctuation level one. It nevertheless seems that rainfalls are not noticeably destabilizing these soft rocks, since the semi-arid conditions couldn't saturate deep and large landslide masses and above all since no other landslides are detected in the same geological formation outside the reservoir shores.

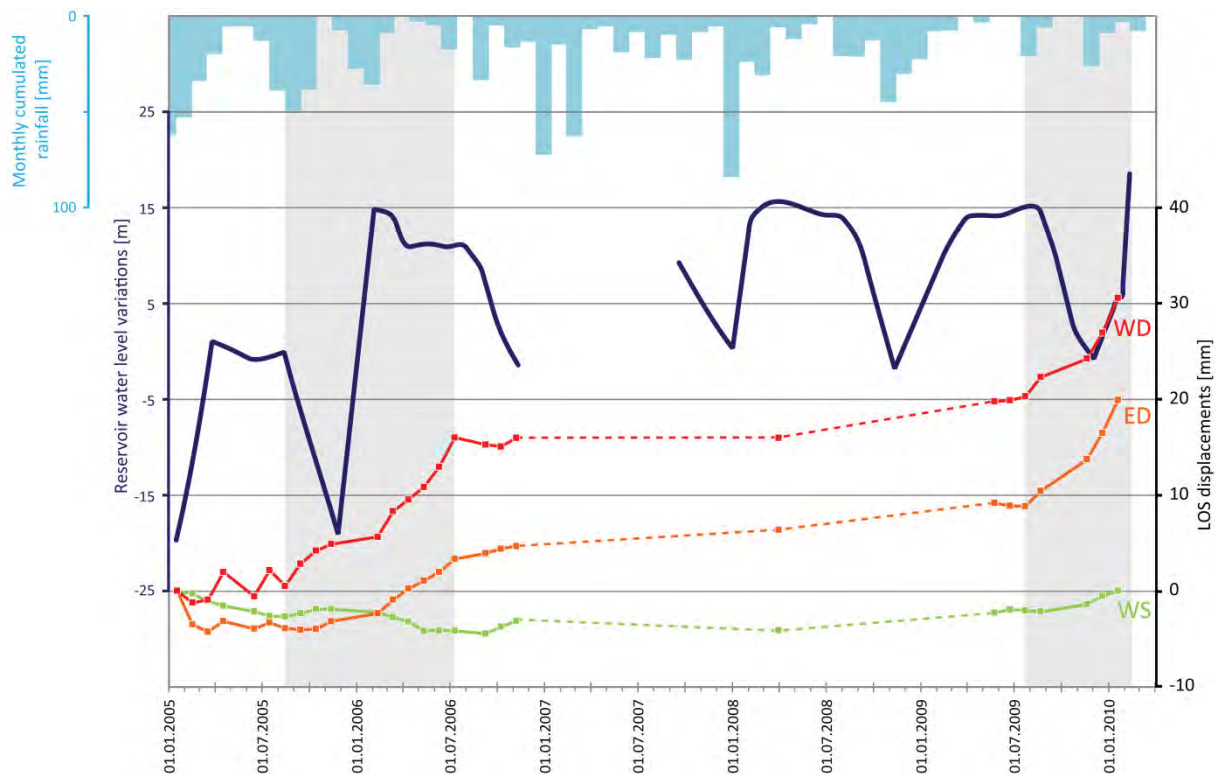


Figure 4.11: Potrerillos reservoir water level variations and monthly cumulated rainfalls compared to cumulated displacements of scatters from the western (WD) and eastern (ED) deformations as well as from a stable part close to the western landslide (WS). The dot lines underline potential fringe unwrapping ambiguity issues. The 2 grey columns are overlapped with displacement acceleration periods. (Potrerillos rainfall data: ©Subsecretaría de Recursos Hídricos).

The stability of the tertiary deposits seems to be therefore very sensitive to significant reservoir level variations, and detailed geotechnical investigations on the field are at this point mandatory to validate this statement.

4.5 Conclusions

The present study aimed to detect large slope deformations using a small baseline InSAR approach (Berardino et al. 2002; Lauknes et al. 2010) along the N7 between Potrerillos and Uspallata since the road is exposed to many natural hazards (Baumann et al. 2005). The Norut GSAR software (Larsen et al. 2005) has been used to process the 27 ascending and the 20 descending SAR scenes acquired by the Envisat satellite (Figure 4.3).

As a result, the regional landslide detection processing did not highlight any large instability along steep elevated slopes of the N7 corridor (Figure 4.5); this outcome does not mean that there is no landslide in this area, but if it does, they are not detected with our input dataset. The major part of pixels within the corridor were indeed (a) invisible from current LOS due to the steep geometry creating shadow radiometric distortion and (b) were also masked out because of very low

coherences created by strong tropospheric delays and long snow cover periods on elevated areas. Both additional 2007-2008 SAR data to reduce temporal baselines as well as unwrapping ambiguities and DEM with higher resolutions to enhance topography-related correction would thus be necessary to improve the landslide detection capability.

Nevertheless, two unsuspected deep extremely slow soft rock slides were detected on gentle shores of the Potrerillos dam reservoir; both have main displacement directions toward the reservoir, with mean velocities up to 8 mm/yr during the 2005-2006 period and up to 20 mm/yr in 2009 (Figure 4.7). After having extracted real displacements vectors from ascending and descending LOS results, a translational sliding surface is assumed for the eastern deformation, while a rotational component is suspected for the western deformation. In addition, a third active landslide not detected by InSAR (but described in the supplementary material), was identified on successive satellite imaging available on *Google™ Earth* showing retrogression of backscarps up to 20 m in 10 years and a general flow of the lower land part of 13 m in 2 years toward the lake.

In order to consider potential reservoir-landslide interactions, the water level variation of the Potrerillos dam reservoir was later assessed, after having extracted from the SRTM DEM the elevation of shoreline pixels isolated on the return amplitude signal of all SAR images (Figure 4.9). Although no formal statement can be obtained from this study, there is however a body of evidences that the three large slope deformations (mainly composed of sandstones and clays) are actually influenced by the Potrerillos reservoir level variations.

To sum up, we show that very precise information on ground surface displacements above all coupled with an original reservoir water level variation survey can be extracted from spaceborne InSAR techniques (Figure 4.11). In addition, detailed geological and rheological investigations, with also displacement and water table monitoring, can thus be planned from this study to (a) investigate in detail landslide destabilizing factors and triggering mechanisms, and (b) forecast if necessary direct consequences of deformations and indirect ones of potential landslide impulse waves on infrastructures and populations.

4.6 Supplementary material: South-eastern landslide

In the south-eastern shore of the Potrerillos dams, successive satellite imaging available on *Google™ Earth* (acquired in 2002.05, 2006.01, 2010.04, 2012.03 and 2012.09) allowed us to characterize the dynamics of a rapid mass movement whose headscarp lies close to the shore of the reservoir (cf. Figures 4.2 and 4.7 of the paper), recently described too by Sales et al. (2014). With a land area of

0.1 km², its extension is limited compared to the 2 other large landslides. But as shown in Figure 4.12, this instability seems particularly active.

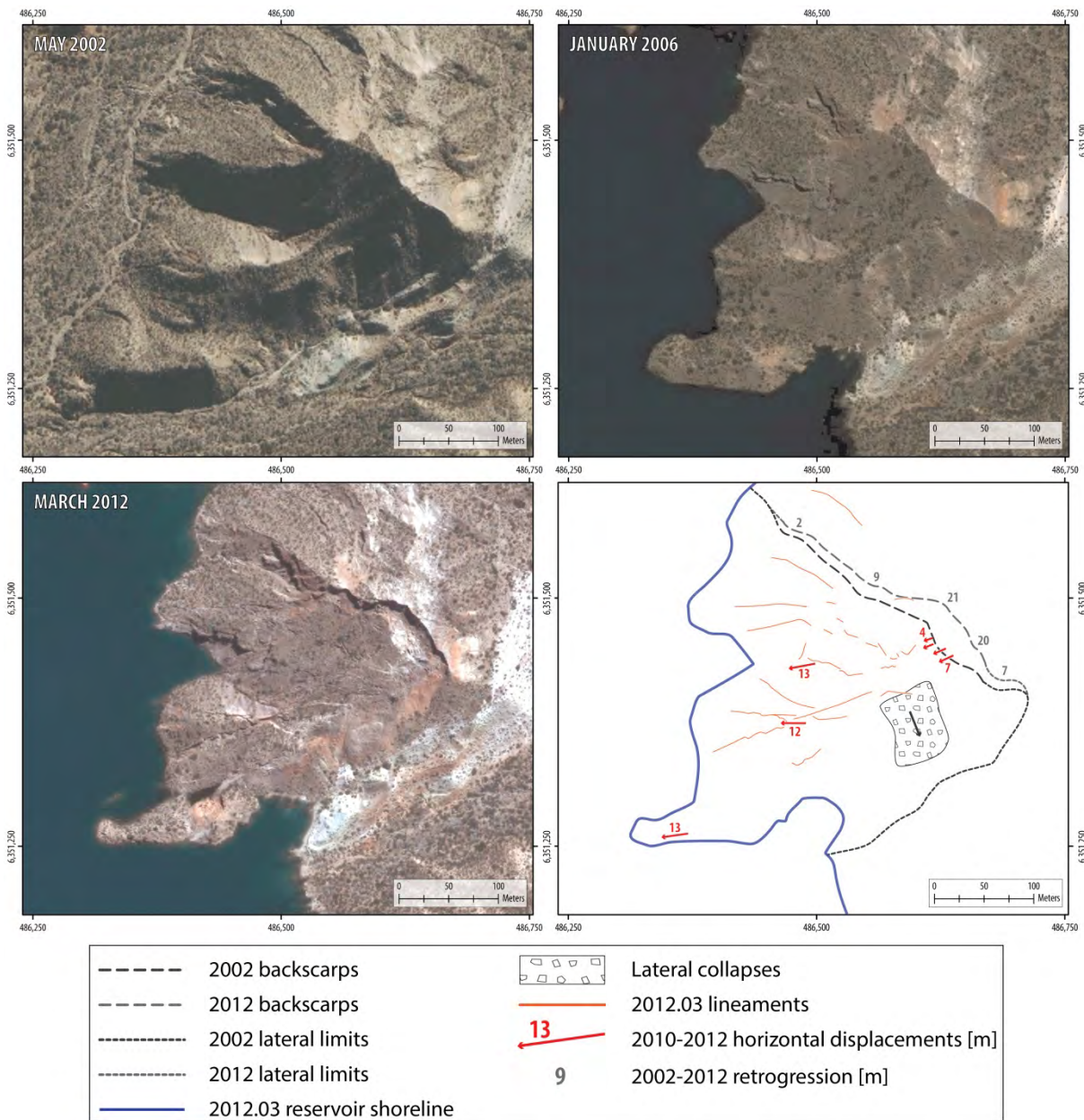


Figure 4.12: Successive satellite imaging and scheme of main geomorphological features of the south-eastern landslide. (Satellite images from ©GoogleEarth)

While no vertical deformation evidences are detected on the SBAS results between 2002 and 2006, important geomorphological changes and large displacements occurred during the 2006-2012 period; we can indeed observe and measure a retrogression along backscarps of the upper crests up to 20 m in 10 years, from 2002 to 2012, coupled with several block collapses, lateral spreading and a general flow of the slope towards the reservoir of 7 m in the upper part up to 13 m in the lower land part measured from 2010 to 2012.

As geometrical decorrelations get really important with the high amplitude of displacements observed in few years only, scatters has very low coherences and are then deleted within the moving area. To be correctly detected and quantified, instabilities must have indeed slow and continuous displacement rates (Massonnet and Feigl 1998; Woodhouse 2006) to avoid strong geometrical decorrelations and phase ambiguities. Because of that, this landslide has not been detected by InSAR processing and no displacement time series is available here. It remains therefore difficult to assess potential correlations between the landslide behaviour and reservoir water level variations; although first geomorphological changes are visible on *Google™ Earth* satellite imaging shortly after the reservoir filling has reached its highest level for the first time in February 2006.

According to the geologic map from Folguera et al. (2003), this active landslide mainly involves sedimentary Triassic rocks (i.e. a succession of conglomerates interlayered with sandstones and clays deposits highly altered on its top). Rheological properties and the presence of these thin deposits could condition the slope instability during fill and drawdown of the dam (cf. Section 4.4.4 of the paper). But further investigations (from field work to numerical modelling) would be definitively required to confirm the landslide behaviour model.

5 Rockfall hazard and risk assessments along roads at a regional scale: example in Swiss Alps

After Michoud C, Derron MH, Horton P, Jaboyedoff M, Baillifard FJ, Loye A, Nicolet P, Pedrazzini A and Queyrel A: Rockfall hazard and risk assessments along roads at a regional scale: example in Swiss Alps. *Natural Hazards and Earth System Sciences*, 12, 615-629, 2012.

Abstract

Unlike fragmental rockfall runout assessments, there are only few robust methods to quantify rock-mass-failure susceptibilities at regional scale. A detailed slope angle analysis of recent *Digital Elevation Models* (DEM) can be used to detect potential rockfall source areas, thanks to the *Slope Angle Distribution* procedure. However, this method does not provide any information on block-release frequencies inside identified areas. The present paper adds to the *Slope Angle Distribution* of cliffs unit its *normalized cumulative distribution* function. This improvement is assimilated to a quantitative weighting of slope angles, introducing rock-mass-failure susceptibilities inside rockfall source areas previously detected. Then rockfall runout assessment is performed using the GIS- and process-based software *Flow-R*, providing relative frequencies for runout. Thus, taking into consideration both susceptibility results, this approach can be used to establish, after calibration, hazard and risk maps at regional scale. As an example, a risk analysis of vehicles traffic exposed to rockfalls is performed along the main roads of the Swiss alpine valley of Bagnes.

Keywords: Rockfall, Road, Risk, Regional assessment, Aerial LiDAR, Swiss Alps.

5.1 Introduction

Mountain roads are frequently exposed to rockfalls (Piteau and Peckover, 1978; Budetta, 2004), involving independent blocks from relatively small sizes characterized by high energy and mobility (Whalley, 1984; Willie and Mah, 2004). Recent advances of high resolution Digital Elevation Models (HRDEM, acronyms are listed in Table 5.1) combined with Geographical Information System (GIS) technologies have made rockfall susceptibility mapping possible (Willie and Mah, 2004; Derron et al. 2005; Cascini 2008; Jaboyedoff et al. 2010). The field of propagation modelling is under fast development, aiming to compute runout probabilities with empirical, process-based and GIS-based models (Dorren, 2003a; Volkwein et al. 2011), such as *CONEFALL* (Jaboyedoff and Labiouse, 2011a), *Rockyfor3D* (Dorren, 2011), *HY-STONE* (Crosta et al. 2004) or *ILWIS* (van Dijke and van Westen, 1990).

However, there are not yet robust and objective methods to detect source areas at a regional scale and quantify rock-mass-failure mean susceptibilities. In the present work, the authors intend to provide information about susceptibility indicators on potential rockfall source areas.

Rockfall are very likely to be found in steep slopes (Heim, 1932; Hoek and Bray, 1981; Crosta and Agliardi, 2003a; Dorren, 2003a). From a basic approach, unstable rock slopes can be delimited through the steepness of the topography. It can be done by fixing a simple slope angle threshold above which we assume that rockfall releases are possible: it can then be defined from distinctive evidence (i.e. cliffs lying above scree deposits, fieldworks or historical events) when it is not arbitrary defined (Toppe, 1987; Dorren and Seijmonsbergen, 2003b; Guzzetti et al. 2003; Jaboyedoff and Labiouse, 2003; Frattini et al. 2008).

Furthermore, several authors showed supplementary conditions influencing rock slope stability (Terzaghi, 1950, 1962; Bieniawski, 1976; Selby, 1982; Willie and Mah, 2004, Jaboyedoff and Derron, 2005a), classified in internal parameters (IP, i.e. lithological, geo-mechanical and structural settings) and external factors (EF, e.g. active tectonic, water infiltration, weathering, etc.). Therefore, more complex models have been developed integrating these conditions to enhance the source detection at regional scale. They introduced rating systems following empirical multi-criteria observations (Pierson et al. 1990; Bunce et al. 1997; Baillifard et al. 2003), structural settings and kinematics analysis (Wagner et al. 1988; Jaboyedoff et al. 1999; Gokceoglu et al. 2000; Günther, 2003), safety factors computations (Hoek and Bray, 1981), or joining IP and EF conditions (Günther et al. 2004; Oppikofer et al. 2007).

But, all these methods depend obviously on the possibility to collect a lot of complex and reliable information on the area of interest. For example, the simplified Rockfall Hazard Rating System method (Pierson et al. 1990; Bunce et al. 1997; Budetta, 2004) requires eleven parameters per outcrop as an input to estimate a rockfall susceptibility index and is designed to be applied only along outcropping road cuts. Moreover, these methods usually use very high resolution datasets that are not often available at regional scale. For instance, Günther (2003) applied his model *SLOPEMAP* to extract structural features of the hard rock terrain using a 5 x 5 m DEM pixel size for a study area of 2.5 km², which is inappropriate when only 10 x 10 up to 30 x 30 m DEM pixel sizes are available at regional scale. These methods therefore require high resolution information and many parameters to be rationally planned on fairly large areas.

However, strong correlations between topography and earth surface processes have been suggested for many years (Powel, 1876 and Gilbert, 1877, cited in Montgomery and Brandon, 2002; Strahler, 1954). Therefore, the terrain morphology reflects the compounded influence of these internal settings (Locat et al. 2000). Hence, Rouiller et al. (1998) and then Loyer et al. (2009) proposed the *Slope Angle Distribution* (SAD) procedure to use the topography as a proxy to detect potential source

locations. The next step is to assess the susceptibility level of rockfall release of the potential source locations previously detected. Therefore, this paper proposes to improve the SAD procedure by linking the cumulative distribution function of the slope angle to quantitative block release susceptibility.

The *Flow-R* software (Horton et al. 2008; Blahut et al. 2010; Kappes et al. 2011) is used to compute rockfall runout areas. It assesses propagations thanks to an open choice of algorithms and parameters of probabilistic spreading and basic energy balance, such as a multiple flow direction model (Holmgren, 1994) coupled with an inertial factor (Gamma, 2000) and a maximum runout distance based on a Coulomb friction model. Moreover, since Horton et al. (2008), the model is now taking into account the susceptibilities of block releases in the resulting spreading.

Finally, this improved methodology allows to draw rockfall susceptibility maps, detecting areas potentially or really exposed to natural hazards, without quantifying landslide intensities and frequencies (Jaboyedoff et al. 2012b). Then, after a calibration based on available rockfall inventories, hazard maps can be obtained, taking into consideration both relative frequencies of block release and propagation (Jaboyedoff et al. 2005b; Corominas and Moya, 2008). Indeed, the hazard is always a challenging parameter to estimate in a *Quantitative Risk Assessment* (QRA) (Corominas et al. 2005a).



Figure 5.1: Photography of a rockfalls event in 2006 that reached twice the road section near *Le Plamproz*, in the Bagnes Valley.

As an example of the applicability of this procedure, the risk of rockfalls to vehicles traffic along the main roads of the Swiss Alpine valley of Bagnes (Figure 5.1) is assessed, and expressed in terms of number of direct impacts per year of blocks on vehicles.

Table 5.1: Table of main acronyms used in chapter 5 to assess rockfall hazard and risks along roads. Bold font: input parameters needed to solve equations; normal font: intermediary or final results solved during the assessment; italic font: useless parameters because deleted during the equations simplifications.

Acronym	Definition
α	Exponent in the Holmgren's (1994) expression
d	Diameter of blocks considered
l	Mean length of the car
m_c	Mean values of cliffs distributions
m_{ss}	Mean values of steep slopes distributions
μ	Friction angle of the runout energy calculation
N_b	Number of rockfall events inventoried along road section
s and β	Slope angle values
σ	Standard deviations of cliffs distributions
T	Traffic per time period t_c
t_i	Time period of the inventory
v	Mean velocity
w	Weighting factor of normal distribution function
x_{rs}	Road section's cells locations
f, f_1, f_2 and f_t	Normal distribution function
F	Cumulative distribution function
F_n	Normalized F: rock-mass-failure susceptibility
H	Hazard
k	Calibration factor of hazard
R	Risk
E	<i>Magnitude of the rockfall event (function of d)</i>
Exp	<i>Exposure</i>
g	<i>Terrestrial acceleration</i>
i and j	<i>Flow directions in the Holmgren's (1994) expression</i>
L	<i>Mean length of the road within a pixel</i>
N_c	<i>Total number of vehicles during t_c</i>
P_{cell}	<i>Probability of a car to be hit inside a pixel</i>
P_f	<i>Relative frequency of propagation (in the Flow-R's results)</i>
t_c	<i>Considered period of time in the Risk equation</i>
x	<i>Punctual location</i>
x_p	<i>Pixel location</i>
Δx	<i>Increment of horizontal displacements in the friction model</i>

5.2 Methodology

5.2.1 Detection of sources areas

a. Slope Angle Distribution procedure

The Strahler's law of constancy of slopes (Strahler, 1950) tells that the morphology of a slope topography tends to group predominantly around several mean slope angle values that are normally distributed with low dispersion. These particular slope angles of convergence can be often related to the most frequently encountered four major morphological units (Oppikofer et al. 2007; Loye et al. 2009):

- *Plains* formed by fluvio-glacial deposit; these correspond to the set of low slope angles;
- Bottom parts of the valley flanks comprising alluvial fans related to debris flow deposits and landslides mass. These correspond to the set of *foot slopes* angles;
- Talus slopes and valley sides (flank) covered by till, screes and debris mantles as well as rocky outcrops lightly covered with soil. These correspond to the set of *steep slopes* angles;
- *Cliffs* and rock faces corresponding to the very steep sets of slope angles.

Hence, the morphology of a terrain displays characteristic slope angles that can be directly related to the geomorphic processes involved in slopes stability. Rockfall source areas are commonly found in the steepest morphological units.

Based on these statements, Rouiller et al. (1998) and then Loye et al. (2009) have established a DEM-based geomorphometric approach to detect these morphological units and therefore rockfall source areas, named the *Slope Angle Distribution* (SAD) procedure. The classification is done by computing the *Slope Angle Frequency Distribution* (SAFD) of the study area, the frequency being normalized considering their real surface of occurrence. The SAFD is then decomposed into several Normal distributions f :

$$f(s) = w \cdot \frac{1}{\sigma\sqrt{2\pi}} \cdot \exp\left[-\frac{1}{2} \cdot \left(\frac{s - m_c}{\sigma}\right)^2\right] \quad \text{Eq. 5.1}$$

where f is the normal probability distribution function (PDF) of the slope angle value s included within the interval $[0;90]$, σ its standard deviation, m_c its mean value (Kreyzig, 2006) and w a weighting factor which is linked to the proportions between unit surfaces inside study areas. The sum of these theoretical normal curves has to rebuild the real SAFD (Figure 5.2A).

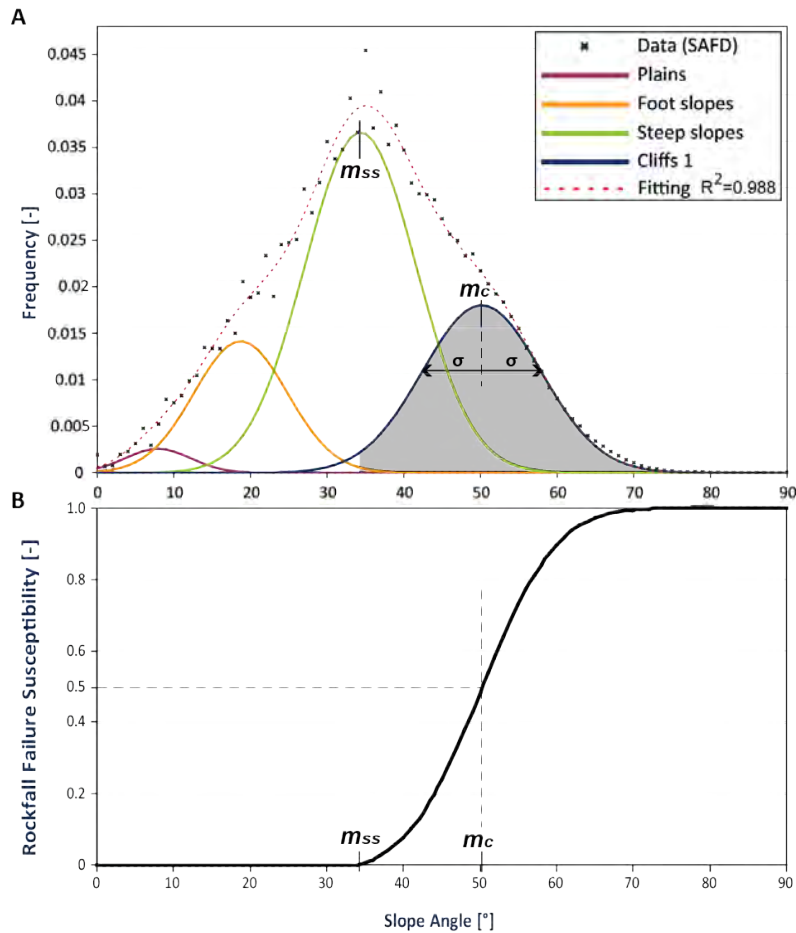


Figure 5.2: (A) Normal distributions of the slope angles of the *granitoids* HMA in the Bagnes Valley, extracted from a 10m-DEM. Three parameters are used to detect potential rockfall source areas: m_c which is the mean angle of the *cliffs* distribution and σ its standard deviation; m_{ss} which is the mean angle of the *steep slopes* distribution. In this case, *cliffs* units are decomposed in only one normal distribution. (B) Normalized cumulative distribution function (F_n) for the *cliffs* units, assimilated to a quantitative weighting of potential rockfall source areas, i.e. to a rock-mass-failure susceptibility. The mean angle of the *steep slopes* distribution m_{ss} is used as first threshold to exclude lower values as potential rockfall source areas.

The above-mentioned sets of morphological units do not always exist in the study area; the number of normal curves is therefore given according to the number of morphological units present in the area of interest (as detailed in Loye et al. 2009). Moreover, in some cases (Figure 5.3A), the distribution of the slope angles of *cliffs* units has to be decomposed in two normal functions f_1 and f_2 . This can be caused by the topography itself (potential high dispersion of this unit that possibly exists from 45° to 90°) or by extent of the support (limits of the study domain). In theory, it could be divided in more than two distributions; but based on previous experiences two distributions are sufficient (Oppikofer et al. 2007; Loye et al. 2009; Jaboyedoff et al. 2012b). Then, the total distribution f_t of *cliffs* units is simply defined as the sum of f_1 and f_2 :

$$f_t(s) = f_1(s) + f_2(s) \tag{Eq. 5.2}$$

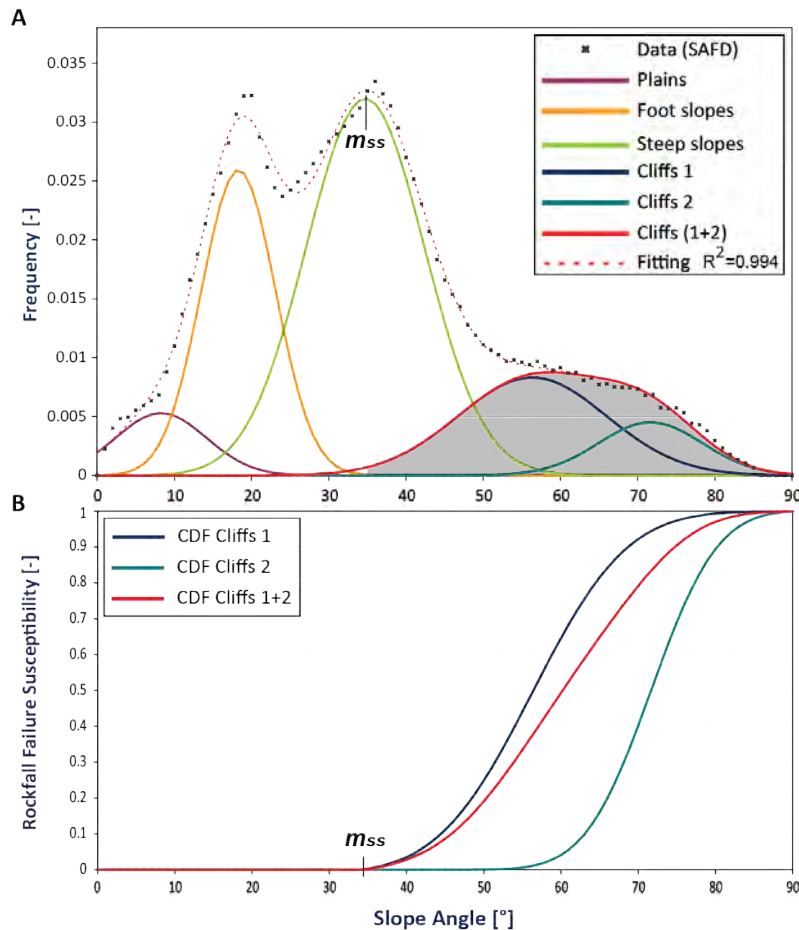


Figure 5.3: (A) Normal distributions of the slope angles of the marbles HMA in the Bagnes Valley. Here, cliffs are decomposed in two normal distributions. (B) The normalized cumulative distribution function (F_n) of the sum of the two cliffs distributions (f_t) is shown by the red line. In comparison, the normalized cumulative distribution functions for the two cliffs distributions are shown in blue (f_1) and cyan (f_2).

Technically, the input values for the initial normal distributions are defined according to the local maximum and minimum that can be visually identified along the SAFD. The fitting process is performed by minimizing the error between the most-likely sets of normal curves and the target function (namely the SAFD) using a simplex optimization solver. The morphological units are then delimited finally according to the sets of normal slope angle distribution, where a normal curve becomes dominant over the others. An example of classified slope steepness map is shown in Figure 5.4. The *cliffs* morphological unit f_i is then considered as the potential rockfall sources areas.

Finally, considering that the local morphology of an Alpine valley is partly controlled by structural settings and rock-mass properties (Terzaghi, 1962; Selby, 1982; Willie and Mah, 2004), different lithological and tectonic units have to be considered in order to refine the morphological analysis. Therefore, the study area is classified in homogeneous morphotectonic areas (HMA), following similar lithological characteristic rock mass structure and geomorphic activity, and one SAD procedure has to be done for each HMA.

To sum up, the SAD is a systematic approach to extract for each HMA a slope angle lower threshold, corresponding to the limit between the *steep slopes* and *cliffs* normal distributions. This procedure leads to Boolean results (i.e. in/out *cliffs* units) and cells included inside these *cliffs* areas are considered as potential sources of fragmental rockfalls.

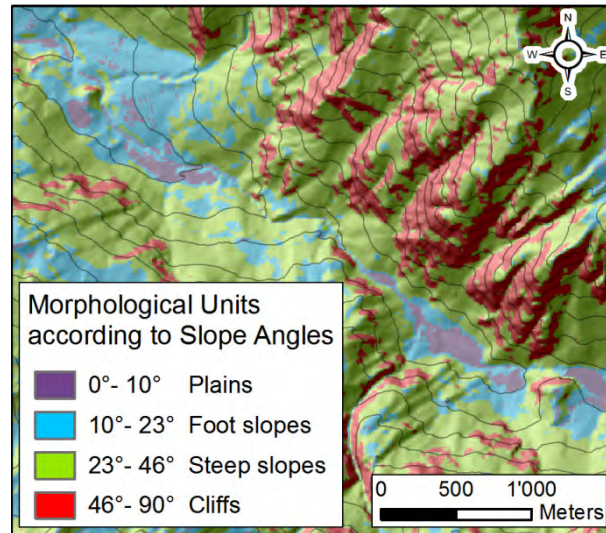


Figure 5.4: Example of main morphological units in a region of the Bagnes valley according to slope angle thresholds got thanks to the SAD procedure. (Hillshade and 10 m isohypses: ©2008 swisstopo)

b. Refinement of the Slope Angle Distribution

As stated in the introduction, taking into account all internal parameters and external factors can require too high resolution dataset and too many parameters to be applied on fairly regional scale in order to precisely detect and rate potential rockfall source areas. But as topographies are strongly correlated with internal rock settings (Locat et al. 2000) and earth surface processes (Montgomery and Brandon, 2002), we do the assumption that for large areas, the block release susceptibility is function of slope angles. Thus, improving the SAD approach, this paper aims to link the cumulative distribution functions of slope angles of *cliffs* units to rock-mass-failure susceptibility inside rockfall source areas previously identified.

The explanations below will illustrate only the situation where *cliffs* units are decomposed in two distributions (Eq. 5.2). When it is not the case, f_i is equal to f_1 . The associated cumulative distribution function F of *cliffs* distribution is defined by:

$$F(\beta) = \int_0^{\beta} f_i(s) \cdot ds \tag{Eq. 5.3}$$

where s and β are two slope angle values included within the interval $[0;90]$. By definition, Eq. 5.3 gives the probability that a slope angle s is lower than β (Kreyzig, 2006).

Therefore, it is by extension assimilated to a quantitative block release susceptibility. Moreover, the mean value of the *steep slopes* distribution m_{ss} , extracted from the SAD procedure (Figures 5.2A and 5.3A), relates to an apparent equilibrium slope angle of scree deposits (usually around 35°, that mainly compose *steep slopes* units).

Thus, for higher slope angle values than m_{ss} , blocks can be mobilized; on the contrary, for lower slope angle values, blocks are not considered. As a consequence, m_{ss} is used as a lower threshold to exclude areas not steep enough to be potential source of rockfalls. Thus, Eq. 5.3 has to be cutoff by m_{ss} and then normalized for slope angle values higher than m_{ss} ; the final cumulative function F_n is shown in Figures 5.2B and 5.3B and defined by:

$$\begin{cases} \forall \beta \in [0; m_{ss}[\Rightarrow F_n(\beta) = 0 \\ \forall \beta \in [m_{ss}; 90] \Rightarrow F_n(\beta) = \frac{F(\beta) - F(m_{ss})}{F(90) - F(m_{ss})} \end{cases} \quad \text{Eq. 5.4}$$

The normalized cumulative distribution function F_n can be assimilated to a quantitative weighting of potential rockfall source areas, i.e. a rock-mass-failure susceptibility indicator (Figure 5.8), identified according to the slope angles and the SAD procedures.

5.2.2 Runout assessment

Many tools were developed to calculate runout areas of rolling, bouncing or falling blocks (Ritchie, 1963) and have been reviewed by Dorren (2003a). In this study, the runout simulation is computed by the *Flow-R* software (Horton et al. 2008). The propagation is assessed by means of a probabilistic spreading and a basic energy balance, controlling respectively the lateral extent and the runout distance, merging several models and approaches. Everything is processed at the cell level and iterated on the DEM grid according to the propagation direction. Thanks to the open choice of algorithms and parameters, it has been possible to parameterize the model according to our needs at regional scale. The model has also been modified to take into account the susceptibilities of the sources (calibrated on the base of F_n) in the resulting spreading, which is a step further in the frequency analysis. It allows us to approach the hazard frequency of a location more consistently than before by relating it to the source susceptibilities.

a. Probabilistic spreading

The probabilistic spreading is based on flow direction algorithms that process a probability for a cell to flow to its neighbors (Horton et al. 2008). The probability is integrated in a continuous way, meaning every neighboring cell having a non-null probability will be propagated further. Flow direction algorithms, that are the basis of the spreading, portion the probabilities according to the slope of the surrounding cells.

Fairfield and Leymarie (1991) have introduced the *multiple flow direction* algorithm as a stochastic method which gives a probability to every cell with a descending slope. Then Holmgren (1994) has suggested a variation of this method by introducing the exponent α on the slope gradient:

$$\forall \begin{cases} \tan \beta_i > 0 \\ \alpha \in [1; +\infty[\end{cases} \Rightarrow P_f(x) = \frac{(\tan \beta_i)^\alpha}{\sum_{j=1}^8 (\tan \beta_j)^\alpha} \quad \text{Eq. 5.5}$$

where i, j are the flow directions, P_f is the probability proportion in direction i , $\tan \beta_i$ is the slope gradient between the central cell and cell in direction i , and α is the exponent to calibrate.

The exponent α allows to better control the spreading extent from the *multiple flow direction* algorithm. When $\alpha = 1$, Eq. 5.5 is equivalent to the *multiple flow direction* algorithm (Fairfield and Leymarie, 1991), and when $\alpha \rightarrow \infty$ to the *D8* algorithm (propagation following only the steepest slope: O'Callaghan and Mark, 1984, Jensen and Domingue, 1988).

In addition to the *flow direction* algorithm, a persistence factor was introduced as in Gamma (2000), which is a weighting of the probability according to a direction change. The chosen values are the same as Gamma (2000), i.e. 1 when there is no change in direction and 2/3 in any other case. The role of this persistence factor is to take in consideration the inertia according to the previous directions of the moving blocks which can therefore deviate from the steepest paths.

b. Runout distance

The runout distance is assessed thanks to a basic energy balance including the potential and kinetic energy components and an energy loss function. As the source mass is unknown, the energy balance is processed on a unit mass. For the energy loss function, a simple Coulomb friction model (with a single friction coefficient) was used:

$$\Delta E_{loss} = g \times \Delta x \times \mu \quad \text{Eq. 5.6}$$

where Δx is the increment of horizontal displacement, g the gravity acceleration and μ is the tangent of the friction angle. To this algorithm, we can add an upper threshold to limit the velocity of blocks or an equivalent kinetic energy (Horton et al. 2008). Then, the maximum runout distance is reached when the energy becomes zero, i.e. when the initial potential energy has been completely lost by friction.

c. Results in Flow-R

Flow-R can be used now to draw maps of relative frequencies of rockfall using: (1) the spreading probability based on a multiple flow algorithm including an inertial factor, and (2) the maximum

In Eq. 5.7, the rockfall hazard H (number of event per year) for a magnitude E is defined for a period of reference t_i at a cell x_p and is equal to the product of rockfall failure susceptibilities F_n times frequencies of propagation P_f up to a cell x_p and times a calibrating factor k , that depends on E .

This coefficient k depends on a known number of rockfall events with a given magnitude E in a cell x_p . However, in a context of rockfall studies along corridors, exact positions of impacts are unknown. For practical issues, inventories are frequently made along road sections. On a DEM, a road section is composed of a group of cells x_{rs} . So the inventoried number of events N_b along the section is the sum of all the rockfalls that occurred within the cells of this section during the time period t_i of the inventory. Thus, N_b has to be distributed in all the cells assessed following:

$$k(E) = N_b(E, t_r, x_{rs}) \times \frac{1}{\sum [F_n \times P_f(x_{rs})]} \times \frac{1}{t_i} \quad \text{Eq. 5.8}$$

where k is calibration factor with a frequency unit, function of a number of rockfall events N_b of magnitude E during a period of time t_i inventoried along a road section of cell x_{rs} divided by the sum of the *Flow-R* results within the whole road section.

5.2.4 Rockfall quantitative risk assessment along roads

Blocks frequently hit cars along Swiss mountain roads and occupants of vehicles are not necessarily killed or injured. Therefore, this paper is focused on the risk R of rockfalls to vehicles traffic; no considerations about vulnerabilities and elements at risk are provided, even if it would give proportional results. Adapting the risk equation of Fell et al. (2005) to this specific case, the annual risk can be defined by:

$$R(E, x_p) = H(E, x_p) \times Exp(x_p) \times N_c(x_p) \quad \text{Eq. 5.9}$$

where R is the risk expressed in terms of number of direct impacts of blocks on cars per year, according to the hazard H and the exposure Exp , i.e. the probability that cars is hit in the hazardous area, and N_c the number of threatened vehicles. Modified after Fell et al. (2005), the exposure is presented as:

$$Exp(x_p) = \frac{L}{v(x_p)} \times \frac{1}{t_c} \times P_{cell}(x_p) \quad \text{Eq. 5.10}$$

Exp depending on the mean length of the road inside cells L and the mean velocity v for a considered time period t_c (one year in this case) and the conditional probability P_{cell} :

$$P_{cell}(x_p) = \frac{d+l}{L} \quad \text{Eq. 5.11}$$

where P_{cell} is the probability that a car of length l is hit by a block of diameter d on average inside a cell of length L , knowing that a block falls into a cell where a car is present. Indeed, in this study hazard and exposure are defined on a cell's scale x_p , not on a punctual location x . It is assumed that d is the minimum size block that will affect significantly the car and the magnitude E is proportional to the block size. The diameter of blocks d has to tally with the inventoried events N_b considered to calibrate the hazard in Eq. 5.8. Then, the total number of vehicles attended on a road section is equal to Eq. 5.12:

$$N_c(x_p) = T(x_p) \times t_c \quad \text{Eq. 5.12}$$

where T correspond to the daily traffic. Finally, the annual risk induced by rockfalls to vehicles traffic for an event with defined magnitude at a pixel x_p can be rewritten as follow:

$$R(E, x_p) = H(E, x_p) \times \frac{d+l}{v(x_p)} \times T(x_p) \quad \text{Eq. 5.13}$$

R being a number of direct impacts of blocks of diameter d on cars of length l per year for a defined magnitude E at a cell x_p , function of the hazard H , the daily road traffic T , the mean velocity v , the mean car length l and the minimum block diameter d . Finally, the total risk along corridors is defined as the integration of all calculated $R(E, x_p)$ within the considered road sections.

5.3 Case study: the Val de Bagnes

5.3.1 Settings

The Val de Bagnes is located in the Canton of Valais in Switzerland. With a surface area of 300 km² and an elevation ranging from 677 m to 4313 m a.s.l., this municipality is under rapid development, in particular because of the fast growing of the Verbier ski resort. Moreover, an important power dam is located in the upper part of the valley. It means that the daily traffic is rather heavy, up to 5'800 cars and 32 bus per day according to open-access databases (SRCE, 2009; CarPostal, 2010). Rockfall susceptibility maps at 1:25'000 were already performed (Michoud et al. 2010a; Jaboyedoff et al. 2012b). In this paper, a QRA of rockfalls to vehicles traffic is performed along the main roads (40 km) of the valley. To achieve this goal, the authors used a 10 m cell size DEM derived from national maps at 1:25'000 (CN25, © swisstopo) to extract slope angles, the geological and tectonic vector atlas at 1:500'000 (© swisstopo) to classify the valley by HMA and the vectorized landscape model of Switzerland (Vector25, © swisstopo) to extract the location of the 40 km of roads.

5.3.2 Rockfall hazard assessments

a. Detection of block release areas

The rock type present is very large, from Cambrian polycyclic basements to Mesozoic and Cenozoic sedimentary covers (Sartori et al. 2006) of the Helvetic, Penninic and Austro-Alpine domains (Trümpy, 1980). Furthermore, large areas are covered by quaternary deposits that are fluvio-glacial deposits, colluvial fans or moraines. As the material diversity is wide, it justifies the importance of the HMA separation before further steps. Thus, each HMA was determined according to similar lithologies extracted from the 1:500'000 vectorised geological Atlas of Switzerland. Height classes were identified (Figure 5.6): basic rocks, conglomerates, flyschs, granitoids, limestones, moraines, marble plus breccias and schists. In addition, some areas, such as lakes or alluvial deposits, were directly mapped as areas without any rockfall sources, due to absence of relief and/or material.

Then SAD analysis was performed from the 10 m DEM (©2008 swisstopo) and the useful slope angles (m_{ss} , m_c and σ for each HMA) were extracted to identify and weight potential rockfall source areas within the height HMAs. Results are presented in Table 5.2. This procedure was done thanks to the freeware *Histofit* (Loye et al. 2009) which decomposes the SAFD extracted from the software *ArcGIS* of *Esri*® and fits it with a predefined number of normal distributions.

With the normal curves defined in *Histofit* and a slope angles map of the region, a *MATLAB*® script allows to calculate directly rock-mass-failure susceptibilities F_n (Eq. 5.4) in each potential rockfall source cell of the map. Finally, the potential onset areas within each HMA were merged in one map (Figure 5.8) before computing one propagation assessment.

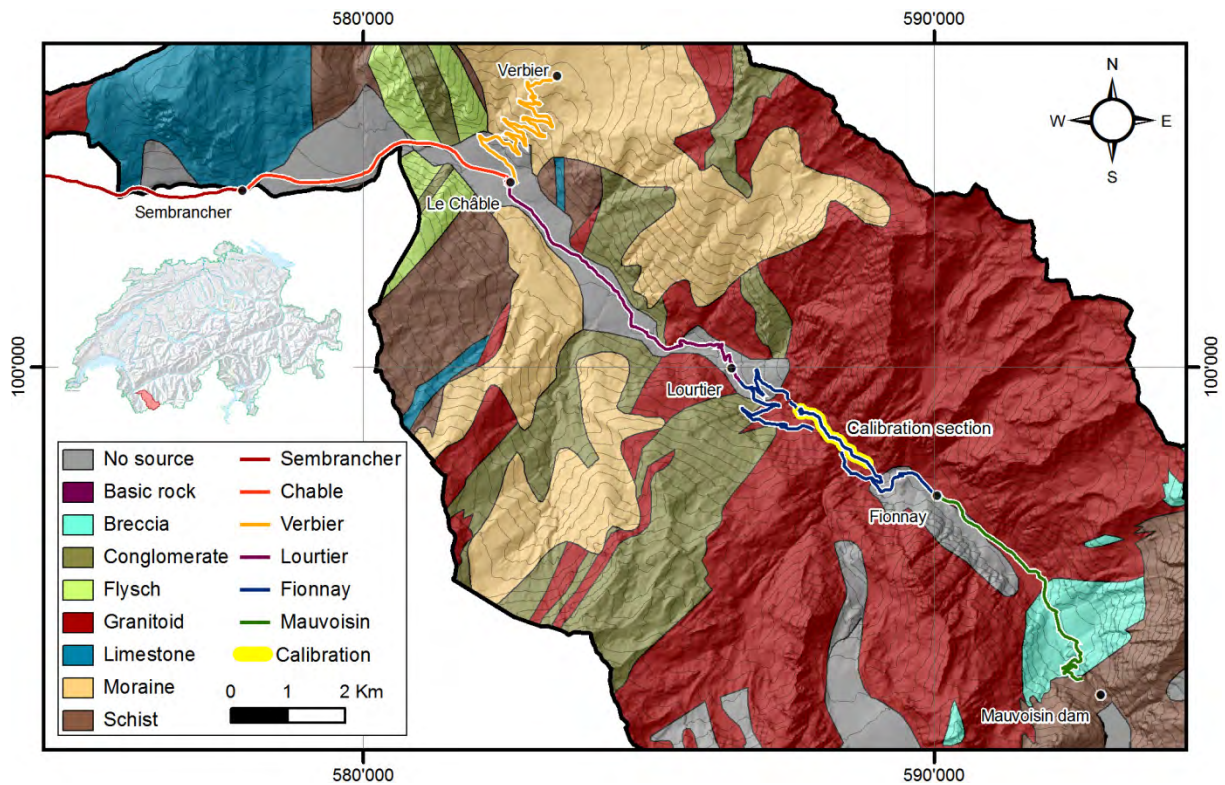


Figure 5.6: Studied road sections and homogenous morphometric areas of the Bagnes Valley, classified according to the national geological atlas and the Vector25 (@swisstopo). They were identified differentiating daily traffic and mean velocities along the roads. The road section used to calibrate the rockfall hazard assessment is located between the second gallery after *Lourtier* and *Les Plamproz*, where the rockfall activity is evident, as shown in Figure 5.1 (Hillshade and 10 m isohypses: ©2008 swisstopo)

Table 5.2: Slope angles extracted from SAD analysis of each HMA. Mean values and standard deviations of *cliffs* distributions correspond respectively to letters m_c and σ , and mean values of the *steep slopes* to letters m_{ss} .

Homogenous Morphometrical Areas	m_{ss}	1 st normal distribution		2 ^d normal distribution	
		m_c	σ	m_c	σ
Basic rocks	33°	53°	8.3°	-	-
Conglomerates	31°	46°	8.7°	-	-
Flyschs	35°	48°	7.5°	60°	7.7°
Granitoids	34°	51°	7.7°	-	-
Limestones	35°	45°	8°	60°	8.0°
Marble and Breccias	33°	50°	6.4°	62°	7.4°
Moraines	33°	44°	6.1°	-	-
Schists	30°	47°	8.3°	61°	8.9°

b. Runout assessment

Taking into account local observations (Jaboyedoff et al. 2012b) and detailed studies including computations of 2D and 3D rockfall modelling made for specific local cliffs into the valley, parameters of the runout assessment by *Flow-R* were calibrated as following: $\alpha = 1$ (Eq. 5.5) and $\mu = \tan 33^\circ$ (Eq. 5.6). Then, only one computation was done for the whole valley merging all the 10 m DEM (Figure 5.9), in order to ensure continuous and homogenous results. Finally, these results were compared with a test simulation performed by the freeware *CONEFALL* (Jaboyedoff and Labiouse, 2011a) based on an *energy line angle* equal to $\tan 33^\circ$ too. On the one hand, both lateral and longitudinal extensions of computed runout areas are quite similar along open slopes, which guarantee the coherence of the *Flow-R* runout assessment. On the other hand, in chenalized slopes, *Flow-R* algorithms better constrain lateral extensions of spreading areas.

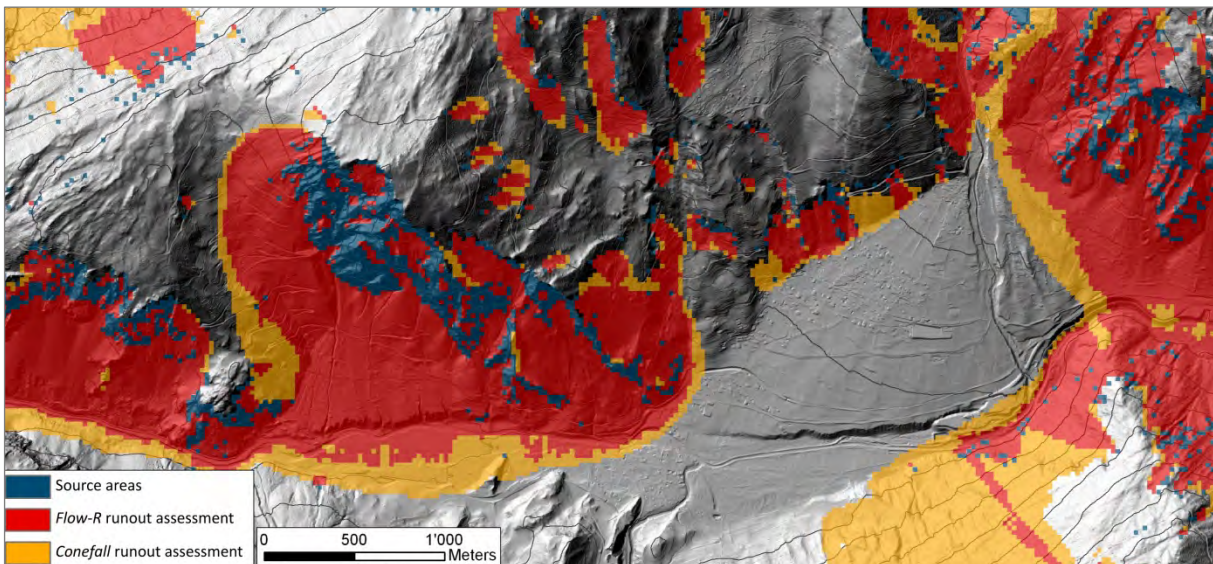


Figure 5.7: Rockfall runout assessment based on *Flow-R* and *Conefall* models.

c. Rockfall hazard assessments

In order to achieve the normalized quantitative hazard assessment along the road sections, it is necessary to calibrate the *Flow-R* results with the factor k (Eq. 5.8 in Section 5.2.3). The road section used to calibrate the model is located on the NW side of the *Dranse* river, between the second gallery after *Lourtier* and *Le Plamproz* (Figure 5.6), where the strong activity of cliffs is well known for many years (Figure 5.1). Along this section, covered by 237 cells with a sum of *Flow-R* results equal to 9'453, it was assumed that 3 blocks with diameters d equal or greater than 25 cm reach the road every year ($t_r = 1$) according to our knowledge of past events. Then according to Eq. 5.8:

$$k(d \geq 25\text{cm}) = 3 \times \frac{1}{9453} \text{ [events / year]} \quad \text{Eq. 5.14}$$

An extract of the hazard map is presented in Figure 5.9 and Figure 5.10.

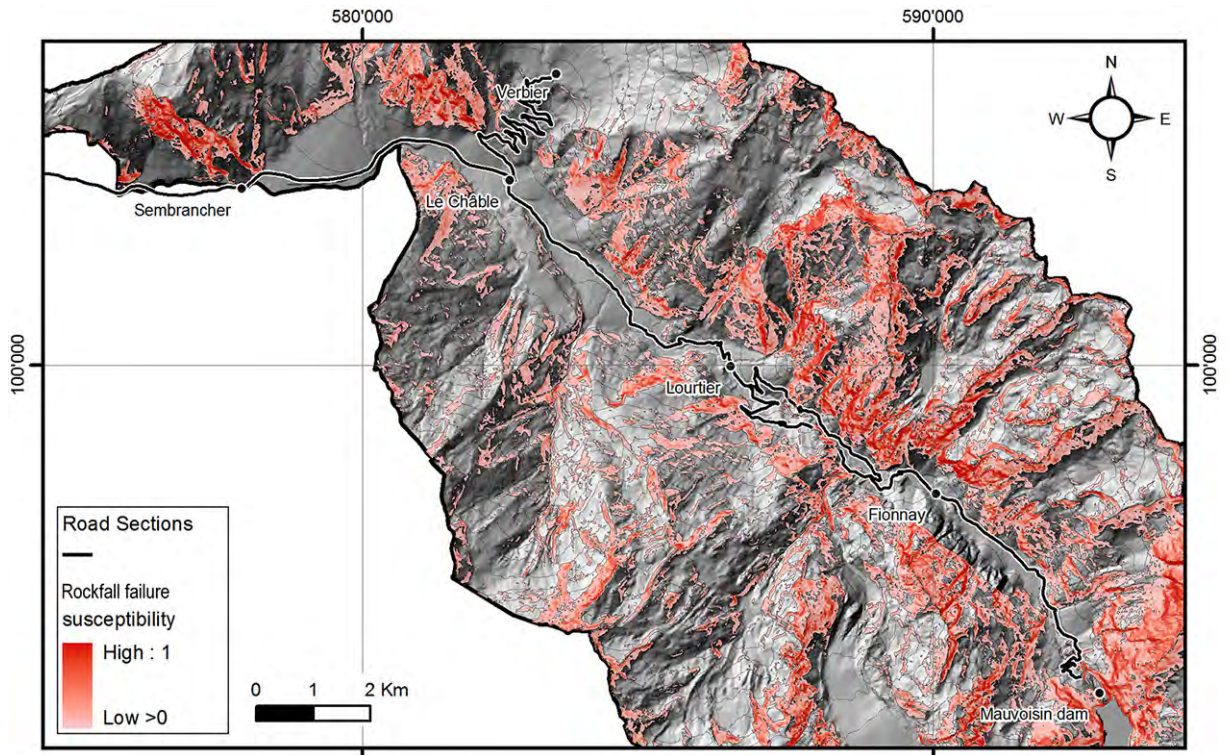


Figure 5.8: Rockfall failure susceptibility in the Bagnes Valley, identified thanks to the improved *Slope Angle Distribution* approach. (Hillshade and 10 m isohyps: ©2008 swisstopo)

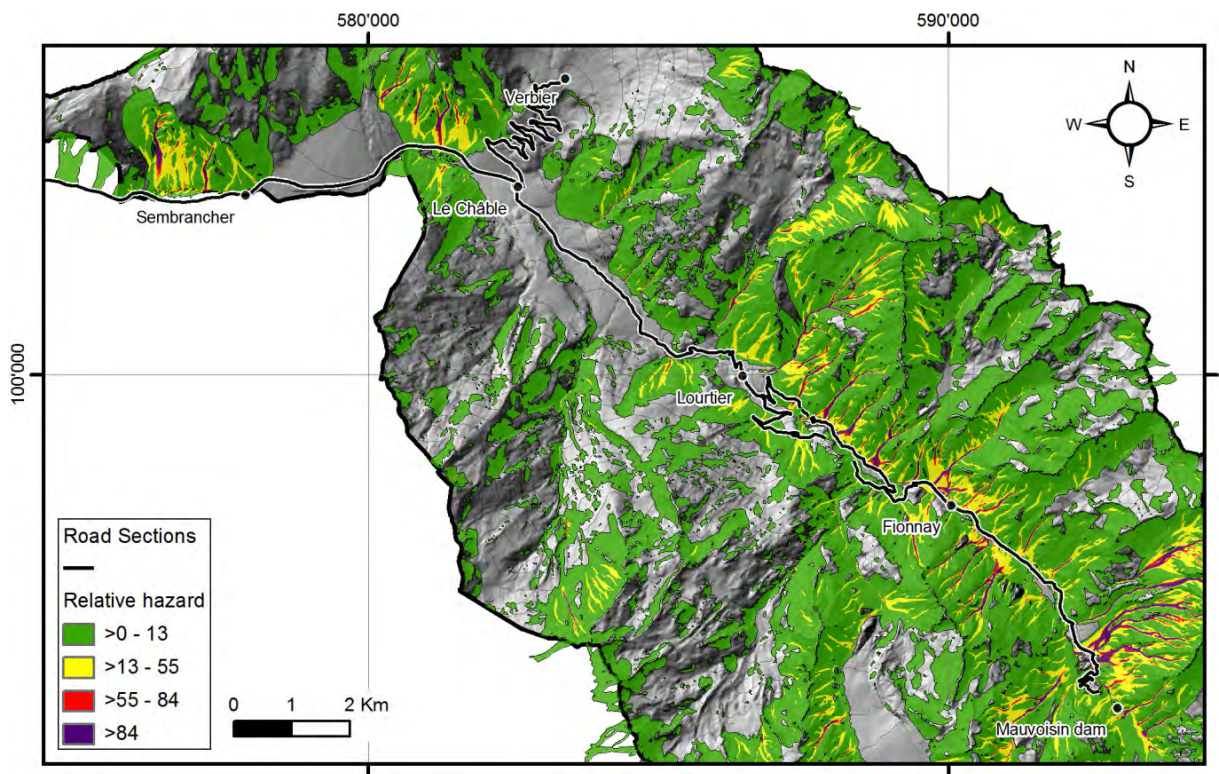


Figure 5.9: Rockfalls relative hazard assessment in a part of the Bagnes Valley, performed by the software *Flow-R*. In the lower part of the valley (Sembrancher, Chable, Verbier), the daily traffic is rather heavy but the exposition is low. On the

contrary, in the upper part of the valley (Fionnay and Mauvoisin), the daily traffic is lower but the hazard is pretty much higher. (Hillshade and 10 m isohypses: ©2008 swisstopo)

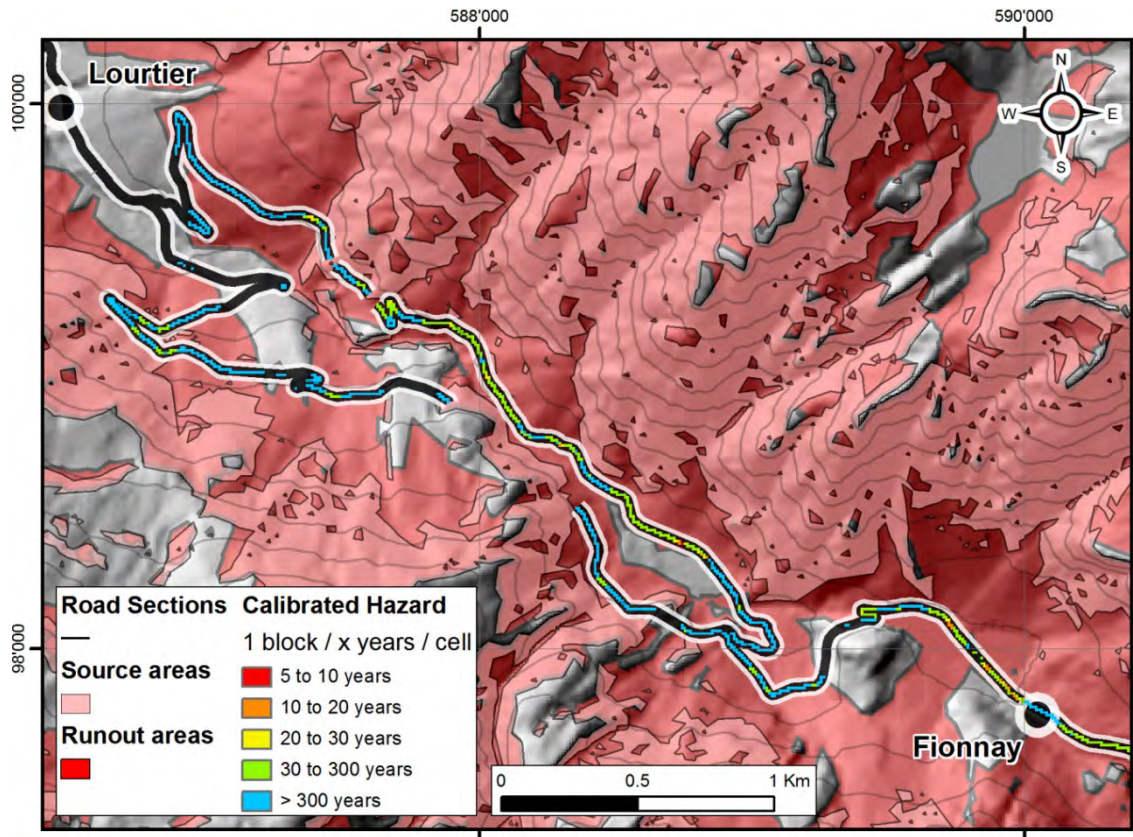


Figure 5.10: “Inverse” hazard once the calibration performed, focused along the road section of *Fionnay*. Gaps along the section correspond to tunnels. (Hillshade and 10 m isohypses: ©2008 swisstopo)

5.3.3 Rockfall risk assessment along the main roads of the valley

a. Inputs

The main important roads of the Val de Bagnes were extracted from the Vector25 (© swisstopo). The daily traffics along roads of the valley considered T were obtained from open-access databases (SRCE, 2010 and CarPostal, 2010). Mean vehicles velocities v were estimated according to the local regulation and the state of the roads (roadwidth and ageing). Therefore, six distinct road sections were distinguished and presented in Figure 5.6 and Table 5.3, differentiating daily traffic and velocities along them. Moreover, the mean car length was set at 4 m, which corresponds to normal European compact cars length. All parameters used in Eq. 5.13 are summarized in Table 5.3.

b. Results

Finally, the annual risk induced by fragmental rockfalls greater or equal to a diameter of 25 cm to vehicles traffic was assessed along each road section of the Val de Bagnes. Results are summarized in

Table 5.4. Along these sections, they vary a lot. In the lower part of the valley (Sembrancher, Chable and Verbier sections), where the daily traffic is important, they are only few rockfalls propagations that reach the road. This is why the risk is evaluated at one hit car every two hundreds to six thousands years. On the opposite, in the upper part of the valley (Lourtier, Fionnay and Barrage sections), the daily traffic is lower but they are a lot of blocks that reach the road; the risk is significantly higher, namely to one hit car every sixty years (Table 5.4). The integrated risk along all the road sections of the Val de Bagnes is evaluated to 0.03414 hit cars per year, i.e. approximately one incident every thirty years.

Table 5.3: Parameters for risk calculation along the different studied road sections (according to CarPostal, 2010, SRCE, 2009 and local road regulations). These road sections are mapped in Figure 5.6.

Road Sections	T [daily traffic]	v [km/h]	d [m]	l [m]
Sembrancher	10'600 cars	80	0.25	4
Chable	5'800 cars	80	0.25	4
Verbier	5'000 cars - 32 bus	60	0.25	4
Lourtier	2'200 cars - 22 bus	70	0.25	4
Fionnay	800 cars - 8 bus	50	0.25	4
Mauvoisin	600 cars - 6 bus	40	0.25	4

Table 5.4: Results of the quantitative risk assessment induced by rockfalls (mean diameter: 25 cm) to vehicles traffic along road sections of the Val de Bagnes. Finally, the whole risk is defined as the sum of all calculated pixel.

Road Sections	Total number of cells	Number of reached cells	Risk [x cars / year]	Inverse Risk [1 car / x years]
Sembrancher	559	197 (35%)	$2.955 \cdot 10^{-3}$	~ 340
Chable	664	178 (27%)	$4.626 \cdot 10^{-3}$	~ 220
Verbier	1031	98 (10%)	$1.668 \cdot 10^{-4}$	~ 6000
Lourtier	851	63 (7%)	$8.369 \cdot 10^{-4}$	~ 1200
Fionnay	1288	976 (76%)	$1.676 \cdot 10^{-2}$	~ 60
Mauvoisin	742	591 (80%)	$8.787 \cdot 10^{-3}$	~ 110
All roads	5135	2103 (41%)	$3.414 \cdot 10^{-2}$	~ 30

5.4 Discussions

5.4.1 Results within the study area

According to the authors' experience and testimonies from local security services and geologists, the results (i.e. the localization of potential rockfall onset areas, the runout computation and the risk assessment) are in agreement with their observations. Nevertheless, the hazard calibration (Eq. 5.14) could be significantly improved with more complete inventories along these roads (detailed discussion in Section 5.4.5). In addition, the calculated risk is approximated and simplified, because it does not take into account some factors. First, the time lapse for the driver to react and the braking

distance in front of blocks already on the road are ignored, considering that the velocity is low enough to avoid a collision along the most exposed sections. Moreover, all surveys and remediation measures already done (such as anchors, nets, removal of unstable blocks, monitoring systems, etc.) are ignored, except for tunnels and galleries which are mapped from orthophotos. Finally, the potential inhomogeneous repartitions of rockfall events and traffic during the day are ignored; for example, during winter periods, workers drive early in the morning and late in the afternoon, when cliffs are frozen.

5.4.2 Recent rockfall event

A recent rockfall occurred on 2 January 2012, during the review process of this paper. The deposit of approx. 1000 m³ cut a small road (Figure 5.11A) on mostly stopped on it. The source area was localized in a zone clearly defined as a potential rockfall source area with a high rockfall failure susceptibility of about 0.8 (scale: no susceptibility = 0 - highest susceptibility = 1; see Figure 5.11B). The trajectories of two blocks that reached a second road 80 m lower fit well with the predicted runout using *Flow-R* (Figure 5.11C). Thus, this event is in agreement with the improved SAD approach and the *Flow-R* results, showing its potential ability to predict hazard and risk zones.

5.4.3 Advantages and limitations of the presented approach

The combination of the improved SAD approach and the *Flow-R* software allows to establish rockfall susceptibility, and when inventories are available, to obtain scaled hazard to assess risk along roads. This methodology is optimized for studies at regional scale with only few available information. Indeed, this procedure requires at least topography DEM and, if possible, geological map in order to improve the rockfall failures susceptibilities and spreading probabilities.

The refinement of the SAD approach is based on the assumption that the release susceptibility is related to the geomorphology, i.e. steepness of the topography, even if it is a simple rockfall activity factor. But, using geological information aims to indirectly take into account rock mass quality that influences the stability conditions too. Nevertheless, it is also true that other very important local factors (such as weathering and/or deburstressing) cannot be taken in consideration for large areas, using documents available at regional scale. Then, regarding propagations, *Flow-R* assesses runout areas using only a DEM, since the parameters of the Holmgren's and the Coulomb's expressions (Eq. 5.5 and 5.6) can be based on literature and/or past event records. This software is particularly optimized for regional studies and computation times are still acceptable with a normal workstation (five days for the study in Bagnes). Moreover, the approach can be even better calibrated according to other potential documents available for the study area (such as landuse maps, aerial images or information about mechanical rock parameters) in order to improve detection and runout settings.

However, this procedure oversimplifies the laws governing rockfall failures and block propagations, which is suitable at regional scale but becomes hazy for small studies areas. Finally, this approach should be used as a preliminary quantitative assessment for large regions, highlighting hotspots requiring more detailed studies.

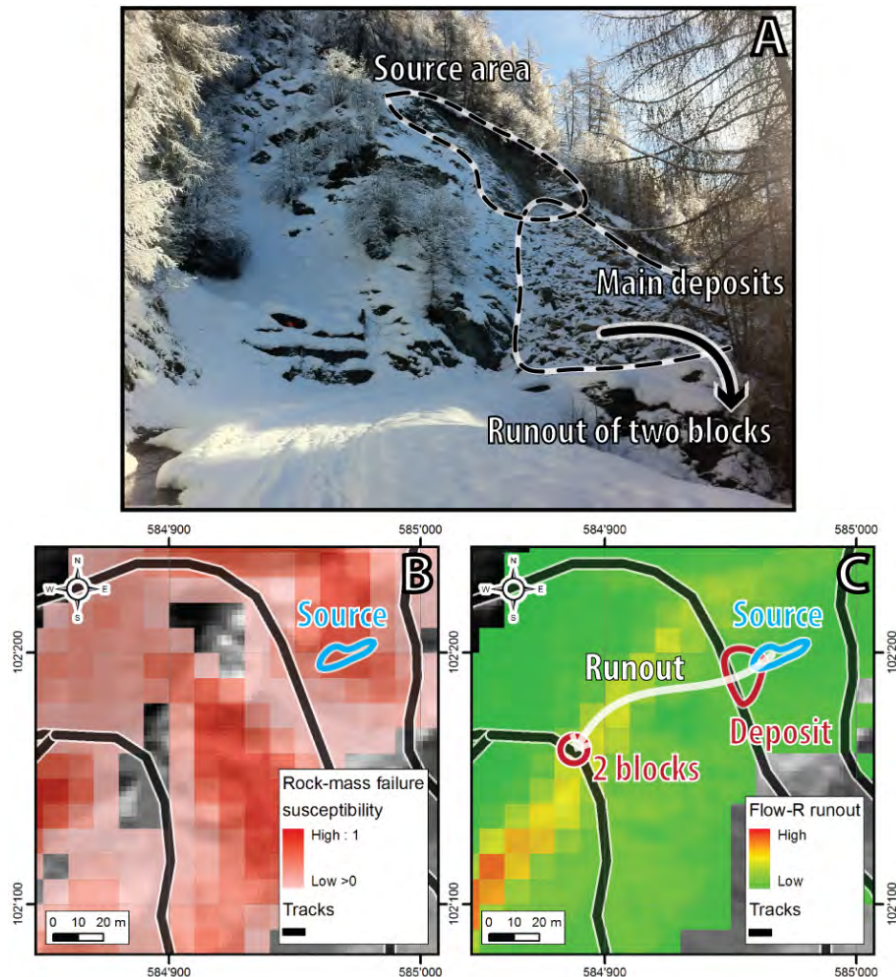


Figure 5.11: (A) A recent rockfall event (2 January 2012) cut a mountain road with a deposit of approx. 1000 m^3 and two single block releases. The height difference between the fresh scarp and the road is about 30 m. (B) The rockfall failure susceptibility map indicates that the onset is clearly defined as a potential rockfall source area with a high rockfall failure susceptibility of about 0.8. (C) The trajectory of two blocks that reached a second road 80 m lower fit well with the predicted runout and confirms *Flow-R* results. (Hillshade: ©2008 swisstopo)

At local scales, robust empirical and physically-based methods have been developed for many years, allowing fine and realistic rockfall failure detections and block propagations. For instance, the *RSS-GIS* method (Günther et al. 2004) allows to deal with internal parameters and external factors of rockfalls. But, it requires a lot of data on topography, structural geology, geotechnical settings and climatic conditions. The *RHRS* method (Pierson et al. 1990) is based on eleven parameters that have to be checked on the field and only on cliffs along roads. These two approaches are therefore indicated for studies at local scales to reliably and accurately detect and rate potential rockfall source

areas; however, they would require substantial efforts for regional works if prioritized locations have not been defined before in-situ investigations. Then, regarding rockfall propagations, software like *HY-STONE* (Crosta et al. 2004; Frattini et al. 2008; Agliardi et al. 2009) is able to deal with both local and regional scale; moreover, it assesses probabilistic runout areas based on physical processes and computations of trajectographies. Furthermore, such software is able to consider countermeasures; fences design and location efficiencies can be estimated before their setup (Agliardi et al. 2009) to optimize them. However, it requires many inputs (such as rolling frictional angles, normal and tangential restitution coefficients) that have to be estimated and spatially distributed for all surfaces type of the study area, depending on landuses as well as superficial and bedrock geologies. Therefore, it involves, for studies at regional scale, more efforts to acquire differentiated input parameters and compute runout than the *Flow-R* model.

5.4.4 Influences of the cell size DEM

The DEM resolution influences rockfall source detections: a coarse DEM tends to smooth high slope angle values.

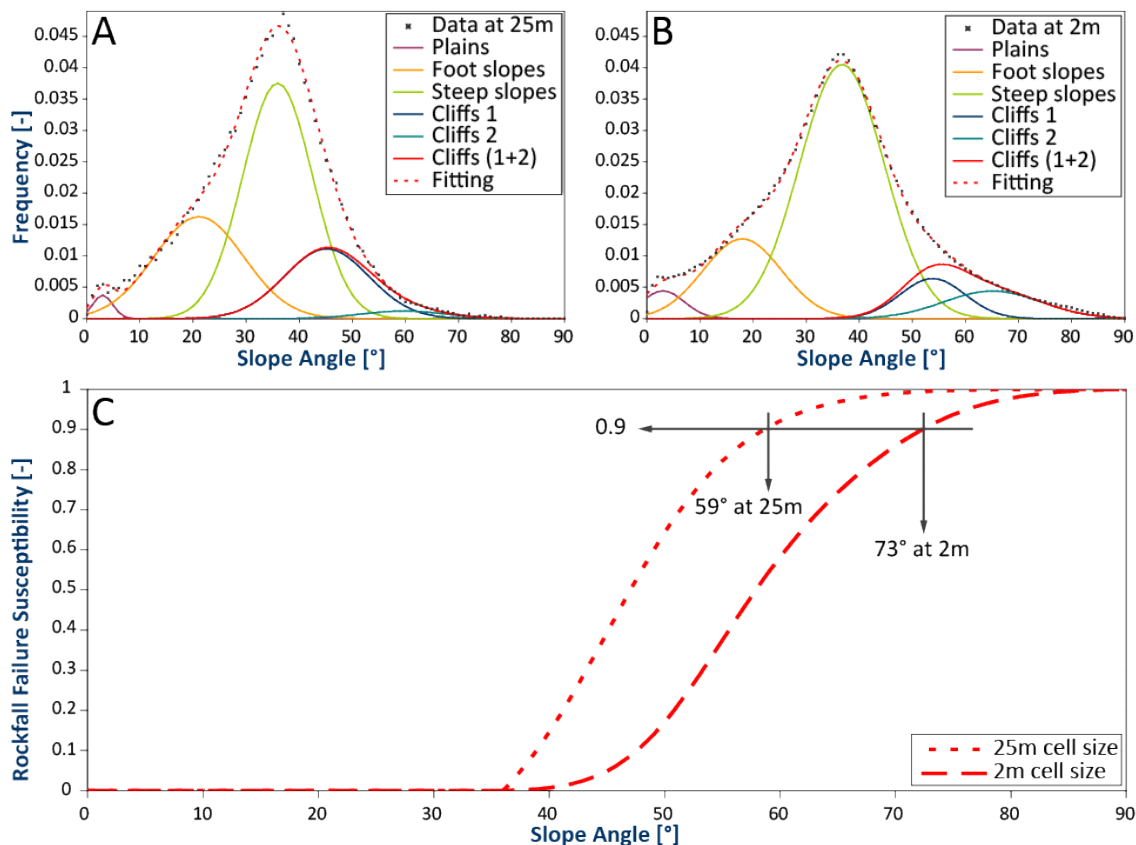


Figure 5.12: (A) Normal distributions of the slope angles of the *limestones* HMA in the Bagnes Valley extracted from a 25 m resolution DEM. (B) Normal distributions of the slope angles of the same *limestones* HMA in the Bagnes Valley extracted now from a 2 m resolution DEM. (C) Cumulative distribution functions are shown for the same limestone HMA, once with a 25 m resolution DEM and once with a 2 m resolution.

As stated in Loye et al. (2009), it implies that the higher resolution the DEM is, the smaller the potential source areas detected are. Furthermore, the coarser the DEM is, the lower the apparent slope angle of a vertical cliff is. For example, a 10 m vertical cliff has an apparent slope angle of 83° on a 2 m DEM instead of 55° on a 10 m DEM (Loye et al. 2009). As threshold angles which are used to identify block release susceptibilities (namely m_{ss} , m_c and σ) are extracted from slope maps, their values directly depend of the DEM cell size.

Thus, for the same detected cliff, the coarser the DEM is, the lower these threshold angles of cliff detection are (Figures 5.11A and 5.11B). It means that the influence of the DEM cell size is implicitly taken into account by the real *Slope Angle Frequency Distribution* and no corrections have to be added. Figure 5.12C illustrates a limestone cliff with an apparent slope angle of 59° on a 25 m DEM and 73° on a 2 m DEM having the same susceptibility of 0.9, regardless of the DEM cell size used during the SAD approach.

5.4.5 Hazard calibration

When it comes to converting rockfall susceptibilities into hazard (i.e. number of blocks per year per cell), the location of the calibration section associated to an inventory has a strong influence. Ideally, the section should be located along a non-forested slope without remediation systems. Therefore, if the calibration section is located along forested slopes, the final hazard would be underestimated along non-forested adjacent slope, because of a biased number of events due to blocks deviated or stopped by trees or anthropogenic countermeasures.

However, due to practical issues, the calibration step has to be achieved with inventories that are available (when they are), even if they are not always performed along optimum road sections. Nevertheless, a preliminary method to calibrate hazard is proposed and is still in progress; enhanced approaches will have to be developed in future works. Up to now, at least one section is needed to perform this calibration, but multiple road sections could also be used. Moreover, introducing during the calibration step (i.e. Eq. 5.8) two adjustment factors to take into account (1) classical censoring effects inside inventories (Hungri et al. 1999) and (2) rockfall-forest interactions along forested slopes based on statistical studies (Dorren et al. 2005) would be the first examples of future evolutions that could improve the reliability of the hazard calibration.

5.5 Conclusions

The improved approach of the *Slope Angle Distribution* and the *Flow-R* software were introduced and carried out along roads of the Val de Bagnes to assess the risk induced by fragmental rockfall to vehicles traffic. Linking the normal distributions of cliffs units with normalized cumulative functions,

rockfall onset areas can be identified with rock-mass-failure susceptibility. Indeed, these indexes can be achieved at regional scale according to slope angle values inside homogeneous morphometric areas thanks to the enhanced SAD procedure. Then *Flow-R* software provides the relative frequencies of block propagations, using several approaches and susceptibilities of source areas. The reach angle that controls the maximum runout extent should be calibrated with back analysis of past events on orthophoto or inventories; in case of limited input data, reach angles can still be extracted from extensive reviews (Toppe 1987; Evans et Hungr 1993; Dorren 2003a). Thanks to these results, i.e. rock-mass-failure susceptibilities and relative frequencies of propagations, hazard maps are achieved and calibrated with an inventoried number of events along a road section.

Even if the obtained quantitative risk assessment is an approximation, this improved approach allows to deal at low cost with real hazard maps at a regional scale, requiring only few documents, namely a DEM and a geological map (if available). So this approach is indicated for regions which cannot afford systematic detailed assessments of the risk due to rockfalls; thus hotspots can be identified in order to prioritize sections on which detailed investigation and mitigation measures will be the most efficient.

SITE-SPECIFIC LANDSLIDE MONITORING AND MODELLING

6 La Perraire rock slope deformation monitoring and modelling by Ground-based InSAR and terrestrial LiDAR integration

After Michoud C, Baillifard FJ, Derron MH, Jaboyedoff M: La Perraire rock slope deformation monitoring and modelling by Ground-based InSAR and terrestrial LiDAR integration. In prep for Engineering Geology

Abstract

La Perraire instability is an active deep seated rock slope deformation involving long-term movements and frequent rockfalls that threaten infrastructures and populations within the Val de Bagnes, in the Swiss Alps. Since 2006, the rockslide has been periodically monitored by ground-based radar interferometry and terrestrial laser scanning. The integrated use of both techniques was decisive to clarify the whole landslide extension as well as its short and long term kinematics. By performing an original wrapping of millimetric daily displacements recorded by GB-InSAR on dense 3D TLS point clouds, we were able to map the rockslide borders and to highlight non-uniform translational displacements along a wedge failure surface. Moreover, based on sequential TLS comparisons, long term displacements and strain monitoring revealed an active extension of the upper part of about 0.085 %/yr; in addition, displacements rates up to 25 cm/yr and a progressive downward decrease movement are implying a compression of the rockslide toe up to -0.17 %/yr. The instability, with calculated volume between 8 and 10 million cubic meters, could evolve into a rock avalanche that could reach the Lourtier village. These investigations are therefore essential requirements to design an early warning system and to set pertinent alert thresholds.

Keywords: Deep seated rock slope deformation, Mapping, Monitoring, GB-InSAR, Terrestrial LiDAR, Swiss Alps.

6.1 Introduction

For the last 15 years, active wave sensors, such as Laser Scanning (LiDAR) and Radar Interferometry (InSAR), have changed our perception and interpretation of slope activities (Jaboyedoff et al. 2012a; Michoud et al. 2012a; Abellán et al. 2014; Caduff et al. 2014; Monserrat et al. 2014); furthermore they are now routinely used for long-term deformation monitoring and can even be integrated in early warning systems (Baroň and Supper 2013; Michoud et al. 2013a; Tofani et al. 2013).

On one hand, long range terrestrial LiDAR (TLS) devices are based on records of time-of-flight (ToF) of laser pulses being back-scattered by natural targets along fixed line of sight (LOS), as detailed in Vosselman and Mass (2010) or Jaboyedoff et al. (2016). TLS have thus been designed to model infrastructures and topographies with very high point density even in steep and inaccessible areas (Beraldin et al. 2000; Gordon et al. 2001; Lichti et al. 2002). Afterward, TLS have been used to detect *cm* to *m* displacements and volume changes of rock slope deformations over small and large blocks by comparing sequential acquisitions (Hunter et al. 2003; Rosser et al. 2005 and 2007; Abellán et al. 2006 and 2014; Teza et al. 2007; Oppikofer et al. 2008 and 2009; Rabatel et al. 2008; Young et al. 2013; Royán et al. 2014; Michoud et al. 2015). In constrained cases, specific data filtering can even improve the movement detection threshold down to mm levels (Gordon and Lichti 2007; Abellán et al. 2009; Kromer et al. 2015).

On the other hand, InSAR technique is based on the measure of the phase decay between two successive radar images, as detailed in Massonnet and Feigl (1998), Woodhouse (2006), Caduff et al. (2014) or Monserrat et al. (2014). Ground-based portable sensors (GB-InSAR) have been also developed to detect and continuously monitor *mm* ground displacements on large blocks (Tarchi et al. 2003c; Casagli et al. 2003, 2008 and 2010; Antonello et al. 2004; Herrera et al., 2009 and 2011; Barla et al., 2010; Luzi, 2010; Del Ventisette et al. 2012; Schulz et al. 2012; Mazzanti et al. 2015).

However both techniques have some limitations: terrestrial LiDAR is good for surface geometry modelling but its precision actually limits our ability to monitor very slow-moving rock deformations over wide areas; GB-InSAR is suitable for small changes imaging, but its metric resolution and particular geometry in azimuth/range may be sometime difficult to visually interpret (cf. Table 6.1).

Table 6.1: Main advantages and limitations of TLS and GB-InSAR devices in Earth Sciences (after Michoud et al. 2012a). Bold font: advantages of both techniques that we aim to couple. Italic font: limitations of both techniques that we aim to avoid by coupling them.

	Advantages	Limitations
Terrestrial LiDAR	<ul style="list-style-type: none"> - cm resolution, even in steep slopes - Good precision for cm to m displacements - Possible mm precisions for constrained cases <ul style="list-style-type: none"> - 3D displacements - Easy visual interpretations - Light and friendly application in the field 	<ul style="list-style-type: none"> - <i>Not adapted for mm displacements</i> - Long post-processing - Vegetation removal very long - <i>Do not yet usually fit with EWS</i>
GB-InSAR	<ul style="list-style-type: none"> - Very good precision for mm to m (for constrained cases) displacements - Continuous monitoring - Long range (up to 4 km) - Suitable for large areas 	<ul style="list-style-type: none"> - <i>m to dam resolution</i> - <i>Difficult visual interpretations</i> - 1D displacements - Affected by atmospheric effects along weeks - Heavy application on the field

La Perraire landslide is an 8 to 10 million m³ active rock slope deformation at 2'200 m a.s.l. that is threatening the population and infrastructures of the Lourtier village 1'000 m downward, in the Western Swiss Alps (Figure 6.1 and Figure 6.2). The rockslide is developed within highly fractured quartzitic micaschists of the Mont Fort Nappe (greenschist facies) in the Middle Penninic unit (Steck et al. 2001). Cracks opening, block fracturing and sliding, tension trenches, ridges, rock falls and shallow landslides are indeed observed on this slope for more than a decade over a surface area of about 280'000 m² (Figure 6.3). With the final aim of investigating potential failure scenarios from surface displacements (Saito 1969; Voight 1989; Fukuzono 1990; Crosta and Agliardi 2003b; Petley et al. 2005a, 2005b; Rose and Hungr 2007; Federico 2012), we set up 4 TLS acquisitions since 2006, as well as 2 GB-InSAR campaigns, in 2011 and 2012 (cf. Section 6.2).

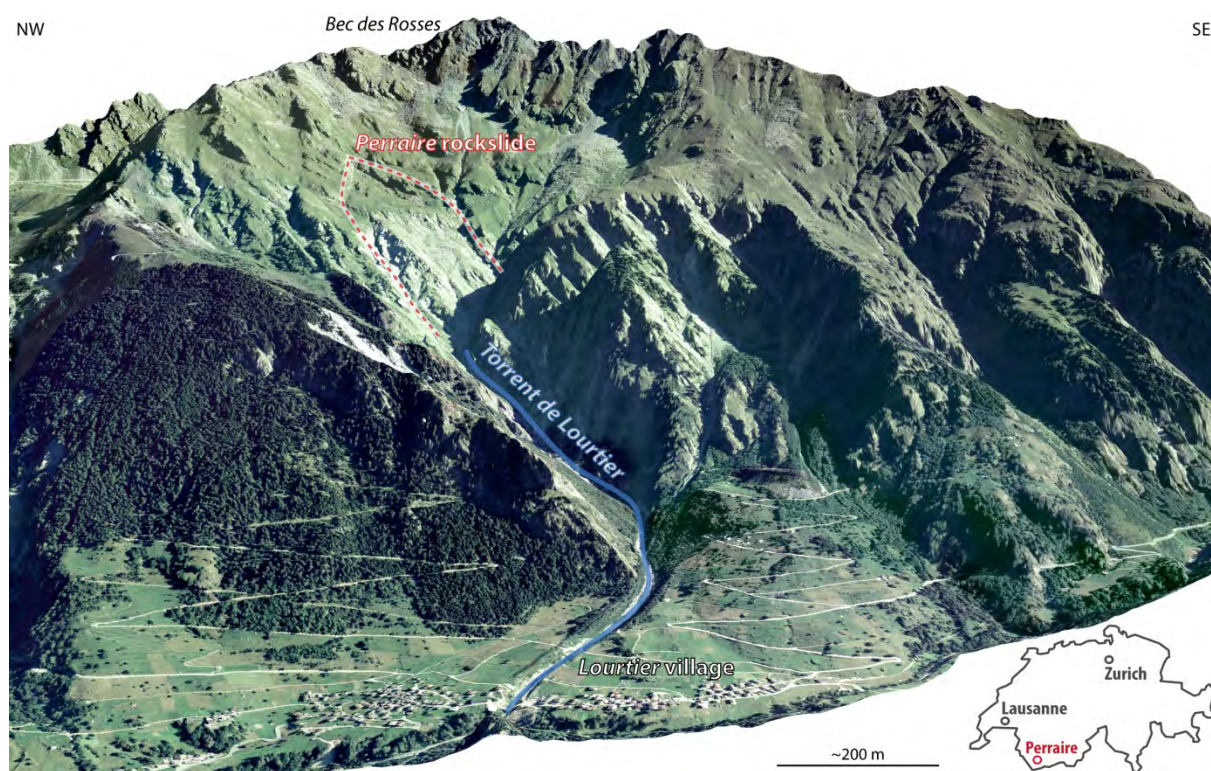


Figure 6.1: Location of La Perraire rockslide and Lourtier village (orthophoto and topography: © swisstopo).

In this paper, we will present results based on these active wave sensors; both of them indeed confirmed decisive and singular capabilities to investigate the rockslide extension and understand its short and long term kinematics (cf. Section 6.3). In addition, to overcome difficulties of visual interpretation of GB-InSAR results due to their singular geometry and resolution, we also designed new tools into LiSAmobile (GB-InSAR device of *Ellegi Ltd*) and Coltop3D (software for geological interpretations from point cloud data, *Terranum Ltd*, Jaboyedoff et al. 2007) to combine advantages of both techniques, by wrapping high precision displacement time series from GB-InSAR on high resolution geometrical data from TLS.



Figure 6.2: Rockslide delimitation in yellow (cf. Section 6.3) and cross-sections locations in blue (cf. Section 6.4) wrapped on general and detailed topographic maps (background maps: © swisstopo).

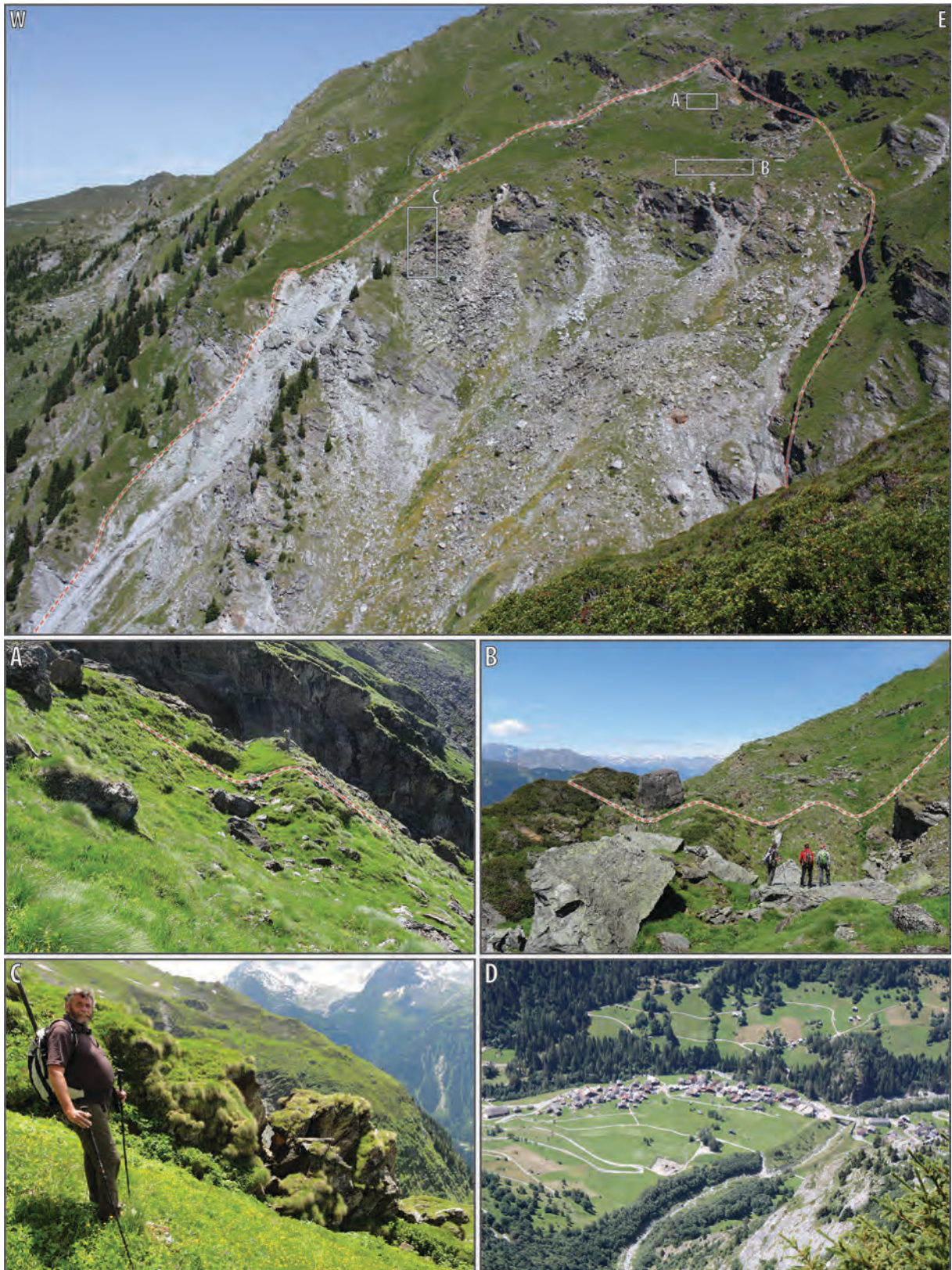


Figure 6.3: (Up) Suspected limits of the La Perraire rockslide. In addition to many rockfalls, scree deposits and shallow landslides visible on the panorama, single and triple ridges systems are shown in (A) and (B), as well as an open trench in a lateral crest in (C), illustrating the extension stresses involved in the upper part of the slope. The downward threatened Lourtier village is displayed in (D).

6.2 Data acquisitions and processing methods

6.2.1 GB-InSAR monitoring campaigns

a. Acquisitions and displacement analysis

Two GB-InSAR monitoring campaigns were carried out with a LiSAMobile™ device during 22 days and 42 days respectively in autumns 2011 and 2012 from Les Toungnes hamlet, at 1'630 m a.s.l. and about 3'500 m of range (Table 6.2). During these two campaigns, we continuously acquired every 10 minutes a SAR image of about 10x1 m pixel size, recording amplitude and phase of the backscattered signals along a South-western LOS (Figure 6.4). To reduce atmospheric artefacts and noises, all SAR images of each day are stacked to increase the signal to noise ratio (SNR). Since displacements projected on the LOS are simply proportional to differences of 24 h stacked backscattered phases with high SNR, they are then retrieved from the standard ground-based interferometry equations (Massonnet and Feigl 1998; Monserrat et al. 2014):

$$\Delta l_{(i,j),t} = \frac{\lambda}{4\pi} \times \Delta \varphi_{s(i,j),t} + e$$

where $\Delta l_{i,j}$ is the projection of the 3D displacements on the LOS of the pixel i,j in [mm] during the time interval t , λ the mean RaDAR wavelength in [mm], $\Delta \varphi_{s(i,j),t}$ the difference of the unwrapped 24 h stacked phase shift of the pixel i,j , measured during the time interval t , and e is the incoherent noise contribution due to environmental and instrumental errors.

Table 6.2: GB-InSAR acquisitions setup.

	19.10.2011 > 10.11.2011	27.09.2012 > 08.11.2012
GB-InSAR device	LiSAMobile	LiSAMobile
Central frequency	Ku band: 17.2 GHz	Ku band: 17.2 GHz
Bandwidth	100 MHz	70 MHz
Rail length	2.5 m	3 m
Number of steps inside the synthetic aperture	601	751
Azimuth resolution at 3'500 m	13 m	10 m
Range resolution at 3'500 m	1.5 m	2 m
Revisiting time	10 min	12 min

b. GB-InSAR and terrestrial LiDAR integration

Because the decametric resolution and the geometry of GB-InSAR acquisitions do not reflect clearly the topography, raw unwrapped interferometry results remain difficult to locate in space and interpret in details at La Perraire.

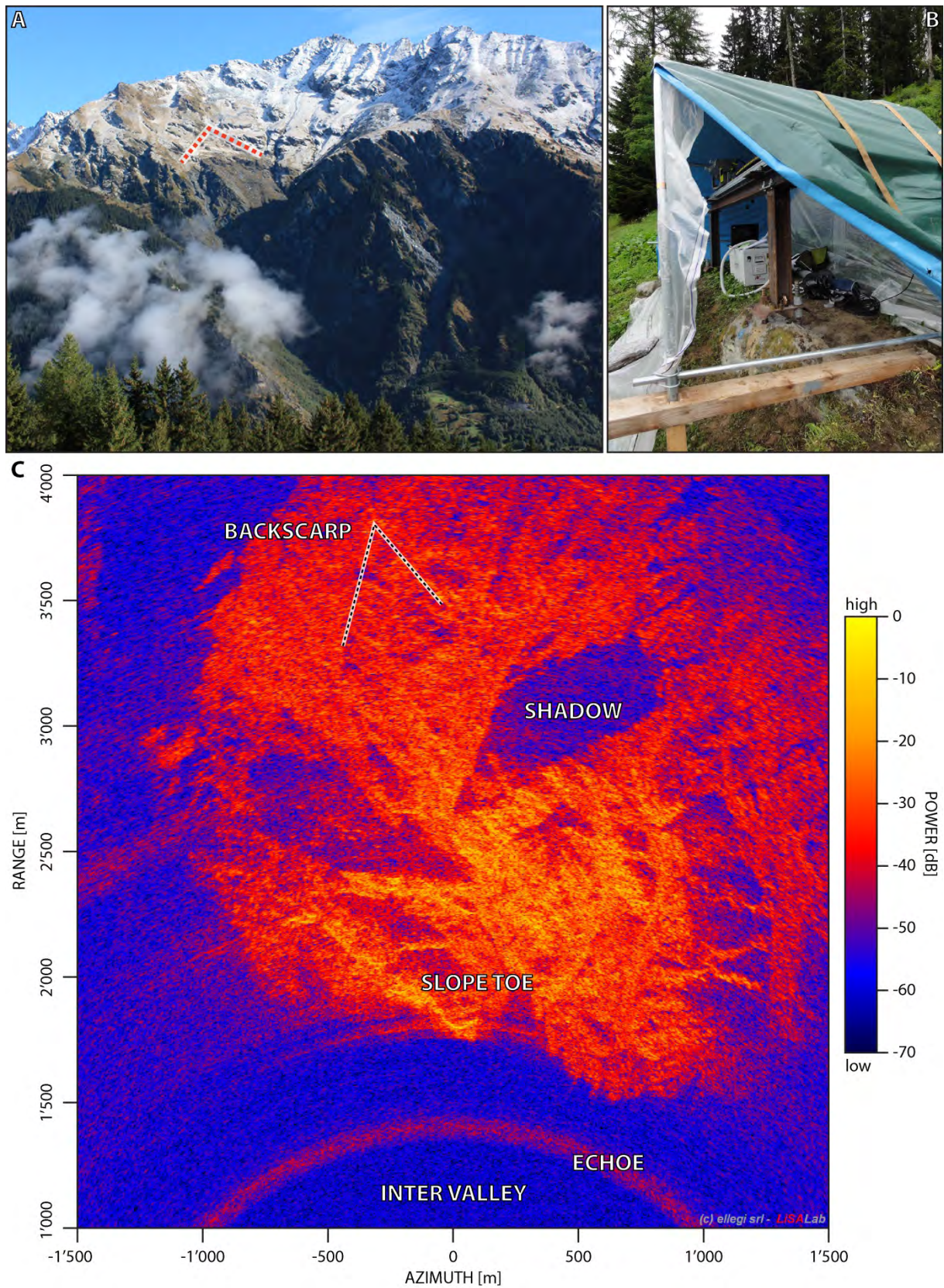


Figure 6.4: (A) GB-InSAR point of view at a mean range of 3'500 m from Les Toungnes hamlet, with the red dashed line underlining the rockslide backscarp. (B) LiSAmobile setup, under its tent. (C) Illustration of an LiSAmobile output data, with the mean amplitude of 24h stacked backscattered SAR signals.

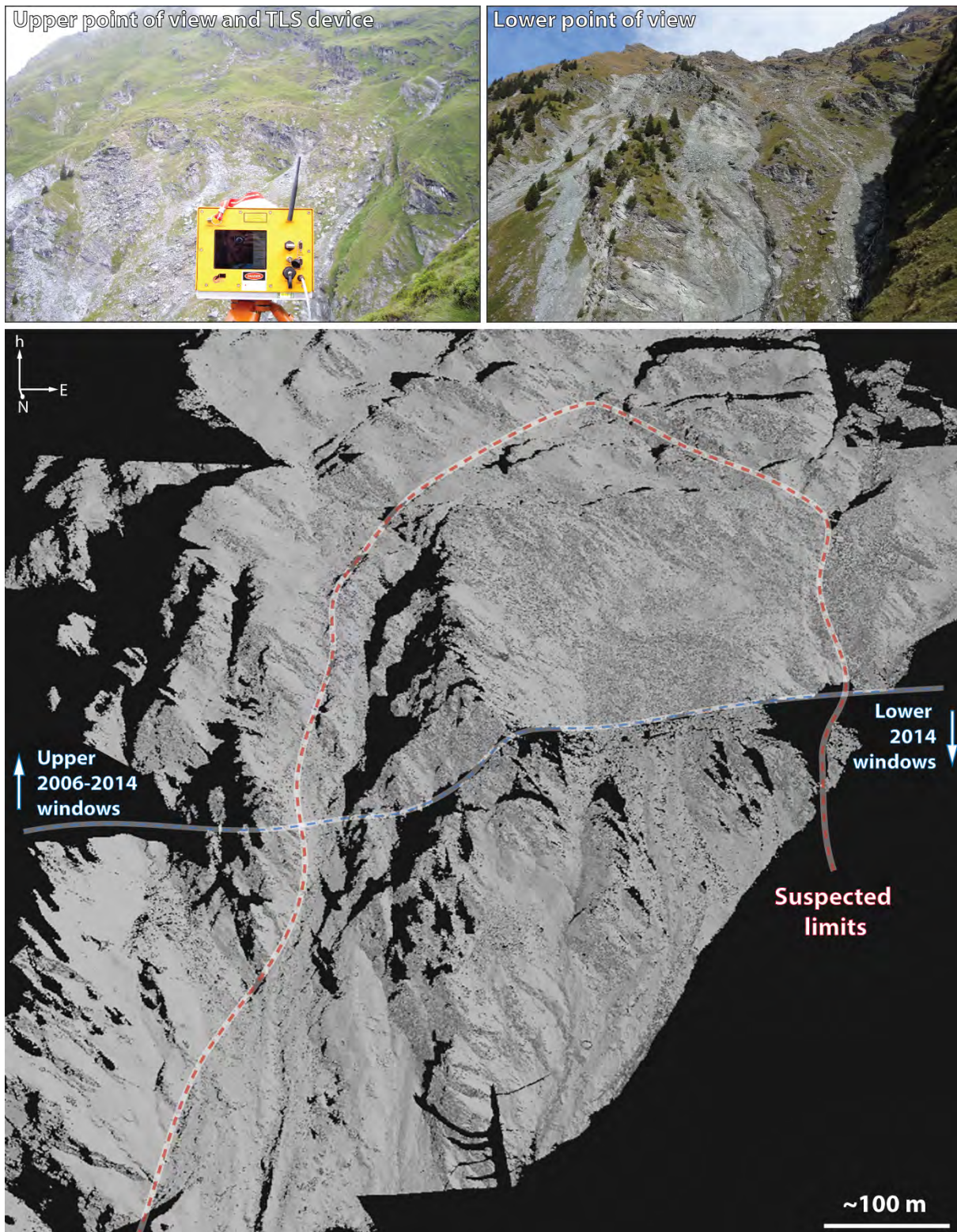


Figure 6.5: (Up) Both upper and lower TLS points of view and TLS setup. (Down) Final point cloud of all cleaned and aligned 08.10.2014 acquisitions, with more than 17 million of points for a mean spacing of about 8 cm.

In order to overcome these complications, additional tools were developed to wrap high precision displacement monitoring from GB-InSAR data on high resolution TLS point clouds clearly modelling topography. In collaboration with *Ellegi Ltd* and the *Åknes/Taffjord Beredskap* centre, we thus added a new exportation module into the processing chain of LiSAmobile devices in order to wrap radar results from their particular geometry on high resolution 3D point clouds with cm mean point spacing. Furthermore, we also added new importation and visualization functionalities into Coltop3D (software for geological interpretations of 3D point cloud) to display these results in 3D and even analysing displacement time series.

6.2.2 TLS monitoring campaign

a. Point clouds acquisitions and geocoding

TLS acquisitions were performed in July 2006, 2011, 2012 and in October 2014, using *Optech™ Ilris3D* devices (Table 6.3). The 2006-2012 scans cover the upper half of the instability with 3 to 6 acquisitions from a single point of view; the 2014 scans cover both upper and lower rockslide parts with 10 different acquisitions from 2 points of view (Figure 6.5).

Table 6.3: TLS acquisitions setup.

	19.07.2006	27.07.2011	18.07.2012	04.10.2014
Terrestrial LiDAR device	Optech Ilris36D	Optech Ilris3D-ER	Optech Ilris3D-LR	Optech Ilris3D-LR
Beam diameter at 500 m (according to Baltsavias 1999)	85 mm	85 mm	125 mm	125 mm
Precision of xyz coordinates at 100 m	7-8 mm	7-8 mm	7-8 mm	7-8 mm
Number of acquisition fences of the upper part	6	4	3	4
Number of acquisition fences of the lower part	-	-	-	6
Weather conditions	Sunny	Wet and cloudy at the top	Sunny	Sunny

Their mean point spacing was set up to about 8 cm, at distances from 500 to 900 m. We then achieved the following steps in order to get cleaned, coregistered and georeferenced point clouds:

1. Each scan is first parsed using the software *Optech™ Parser 5.0.3.1* in order to convert the point coordinates from a spherical system (the device recording each pulse ToF, as well as azimuthal and zenithal angles) to a Cartesian xyz system relative to the device setup.
2. Each scan is then manually and iteratively cleaned from points visually interpreted as noise (as sun artefacts, birds, air dust, etc.) and non-ground points (mainly pine trees and berry shrubs) using the software *Polyworks™ PIFedit 10.1*.

3. All scans (from the different windows) acquired the same day are then coregistered in one merged point cloud, first with a manual selection of common points within overlapping areas. The coregistration is then adjusted using an Iterative Closest Point – based (ICP, Friedman et al. 1977; Besl and Mac Key 1992) algorithm implemented in the software *Polyworks™ ImAlign 10.1*, automatically minimizing distances between points from different scans in overlapping areas.
4. The 2014 point cloud, used as reference since it has the greater extent, is then georeferenced by coregistering it on the SwissALTI3D Digital Elevation Model (2 m cell size aerial LiDAR-based high resolution DEM, ©*swisstopo*), following the same procedure as step 3.
5. The 2006 to 2012 acquisitions are finally georeferenced by aligning them on the 2014 point cloud, following the same procedure as step 3, yet ignoring the unstable part (mapped from GB-InSAR results) for this alignment.

b. Surface change and roto-translation measures

As detailed in the previous section, the 2006 to 2014 point clouds are cleaned, georeferenced and coregistered on the 2014 point cloud used as reference. Topography changes between 2006 and 2012 are consequently obtained by computing the shortest distances from each 2006 point to the 2012 meshed surface using the ICP-based algorithm. In addition, the 2012-2014 changes are computed following the same procedure.

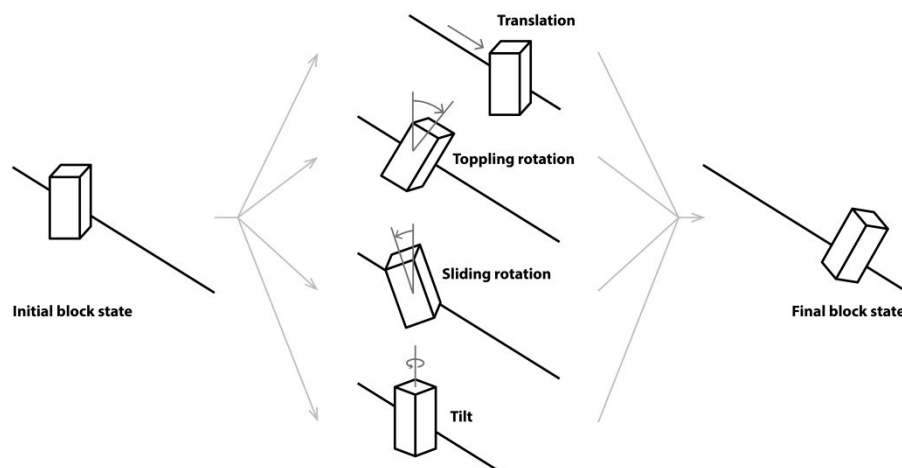


Figure 6.6: Singular rigid body movement types identifiable with roto-translation matrixes.

Furthermore, since we aim to understand strain and stress fields within the instability, real displacements of selected compartments have to be assessed to model the rockslide kinematic. Indeed, movements of a delimited compartment, inside which we assume homogeneous behaviours, can be decomposed into rock-mass toppling and tilt, as well as translation of its centre point (Figure

6.6). Therefore, for each delimited moving compartments, the ICP-based alignment of the isolated point cloud on its initial reference surface can be expressed by a 4x4 matrix recording the roto-translation behaviour of the rock mass between the two TLS acquisitions (Tupling and Pierrynowski 1987; Lichti et al. 2002; Monserrat and Crosetto 2008; Oppikofer et al. 2009).

c. Strain rate assessment

Short term forecasting of time to slope failure is usually based on the acceleration of surface displacements and the inverse velocity method (Saito 1969; Voight 1989; Fukuzono 1990; all reviewed by Federico 2012), especially in brittle materials (Petley et al. 2005a). But this methodology can provide realistic forecasts only during the last acceleration phase prior to final collapse (Petley et al. 2005b; Rose and Hungr 2007). Then, long term predictions can be supported as well with deformation states and strain rates assessments (Jaboyedoff et al. 2012c).

For the upper triangular part of La Perraire instability, where an important extension is being seen in cracks opening and ridge systems (cf. Figure 6.3), the deformation state is estimated on TLS –based longitudinal cross section (cf. Figure 6.7) according to:

$$\bar{\varepsilon}_t = \frac{\Delta l_t}{l_0} = \frac{\Delta l_t}{l_t - \Delta l_t}$$

where $\bar{\varepsilon}_t$ is the deformation state of the upper triangular compartment C1 at time step t in [%], Δl_t the length l_t of this compartment at time step t minus its initial length l_0 in [m]. As a result, positive outputs mean extension processes, while negative results indicate compression ones.

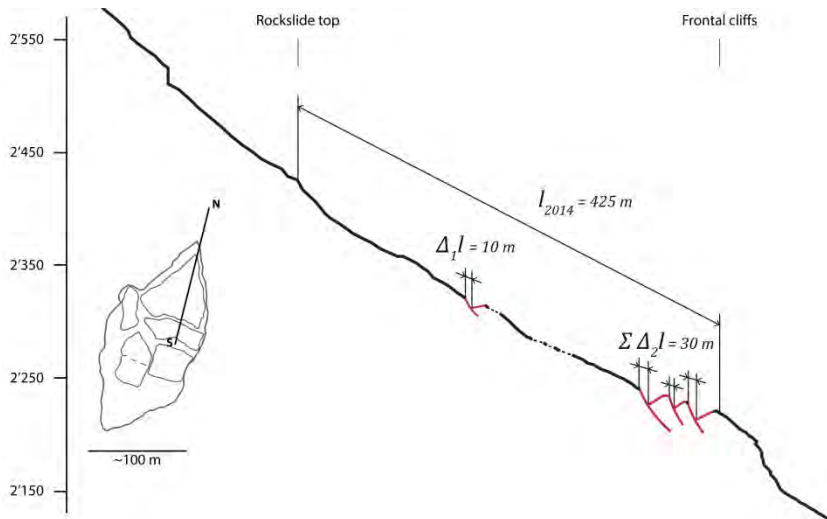


Figure 6.7: Scheme of the deformation state of the upper compartment, based on the 2014 longitudinal cross section. All lengths were measured on the 04.10.2014 TLS points cloud. $\Delta_1 l$ and $\Delta_2 l$ refer respectively to Figures 6.3A and B. (Topography extracted from the 04.10.2014 TLS acquisitions.)

More precisely, strain rates can be computed for each sequential acquisition over the whole rockslide surface (Teza et al. 2008; Travelletti et al. 2014). Here strain rates are punctually but accurately computed at centre of each compartment over time on sequential TLS acquisitions according to (Jaboyedoff et al. 2012c):

$$\dot{\bar{\epsilon}}_{n,t} = \frac{\Delta \bar{\epsilon}_{n,t}}{\Delta t} = \frac{\Delta l_{n,t}}{l_{n,t-1}} \times \frac{1}{\Delta t}$$

where $\dot{\bar{\epsilon}}_{n,t}$ is the strain rate at the centre of the compartment n at time step t in [%/yr], $\Delta l_{n,t}$ the length between the reference point located at the top (but outside) of the rockslide and the centre n at time step t minus the same length $l_{n,t-1}$ at time step $t-1$ in [m] and Δt the time interval between time steps $t-1$ and t in [yr]. In the same way, internal strain rates of the lateral western crest can be assessed by fixing the reference point at the top of this crest, instead of the top of the whole instability (cf. Figure 6.13). This point located within the rockslide on a well identifiable block is also moving and its coordinates have to be picked at each acquisition.

6.2.3 TLS-based geometry modelling

a. Structural settings

The orientation of the discontinuity planes can be extracted from georeferenced point clouds imported into Coltop3D™. The software indeed assigns to all points a colour code according to azimuth and orientation of their normal vector (Jaboyedoff et al. 2007). By manually picking hundreds of selected points displaying with the same colour, we then extract normal vector orientations belonging to the same discontinuity set. Mean orientations of all selected points are then extracted for each identified discontinuity sets, with a semi-automatic clustering assessment based on Fisher distributions using Dips™ software (Diederichs, 1990). All discontinuity orientations are defined according to the dip direction / dip angle convention.

b. Volumes estimations

Volumes are then estimated using the sloping local base level (SLBL: Jaboyedoff et al. 2004, 2009c and 2015), derived from isobases and base level surfaces defined in geomorphology (Golts and Rosenthal 1993; Mills 2003). The SLBL indeed computes volumes of delimited instable slope masses that are not buttressed at the toe and assumed as erodible, by computing a curved surface joining the top to the bottom of the spur which is considered as the most probable slip surface. This model is constrained by a former electrical-resistivity tomographies carried out in the upper triangular part in 2006 (Borle et al. 2007), that first estimated a mean surface failure close to 50 m deep above frontal cliffs.

6.3 Processing results

6.3.1 Short term continuous monitoring

After having excluded InSAR acquisitions affected by two much atmospheric decorrelations on the 2011 GB-InSAR monitoring campaign, we quantified the Perraire slope displacements projected on the radar LOS from 28 October to 7 November 2011 (cf. Section 6.2.1a). Cumulated unwrapped displacements projected on the radar LOS measured are displayed in Figure 6.8.

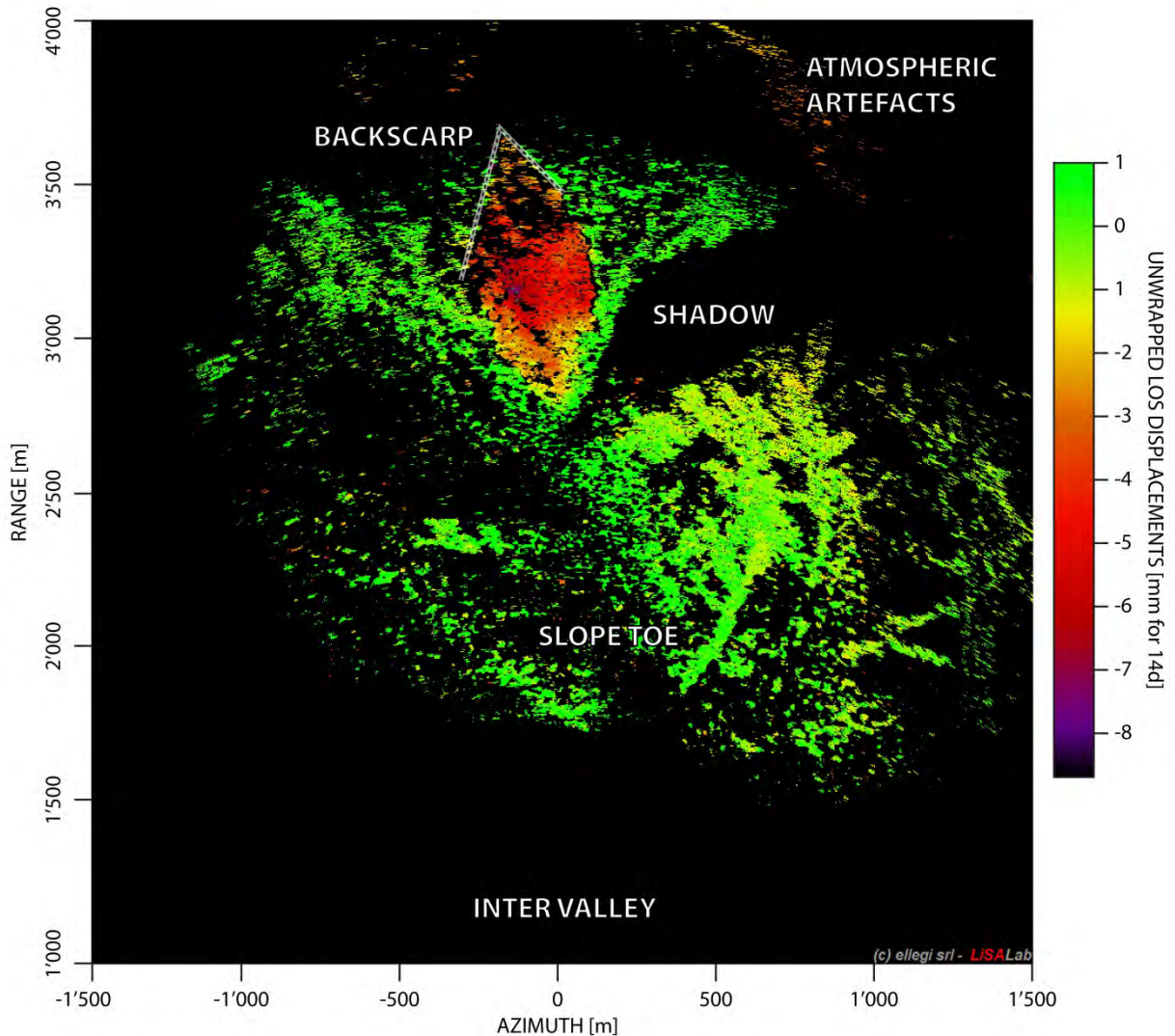


Figure 6.8: GB-InSAR unwrapped displacements projected on the radar LOS measured from 28 October to 7 November 2011 (period of 10 days). We can first note that the backscarp is clearly delimited by the wedge cliffs (negative displacement values indicate movements toward the device).

During this period of 14 days, movements up to 10 mm have been recorded within the upper part of the rockslide, and displacements progressively decrease at the toe, imaged for the first time. We can notice as well a clear triangular upper delimitation of the instability, whereas the lower limit is more

diffuse. In addition, 2012 GB-InSAR results confirm displacement rates measured in 2011. Finally, no movement computations can be performed by comparing 2011 with 2012 SAR images, since geometric decorrelations, due to the important slope deformation, drastically decreased the signal coherence.

Furthermore, these monitored high precision displacements are projected on the high resolution topography modelling (cf. Section 6.2.1b), as illustrated in Figures 6.9 and 6.10; the prior observations from raw output can then be refined. First, by checking displacement time series of 9 stable scatterers (Figure 6.10), measurements errors of the 2011 GB-InSAR monitoring campaign are estimated at ± 1 mm, in agreement with LiSAmobile specifications (Ellegi Srl pers. comm.); in addition, time series of moving scatterers are consistent over days, with low noise level. Monitored displacements, based on 24 h stacked phase scenes (cf. Section 6.2.1a), seem then reliable. We then observe that the wedge created by the 2 cliff systems is a clear upper limit and acts thus as the Perraire backscarps. In the lower part of the slope, displacements are progressively decreasing down to 2 mm in 14 ; for the first time, the rockslide diffuse lower extension is thus monitored and mapped at an altitude of about 1'750 m.a.s.l.

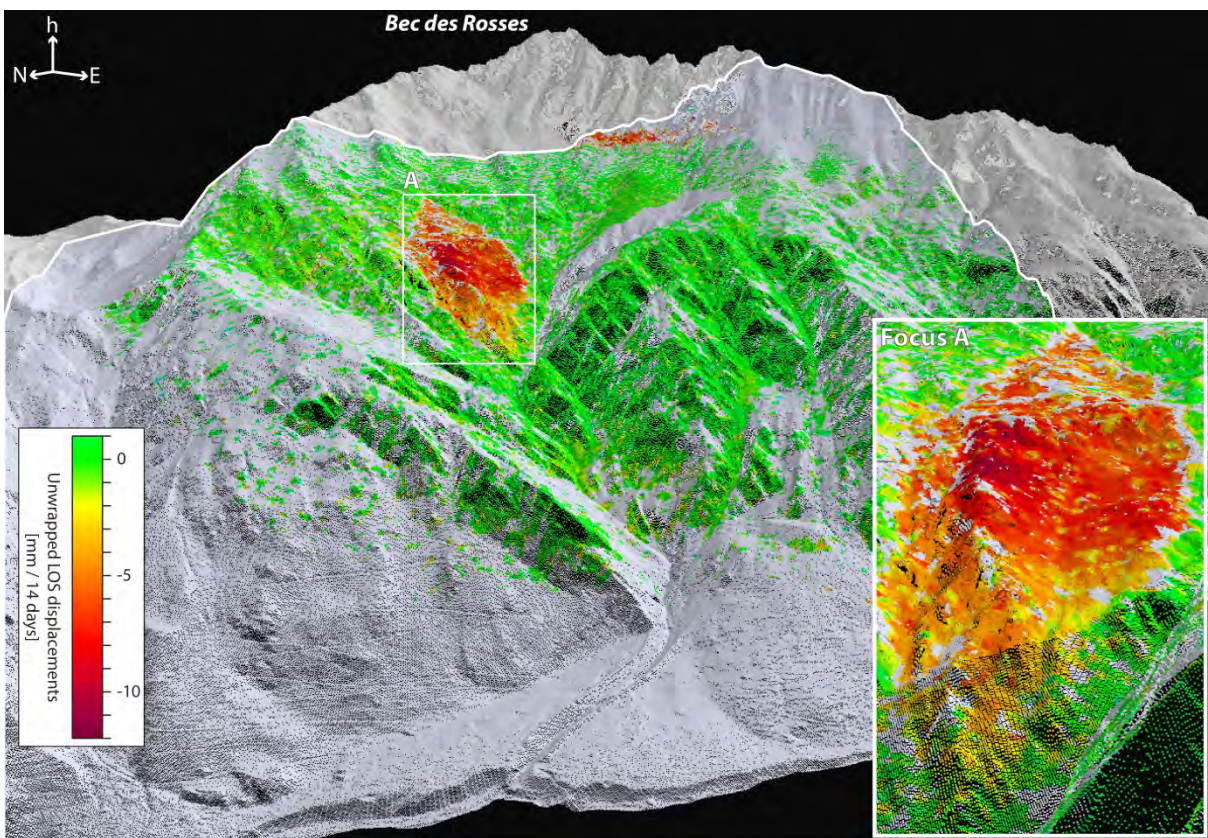


Figure 6.9: Autumn 2011 GB-InSAR unwrapped displacements displayed in Coltop3D on ALS and TLS point cloud. For the first time, were able to map the lower rockslide limits and measure a non-uniform translation along a crone-toe axe. In addition, the upper wedge composed by the 2 cliff system is confirmed as upper scarp of the instability. (ALS points: © swisstopo)

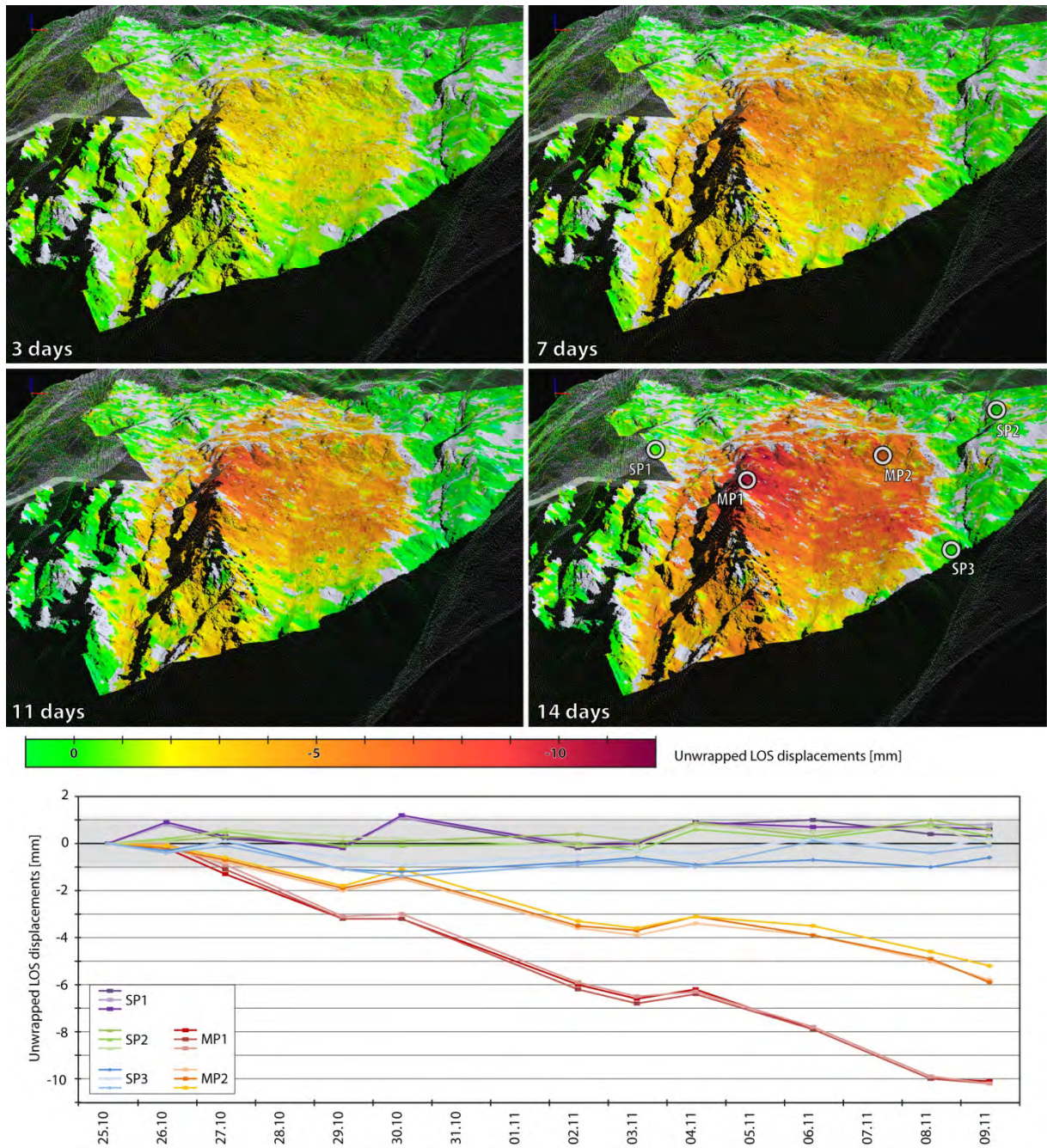


Figure 6.10: Autumn 2011 GB-InSAR displacement time series of 9 stable scatterers (selected in 3 locations) and 6 moving ones (selected in 2 locations). Uncertainties estimated with noise level of points located in stable areas are close to ± 1 mm, corresponding to LiSAmobile specifications. Displacements of points located on frontal cliffs and lateral western crest are quite regular within this short period of 14 days, to reach respectively -6 and -10 mm. (ALS points: © swisstopo)

In addition, short-term displacement field is not uniform within the whole instability: the largest movements are indeed measured on the lateral western crest, with displacements up to 12 mm southward, while movements of surrounding areas are closer to 6 to 8 mm southward. In addition, a clear progressive attenuation of displacements from the top to the toe of the lateral crest and the scree deposit area is visible.

6.3.2 Long term sequential monitoring

a. Change detection

By applying ICP algorithms on sequential point clouds (cf. Section 6.2.2a), we identify main surface changes that occurred during time interval between TLS acquisitions.

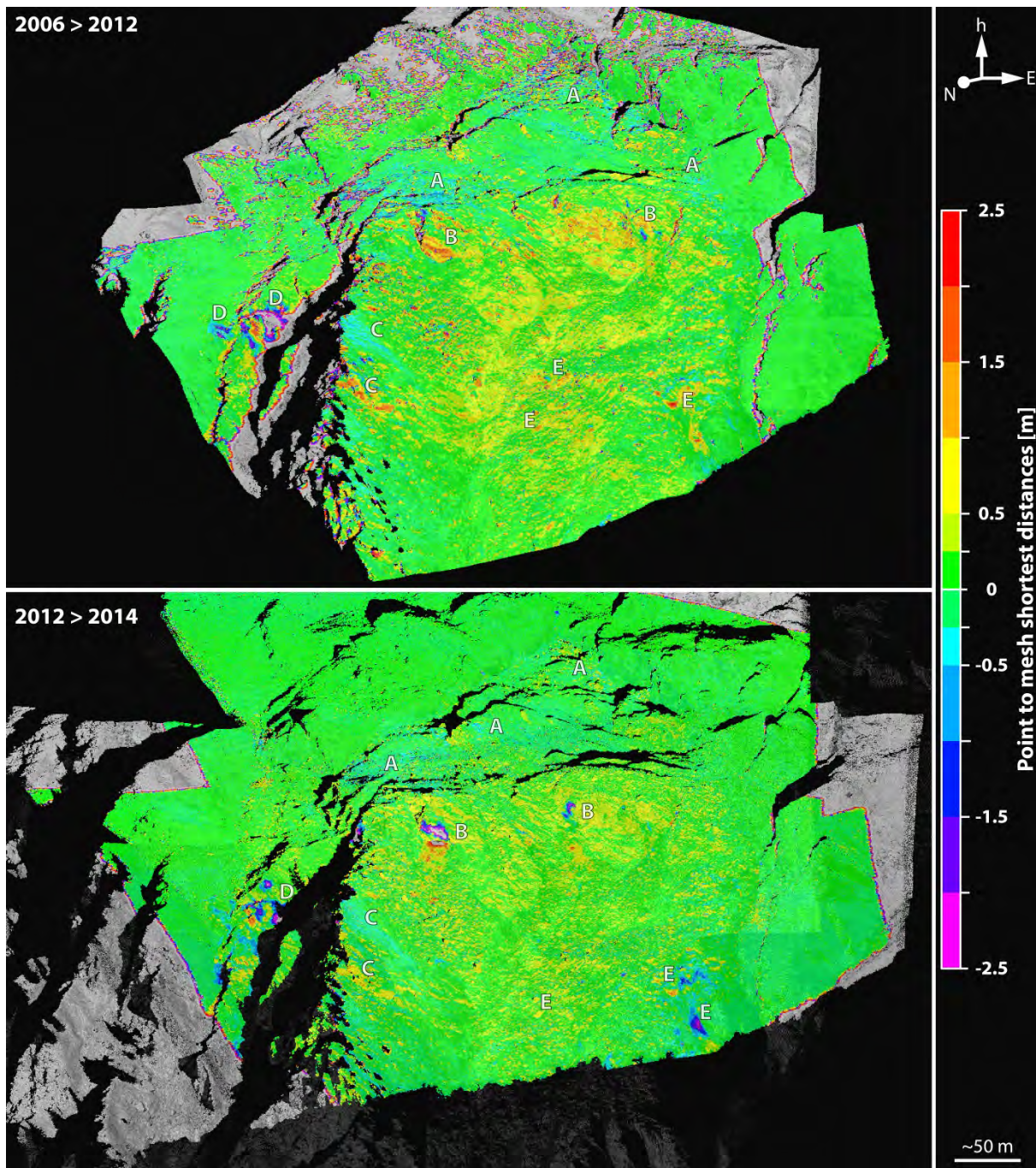


Figure 6.11: TLS-based change detection, using ICP-based shortest distance comparison algorithm between (up) the 2006 mesh and the 2012 points and (down) the 2012 mesh and the 2014 points. The letters refer to the description list of this section. (Positive values: displacements toward the slope or accumulated material. Negative values: subsidence or eroded material).

Letters on Figure 6.11 refer to all changes listed hereafter.

Between July 2006 and 2012 (period of 7 years):

- a. Some sectors of the upper part have subsided of about 4 cm/yr (i.e. 30 cm), even up to 14 cm/yr (i.e. 1 m) just upward the lateral crest ;
- b. The frontal cliffs are displaced of 14 to 22 cm/yr (i.e. 1 to 1.5 m), and several rockfalls are also detected;
- c. The outcrop in the middle of the lateral crest shows downward displacements up to 18 cm/yr (i.e. 1.25 m), and the upward thalweg is being eroded;
- d. On the rockslide western side, a large rockfall is detected;
- e. Some blocks in the scree deposit areas, below the frontal cliffs, slid of about 14 cm/yr (i.e. 1 m), and even up to 29 cm/yr for some of them (i.e. 2 m).
- f. No other significant changes are detected with TLS data outside the rockslide limits mapped from the GB-InSAR short-term measures.

Furthermore, between July 2012 and October 2014 (period of 2.25 years):

- a. Some sectors of the upper part have subsided up to 11 cm/yr (i.e. 25 cm);
- b. The frontal cliffs are displaced of about 33 cm/yr (i.e. 0.75 m), and 2 large rockfalls are detected;
- c. The outcrop in the middle of the lateral crest shows downward displacements up to 45 cm/yr (i.e. 1 m), and the upward thalweg is still being eroded;
- d. On the western rockslide sides, several small rockfalls have been detected;
- e. Some blocks in the scree deposit areas slid of about 11 and 22 cm/yr (i.e. 0.25 and 0.5 m), and even up to 45 cm/yr (i.e. 1 m) downward, where a large rockfall is detected as well.

b. Roto-translation of compartments

Within the upper part of the rockslide, six different compartments were distinguished (Figure 6.12) over large areas in order to assume deep-seated failure surfaces of compartments (Carter and Bentley 1985; Jaboyedoff and Derron 2015):

- Test compartment: upper part of the slope, supposed as stable in regards of short term displacements and long term changes detection. This compartment is used to estimate uncertainties, since measurement errors might be introduced during TLS acquisitions and point clouds coregistration and georeferencing steps ;
- Compartment C1: triangular upper part, where the observation of recent crack opening, rock fracturing and ridges are evidences of active extension stresses;
- Compartment C2: upper western section, where displacements can be observed on GB-InSAR data although evidences of movements are not clear in the field;

- Compartment C3: lateral western crest, where high displacements are detected by GB-InSAR, and large trenches and recent rockfalls were observed as well. Because we noticed on short-term displacements a progressive attenuation of movements downwards, the compartment 3 is subdivided in 2 areas, the upper 3.1 and the lower 3.2 ones, in order to quantify the long term deformation of the lateral crest;
- Compartment C5: all the frontal cliffs, where rockfalls and metric displacements toward the slope are recorded;
- Compartment C6: scree deposit areas, where the highest displacements were detected on previous point cloud comparisons.

For all these compartments, roto-translation movement types (Figure 6.6) are extracted from TLS alignment matrixes (cf. Section 6.2.2b) and are summed up in Table 6.4 and Figure 6.13. We can first notice that uncertainties from measurement and ICP-based alignment errors of the stable compartment are estimated of about 4 cm for the translation values and close to 0.01° for rotation and tilt angle. Moreover, errors on absolute azimuths and dip cannot be assessed without other external monitoring method; directions might thus vary of few degrees, while it would not change the relative movement variation of compartments over time.

Table 6.4: Translation (dip direction, dip and amplitude) - Rotation (direction -northward azimuth: sliding rotation; southward azimuths: toppling rotation- and amplitude) - Tilt angle, detected by roto-translation matrixes on all compartments.

	19.07.2006 > 8.10.2014	27.07.2011 > 8.10.2014	18.07.2012 > 8.10.2014
Stable compartment	$\begin{pmatrix} 058^{\circ}40^{\circ} \\ 5 \text{ cm} \end{pmatrix} - \begin{pmatrix} 291^{\circ} \\ 0^{\circ} \end{pmatrix} - 0^{\circ}$	$\begin{pmatrix} 070^{\circ} - 16^{\circ} \\ 3 \text{ cm} \end{pmatrix} - \begin{pmatrix} 202^{\circ} \\ 0^{\circ} \end{pmatrix} - 0^{\circ}$	$\begin{pmatrix} 035^{\circ}03^{\circ} \\ 4 \text{ cm} \end{pmatrix} - \begin{pmatrix} 200^{\circ} \\ 0^{\circ} \end{pmatrix} - 0^{\circ}$
Compartment 1	$\begin{pmatrix} 206^{\circ}42^{\circ} \\ 172 \text{ cm} \end{pmatrix} - \begin{pmatrix} 335^{\circ} \\ 0.1^{\circ} \end{pmatrix} - 0^{\circ}$	$\begin{pmatrix} 197^{\circ}41^{\circ} \\ 70 \text{ cm} \end{pmatrix} - \begin{pmatrix} 340^{\circ} \\ 0^{\circ} \end{pmatrix} - 0^{\circ}$	$\begin{pmatrix} 202^{\circ}43^{\circ} \\ 54 \text{ cm} \end{pmatrix} - \begin{pmatrix} 308^{\circ} \\ 0^{\circ} \end{pmatrix} - 0^{\circ}$
Compartment 2	$\begin{pmatrix} 198^{\circ}31^{\circ} \\ 133 \text{ cm} \end{pmatrix} - \begin{pmatrix} 68^{\circ} \\ 0.2^{\circ} \end{pmatrix} - 0^{\circ}$	$\begin{pmatrix} 206^{\circ}33^{\circ} \\ 61 \text{ cm} \end{pmatrix} - \begin{pmatrix} 68^{\circ} \\ 0.1^{\circ} \end{pmatrix} - 0^{\circ}$	$\begin{pmatrix} 213^{\circ}26^{\circ} \\ 42 \text{ cm} \end{pmatrix} - \begin{pmatrix} 78^{\circ} \\ 0.1^{\circ} \end{pmatrix} - 0^{\circ}$
Compartment 31	$\begin{pmatrix} 189^{\circ}34^{\circ} \\ 259 \text{ cm} \end{pmatrix} - \begin{pmatrix} 268^{\circ} \\ 0.4^{\circ} \end{pmatrix} - 0^{\circ}$	$\begin{pmatrix} 192^{\circ}33^{\circ} \\ 119 \text{ cm} \end{pmatrix} - \begin{pmatrix} 264^{\circ} \\ 0.2^{\circ} \end{pmatrix} - 0^{\circ}$	$\begin{pmatrix} 197^{\circ}38^{\circ} \\ 89 \text{ cm} \end{pmatrix} - \begin{pmatrix} 245^{\circ} \\ 0.1^{\circ} \end{pmatrix} - 0^{\circ}$
Compartment 32	$\begin{pmatrix} 200^{\circ}33^{\circ} \\ 132 \text{ cm} \end{pmatrix} - \begin{pmatrix} 13^{\circ} \\ 0.1^{\circ} \end{pmatrix} - 0^{\circ}$	$\begin{pmatrix} 213^{\circ}25^{\circ} \\ 55 \text{ cm} \end{pmatrix} - \begin{pmatrix} 65^{\circ} \\ 0^{\circ} \end{pmatrix} - 0^{\circ}$	$\begin{pmatrix} 219^{\circ}41^{\circ} \\ 59 \text{ cm} \end{pmatrix} - \begin{pmatrix} 65^{\circ} \\ 0^{\circ} \end{pmatrix} - 0^{\circ}$
Compartment 5	$\begin{pmatrix} 199^{\circ}32^{\circ} \\ 203 \text{ cm} \end{pmatrix} - \begin{pmatrix} 333^{\circ} \\ 0.1^{\circ} \end{pmatrix} - 0.1^{\circ}$	$\begin{pmatrix} 196^{\circ}33^{\circ} \\ 87 \text{ cm} \end{pmatrix} - \begin{pmatrix} 323^{\circ} \\ 0^{\circ} \end{pmatrix} - 0.1^{\circ}$	$\begin{pmatrix} 197^{\circ}32^{\circ} \\ 62 \text{ cm} \end{pmatrix} - \begin{pmatrix} 301^{\circ} \\ 0^{\circ} \end{pmatrix} - 0.1^{\circ}$
Compartment 6	$\begin{pmatrix} 198^{\circ}26^{\circ} \\ 244 \text{ cm} \end{pmatrix} - \begin{pmatrix} 133^{\circ} \\ 0.2^{\circ} \end{pmatrix} - 0^{\circ}$	$\begin{pmatrix} 199^{\circ}27^{\circ} \\ 119 \text{ cm} \end{pmatrix} - \begin{pmatrix} 129^{\circ} \\ 0.1^{\circ} \end{pmatrix} - 0^{\circ}$	$\begin{pmatrix} 203^{\circ}34^{\circ} \\ 90 \text{ cm} \end{pmatrix} - \begin{pmatrix} 144^{\circ} \\ 0.1^{\circ} \end{pmatrix} - 0^{\circ}$

Regarding the rockslide kinematic, the main movement component of these last 8 years is a mean translation toward 200° / 35° to 40° (plunge direction and dip angle convention) with different amplitudes according to the instability sectors. Displacements from 1.3 to 1.7 m were extracted for the upper compartments 1 and 2, whereas we measure a translation of 2.0 m of the frontal cliffs. Furthermore, the upper part of the lateral crest was displaced of 2.6 m, which is almost two times higher than the 1.3 m measured for its lower part. In addition, the rockslide is also affected by a small sliding rotation of about 0.1°, noticed on compartments 1, 2 and 5. No significant tilt angles are measured.

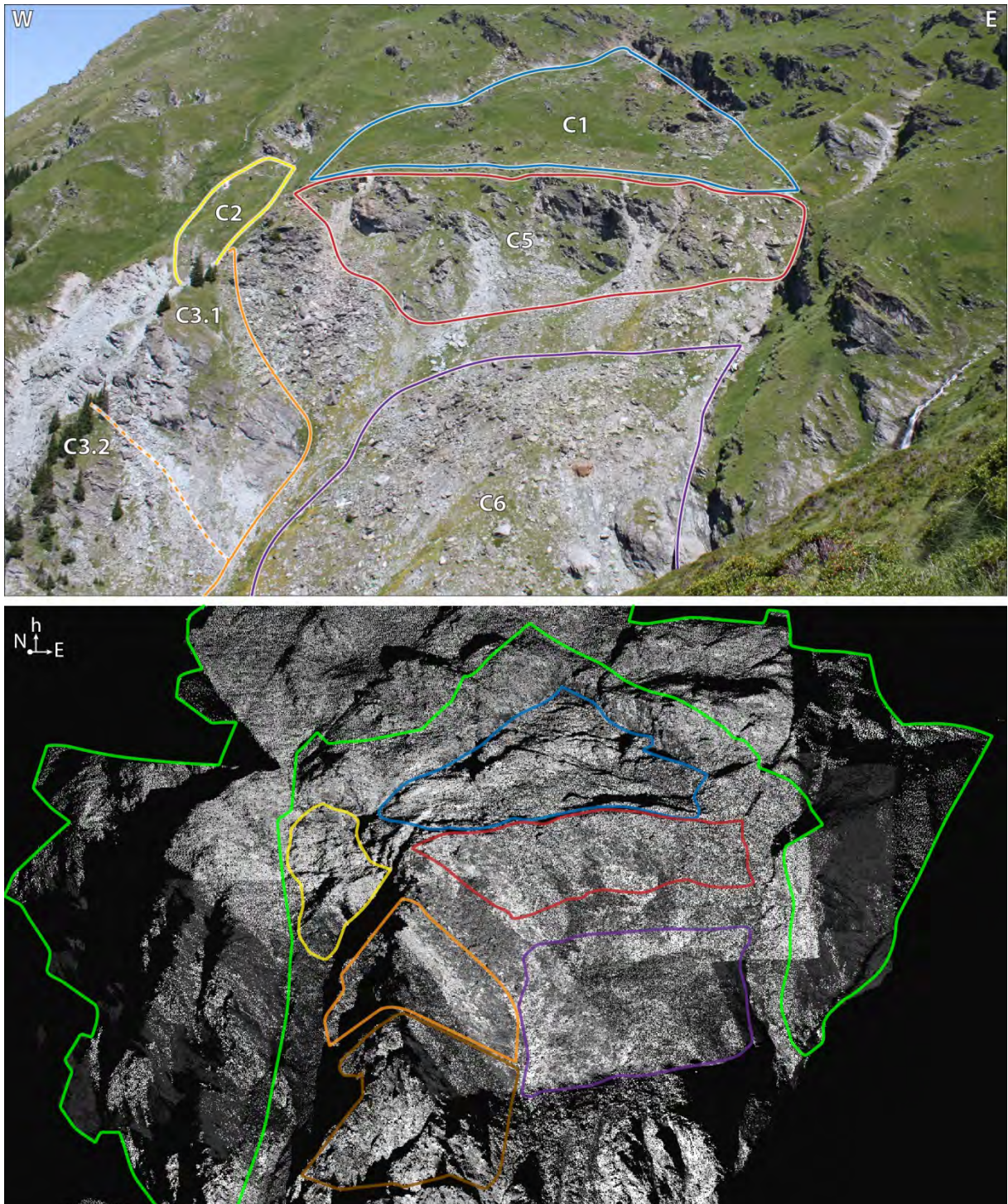


Figure 6.12: Delimitation of all compartments, both on photo (up) and TLS point cloud (down).

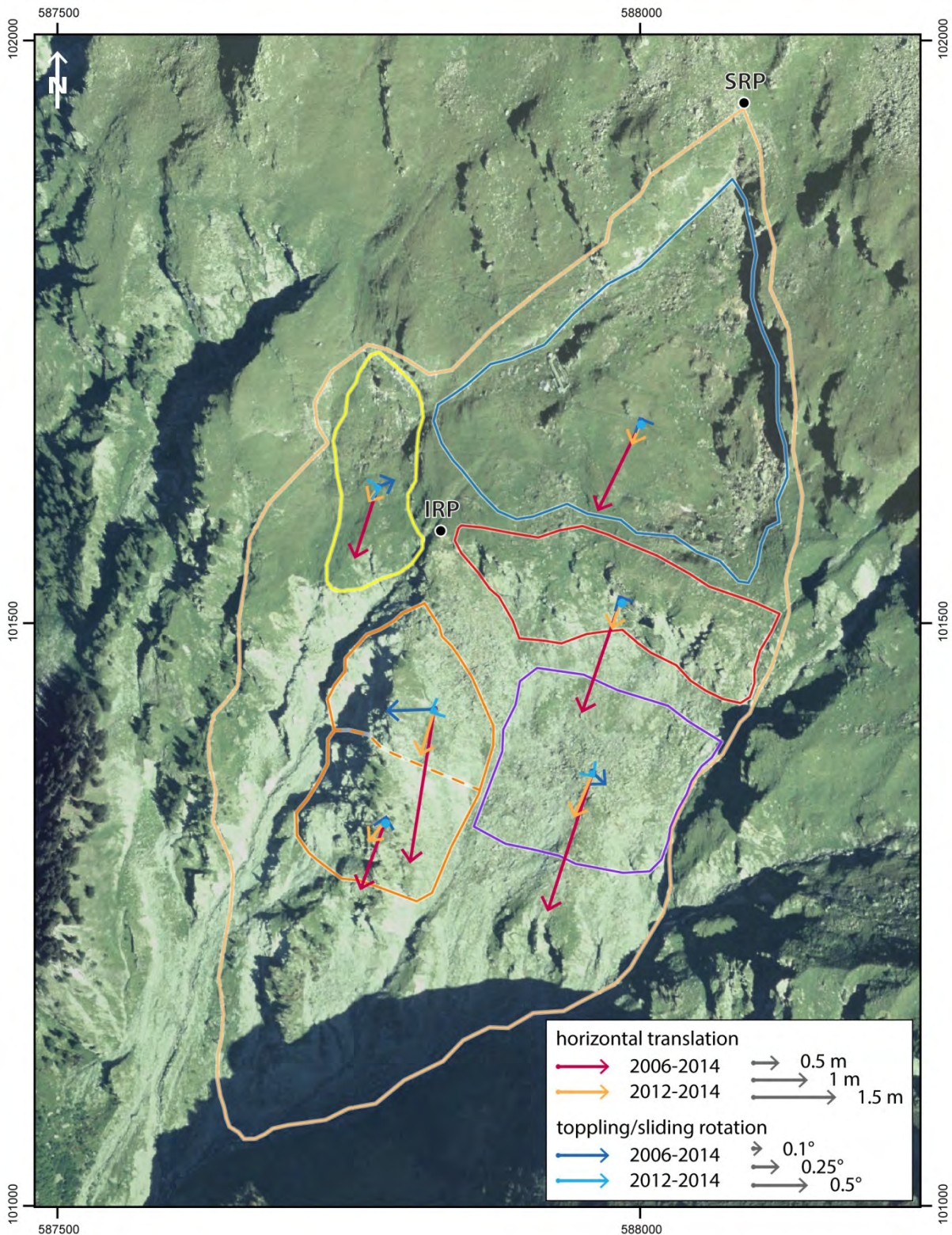


Figure 6.13: XY directions of translation and rotation vectors affecting the 6 compartments delimited within the upper part of the rockslide. Sliding and toppling rotations are respectively highlighted by upward and downward vectors. SRP and IRP identify respectively (1) the stable reference point used to measure strain rates and (2) the internal reference point used to measure internal strain rates of the lateral western crest. (Orthophoto and shaded topography: © swisstopo)

Finally, a progressive increase of mean rockslide compartment velocities is noticed from 2006 to 2014; as reported in Table 6.5 and Figure 6.14, they increase for the beginning of TLS –based measures from 20 to 24 cm/yr on the upper part, from 23 to 28 cm/yr on the frontal cliffs and even from 28 to 40 cm/yr for the top part of the lateral crest.

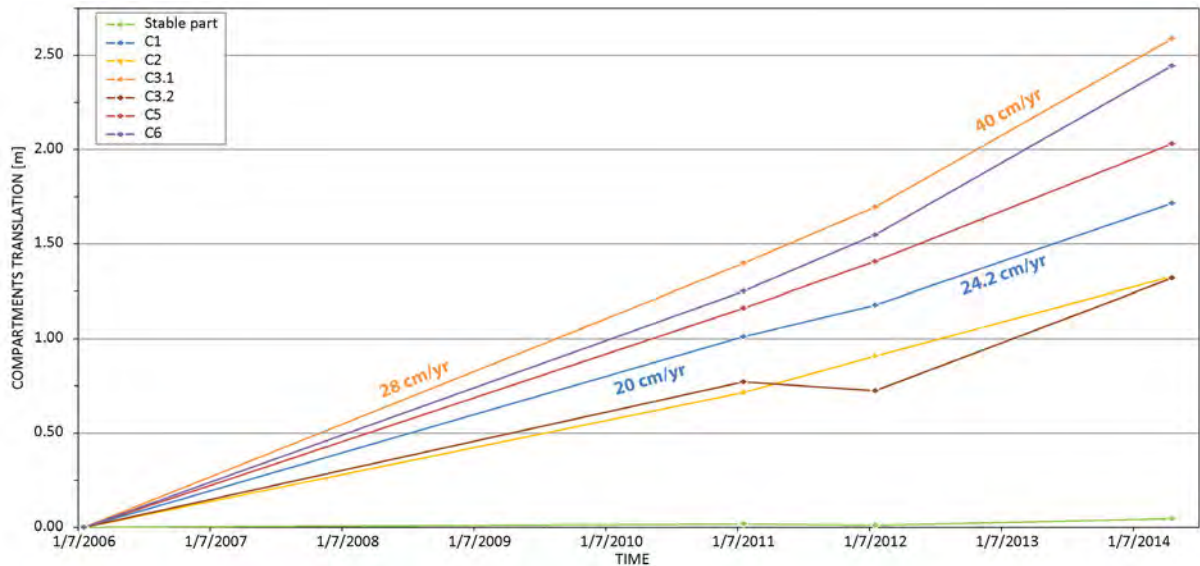


Figure 6.14: Cumulated translation displacements of all compartments computed on TLS roto-translation matrixes. A small acceleration is thus measured between 2012 and 2014.

Table 6.5: Mean compartment velocity (in cm/yr). In bold typo are velocities higher than 36.5 cm/yr, i.e. 1 mm/day.

	19.07.2006 > 27.07.2011	27.07.2011 > 18.07.2012	18.07.2012 > 8.10.2014
Stable compartment	0.4	0.7	1.6
Compartment 1	20.1	17.1	24.2
Compartment 2	14.2	19.7	18.9
Compartment 3.1	27.8	30.5	40.1
Compartment 3.2	14.3	4.8	26.7
Compartment 5	23.1	25.2	28.0
Compartment 6	24.9	30.4	40.3

c. Strain rates

The deformation state of the upper compartment, in extension, is now assessed (cf. Section 6.2.2c). With TLS mean point spacing of about 8 cm and shadowing biases (Abellán et al. 2014), micro rock fracturing and fresh opened cracks are not modelled on cross-sections; the C1 compartment opening Δl_i is thus underestimated, but can still be approximated close to 40 m long by measuring extensions of the large single and triple ridge systems (cf. Figures 6.3 and 6.7). In addition, this compartment measures 425 m long (l_i). Therefore, the deformation state of the upper compartment in extension is estimated at minimum 10 %.

In addition, accurate strain rates are monitored at compartment centres over time on sequential TLS acquisitions (cf. Section 6.2.2c). Computed results are then resumed in Table 6.6: delimited by the compartment 1, mean strain rates of the triangular upper part reaches 0.08 %/yr, while extensions of the frontal cliffs are of about 0.06 %/yr. Regarding internal deformations of the 1 million m³ lateral western crest, the upper compartment 3.1 is putting up with a mean extension of 0.04 %/yr whereas the lower compartment 3.2 is dealing with a mean compression of -0.01 %/yr; furthermore, a major compression period of this lateral crest was noticed between summers 2011 and 2012, with strain rates down to -0.12 %/yr on its top and -0.17 %/yr on its toe.

Table 6.6: Strain rates of all compartments and internal strain rates of the lateral western crest.

	19.07.2006 > 27.07.2011	27.07.2011 > 18.07.2012	18.07.2012 > 8.10.2014
C1	0.0715 %/yr	0.0605 %/yr	0.0856 %/yr
C2	0.0384 %/yr	0.0402 %/yr	0.0385 %/yr
C3.1	0.0438 %/yr	0.0480 %/yr	0.0630 %/yr
C3.2	0.0201 %/yr	-0.0063 %/yr	0.0350 %/yr
C5	0.0510 %/yr	0.0556 %/yr	0.0617 %/yr
C6	0.0390 %/yr	0.0476 %/yr	0.0630 %/yr
Internal C3.1	0.0384 %/yr	-0.1160 %/yr	0.0456 %/yr
Internal C3.2	0.0092 %/yr	-0.1755 %/yr	-0.0108 %/yr

6.3.3 Geometry modelling

Structural settings of the upper wedge cliff system acting as the main backscarp are assessed on TLS point clouds (cf. Section 6.2.3a). As a result, the western cliffs of the wedge are mainly formed by joints J1 (167°/52°), while the eastern cliffs are mostly shaped by joints J2 (086°/53°) and J3 (254°/74°); a last set, J4 (040°/79°), is cutting the entire wedge, although being not extensively expressed at the outcropping rock.

With a mean topography of 211°/43° assessed close to the upper scarp, wedge and toppling kinematic tests are applied on these identified discontinuities (cf. Figure 6.15). First, azimuth directions of wedge failure criteria match to the measured general translation, i.e. about 200°. In addition, the wedge shaped by J1 and J3 intersections (mean orientation of 184°/51°) can verify this failure mechanism if it flattens in depth or if it is completed by a 3rd flat discontinuity set (undetected yet). Moreover, kinematic tests also confirm the possible toppling rotation on the J4 discontinuity.

According to SLBL simulations (cf. Section 6.2.3b), all computed volumes range from 8 to 10 million cubic meters; in addition, the individual volume of the very active lateral western crest is estimated to about 1 million cubic meter. Nevertheless, these volumes should be confirmed and refined by new core logging or additional geophysical investigations to better constrain basal surface modelling, especially in the lower rockslide part.

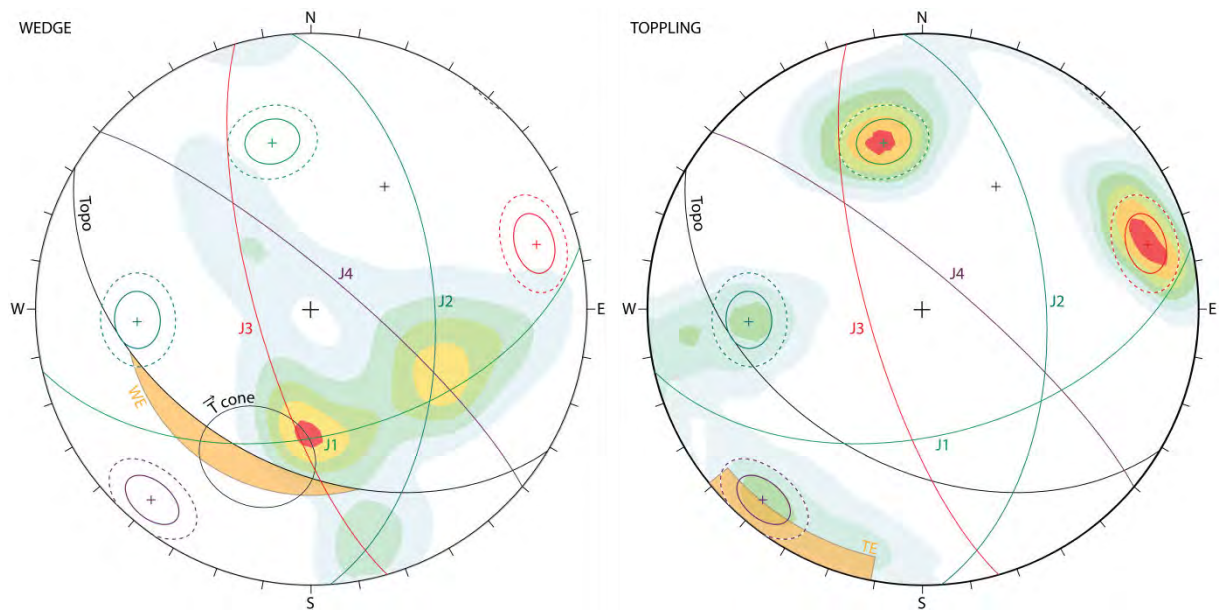


Figure 6.15: Wedge (left) and toppling (right) kinematic tests on Schmidt lower hemisphere stereonet, according to the four major discontinuity sets detected on the upper wedge cliff system and the mean orientation of the topography close to the upper scarp ($211^{\circ}43^{\circ}$). Circles around mean poles represent the 1σ and 2σ variability cones, contour plots highlight Fisher distributions of wedge intersections (left) and discontinuity poles (right), the \vec{T} cone ($200^{\circ}42^{\circ}\pm 16^{\circ}$) displays the mean orientation of the rockslide translation and WE and TE identify respectively wedge and toppling failure criteria envelopes.

6.4 Synthesis and discussion

The original integration of GB-InSAR data on high resolution TLS and ALS point clouds in Coltop3D software has been mandatory to allow a reliable visual interpretation of mm surface displacements over the whole La Perraire slope surface. Therefore, the rockslide extension has been precisely mapped for the first time. The coupled RaDAR and LiDAR data indeed confirm that (a) the upper cliff wedge system is acting as the major backscarp at 2'400 m.a.s.l and (b) the rockslide is affecting the slope at least down to an elevation of 1'750 m.a.s.l, close to the alpine Lourtier torrent shaped by the opposite northward slope flank. The rockslide reaches then a maximum length and width of 1'000 by 500 m for a surface of about 280'000 m^2 . Based on SLBL computations, the total instability volume is estimated between 8 to 10 million m^3 with a basal failure surface 50 m deep.

During these last 8 years, La Perraire rockslide is mainly affected by a deep-seated translation with representative plunges of about $200^{\circ}/42^{\circ}$ and velocities of 20 to 28 cm/yr the upper western section and about 30 to 40 cm/yr in the upper part of the lateral western crest. The kinematic tests corroborate a wedge failure mechanism; the translation may indeed occur on a basal surface formed by the J1 and J3 wedge system that requires to be flattened in depth or to be completed by a third flat discontinuity set to match with both wedge failure criteria and the mean translation orientation (cf. Figure 6.15 left). Moreover, this wedge flattening could also explained the small sliding rotation of 0.1° downward affecting the whole instability as well.

In addition to these long term and deep seated movements, roto-translation matrix carried out on small superficial blocks are highlighting shallower displacements as well; shallow block toppling can indeed be observed and measured on TLS data in the upper part, as well as south-western displacements along upper west flanks (confirmed by the unique permanent GNSS antennas surveying the top of the rockslide) and south-eastern displacements along the upper east flanks.

Moreover, both GB-InSAR and TLS monitoring campaigns emphasize non-uniform displacements involving different strain rates in the rockslide top and its toe (cf. Figures 6.10 and 6.13). In one hand, the survey measured a translation of 1.7 m of the upper triangular compartment, while surrounding compartments have lower displacements of 0.3 up to 0.9 m (cf. Tables 6.4 and 6.5). Because of the free space created by the greater translation of the frontal cliffs and the upper lateral crest, a significant extension close to 10 % and current strain rates to 0.085 %/yr are estimated on the upper rockslide part (cf. Figure 6.7 and Table 6.6), manifested in observed fresh cracks, trenches and multiple ridges systems in compartment 1 (cf. Figure 6.3). On the other hand, GB-InSAR results highlighted a downward attenuation of movements (cf. Figure 6.10), verified by TLS 3D displacements along the lateral crest as well. It is hence suggesting the possibility of a compression of the lower rock mass.

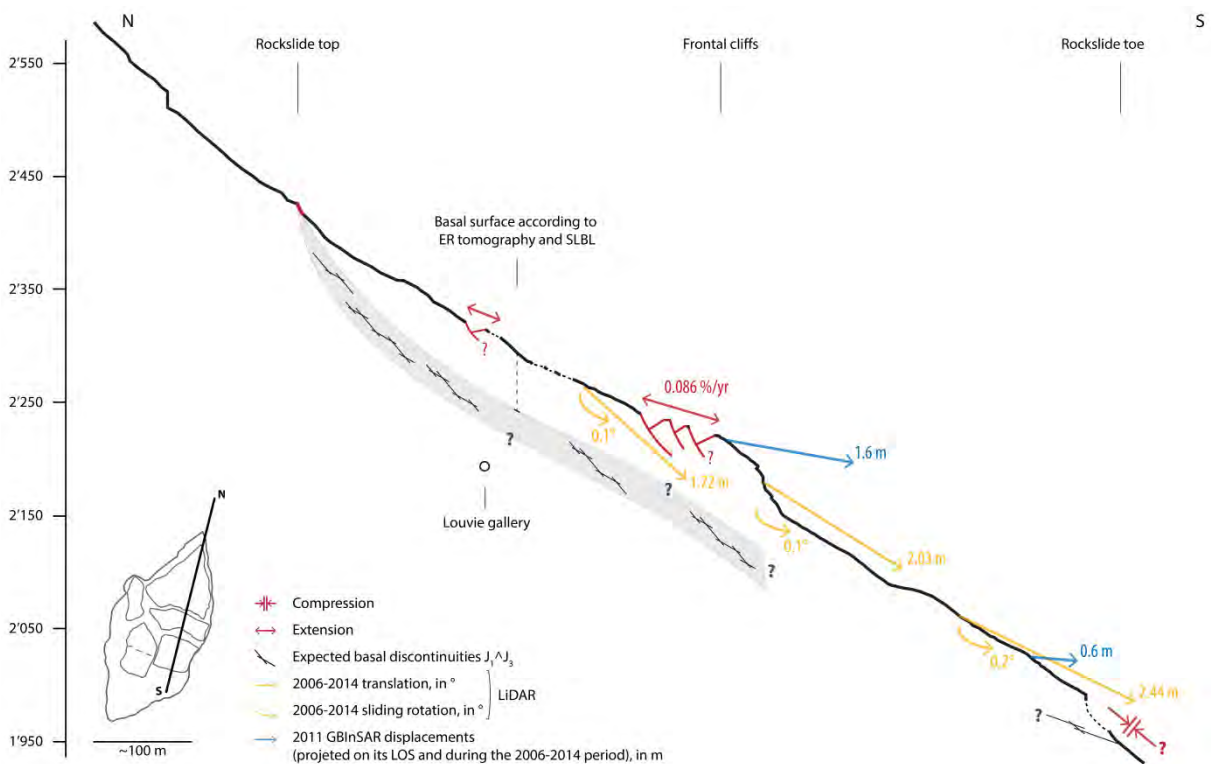


Figure 6.16: Rockslide cross section synthetizing information retrieved on field observations, numerical modelling as well as GB-InSAR and TLS monitoring campaigns. (Topography extracted from the 04.10.2014 TLS acquisitions and cf. cross-section location on Figure 6.2.)

Furthermore, both biggest and smallest short and long term displacements are measured within the lateral western crest according to GB-InSAR and TLS data (cf. Figures 6.10 and 6.13). This compartment of 1 million m³ is then the most active area of the rockslide these last 8 years with velocities about 31 cm/yr, and a westward toppling rotation of 0.4° in its upper part. According to kinematic tests, the rock mass toppling can be developed on J4 discontinuities (cf. Figure 6.15 right). Moreover, this current and important activity is moreover confirmed by large trenches (cf. Figure 6.3C), rockfalls and opening cracks and scarps upward observed by local mountain guides. On the other hand, only translational displacements of 16 cm/yr without relevant toppling rotation are measured in the lower part of the lateral crest.

In the meantime, internal strain rates of this lateral crest indicate as well a current extension of 0.045 %/yr of the upper compartment, while a major compression of -0.011 %/yr is measured on its lower one (cf. Table 6.6). The high compression strain of the lower part is also implying a high stress accumulation within the crest toe. Furthermore, even the upper part of the crest and de facto the entire lateral crest can be compressed by the upper triangular compartment, as during the year between summers 2011 and 2012 with strain rates assessed from -0.11 to -0.18 %/yr. This alternation of extension and compression of the upper lateral crest tends to increase the rock mass fatigue behaviour by enlarging opened micro-cracks (Costin and Holcomb 1981); it can thus significantly reduce the whole crest failure strength (Attewell and Farmer 1973; Scholz and Koczyński 1979; Costin and Holcomb 1981).

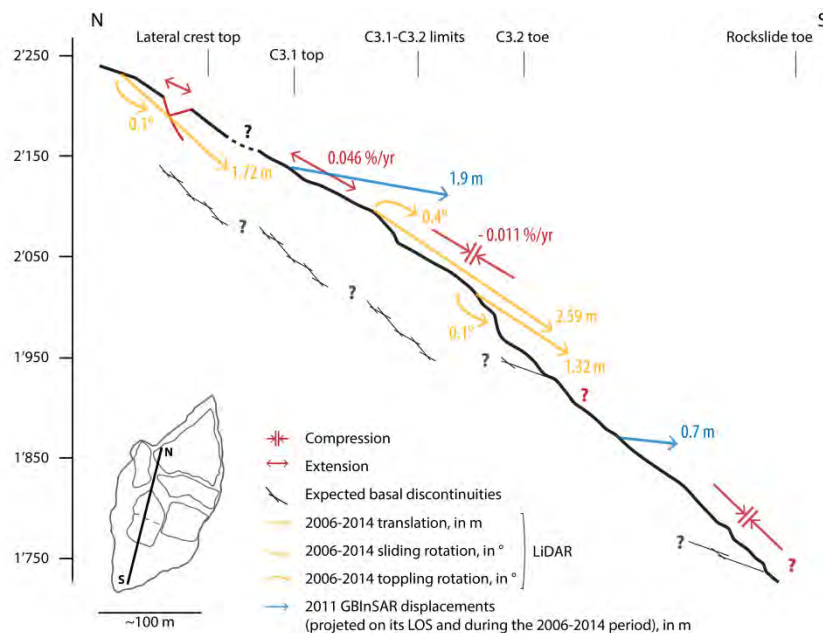


Figure 6.17: Lateral western crest cross section synthesizing information retrieved on field observations, numerical modelling, as well as GB-InSAR and TLS monitoring campaigns. (Topography extracted from the 04.10.2014 TLS acquisitions and cf. cross-section location on Figure 6.2.)

Nevertheless, those significant deformation rates (0.085 %/yr in its upper part, cf. Table 6.6) in rock slopes do not always imply general instability collapse. On the one hand, strain rates of the Kilchenstock rockslide (Heim 1932; Löw 1997) were actually estimated in 1932 of about 0.33 %/yr over 4 years and even up to 25 %/yr during 2.5 months; up to date, Kilchenstock's slopes has still not collapsed. But on the other hand, several rockslides with rates close to La Perraire's ones confirm the importance of long term strain-based collapse assessments. Pre-failure strain rates of the Randa rockslide were indeed measured between 0.1 and 1 %/yr during the 2 decades before its second collapse (Jaboyedoff et al. 2012c). In addition, strain rates of the very active Åknes rockslide (Blikra 2008 and 2012) are currently reaching 0.015 %/yr in its upper part and decrease in the lower part as well. Nevertheless, stress accumulation on toes are commonly creating fold and bulge features (Jaboyedoff et al. 2013) that are not yet observed in the field because of harsh rockslide toe accesses.

6.5 Conclusions

The active la Perraire rockslide is monitored since 2006 with sequential GB-InSAR and TLS acquisitions (cf. Figure 6.3); both active wave sensors were necessary to understand the whole landslide kinematic. During autumnal GB-InSAR monitoring campaigns, we recorded millimetric daily displacements (cf. Figure 6.8). Then by wrapping precise monitored movements from GB-InSAR measures on dense 3D TLS point clouds, we were able to map the rockslide limits and to verify that the upper cliff wedge acts as the major backscarp (cf. Figure 6.9); structural analyses moreover suggest that the J1 and J3 discontinuities within this upper wedge may act as the basal rockslide surface if they are flattened in depth (cf. Figure 6.15). We also highlighted non-uniform displacements, with the greatest amplitudes noticed on the upper western part and a gradual downward decrease (cf. Figures 6.10 and 6.15). Long term observations based on the sequential TLS acquisitions afterwards confirms the movement amplitude recorded by GB-InSAR data, with mainly translational displacements in the upper part from 1.5 to 2.5 m in 8 years towards about 200°40° (cf. Figure 6.13); deformation states indicate hence a current extension of 0.085 %/yr of the triangular upper part. On the other hand, the smaller displacements measured in the lower rockslide part are producing a compression strain close to -0.011 %/yr at the crest toe (cf. Table 6.6). All these notes are summarized in the two rockslide cross-sections displayed in Figures 6.16 and 6.17. To sum up, in regards to high displacements that tend to accelerate, significant strain rates, and volumes of 8 to 10 million cubic meters, the scenario of a rock slope failure behaving as a rock avalanche and reaching the Lourtier village has to be considered.

Based on this study, new investigations are therefore necessary to design an early warning system for populations and infrastructures downward. First, the rockfall activity in frontal cliffs and western

lateral crest has to be surveyed, since an increasing of event might be precursor of slope collapses (Voight 1988; Suwa 1991; Azzoni et al. 1993; Rosser et al. 2007; Baroň et al. 2012; Jaboyedoff et al. 2012c). In the meantime, new TLS acquisitions as well as high resolution panoramic photos covering both upper and lower rockslide parts will be mandatory to survey geological compression structures and measure strain rates within the rockslide toe and to regularly update the instability displacement and strain monitoring. Furthermore, it is also important to achieve new investigations on surface and sub-surface processes. Indeed, TLS-based structural settings must be completed with field mapping within the rockslide area and its entire surrendering slope; in addition, the effects of underground water on La Perraire slope destabilizing processes are nowadays unknown. Core logging will also be required to monitor sub-surface parameters via inclinometers and piezometers. Finally, rock avalanche runout areas could first be assessed using an empirical approach, such as the 1973 Scheidegger's equation linking instability volumes and Fahrböschung angles that control the avalanche mobility (Heim 1932; Scheidegger 1973; Corominas 1996; Locat et al. 2006). These new investigations will therefore be fundamental to process reliable numerical modelling and to set a pertinent EWS with reliable warning criteria (Michoud et al. 2013a; Cloutier et al. 2015).

7 Experiences from site-specific landslide Early Warning Systems

After Michoud C, Bazin S, Blikra LH, Derron MH and Jaboyedoff M: Experiences from Site-Specific Landslide Early Warning Systems. *Natural Hazards and Earth System Sciences*, 13, 2659–2673, 2013.

Abstract

Landslide early warning systems (EWSs) have to be implemented in areas with large risk for populations or infrastructures when classical structural remediation measures cannot be set up. This paper aims to gather experiences of existing landslide EWSs, with a special focus on practical requirements (e.g. alarm threshold values have to take into account smallest detectable signal levels of deployed sensors before being established) and specific issues dealing with system implementations. Within the framework of the SafeLand European project, a questionnaire was sent to about a hundred of institutions in charge of landslide managements. Finally, we interpreted answers from experts belonging to 14 operational units related to 23 monitored landslides. Although no standard requirements exist for designing and operating EWSs, this review highlights some key elements, such as the importance of pre-investigation work, the redundancy and robustness of monitoring systems, the establishment of different scenarios adapted to gradual increasing of alert levels, and the necessity of confidence and trust between local populations and scientists. Moreover, it also confirms the need to improve our capabilities on failure forecasting, monitoring techniques and integration of water processes in landslide conceptual models.

Keywords: Early Warning System, Survey, Experience, Landslides.

7.1 Introduction

Landslides are frequent phenomena in many natural environments and remediation measures ought to be implemented in areas with high risk due to the presence of populations or infrastructures. Structural remediation measures have been extensively used for reducing and even eliminating the hazard (Piteau and Peckover, 1978; Holtz and Schuster, 1996; Wyllie and Mah, 2004; Cornforth, 2005; Vaciago et al. 2011). However, classical countermeasures, such as modifications of mass distributions or water regimes, are often too expensive or difficult, if not impossible, when dealing with complex instabilities of large volumes (Crosta and Agliardi, 2003b; Blikra, 2012).

In such situations, other types of mitigations have to be performed in order to decrease the risk, mainly imposed to human lives. A proper measure is to reduce the number of exposed people by

implementing reliable landslides early warning systems (EWSs) that are capable of alerting and evacuating populations based on the monitoring of stability conditions of the landslide (e.g. parameter values exceeding established thresholds). Indeed, EWSs are defined by the United Nations as “the set of capacities needed to generate and disseminate timely and meaningful warning information to enable individuals, communities and organizations threatened by a hazard to prepare and to act appropriately and in sufficient time to reduce the possibility of harm or loss” (UN-ISDR, 2009). Efficient landslides EWSs require four major elements that have to be well integrated: (1) risk assessment, (2) phenomenon monitoring and forecasting, (3) warning communication and alert dissemination and (4) local response aptitudes (UN-ISDR, 2009).

These elements have been described in detail in many papers and useful concepts and recommendations can be extracted, such as in (1) Turner and Schuster (1996) or Fell et al. (2005) for hazard and risk assessments, (2) Stumpf et al. (2011), Michoud et al. (2012a) or Tofani (2013) for monitoring techniques, (3) Saito (1969), Fukuzono (1990), Crosta and Agliardi (2003b) or Meyer et al. (2012) for slope failure and flow initiation forecasts and (4) Basher (2006) or Dash and Gladwin (2007) for alerts and associated social processes. Furthermore, some papers describe how to integrate all tasks together (Angeli et al. 2000; Lacasse and Nadim, 2009). For shallow landslides and debris flows, a huge effort has been performed in order to develop complete and efficient EWSs at regional scales; they are based on rainfall intensity forecasting, soil moisture content and/or antecedent water index, etc. (Keefer et al. 1987; Aleotti, 2004; Baum and Godt, 2010; Jakob et al. 2012; Mercogliano et al. 2013). Nevertheless, it seems that there are only few reviews dealing with practical considerations and specific requirements in order to implement reliable single landslide EWSs that are site related.

For this purpose, the SafeLand project (2009-2012), funded by the European Commission in the 7th Framework Programme (Grant Agreement No. 226479), intended to develop generic risk management tools and strategies for landslides. Thus, one of its main objectives has been to provide guidelines that would facilitate the establishment of new EWSs and increase the quality of existing systems (Bazin, 2012; Intrieri et al. 2013). Consequently, the first step of this study was to gather experiences from existing EWSs strategies and expert judgments. In this way, we prepared a four-page questionnaire that has been filled by 15 institutions in charge of 24 landslide EWSs. Primary analyses have been first presented in Bazin (2012). This paper therefore aims to present the results of experiences of those European and North-American landslide EWSs, focused on implementation requirements and potential practical issues of importance for landslide specialists dealing with risk management.

7.2 Design of the questionnaire

As a part of the SafeLand project, a screening study was intended to gather information about the state of the technologies and existing strategies for the establishment of landslide EWSs. A four-page questionnaire was compiled to illustrate the wide spectra of monitoring and integrated platforms and to merge actual knowledge and expert judgments from existing systems. It aimed to collect information about:

- operational units in charge of the EWS;
- monitored landslide settings and consequences of past events (if any);
- pre-investigations used to design the EWSs;
- monitoring parameters, thresholds and sensors;
- warnings, communication and decision making process.

Questions were focused on practical considerations and specific requirements, such as technical challenges to install and maintain the EWS. In addition, it was also oriented to understand advantages and disadvantages and reveal potential lack of existing techniques to propose directions that current researches should follow.

In order to maximize the number of potential answers, the questionnaire has been designed to be as short, user-friendly and simple as possible (Lapointe et al. 2010). Indeed, it mainly contained a list of closed questions with pre-established answers clickable in checkboxes. Moreover, a few open questions were also kept in order to leave the compiler free to provide any further considerations and points of view especially about:

- advantages, limitations and upcoming improvements of current monitoring systems;
- how could actual EWSs be improved.

In practice, units in charge of EWSs have often the responsibility for several landslides and the questionnaire was therefore designed to fit systems that monitor multiple sites as well as single landslides. The questionnaire was then compiled into a Portable Document Format (*pdf*) document, one of the most standard formats, in order to ensure that everyone could open and read it. Finally, each user had the possibility to include with his answer, some supplementary material such as extra text and maps.

The questionnaire is available in the supplementary material.

7.3 Results and interpretations

The questionnaire was sent and spread in June 2011 to about a hundred of institutions in charge of landslide hazard and risk management. These Asian, European and North-American institutions were

identified within the professional network of SafeLand's participants, national experts and colleagues in the landslide scientific community. The list was also completed by reviewing EWS publications, conferences on landslides and also by looking for internet websites. Finally, in autumn 2011, we received answers from experts belonging to 15 operational units from 9 different countries and related to 24 landslides, i.e. 23 site-specific landslides and 1 regional EWS. Among them, 21 systems are in operation, 1 is under construction and 2 are stopped. The Table 7.1 sums up the list of institutions (and investigated landslides) that answered to the questionnaire. Some slope movements are well-known within the landslide community, such as the landslides of *Åknes* in Norway (Blikra, 2008 and 2012; Oppikofer et al. 2009; Jaboyedoff et al. 2011b), *Ancona* (Cotecchia, 2006; Cardellini, 2011) and *Ruinon* in Italy (Agliardi et al. 2001; Crosta and Agliardi, 2003b; Tarchi et al. 2003b), *Turtle Mountain* in Canada (Terzaghi, 1950; Cruden and Krahn, 1973; Benko and Stead, 1998; Froese and Moreno, 2011) and *Vallcebre* in Spain (Gili et al. 2000; Corominas and Santacana, 2003; Corominas et al. 2005b). On the other hand, the *Hong Kong Engineering Office* provided the only one response dealing with a regional EWS for shallow landslides (Hong Kong Slope Safety, 2012); this case is not included hereafter since many questions were not designed and thus not applicable for regional systems and also since this singular experience is too different from the other 14 operational units and their 23 related site-specific case studies.

Although 23 answers have not a high statistical significance, interesting practical trends can still be extracted from the dataset, especially since some of them are about the most studied landslides worldwide and valuable experiences have thus been accumulated for many years.

7.3.1 Units in charge of the EWSs

The first part of the questionnaire is related to the functioning of operational units. The 14 reported institutions, in charge of site-specific landslides monitoring and/or EWSs, operate mostly at national and regional levels; however, two third of them are also responsible for monitoring other natural processes, such as weather conditions, volcanoes and/or earthquakes. These units employ especially for their EWSs between 0 (monitoring carried out by universities) and 15 people (*IPGP - Martinique*).

All these institutions are financed by public funds, except one which receives additional private resources. On average, they need to operate about 175'000 € per year, with a minimum of 60'000 € for a Czech office in charge of 10 landslides and a maximum of 500'000 € for the *Centro di Monitoraggio Geologico of the ARPA Lombardia* in charge of 24 single landslides. But annual operational costs are highly depending on the different living standards in each country and also on how the unit is organized; moreover, the funding for replacing and implementing new monitoring systems can highly change from year to year. This highly changing budget and resources from year to year can be a reason that only 7 institutions answered to this question.

Table 7.1: Exhaustive list of the monitored landslides and their related operational units that answered to the questionnaire during Summer 2011: ^a system in operation. ^b system under-construction. ^c stopped system. ^x results not included in this study.

Country	Operational Unit	Monitored landslide
Canada	Alberta Geological Survey	Turtle Mountain ^a
	University Laval	Gascon Rockslide ^b
Czech Republic	Geo-Tools	unnamed ^a
	National Park Bohemian Switzerland	Hrensko ^a
France	Service de Restauration des Terrains en Montagne	La Valette ^a
	Institut de Physique du Globe de Paris à la Martinique	Prêcheur River ^c
China	Geotechnical Engineering Office	Entire Hong Kong province ^{a x}
Italy	Ancona Monitoring Center	Ancona ^a
	Centro di Monitoraggio Geologico – ARPA Lombardia	Ruina ^a
	Servizio Geologico Aosta	Becca di Nona ^a
		Bosmatto ^a
		Chervaz ^a
		Citrin ^a
		La Saxe ^a
Vollein ^a		
Norway	Università degli Studi di Firenze	Torgiovanetto ^c
		Åknes ^a
	Åknes/Tafjord Early warning Centre	Hegguraksla ^a
		Jettan ^a
		Mannen ^a
Slovakia	Nebbet Monitoring Center	Nebbet Mountain ^a
	State Geological Institute of Diunyz Stur	Okolicne ^a
		Velka Causa ^a
Spain	Universitat Politècnica de Catalunya	Vallcebre ^a

7.3.2 Landslides Settings

a. Hazard

The second part of the questionnaire was related to the context of the 23 monitored instabilities, their previous displacement activities and their potential consequences. It includes a wide range of phenomena (Figure 7.1) mostly related to natural slopes, from small rock falls of less than 10 m³ to large rock slides of more than 50 million m³ or regional debris flows and earth slide. Moreover, landslide events already occurred for 20 of them.

The studied instability crisis are mainly triggered by intensive rainfall (Figure 7.2). Snowmelt and permafrost, human activities, erosion processes, tectonic activities, or even their intrinsic dynamics are the other triggering mechanisms sometimes involved. Half of the events happened due to a combination of several factors. Furthermore, classifying triggering factors according to the four

physical agents responsible of slope destabilizations described by Terzaghi in 1950 (i.e. material transport, tectonic stresses, water and weight of slope-forming material), water is surely the most important agent, destabilizing more than 87 % of the slopes (Figure 7.2).

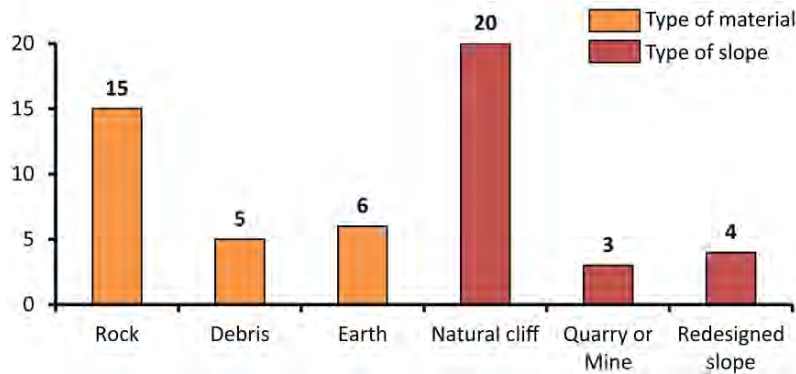


Figure 7.1: Type of landslide materials and slopes involved in this study. The total number is over 23, due to multiple possible settings.

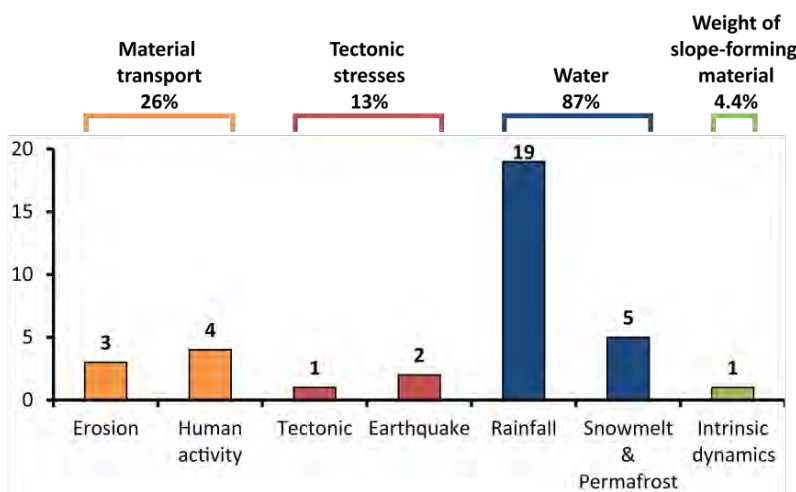


Figure 7.2: Triggering mechanisms involved for the 23 reported instabilities and grouped according to Terzaghi (1950)'s agents. The total can be over than 23 (and 100 %) since the reported studies can be affected by more than one triggering mechanism.

b. Risk

As introduced before, remediation measures have to be considered when there is an unacceptable risk. Indeed, as shown in Figure 7.3, these 23 landslides are directly threatening infrastructures such as roads or railways (for 20 of them), buildings (for 14 of them) and human lives (for 12 of them). Moreover, 8 of them could even lead to significant indirect consequences, such as tsunami induced by rockslides (Blikra, 2008 and 2012; L’Heureux et al. 2011) or outbursts resulting from landslide dam failures (Costa and Schuster, 1988; Korup, 2002).

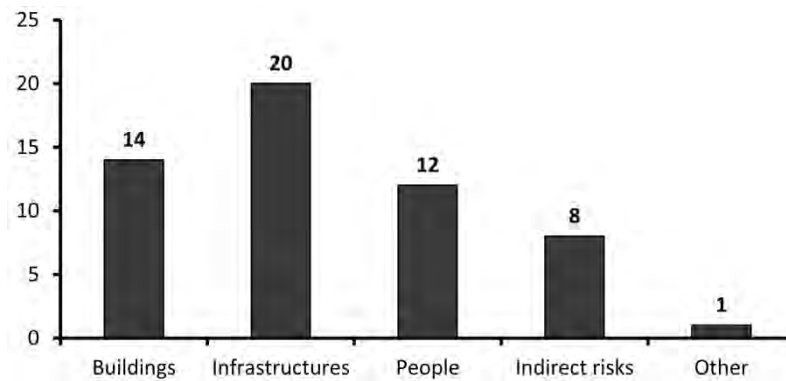


Figure 7.3: Number of landslides that are endangering buildings, transportation infrastructures, people and create indirect risks or even other issues. The total number is over 23, because consequences of a landslide can affect more than a single target.

In the past, the 20 reported landslides that are now active or dormant (cf. the classification of Cruden and Varnes, 1996) produced considerable economic losses that are difficult to quantify (even if estimated at about 400 million € by their Operational Units). Furthermore, they had important social consequences, destroying roads and villages, isolating populations and even killing more than 110 people. For example, the rock avalanche at Turtle Mountain in 1903 buried more than 70 citizens of the village of Frank during their sleep (McConnell and Brock, 1904). In 1934, the Hegguraksla rockslide indirectly killed 40 people due to the landslide-induced tsunami that destroyed several villages along the fjord with a wave reaching a maximum height of 62 m a.s.l. (Kaldhol and Kolderup, 1936; Bugge, 1937).

For 10 of the reported landslides, some physical mitigation works were performed to prevent new catastrophic events, such as retaining basins for debris flows or retaining walls for rock falls, when the context allowed it. Moreover, revision of the land-use plans has been implemented in the hazard zones for almost 75 % of the reported landslides, essentially updating land-use restrictions and construction norms for new inhabitants and infrastructures to reduce the number of elements at risk, their vulnerability and/or the population exposition.

c. Pre-investigations for EWSs

The third part of the questionnaire was related to investigations performed before the design of the monitoring systems. Several issues are usually investigated in order to get a sufficient understanding of the unstable systems, which is required for designing a proper and pertinent monitoring network (Figure 7.4).

The most investigated criteria are obviously the landslide geology and the geomorphology (for 19 of them), completed by surface movement data (for 14 of them). Indeed, geological and geomorphological studies are crucial to understand unstable slope behavior and to provide relevant

conceptual models. This includes mapping of landslide features (e.g. main and minor scarps, open fractures, surfaces of rupture, compression zones) and evidences of recent activities. Furthermore, investigating surface and sub-surface displacements is often crucial for making reliable landslide conceptual models. The coupling of geological, geomorphological and displacement maps is an important fundament for designing monitoring networks and sensor locations.

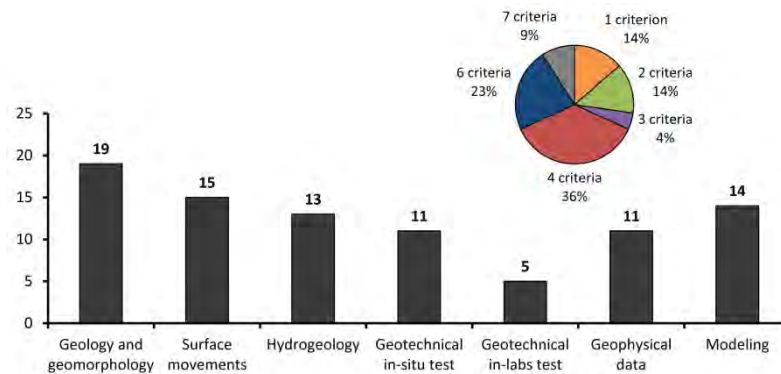


Figure 7.4: Inventory of investigations performed before designing the 23 reported EWSs performed and percentage of total number of criteria investigated per site. The total number of investigations is over 23, because 86 % of the landslides required more than one type of criterion.

The monitoring network of the Norwegian rockslide in Mannen (Figure 7.5) illustrates how a monitoring network can be designed, with in-place instrumentations in the accessible upper areas, close to the open fractures, and with ground-based remote-sensing techniques to cope with less accessible lower parts. Moreover, sub-surface monitoring in deep boreholes is performed at two accessible localities in order to fulfill the Norwegian requirements for EWS.

In addition, numerical models are computed for 14 instabilities in order to (1) determine stability factors and (2) map potential run-out areas of rock falls, rock avalanches, debris flows, as well as rockslide-induced tsunamis. Therefore, simulation models are essential to identify exposed populations and infrastructures. Geophysical measurements (mainly seismic refraction and electrical resistivity) and geotechnical in-situ tests (such as standard or cone penetration tests) are performed in approximately 50 % of the cases, providing useful complementary information on sub-surface conditions. Geotechnical in-lab tests are usually less employed than other criteria.

Surprisingly, hydrogeological conditions are only investigated for half of the cases (mainly piezometers and/or rain gauges mostly). It contrasts with the fact that in the 2nd part of the questionnaire, water is considered as a physical destabilizing agent for 87 % of the reported instabilities (Figure 7.2) and ground-water conditions is also required for reliable landslide models. For example, Bonnard and Steiger (2012) advise a minimum of two years of water-table monitoring before designing any drainage systems.

Finally, it is also important to note the common use of a multi-criteria approach. Thus, as seen in Figure 7.4, operational units have designed their EWS on 4 types of criteria and even more in 69 % of the cases. The use of only one criterion is a method used for 14 % of the cases, and this is mostly implemented for cases where debris flows are triggered by heavy precipitations.

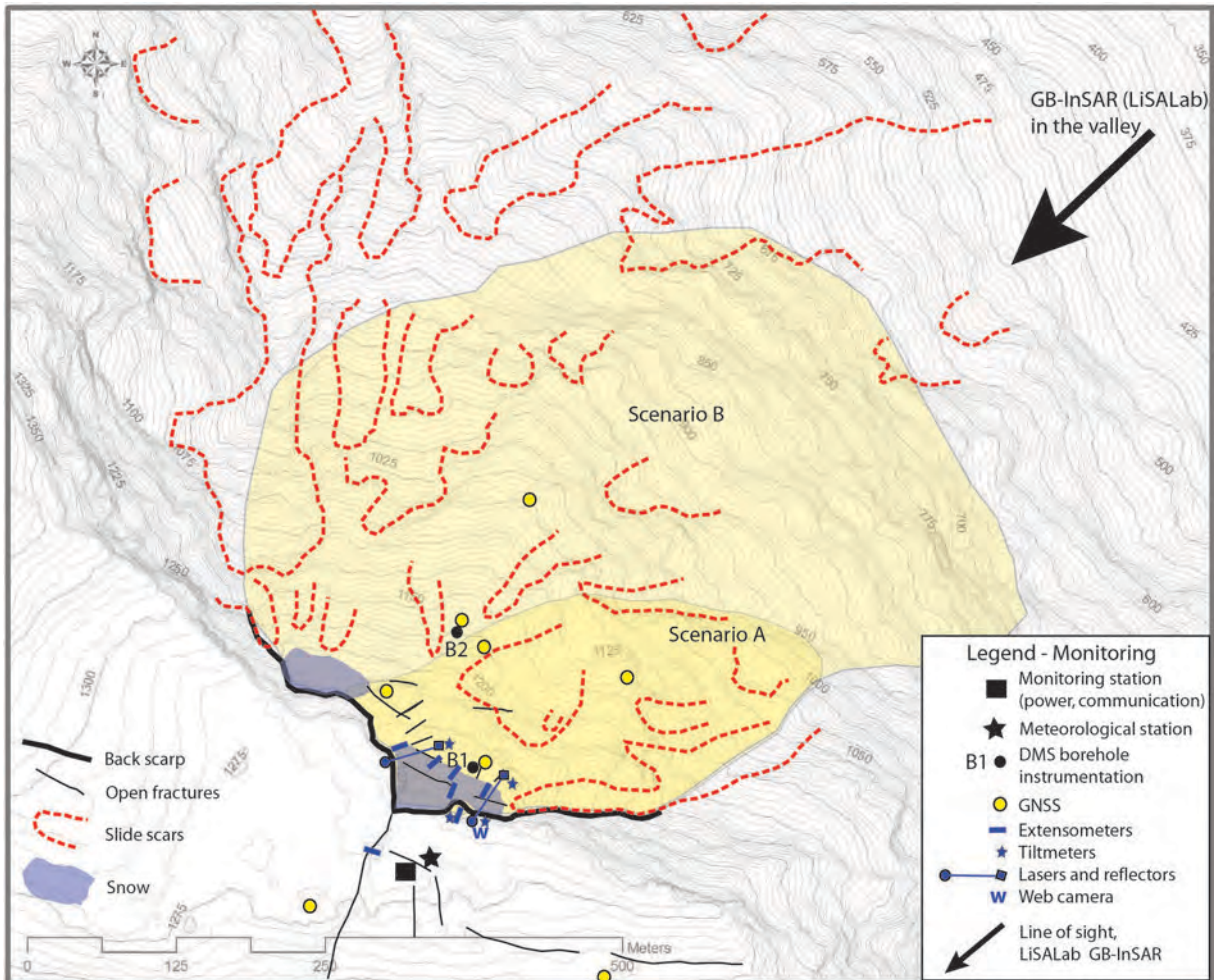


Figure 7.5: Mannen rockslide monitoring network. Ground-based in-place instrumentation is concentrated close to the back scarp, while the GB InSAR system is placed in the valley below. Two deep boreholes are instrumented by 120 m long DMS columns. Open fractures and slide scars were identified and mapped during previous field investigations. Theoretical and technical details of those techniques are developed in Stumpf et al. (2011) and Michoud et al. (2012a).

7.3.3 Monitoring systems

a. Sensor network

The fourth part of the questionnaire is related to instruments and sensors used to monitor the instabilities. Two of our partners, monitoring fragmental rockfall events, reported to us difficulties to fill this section table because of its *pdf* format; the following interpretations are thus based on the 21

other case studies. Figure 7.6 displays the different types of observed parameters and Figure 7.7 sums up the different setup sensors. Detailed theoretical and technical aspects on all these landslide monitoring sensors are developed in Stumpf et al. (2011) and Michoud et al. (2012a).

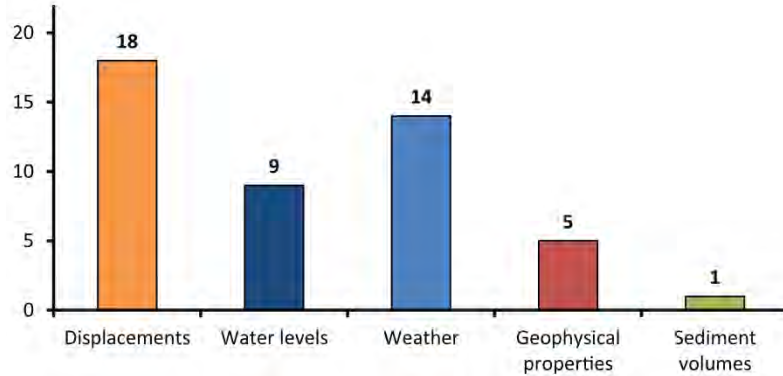


Figure 7.6: Inventory of monitored parameter types for the 21 reported monitoring networks. The total number is over 21, because more than one parameter is monitored for 15 of the landslides.

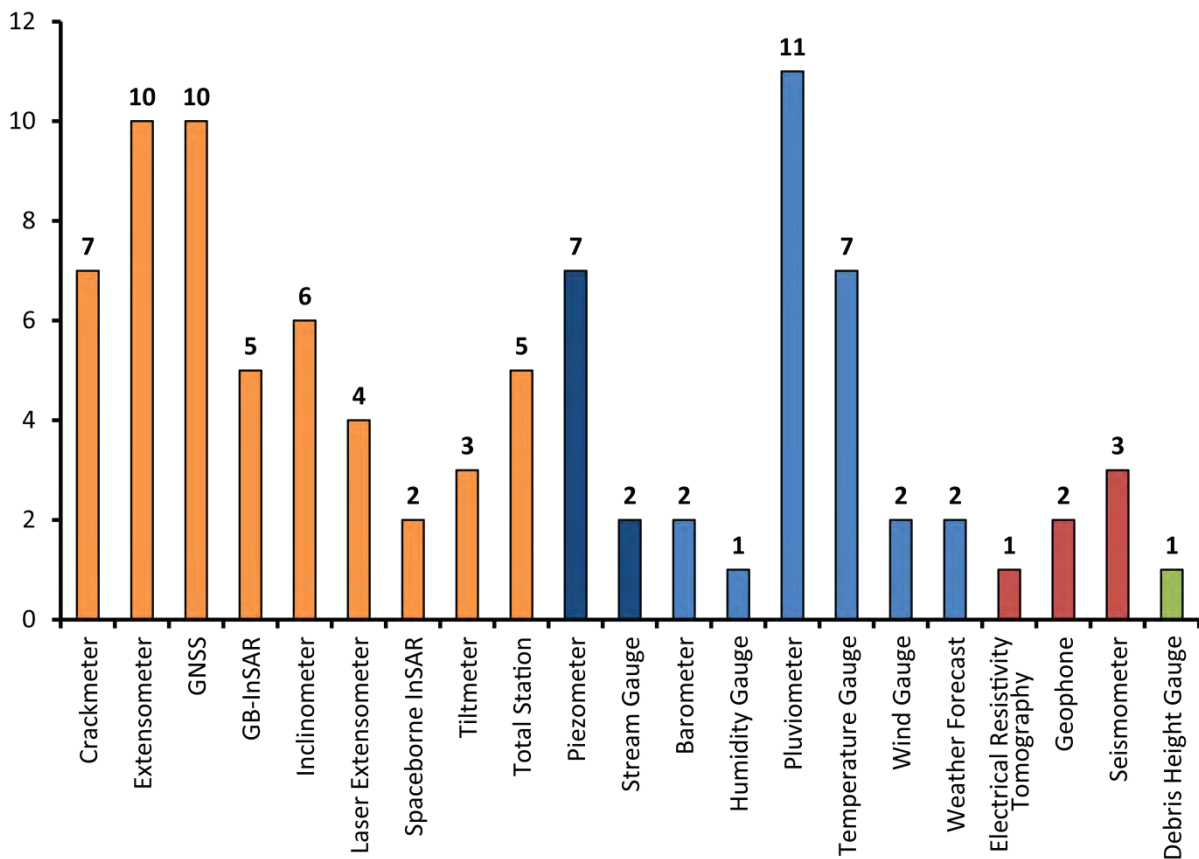


Figure 7.7: Inventory of the different techniques used for the 21 reported monitoring networks in order to measure surface and sub-surface displacements (in orange), water and groundwater table levels (in dark blue), weather conditions (in light blue), geophysical properties (in red) and available sediment volumes (in light green). Theoretical and technical details of those techniques are developed in Stumpf et al. (2011) and Michoud et al. (2012a).

The large majority of the EWSs is based on the monitoring of surface and sub-surface displacements (for 18 of them), certainly because they show direct evidences of active deformations. In order to measure movements, half of the networks are based on extensometers and/or Global Navigation Satellite Systems (GNSS); crackmeters and inclinometers are also frequently used. These sensors deliver reliable data and they are robust and cheap (except for GNSS). Regarding GNSS, even if antennas and receivers are more expensive than other systems and the data processing more complicated, they have the major advantage that they provide 3D displacement information. Other techniques such as ground-based interferometric radar (GB-InSAR), total station, laser, or tiltmeters are less used. Up to now, they were considered to be expensive as well as to create some difficulties related to setup and data processing in comparison with other methods. Furthermore, some instruments as crackmeters or GB-InSAR may become fragile in harsh environments and good protections (against heavy rainfall, snow load or snow creep for example) have to be considered to protect them. Subsurface monitoring in boreholes is common on some of the largest and more complex landslides, and is used in 6 of the reported cases. Several of the landslides have now changed the instrumentation from traditional manual inclinometric probe measurements to automatic and long columns, such as the DMS system (Lovisol et al. 2003), consisting of a large number of sensors managing to monitor continuous sequences.

It is also interesting to note that the Turtle Mountain and Åknes instabilities are monitored using spaceborne radar interferometry (InSAR) techniques as well. Even if it does not provide real-time data and de facto cannot be used for operative early warnings, it is a useful approach to understand and update the landslide dynamics using images from space agencies' archives. Moreover Spaceborne InSAR can be helpful during pre-investigation works and also provide complementary information to EWSs. Indeed, an overview of the regional stability in the neighborhood of the monitored slopes is important in many cases, since large landslides as sackungs are able to destabilize small monitored landslides inside the large deformed masses (Agliardi et al. 2001).

In addition to displacement data, meteorological parameters are crucial to be monitored since rainfall, snowmelt and permafrost are considered as a triggering factor for 20 (87%) of the instabilities (Figure 7.2). Meteorological parameters are thus very frequently measured (in 14 EWSs) as well as water table levels and water discharge in streams (in 9 EWSs); indeed, rain gauges are included in half of the monitoring networks, and piezometers and temperature gauges for 7 of them.

Near-surface geophysical methods have been considerably improved during the last two decades and their uses for landslide investigation purposes have been reviewed in Jongmans and Garambois (2007). Nevertheless, geophysical applications for operational EWSs are still under developments (Spillman et al. 2007; Roth, 2012; Mainsant et al. 2012a, Navratil et al. 2013), largely explaining why they are applied only for 5 of the 21 reported case studies.

An EWS implemented in debris and earthflow source areas is also monitoring the volume of available sediments that can be mobilized in case of heavy rainfall using gauges that measure the sediment heights, in order to be able to forecast potential event intensities.

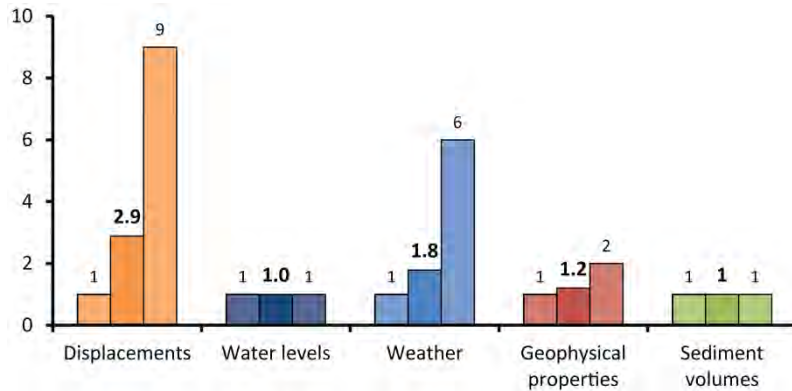


Figure 7.8: Minimum, mean and maximum instrument types used to monitor each parameter (when it is done) per landslide.

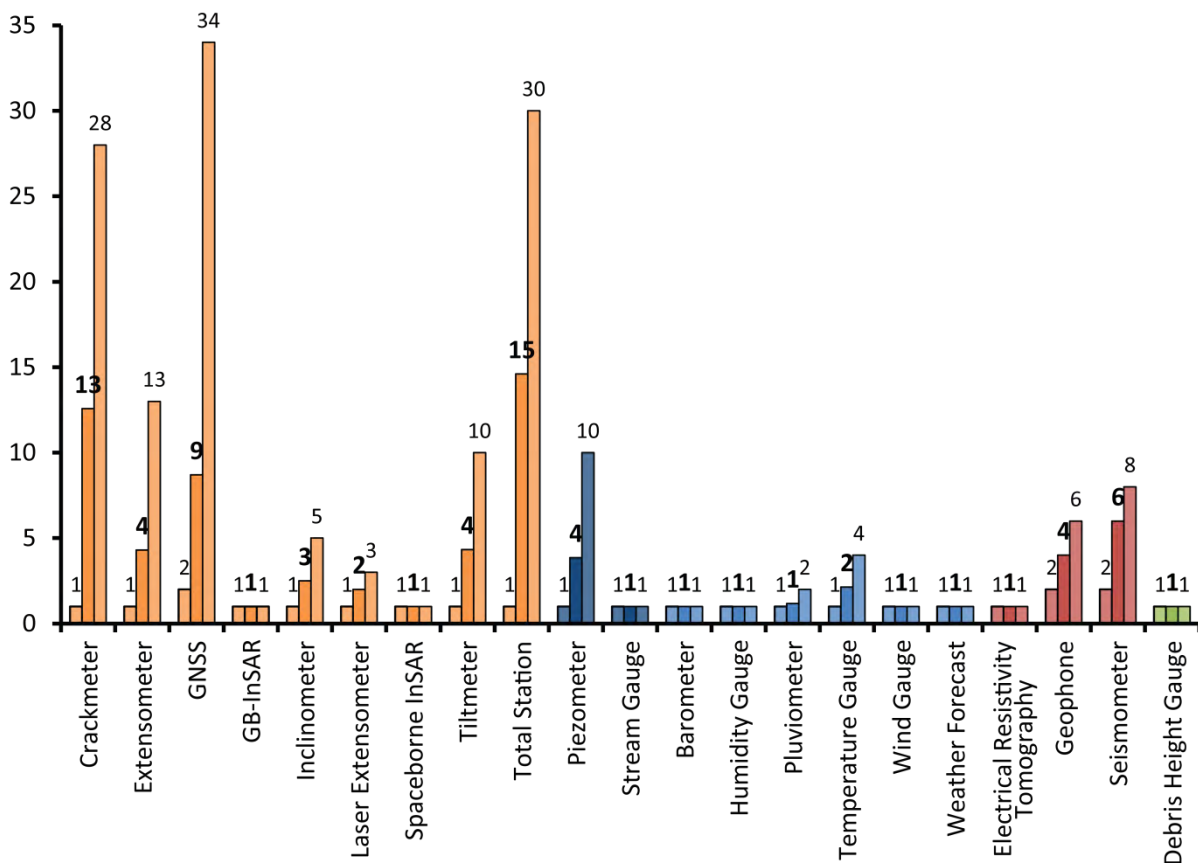


Figure 7.9: Minimum, mean and maximum number of sensors of each type per landslide, when used, in order to monitor surface and sub-surface displacements (in orange), water and groundwater table levels (in dark blue), weather conditions (in light blue), geophysical properties (in red) and available sediment volumes (in light green). Theoretical and technical details of those techniques are developed in Stumpf et al. (2011) and Michoud et al. (2012a).

Redundancy is important in EWSs (Figures 7.8 and 7.9). This is particularly evident for robust monitoring networks that measure displacements and groundwater. For example, on the Åknes instability, displacements are monitored by 8 instrument types: 8 crackmeters, 8 GNSS antennas, 2 laser devices, 1 ground-based radar, 3 extensometers, 1 total station coupled with 30 prisms, 2 surface tiltmeters and 3 deep boreholes instrumented with inclinometers and water-pressure measurement cells (DMS columns). It allows to (1) monitor several sectors with different dynamics and displacement rates in surface and sub-surface, (2) discriminate unwanted false alarms coming from large noise or one defective sensor and (3) have instruments fed by several power supply and data communication lines. On the contrary, only one meteorological station (e.g. with rainfall, temperature, snow depth or humidity gauges) is usually installed to monitor weather conditions since landslides are usually confined in small areas with relative similar conditions.

In conclusion, based on the experiences of the reported institutions in charge of landslides EWSs, a good monitoring network is characterized by:

1. Simplicity;
2. Robustness;
3. Presence of multiple sensors;
4. Power and communication lines back-ups (detailed in Section 7.3.3).

The following characteristics are also important for the choice of an instrumentation:

1. Implication for understanding the landslide evolution;
2. Long-life expectancy;
3. Robustness;
4. Price;
5. Level of real-time data;
6. Noise level of the sensors.

On the other hand, a system is limited if it is based only on surface displacements and if it can be damaged by weather conditions and/or landslide events themselves before sending data or alarms to the operational centre. Present monitoring networks can still be improved by a better integration and near real-time compilation of all monitoring data, for example by coupling displacements with weather conditions, groundwater and/or seismic activities.

b. Power and data management networks

The principle of redundancy is also important for power and data management networks, as shown in detail in Froese and Moreno (2011). Those networks supply monitoring sensors with electricity and allow manual remote data accesses for expert's periodical checks and automatic data transmissions

to operational units based on Internet protocols. Regarding the 23 reported sites, two third of monitoring networks are equipped with power supplies, communication lines and systems back-ups for monitoring sensors and for operational centres, in order to ensure continuous data measurement, transmission and analyse.

c. Alarms

The fifth and last part of the questionnaire is focused on the way to use monitored data, establishing alarms and associated responses to protect endangered populations and infrastructures.

Threshold values for alarm messages are normally based on the evaluation of different sensors and an expert interpretation of the stability conditions, mainly during the pre-investigation work (Blikra, 2008; Froese and Moreno, 2011). Because they are direct evidences of activity, almost all threshold parameters are based on displacement data (for 13 of the 15 reported answers), sometime coupled with rainfall data (for 6 cases). More rarely, 2 earth slides in Slovakia use groundwater table level monitored by piezometers as threshold parameter.

Figure 7.10 highlights essential characteristics for the establishment of alarm procedures. In order to limit false alarms, threshold values are based on multiple identical devices and/or several redundant types of sensor for 19 of the EWSs. But curiously, only 9 of the threshold values are taking into account technical sensor limitations, such as the smallest detectable signal and noise levels, before establishing them, even if it allows to increase the alarms reliability. Furthermore, several levels of alarms (such as Table 7.2) have been established for one third of the reported systems.

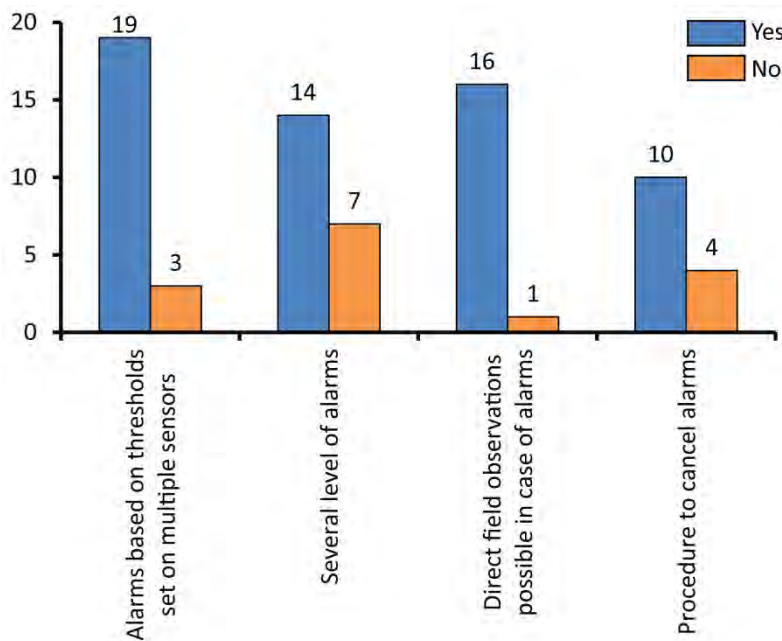


Figure 7.10: Inventory of the essential characteristics of alarm procedures for the 23 reported monitoring networks.

Table 7.2: Example from the Emergency Preparedness Centre in Stranda (Norway) of gradual alert levels based on different threshold values and experts evaluations leading to planned responses (modified from Blikra et al. 2007).

Velocities [mm/day]	Alarm level	Activities and alarms	Response
0.1 – 0.5	Level 1 - Green Normal Situation	Minor seasonal variations No alarm	Technical maintenance EPC staff
0.5 – 2	Level 2 - Blue Awareness	Important seasonal fluctuations for individual and multiple sensors Values < excess thresholds for Level 2	Increase frequency of data review and comparison of different sensors EPC staff
2 – 5	Level 3 - Yellow Increase awareness	Increased displacement velocity, seen on several individual sensors Values < excess thresholds for Level 3	Do continuous reviews and field survey Geo-expert team at EPC full time Inform police and emergency preparedness teams in municipalities
5 – 10	Level 4 – Orange High hazard	Acceleration in displacement velocity observed on multiple sensors Values < excess thresholds for Level 4	Increase preparedness, continuous data analysis Alert municipalities to stand prepared for evacuation
> 10	Level 5 – Red Critical situation	Further acceleration Values > excess thresholds for Level 4	Evacuation

As soon as a threshold value is reached by a predefined number of sensors, 22 of the 23 monitoring networks automatically send an alarm message to an operator on call 24/7. The most used communication technique is largely an automatic SMS sent to operators cellular and is too rarely coupled with other redundant systems, such as emails or voice phone message (Figure 7.11).

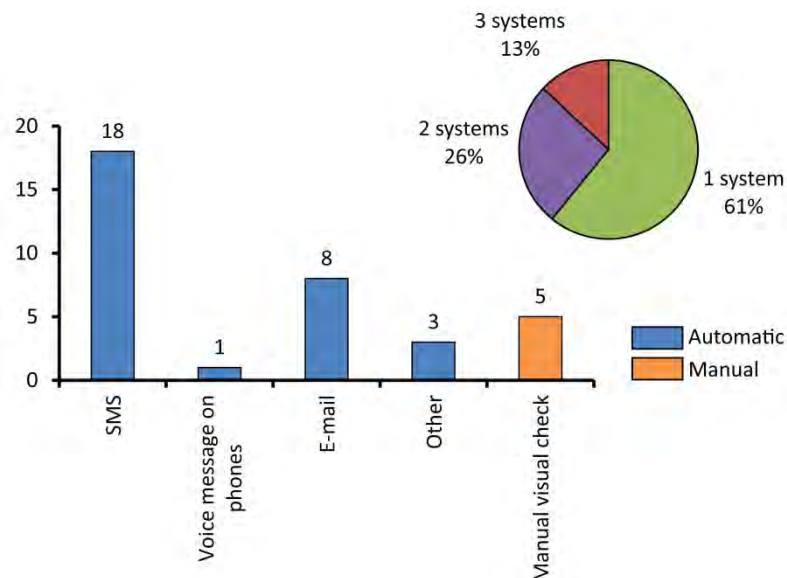


Figure 7.11: Inventory of automatic and manual techniques used to send alarms from the monitoring network to the operational unit and percentage of number of techniques used simultaneously for the 23 reported monitoring networks. The total number is above 23, since 39 % of the monitoring networks use more than one technique.

These alarms prompt the responsible person on duty to inspect the monitored data. Moreover, direct field observations are possible in many cases to get additional information about the stability conditions, especially during critical stages, by checking visible changes, such as local activities (e.g. sliding and/or fall) within the whole landslide area,

Finally, according to expert judgment based on the monitored data and these field observations, procedures to manually cancel alarms have been established for two thirds of the reported case studies.

7.3.4 Dealing with populations

a. Decision making processes

Tailored strategies have to be adopted depending on the landslide state of activity and two third of the reported EWSs have established different thresholds for different scenarios. For example, the *Emergency Preparedness Centre in Stranda* established gradual alert postures based on different threshold values and expert evaluations leading to appropriated responses, as the evacuation of endangered populations (Table 7.2). The execution of these strategies requires a close collaboration between the operational units and local and/or regional authorities. Rigorous protocols have to be established in order to clearly define roles and responsibilities of each institution according to the alert levels; a detailed example of the Turtle Mountain Monitoring Project protocols is illustrated in Moreno and Froese (2009). The flowchart is a common representation that gives an evident check list reviewing necessary procedures, as shown for instance in Figure 7.12. The design of decision making processes should take care of legislation and cultural issues, as well as of the prerogatives of the involved agencies. Three fourth of the reported strategies have been designed by the operational units, with the help for about one third of them from local authorities and/or regional and governmental institutions (Figure 7.13). Moreover, the procedures have almost all been reviewed by operational check lists (in 16 cases), completed in 8 cases by reviews from external groups.

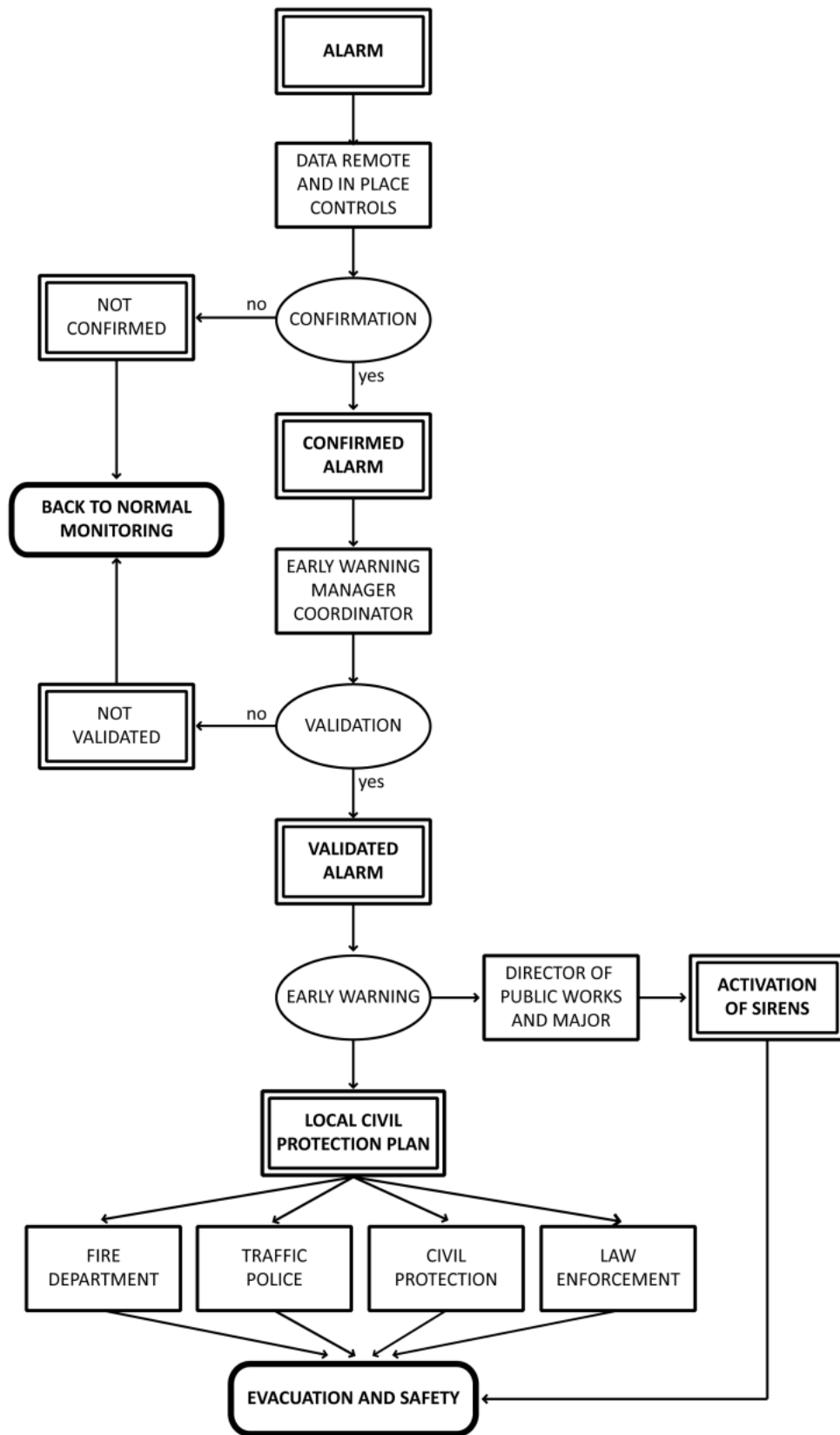


Figure 7.12: Flowchart of the protocol that has to be followed in case of alarm in Ancona, Italy (modified after Cardellini, 2011).

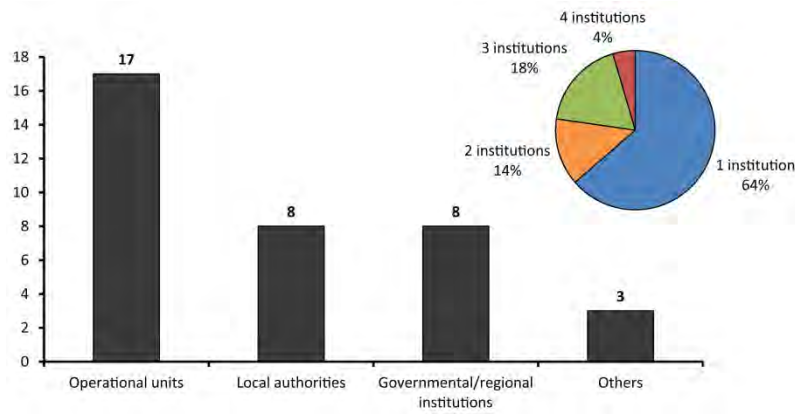


Figure 7.13: Inventory of institutions involved in the establishment of strategies in case of alerts and percentage of number of institutions involved together for the 23 reported EWSs. The total number is above 22, because 36 % of the strategies have been designed by more than one institute.

b. Alert broadcasts

When circumstances require the evacuation of local populations, the most used communication vectors to inform people are radio, siren and SMS, coupled sometime with phone and TV (Figure 7.14); but also normal evacuation approaches by policemen walking door-to-door are important routines. Websites and e-mails are rarely used, since it is not sure that they manage to reach the population in time for an imminent danger. Regarding the closing of road sections, the most frequent system is simple traffic lights that can actually be completed by policemen. According to our ability to predict in advance the time to slope failure or to flow initiation (Fukuzono, 1990; Crosta and Agliardi, 2003b; Baum and Godt, 2010; Federico et al. 2012; Meyer et al. 2012) and the stakes of each site, reaction times after warning are from 10 minutes to close roads, as in Torgiovanetto, to 72 hours to evacuate populations, as for Norwegian rockslides.

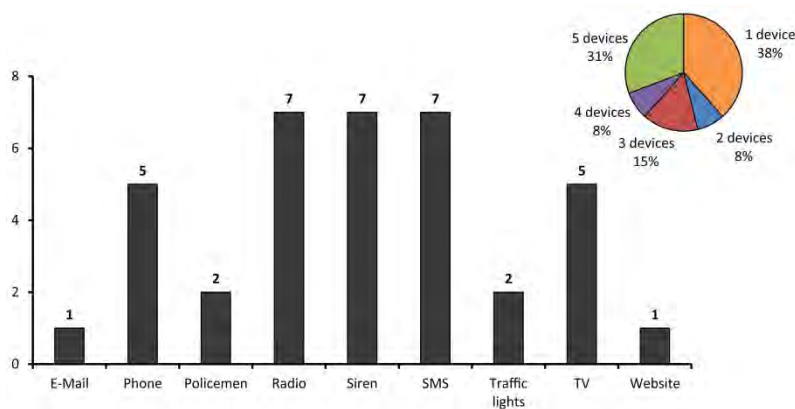


Figure 7.14: Inventory of the different ways used to issue the alerts to local populations and percentage of number of communication devices coupled for the 13 reported answers got from questionnaires. The total number of communication vectors for alerts is over 13, because 38 % of the systems use more than one type of device.

Prior to real evacuations, operational units and local units have imperatively to ensure that public has been well informed about the adopted strategies, in order to guarantee that the plan comes together with proper cooperation and behavior of the local populations (as detailed in Section 7.3.4). In addition, evacuation exercises, which have been performed once or twice for 12 reported case studies, recently turn out to be necessary to test the efficiency of established plans and procedures (Moreno and Froese, 2009).

c. Risk communications

The trust of local populations in EWSs and a proper risk perception are fundamental for the success of an EWS (Dash and Gladwin, 2007) since cooperating and collective actions are required in case of alerts. Due to socio-cultural heritages, fair judgments need openness, involvement and good consultation processes. Ostrom (1998) further recommends the face-to-face communication. It provides the best positive effects on cooperative tasks, allowing, among other things, the exchange of mutual commitments and the assurance of proper expectations of population behaviors in case of evacuation for instance.

For half of the reported cases, the information is given thanks to public meetings, reports, as well as websites (Figure 7.15). Other solutions, such as newspapers, are still anecdotic. No answers referred to any information provided by some TV-programs. A good risk communication also means that public meetings have to be organized to inform and consult local populations during and/or after every round of the decision making process.

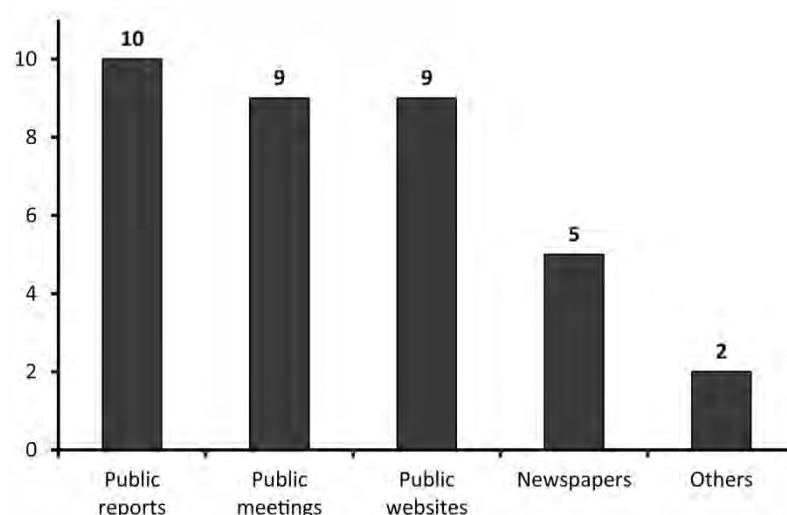


Figure 7.15: Inventory of communication vectors used to inform local populations for the 23 reported EWSs. The total number of vectors is over 23, because several institutions communicated by several ways.

Finally, a last point is also clear: monitoring centers are in charge of sensitive and complex data. Indeed, even if they are all partially or totally financed by public funds, two third of the institutions

still do not open a free and easy access to data for anyone. It can be also a question about letting the public having access to raw data that can be difficult to interpret due to noise in the sensor measurements. Although not communicating the monitored data could make local people suspicious, incorrect readings could also certainly lead to major misunderstandings and unnecessary concerns (Mileti and Sorensen, 1990). Therefore, the right communication level is difficult to reach.

7.3.5 Practical challenges

The last part of the questionnaire is related to practical challenges encountered during the design, the construction and the maintenance of the EWSs (Figure 7.16). Most of them (20) related some problems during the installation and the maintenance of the sensors. Indeed, more than half of the instrumentation deals with harsh weather and site conditions, suffering from heavy rainfall, ice, thick snow cover, avalanches, wind, etc. On the other hand, funding and human resources are sources of problems for less than one third of the EWSs.

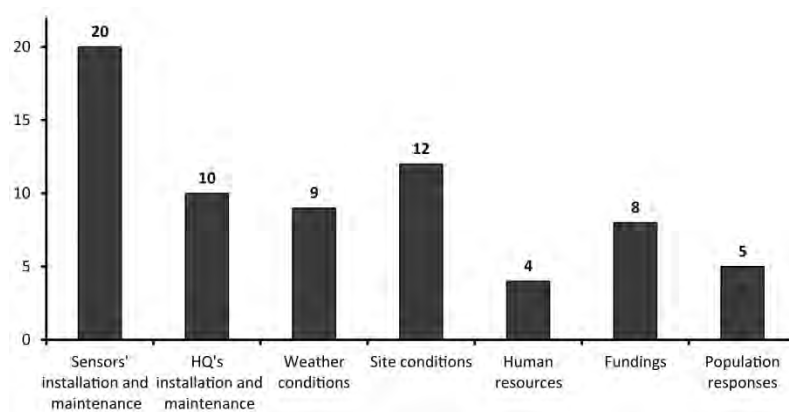


Figure 7.16: Inventory of practical challenges met by the 23 reported EWSs. The total number of challenges is over 23, because EWSs usually encountered more than issue during its life cycle.

From the 8 participating countries, only Norway legislated on EWS in order to define the roles of institutions in charge of landslide EWSs and to direct them (Technical requirements in the Norwegian building codes). In addition, Slovakia produced a guideline about general strategies to adopt and Canada is on the way (Couture et al. 2012).

As a consequence, the operational units in charge of EWSs have to look for scientific and practical supports from other expert groups and/or international experience.

7.4 Discussions and conclusions

This paper aims to present some reflections for implementing site-specific landslide EWSs focused on specific requirements and practical issues based on current on-going experiences. A questionnaire on

these purposes was created and sent to about a hundred of institutions in charge of landslide managements. About one fourth of the requests received an answer. One reason could be the lack of availability from the persons in charge. Another reason could be the questionnaire format (a *pdf* file including questions and tables sent by emails), even if it seemed to be easy accessible for everybody. Several institutions reported to us indeed difficulties to fill some parts of the questionnaire and had to print it to write answers by hand. For future investigations, we would recommend the use of interactive web-based survey tools (e.g. as in Tofani et al. 2013); they are indeed more user-friendly to fill by respondents (maximizing the number of potential answers as shown in Lapointe et al. 2010) and also to analyze afterwards. Although the small number of answers has not a high statistical significance, several of the reported EWSs are among the most studied landslides in the Western countries. They have also accumulated high-quality knowledge after many constructive studies and experiments; valuable results and future recommendation can thus be extracted from these sites.

There are no standard requirements for designing and operating EWSs. Actually, we cannot provide solutions to all questions since every situation is unique, depending on landslide hazard and risk settings, local legislations and available resources. Such guidelines are provided in a comprehensive report (Bazin, 2012). Nevertheless, this review based on current experiences highlights specific requirements and potential practical issues that operational units would have to take into consideration when designing their system:

- It is crucial to acquire a proper understanding of instabilities through hazard and risk pre-investigations, and to constantly update landslide conceptual models with the newer monitored data of EWSs;
- Redundancy, simplicity, robustness, communication and power supply back-ups are necessary for a reliable monitoring system. This should support a near real-time interpretation of the stability conditions by experts;
- The establishment of different scenarios adapted to gradual increasing of alert levels based on reliable landslide models is important. Procedures should clearly define the role and the responsibilities of all involved institutions. Alerts should be as quick and as direct as possible;
- Public meetings for properly informing and consulting local population are important in order to ensure a trust atmosphere and an appropriate behavior of people in case of alert.

Nevertheless, some EWS are limited by theoretical and practical issues that are currently investigated:

- First, operational units also underline that most of the time, monitoring networks are located in harsh conditions and therefore that it is difficult to install and maintain sensors. This point emphasizes the importance for manufactures to improve long term sensor robustness and for operational units to ensure a proper maintenance budget.

- EWSs could be significantly improved by current research, focusing on a better near real time integration of monitoring data from different sensor types (Bichler et al. 2004; Travelletti et al. 2012; Michoud et al. 2013c). Sensors and their data processing are under fast developments (Tofani et al. 2011), getting to the continuous integration of GB-InSAR data (Casagli et al. 2010; Chantry et al. 2013; Montserrat et al. 2013), LiDAR data (Riegler, 2013) and geophysical measurements (Mainsant et al. 2012a; Navratil et al. 2013) to monitor landslides. Due to this fast evolution, monitoring systems have to be regularly updated, having once again an impact on EWS deployments and maintenance costs (Froese, 2013).
- In addition to technical limitations, this survey highlights also some EWS conceptual issues. For instance, it seems there is lack of investigation about hydrological factors in landslide processes since water is involved in about 86 % of slope destabilizations and/or landslide triggering but is investigated with rain gauges or piezometers for only half of the cases.
- Moreover, an important challenge is to improve the reliability and pertinence of automatic alarms in the future. Surprisingly about half of the reported systems did not take into considerations technical sensor limitations before establishing threshold values, even if it would surely decrease the frequency of false alarms. In addition, recent research are focused on failure forecasting and/or flows initiations by looking for mass movement indicators (Baroň et al. 2012), such as precursory displacements (Abellán et al. 2010; Federico et al. 2012), changes in slope rheological settings (Mainsant et al. 2012b), strain rates (Jaboyedoff et al. 2012c), or hydrological conditions (Abellán et al. 2013; Mercogliano et al. 2013).

We can also add that a recent workshop (*"The 1st International Workshop on Warning Criteria for Active Slides"*), held in Courmayeur, Italy (Cloutier et al. 2015), during the review process of this paper (10-12 June 2013), showed one additional issue. After a decade of services, it indeed seems that some EWSs need to be redeployed because of low activity of the landslides and budget issues. This leads to learn how to go from expensive and complex EWS to simpler and cheaper monitoring systems (Troisi and Negro, 2013; Froese, 2013).

Finally, the collected feedbacks and experiences, in addition to current researches, will therefore contribute to modify and improve existing and future EWS strategies.

7.5 Supplementary material

The following questionnaire has been sent in June 2011 to more than hundred institutions in charge of landslides monitoring and/or early warning centers in Asia, Europe and North-America. The results of the present paper are based on answers that we received till autumn 2011.



Oslo and Lausanne, the 23rd of June 2011.

Subject: Invitation to participate to a screening survey about landslides Early Warning Systems

To whom it may concern,

The large, integrating project SafeLand, funded by the European Commission in the 7th Framework Programme, is intended to develop generic risk management tools and strategies for landslides. SafeLand is a collaborative project between 27 partners from 12 countries and coordinated by the International Centre for Geohazards (ICG) in Oslo, Norway. One of the main objectives of the Safeland project is to merge experience and expert judgment and therefore to create synergies on EC-level and to make these results available to end users and local stakeholders. More information on this project is available at www.safeland-fp7.eu.

As part of this study, we are **gathering information about the responsible organizations for landslide early warning system and risk management in selected countries**. You have been identified on internet or by colleagues as an organization in charge of one or several Early Warning System(s). Thus, we would very appreciate that you fill the attached form. **This short (four-page) questionnaire aims to compile information about the state of the art technologies and existing strategies**. The intention of this screening study is **to provide guidelines that will facilitate the establishment of new Early Warning Systems**. Additional information could be sent as attached documents. As our project is limited in time, we would very much appreciate if you **return this form before the 15th of September 2011** to safeland@igar.org.

Do not hesitate to spread this questionnaire to other people involved in Early Warning Systems. Of course, if you have any additional question, do not hesitate to contact us. We look forward to receiving your information.

Sincerely yours,

Sara Bazin for SafeLand Project Coordinator, Norway
Clément Michoud and Prof. Michel Jaboyedoff, for University of Lausanne, Switzerland
safeland@igar.org



Questionnaire

on landslide early warning systems

1. GENERAL INFORMATION ON THE UNIT IN CHARGE OF THE EWS

Name of the operational unit			
Country		Location	
Person in charge of the operational unit	Name		
	Email address		
Level of operational unit	<input type="checkbox"/> National <input type="checkbox"/> Regional <input type="checkbox"/> Local <input type="checkbox"/> Private		
Source of funding			Yearly cost of unit
Are there any codes for EWS in your country?	<input type="checkbox"/> Yes <input type="checkbox"/> No	Are there any guidelines for EWS in your country?	<input type="checkbox"/> Yes <input type="checkbox"/> No
Is the unit also responsible for monitoring other than landslides?	<input type="checkbox"/> Yes <input type="checkbox"/> No If yes, specify <input type="checkbox"/> volcanoes <input type="checkbox"/> earthquakes <input type="checkbox"/> tsunamis <input type="checkbox"/> weather <input type="checkbox"/> other (specify):	Number of monitored landslides with implemented EWS?	
		Number of monitored landslides without EWS?	
Scale of landslide	<input type="checkbox"/> Single slide <input type="checkbox"/> Multiple slide <input type="checkbox"/> Regional slide		
Are the warning systems in operation?	<input type="checkbox"/> Yes <input type="checkbox"/> No	If not, is it: <input type="checkbox"/> planned <input type="checkbox"/> under construction <input type="checkbox"/> damaged <input type="checkbox"/> stopped	
Number of persons employed at the unit		A person is present on duty 24/7 <input type="checkbox"/> Yes <input type="checkbox"/> No A person is on call 24/7 <input type="checkbox"/> Yes <input type="checkbox"/> No	
Confidentiality/ Access to data	<input type="checkbox"/> Public (full access of general data (e.g. Topography, geology, structural, borehole, hazard/risk etc.), detailed monitoring data accessible on request) <input type="checkbox"/> Not Public (specify whether authorization is already available/requested):		
Web site			

Questionnaire on landslide EW systems

2. MONITORED LANDSLIDES

Please fill this table for each landslide that you monitor

Name of the site:			
Slide has occurred yet?	<input type="checkbox"/> Yes <input type="checkbox"/> No (slide prone)	If yes, potential for future sliding?	<input type="checkbox"/> Yes <input type="checkbox"/> No
Type of landslide	<input type="checkbox"/> rock <input type="checkbox"/> debris <input type="checkbox"/> earth <input type="checkbox"/> other (specify):	Type of slope	<input type="checkbox"/> natural cliff <input type="checkbox"/> quarry or mine <input type="checkbox"/> redesigned slope <input type="checkbox"/> other (specify):
Triggering mechanism	<input type="checkbox"/> rainfall <input type="checkbox"/> earthquake <input type="checkbox"/> erosion <input type="checkbox"/> human activity <input type="checkbox"/> other (specify):	Volume of landslide	
Elements at risk, specify and quantify for each case		<input type="checkbox"/> buildings (private, public...) <input type="checkbox"/> infrastructure (railways, roads, bridges, power lines...) <input type="checkbox"/> people (inhabitants, workers, tourists...) <input type="checkbox"/> indirect risk (tsunami, flooding...) <input type="checkbox"/> other (specify):	
Human losses (death and injuries) due to previous events	<input type="checkbox"/> Yes <input type="checkbox"/> No	If yes, quantify:	
Economic loss due to previous events	<input type="checkbox"/> Yes <input type="checkbox"/> No	If yes, quantify in €:	
Social consequences due to previous events	<input type="checkbox"/> Yes <input type="checkbox"/> No	If yes, specify:	
Mitigation (already performed or envisaged)	<input type="checkbox"/> Yes <input type="checkbox"/> No	If yes, describe (structural/non-structural):	
Land planning already established for the case	<input type="checkbox"/> Yes <input type="checkbox"/> No	If yes, specify:	

3. PRE-INVESTIGATIONS USED TO DESIGN THE EWS

Was geology or geomorphology a design criterion?	<input type="checkbox"/> Yes <input type="checkbox"/> No	If yes, specify:
Were geophysical data a design criterion?	<input type="checkbox"/> Yes <input type="checkbox"/> No	If yes, specify (technique, profiles, scale etc.):
Was hydrogeology a design criterion?	<input type="checkbox"/> Yes <input type="checkbox"/> No	If yes, specify (piezometers, suction etc.):
Were geotechnical data used to design the EWS?	In situ data: <input type="checkbox"/> Yes <input type="checkbox"/> No	If yes, specify (type of test, drilling depth, location, maps availability etc.):
	Lab data: <input type="checkbox"/> Yes <input type="checkbox"/> No	If yes, specify (type and number of tests, material tested):
Were surface movement data used to design the EWS?	<input type="checkbox"/> Yes <input type="checkbox"/> No	If yes, specify type (technique), scale and date:
Was modeling used to design the EWS?	<input type="checkbox"/> Yes <input type="checkbox"/> No	If yes, specify type (technique):

Please return this form to safeland@igar.org

Page 2



Questionnaire on landslide EW systems

5. WARNINGS, COMMUNICATION, AND DECISION MAKING PROCESS

How is operated the data monitoring?	<input type="checkbox"/> automatic, then specify by <input type="checkbox"/> SMS, <input type="checkbox"/> voice message, <input type="checkbox"/> e-mail, <input type="checkbox"/> other <input type="checkbox"/> manual, then specify the frequency of data check and operator:		
Are the warning based on thresholds set on?	<input type="checkbox"/> single sensors <input type="checkbox"/> multiple sensors	Are thresholds based on minimum resolution and noise level?	<input type="checkbox"/> yes <input type="checkbox"/> no
Are there any power supply back-ups?	<input type="checkbox"/> for the sensors <input type="checkbox"/> for the operational center <input type="checkbox"/> for the communication		
Are there any back-ups for communication?	<input type="checkbox"/> for the data transfer <input type="checkbox"/> for the operational center communication (internet, phone, radio...)		
Type of software and integrated systems?			
Who designed the alarm chain?	<input type="checkbox"/> responsible of operational unit <input type="checkbox"/> local authorities <input type="checkbox"/> governmental/regional institutions <input type="checkbox"/> other, specify		
Are there several levels of warning?	<input type="checkbox"/> Yes <input type="checkbox"/> No <input type="checkbox"/> Envisaged If yes, specify how it works :		
Do you have different thresholds for different scenarios?	<input type="checkbox"/> Yes <input type="checkbox"/> No <input type="checkbox"/> Envisaged If yes, specify how it works :		
Can you perform direct field observations in case of a warning?	<input type="checkbox"/> Yes <input type="checkbox"/> No	Is there a procedure to cancel the warning once issued?	<input type="checkbox"/> Yes <input type="checkbox"/> No If yes, describe:
Procedure in case of a warning?			
Evacuation time after a warning?			
How is issued the warning to the population?	<input type="checkbox"/> siren <input type="checkbox"/> SMS <input type="checkbox"/> TV <input type="checkbox"/> radio <input type="checkbox"/> other, specify		
Do you have review procedures?	<input type="checkbox"/> operational check list <input type="checkbox"/> report to review group <input type="checkbox"/> other, specify:		
How do you communicate with the public?	<input type="checkbox"/> public reports specifying status of the landslide, if yes specify frequency: <input type="checkbox"/> public meetings, if yes specify frequency: <input type="checkbox"/> public website <input type="checkbox"/> newspaper <input type="checkbox"/> other, specify:		
Tests and evacuation exercises performed?	<input type="checkbox"/> Yes <input type="checkbox"/> No <input type="checkbox"/> Envisaged If yes, specify extent and frequency:		
What are your practical challenges for the EWS?	<input type="checkbox"/> installation and maintenance of the sensors <input type="checkbox"/> installation and maintenance of the operational unit <input type="checkbox"/> weather conditions <input type="checkbox"/> site conditions <input type="checkbox"/> human resources <input type="checkbox"/> funding <input type="checkbox"/> population response <input type="checkbox"/> other, please specify:		
How could the actual EWS be improved?			

Please return this form to safeland@igar.org

Page 4

CONCLUSIONS

8 Synthesis

8.1 Summary of specific conclusions

As introduced in Section 1, this PhD thesis aimed to investigate capabilities of LiDAR and RaDAR techniques at multiple scales and for various landslide types to support landslide hazard assessments and management from regional scales to site-specific instabilities.

1. Landslides detection and characterization at regional scales

Regarding the regional landslide detection and characterization matter, we first validated the suitable capabilities of recent boat-based mobile LiDAR devices to properly model the topography with a decimetric resolution of km long Normand chalk coastal cliffs, from tossed water of the Channel Sea. Parameters controlling point cloud resolution and precision were also discussed and quantified. Then by comparing annual acquisitions, we validated as well our approach to detect surface changes and thus map rock collapses, landslides and toe erosions at a county scale. The spatial repartition of detected events is now supporting researches to improve our understanding of chalk coastal cliff destabilization processes.

In the Argentine Andes, we applied a spaceborne small baseline InSAR approach to detect large slope instabilities along the national road 7. The low coherence of resulted processes limits the capability of advanced InSAR methods to survey surface changes in such steep reliefs and harsh environments. Nevertheless, we detected, characterized and monitored two unknown deep extremely slow soft rock slides along gentle shores of the Potrerillos dam reservoir. We then identified a body of evidences that those large slope instabilities mainly formed by sandstones and clays are influenced by the reservoir level variations. We therefore demonstrated that geometries and displacements of extremely slow landslides, as well as survey of the reservoir water level variations, can all be extracted from spaceborne advanced InSAR images using both phase and amplitude signals.

2. Spatial risk assessment over large areas

Advanced investigations on fragmental rockfall risk assessment for were conducted along roads of the whole Bagnes valley, based on HR-DEM and the Swiss geological atlas. By improving approaches of the Slope Angle Distribution and the FlowR software, both rock-mass-failure susceptibilities and relative frequencies of block propagations were evaluated at the valley scale and thus rockfall hazard maps could be established. Finally, based on the hazard mapping and additional information about

traffic, we then were able to process rockfall risk assessments along all roads of the valley. As a result, even if the resulting risk is an approximation, this improved approach allowed (1) to deal at affordable cost with real hazard maps at regional scales and (2) to identify hotspots where expensive detailed investigations are necessary in priority.

3. Slope instability monitoring and modelling at site-specific scales

At slope-specific scales in the Swiss Alps, we integrated Ground-based InSAR and terrestrial LiDAR acquisitions to map, monitor and model the La Perraire rock slope deformation. By interpreting both methods individually and originally integrated as well, we therefore delimited the rockslide borders, computed volumes between 8 and 10 million cubic meters, and highlighted non-uniform translational displacements along a wedge failure surface. Computed strain rates stressed an active extension of the upper part of about 0.085 %/yr with displacements rates up to 25 cm/yr, and a progressive movement decrease downward that implies a worrying compression of the rockslide toe. The instability may behave as rock avalanche in case of sudden total failure; these investigations are therefore essential requirements to design an early warning system.

Finally, we studied specific requirements and practical issues experienced on early warning systems set up for some of the most studied landslides worldwide that accumulated high-quality knowledge after many constructive studies and experiments. We then extracted valuable recommendations to set a reliable EWS, such as the importance of pre-implementation works or the establishment of different scenarios adapted to gradual increasing of alert levels. We also underlined some current conceptual issues that must be solved, especially regarding failure forecasting and integration of water processes in landslide conceptual models. For instance, water is indeed involved in about 86 % of slope destabilizations and/or landslide triggering but is investigated with rain gauges or piezometers for only half of the cases. To sum up, this review, in addition to current researches, will thus support the design and improvement of future systems.

8.2 Current sensors capabilities

Spaceborne DInSAR methods extract extremely slow surface displacements with sparse resolutions at regional scales (Massonnet 1985; Ferretti et al. 2001 and 2011; Berardino et al. 2002). Therefore, they are indicated to detect large and active slope instabilities with continuous displacements, such as mountain and rock slope deformations, rock and soil slides, or even earthflows (Berardino et al. 2003; Herrera et al. 2010, 2013; Lauknes et al. 2010; Henderson et al. 2011; Schlögel et al. 2015; Section 4 of this manuscript). Thus, DInSAR methods are not sufficient to achieve complete active landslide inventories (Bianchini et al. 2012; Herrera et al. 2013) and cannot point out former and stabilized landslides; but it can still monitor a dormant delimited instability to survey its potential

reactivation (Herrera et al. 2011; Crosetto et al. 2013; Sigleton et al. 2014). Nevertheless, those limitations are nowadays being overcome: indeed, a new generation of spaceborne SAR sensors is currently under deployment within the European Space Agency Sentinel program (Malenovský et al. 2012). The constellation of Sentinel 1A and 1B will allow a revisiting time of 12 days and even 6 days in tandem modes (Berger et al. 2012). These short temporal baselines will definitely refine coherence of A-DInSAR scenes reducing spatial decorrelation and increasing the SNR by stacking (cf. annex B1). Therefore, these new products will surely improve the landslide detection at regional scales, which are currently suffering of large masked areas with no data due to low coherence issues (cf. Section 4.4.2). In addition, they will also enhance displacement monitoring of site-specific landslides, such as in Turtle Mountain or Åknes (cf. Section 7.3.3). Those measurements recorded on a weekly base will then support long term investigations at low cost, requiring only the setup of corner reflectors on studied slopes. Now, prior to any applications, it is important to take care of specific points in order to ensure the most consistent processing as possible (Massonnet and Feigl 1998; Hanssen 2001; Cascini et al. 2009). Indeed, the natural features of the region of interest, such as slope steepness and aspect, land-use, landslide type and velocities, will condition the choice of SAR sensors according to their resolution, orbits and wavelengths. Furthermore, the availability and costs of archived scenes are also decisive to confirm the choice of the sensor: without any archives, we would have to wait more than 15 snow-free SAR acquisitions (repeat intervals of respectively 35 and 11 days for Envisat and TerraSar-X) to get enough images to process reliable stacked interferograms. In addition, archived SAR images from mid-resolution ESA sensors (ERS, Envisat, etc.) can be relatively low cost or even free, allowing to get InSAR results at affordable costs when necessary. Moreover, even if DInSAR processing are time consuming and complex, they are nowadays semi-automatic and many tests can be performed to set the most relevant parameters as possible.

Ground-based InSAR devices have been developed to continuously monitor delimited unstable compartments (Tarchi et al. 1997; Casagli et al. 2003; Herrera et al. 2009; Barla et al. 2010; Section 6 of this manuscript). In order to ensure a consistent monitoring, extents, velocities and directions of mass movements must be estimated as best as possible. Indeed, it will condition GB-InSAR monitoring feasibilities and potential device locations. First, GB-InSAR devices usually have metric resolutions and are optimized to detect millimetric mass movements. Then regarding GB-InSAR locations, device LOS must be as parallel and less orthogonal as possible to the expected movement directions to maximize the possibility to monitor them, since recorded displacements are the projection of real ones on the LOS. In addition and only if several location can fit with the previous points, devices should be set up as close to the instability as possible to improve their resolution, and at same elevations as surveyed masses to avoid that potential atmospheric layering induces decorrelations (Hanssen et al. 2001; Lauknes et al. 2011). Once device location and parameters are optimized, data acquisitions and displacement processing can be automatically executed; therefore GB-InSAR methods are indicated for early warning systems of large unstable masses by monitoring

extremely to very slow precursory displacements (Luzi 2010; Caduff et al. 2014; Monserrat et al. 2014; Section 7 of this manuscript).

Aerial LiDAR sensors are mainly used to produce HR-DEM at regional scales (Baltsavias 1999b; Carter et al. 2001). On the one hand, semi-automatic procedures were developed to spatially assess landslide susceptibilities, mapping areas that can potentially be reached by natural processes with no indications on their current activity (Chigira et al. 2004; Jaboyedoff et al. 2012b; Section 5 of this manuscript). These approaches can be applied to rockfall, debris flows, shallow landslides, snow avalanches or even dynamic floods. On the other hand, active or dormant slope instabilities (slides and flows) can be manually mapped based on the visual interpretation of landslide geomorphological markers, such as crones, bulges, shallow flow, toe erosion or scree deposits (McKean and Roering 2004; Ardizzone et al. 2007; Haneberg et al. 2009; Schulz 2007; Jaboyedoff et al. 2012b; Crosta et al. 2013). This visual expertise is technically simple but very time-consuming and asks rigour to provide consistent and coherent results over large areas. Before any application, we must be aware that land-uses (especially dense forests), slope angles (in particular vertical cliffs) and elevations of studied areas will affect the quality of the ALS surface point clouds and limitate HR DEM-based geological mapping capabilities. In addition, costs of aerial LiDAR acquisitions were reletaviley high, limiting so far the use of sequential acquisitions for surface change detection and monitoring.

Terrestrial LiDAR sensors provide 3D point clouds of the topography with very high resolution, especially on steep rock slopes at site-specific scales (Gordon et al. 2001; Lichti et al. 2002). First, in order to ensure reliable results, it is important to optimize TLS acquisitions according to slope geometry. Indeed, the number of different acquisitions covering the whole moving mass has to minimize shadow areas by usually increasing the number of point of views; on the contrary, they also have to be as low as possible to avoid scan alignment errors. Therefore, the optimization of number of windows should be seriously considered before any acquisition, since it will definitively influence result capabilities. Once clouds are processed, landslide geological and geomorphological features can be precisely mapped based on visual point interpretations (Jaboyedoff et al. 2007; Matasci et al. 2014). In addition, semi-automatic approaches to assess structural settings and surface changes are under constant developments (Sturzenegger et al. 2007; Teza et al., 2007; Oppikofer et al. 2008; Abellán et al. 2010; Carrea et al. 2012). Indeed, TLS are widely used for accurate and complete sequential monitoring of surface changes and 3D displacements of various landslide types (Oppikofer et al. 2008; Travelletti et al. 2014; Section 6 of this manuscript). Nevertheless, some critical post-processing steps remain manual, tedious and time consuming, such as vegetation removal, volume estimations or roto-translation matrixes extraction; thus, uses of TLS devices for continuous monitoring including early warning systems are nowadays limited to small slide monitoring in mines

(TLS manufacture communications), and automatic routines for more complex slope instabilities are under developments (Kromer et al. 2015).

Mobile LiDAR sensors have been designed to fill gaps between aerial and terrestrial LiDAR sensors. Indeed, these sensors are able to acquire points on vertical cliffs (only sparsely covered by aerial sensors) confined along transportation corridors, such as cut slopes or coastal cliffs (Kukko et al. 2012; Glennie et al. 2013). Therefore, in addition to common expertise based on visual interpretations of landslide geomorphological features, rock fall activity as well as surface changes and displacements can be assessed as for TLS approaches (Alho et al. 2009; Vaaja et al. 2011 and 2013; Kukko et al. 2012; Glennie et al. 2013; Section 3 of this manuscript). Prior to any MLS study, specific conditions must be assessed to ensure possible acquisitions. First, the GNSS horizon must be clear enough and satellites must be consistently located, which can thus limit acquisitions on polar latitudes and along vegetated or incised corridors. Then ranges of acquisition have to fit with device specifications (from hundred to thousand meters). Finally, external factors, such as marine streams and waves on boats or traffic on cars, must be considered as well to ensure reliable acquisition conditions.

8.3 Research perspectives

As pointed out in previous sections of the manuscript, some achievements would require more tests and methodological issues have risen; then, further studies would be really stimulating to improve landslide-related sensor capabilities and should therefore be intended:

1. Spaceborne InSAR capabilities for landslide detection at regional scales

We stressed in Argentina issues to record pertinent and stable reflectors, since the signal is hampered by steep slope geometry and is interfered by strong tropospheric delays and long snow cover periods on elevated areas (cf. Section 4.4.2). The general trend introduced by the atmospheric artefacts has been removed by fitting a quadratic polynomial function on mean LOS velocities according to azimuths and elevations. Even if it improved final results, it could not retrieve all interfered reflectors that were masked out before the prior interferogram unwrapping step (cf. Section 4.3.2a). Then complex atmospheric corrections (Lauknes 2011) included within the whole SBAS processing chain and before the unwrapping step still need to be developed and improved.

Furthermore, spaceborne InSAR method could be applied in the Val de Bagnes. Indeed, in addition to rockfall hazard maps (cf. Section 5), landslides affecting the whole valley were inventoried on the aerial LiDAR -based DEM (cf. annex B3; Michoud et al. 2010a; Jaboyedoff et al. 2012b). It then would be interesting to compare the InSAR detection capabilities for various land-uses, altitudes, slope

geometries, and for different landslides types and activities, according to the inventory map. It could also be integrated into initiated studies on the identification of distinct InSAR signal patterns according to landslide types (Derron et al. 2015; Schlögel et al. 2015).

2. GB-InSAR capabilities for landslide monitoring

As experimented at La Perraire (cf. Section 6), La Barmasse (Figure 2.10) and in Norway (Rouyet et al. submitted), algorithms to post-process GB-InSAR images are not as complete as the one for spaceborne interferometry. In the one hand, it is normal since spaceborne-related phase contributions mainly due to orbital and topographic effects (Hanssen 2001) do not affect terrestrial SAR images. But on the other hand, there are only few tools to correct atmospheric noises; currently, this contribution is corrected by low coherence filtering, pixel focusing and mainly image stacking, in order to increase the signal to noise ratio. Nevertheless in some cases, the selection of stacking time-interval can drastically influence the amplitude of monitored displacements. Tools to select the best compromise between the lowest stack influences and highest signal to noise ratio, and to filter GB-InSAR images according to rain and humidity gauges, should then be studied to remove atmospheric phase contributions.

In addition and to complete spaceborne InSAR perspectives, other investigations were began in parallel to improve our understanding of the back scattered signal according to landslide types; indeed, tests were started at the Roche quarry, acquiring GB-InSAR images while controlling displacement amplitudes and types of artificial rock blocks. Nevertheless, those tests and interpretations remained uncompleted and should therefore be finished and compare with the DInSAR simulator developed by Derron et al. (2015).

3. Terrestrial LiDAR capabilities for landslide early warning

A reflexion on the use of continuous terrestrial LiDAR to monitor mass balance in landslide warning systems has been initiated for the SafeLand project. This kind of system is indeed regularly used for snow avalanches (Rice et al. 2002; Sailer et al. 2008): first LiDAR devices record the thickness of snow mantle, particularly in locations where wind is expected to accumulate it. Once the volume reaches a predefined critical value, automatic warning procedures can be executed.

But presently we are not aware of any actual application of it to landslides, even if it could theoretically be implemented. Indeed, the monitoring of the volume of potentially mobile material in key locations in watersheds could help to prevent large debris flows with long run out. In addition, the monitoring of foot slope volume changes, as for example erosion of quick clays toe (Jaboyedoff et al. 2009a) or bulging of earthflows (Mainsant et al. 2012a), could be a reliable indicator prior to failures. Nevertheless, two major issues can explain why the mass balances concepts are not used in

EWS as far as we know. First it requires the assessment of reliable volume threshold values complex models. Then there are only few published routines allowing a continuous monitoring with a TLS device (Kromer et al. 2015), since estimations of mass balances and surface displacements in complex situations from point clouds comparisons still require manual steps. These limitations should then be investigated, especially on development of automatized LiDAR routines.

4. Multi-sensors integration tools

Finally, landslide experts need tools to integrate in one model all acquisitions from different sensor types, in order to provide a consistent decision support (cf. Section 7.4). A first step toward this objective was achieved, with the implementation in Coltop3D of a module to fuse displacement data from GB-InSAR and 3D point clouds from LiDAR acquisitions (cf. Section 6.2.1). Nevertheless, it might be interesting to go further, developing tools to add other dataset, such as displacement vectors from punctual GNSS campaigns or sub-surface movements recorded on inclinometers.

9 Epilogue

This thesis investigated LiDAR and DInSAR capabilities on various landslide types, at several scales and for different objectives. Therefore, the diversity of experimented situations brought an extensive experience that revealed the potential and limitations of both methods and highlighted as well the necessity of their complementary and integrated uses. Furthermore, during seven years of this PhD, we saw the technical improvement of devices continuously more portable, accurate and affordable; in addition, recent algorithms also tend to refine and automatize post-processing routines. Current developments of mobile LiDAR mounted on UAVs and photogrammetry based on Structure-for-Motion—Multiview-Stereo algorithms illustrate this trend. Thereby, we can reasonably assume that slope instability surveying and monitoring will be steadily less technically challenging and then, efforts should be focused on stimulating questions, i.e. landslide mechanism understanding and time to failure forecasting.

REFERENCES

- Abellán A, Vilaplana JM, Martínez J (2006) Application of a long-range Terrestrial Laser Scanner to a detailed rockfall study at Vall de Núria (Eastern Pyrenees, Spain). *Engineering Geology* 88:136–148
- Abellán A, Jaboyedoff M, Oppikofer T, Vilaplana JM (2009) Detection of millimetric deformation using a terrestrial laser scanner: experiment and application to a rockfall event. *Nat. Hazards Earth Syst. Sci.* 9:365–372
- Abellán A, Oppikofer T, Jaboyedoff M, Rosser NJ, Lim M, Lato MJ (2014) Terrestrial laser scanning of rock slope instabilities. *Earth Surf. Process. Landforms*, 39:80–97
- Abellán A, Calvet J, Vilaplana JM, Blanchard J (2010) Detection and spatial prediction of rockfalls by means of terrestrial laser scanner monitoring. *Geomorphology* 119:162–171
- Abellán A, Vilaplana JM, Calvet J, García-Sellés D, Asensio E (2011) Rockfall monitoring by Terrestrial Laser Scanning – case study of the basaltic rock face at Castellfollit de la Roca (Catalonia, Spain). *Nat. Hazards Earth Syst. Sci.* 11:829–841
- Abellán, A., Moya, J., Jaboyedoff, M. and Corominas, J. (2013) Predicción de la velocidad de un deslizamiento en base a la precipitación. Aplicación en la zona de estudio piloto de Vallcebre (Pirineos Catalanes), in: *Proceedings of the VII Simposio Nacional sobre Taludes y Laderas Inestables* (in Spanish), Palma de Mallorca, Spain, 11-14 June 2013, 1081-1092
- Abshire JB, Sun X, Riris H, Sirota JM, McGarry JF, Palm S, Yi D, Liiva P (2005) Geoscience Laser Altimeter System (GLAS) on the ICESat Mission: On-orbit measurement performance. *Geophysical Research Letters* 32
- Adams JC, Chandler JH (2002) Evaluation of LiDAR and medium scale photogrammetry for detecting soft-cliffs coastal change. *The Photogrammetric Record* 17:405-418
- Agliardi F, Crosta GB, Zanchi A (2001) Structural constraints on deep-seated slope deformation kinematics. *Engineering Geology* 59:83–102
- Agliardi F, Crosta GB, Frattini P (2009) Integrating rockfall risk assessment and countermeasure design by 3D modelling techniques, *Nat. Hazards Earth Syst. Sci.*, 9, 1059-1073
- Aleotti, P (2004) A warning system for rainfall-induced shallow failures, *Engineering Geology*, 73, 247-265
- Alho P, Kukko A, Hyypä H, Kaartinen H, Hyypä J, Jaakkola A (2009) Application of boat-based laser scanning for river survey. *Earth Surf. Process. Landforms* 34:1831-1838
- Andrew RD, Arndt B, Turner KA (2012) Instrumentation and Monitoring Technologies. In: Turner A, Schuster R (Eds.) *Rockfall, Characterization and Control*. Transportation Research Board, Special Report , Washington, DC, 212-284
- Angeli, M.-G., Pasuto, A. and Silvano, S. (2000) A critical review of landslide monitoring experiences, *Engineering Geology*, 55, 133-147
- Antoine P, Fabre D, Giraud A, Al Hayari M (1988) Geotechnical properties of some geological formations responsible for landslides (French Alps). In: *Proceedings of the 5th International Symposium on Landslides, Lausanne*, 2:1301-1306
- Antonello G, Casagli N, Farina P, Leva D, Nico G, Sieber AJ, Tarchi D (2004) Ground-based SAR interferometry for monitoring mass movements. *Landslides* 1:21-28
- Applanix Corporation (2001) POS MV V5 Installation and Operation Guide, revision 3
- Ardizzone F, Cardinali M, Galli F, Guzzetti F, Reichenbach P (2007) Identification and mapping of recent rainfall-induced landslides using elevation data collected by airborne Lidar. *Natural Hazards Earth System Sciences* 7:637–650.
- Aryal A, Brooks BA, Reid ME, et al (2012) Displacement fields from point cloud data: Application of particle imaging velocimetry to landslide geodesy. *J Geophys Res* 117:F01029
- Aryal A, Brooks BA, Reid ME (2015) Landslide subsurface slip geometry inferred from 3-D surface displacement fields. *Geophys Res Lett* 42:1411–1417
- Attewell PB, Farmer IW (1973) Fatigue Behavior of Rock. *Int. J. Mech. Sci.* 10:1-9
- Azzoni A, Chiesa S, Frassoni A, Govi M (1992) The Valpola landslide. *Engineering Geology* 33(1):59-70
- Baillifard, F.J., Jaboyedoff, M. and Sartori, M. (2003) Rockfall hazard mapping along a mountainous road in Switzerland using a GIS-based parameter rating approach, *Natural Hazards and Earth System Sciences*, 3: 431-438
- Bakkehoi S, Domaas U, Lied K (1983) Calculation of snow avalanche runout distance. *Annals of Glaciology* 4:24-29
- Balbarani S, Euillades PA, Euillades LD, Casu F, Riveros NC (2013) Atmospheric corrections in interferometric synthetic aperture radar surface deformation – a case study of the city of Mendoza, Argentina. *Advances in Geosciences* 35:105–113
- Baltsavias EP (1999a) Airborne laser scanning: basic relations and formulas. *ISPRS Journal of Photogrammetry & Remote Sensing* 54:199-214
- Baltsavias EP (1999b) A comparison between photogrammetry and laser scanning. *ISPRS Journal of Photogrammetry & Remote Sensing* 54:83-94

- Bamler R (1992) A Comparison of Range-Doppler and Wavenumber Domain SAR Focusing Algorithms. *IEEE Transactions on Geoscience and Remote Sensing* 30(4):706-713
- Bamler R, Hart P (1998) Synthetic aperture radar interferometry. *Inverse Problems* 14:R1–R54
- Bardi B, Frodella W, Ciampalini A, Bianchini S, Del Ventisette C, Gigli G, Fanti R, Moretti S, Basile G, Casagli N (2014) Integration between ground based and satellite SAR data in landslide mapping: The San Fratello case study. *Geomorphology* 223:45–60
- Barla G, Antolini F, Barla M, Mensi E, Piovano G (2010) Monitoring of the Beaugregard landslide (Aosta Valley, Italy) using advanced and conventional techniques. *Engineering Geology* 116:218–235
- Baroň I, Supper R, Ottowitz D, Eds. (2012) SafeLand deliverable 4.6.: Report on evaluation of mass movement indicators, European Project SafeLand, Grant Agreement No. 226479, 382 pp., available at: <http://www.safeland-fp7.eu>
- Baroň I, Supper R (2013) Application and reliability of techniques for landslide site investigation, monitoring and early warning – outcomes from a questionnaire study. *Nat. Hazards Earth Syst. Sci.* 13:3157–3168
- Basher R (2006) Global early warning systems for natural hazards: systematic and people-centered, *Phil. Trans. R. Soc.*, 364, 2167-2182
- Baum RL, Godt JW (2010) Early warning of rainfall-induced shallow landslides and debris flows in the USA. *Landslides* 7:259-272
- Baumann V, Coppolecchia M, González MA, Fauqué LE, Rosas M, Altobelli S, Wilson C, Hermanns RL (2005) Landslide Processes in the Puente del Inca region, Mendoza, Argentina. In: Hungr O, Fell R, Couture R, Eberhardt E (eds) *Proceedings of the International Conference on Landslide Risk Management, Vancouver, Canada*. A.A. Balkema Publishers, London, Supplementary Volume (CD), pp 61-62
- Baumann V, Wick E, Horton P, Jaboyedoff M (2011) Debris flow susceptibility mapping at a regional scale along the National Road N7, Argentina. In: *Proceedings of the 2011 Pan-Am CGS Geotechnical Conference, Toronto, Canada*, 7 p
- Bazin S, Ed. (2012) SafeLand deliverable 4.8.: Guidelines for landslide monitoring and early warning systems in Europe – Design and required technology, European Project SafeLand, Grant Agreement No. 226479, 153 pp., available at: <http://www.safeland-fp7.eu>
- Bell FG (2007) *Engineering Geology*, 2nd edn. Butterworth-Heinemann
- Bellian JA, Kerans C, Jennette DC (2005) Digital Outcrop Models: Applications of Terrestrial Scanning Lidar Technology in Stratigraphic Modeling. *Journal of Sedimentary Research* 75(2):166-176
- Benko B, Stead D (1998) The Frank slide: a reexamination of the failure mechanism, *Canadian Geotechnical Journal* 35:299-311
- Beraldin JA, Blais F, Boulanger P (2000) Real world modelling through high resolution digital 3D imaging of objects and structures. *ISPRS Journal of Photogrammetry & Remote Sensing* 55:230–250
- Berardino P, Fornaro G, Lanari R, Sansosti E (2002) A New Algorithm for Surface Deformation Monitoring Based on Small Baseline Differential SAR Interferograms. *IEEE Transactions on Geoscience and Remote Sensing* 40(11):2375-2383
- Berardino P, Costantini M, Franceschetti G, Iodice A, Pietranera L, Rizzo V (2003) Use of differential SAR interferometry in monitoring and modelling large slope instability at Maratea (Basilicata, Italy). *Engineering Geology* 68:31-51
- Berger M, Moreno J, Johannessen JA, Levelt PF, Hanssen RF (2012) ESA's sentinel missions in support of Earth system science. *Remote Sensing of Environment* 120:84-90
- Besl PJ, McKay ND (1992) A Method for Registration of 3D Shapes. *IEEE Transaction on Pattern Analysis and Machine Intelligence* 14:239-256
- Bianchini S, Cigna F, Righini G, Proietti C, Casagli N (2012) Landslide HotSpot Mapping by means of Persistent Scatterer Interferometry. *Environ Earth Sci* 67:1155–1172
- Bichler A, Bobrowsky P, Best M, Douma M, Hunter J, Calvert T, Burns R (2004) Three-dimensional mapping of a landslide using a multi-geophysical approach: the Quesnel Forks landslide, *Landslides* 1:29-40
- Bieniawski ZT (1976) Rock mass classification in rock engineering, in: *Proceeding of the Symposium on Exploration for Rock Engineering, Vol. 1, Bieniawski, Z.T (ed.), Johannesburg, South Africa, 1-5 November 1976*, 97-106
- Blahut J, Horton P, Sterlacchini S, Jaboyedoff M (2010) Debris flow hazard modelling on medium scale: Valtellina di Tirano, Italy, *Nat. Hazards Earth Syst. Sci.*, 10, 2379–2390
- Blikra LH (2008) The Åknes rockslide: Monitoring, threshold values and early-warning. *Landslides and Engineering Slopes: From the Past to the Future, Proceedings of the 10th International Symposium on Landslides and Engineering Slopes, Xi'an, China, 30 June–4 July 2008*, 1089–1094
- Blikra LH (2012) The Åknes rockslide, Norway. In: *Landslides: Types, Mechanisms and Modeling*, Clague JJ, Stead D (Eds.), Cambridge, 323–335

- Bonnard C, Steiger H (2012) Control of an unstable slope by horizontal drainage boreholes and soil nailing during the widening of a major road, Laubegg gorge Switzerland, in: Landslides and Engineering Slopes: Protecting Society through Improved Understanding, Proceedings of the 11th International and 2nd North American Symposium on Landslides and Engineered Slopes, Banff, Canada, 3-8 June 2012, 1575-1580
- Borle Y (2007) Phénomènes érosifs dans le bassin versant de Lourtier (Valais, Suisse) - Etude d'une instabilité rocheuse et établissement d'un bilan sédimentaire à l'aide d'une cartographie de terrain détaillée : méthodologie et application. Master of Sciences of the University of Lausanne, Switzerland, supervised by M Jaboyedoff, 150 p
- Braathen A, Blikra LH, Berg SS, Karlsen F (2004) Rock-slope failures in Norway; type, geometry, deformation mechanisms and stability. *Norwegian Journal of Geology* 84:67-88
- Brock JC, Purkis SJ (2009) The Emerging Role of Lidar Remote Sensing in Coastal Research and Resource Management. *Journal of Coastal Research* SI(53):1-5
- Brooker G (2009) Introduction to sensing. Introduction to Sensors for Ranging and Imaging; SciTech Publishing Inc.: Raleigh, USA 1-22
- Bründl M, Romang HE, Bischof N, Rheinberger CM (2009) The risk concept and its application in natural hazard risk management in Switzerland. *Nat. Hazards Earth Syst. Sci.* 9:801-813
- Brunetti MT, Guzzetti F, Rossi M (2009) Probability distributions of landslide volumes. *Nonlinear Process. Geophys.* 16:179-188
- Buckley SJ, Howell JA, Enge HD, et al. (2008) Terrestrial laser scanning in geology: data acquisition, processing and accuracy considerations. *Journal of the Geological Society* 165, 625-638
- Buckley SJ, Kurz TH, Howell JA, Schneider D (2013) Terrestrial lidar and hyperspectral data fusion products for geological outcrop analysis. *Computers & Geosciences* 54:249-258
- Budetta P (2004) Assessment of rockfall risk along roads, *Nat. Hazards Earth Syst. Sci.*, 4, 71-81, 2004
- Bugge A (1937) Fjellscred fra topografisk og geologisk synspunkt, *Norsk Geografisk Tidsskrift*, 6, 342-360, 1937
- Caduff R, Schlunegger F, Kos A, Wiesmann A (2014) A review of terrestrial radar interferometry for measuring surface change in the geosciences. *Earth Surf. Process. Landforms*, published online, 21 p
- Cajos J, Trocmé-Maillard M, Huber M, Arnold P, Vollmer U, Sandri A, Raetzo H, Dorren L, Egli T, Eberli J, Knuchel R, Kienholz H, Donzel M, Utelli HH, Perren B (2009) Risk concept for natural hazards on national roads, Federal Roads Office (Eds.), 108 pp., available at <http://www.astra.admin.ch/>
- Cardellini S (2011) The Early Warning System of Ancona for Managing and Reducing Landslide Risks, Climate change adaptation and disaster risk reduction, making cities resilient conference, Stockholm, Sweden, 17 May 2011, available at: <http://www.unisdr.org/we/inform/events/19823>
- Carne C, Massonnet D, King C (1996) Two example of the use of SAR interferometry on displacement fields of small spatial extent. *Geophysical Research Letters* 23(24):3579-3582
- CarPostal (2010) <http://www.carpostal.ch/>, last access: 3 December 2010
- Carrea D, Abellán A, Derron M-H, et al (2012) Using 3D surface datasets to understand landslide evolution: From analogue models to real case study. In: Eberhardt E, Froese C, Turner K, Leroueil S (eds) *Landslides and Engineered Slopes: Protecting Society through Improved Understanding*. CRC Press, pp 575-579
- Carrea D, Abellán A, Derron MH, Jaboyedoff M (2014) Automatic rockfalls volume estimation based on Terrestrial Laser Scanning data. In: Proceedings of the IAEG XII Congress, 15-19 September 2014, Turin Italy, 6 p
- Carter M, Bentley SP (1985) A procedure to locate slip surface beneath active landslides using surface monitoring data. *Computers and Geotechnics*, 1:139-153
- Carter W, Shrestha R, Tuell G, et al. (2001) Airborne Laser Swath Mapping Shines New Light on Earth's Topography. *EOS* 82(46), 549-564
- Casagli N, Farina P, Guerri L, Tarchi D, Fortuny J, Leva D and Nico G (2003) Preliminary results of SAR monitoring of the Sciara del Fuoco on the Stromboli volcano, Occurrence and Mechanisms of Flow-like Landslides in Natural Slopes and Earthfills, Sorrento, Italy, Patron Editore, Bologna
- Casagli N, Catani F, del Ventisette C, Guerri L, Tarchi D, Fortuny J, Antonello G, Leva D, Rivolta C (2008) Ground-Based InSAR Monitoring of an Active Volcano and Related Landslides, The First World Landslide Forum, Tokio, 3 p
- Casagli N, Catani F, del Ventisette C, Luzi G (2010) Monitoring, prediction, and early warning using ground-based radar interferometry, *Landslides* 7:291-301
- Cascini L (2008) Applicability of landslide susceptibility and hazard zoning at different scales, *Engineering Geology* 102:164-177
- Cascini L, Fornaro G, Peduto D (2009) Analysis at medium scale of low-resolution DInSAR data in slow-moving landslide-affected areas. *ISPRS Journal of Photogrammetry and Remote Sensing* 64:598-611

- Chantry R, Pedrazzini A, Jaboyedoff M, Stampfli E (2013) Caractérisation, suivi et assainissement des instabilités rocheuses à la carrière d'Arvel, in: Les dangers naturels en Suisse: pratiques et développement, Comptes rendus de la deuxième Journée de Rencontre sur les Dangers Naturels, Lausanne (in French), Switzerland, 18 February 2011, 243-261
- Chen CW, Zebker HA (2001) Two-dimensional phase unwrapping with use of statistical models for cost functions in nonlinear optimization. *Journal of the Optical Society of America* 18(2):338–351
- Chigira M (1992) Long-term gravitational deformation of rocks by mass rock creep. *Engineering Geology* 32:157-184
- Chigira M, Duan F, Yagi H, Furuya T (2004) Using an airborne laser scanner for the identification of shallow landslides and susceptibility assessment in an area of ignimbrite overlain by permeable pyroclastics. *Landslides* 1:203–209
- Cigna F, Bianchini S, Casagli N (2013) How to assess landslide activity and intensity with Persistent Scatterer Interferometry (PSI): the PSI-based matrix approach. *Landslides* 10:267–283
- Clague JJ, Roberts NJ (2012) Landslide hazard and risk. In: *Landslides: Types, Mechanisms and Modeling*, Clague JJ, Stead D (Eds.), Cambridge, 1–9
- Cloutier C, Agliardi F, Crosta G, Frattini P, Froese C, Jaboyedoff M, Locat J, Michoud C, Marui H (2015) The First International Workshop on Warning Criteria for Active Slides: technical issues, problems and solutions for managing early warning systems. *Landslides* 12:205-2012
- Colesanti C, Wasowski J (2006) Investigating landslides with space-borne Synthetic Aperture Radar (SAR) interferometry. *Engineering Geology* 88:173-199
- Collins B, Sitar N (2008) Processes of coastal bluff erosion in weakly lithified sands, Pacifica, California, USA. *Geomorphology* 97:483–501
- Cornforth DH (2005) *Landslides in Practice: Investigation, Analysis and Remedial/Preventive Options in Soils*, John Wiley & Sons, Hoboken, New Jersey, 624 pp
- Corominas J (1996) The angle of reach as a mobility index for small and large landslides. *Can. Geotech. J.* 33:260–271
- Corominas J, Santacana N (2003) Stability analysis of the Vallcebre translational slide, Eastern Pyrenees (Spain) by means of a GIS, *Natural Hazards* 30: 473–485
- Corominas J, Copons R, Moya J, Vilaplana J, Altimir J, Amigó J (2005a) Quantitative assessment of the residual risk in a rockfall protected area, *Landslides*, 2, 343-357
- Corominas J, Moya J, Ledesma A, Lloret A, Gili J (2005b) Prediction of ground displacements and velocities from groundwater level changes at the Vallcebre landslide (Eastern Pyrenees, Spain), *Landslides*, 2, 83-96
- Corominas J, Moya J (2008) A review of assessing landslide frequency for hazard zoning purposes, *Engineering Geology*, 102, 193-213
- Corominas J, Mavrouli O et al., Eds. (2011) SafeLand deliverable 2.4: Guidelines for landslide susceptibility, hazard and risk assessment and zoning, European Project SafeLand, Grant Agreement No. 226479, 173 p., available at: <http://www.safeland-fp7.eu>
- Corominas J, Mavrouli O et al., Eds. (2012) SafeLand deliverable 2.9: Toolbox for landslide quantitative risks assessment, European Project SafeLand, Grant Agreement No. 226479, 39 p., available at: <http://www.safeland-fp7.eu>
- Corominas J, van Westen C, Frattini P, Cascini L, Malet JP, Fotopoulou S, Catani F, van den Eeckhaut M, Mavrouli O, Agliardi F, Pitilakis K, Winter MG, Pastor M, Ferlisi S, Tofani V, Hervás J, Smith JT (2014) Recommendations for the quantitative analysis of landslide risk. *Bull Eng Geol Environ* 73:209–263
- Cortés JM, Casa A, Pasini M, Yamín M, Terrizzano C (2006) Fajas oblicuas de deformación neotectónica en Precordillera y Cordillera Frontal (31°30'–33°30'): Controles paleotectónicos. *Revista de la Asociación Geológica Argentina* 61:639-646
- Costa JE, Schuster RL (1988) The formation and failure of natural dams, *Geological Society of America Bulletin*, 100, 1054-1068
- Costa S (1997) *Dynamique littorale et risques naturels: L'impact des aménagements, des variations du niveau marin et des modifications climatiques entre la Baie de Seine et la Baie de Somme*. PhD thesis of the University of Paris I (Panthéon Sorbonne), 347 p
- Costa S, Delahaye D, Freiré-Díaz S, Davidson R, Di-Nocera L, Plessis E (2004) Quantification by photogrammetric analysis of the Normandy and Picardy rocky coast dynamic (Normandy, France). In: Mortimore RN, Duperré A (eds.) *Coastal chalk cliff instability*, Engineering Geology Special Publications, Geological Society, London, pp 139–148
- Costa S (2014) The High Normandy Chalk Cliffs: An Inspiring Geomorphosite for Painters and Novelists. In: Fort M, André MF (eds.) *Landscapes and Landforms of France*, Springer, pp 29-39
- Costin LS, Holcomb DJ (1981) Time-Dependent Failure of Rock Under Cyclic Loading. *Tectonophysics* 79:279-296
- Cotecchia V (2006) The Second Hans Cloos Lecture: Experience drawn from the great Ancona landslide of 1982, *Bull. Eng. Geol. Env.*, 65, 1-41

- Couture R, Bobrowsky PT, Blais-Stevens A, Wang B, VanDine DF (2012) An introduction to the Canadian technical guidelines and best practices related to landslides, in: *Landslides and Engineering Slopes: Protecting Society through Improved Understanding*, Proceedings of the 11th International and 2nd North American Symposium on Landslides and Engineered Slopes, Banff, Canada, 3-8 June 2012, 217-222
- Crosetto M, Gili J, Monserrat O, Cuevas-González M, Corominas J, Serral D (2013) Interferometric SAR monitoring of the Vallcebre landslide (Spain) using corner reflectors. *Nat. Hazards Earth Syst. Sci.* 13:923–933
- Crosta GB, Agliardi F (2003a) A methodology for physically based rockfall hazard assessment, *Nat. Hazards Earth Syst. Sci.*, 3, 407-422
- Crosta GB, Agliardi F (2003b) Failure forecast for large rock slides by surface displacement measurements. *Canadian Geotechnical Journal* 40:176–191
- Crosta GB, Agliardi F, Frattini P, Imposimato S (2004) A three-dimensional hybrid numerical model for rockfall simulation, *Geophysical Research Abstracts* 6, n. 04502
- Crosta GB, Chen H, Frattini P (2006) Forecasting hazard scenarios and implications for the evaluation of countermeasure efficiency for large debris avalanches. *Engineering Geology* 83:236– 253
- Crosta GB, Frattini P, Agliardi F (2013) Deep seated gravitational slope deformations in the European Alps. *Tectonophysics* 605:13-33
- Cruden D, Krahn J (1973) A re-examination of the geology of Frank Slide, *Canadian Geotechnical Journal*, 10, 581-591
- Cruden D, Varnes D (1996) *Landslides Types and Processes*. In: Turner A, Schuster R (Eds.) *Landslides, Investigations and Mitigations*, Transportation Research Board, Special Report 247, Washington, DC, 36-75
- Dallaire EE (1974) Electronic distance measuring revolution well under way; *Civil Engineering*, 44, 66-71
- Dash, N. and Gladwin, H. (2007) *Evacuation Decision Making and Behavioral Responses: Individual and Household*, *Natural Hazards, Review*, 8, 69-77
- Del Ventisette C, Casagli N, Fortuny-Guasch J, Tarchi D (2012) Ruinon landslide (Valfurva, Italy) activity in relation to rainfall by means of GBInSAR monitoring. *Landslides* 9:497–509
- Delacourt C, Allemand P, Berthier E, Raucoles D, Casson B, Grandjean P, Pambruns C, Varel E (2007) Remote-sensing techniques for analysing landslide kinematics: a review. *Bull. Soc. géol. Fr.* 178(2):89-100
- Delmonaco G, Leoni G, Margottini C, Puglisi C, Spizzichino D (2003) Large scale debris-flow hazard assessment: a geotechnical approach and GIS modelling, *Nat. Hazards Earth Syst. Sci.*, 3, 443–455
- Derron MH, Jaboyedoff M, Blikra LH (2005) Preliminary assessment of rockslide and rockfall hazards using a DEM (Oppstadhornet, Norway), *Nat. Hazards Earth Syst. Sci.*, 5, 285–292
- Derron MH, Jaboyedoff M, Pedrazzini A, Michoud C, Villemin T (2011) Remote Sensing and Monitoring Techniques for the Characterization of Rock Mass Deformation and Change Detection. In: *Rockfall Engineering*, Lambert S., Nicot F. (Eds.), John Wiley & Sons, New York, ISTE Ltd, London, 2011. ISBN 978-1-84821-256-5. 464 p
- Derron MH, Carrea D, Michoud C, Jaboyedoff M (2015) DInSAR fringes simulation of sandbox models. *Geophysical Research Abstracts*, EGU2015-9332
- Dewez T, Rohmer J, Regard V, Cnudde C (2013) Probabilistic coastal cliff collapse hazard from repeated terrestrial laser surveys: case study from Mesnil Val (Normandy, northern France). *Journal of Coastal Research*, Special Issue No. 65:702-707
- Diederichs MS (1990) *Dips, an interactive and graphical approach to the analysis of orientation based data*. Applied Sciences master thesis in of the University of Toronto, Canada, 145 p
- DiMarzio JP (2007) *GLAS/ICESat 500 m Laser Altimetry Digital Elevation Model of Antarctica*. Boulder, Colorado USA: National Snow and Ice Data Center
- Dirección Nacional de Vialidad (2013) Road traffic statistics available at: http://transito.vialidad.gov.ar:8080/SelCE_WEB/intro.html2013. Accessed 6 November 2013
- Doin MP, Lasserre C, Peltzer G, Cavalié O, Doubre C (2009) Corrections of stratified tropospheric delays in SAR interferometry: Validation with global atmospheric models. *Journal of Applied Geophysics* 69:35–50
- Dorren LKA (2003a) A review of rockfall mechanics and modelling approaches, *Progress in Physical Geography*, 27, 69–87
- Dorren LKA, Seijmonsbergen AC (2003b) Comparison of the three GIS-based models for predicting rockfall runout zones at a regional scale, *Geomorphology*, 56, 49-64
- Dorren LKA, Berger F, le Hir C, Mermin E, Tardif P (2005) Mechanisms, effects and management implications of rockfall in forests, *Forest Ecology and Management*, 215, 183-195
- Dorren LKA (2011) *Rockyfor3D (v4.0) revealed – Transparent description of the complete 3D rockfall model*, ecorisQ paper, 28 pp
- Dunncliff J (1988) *Geotechnical instrumentation for monitoring field performance*. Wiley-Intersciences, 577 p

- Duperret A, Genter A, Mortimores RN, Delacourt B, De Pomerai MR (2002) Coastal Rock Cliff Erosion by Collapse at Puys, France: The Role of Impervious Marl Seams within Chalk of NW Europe. *Journal of Coastal Research* 18:52-61
- Dussauge C, Grasso JR, Helmstetter A (2003) Statistical analysis of rockfall volume distributions: Implications for rockfall dynamics. *Journal of Geophysical Research* 108, 11 p
- Dussauge-Peisser C, Helmstetter A, Grasso JR, Hantz D, Desvarreux P, Jeannin M, Giraud A (2002) Probabilistic approach to rock fall hazard assessment: potential of historical data analysis. *Natural Hazards and Earth System Sciences* 2: 15–26
- Earlie CS, Masselink G, Russell PE, Shail RK (2014) Application of airborne LiDAR to investigate rates of recession in rocky coast environments. *J Coast Conserv* 15 p
- Eberhardt E (2012) Landslide monitoring: the role of investigative monitoring to improve understanding and early warning of failure. *Landslides in the Earth System*. In: *Landslides: Types, Mechanisms and Modeling*, Clague JJ, Stead D (Eds.), Cambridge, 222-234
- Edelsbrunner H, Mücke EP (1994) Three-dimensional alpha shapes. *ACM Trans. Graphics* 13:43-72
- Einstein HH (1988) Special lecture: Landslide risk assessment procedure. *Proceedings of 5th International Symposium on Landslides in Lausanne* 2:1075–1090
- Eisbacher GH, Clague JJ (1984) Destructive mass movements in high mountains : hazard and management. *Geol. Surv. Can. Paper* 84-16, 230 p
- Evans S and Hungr O (1993) The assessment of rockfall hazard at the base of talus slopes, *Can. Geotech. J.*, 30, 620–636, doi:10.1139/t93-054
- Fairfield J, Leymarie P (1991) Drainage Networks from Grid Digital Elevation Models, *Water Resources Research*, 27(5), 709-717
- Fardin N, Feng Q, Stephansson O (2004) Application of a new in situ 3D laser scanner to study the scale effect on the rock joint surface roughness. *International Journal of Rock Mechanics & Mining Sciences* 41, 329–335
- Fauqué L, Cortés JM, Folguera A, Etcheverría M (2000) Avalanchas de roca asociadas a neotectónica en el valle del río Mendoza, al sur de Uspallata. *Revista de la Asociación Geológica Argentina* 55:419- 423
- Fauqué L, Baumann V, Rosas M, González MA, Coppolecchia M, Di Tommaso I, Wilson CGJ (2005) Natural Dams in the Mendoza River Basin, Mendoza Province, Argentina. Argentina. In: Hungr O, Fell R, Couture R, Eberhardt E (eds) *Proceedings of the International Conference on Landslide Risk Management*, Vancouver, Canada. A.A. Balkema Publishers, London, CD
- Federico A, Popescu M, Elia G, Fidelibus C, Internò G, Murianni A (2012) Prediction of time to slope failure: a general framework. *Environmental Earth Sciences* 66(1):245-256
- Fell R, Ho KKS, Lacasse S, Leroi E (2005) A framework for landslide risk assessment and management, in: *Landslide Risk Management*, Hungr, O., Fell, R., Couture, R. and Eberhardt, E. (Eds.), *Proceedings of the International Conference on Landslide Risk Management in Vancouver, Canada*, 31 May – 3 June 2005, 3-25
- Fell R, Corominas J, Bonnard C, Cascini L, Leroi E, Savage WZ, on behalf of the JTC-1 Joint Technical Committee on Landslides and Engineered Slopes (2008) *Guidelines for Landslide Susceptibility, Hazard and Risk Zoning for Land Use Planning*. *Engineering Geology* 102:85-98
- Feng QH, Röschoff K (2004) In-situ mapping and documentation of rock faces using a full-coverage 3-D laser scanning technique. *International Journal of Rock Mechanics & Mining Sciences* 41(3)
- Fernández García F, Polimeni M (2003) Características Climáticas de los valles del Río Aconcagua (Chile) y del Río Mendoza (Argentina). In: Fernández García F, Mikkan R (eds) *Evaluación Global del Medio Geográfico como base de un ordenamiento racional en el principal corredor Bioceánico del Plan Mercosur: Valles del Río Mendoza (Argentina) y Aconcagua (Chile)*. Universidad Nacional de Cuyo-Universidad Autónoma de Madrid. Mendoza, pp 88-92
- Ferretti A, Prati C, Rocca F (2000) Nonlinear Subsidence Rate Estimation Using Permanent Scatterers in Differential SAR Interferometry, *IEEE Transactions on Geoscience and Remote Sensing*, 38(5), 2202-2012
- Ferretti A, Prati C, Rocca F (2001) Permanent Scatterers in SAR Interferometry. *IEEE Transactions on Geoscience and Remote Sensing* 39(1):8-20
- Ferretti A, Monti-Guarnieri A, Prati C, Rocca F, Massonnet D, Lichtenegger J (2007) *InSAR Principles : Guidelines for SAR Interferometry Processing and Interpretation*. ESA Publications, 234p
- Ferretti A, Fumagalli A, Novali F, Prati C, Rocca F, Rucci A (2011) A New Algorithm for Processing Interferometric Data-Stacks: SqueeSAR. *IEEE Transactions on Geoscience and Remote Sensing* 49(9):3460 – 3470
- Folguera A, Etcheverría M, Pazos PJ, Giambiagi L, Fauqué L, Cortés JM, Rodríguez MF, Irigoyen MV, Fusari C (2003) *Hoja Geológica* 3369-15, Potrerillos, Provincia de Mendoza, 1:100 000. Instituto de Geología y Recursos Minerales, Servicio Geológico Minero Argentino, Buenos Aires

- Fornaro G, Pauciuolo A, Serafino F (2009) Deformation monitoring over large areas with multipass differential SAR interferometry: a new approach based on the use of spatial differences. *International Journal of Remote Sensing* 30(6):1455-1478
- Francis P, Rothery D (2000) Remote Sensing of Active Volcanoes, *Annual Review of Earth Planetary Sciences*, 28, 81–106
- Frattini P, Crosta G, Carrara A, Agliardi F (2008) Assessment of rockfall susceptibility by integrating statistical and physically-based approaches, *Geomorphology*, 94, 419-437
- Friedman JH, Bentely J, Finkel RA (1977) An Algorithm for Finding Best Matches in Logarithmic Expected Time. *ACM Transactions on Mathematical Software* 3:209-226
- Froese C, Moreno, F (2011) Structure and components for the emergency response and warning system on Turtle Mountain, Alberta, Canada, *Natural Hazards*, DOI 10.1007/s11069-011-9714-y
- Froese C (2013) Lessons Learned from 10 Years of Early Warning at Turtle Mountain, Alberta, Canada, in: *Proceedings of the 1st International Workshop on Warning Criteria for Active Slides*, Courmayeur, Italy, 10-12 June 2013, 48-49, available at: <http://www2.ggl.ulaval.ca/iwwcas/>
- Fruneau B, Apache J (1996) Observation and modelling of the Saint-Etienne-de-Tinée landslide using SAR interferometry. *Tectonophysics* 265:181-190
- Fu W, Guo H, Tian Q, Guo X (2010) Landslide monitoring by corner reflectors differential interferometry SAR. *International Journal of Remote Sensing* 31(24):6387–6400
- Fukuzono T (1990) Recent Studies on Time Prediction of Slope Failure. *Landslide news* 4:9-12
- Gabriel AK, Goldstein RM, Zebker HA (1989) Mapping Small Elevation Changes Over Large Areas: Differential Radar Interferometry. *Journal of Geophysical Research* 94:9183-9191
- Gamma P (2000) Dfwalk - Ein Murgang-Simulationsprogramm zur Gefahrenzonierung, Geographisches Institut der Universität Bern, Switzerland, 158 pp
- Gansser A (1973) Facts and theories on the Andes. *Journal of the Geological Society* 129:93-131
- García-Davalillo J, Herrera G, Notti D, Strozzi T, Álvarez-Fernández I (2014) DInSAR analysis of ALOS PALSAR images for the assessment of very slow landslides: the Tena Valley case study. *Landslides* 11:225–246
- Geertsema M, Highland L, Vaugeouis L (2009) Environmental Impact of Landslides. In: *Landslides – Disaster Risk Reduction*, Sassa K, Canuti P (eds.), Springer-Verlag Berlin Heidelberg, 589-608
- Giambiagi L, Martinez AN (2008) Permo-Triassic oblique extension in the Potrerillos-Uspallata area, western Argentina. *Journal of South American Earth Sciences* 26:252-260
- Giambiagi L, Mescua J, Bechis F, Martinez A, Folguera A, (2011) Pre-Andean deformation of the Precordillera southern sector, southern Central. *Geosphere* 7:219-239
- Gigli G, Casagli N (2011) Semi-automatic extraction of rock mass structural data from high resolution LIDAR point clouds; *International Journal of Rock Mechanics & Mining Sciences*, 48:187–198.
- Gilbert GK (1877) *Geology of the Henry Mountains*, US Geological and Geographical Survey of the Rocky Mountain Region, Government Printing Office, Washington, DC
- Gili J, Corominas J, Rius J (2000) Using Global Positioning System techniques in landslide monitoring. *Engineering Geology* 55:167–192
- Glennie C, Brooks B, Ericksen T, Hauser D, Hudnut K, Foster J, Avery J (2013) Compact Multipurpose Mobile Laser Scanning System – Initial Tests and Results. *Remote Sensing* 5:521-538
- Gokceoglu C, Sonmez H, Ercanoglu M (2000) Discontinuity controlled probabilistic slope failure risk maps of the Altindag (settlement) region in Turkey, *Engineering Geology*, 55, 277–296
- Goldstein RM, Engelhardt H, Kamb B, Frolich RM (1993) Satellite Radar Interferometry for Monitoring Ice Sheet Motion: Application to an Antarctic Ice Stream. *Science* Vol. 262 no. 5139. pp 1525-1530
- Golts S, Rosenthal E (1993) A morphotectonic map of the northern Arava in Israel, derived from isobase lines. *Geomorphology* 7: 305-315
- Gordon S, Lichti D, Stewart M (2001) Application of a High-Resolution, Ground-Based Laser Scanner for Deformation Measurements. In: *Proceedings of the 10th International Symposium on Deformation Measurements*, 19-22 March 2001; Orange USA, 23-32
- Gordon S, Lichti D (2007) Modeling Terrestrial Laser Scanner Data for Precise Structural Deformation Measurement. *J. Surv. Eng.* 133:72-80
- Günther A (2003) SLOPEMAP: programs for automated mapping of geometrical and kinematical properties of hard rock hill slopes, *Computers and Geosciences*, 29, 865-875
- Günther A, Cartensen A, Pohl W (2004) Automated sliding susceptibility mapping of rock slopes, *Nat. Hazards Earth Syst. Sci.*, 4, 95-102

- Guthries RH, Evans SG (2004) Analysis of Landslide Frequencies and Characteristics in a Natural System, Coastal British Columbia. *Earth Surface Processes and Landforms* 29:1321-1339
- Guzzetti F, Malamud BD, Turcotte DL, Reichenbach P (2002) Power-law correlations of landslide areas in central Italy. *Earth and Planetary Science Letters* 195:169-183
- Guzzetti F, Reichenbach P, Wieczorek GF (2003) Rockfall hazard and risk assessment in the Yosemite Valley, California, USA, *Nat. Hazards Earth Syst. Sci.*, 3, 491-503, 2003.
- Guzzetti F, Mondini AC, Cardinali M, Fiorucci F, Santangelo M, Chang KT (2012) Landslide inventory maps: New tools for an old problem. *Earth-Science Reviews* 112:42–66.
- Haala N, Brenner C (1999) Extraction of buildings and trees in urban environments. *ISPRS Journal of Photogrammetry & Remote Sensing* 54, 130-137.
- Haneberg WC, Cole WF, Kasali G (2009) High-resolution LiDAR-based landslide hazard mapping and modeling, UCSF Parnassus Campus, San Francisco, USA. *Bull Eng Geol Environ* 68, 263–276.
- Hanssen RF (2001) *Radar Interferometry: Data Interpretation and Error Analysis*. Kluwer Academic Publishers, Dordrecht, The Netherlands, 308 p
- Hecht J (1994) *Understanding Lasers: An Entry Level Guide*, 2nd Ed.; IEEE Press: New York, USA
- Heim A (1882) Der Bergsturz von Elm, *Deutsche Geologische Gesellschaft*, 34: 74-115
- Heim A (1932) Bergsturz und Menschenleben. *Beiblatt zur Vierteljahrschrift der Naturforschenden Gesellschaft*. Zürich 77, 218 p
- Heinimann HR (1998) *Methoden zur Analyse und Bewertung von Naturgefahren*, Bundesamt für Umwelt, Wald und Landschaft (BUWAL), 85, 247 pp., (in German)
- Henderson IHC, Lauknes TR, Osmundsen PT, Dehls J, Larsen Y, Redfield TF (2011). A structural, geomorphological and InSAR study of an active rock slope failure development. In: Jaboyedoff (ed) *Slope Tectonics*, Geological Society, London, 351:185-189
- Hermanns RL, Fauqué L, Wilson CGL (2014) ³⁶Cl terrestrial cosmogenic nuclide dating suggests Late Pleistocene to Early Holocene mass movements on the south face of Aconcagua mountain and in the Las Cuevas-Horcones valleys, Central Andes, Argentina. In: Sepúlveda, Giambiagi, Moreiras, Pinto, Tunik, Hoke, Farías (eds) *Geodynamic Processes in the Andes of Central Chile and Argentina*, Geological Society, London, 24 p.
- Herrera G, Fernández-Merodo JA, Mulas J, Pastor M, Luzi G, Monserrat O (2009) A landslide forecasting model using ground based SAR data: The Portalet case study. *Engineering Geology* 105:220–230
- Herrera G, Tomás R, Vicente F, Lopez-Sanchez JM, Mallorquí JJ, Mulas J (2010) Mapping ground movements in open pit mining area as using differential SAR interferometry, *International Journal of Rock Mechanics & Mining Sciences*, 47, 1114–1125.
- Herrera G, Notti D, García-Davalillo JC, Mora O, Cooksley G, Sánchez M, Arnaud A, Crosetto M (2011) Analysis with C- and X-band satellite SAR data of the Portalet landslide area. *Landslides* 8:195–206
- Herrera G, Gutiérrez F, García-Davalillo JC, Guerrero J, Notti D, Galve JP, Fernández-Merodo JA, Cooksley G (2013) Multi-sensor advanced DInSAR monitoring of very slow landslides: The Tena Valley case study (Central Spanish Pyrenees). *Remote Sensing of Environment* 128:31–43.
- Hoek E, Bray JW (1981) *Rock Slope Engineering*, 3rd edition, Institution of Mining and Metallurgy, London
- Hoek E, Marinos P, Benissi M (1998) Applicability of the Geological Strength Index (GSI) classification for very weak and sheared rock masses. The case of the Athens Schist Formation, *Bull. Engng Geol. Env.*, 57 (2), 151-160
- Hoge FE, Swift RN, Frederick EB (1980) Water depth measurement using an airborne pulsed neon laser system; *Applied Optics*, 19, 871-883
- Höhle J, Höhle M (2009) Accuracy assessment of digital elevation models by means of robust statistical methods. *ISPRS Journal of Photogrammetry and Remote Sensing* 64:398-406
- Holmgren P (1994) Multiple flow direction algorithms for runoff modeling in grid based elevation models: an empirical evaluation, *Hydrological Processes*, 8, 327-334
- Holtz RD, Schuster RL (1996) Stabilization of soil slopes, in: *Landslides, Investigations and Mitigations*, Transportation Research Board, Special Report 247, Turner, A., Schuster, R. (Eds.), Washington, DC, 439-473
- Hong Kong Slope Safety (2012) <http://hkss.cedd.gov.hk/hkss/eng/index.aspx>, last access: 19 November 2012
- Horn R, Nottensteiner A, Reigber A, Fischer J, Scheiber R (2009) F-SAR — DLR's new multifrequency polarimetric airborne SAR. In: *Geoscience and Remote Sensing Symposium, IGARSS 2009* 2:II.902-II.905
- Horton P, Jaboyedoff M, Rudaz B, Zimmermann M (2013) Flow-R, a model for susceptibility mapping of debris flows and other gravitational hazards at a regional scale. *Nat. Hazards Earth Syst. Sci.*, 13, 869–885

- Horton P, Jaboyedoff M, Bardou E (2008) Debris flow susceptibility at a regional scale, 4th Canadian Conference on Geohazards, Université Laval, Quebec, Canada, 20-24 May 2008, 8 pp
- Hovius N, Stark CP, Hao-Tsu C, Jiun-Chuan L (2000) Supply and removal of sediment in a landslide-dominated mountain belt: Central Range, Taiwan. *Journal of Geology* 108:73–89
- Hungr O, Evans SG, Hazzard J (1999) Magnitude and frequency of rock falls and rock slides along the main transportation corridors of southwestern British Columbia, Can. Geotech. J., 36, 227-238
- Hungr O, McDougall S (2009) Two numerical models for landslide dynamic analysis. *Computers & Geosciences* 35:978–992
- Hungr O, Leroueil S, Picarelli L (2014) The Varnes classification of landslide types, an update. *Landslides* 11:167–194
- Hunter G, Pinkerton H, Airey R, Calvari S (2003) The application of a long-range laser scanner for monitoring volcanic activity on Mount Etna. *Journal of Volcanology and Geothermal Research* 123:203-210
- Hutchinson JN (1988) General report: morphological and geotechnical parameters of landslides in relation to geology and hydrogeology. In: *Proceedings of the 5th International Symposium on Landslides, Lausanne*, 1:3–35
- Hutchinson JN (1955). Keynote paper: Landslide hazard assessment. *Landslides*, Bell DH (ed), 1805–1841
- Intrieri E, Gigli G, Casagli N, Nadim F (2013) Brief communication: Landslide Early Warning System: toolbox and general concepts, *Natural Hazards and Earth System Sciences*, 13, 85-90
- Iovine G, D’Ambrosio D, Di Gregorio S (2005) Applying genetic algorithms for calibrating a hexagonal cellular automata model for the simulation of debris flows characterised by strong inertial effects, *Geomorphology*, 66, 287–303
- Irish JL, Lillycrop WJ (1999) Scanning laser mapping of the coastal zone: the SHOALS system. *ISPRS Journal of Photogrammetry & Remote Sensing* 54:123–129
- Iverson RM, Schilling SP, Vallance JW (1998) Objective delineation of lahar-inundation hazard zones, *Geol. Soc. Am. Bull.*, 110, 972–984
- Jaakkola A, Hyypä J, Hyypä H, Kukko A (2008) Retrieval Algorithms for Road Surface Modelling Using Laser-Based Mobile Mapping. *Sensors* 8:5238-5249
- Jaboyedoff M, Baillifard F, Couture R, Locat J, Locat P (2004) Toward preliminary hazard assessment using DEM topographic analysis and simple mechanical modeling by means of sloping local base level. In: *Landslides: Evaluation and Stabilization*. Lacerda, Ehrlich, Fontoura, Sayao (eds.). Taylor & Francis Group, London, 199-204
- Jaboyedoff M, Penna I, Pedrazzini A, Baroň I, Crosta GB (2013) An introductory review on gravitational-deformation induced structures, fabrics and modelling. *Tectonophysics* 605:1–12
- Jaboyedoff M, Derron MH (2015) Methods to Estimate the Surfaces Geometry and Uncertainty of Landslide Failure Surface. In: *Engineering Geology for Society and Territory. Proceedings of the IAEG XII Congress*. Lollino G et al. (eds.), Torino, Italy, 15-19 September 2014, 2:339-343
- Jaboyedoff M, Baillifard FJ, Marro C, Philippossian F, Rouiller JD (1999) Detection of rock instabilities: Matterock Methodology, Joint Japan-Swiss Scientific on Impact Load by Rock Falls and Design of Protection Structures, Kanazawa, Japan, 4-7 October 1999, 37-43
- Jaboyedoff M, Labiouse V (2003) Preliminary assessment of rockfall hazard based on GIS data, in: *Proceedings of the 10th International Congress on Rock Mechanics ISRM 2003 – Technology roadmap for rock mechanics*, South African Institute of Mining and Metallurgy, Johannesburg, South Africa, 8-12 September 2003, 575-778
- Jaboyedoff M, Derron MH (2005a) Integrated risk assessment process for landslides, in: *Landslide risk management*, edited by Hungr, O., Fell, R., Couture, R. and Eberhardt, E., p. 776, Taylor and Francis
- Jaboyedoff M, Dudt JP, Labiouse V (2005b) An attempt to refine rockfall hazard zoning based on the kinetic energy, frequency and fragmentation degree, *Nat. Hazards Earth Syst. Sci.*, 5, 621-632
- Jaboyedoff M (2006) Rapport de visite de terrain du 9 septembre 2006 dans le versant au dessus du lieu dit Pont Bourquin (Les Diablerets). Rapport publié sur www.quanterra.org. 8 pages
- Jaboyedoff M, Metzger R, Oppikofer T et al. (2007) New insight techniques to analyze rock-slope relief using DEM and 3D-imaging cloud points: COLTOP-3D software. In *Rock mechanics: Meeting Society’s Challenges and Demands*, Proceedings of the 1st Canada-US Rock Mechanics Symposium, Vancouver, Canada, May 27–31 2007; 61-68
- Jaboyedoff M, Demers D, Locat J, Locat A, Locat P, Oppikofer T, Robitaille D, Turmel D (2009a) Use of Terrestrial Laser Scanning for the characterization of retrogressive landslides in sensitive clay and rotational landslides in river banks. *Canadian Geotechnical Journal* 46:1379-1390
- Jaboyedoff M, Pedrazzini A, Loye A, Oppikofer T, Güell i Pons M, Locat J (2009b) Earth Flow in a complex geological environment : the example of Pont Bourquin, Les Diablerets (Western Switzerland). In : *Landslide Processes : from Geomorphologic Mapping to Dynamic Modelling*. Edited by Malet J.-P., Remaître A. and Boga
- Jaboyedoff M, Couture R, Locat J (2009c) Structural analysis of Turtle Mountain (Alberta) using digital elevation model: Toward a progressive failure. *Geomorphology* 103:5–16

- Jaboyedoff M, Labiouse V (2011a) Technical Note: Preliminary estimation of rockfall runout zones, *Nat. Hazards Earth Syst. Sci.*, 11, 819–828
- Jaboyedoff M, Oppikofer T, Derron MH, Blikra LH, Böhme M., Saintot A (2011b) Complex landslide behaviour and structural control: a three-dimensional conceptual model of Åknes rockslide, Norway, in: *Slope Tectonics, Special Publication 351*, Jaboyedoff, M. (Ed.), Geological Society of London, 147-161
- Jaboyedoff M, Oppikofer T, Abellán A, Derron MH, Loye A, Metzger R, Pedrazzini A (2012a) Use of LIDAR in landslide investigations: a review. *Natural Hazard* 61:5-28
- Jaboyedoff M, Choffet M, Derron MH, Horton P, Loye A, Longchamp C, Mazotti B, Michoud C, Pedrazzini A (2012b) Preliminary slope mass movements susceptibility mapping using DEM and LiDAR DEM. In: Pradhan, Buchroithner (eds) *Terrigenous Mass Movements*, Springer-Verlag, Berlin Heidelberg, pp 109-169.
- Jaboyedoff M, Derron MH, Pedrazzini A, Blikra LH, Crosta GB, Froese CR, Hermanns RH, Oppikofer T, Böhme M, Stead D (2012c) Fast assessment of susceptibility of massive rock instabilities. In: *Proceeding of the 11th ISL, Landslides and Engineered Slopes: Protecting Society through Improved Understanding*. Eberhardt et al. (Eds), Banff, Canada, 2-8 June 2012, 459-465
- Jaboyedoff M, Derron MH (2015) Methods to Estimate the Surfaces Geometry and Uncertainty of Landslide Failure Surface. In: Lollino G et al. (Eds.) *Engineering Geology for Society and Territory. Proceedings of the IAEG XII Congress*, Torino, Italy, 15-19 September 2014, 2:339-343.
- Jaboyedoff M, Abellán A, Carrea D, Derron MH, Matasci B, Michoud C (2016) LiDAR use for Mapping and Monitoring of Landslides. In: *Encyclopedia of Natural Hazards*, Taylor and Francis, 39 p.
- Jaedicke C et al., Eds. (2010) SafeLand deliverable 2.10: Identification of landslide hazard and risk “hotspots” in Europe, European Project SafeLand, Grant Agreement No. 226479, 132 p., available at: <http://www.safeland-fp7.eu>
- Jakob M, Holm K (2012) Risk assessments for debris flows. In: *Landslides: Types, Mechanisms and Modeling*, Clague JJ, Stead D (Eds.), Cambridge, 71–82
- Jakob M, Owen T, Simpson T (2012) A regional real-time debris-flow warning system for the District of North Vancouver, Canada, *Landslides*, 9, 165-178
- Jarvis A, Reuter HI, Nelson A, Guevara E (2008) Hole-filled seamless SRTM data V4. International Centre for Tropical Agriculture. <http://srtm.csi.cgiar.org>. Accessed 31 March 2014.
- Jenson SK, Domingue JO (1988) Extracting topographic structure from digital elevation data for geographic information system analysis, *Photogramm. Eng. Remote Sens.*, 54 (11), 1593–1600
- Jongmans D, Garambois S (2007) Geophysical investigations of landslides. A review, *Bulletin de la Société Géologique de France*, 178, 101-112
- Kaldhol H, Kolderup NH (1936) Skredet i Tafjord 7. April 1934, *Bergens Museums Årbok 1936 Naturvitenskapelig Rekke*, 11, 1– 15
- Kappes MS, Malet JP, Rémaitre A, Horton P, Jaboyedoff M, Bell R (2011) Assessment of debris-flow susceptibility at medium-scale in the Barcelonnette Basin, France, *Nat. Hazards Earth Syst. Sci.*, 11, 627–641
- Keefer DK, Wilson RC, Mark RK, Brabb EE, Brown WM, Ellen SD, Harp EL, Wieczorek GF, Alger CS, Zarkin RS (1987) Real time landslide warning system during heavy rainfall, *Science*, 238, 921–925
- Keefer DK (1984) Landslides caused by earthquakes. *Geological Society of America Bulletin* 95:406-421
- Kendrick EC, Bevis M, Smalley Jr RF, Cifuentes O, Galban F (1999) Current rates of convergence across the Central Andes: estimates from continuous GPS observations. *Geophysical Research Letters* 26(5):541-544
- Kimura H, Yamaguchi Y (2000) Detection of Landslide Areas Using Satellite Radar Interferometry. *Photogrammetric Engineering & Remote Sensing* 66(3): 337-344
- Kjekstad O, Highland L (2009) Economic and Social Impact of Landslides. In: *Landslides – Disaster Risk Reduction*, Sassa K, Canuti P (eds.), Springer-Verlag Berlin Heidelberg, 573-588
- Korup O (2002) Recent research on landslide dams – a literature review with special attention to New Zealand, *Progress in Physical Geography*, 26, 206-235
- Korup O (2012) Landslides in the Earth System. In: *Landslides: Types, Mechanisms and Modeling*, Clague JJ, Stead D (Eds.), Cambridge, 323–335
- Kovári K (1988) General report: methods of monitoring landslides. In: *Proceedings of the 5th International Symposium on Landslides*, Lausanne, 3:1421-1433
- Kozłowski EE, Mancado R, Ramos VA (1993) Geología y Recursos Naturales de Mendoza. In: *Proceedings of the 12th Servicio Geológico Argentino Conference and 2nd Congreso de Exploración de Hidrocarburos*, 1(18):235-256
- Krabill WB, Collins JG, Link LE, Swift RN, Butler ML (1984) Airborne laser topographic mapping results; *Photogramm Eng Remote Sens*, 50, 685-694

- Krabill WB, Thomas RH, Martin CF, Swift RN, Frederick EB (1995) Accuracy of airborne laser altimetry over Greenland ice sheet; *Int J Remote Sens*, 16, 1211-1222
- Krabill WB, Frederick EB, Manizade S, Martin CF, Sonntag J, Swift RN, Thomas R, Wright W, Yungel J (1999) Rapid Thinning of Parts of the Southern Greenland Ice Sheet; *Science*, 283, 1522-1524
- Kreyszig E (2006) *Advanced Engineering Mathematics*, 9th edition, John Wiley and Sons (Ed.), 1248 pp
- Kromer RA, Abellán A, Hutchinson DJ, Lato MJ, Edwards T, Jaboyedoff M (2015) A 4D Filtering and Calibration Technique for Small-Scale Point Cloud Change Detection with a Terrestrial Laser Scanner. *Remote Sensing* 7:13029-13052
- Kukko A, Kaartinen H, Hyypä J, Chen Y (2012) Multiplatform Mobile Laser Scanning: Usability and Performance. *Sensors* 12:11712-11733
- Kurz TH, Buckley SJ, Howell JA et al. (2008) Geological outcrop modeling and interpretation using ground based hyperspectral and laser scanning data fusion. In *WG VIII/12: Geological Mapping, Geomorphology and Geomorphometry, Proceedings of the International Society for Photogrammetry and Remote Sensing Conference, Beijing, China, July 3-11 2008*; 1229-1234
- Kurz TH, Buckley SJ, Howell JA (2011) Integration of Panoramic Hyperspectral Imaging with Terrestrial LiDAR data. *The Photogrammetric Record* 26(134): 212–228
- L'Heureux JS, Glimsdal S, Longva O, Hansen L, Harbitz CB (2011) The 1888 shoreline landslide and tsunami in Trondheimsfjorden, central Norway, *Mar. Geophys. Res.*, 32, 313–329
- Lacasse S, Nadim F (2009) Landslide Risk Assessment and Mitigation Strategy, in: *Landslides – Disaster Risk Reduction*, Sassa, K. and Canuti, P. (Eds.), Springer-Verlag Berlin Heidelberg, 31-61
- Lambert S, Bourrier F (2013) Design of rockfall protection embankments: a review. *Engineering Geology* 154:77-88
- Lanari R, Lundgren P, Sansoti E (1998) Dynamic deformation of Etna volcano observed by satellite radar interferometry, *Geophysical Research Letters*, 25, 1541–1544
- Lapointe F, Baulne J, Bélanger L, Breton A, Camirand J, Chevalier R, Cloutier R, Godbout M, Lepage H, Thibault MT, Vecerina C, Bilodeau D, des Groseilliers L, Haché M (2010) Gestion de la qualité – Document de principes sur la qualité dans les enquêtes, Public report (in french), Institut sur la statistique du Québec, Québec, Canada, 65 pp
- Larsen Y, Eigen G, Lauknes TR, Malnes E, Høgda KA (2005) A generic differential interferometric SAR processing system, with applications to land subsidence and snowwater equivalent retrieval. In: *Proceedings of the Fringe 2005 Workshop, Frascati, Italy, 28 November – 2 December 2005*, 6 p.
- Lateltin O (1997) *Recommandations 1997: Prise en compte des dangers dus aux mouvements de terrain dans le cadre des activités de l'aménagement du territoire*. Office fédéral de l'aménagement du territoire. OFAT, 42 p
- Lato M, Diederichs MS, Hutchinson DJ et al. (2009) Optimization of LiDAR scanning and processing for automated structural evaluation of discontinuities in rock masses. *International Journal of Rock Mechanics & Mining Sciences* 46, 194–199.
- Lauknes TR, Piyush Shanker A, Dehls JF, Zebker HA, Henderson IHC, Yarsen Y (2010) Detailed rockslide mapping in northern Norway with small baseline and persistent scatterer interferometric SAR time series methods. *Remote Sensing of Environment* 114:2097–2109.
- Lauknes TR (2011) InSAR Tropospheric Stratification Delays: Correction Using a Small Baseline Approach. *IEEE Geoscience and Remote Sensing Letters* 8(6):1070-1074.
- Leroi E (1996) Landslides hazard – risk maps at different scales: objectives, tools and developments, in: *Proceedings of the 7th Int. Symp. on Landslides, Trondheim, Norway, 1, 35–51*
- Leroueil S, Locat J, Vaunat J, Picarelli L, Lee H, Faure R (1996) Geotechnical characterization of slope movements, *Landslides, Senneset* (ed.), 53-73
- Leroueil S (2001) Natural slopes and cuts: movement and failure mechanisms. *Géotechnique* 51(3):197-243
- Letortu P, Costa S, Cantat O (2012) Les submersions marines en Manche Orientale: approche inductive et naturaliste pour la caractérisation des facteurs responsables des inondations par la mer. *Climatologie* 9 :31-57
- Letortu P (2013) Le recul des falaises crayeuses haut-normandes et les inondations par la mer en Manche centrale et orientale: de la quantification de l'aléa à la caractérisation des risques induits. PhD thesis of the University of Caen Basse-Normandie 414 p.
- Letortu P, Costa S, Bensaid A, Cador JM, Quénot H (2014) Vitesses et rythmes de recul des falaises crayeuses de Haute-Normandie (France). *Géomorphologie, relief, processus et environnement* 2:133-144
- Lichti D, Gordon S, Stewart M (2002) Ground-based Laser Scanners: Operation, Systems and Applications. *Geomatica* 56:21–33
- Lichti D, Gordon S, Tipdecho T (2005) Error Models and Propagation in Directly Georeferenced Terrestrial Laser Scanner Networks. *Journal of Surveying Engineering* 131:135-142
- Lillesand TM, Kiefer RW, Chipman JW (2008) *Remote Sensing and Image Interpretation*, 6th edn. John Wiley & Sons, 756 p.

- Lim M, Petley DN, Rosser NJ, Allison RJ, Long AJ, Pybus D (2005) Combined digital photogrammetry and time-of-flight laser scanning for monitoring cliff evolution. *Photogrammetric Record* 20:109–129
- Locat J, Leroueil S, Picarelli L (2000) Some considerations on the role of geological history on slope stability and estimation of minimum apparent cohesion of a rock mass, in: *Landslides in research, theory and practice*, Bromhead, E., Dixon, N. and Ibsen, M.L. (Eds.), The 8th International Symposium on Landslides in Cardiff, Wales, 26-30 June 2000, 935-942
- Locat P, Couture R, Leroueil S, Locat J, Jaboyedoff M (2006) Fragmentation energy in rock avalanches. *Can. Geotech. J.* 43:830-851
- López F, Rodríguez A, Dölling OR (2011) *Inventario de Presas y Centrales Hdroeléctricas de la República Argentina*. Ministerio de la Planificación Federal, Inversión pública y Servicios, Buenos Aires, 224 p.
- Lovisolò M, Ghirotto S, Scardia G, Battaglio M (2003) The use of Differential Monitoring Stability (D.M.S.) for remote monitoring of excavation and landslide movements, in: *Proceedings of the Sixth International Symposium on Field Measurements in Geomechanics*, Myrvol, A. (Ed.), Oslo, Balkema, 519-524
- Löw S (1997) Wie sicher sind geologische Prognosen? *Bulletin für Angewandte Geologie* 2(2):83–97
- Loye A, Jaboyedoff M, Pedrazzini A (2009) Identification of potential rockfall source areas at a regional scale using a DEM-based geomorphometric analysis, *Nat. Hazards Earth Syst. Sci.*, 9, 1643-1653
- Lu Z, Mann D, Freymueller J (1998) Satellite radar interferometry measures deformation at Okmok volcano, *EOS Transactions, American Geophysical Union*, 79(39),461–468
- Luzi G (2010) Ground based SAR interferometry: a novel tool for Geoscience. In: *Geoscience and Remote Sensing, New Achievements*. Imperatore P, Riccio D (Eds), ISBN: 978-953-7619-97-8, 26 p
- Mainsant G, Larose E, Brönnimann C, Jongmans D, Michoud C, Jaboyedoff M (2012a) Ambient seismic noise monitoring of a clay landslide: Toward failure prediction, *Journal of Geophysical Research*, 117, 12 pp
- Mainsant G, Jongmans D, Chambon G, Larose E, Baillet L (2012b) Shear-wave velocity as an indicator for rheological changes in clay materials: Lessons from laboratory experiments, *Geophysical Research Letters*, 39, 5 pp
- Malenovský Z, Rott H, Cihlar J, Schaepman ME, García-Santos G, Fernandes R, Berger M (2012) Sentinels for science: Potential of Sentinel-1, -2 and -3 missions for scientific observations of ocena, cryosphere, and land. *Remote Sensing of Environment* 120:91-101
- Mangeny A, Bouchut F, Thomas N, Vilotte JP, Bristeau MO (2007) Numerical modeling of self-channeling granular flows and of their levee-channel deposits. *Journal of Geophysical Research* 112: F02017
- Massonnet D (1985) *Etude de Principe d'une Détection de Mouvements Tectoniques par Radar*. Internal memo No. 326, Centre National d'Etude Spatial (CNES), Toulouse, France.
- Massonnet D, Rossi M, Carmona C, Adragna F, Peltzer G, Feigl K, Rabaute T (1993) The displacement field of the Landers earthquake mapped by radar interferometry. *Nature* 364:138-142
- Massonnet D, Briole P, Arnaud A (1995) Deflation of Mount Etna monitored by spaceborne radar interferometry. *Nature* 375:567–570
- Massonnet D, Thatcher W, Vadon H (1996) Detection of postseismic fault zone collapse following the Landers earthquake, *Nature*, 382, 612-616
- Massonnet D, Feigl KL (1998) Radar interferometry and its applications to changes in the Earth's surface. *Review of Geophysics* 36:441-500
- Matasci B, Guerin A, Putman R, Stock GM, Jaboyedoff M, Glazner AF (2014) Three dimensional geological mapping of the vertical rock face of El Capitan, Yosemite (California, USA), with field work, gigapixel photography, and terrestrial laser scanning. In: *Vertical Geology, from remote sensing to 3D geological modelling*. Proceedings of the 1st Vertical Geology Conference. Humair F, Matasci et al. (eds.) 5-7 February 2014, Lausanne, Switzerland, 155-159.
- Matasci B, Jaboyedoff M, Loye A., Pedrazzini A, Derron MH, Pedrozzi G (2015) Impacts of fracturing patterns on the rockfall susceptibility and erosion rate of stratified limestone. *Geomorphology* 241:83-97
- Mazzanti P, Bozzano F, Cipriani I, Prestininzi A (2015) New insights into the temporal prediction of landslides by a terrestrial SAR interferometry monitoring case study. *Landslides* 12:55–68
- McConnell RG, Brock RW (1904) Report on the great landslide at Frank, Alberta, Canada. Canadian Department of Interior, Annual Report, 1902-1903, Part 8
- McKean J, Roering J (2004) Objective landslide detection and surface morphology mapping using high-resolution airborne laser altimetry. *Geomorphology* 57:331–351.
- Mercogliano P, Segoni S, Rossi G, Sikorsky B, Tofani V, Schiano P, Catani F, Casagli N (2013) Brief communication "A prototype forecasting chain for rainfall induced shallow landslides", *Nat. Hazards Earth Syst. Sci.*, 13, 771–777
- Meyer NK, Dyrddal AV, Frauenfelder R, Etzlermüller B, Nadim F (2012) Hydrometeorological threshold conditions for debris flow initiation in Norway, *Nat. Hazards Earth Syst. Sci.*, 12, 3059–3073

- Michoud C, Mazotti B, Choffet M, Dubois J, Breguet A, Métraux V, Jaboyedoff M (2010a) Advanced Susceptibility Mapping for Natural Hazards at a Local Scale – The Case of the Swiss Alpine Valley of Bagnes, EGU General Assembly, Vienna, Austria, 3-7 May 2010, EGU2010-4606
- Michoud C, Longchamp C, Derron MH, Jaboyedoff M, Blikra LH, Kristensen L, Oppikofer T (2010b) The terrestrial and offshore laser scanning acquisitions of September 2010 in Sunndalsøra (Møre og Romsdal, Norway) - Techniques, processing and data. Internal technical report University of Lausanne, 10 p.
- Michoud C, Jaboyedoff M, Derron MH, Nadim F, Leroi E (2011a) Classification of landslide-inducing anthropogenic activities. 5th Canadian Conference on Geotechnique and Natural Hazards, Kelowna, Canada, 10 p
- Michoud C, Metzger R, Fragnol B, Longchamp C, Derron MH, Jaboyedoff M, Blikra LH, Kristensen L, Oppikofer T (2011b) Coastal rockfall hazard assessment: Offshore Laser Scanning and structural analysis with Coltop3D in Sunndalsøra, Norway. Innovative LiDAR Solutions Conferences, Toronto, Canada
- Michoud C, Abellán A, Derron MH and Jaboyedoff M, Eds. (2012a) SafeLand deliverable 4.1.: Review of Techniques for Landslide Detection, Fast Characterization, Rapid Mapping and Long-Term Monitoring, 2nd Edition, European Project SafeLand, Grant Agreement No. 226479, 401 pp., available at: <http://www.safeland-fp7.eu>
- Michoud C, Derron MH, Horton P, Jaboyedoff M, Baillifard FJ, Loye A, Nicolet P, Pedrazzini A and Queyrel A: Rockfall hazard and risk assessments along roads at a regional scale: example in Swiss Alps. *Natural Hazards and Earth System Sciences*, 12, 615-629, 2012b.
- Michoud C, Nicolet P, Jaboyedoff M, Larose E, Mainsant G, Jongmans D, Brönnimann C (2012c) Glissement de Pont Bourquin - Rapport de synthèse des travaux menés par l'IGAR et ses partenaires de 2006 à 2012, 125 p
- Michoud C, Bazin S, Blikra LH, Derron MH, Jaboyedoff M (2013a) Experiences from site-specific landslide early warning systems. *Natural Hazards Earth System Sciences* 13:2659–2673
- Michoud C, Derron MH, Jaboyedoff M (2013b) Surveillance du glissement rocheux de la Barmasse - Suivi des déplacements mesurés entre 2007 et 2012 par LiDAR terrestre, GPS différentiel et RaDAR terrestre, 40 p
- Michoud C, Derron MH, Jaboyedoff M, Abellán A, Bazin S, Blikra LH (2013c) On the importance of landslide conceptual models by integrating and coupling different sources of data to set pertinent thresholds and proper EWS, in: *Proceedings of the 1st International Workshop on Warning Criteria for Active Slides*, Courmayeur, Italy, 10-12 June 2013, 19-20, available at: <http://www2.ggl.ulaval.ca/iwwcas/>
- Michoud C, Carrea D, Costa S, Derron MH, Jaboyedoff M, Delacourt C, Maquaire O, Letortu P, Davidson R (2015) Landslide detection and monitoring capability of boat-based mobile laser scanning along Dieppe coastal cliffs, Normandy. *Landslides* 12:403–418
- Michoud C, Baumann V, Lauknes TR, Penna I, Derron MH, Jaboyedoff M (in press) Large Slope Deformations Detection and Monitoring along Shores of the Potrerillos Dam Reservoir, Argentina, based on a Small-Baseline InSAR Approach. *Landslides*, 24 p., published online 30 April 2015
- Mileti D, Sorensen J (1990) Communication of emergency public warnings - A social science perspective and state-of-the-art assessment, Oak Ridge National Laboratory, Tennessee, USA, 166 pp
- Miller B (1965) Laser altimeter may aid photo mapping; *Aviat Week Space Technol*, 88, 60-64
- Mills HH (2003) Inferring erosional resistance of bedrock units in the east Tennessee mountains from digital elevation data. *Geomorphology* 55:263-281
- Monserrat O, Crosetto M (2008) Deformation measurement using terrestrial laser scanning data and least squares 3D surface matching. *ISPRS Journal of Photogrammetry & Remote Sensing* 63:142–154
- Monserrat O, Moya J, Luzi G, Crosetto M, Gili JA, Corominas J (2013) Non interferometric GBSAR measurement. Application to the Vallcebre Landslide (Eastern Pyrenees, Spain). *Natural Hazards and Earth System Sciences*, 13, 1873-1887
- Monserrat O, Crosetto M, Luzi G (2014) A review of ground-based SAR interferometry for deformation measurement. *ISPRS Journal of Photogrammetry and Remote Sensing* 93:40–48
- Montgomery DR, Brandon MT (2002) Topographic controls on erosion rates in tectonically active mountain ranges, *Earth and Planetary Science Letters*, 201, 481-489
- Moreiras SM (2004) Landslide incidence zonation in the Rio Mendoza Valley, Mendoza Province, Argentina, *Earth Surface Processes and Landforms*, 29: 255-266
- Moreiras SM (2005) Landslide susceptibility zonation in the Rio Mendoza Valley, Argentina. *Geomorphology* 66:345–357
- Moreiras SM (2006) Frequency of debris flows and rockfall along the Mendoza river valley (Central Andes), Argentina: Associated risk and future scenario. *Quaternary International* 118:110-121
- Moreno F, Froese C (2009) ERCB/AGS Roles and Responsibilities Manual for the Turtle Mountain Monitoring Project, Alberta, ERCB/AGS, Open File Report 2009-06, 35 p, available at: http://www.ags.gov.ab.ca/geohazards/turtle_mountain/

- Moussavi MS, Abdalati W, Scambos T, Neuenschwander A (2014) Applicability of an automatic surface detection approach to micropulse photon-counting lidar altimetry data: implications for canopy height retrieval from future ICESat-2 data. *International Journal of Remote Sensing* 35(13):5263–5279
- Müller L (1964) The Rock Slide in the Vaiont Valley. *Rock Mech. Eng. Geol.* 2:148-212
- Nadim F, Høydal Ø, Haugland H, McLean A, Eds. (2010) SafeLand deliverable 1.6: Analysis of Landslides triggered by anthropogenic factors in Europe, European Project SafeLand, Grant Agreement No. 226479, 81 pp., available at: <http://www.safeland-fp7.eu>
- Navratil O, Liébault F, Bellot H, Travaglini E, Theule J, Chambon G, Laigle D (2013) High-frequency monitoring of debris-flow propagation along the Réal Torrent, Southern French Prealps, *Geomorphology*, 201:157-171
- Nemčok A (1982) Zosuvy v Slovenských Karpatoch (Landslides in the Slovak Carpathians). Slovak Academy of Sciences, Bratislava
- Neumann GA, Smith DE, Zuber MT (2003) Two Mars years of clouds detected by the Mars Orbiter Laser Altimeter, *Journal of Geophysical Research*, 108(E4), 5023, doi:10.1029/2002JE001849
- Nicolet P, Derron MH, Jaboyedoff M, et al. (2013) Glissements de terrain superficiels aux Avants (Commune de Montreux) - Analyse des phénomènes de glissements superficiels spontanés (GSS) et des méthodologies utilisées pour la carte indicative de dangers (CID) et les cartes de dangers naturels (CDN). Rapport de recherche établis pour l'Unité des Dangers Naturels du canton de Vaud, 119 p
- Nissen E, Krishnan AK, Arrowsmith JR, Saripalli S (2012) Three-dimensional surface displacements and rotations from differencing pre- and post-earthquake LiDAR point clouds. *Geophys Res Lett* 39:1–6
- Nissen E, Maruyama T, Ramon Arrowsmith J, et al (2014) Coseismic fault zone deformation revealed with differential lidar: Examples from Japanese Mw ~7 intraplate earthquakes. *Earth Planet Sci Lett* 405:244–256
- O'Callaghan JF, Mark DM (1984) The extraction of drainage networks from digital elevation data, *Comput. Vision Graphics Image Process.*, 28, 328–344
- Oppikofer T, Jaboyedoff M, Keusen H.R (2008) Collapse at the eastern Eiger flank in the Swiss Alps. *Nature Geoscience* 1:531-535
- Oppikofer T, Jaboyedoff M, Coe JA (2007) Rockfall hazard at Little Mill Campground, Uinta National Forest: Part 2. DEM analysis, in: First North American Landslide Conference - Landslides and Society: Integrated Science, Engineering, Management, and Mitigation, Vail, USA, 3-8 June 2007, 1351-1361
- Oppikofer T, Jaboyedoff M, Blikra LH, Derron MH, Metzger R. (2009) Characterization and monitoring of the Åknes rockslide using terrestrial laser scanning. *Nat. Hazards Earth Syst. Sci.* 9:1003–1019
- Ostrom E (1998) A Behavioral Approach to the Rational Choice Theory of Collective Action: Presidential Address, American Political Science Association, 1997. *The American Political Science Review*, 92, 1-22
- Pedrazzini A (2012) Characterization of gravitational rock slope deformations at different spatial scales based on field, remote sensing and numerical approaches, PhD thesis of the University of Lausanne
- Perla R, Cheng TT, McClung DM (1980) A two-parameter model of snow-avalanche motion. *J. Glaciol.*, 26, 197-207
- Petley DN, Mantovani F, Bulmer MH, Zannoni A (2005a) The use of surface monitoring data for the interpretation of landslide movement patterns. *Geomorphology* 66:133–147
- Petley DN, Higuchi T, Petley DJ, Bulmer MH, Carey J (2005b) Development of progressive landslide failure in cohesive materials. *Geology* 33(3):201-204
- Petri G (1990) Laser-based surveying instrumentation and methods. In *Engineering Surveying Technology*; Kennie, T.J.M., Petrie, G., Eds.; Blackie, Glasgow & London and Halsted Press, New York, USA, 48-83
- Petrie G, Toth C (2009) Introduction to Laser Ranging, Profiling, and Scanning. In *Topographic Laser Ranging and Scanning*; Shan, J., Toth, C.K., Eds.; CRC Press, Boca Raton, USA, 1-27.
- Pfitzner M, Langemeyer S, Pirsch P, Blume H (2011) A flexible real-time SAR processing platform for high resolution airborne image generation. In: *Radar, 2011 IEEE CIE International Conference on Radar*, 1:26-29
- Pierson LA, David SA, Van Vickler R (1990) Rockfall Hazard Rating System Implementation Manual, Oregon
- Pinyol NM, Alonso EE, Corominas J, Moya J (2012) Canelles landslide: modelling rapid drawdown and fast potential sliding. *Landslides* 9:33-51
- Piteau DR, Peckover FL (1978) Engineering of Rock Slope, in: *Landslides, Analysis and Control*, Transportation Research Board, Special Report 176, Schuster, R.L. and Krizek, R.J. (Eds.), Washington, DC, 192-228
- Point of Beginning (2008) 3D laser scanner hardware and software surveys. Available from laser.jadaproductions.net, last accessed 7 January 2009
- Polansky J (1963) Estratigrafía, neotectónica y geomorfología del Pleistoceno pedemontano entre los ríos Diamante y Mendoza. *Asociación Geológica Argentina, Revista* 17:127-349

- Powell JW (1876) Report on the Geology of the Eastern Portion of the Uinta Mountains and a Region of Country Adjacent Thereto, US Geological and Geographical Survey of the Territories, Government Printing Office, Washington, DC
- Preissner J (1978) The influence of the atmosphere on passive radiometric measurements. In: Proceedings of the Symposium on Millimeter and Submillimeter Wave Propagation Circuits: AGARD Conferene, 245:1:13
- Rabatel A, Deline P, Jaillet S, Ravanel L (2008) Rock falls in high-alpine rock walls quantified by terrestrial lidar measurements: A case study in the Mont Blanc area. *Geophysical Research Letters* 35:L10502
- Ramos VA (1997) El Segmento de Subducción Subhorizontal de los Andes Centrales Argentino-Chilenos. *Acta Geológica Hispánica* 32:5-16
- Ramos VA (1999) Plate tectonic setting of the Andean Cordillera. *Episodes* 22(3):183-190
- Rib HT, Liang T (1978) Recognition and identification, in: Landslides, Analysis and Control. In: Schuster, R. and Krizek, R.J. (eds) Transportation Research Board, Special Report 176, Washington DC, pp 34–80
- Rice R Jr, Decker R, Jensen N, Patterson R, Singer S, Sullivan C, Wells L (2002) Avalanche hazard reduction for transportation corridors using real-time detection and alarms. *Cold Regions Science and Technology* 34:31-42
- Rickenmann D, Zimmermann M (1993) The 1987 debris flows in Switzerland: documentation and analysis, *Geomorphology*, 8, 175–189
- Rickenmann D (2005) Runout prediction methods, in: Debris-Flow Hazards and Related Phenomena, edited by: Jakob, M. and Hungr, O., Springer Praxis, Chichester, 305–324
- Riegl (2013) <http://www.riegl.com/media-events/newsletter/0512-rimonitor-and-rimining/>, access date: 11 July 2013
- Riemer W (1995) Keynote paper: Landslides and reservoirs. In: Bell FG (ed.) Landslides, Balkema, Rotterdam, pp 1973-2004
- Ritchie AM (1963) Evaluation of rockfall and its control, in: Highway Research Record, 17, Highway Research Board, National Research Council, Washington, DC, 13-28
- Rose ND, Hungr O (2007) Forecasting potential rock slope failure in open pit mines using the inverse-velocity method. *International Journal of Rock Mechanics & Mining Sciences* 44:308–320
- Rosser NJ, Petley DN, Lim M, Dunning SA, Allison RJ (2005) Terrestrial laser scanning for monitoring the process of hard rock coastal cliff erosion. *Quarterly Journal of Engineering Geology and Hydrogeology* 38:363–375
- Rosser NJ, Lim N, Petley DN, Dunning S, Allison RJ (2007) Patterns of precursory rockfall prior to slope failure. *Journal of Geophysical Research* 112: F04014
- Roth M (2012) Microseismic monitoring at the unstable rock slope at Åknes, Norway, in: SafeLand deliverable 4.1.: Review of Techniques for Landslide Detection, Fast Characterization, Rapid Mapping and Long-Term Monitoring, 2nd Edition, Michoud, C., Abellán, A., Derron, M.-H. and Jaboyedoff, M. (Eds.), European Project SafeLand, Grant Agreement No. 226479, 313-317, available at: <http://www.safeland-fp7.eu>
- Rouiller JD, Jaboyedoff M, Marro C, Philipposian F and Mamin M (1998) Pentes instables dans le Pennique Valaisan. MATTEROCK: une méthodologie d'auscultation des falaises et de detection des éboulements majeurs potentiels, Rapport final du PNR31, VDF Hochschulverlag AG, ETH Zürich, Switzerland
- Rouyet L (2013) Monitoring and characterization of rock slope instabilities in Norway using GB-InSAR. MSc. thesis of the Faculty of Geosciences and Environment of the University of Lausanne, 261 p
- Rouyet L, Kristensen L, Derron MH, Michoud C, Blikra LH, Jaboyedoff M, Lauknes TR (submitted) Evidence of rock slope breathing using Ground-Based InSAR. Submitted to *Geomorphology* in 2015, 27p
- Royán MJ, Abellán A, Jaboyedoff M, Vilaplana JM, Calvet J (2014) Spatio-temporal analysis of rockfall pre-failure deformation using Terrestrial LiDAR. *Landslides* 11:697–709
- Royán MJ, Abellán A, Vilaplana JM (2015) Progressive failure leading to the 3 December 2013 rockfall at Puigcercós scarp (Catalonia, Spain). *Landslides*, published online, 11 p
- Sailer R, Fellin W, Fromm R, Jörg P, Rammer L, Sampl P, Schaffhauser A (2008) Snow avalanche mass-balance calculation and simulation-model verification. *Annals of Glaciology* 48:183-192
- Saito M (1969) Forecasting time of slope failure by tertiary creep. In: Proceedings of 7th international conference on soil mechanics and foundation engineering, Mexico, pp 677–683
- Sales DA, Moreiras SM, Gardini CE (2014) Análisis de estabilidad del deslizamiento rotacional en el cerro Los Baños, Potrerillos, Provincia de Mendoza, Argentina. XIX Congreso Geológico Argentino, Jujuy, Abstracts
- Saroli M, Stramondo S, Moro M, Doumaz F (2005) Movements detection of deep seated gravitational slope deformations by means of InSAR data and photogeological interpretation: northern Sicily case study. *Terra Nova* 17:35–43
- Sartori M, Gouffon Y, Marthaler M (2006) Harmonisation et définition des unités lithostratigraphiques briançonnaises dans les nappes penniques du Valais, *Eclogae Geologicae Helvetiae*, 99, 363-407
- Sassa K (1988) Special lecture: Geotechnical model for the motion of landslides. In: Proceedings of the 5th International Symposium on Landslides, Lausanne, 2:37-56

- Scheidegger AE (1973) On the Prediction of the Reach and Velocity of Catastrophic Landslides. *Rock Mechanics* 5:231-236
- Schlögel R, Doubre C, Malet JP, Masson F (2015) Landslide deformation monitoring with ALOS/PALSAR imagery: A D-InSAR geomorphological interpretation method. *Geomorphology* 231:314-330
- Scholz CH, Koczyński TA (1979) Dilatancy Anisotropy and the Response of Rock to Large Cyclic Loads. *Journal of Geophysical Research* 84:5525-5534
- Schulz WH (2004) Landslides mapped using LiDAR imagery, Seattle, Washington, U.S. Geological Survey Open-File Report 2004-1396; U.S. Department of the Interior: Seattle, USA, 1-11
- Schulz WH (2007) Landslide susceptibility revealed by LIDAR imagery and historical records, Seattle, Washington, *Engineering Geology*, 89: 67-87
- Schulz WH, Coe JA, Shurtleff BL, Panosky J, Farina P, Ricci PP, Barsacchi G (2012) Kinematics of the Slumgullion landslide revealed by ground-based InSAR surveys. In: *Landslides and Engineered Slopes: Protecting Society through Improved Understanding*. Proceedings of the ISL Congress. Eberhardt et al. (eds.), Banff, Canada, 2-8 June 2012, 1273:1279
- Schuster RL (1996) Socioeconomic Significance of Landslides. In: Turner A, Schuster R (Eds.) *Landslides, Investigations and Mitigations*, Transportation Research Board, Special Report 247, Washington, DC, 12-35
- Schuster RL (2006) Interaction of Dams and Landslides – Case Studies and Mitigation. Professional Paper 1723, U.S. Geological Survey
- Schutz BE, Zwally HJ, Shuman CA, Hancock D, DiMarzio JP (2005) Overview of the ICESat Mission. *Geophysical Research Letters*, Vol. 32
- Selander JM (1998) Initial progress in the recording of crime scene simulations using 3D laser structured light imagery techniques for law enforcement and forensic applications. *Proceedings of 26th AIRP workshop*
- Selby MJ (1982) Controls on the stability and inclinations of hillslopes formed on hard rock, *Earth Surface Processes and Landforms*, 7, 449-467
- Shapiro II, Zisk SH, Rogers AEE, Slade MA, Thompson TW (1972) Lunar Topography: Global Determination by Radar. Delay-Doppler stereoscopy and Radar interferometry yield high-resolution three-dimensional views of the moon. *Science* 178(4064):939-948
- Shepherd EC (1965) Laser to watch height, *New Scientist*, 1, 33-37
- Sigmundsson F, Vadon H, Massonnet D (1997) Readjustment of the Krafla spreading segment to crustal rifting measured by satellite radar interferometry. *Geophysical Research Letters* 24(15):1843-1846
- Singhroy V, Molch K (2004) Characterization and monitoring rockslides from SAR techniques, *Advances in Space Research*, 33, 290-295
- Singleton A, Li Z, Hoey T, Muller JP (2014) Evaluating sub-pixel offset techniques as an alternative to D-InSAR for monitoring episodic landslide movements in vegetated terrain. *Remote Sensing of Environment* 147:133-144
- Slob S, Hack R, Keith T (2002) An approach to automate discontinuity measurements of rock faces using laser scanning techniques. In the Proceedings of the International Symposium on Rock Engineering for Mountainous Regions – Eurock, Funchal, Portugal, November 25-28 2002; 87-94
- Smith DE, Muhleman DO, Ivanov AB (2001) Mars Orbiter Laser Altimeter: Experiment summary after the first year of global mapping of Mars, *Journal of Geophysical Research*, 106, E10, 23,689-23,722
- Spillman T, Maurer H, Green GA, Heincke B, Willenberg H, Husen S (2007) Microseismic investigation of an unstable mountain slope in the Swiss Alps, *Journal of Geophysical Research*, 112, 25 pp
- Squarzonni C, Delacourt C, Allemand P (2003) Nine years of spatial and temporal evolution of the La Valette landslide observed by SAR interferometry. *Engineering Geology* 68:53-66
- SRCE (2009) Daily Traffic during 2007, by the Roads and Rivers Office of the Canton of Valais: <http://mapserver-srce.kiperti.com/srce/carte.html>, last access: 3 December 2010
- Steck A, Epard JL, Escher A, Gouffon Y, Masson H (2001) Notice explicative de la carte tectonique des Alpes de Suisse occidentale et des régions avoisinantes au 1:100000. Sheet 123, special geological atlas, OFEG, 73 p
- Stipanovic PN (1979) El Triásico del valle del Río de los Platos (Provincia de San Juan). In: Turner JCM (ed) *Segundo Simposio de Geología Regional Argentina: Córdoba*, Academia Nacional de Ciencias 1:695:744
- Strahler AN (1950) Equilibrium theory of erosional slopes approached by frequency distribution analysis, *Am. J. Sci.*, 248, 673-696, 800-814
- Strahler AN (1954) Quantitative geomorphology of erosional landscapes, *Compt. Rend, 19th Intern. Geol. Cong., Sec. 13*, 341-354
- Stumpf A, Kerle N, Malet JP, Eds. (2011) *SafeLand deliverable 4.4.: Guidelines for the selection of appropriate remote sensing technologies for monitoring different types of landslides*, European Project SafeLand, Grant Agreement No. 226479, 91 pp., available at: <http://www.safeland-fp7.eu>

- Stumpf A, Malet JP, Kerle N, Michoud C, Tofani V, Segoni S, Jaboyedoff M, Casagli N (submitted) Appropriate remote sensing techniques for landslide monitoring: review and selection criteria. Submitted to *Earth-Science Reviews* in November 2013, 80 p
- Sturzenegger M, Yan M, Stead D et al. (2007) Application and limitations of ground-based laser scanning in rock slope characterization. In *Rock mechanics: Meeting Society's Challenges and Demands, Proceedings of the 1st Canada-US Rock Mechanics Symposium, Vancouver, Canada, May 27–31 2007*, 29–36
- Subsecretaría de Recursos Hídricos (2013) Rio Mendoza discharge. <http://www.hidricosargentina.gov.ar>. Accessed 11 October 2013
- Suwa H (1991) Visual observed failure of a rock slope in Japan. *Landslide News* 5:8–9
- Takahashi T (1981) Estimation of potential debris flows and their hazardous zones: Soft countermeasures for a disaster, *Journal of Natural Disaster Science*, 3, 57–89
- Tarayre H, Massonnet D (1996) Atmospheric propagation heterogeneities revealed by ERS-1 interferometry. *Geophysical Research Letters* 23(9):989-992
- Tarchi D, Ohlmer E, Sieber A: Monitoring of Structural Changes by Radar Interferometry. *Research in Nondestructive Evaluation* 9(4): 213-225:1997
- Tarchi D, Casagli N, Fanti R, Leva D, Luzi G, Pasuto A, Pieraccini M, Silvano S (2003a) Landslide Monitoring by Using Ground-Based SAR Interferometry: an example of application to the Tessina landslide in Italy, *Engineering Geology*, 68, 15-30
- Tarchi D, Casagli N, Moretti S, Leva D, Sieber AJ (2003b) Monitoring landslide displacements by using ground-based synthetic aperture radar interferometry: Application to the Ruinon landslide in the Italian Alps, *Journal of Geophysical Research - Solid Earth*, 108, 14 pp
- Tarchi D, Casagli N, Fanti R, Leva D, Luzi G, Pasuto A, Pieraccini M, Silvano S (2003c) Landslide Monitoring by Using Ground-Based SAR Interferometry: an example of application to the Tessina landslide in Italy. *Engineering Geology* 68:15-30
- Terzaghi K (1950) Mechanism of Landslides. The Geological Society of America, *Engineering Geology (Berkeley) Volume*, 83-123
- Terzaghi K (1962) Stability of Steep Slopes on Hard Unweathered Rock, *Géotechnique*, 12, 251-270
- Teza G, Galgaro A, Zaltron N, Genevois R (2007) Terrestrial laser scanner to detect landslide displacement fields: a new approach. *International Journal of Remote Sensing* 28(16):3425-3446
- Teza G, Pesci A, Genevois R, Galgaro A (2008) Characterization of landslide ground surface kinematics from terrestrial laser scanning and strain field computation. *Geomorphology* 97:424-437
- Tofani V, Segoni S, Catani F, Casagli N., Eds. (2012) SafeLand deliverable 4.5.: Evaluation report on innovative monitoring and remote sensing methods and future technology, European Project SafeLand, Grant Agreement No. 226479, 280 pp., available at: <http://www.safeland-fp7.eu>
- Tofani V, Segoni S, Agostini A, Catani F, Casagli N (2013) Technical Note: Use of remote sensing for landslide studies in Europe. *Nat. Hazards Earth Syst. Sci.* 13:299–309
- Tomás R, Li Z, Liu P, Singleton A, Hoey T, Cheng X (2014) Spatiotemporal characteristics of the Huangtupo landslide in the Three Gorges region (China) constrained by radar interferometry. *Geophysical Journal International*, doi: 10.1093/gji/ggu017, 20 p
- Toppe R (1987) Terrain models – a tool for natural hazard mapping, *IAHS*, 162, 629–638
- Travelletti J, Malet JP, Delacourt C (2014) Image-based correlation of Laser Scanning point cloud time series for landslide monitoring. *International Journal of Applied Earth Observation and Geoinformation* 32:1–18
- Travelletti J, Malet JP (2012) Characterization of the 3D geometry of flow-like landslides: A methodology based on the integration of heterogeneous multi-source data, *Engineering Geology*, 128, 30–48
- Troisi C, Negro N (2013) Managing of EW systems by public agencies: related problems, in: *Proceedings of the 1st International Workshop on Warning Criteria for Active Slides, Courmayeur, Italy, 10-12 June 2013*, 43-45, available at: <http://www2.ggl.ulaval.ca/iwwcas/>
- Trombotto D, Borzotta E (2009) Indicators of present global warming through changes in active layer-thickness, estimation of thermal diffusivity and geomorphological observations in the Morenas Coloradas rockglacier, Central Andes of Mendoza, Argentina. *Cold Regions Science and Technology* 55:321–330
- Trümpy R (1980) *Geology of Switzerland - A Guide Book, Part A: An Outline of the Geology of Switzerland*, Wepf & Co, Basel, 104 pp
- Tupling SJ, Pierrynowski MR (1987) Use of cardan angles to locate rigid bodies in three-dimensional space. *Medical and Biological Engineering and Computing* 25(5):527-532
- Turner A, Schuster R, Eds. (1996) *Landslides, Investigations and Mitigations*, Transportation Research Board, Special Report 247, Washington, DC, 685 pp

- UN-ISDR (2009) Terminology on Disaster Risk Reduction, United Nation International Strategy for Disaster Reduction, Geneva, Switzerland, 35 pp
- Vaaja M, Hyyppä J, Kukko A, Kaartinen H, Hyyppä H, Alho P (2011) Mapping Topography Changes and Elevation Accuracies Using a Mobile Laser Scanner. *Remote Sensing* 3:587-600
- Vaaja M, Kukko A, Kaartinen H, Kurkela M, Kasvi E, Flener C, Hyyppä H, Hyyppä J, Järvelä J, Alho P (2013) Data Processing and Quality Evaluation of a Boat-Based Mobile Laser Scanning System. *Sensors* 13:12497-12515
- Vaciago G, Rocchi G, Riba I, Davì M, Bianchini A, Callerio A, Costi M, Eds. (2011) SafeLand deliverable 5.1.: Compendium of tested and innovative structural, non-structural and risk-transfer mitigation measures for different landslide types, European Project SafeLand, Grant Agreement No. 226479, 340 pp., available at: <http://www.safeland-fp7.eu>
- Van Den Eeckhaut M, Poesen J, Govers G, Verstraeten G, Demoulin A (2007) Characteristics of the size distribution of recent and historical landslides in a populated hilly region, *Earth and Planetary Science Letters*, 256: 588-603
- Van Dijke JJ, Van Westen CJ (1990) Rockfall hazard: a geomorphological application of neighbourhood analysis with ILWIS, *ITC Journal*, 1, 40-44
- Varnes D (1978) Slope Movement Types and Processes, in: *Landslides, Analysis and Control*, Transportation Research Board, Special Report 176, Turner, A., Krizek, R. (Eds.), Washington, DC, 12-33
- Varnes DJ (1984) Landslide hazard zonation: a review of principles and practices. *Natural hazards*, 63 p
- Vaunat J, Leroueil S, Faure R (1994) Slope movements: a geotechnical perspective. *Proc. 7th Int. Congress of Int. Association of Engineering Geology*, Oliveira (ed.), 1637-1646
- Voellmy A (1955) Über die Zerstörungskraft von Lawinen, *Schweizerische Bauzeitung*, 73, 212-285
- Voight B (1988) A method for prediction of volcanic eruption. *Nature* 332:125– 130
- Voight B (1989) A relation to describe rate-dependent material failure. *Science* 243(4888):200-203
- Volkwein A, Schellenberg K, Labiouse V, Agliardi F, Berger F, Bourrier F, Dorren LKA, Gerber W, Jaboyedoff M (2011) Rockfall characterisation and structural protection – a review, *Nat. Hazards Earth Syst. Sci.*, 11, 2617–2651
- Vosselman G, Maas H (2010) *Airborne and terrestrial laser scanning*. CRC Press, Boca Raton (USA)
- Wagner A, Leite E, Olivier R (1988) Rock and debris-slides risk mapping in Nepal – A user-friendly PC system for risk mapping, in: *Proceedings of the fifth international symposium on landslides*, Lausanne, Switzerland, 10-15 July 1988, 1251-1258
- Wang F, Zhang Y, Huo Z, Peng X, Araiba K, Wang G (2008) Movement of the Shuping landslide in the first four years after the initial impoundment of the Three Gorges Dam Reservoir, China. *Landslides* 5:321–329
- Wehr A, Lohr, U (1999) Airborne laser scanning – an introduction and overview. *ISPRS Journal of Photogrammetry & Remote Sensing* 54, 68-82
- Whalley WB (1984) Rockfalls, in: *Slope Instability*, edited by: Brunsden, D. and Prior, D. B., Wiley, Chichester, 217–256
- Wick E, Baumann V, Jaboyedoff M (2010a) Brief communication: “Report on the impact of the 27 February 2010 earthquake (Chile, Mw 8.8) on rockfalls in the Las Cuevas valley, Argentina”. *Natural Hazards and Earth System Sciences* 10:1989–1993.
- Wick E, Baumann V, Favre-Bulle G, Jaboyedoff M, Loye A, Marengo H, Rosas M (2010b) Flujos de detritos recientes en la cordillera frontal de Mendoza: Un ejemplo de riesgo natural en la ruta 7. *Revista de la Asociación Geológica Argentina* 66:460-465
- Wiley CA (1954) Pulsed Doppler Radar Methods and Apparatus, United States Patent No. 3196436
- Williams K, Olsen MJ, Roe GV, Glennie C (2013) Synthesis of Transportation Applications of Mobile LiDAR. *Remote Sensing* 5:4652-4692
- Wilson SD, Mikkelsen PE (1978) Field Instrumentation, in: *Landslides, Analysis and Control*, Transportation Research Board, Special Report 176, Turner, A., Krizek, R. (Eds.), Washington, DC, 112-138
- Woodhouse IH (2006) *Introduction to Microwaves Remote Sensing*. CRC Taylor & Francis, Boca Raton, 370p
- Wu TH, Tang WH, Einstein HH (1996) Landslide Hazard and Risk Assessment. In: Turner A, Schuster R (Eds.) *Landslides, Investigations and Mitigations*, Transportation Research Board, Special Report 247, Washington, DC, 106-120
- Wyllie DC, Mah CW (2004) *Rock Slope Engineering*, Civil and Mining, 4th Edition, Taylor & Francis, London and New-York
- Xia M, Ren GM, Ma XL (2013) Deformation and mechanism of landslide influenced by the effects of reservoir water and rainfall, Three Gorges, China. *Natural Hazards* 68:467–482
- Yin Y, Zheng W, Liu Y, Zhang J, Li X (2010) Integration of GPS with InSAR to monitoring of the Jiaju landslide in Sichuan, China. *Landslides* 7:359–365

- Young AP, Olsen MJ, Driscoll N, Flick RE, Gutierrez R, Guza RT, Johnstone E, Kuester F (2013) Comparison of Airborne and Terrestrial LiDAR estimates of Seacliff Erosion in Southern California. *Photogrammetric Engineering & Remote Sensing* 76:421-427
- Záruba Q, Mencl V (1982) *Landslides and their control: developments in geotechnical engineering* 31. Academia Publishing House of the Czechoslovak Academy of Sciences, Prague
- Zebker HA, Rosen PA, Goldstein RM, Gabriel A, Werner C (1994) On the derivation of coseismic displacement fields using differential RaDAR interferometry: the Landers earthquake. *Journal of Geophysical Research: Solid Earth* 99(B10):19617–19634
- Zebker HA, Rosen PA, Hensley S (1997) Atmospheric effects in interferometry synthetic aperture radar surface deformation and topographic maps. *Journal of Geophysical research* 102:7547-7563
- Zischinsky U (1969) *Über Sackungen*. *Rock Mechanics* 1:30–52
- Zwally HJ, Schutz B, Abdalati W, Abshire J, Bentley C, Brenner A, Bufton J, Dezio J, Hancock D, Harding D, Herring T, Minster B, Quinn K, Palm S, Spinhirne J, Thomas R (2002) ICESat's laser measurements of polar ice, atmosphere, ocean, and land. *Journal of Geodynamics*, 34,405–445



UNIL | Université de Lausanne
Faculté des Géosciences et de l'Environnement
Institut des Sciences de la Terre

FROM REGIONAL LANDSLIDE DETECTION TO SITE-SPECIFIC SLOPE DEFORMATION MONITORING AND MODELLING BASED ON ACTIVE REMOTE SENSORS

ANNEXES

Thèse de doctorat

présentée à la faculté des géosciences et de l'environnement par

Clément Michoud

ingénieur géologue diplômé de l'université de Lausanne

Devant le Jury composé de
Monsieur le professeur Michel Jaboyedoff, directeur
Monsieur le docteur Marc-Henri Derron, co-directeur
Monsieur le docteur François Joseph Baillifard, expert
Monsieur le professeur Lars Harald Blikra, expert
Monsieur le professeur Jacques Locat, expert
Sous la présidence de monsieur le doyen François Bussy

Lausanne, 2016

Table of Annexes

Foreword

Curriculum Vitae and Publication List

Annexes A: publications in peer-reviewed journals, as co-author

- A1: Mainsant G, Larose E, Brönnimann C, Jongmans D, Michoud C and Jaboyedoff M: Ambient seismic noise monitoring of a clay landslide: toward failure prediction. *Journal of Geophysical Researches Earth Surface* 117, 12 p., 2012
- A2: Cloutier C, Agliardi F, Crosta G, Frattini P, Froese C, Jaboyedoff M, Locat J, Michoud C and Marui H: The First International Workshop on Warning Criteria for Active Slides: technical issues, problems and solutions for managing early warning systems. *Landslides* 12, 205-2012, 2015
- A3: Rouyet L, Kristensen L, Derron MH, Michoud C, Blikra LH, Jaboyedoff M and Lauknes TR: Evidence of rock slope breathing using GB-InSAR. Submitted to *Geomorphology*, 27 p, May 2015

Annexes B: selection of other relevant publications

- B1: Michoud C, Derron MH, Abellán A, Jaboyedoff M and Fornaro G: Radar Wave Principles, Interferometric Radar Distance-Meter and Differential SAR Interferometry. Deliverable 4.1 of the European project SAFELAND: Review of Techniques for Landslide Detection, Fast Characterization, Rapid Mapping and Long-Term Monitoring. Edited in 2010 by Michoud C, Abellán A, Derron MH and Jaboyedoff M, 105-125, 2010
- B2: Jaboyedoff M, Abellán A, Carrea D, Derron MH, Matasci B and Michoud C: LiDAR use for Mapping and Monitoring of Landslides, Accepted in *Encyclopedia Natural Hazards*, Taylor & Francis
- B3: Jaboyedoff M, Choffet M, Derron MH, Horton P, Loyer A, Longchamp C, Mazotti B, Michoud C and Pedrazzini A: Preliminary slope mass movements susceptibility mapping using DEM and LiDAR DEM. In: *Terrigenous Mass Movements*, Pradhan and Buchroithner (Eds.), Springer-Verlag Berlin Heidelberg, 109-170, 2012
- B4: Jaboyedoff M, Horton P, Derron MH, Longchamp C and Michoud C: Monitoring Natural Hazards. In: *Encyclopedia of Natural Hazards*, Bobrowsky P.T. (Ed.), Springer Science+Business Media B.V., 12 pp., 2012
- B5: After Michoud C, Jaboyedoff M, Derron MH, Nadim F and Leroi E: Classification of landslide-inducing anthropogenic activities. 5th Canadian Conference on Geotechnique and Natural Hazards, Kelowna, Canada, 10 p., 2011

Clément Michoud

Impasse Docteur Tissot 5
CH-1117 Grancy
clement.michoud@terranum.ch

French (Permis C), married
29 years old, driving license

MASTER OF SCIENCES ENGINEERING GEOLOGIST

Present jobs

- Since April 2015: Engineering geologist and manager at Terranum Sàrl, a private office for rock-solid geosciences and Software solutions
- Since Summer 2014: Farmer of a Swiss estate (secondary activity)

Personal skills

Natural hazard

- Landslides susceptibility mapping at regional scales (shallow landslides, large instabilities and rockfalls) using Geographic Information Systems and remote sensing data (aerial and mobile LiDAR, spaceborne radar interferometry and optical imagery)
- Slope-specific stability assessments based on field works, water and displacement monitoring (terrestrial LiDAR, ground-based InSAR, GNSS, etc.), safety factor computation, runout modelling, Early Warning Systems

Engineering geology

- Rock and soil mechanics, knowledge of core drilling, subsurface geophysics, etc.

Environment

- Regulations, practices, obligations and needs of Agriculture in Switzerland

Technic

- LiDAR systems: Optech, Applanix and Leica (field acquisitions and post-processing)
- GNSS and total station: Topcon (field acquisitions and post-processing)
- Software: ArcGIS, QGIS, Polyworks, Rocscience, Surfer, Coltop3D, MatLAB, Adobe

Languages

- English: bachelor's degree, professional vocabulary
- Spanish: intermediary level (European level B1)
- German: basis level

Recent collaborations

- Bagnes municipality, Valais, Switzerland
- Forestry Service, Canton of Fribourg, Switzerland
- Forestry and Road Services, Canton of Vaud, Switzerland
- Geological Survey of Norway, Norway
- Institute of Earth Sciences (ISTERRE), UJF, France
- Laboratory of Physical Geography and Environment (GEOPHEN), UniCaen, France
- LiSALab Ellegi SRL, Italy

- Northern Research Institute Tromsø (Norut), Norway
- Norwegian Water Resources and Energy Directorate (NVE), snow avalanches and rockslides sections, Norway

Former activities

- From April 2011 to April 2015: Engineering geologist and partner at Terranum Sàrl
- From March 2009 to May 2014: Teaching and research Assistant at the "Risk" group of the Prof. Jaboyedoff (IGAR then ISTE) at the University of Lausanne
- From July to November 2008: assistant at the Laboratory of Engineering and Environmental Geology (GEOLEP), Swiss Federal Institute of Technology of Lausanne (EPFL)
- Summers 2006-2007: renovation, maintenance of villas and gardens

Teaching domains

- Risks and Natural Hazards, with Prof. Jaboyedoff, BSc level, 2009-2014
- Cliff instabilities, with Prof. Jaboyedoff, MSc level, 2009-2012
- 3D surveying Techniques, with Dr. Derron, MSc level, 2010-2012
- Radar Interferometry, with Dr. Derron, MSc level, 2011-2014
- LiDAR Applied to Landslides, with Prof. Jaboyedoff, for professionals, 2012-2014
- Rockfall Susceptibility and Hazard Mapping, for professionals, 2014

University thesis

- PhD thesis in Earth Sciences of the University of Lausanne: *From Regional Landslide Detection to Site-Specific Slope Deformation Monitoring and Modelling Based on Active Remote Sensors*. Viva voce in January 2016
- Master thesis in Engineering geology of the University of Lausanne: *Differential Synthetic Aperture Radar Interferometry in Monitoring La Frasse Landslide, Swiss' Alps*. Viva voce in February 2009

Education

- 2009-2016: PhD in Earth Sciences at the Institute of Earth Sciences (Risk group), University of Lausanne, supervised by Michel Jaboyedoff and Marc-Henri Derron
- 2007-2009: Master of Sciences in Engineering Geology. Lemanic School of Earth and Environmental Sciences (Universities of Lausanne and Geneva, Swiss Federal Institute of Technology of Lausanne), Switzerland
- 2004-2007: Bachelor of Sciences and Technologies in Earth and Environmental Sciences. Passed with distinction, 2nd of the promotion. University of Savoy, France

Interests

- Lacrosse, alpinism, skiing, snowshoes, squash
- History of Sciences and ancient civilizations
- Comics and movies

List of publications

Papers in international peer-reviewed journals

- Michoud C.**, Baumann V., Lauknes T.R., Penna I., Derron M.-H. and Jaboyedoff M.: Large Slope Deformations Detection and Monitoring along Shores of the Potrerillos Dam Reservoir, Argentina, based on a Small-Baseline InSAR Approach, *Landslides*, 20 p., in press.
- Michoud C.**, Carrea D., Costa S., Derron M.-H., Jaboyedoff M., Delacourt C., Maquaire O., Letortu P. and Davidson R.: Landslide detection and monitoring capability of boat-based mobile laser scanning along Dieppe coastal cliffs, Normandy, *Landslides*, 12, 403–418, 2015.
- Michoud C.**, Bazin S., Blikra L.-H., Derron M.-H. and Jaboyedoff M.: Experiences from Site-Specific Landslide Early Warning Systems, *Natural Hazards and Earth System Sciences*, 2659–2673, 2013.
- Michoud C.**, Derron M.-H., Horton P., Jaboyedoff M., Baillifard F.-J., Loye A., Nicolet P., Pedrazzini A. and Queyrel A.: Rockfall hazard and risk assessments along roads at a regional scale: example in Swiss Alps. *Natural Hazards and Earth System Sciences*, 12, 615-629, 2012.
- Rouyet L., Kristensen L., Derron M.-H., **Michoud C.**, Blikra L.H., Jaboyedoff M. and Lauknes T.R.: Evidence of rock slope breathing using GB-InSAR. Submitted to *Geomorphology*, May 2015.
- Stumpf A., Malet J.-P., Kerle N., **Michoud C.**, Tofani V., Segoni S., Jaboyedoff M. and Casagli N.: Appropriate remote sensing techniques for landslide monitoring: review and selection criteria. Submitted to *Earth Sciences Review*, November 2013.
- Cloutier C., Agliardi F., Crosta G., Frattini P., Froese C., Jaboyedoff M., Locat J., **Michoud C.** and Marui H.: The First International Workshop on Warning Criteria for Active Slides: technical issues, problems and solutions for managing early warning systems, *Landslides*, 12, 205-2012, 2015.
- Mainsant G., Larose E., Brönnimann C., Jongmans D., **Michoud C.** and Jaboyedoff M.: Ambient seismic noise monitoring of a clay landslide: toward failure prediction. *Journal of Geophysical Researches - Earth Surface*, 117, 12 pp., 2012.

Book chapters and edition

- Jaboyedoff M., Abellán A., Carrea D., Derron M.-H., Matasci B. and **Michoud C.**: LiDAR use for Mapping and Monitoring of Landslides, Accepted in *Encyclopedia Natural Hazards*, Taylor & Francis.
- Humair F., Matasci B., Jaboyedoff M., Abellan A., Carrea D., Derron M.-H., Guerin A., **Michoud C.**, Nicolet P., Nguyen L., Penna I., Voumard J., Wyser M. (Eds). *Vertical Geology: from remote sensing to 3D geological modelling*. Proceedings of the first Vertical Geology conference, 5-7 February 2014, University of Lausanne, Switzerland, 254 p.
- Jaboyedoff M., Horton P., Derron M.-H., Longchamp C., **Michoud C.**: Monitoring Natural Hazards. In: *Encyclopedia of Natural Hazards*, Bobrowsky P.T. (Ed.), Springer Science+Business Media B.V., 12 pp., 2012.
- Jaboyedoff M., Choffet M., Derron M.-H., Horton P., Loye A., Longchamp C., Mazotti B., **Michoud C.** and Pedrazzini A.: Preliminary slope mass movements susceptibility mapping using DEM and LiDAR DEM. In: *Terrigenous Mass Movements*, Pradhan and Buchroithner (Eds.), Springer-Verlag Berlin Heidelberg, 109-170, 2012.
- Derron M.-H., Jaboyedoff M., Pedrazzini A., **Michoud C.** and Villemin T.: Remote Sensing and Monitoring Techniques for the Characterization of Rock Mass Deformation and Change Detection. In: *Rockfall Engineering*, Lambert S., Nicot F. (Eds.), John Wiley & Sons, New York, ISTE Ltd, London, 2011. ISBN 978-1-84821-256-5. 464 p., 2011.

Proceeding in peer-reviewed conferences (as 1st author)

Oral presentations

- Michoud C.**, Baumann V., Derron M.-H., Jaboyedoff M. and Lauknes T.R.: Slope Instability Detection along the National 7 and the Potrerillos Dam Reservoir, Argentina, Using the Small-Baseline InSAR Technique. 12 IAEG Congress, Turin, Italy, 6 p., 2014.

- Michoud C., Carrea D., Costa S., Davidson R., Delacourt C., Derron M.-H., Jaboyedoff M. and Macquaire O.:** Rockfall Detection and Landslide Monitoring Ability of Boat-based Mobile Laser Scanning along Dieppe Coastal Cliffs. 1st Vertical Geology Conference, University of Lausanne, Switzerland, 23-27, 2014.
- Michoud C., Jaboyedoff M., Derron M.-H., Nadim F. and Leroi E.:** Classification of landslide-inducing anthropogenic activities. 5th Canadian Conference on Geotechnique and Natural Hazards, Kelowna, Canada, 10 p., 2011.

Abstracts in conferences (as 1st author)

Oral presentations

- Michoud C., Baillifard F.J., Blikra L.H., Derron M.-H., Jaboyedoff M., Kristensen L., Leva D., Metzger R. and Rivolta C.:** Coupling high resolution 3D point clouds from terrestrial LiDAR with high precision displacement time series from GB-InSAR to understand landslide kinematic: example of the La Perraire instability, Swiss Alps. European Geosciences Union General Assembly, Vienna, EGU2014-8169, 2014.
- Michoud C., Bazin S., Blikra L.H., Derron M.-H., Jaboyedoff M. and Abellán A.:** On the importance of landslide conceptual models by integrating and coupling different sources of data to set pertinent thresholds and proper EWS. 1st International Workshop on Warning Criteria for Active Slides, Courmayeur, Italy, 2013.
- Michoud C., Carrea D., Augereau E., Cancouët R., Costa S., Davidson R., Delacourt C., Derron M.-H., Jaboyedoff M., Letortu P. and Maquaire O.:** Mobile Laser Scanning along Dieppe coastal cliffs: reliability of the acquired point clouds applied to rockfall assessments. European Geosciences Union General Assembly, Vienna, EGU2013-5254-4, 2013.
- Michoud C., Abellán A., Baillifard F., Derron M.-H., Jaboyedoff M. and May-Delasoie F.:** Using active terrestrial remote sensing techniques to monitor and model the structurally-controlled rockslide of La Barmasse (Valais, Switzerland). Innovative LiDAR Solutions Conferences, Nice, France, 2012.
- Michoud C., Derron M.-H., Jaboyedoff M.:** Surveillance des glissements de terrain: du LiDAR terrestre au GB-InSAR. Séminaire de recherche en environnement pour le master en géosciences de l'environnement, 2011.
- Michoud C., Metzger R., Fragnol B., Longchamp C., Derron M.-H., Jaboyedoff M., Blikra L.H., Kristensen L. and Oppikofer T.:** Coastal rockfall hazard assessment: Offshore Laser Scanning and structural analysis with Coltop3D in Sunndalsøra, Norway. Innovative LiDAR Solutions Conferences, Toronto, Canada, 2011.
- Michoud C., Abellán A., Derron M.-H. and Jaboyedoff M.:** Review of Techniques for Landslides Detection, Fast Characterization, Rapid Mapping and Long-Term Monitoring. "Mountain Risk" International Conference, Firenze, Italy, 2010.
- Michoud C., Mazotti B., Choffet M., Dubois J., Breguet A., Métraux V., Jaboyedoff J. et al.:** Advanced Susceptibility Mapping for Natural Hazards at a Local Scale – The Case of the Swiss Alpine Valley of Bagnes. European Geosciences Union General Assembly, Vienna, EGU2010-4606, 2010.
- Michoud C., Abellán A., Derron M.-H. and Jaboyedoff M.:** A Review of Remote Sensing and Ground-Based Techniques for Landslides Detection, Fast Characterization, Rapid Mapping and Long-Term Monitoring. International workshop on landslide monitoring technologies and early warning systems, Vienna, 2010.

Poster presentations

- Michoud C., Carrea D., Augereau E., Cancouët R., Costa S., Davidson R., Delacourt C., Derron M.-H., Jaboyedoff M., Letortu P. and Macquaire O.:** Acquisition, Resolution and Precision of Dieppe Coastal Cliffs Point Clouds from Mobile Laser Scanning. 8th International Conference on Geomorphology, Paris, Switzerland, 2013.
- Michoud C., Derron M.-H., Baumann V., Jaboyedoff M. and Lauknes T.R.:** Detection of Slope Instabilities Along the National Road 7, Mendoza Province, Argentina, Using Multi-Temporal InSAR. European Geosciences Union General Assembly, Vienna, EGU2013-5157-1, 2013.
- Michoud C., Abellán A., Baillifard F.-J., Demierre J., Derron M.-H., Jaboyedoff M., Jakubowski J., and May-Delasoie F.:** The structurally-controlled rockslide of Barmasse (Valais, Switzerland): structural geology, ground-based monitoring and displacement vs. rainfall modeling. European Geosciences Union General Assembly, Vienna, EGU2012-2914-2, 2012.
- Michoud C., Bazin S., Blikra L.-H., Derron M.-H. and Jaboyedoff M.:** Overview of Existing Landslide Early-Warning Systems in Operation. European Geosciences Union General Assembly, Vienna, EGU2012-2919-1, 2012.
- Michoud C., Jaboyedoff M., Derron M.-H., Nadim F. and Leroi E.:** New classification of landslide-inducing anthropogenic activities. European Geosciences Union General Assembly, Vienna, EGU2012-2923-1, 2012.

- Michoud C.**, Derron M.-H., Horton P., Queyrel A., Jaboyedoff M., Baillifard F.-J., Loye A., Nicolet P. and Pedrazzini A.: New improvement of the Slope Angle Distribution approach in order to assess hazard and risk along roads exposed to rockfalls: example of the Bagnes valley, Swiss Alps. European Geosciences Union General Assembly, Vienna, EGU2011-7553, 2011.
- Michoud C.**, Baumann V., Derron M.-H., Jaboyedoff M., Lauknes T.R. and Wick E.: Detection of Large Slope Instabilities using Spaceborne Radar Interferometry along the National Road 7, Mendoza Province, Argentina. European Geosciences Union General Assembly, Vienna, EGU2011-7619, 2011.
- Michoud C.**, Lauknes T.R., Pedrazzini A., Jaboyedoff M., Tapia R. and Steinmann G.: Differential Synthetic Aperture Radar Interferometry in monitoring large landslide (La Frasse, Switzerland). European Geosciences Union General Assembly, Vienna, EGU2009-5129, 2009.

SafeLand European Project

Edition of technical peer-reviewed deliverable

- Michoud C.**, Abellán A., Derron M.-H. and Jaboyedoff M. (Eds.): SafeLand deliverable 4.1: Review of Techniques for Landslide Detection, Fast Characterization, Rapid Mapping and Long-Term Monitoring. 401 p., 2010.

Chapters in technical peer-reviewed deliverable

- Michoud C.**, Derron M.-H., Jaboyedoff M., Bazin S., Blikra L.H.: Overview of existing landslide Early Warning Systems in operation. Deliverable 4.8 of the European project SAFELAND: Guidelines for landslide monitoring and early warning systems in Europe – Design and required technology. Edited in 2012 by Bazin S., 17 pp., 2012.
- Michoud C.**, Derron M.-H., Abellán A., Jaboyedoff M. and Fornaro G.: Radar Wave Principles, Interferometric Radar Distance-Meter and Differential SAR Interferometry. Deliverable 4.1 of the European project SAFELAND: Review of Techniques for Landslide Detection, Fast Characterization, Rapid Mapping and Long-Term Monitoring. Edited in 2010 by Michoud C., Abellán A., Derron M.-H. and Jaboyedoff M., pp. 105-125, 2010.
- Michoud C.**, Blikra L.H., Abellán A., M.-H. Derron and Jaboyedoff M.: Introduction to Core Logging. Deliverable 4.1 of the European project SAFELAND: Review of Techniques for Landslide Detection, Fast Characterization, Rapid Mapping and Long-Term Monitoring. Edited in 2010 by Michoud C., Abellán A., Derron M.-H. and Jaboyedoff M., pp. 247-250, 2010.
- Abellán A., Jaboyedoff M., **Michoud C.**, Derron M.H. and Oppikofer, T.: Active Optical Sensors (LASERS). Deliverable 4.1 of the European project SAFELAND: Review of Techniques for Landslide Detection, Fast Characterization, Rapid Mapping and Long-Term Monitoring. Edited in 2010 by Michoud C., Abellán A., Derron M.-H. and Jaboyedoff M., pp. 66-102, 2010.
- Lecomte I., Bazin S., Grandjean G. and **Michoud C.**: Ground-Based Geophysical Investigations. Deliverable 4.1 of the European project SAFELAND: Review of Techniques for Landslide Detection, Fast Characterization, Rapid Mapping and Long-Term Monitoring. Edited in 2010 by Michoud C., Abellán A., Derron M.-H. and Jaboyedoff M., pp. 167-195, 2010.

Technical reports (as 1st author)

- Michoud C.**, Derron M.-H. and Jaboyedoff M.: Surveillance du glissement rocheux de la Barmasse - Suivi des déplacements mesurés entre 2007 et 2012 par LiDAR terrestre, GPS différentiel et RaDAR terrestre, 40 d, March 2013.
- Michoud C.**, Derron M.-H. and Jaboyedoff M.: Surveillance du glissement rocheux de la Perraire - Suivi des déplacements mesurés entre 2006 et 2012 par LiDAR terrestre et RaDAR terrestre, 23 d, March 2013.
- Michoud C.**, Carrea D., Derron M.-H. and Jaboyedoff M.: Acquisitions par Scanner Laser Mobile de falaises de craie près de Dieppe, France - Rapport technique : acquisitions, traitements et qualité des données, 45 p., March 2013
- Michoud C.**, Nicolet P., Jaboyedoff M., Larose E., Mainsant G., Jongmans D. and Brönnimann B.: Glissement de Pont Bourquin - Rapport de synthèse des travaux menés par l'IGAR et ses partenaires de 2006 à 2012, 125 p., May 2012.
- Michoud C.**, Nicolet P., Carrea D. and Jaboyedoff M. : Glissement au lieu dit Pont Bourquin - Compte-rendu des événements d'août 2010 et premières interprétations, 31 p., November 2010.
- Michoud C.**, Oppikofer T. and Jaboyedoff M. : Falaise de la Barmette, Route de Vens - Etude d'un bloc potentiellement instable par scanner laser terrestre, 14 p., October 2010.

- Michoud C., Longchamp C., Derron M.-H. and Jaboyedoff M.:** Technical report: the terrestrial and offshore laser scanning acquisitions of September 2010 in Sunndalsøra (Møre og Romsdal, Norway): Techniques, processing and data, 10 p., October 2010.
- Michoud C., Mazotti B., Choffet M., Dubois J., Breguet A., Métraux V., Jaboyedoff J. et al.:** Cartes indicatives de Dangers - Communes de Bagnes et de Vollèges / VS, Carnets « méthodologie » et « résultats », 207 p., March 2010.

Assisted master thesis

- Vioget A.:** Analyse de l'évolution morphostructurale des falaises littorales du Bessin, Basse-Normandie, France. MSc. thesis of the Faculty of Geosciences and Environment of the University of Lausanne, supervised by Prof. Dr. Jaboyedoff M. and Prof. Dr. Maquaire O., assisted by **Michoud C.**, 2013-2015.
- Egli T.:** Cartes de danger de chutes de blocs sur le village des Morgnes (Bagnes). MSc. thesis of the Faculty of Geosciences and Environment of the University of Lausanne and the EPFL, supervised by Prof. Dr. Jaboyedoff M. and Dr. Labiouse V. M.-H., assisted by **Michoud C.**, 2012-2013.
- Rouyet L.:** Monitoring and characterization of rock slope instabilities in Norway using GB-InSAR. MSc. thesis of the Faculty of Geosciences and Environment of the University of Lausanne, supervised by Prof. Dr. Jaboyedoff M. and Dr. Derron M.-H., assisted by **Michoud C.**, 2011-2013.
- Franz M.:** La falaise des Bornes du Diable: de l'Instabilité au Tsunami. MSc. thesis of the Faculty of Geosciences and Environment of the University of Lausanne, supervised by Prof. Dr. Jaboyedoff M. and assisted by **Michoud C.**, 2009-2011.
- Fournier L.:** Analyse du risque de chutes de blocs le long de la route cantonale Aigle – Les Diablerets (Canton de Vaud). MSc. thesis of the Faculty of Geosciences and Environment of the University of Lausanne, supervised by Prof. Dr. Jaboyedoff M. and assisted by **Michoud C.** and Nicolet P., 2011.
- Delasoie F.:** Etudes des instabilités de versants de la Barmasse (Valais, Suisse) par une approche multidisciplinaire. MSc. thesis of the Faculty of Geosciences and Environment of the University of Lausanne, supervised by Prof. Dr. Jaboyedoff M. and assisted by **Michoud C.** and Pedrazzini A., 2009-2010.

Annex A1

Mainsant G, Larose E, Brönnimann C, Jongmans D, Michoud C and Jaboyedoff M: Ambient seismic noise monitoring of a clay landslide: toward failure prediction. *Journal of Geophysical Researches Earth Surface* 117, 12 p, 2012

Ambient seismic noise monitoring of a clay landslide: Toward failure prediction

Guérolé Mainsant,¹ Eric Larose,¹ Cornelia Brönnimann,² Denis Jongmans,¹ Clément Michoud,³ and Michel Jaboyedoff³

Received 29 July 2011; revised 1 February 2012; accepted 6 February 2012; published 22 March 2012.

[1] Given that clay-rich landslides may become mobilized, leading to rapid mass movements (earthflows and debris flows), they pose critical problems in risk management worldwide. The most widely proposed mechanism leading to such flow-like movements is the increase in water pore pressure in the sliding mass, generating partial or complete liquefaction. This solid-to-liquid transition results in a dramatic reduction of mechanical rigidity in the liquefied zones, which could be detected by monitoring shear wave velocity variations. With this purpose in mind, the ambient seismic noise correlation technique has been applied to measure the variation in the seismic surface wave velocity in the Pont Bourquin landslide (Swiss Alps). This small but active composite earthslide-earthflow was equipped with continuously recording seismic sensors during spring and summer 2010. An earthslide of a few thousand cubic meters was triggered in mid-August 2010, after a rainy period. This article shows that the seismic velocity of the sliding material, measured from daily noise correlograms, decreased continuously and rapidly for several days prior to the catastrophic event. From a spectral analysis of the velocity decrease, it was possible to determine the location of the change at the base of the sliding layer. These results demonstrate that ambient seismic noise can be used to detect rigidity variations before failure and could potentially be used to predict landslides.

Citation: Mainsant, G., E. Larose, C. Brönnimann, D. Jongmans, C. Michoud, and M. Jaboyedoff (2012), Ambient seismic noise monitoring of a clay landslide: Toward failure prediction, *J. Geophys. Res.*, 117, F01030, doi:10.1029/2011JF002159.

1. Introduction

[2] All mountainous areas are affected by gravitational mass movements of various types, sizes and velocities, which could have a major impact on life and property. Landslides in clay-rich formations, which are widespread over the world, are characterized by unpredictable acceleration and liquefaction phases [Iverson *et al.*, 1997; Malet *et al.*, 2005]. Of particular concern for hazard assessment is the triggering of earthflows and debris flows, the rheology of which switches from solid to fluid. This phenomenon has been widely reported in all types of recent clay deposits, including Quaternary marine sensitive [Crawford, 1968; Eilertsen *et al.*, 2008] or nonsensitive clays [Picarelli *et al.*, 2005] and lacustrine clay deposits [Bièvre *et al.*, 2011]. But flow-like movements have also been frequently observed in fractured and weathered clay-rich rocks, such as shales, marls and flyschs [Angeli *et al.*, 2000; Picarelli *et al.*, 2005; Malet *et al.*, 2005], and in volcanic rocks in which primary minerals were altered to clays [Coe *et al.*, 2003].

[3] Predicting these sudden events, primarily controlled by groundwater conditions, has been an active research topic for the last two decades [Lee and Ho, 2009]. Empirical prediction methods have been proposed, relying on two types of measurements: (1) surface displacements, whose change to rupture is usually interpreted using slope creep theories [Petley *et al.*, 2005], and (2) hydrological factors such as precipitation, soil water content or pore pressure, used as predictors with threshold values determined in an empirical or statistical manner [Keefer *et al.*, 1987]. Although these empirical methods have been successfully applied in some specific cases, they do not provide a real insight into the mechanisms involved, and have proved to be very sensitive to changes in landslide geometry and deformation. Recently, theoretical models coupling a slope instability mechanism and hydrological modeling have been developed for predicting landslide occurrence [Keefer *et al.*, 1987; Crosta and Frattini, 2008]. However, in 3D, such approaches require considerable investigation and computational effort.

[4] For debris flows and earthflows occurring in fine-grained soils during or after heavy and sustained rainfalls, the triggering mechanism most often proposed is the partial or total liquefaction of the mass, resulting from an increase in pore water pressure [Picarelli *et al.*, 2005; van Asch *et al.*, 2007]. As the shear wave velocity (V_s) in a fluid tends to 0 [Reynolds, 1997], the bulk shear wave velocity should

¹ISTerre, CNRS, Université de Grenoble, Grenoble, France.

²GEOLEP, EPFL, Lausanne, Switzerland.

³IGAR, University of Lausanne, Lausanne, Switzerland.

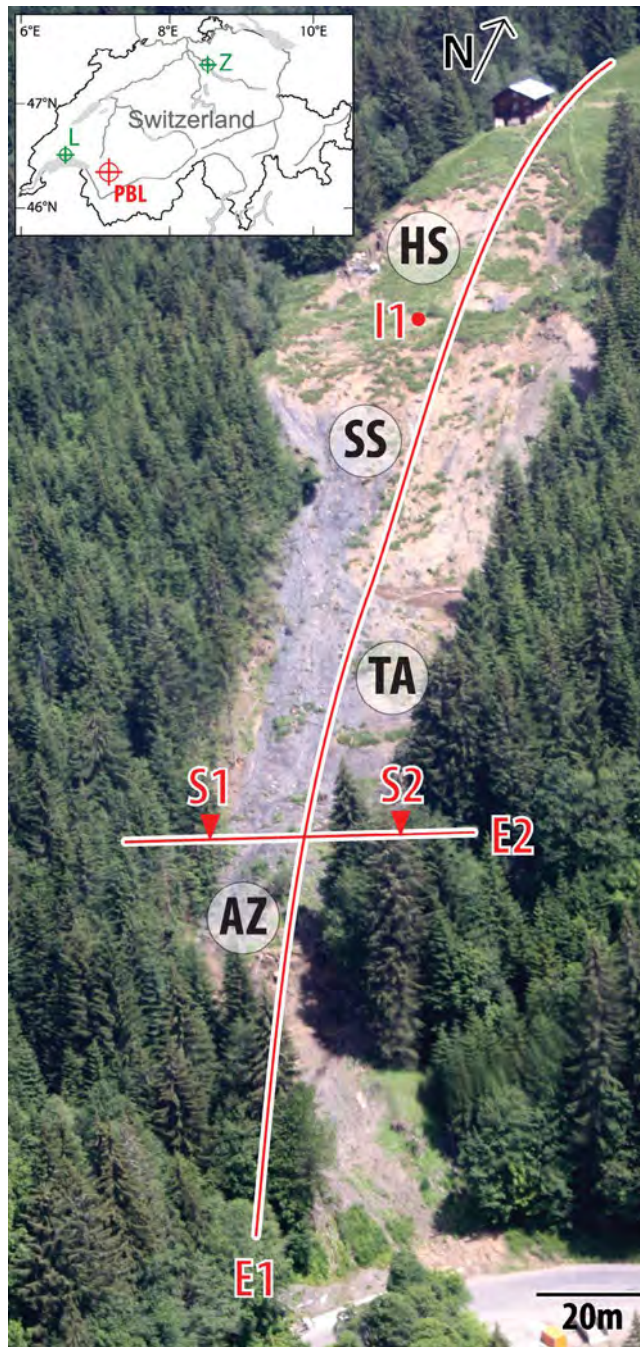


Figure 1. Aerial photo of the Pont Bourquin landslide in June 2009, with the location of the two electrical profiles E1 and E2, the two seismometers S1 and S2 installed on stable ground, and the inclinometer I1. The headscarp (HS), main secondary scarp (SS), transportation area (TA), and accumulation zone (AZ) are also indicated. The Pont Bourquin landslide (red cross) is located on the topographic inset map of Switzerland (L, Lausanne; Z, Zurich). The gravitational instability threatens the road carrying heavy traffic over the Pillon pass (bottom of the photo).

dramatically decrease in the vicinity of liquefied zones. Moreover, it has been recently shown that, in a clay-rich landslide, V_s also significantly decreases with the extent of damage in the material [Renalier et al., 2010]. This suggests

that continuous V_s measurement could be valuable for monitoring clay slope degradation and would constitute an alternative to the classical prediction methods. V_s is usually obtained from active source-receiver experiments. However, the reproducibility of seismic sources is very limited, and it is difficult to ascertain whether seismic response changes actually result from a change in the mechanical properties of the medium or from the source. The ambient noise correlation technique developed over the last 10 years [Weaver and Lobkis, 2001; Shapiro and Campillo, 2004] offers a realistic alternative to using controlled sources. The local Green's function (or impulse response) can in fact be determined from the cross correlation of ambient noise continuously acquired by two passive sensors as if one of them was a source. This method has found considerable applications in seismic imaging at different scales [Shapiro et al., 2005; Larose et al., 2006]. More recently, it was demonstrated that the tail portion of the correlograms, the so-called coda part formed by scattered waves, is extremely sensitive to small changes in the medium [Sens-Schönfelder and Wegler, 2006; Brenguier et al., 2008a, 2008b]. By comparing the phases of the waves in the coda, apparent relative velocity changes of the material can be measured with a precision better than 0.1%. This can be performed even if the correlograms do not give the exact Green's function between the sensors. Correlograms are however required to be stable in time, implying a relatively constant background noise over the period of interest [Hadziioannou et al., 2009]. In the present manuscript we will apply the noise correlation technique on a landslide where the noise is in part due to traffic on the road, which constitutes a spatially stable background noise. The purpose of the paper is to detect mechanical changes in an active clay landslide where failure is expected.

2. The Pont Bourquin Landslide History and Geology

2.1. Historical Context

[5] The Pont Bourquin landslide is located in the Swiss Prealps, 40 km to the east of the town of Lausanne (Figure 1). Although the whole area has been affected by landslide phenomena since the last glacial retreat (more than 10,000 years ago), aerial photos show that gravitational deformation appeared in the mid 90s in the upper part of the hillside and that the slope instability gradually developed over a period of about 10 years [Jaboyedoff et al., 2009]. In 2006, displacements of up to 80 cm created the head scarp of a 240 m long translational landslide affecting an area of about 8,000 m², with a width varying from 15 m to 60 m (Figure 1). On 5 July 2007, a 3 day period of heavy rainfall (cumulative depth of 95 mm) triggered an earthflow, which started from the main secondary scarp (SS in Figures 1 and 2) and cut the frequently used Pillon Pass road located at the toe of the Pont Bourquin landslide. This earthflow, with an estimated volume of 3,000 to 6,000 m³, affected a layer a few meters thick in the transportation area (TA) of the Pont Bourquin landslide [Jaboyedoff et al., 2009]. During the following 3 years, the entire landslide has exhibited a general translational motion associated with high internal deformation and numerous small superficial translational or rotational landslides, earthflows and debris flows. These

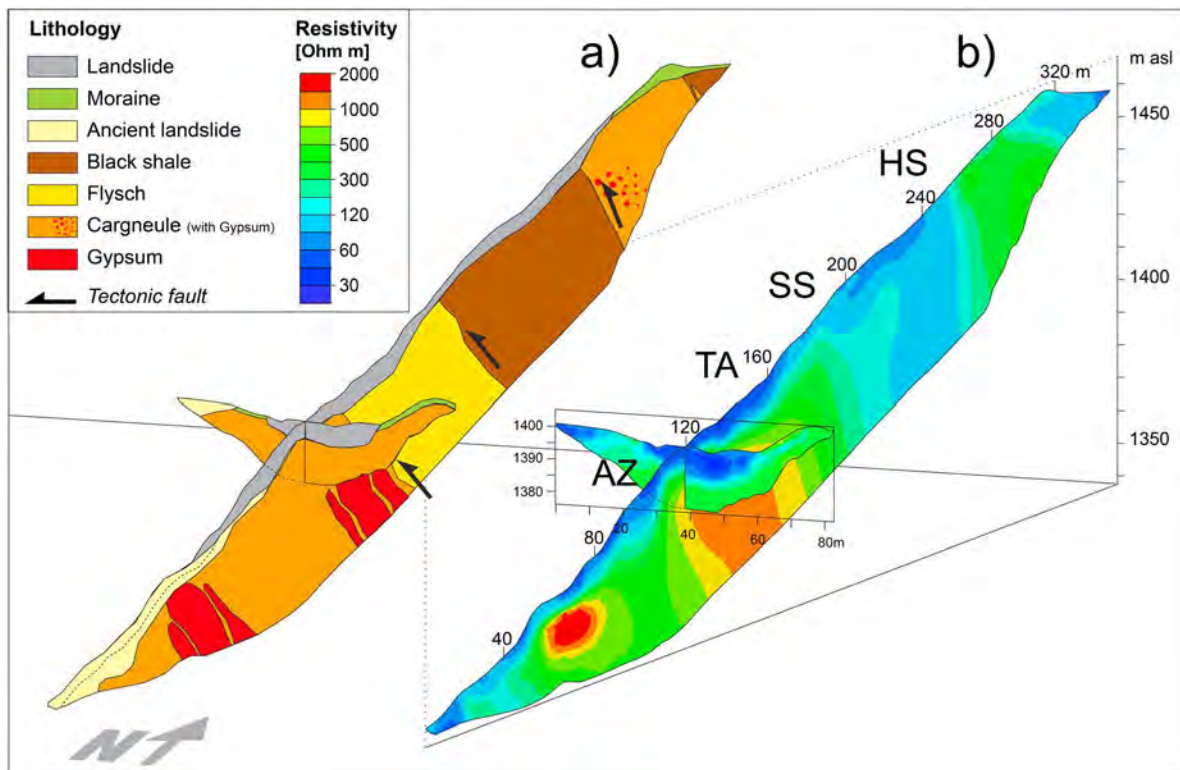


Figure 2. (a) North-south geological cross section along the Pont Bourquin landslide, constructed from the local geological atlas [Badoux *et al.*, 1990] and the electrical images shown in Figure 2b. (b) North-south and east-west oriented electrical resistivity tomography profiles (see location in Figure 1). The head-scarp (HS), main secondary scarp (SS), transportation area (TA), and accumulation zone (AZ) are also indicated.

multiple erosive processes gradually created a bulge of highly deformed material (accumulation zone labeled AZ in Figures 1 and 2) that progressively loaded the lower part of slope (see also Text S1 in the auxiliary material).¹ This material accumulation led to the toe failure between 18 and 20 August 2010, following significant cumulative rainfall in July.

2.2. Geological Context

[6] According to the geological map [Badoux *et al.*, 1990] the Pont Bourquin landslide is located in a tectonically very complex zone. Three thrust faults dipping approximately 35° toward the North cross the landslide and separate distinctive geological formations (Figure 2a). In the upper and lower parts of the slope, the bedrock is composed of Triassic cargneule (cellular dolomite) associated with gypsum. These highly soluble and deformable rocks could have promoted slope destabilization at the landslide toe. Below the cargneule layer, the upper part of the slope is made of Aalenian black shale, the weathering of which is the main source of the sliding clay material. In the middle part of the slope, the landslide overlies flysch consisting of thin-bedded turbidites including siltstone and conglomerate. The top of the hill is covered by several meters of moraine deposits. The rocks have been heavily fractured by the Alpine orogeny and

subsequently affected by toppling, chemical weathering and freeze and thaw cycles, which contributed to a high degree of fragmentation of the outcropping rocks. These alterations have resulted in muddy material that can give rise to numerous small earthflows and debris flows along the slope. Deposits resulting from ancient mass movements locally cover the lower part of the slope. The present day landslide mass is mainly composed of a mixture of moraine material, mainly visible in the upper part, and weathered debris from the Aalenian black shale, flysch sandstone and marl alternations, making the sliding material predominantly clayey. According to the classification proposed by Cruden and Varnes [1996], this landslide can be termed an active composite earthslide-earthflow.

2.3. Geophysical Investigation

[7] In order to clarify the landslide geometry and the geological structure underneath, two electrical resistivity tomography (ERT) profiles E1 and E2 were collected (see location in Figure 1), along and perpendicular to the slope, respectively. Data were acquired using the Wenner-Schlumberger configuration [Dahlin and Zhou, 2004] with 64 electrodes and an electrode spacing of 5 m and 1.5 m for E1 and E2, respectively. Data were inverted through a least squares inversion (L2-norm) using the RES2DINV software [Loke, 1998]. ERT images have been obtained for a RMS value lower than 5%. Electrical images are shown in Figure 2b. The superficial clay-rich sliding layer is clearly

¹Auxiliary materials are available in the HTML. doi:10.1029/2011JF002159.

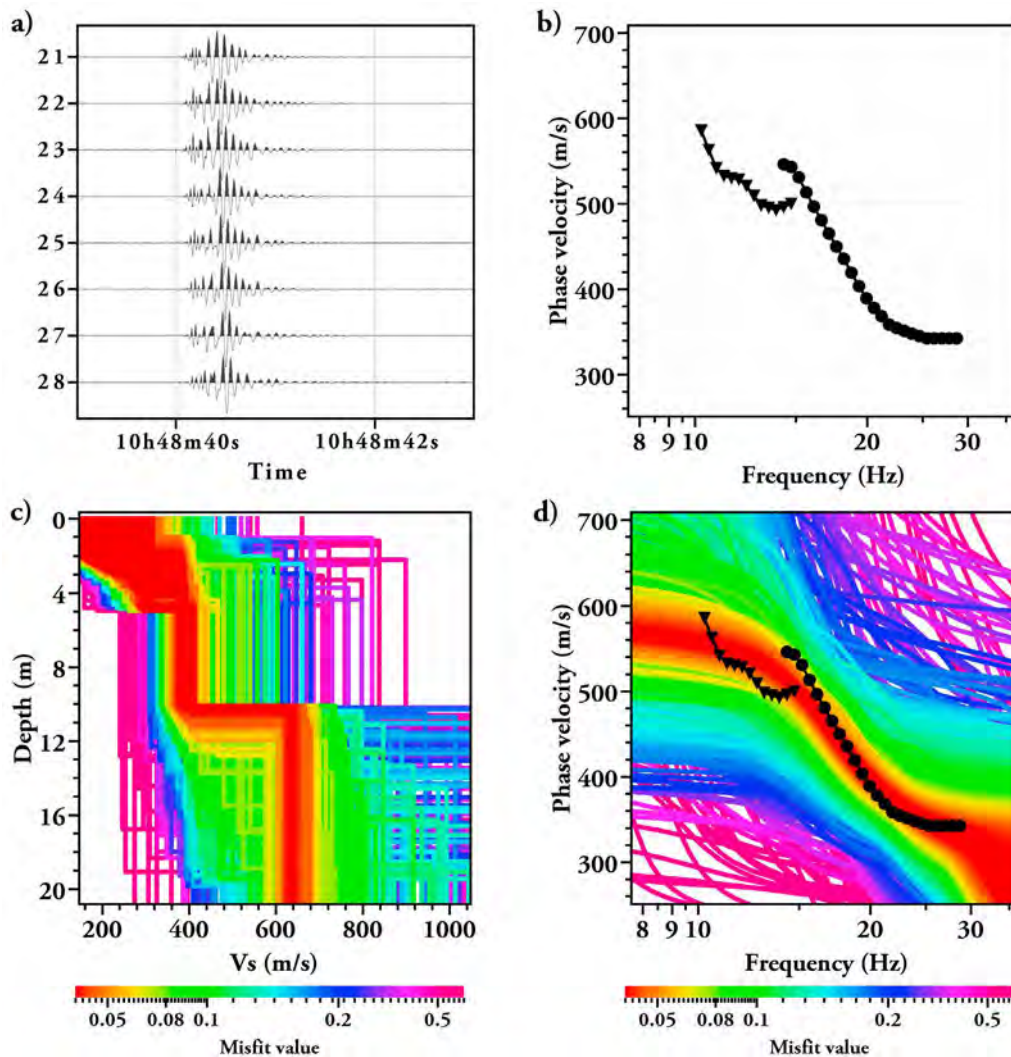


Figure 3. Shear wave velocity determination from the Rayleigh waves measured along two perpendicular profiles (same location as E1 and E2, Figure 1). (a) Normalized raw signals along profile 1. The spacing between geophones is 5 m. (b) Phase velocity dispersion curves computed from profiles 1 (triangles) and 2 (circles). (c) V_s profiles resulting from the inversion of dispersion curves with a three-layer model. (d) Dispersion curves corresponding to the models shown in Figure 3c.

evidenced by a resistivity lower than 100 ohm m, with a thickness varying from a few meters to locally more than 10 m along the profile. This low resistivity results from the high percentage of saturated clay in the sliding mass and from the high salinity of the water (total salinity greater than 1500 mg/l in superficial water between S1 and S2, Figure 1). The potentially mobilized volume of the whole landslide is estimated to be 30,000 to 40,000 m³. Below the sliding material, the cargneule and gypsum formations at the top and bottom of the slope can be distinguished by their higher resistivity (from 200 to 500 ohm m in the cargneule and up to 2000 ohm m in gypsum). Conversely, the black shales are characterized by low resistivity values ranging from 100 to 200 ohm m. Finally, the flysch formation has a resistivity between 200 and 500 ohm m, a range similar to that measured for the cargneule. The combination of the two electrical images and geological observations has yielded the interpretative cross section of Figure 2a.

[8] Two active seismic profiles were performed along and across the landslide (same location as the electrical profiles E1 and E2). The surface wave inversion technique was applied to 8 signals recorded in the accumulation zone of the landslide to infer the shear wave velocity profile in this area. For the longitudinal profile, signals were generated with explosive shots and recorded by 8 geophones 5 m apart (channels 21 to 28, Figure 3a). For the second transverse profile (between S1 and S2), the source was a hammer striking a plate, and the records from 8 geophones located within the landslide (4 m intertrace distance) were processed. The Rayleigh wave phase velocity dispersion curves were computed along the two perpendicular travel paths (Figure 3b), using the frequency-wave number technique [Lacoss *et al.*, 1969]. The two dispersion curves cover the 10–30 Hz frequency range, according to the frequency of the sources (explosive and hammer), and partly overlap around 15 Hz. The 10% difference in phase velocity around 15 Hz

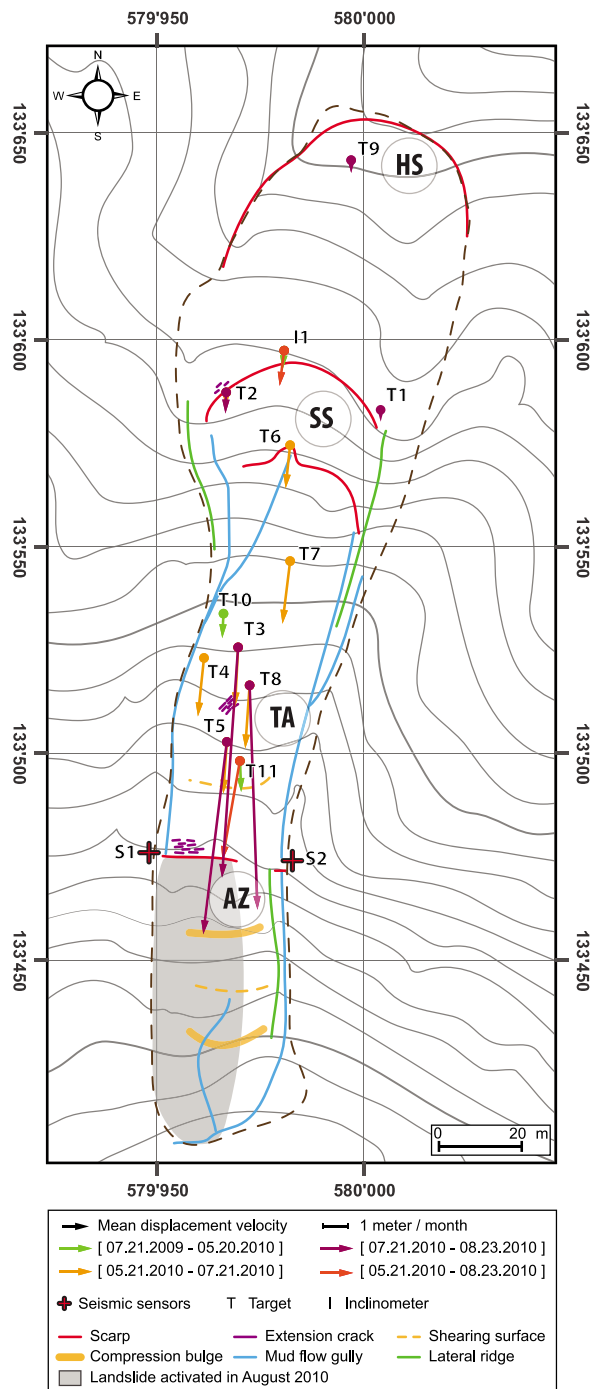


Figure 4. Mean velocity (meters per month) of 12 targets (T1–T11 and I1), monitored since July 2009 by Differential Global Navigation Satellite System (D-GNSS) and May 2010 by Electronic Distance Meter (EDM). In the top part of the landslide, displacements did not exceed 1 m between 20 May 2010 and 23 August 2010, while they exceeded 20 m in the middle of the transportation area during these 3 months, which considerably loaded the accumulation zone (AZ). (Topography outside the landslide: high-resolution Digital Elevation Model data from Swisstopo; topography inside the landslide: terrestrial laser scanning (TLS) data from UNIL.)

(500 to 550 m/s) probably results from different spatial variations along the two profiles. Dispersion curves were inverted using the enhanced neighborhood algorithm [Wathelet, 2008], assuming a 1D structure along the two directions below the accumulation zone. The misfit function is defined by the following equation:

$$misf = \sqrt{\frac{1}{n} \sum_{i=1}^n \frac{(c_{di} - c_{ci})^2}{c_{di}^2}}, \quad (1)$$

where c_{di} is the phase velocity of the data curve at frequency f_i , c_{ci} is the velocity of the calculated curve at frequency f_i , and n is the number of frequency samples. The inversion was constrained by imposing a thickness higher than 10 m for the clay-rich sliding layer, in agreement with the electrical data.

[9] Figure 3c shows the computed S wave velocity profiles with the misfit values for a three-layer model. The shear wave velocity in the superficial layer of a few meters thick is poorly constrained, owing to the lack of information at high frequency. Below, the best fitting models (misfit lower than 5%) show that the seismic velocity in the landslide is between 360 and 420 m/s. The bottom of this layer is found at a depth of about 11 m. Below this depth, the velocity increased to about 640 m/s in the undisturbed layers. Figure 3d displays all dispersion curves corresponding to the models obtained, with good agreement being shown between models and observations.

2.4. Groundwater Level Monitoring

[10] The level of the water table was measured in one 5 m deep borehole located in the accumulation zone (see Figure 4 for location). The system consists of a piezometer sensor connected to a data logger operated continuously, and a barometer to correct the water table height from the atmospheric pressure fluctuations. During the experiment time (April to August 2010), the measured water table fluctuated from 3.7 m depth to less than 1 m (see section 4.1).

3. Displacement Monitoring

3.1. Surface Displacement From GNSS and Electronic Distance Meter

[11] In order to evaluate the activity of the Pont Bourquin landslide, the displacement of twelve targets placed on the surface was recorded. Three targets (I1, T10 and T11, see location in Figures 1 and 4), were monitored from summer 2009 until August 2010 using a Differential Global Navigation Satellite System (D-GNSS) [U.S. Army Corps of Engineers, 2003]. The data were acquired by two Topcon HiPer® Pro antennas tracking their position from the Russian and American geodesic satellite constellations. The field procedure followed the Real Time Kinematic (RTK) method. A base station antenna was set up on a unique reference point location close to the landslide (about 650 m away). Targets on the landslide were 3D located with the second GNSS antenna (rover station), using the correction information communicated by the base station. Instrumental accuracy is ~ 12 mm [Gili et al., 2000], which is considered negligible with regards to the observed meter-scale displacements. Nine additional targets (T1–T9) were installed

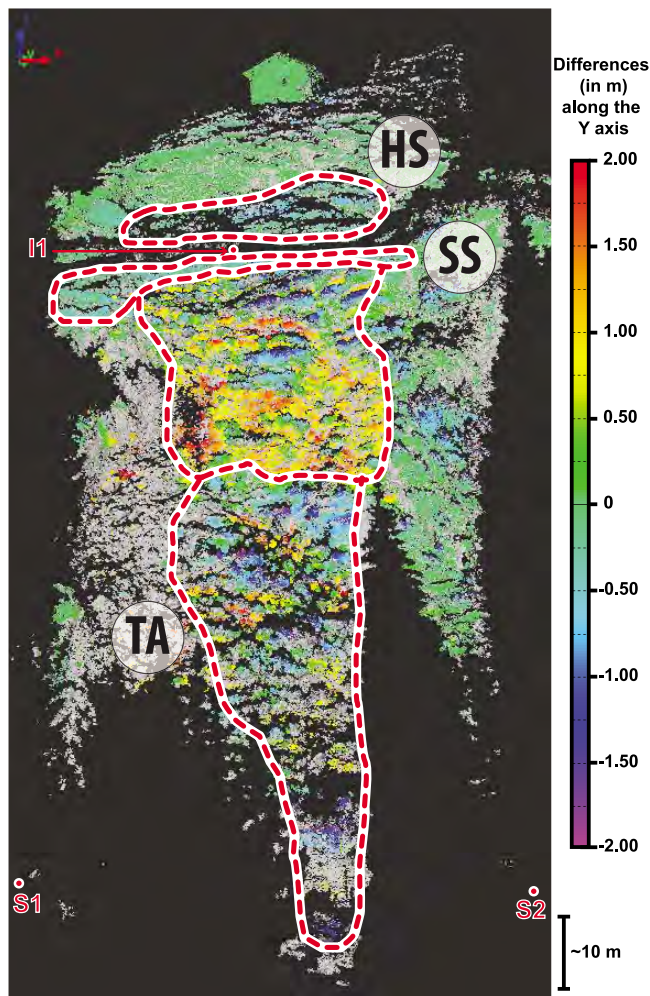


Figure 5. Differences (in m, southward, i.e., along the y axis) between two point clouds acquired by TLS on 19 May 2010 and on 20 July 2010. Positive (accumulated material) and negative (eroded material) movements are shown in red and blue, respectively. Black indicates no data, and gray indicates unreliable data. Red dashed lines isolate particular areas of the landslide. Small erosion of the head scarp (HS) by flowing processes. Retrogression of the most active secondary scarp (SS) through small and discontinuous translational landslides. Very active creeping inside the transportation area (TA). The locations of the inclinometer (I1) and the seismometers (S1 and S2) are indicated. The accumulation zone located between S1 and S2 could not be monitored by TLS because of forest cover.

in spring 2010 and have been periodically monitored with a Topcon GPT-9003M reflector total station [U.S. Army Corps of Engineers, 2007]. For each measurement campaign, the device was first installed at a reference point (the same as the GNSS base station) having a direct line of sight to the landslide and orientated by shooting at a reference prism located in a stable area close to the landslide, the coordinates of which were measured by D-GNSS.

[12] The surface displacements presented in Figure 4 exhibit an acceleration during summer 2010, before the slope failure. Active creeping in and above the accumulation

zone was evidenced by D-GNSS and EDM data (arrows in Figure 4). From July 2009 to May 2010 (green arrows), displacement rate values were lower than 1 m/month. From 21 May to 21 July 2010 (orange arrows), a mean displacement rate of 6 m/month was measured by four targets in the transportation zone. The motion in this zone accelerated from 21 July to 23 August 2010 (purple arrows), when displacements ranging from 17 m up to 21 m were recorded in one month on the same targets. In the meantime, sliding velocities at the head and the secondary scarps were lower than 0.5 m/month.

3.2. Terrestrial Laser Scanning

[13] Terrestrial laser scanning (TLS) was regularly performed from April to September 2010 in order to monitor ground motions over the whole slope. TLS is a remote sensing technique capable of obtaining local images of the earth's 3D topography by acquiring point clouds of the ground position [Baltsavias, 1999; Lichten et al., 2002]. TLS involves sending a laser pulse in a known direction and the distance is evaluated by measuring the return time of the pulse reflected by the ground surface. Scanning on a regular grid provides images of several million points. The TLS device was an Optech ILRIS-3D-ER using a laser with a 1500 nm wavelength and with maximum acquisition distance ranging from 800 to 1200 m.

[14] The TLS data acquisition and processing followed these main stages: (1) the point clouds of the upper part of the Pont Bourquin landslide were acquired from the same scanning point of view at different epochs with a mean resolution of 30 mm (average distance between points); (2) two TLS points clouds, from May and July 2010, were selected in order to extract the two months displacements prior to the August event; (3) each points cloud was cleaned, deleting outliers and vegetation masking the ground, using the Pifedit software (InnovMETRIC); (4) the reference point cloud (May 2010) was georeferenced using PolyWorks® v10, ImAlign module, wrapping it on the regional 1 m DEM using the iterative closest point algorithm [Besl and McKay, 1992] implemented in PolyWorks®; (5) the second point cloud (July 2010) was aligned and wrapped on the reference cloud with the iterative closest point algorithm, ignoring the unstable area; and (6) the displacements were measured using PolyWorks® v10, ImInspect module. The method computed the horizontal difference between the two surfaces along a north-south axis (i.e., the y axis, parallel to the landslide main displacement direction). The error was assumed to be smaller than the alignment error (standard deviation of 35 mm) using the iterative closest point algorithm between the two scans, which was considered small compared to the total displacement.

[15] As shown in Figure 5, TLS surface displacement data, acquired between May and July 2010, can be separated into several distinct areas. On the head scarp, erosion has been recorded, highlighting the occurrence of small earthflow events with a topographic change of less than 0.7 m. In contrast, the middle section of the Pont Bourquin landslide, below the secondary scarp, has been very active and affected by several small translational sliding events shown by positive and negative displacements greater than 1 m in two

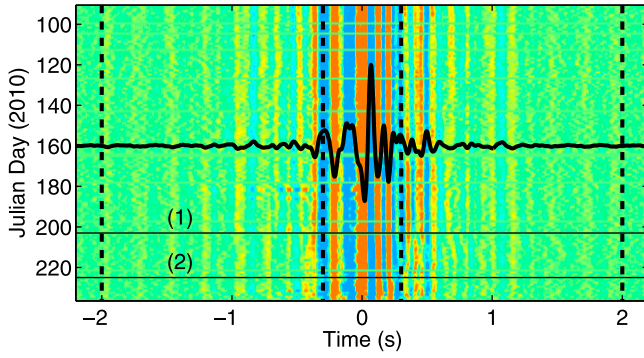


Figure 6. Daily cross correlations of ambient seismic noise recorded by S1 and S2 from day 91 to day 236, in the 4–25 Hz frequency range. Amplitude is normalized each day. The reference trace, averaged over all the correlograms, is displayed by the continuous thick line. Vertical dotted lines mark the time window of the coda used to estimate the relative velocity change dV/V . Early arrivals (between -0.2 s and $+0.2$ s) are not taken into account in this study. Horizontal lines 1 and 2 mark the days for which a velocity drop is observed (see Figure 7).

months. Large positive motions exceeding 1 m were recorded in the transportation zone (see also Text S1).

4. Ambient Noise Monitoring

4.1. Experimental Procedure and Relative Velocity Change

[16] In order to monitor the change in seismic properties of the material constituting the bulk of the landslide, two seismic sensors S1 and S2 (2 Hz three-component velocimeters) were placed 35 m apart in stable ground on both sides of the landslide (Figures 1, 4, and 5), outside of the active landslide. Moreover, no evidence of recent ground deformations was observed at the two seismometer locations. They were buried at a depth of about 40 cm, to avoid atmospheric thermal effects. They were both connected to the same 24 bit Kephren acquisition station for digitization (at 250 Hz) and data storage. Vertical vibrations were continuously recorded from 1 April to 24 August 2010 and stored in 1 hour long records named $s_1(day, i, t)$ and $s_2(day, i, t)$, respectively, where the subscripts stand for the sensor number, day for the date and i for the hour.

[17] The records were studied in the 4–25 Hz frequency range, which corresponds to Rayleigh wave penetration depths ranging from a few meters to a few tens of meters, thus sampling the landslide properly. From direct observations during the field experiments, two main sources of ambient noise were identified in this frequency band: the wind in the trees and the traffic along the road at the foot of the landslide. While the noise from both sources may be variable in time, the important feature for monitoring is that their locations are stable [Hadziioannou et al., 2009]. Moreover, although the traffic is not stable in the short term, it statistically stabilizes when averaging over a day, as will be shown below. Although these two sources dominate the seismic noise records, it cannot be excluded that additional distant sources might play a role here, but this issue cannot be studied using a two-sensor experimental setup.

[18] As a first processing step, records were whitened in the 4–25 Hz frequency band. This procedure renormalizes the Fourier transform of s_i at each frequency by its absolute value to ensure that all frequencies in the bandwidth of interest have a similar statistical contribution:

$$\tilde{s}_i(day, i, t) = IFFT \left(\frac{FFT(s_i(day, i, t))}{|FFT(s_i(day, i, t))|} A(\omega) \right), \quad (2)$$

where $A(\omega)$ is an apodization window in the frequency domain, which shows a smooth transition from 0 (out of the 4–25 Hz range) to 1 (within the 4–25 Hz range).

[19] Then, 24 h cross correlations were calculated and averaged each day, yielding 146 daily correlograms h_{day} for the period of interest:

$$h_{day}(\tau) = \left\langle \int \tilde{s}_1(day, i, t) \tilde{s}_2(day, i, t + \tau) dt \right\rangle_{i=0..23}. \quad (3)$$

Figure 6 shows the daily cross correlations obtained from Julian day 91 to Julian day 236, along with the reference waveform h_{ref} obtained by averaging all the correlograms. Daily correlations were then filtered at successive center frequencies f_c from 5 Hz to 23 Hz with a 2 Hz bandwidth. For each frequency f_c , correlations are compared to the reference. In the case of a homogeneous velocity change dV , all the waveforms constituting the correlograms are shifted in time by a factor dV/V . To measure this relative velocity change, the stretching technique [Sens-Schönfelder and Wegler, 2006; Hadziioannou et al., 2009] was applied, which consists in testing several possible velocity changes dV/V by resampling the correlograms in time $h_{day}^f(t) \rightarrow h_{day}^f(t(1 + dv/v))$. The actual relative velocity change dV/V at a given date day maximizes the correlation coefficient:

$$CC \left(\frac{dV}{V} \right) = \frac{\int h_{day}(t(1 + dV/V)) h_{ref}(t) dt}{\sqrt{\int h_{day}(t(1 + dV/V))^2 dt \int h_{ref}(t)^2 dt}}. \quad (4)$$

The asymmetry of the correlograms in the central part $[-0.2$ s– 0.2 s] (Figure 6) is due to the imperfect spatial distribution of noise sources. Signals observed around $\tau = 0$ correspond to waves traveling from the (unknown) sources to the receivers. As these early direct waves (P, S and Rayleigh) are very sensitive to changes in the noise source position, they were removed by considering the portion of the correlograms in the range $[-0.2$ s– -2 s] and $[0.2$ s– 2 s], delimited by vertical broken lines in Figure 6). This time range begins after the slowest Rayleigh wave between the two sensors and ends when the amplitude of the correlations is low and the waveforms fluctuate too much from one day to another. Consequently, these time windows correspond to coda waves which have sampled the region around and between the seismic sensors [Pacheco and Snieder, 2005; Rossetto et al., 2011]. The coda is essentially made up of surface waves [Larose et al., 2006; Sens-Schönfelder and Wegler, 2006; Brenguier et al., 2008a, 2008b], i.e., Rayleigh waves for the vertical components used here. The relative phase velocity changes were analyzed for 2 Hz wide frequency bands between 4 and 25 Hz. A significant variation versus time was found in the 10–12 Hz range (Figure 7a). Figure 7a also shows the water table level. Figure 7b displays the plot of the correlation coefficient CC between the reference and the current

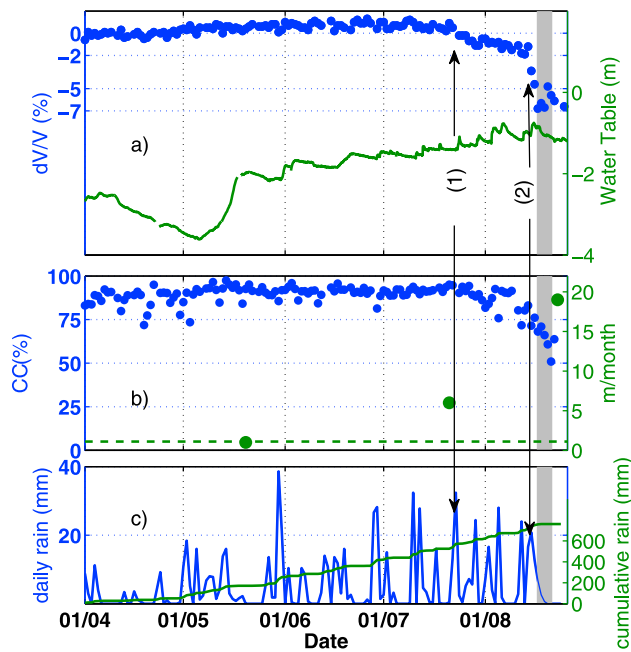


Figure 7. (a) Green represents the water table, and blue represents the relative Rayleigh wave seismic velocity change of the material obtained by comparing daily seismic noise correlograms in the 10–12 Hz frequency range. Vertical line 1: the first velocity reduction starts after rainfall on 23 July and represents a drop of 2% developing over 20 days. Vertical line 2: the major drop starts after rainfall on 14 August, with a total decrease of 7% over the 4 days preceding a major failure of the landslide. The vertical shaded area marks the days of the failure (around 19 August). The correlation coefficient CC , from which the absolute error in estimating dV/V can be derived. This absolute error is 1% for all the data except the last 10 days, where it increases to 2%. (c) Daily (blue) and cumulative (green) precipitation, which cannot alone be used to predict the failure.

correlation (see equation (4)). From this coherence, the absolute error of dV/V can be estimated following *Weaver et al.* [2011]. This error is 1% for all the data except during the last 10 days when it increases to 2%. Figure 7b also gives the average monthly displacement of the landslide computed from the four D-GNSS campaigns. These data show an acceleration of the landslide during summer 2010, but with a limited temporal resolution inherent to this observational technique. Finally, the daily precipitation and the cumulative rainfall are displayed in Figure 7c.

[20] From the beginning of April to the middle of July 2010, the apparent Rayleigh wave velocity was relatively stable: observed velocity fluctuations are smaller than 1%. From mid-May to mid-July, the cumulative rainfall, along with the groundwater level in the piezometer borehole (Figures 7a and 7c), rose linearly with time. Groundwater reacted with a delay of about 20 h to rainfall inputs, suggesting that water infiltration was controlled by soil permeability. On July 24, after a short rainfall event and the corresponding delayed groundwater elevation, the apparent Rayleigh wave velocity (Figure 7a) underwent a gradual decrease of 2% over 20 days. On 15 August, after a series of intense precipitation events and related increases in the water

table, the apparent velocity dropped by 7% in only 4 days. While losing its rigidity, the creeping material reached its stability limit and the slope failed, with a composite earthslide-earthflow event. This catastrophic event occurred between 18 and 20 August. As the mud accumulation at the slope toe directly threatened the road, slope reprofiling and drainage works were initiated on 21 August, which led to the seismic devices being dismantled.

4.2. Spectral Analysis of the Relative Velocity Change

[21] Figure 8 displays the Rayleigh wave phase velocity variation evaluated for each frequency band during the

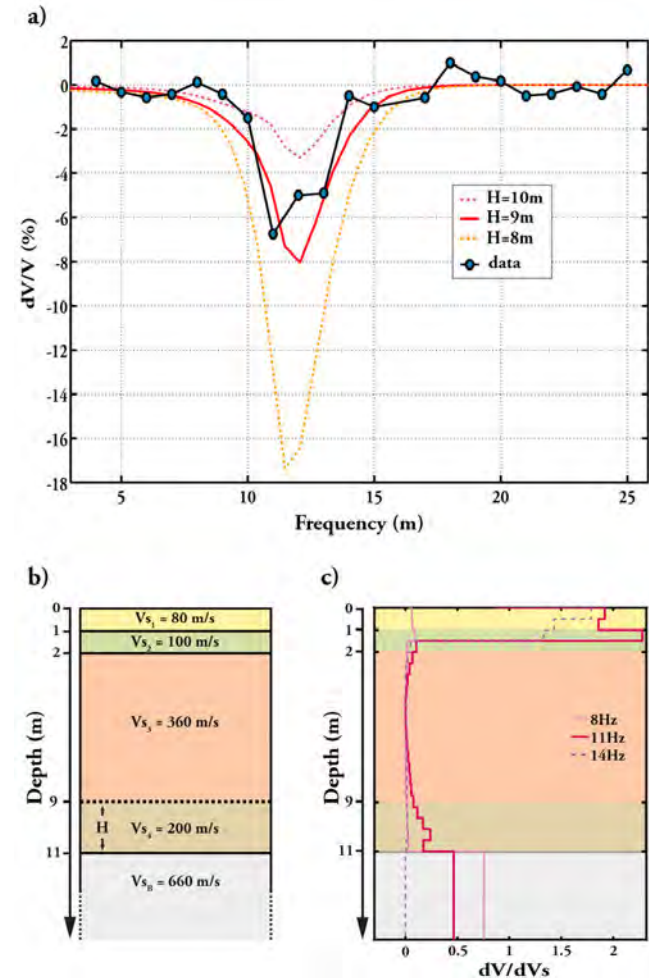


Figure 8. (a) Relative velocity variation dV/V (%) observed in the coda of the correlations for the 5 days preceding the slope failure, for various frequencies (± 1 Hz around central frequency). The velocity drop is observed mainly in the 10–14 Hz frequency range, corresponding to the lower layer of the sliding material (depth from about 9 to 11 m). Models with different thickness layer (continuous and dotted lines) were tested, and a good fit was obtained with $H = 2$ m and $V_s = 200$ m/s in the layer (Figure 8b). (b) V_s model obtained from geophysical prospecting and by fitting the characteristics of the low-velocity layer above bedrock (see section 4.2 for details). (c) Rayleigh wave depth sensitivity kernel computed at the frequencies 8 Hz, 11 Hz, and 14 Hz for the model in Figure 8b.

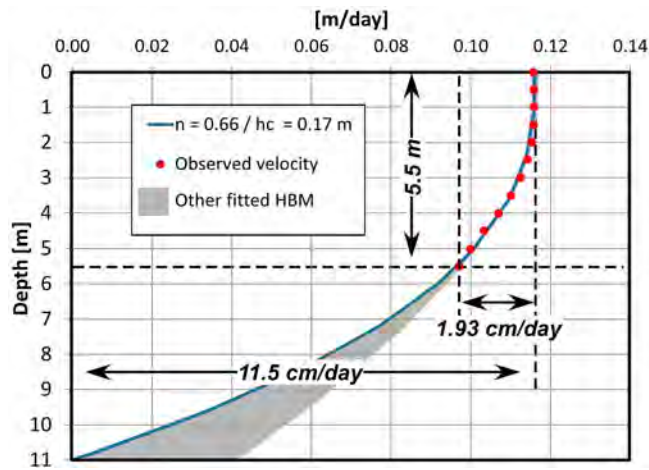


Figure 9. Red dots are observed displacement rates versus depth. Blue line represents velocity profile (corrected for the slope) computed from the Herschel-Bulkley model (HBM) with the fit parameters $n = 0.66$, $h_C = 0.17$ m ($t_C = 1.4$ kPa), and $\mu_n = 1.7 \times 10^{9N} \text{ m}^{-2} \text{ s}^n$. The shaded area shows all the HBMs fitting well the data (the coefficient of determination of the fitted law is $r^2 = 0.98$). The model giving the greatest velocity at the surface was chosen because it is closer to the observed surface velocities.

5 days before slope failure. It shows that the seismic velocities for frequencies below 10 Hz and above 14 Hz remained unaffected during the course of the experiment and that the velocity drop occurred at a depth related to the sensitivity of Rayleigh waves in the range 10–14 Hz.

[22] In order to define the depth of the change in the sliding material, an analysis of the depth sensitivity of the Rayleigh wave versus frequency is performed similarly to Rivet *et al.* [2011]. An initial numerical model was created from geophysical a priori information and field observations (Figures 2 and 3). From the active seismic profiles, the bedrock depth was fixed at 11 m with $V_{sB} = 640$ m/s. This bedrock is overlain with a softer layer with a velocity $V_{s3} = 360$ m/s. Several tests quickly showed that the change at 14 Hz observed in Figure 8a can only be obtained when introducing superficial low V_s layers ($V_{s1} = 80$ m/s; $V_{s2} = 100$ m/s) with a total thickness of 2 m. From this model (Figure 8b) the initial dispersion curve of Rayleigh waves (similar to observations before the slope failure) was then computed, using the method proposed by Dunkin [1965] and implemented in the geopsy software (<http://www.geopsy.org>). A series of models with a soft layer (thickness H and V_{s4}) added at the bedrock top was then tested. Figure 8a shows the relative phase velocity differences between the initial and perturbed models, computed for three different thickness values ($H = 1, 2$ and 3 m) and for a shear wave velocity of $V_{s4} = 200$ m/s. The best correlation with experimental data was obtained for a thickness $H = 2$ m (red line). A multitude of realistic models (changing H and V_{s4}) were created to test the uniqueness of this solution and no other simulated model was found consistent with observations. Finally, we computed the Rayleigh wave sensitivity kernels dV/dV_s as a function of depth for the fundamental mode in order to assess how well the depth localization of the low-

velocity layer is constrained. Computations were made for the proposed velocity model at the three frequencies 8 Hz, 11 Hz and 14 Hz (Figure 8c), using the software developed by Herrmann (<http://www.eas.slu.edu/People/RBHerrmann/>), and the sensitivity curves are displayed in Figure 8c. At 8 Hz and 14 Hz, phase velocities are only sensitive to V_s variations in the bedrock and in the shallow layers, respectively. In contrast, the phase velocity at 11 Hz is sensitive to V_s changes both in the shallow layers and, to a less extent, in the two meters above the bedrock interface. However, as no variation was observed on the dV/V curve for 14 Hz (Figure 8a), the drop at 11 Hz results from a variation in V_s above the bedrock, corroborating our analysis. The frequency range for which a velocity reduction is observed then corresponds to a V_{s4} decrease from 360 m/s to 200 m/s in a 2 m thick zone located in the lower part of the sliding layer (from 11 to 9 m depth). These results have proved to be robust when varying the characteristics of the soft superficial layers.

4.3. Rheological Analysis of the Inclinometer Data

[23] The depth and intensity of the relative velocity change has been compared with inclinometric data collected in 2009, and with the subsequent rheological considerations derived from them. The 17–21 m surface displacements measured from 21 July to 23 August 2010 can be explained by (1) basal sliding, (2) deformation over a given thickness resulting from a change in rheological properties or (3) both the above factors. Simulating the propagation of the 2007 mudflow using the BING software [Imran *et al.*, 2001] demonstrated that the first hypothesis was not valid [Jaboyedoff *et al.*, 2009]. The only way to explain surface displacements was to introduce a viscoplastic law, like the Herschel-Bulkley model (HBM) [Coussot, 1997; Huang and Garcia, 1998]. A change in the rheological properties over a certain thickness is also strongly supported by the seismic velocity changes observed in the bulk of the lower part of the sliding material. Here we investigate the most probable rheological model, analyzing the inclinometer data.

[24] In June 2009, about 1 year before the seismic noise experiment, a borehole (I1; 5.5 m deep) was drilled at the top of the Pont Bourquin landslide (see location in Figures 1 and 4). It was equipped with an inclinometer casing. Inclinometer measurements were taken over a short period of time (a few days) after which the high deformation rates destroyed the casing. Since the landslide did not evolve too much from June 2009 to June 2010, the vertical distribution of the deformations in 2010 must be similar to the one obtained in 2009. The velocities were calculated from the inclinometric data. Measurements were projected along the vertical direction assuming an average slope of $\beta = 25^\circ$. These data indicate a maximum southward surface displacement of 15.5 cm in 8 days, from 24 June 2009 to 1 July 2009. This motion corresponds to a surface velocity of 1.93 cm/d over a thickness of 5.5 m (Figure 9), with a thin layer in rigid motion overlying a thick layer affected by continuous shearing. The strain rate was found to be negligible at the surface of the profile and accelerates below a depth h_C . This suggests a viscoplastic behavior of the sliding material. Rheological studies of mud have shown that it can be modeled as a non-Newtonian fluid exhibiting a yield

stress and the HBM was found to be appropriate in fitting the rheological data [Cousso, 1997]. In the HBM, the velocity profile $u(z-h_c)$ at a depth $z \geq h_c$ follows the equation

$$u(z) = u_s - \frac{n}{n+1} \left(\frac{\rho g (z - h_c)^{n+1} \sin(\beta)}{\mu_n} \right)^{1/n}, \quad (5)$$

where u_s is the velocity at the surface, n is the exponent of the HBM, h_c is the plug layer (unsheared) thickness, ρ the material density, g the gravity, β the slope angle, μ_n the dynamic viscosity [$\text{N m}^{-2} \text{s}^n$], and z is the axis perpendicular to the slope.

[25] The yield stress τ_C is related to h_C by

$$\tau_C = \rho g h_C \sin(\beta). \quad (6)$$

The HBM was fitted by minimizing the absolute difference between theoretical values and raw data. The best fitting curve (Figure 9) was obtained for the following parameters: $\mu_n = 1.7 \times 10^9 \text{ N m}^{-2} \text{ s}^n$, $n = 0.66$, $h_c = 0.17 \text{ m}$ and $\tau_C = 1.4 \text{ kPa}$. The HBM was then used to extrapolate the surface displacement velocity to the base of the sliding material at a depth of 11 m. This depth was deduced from the electrical tomography and the V_s profile. The surface velocity obtained from the HBM is equal to 11.5 cm/d (Figure 9). This surface displacement rate is of the order of magnitude of the observed surface velocity at the center of the landslide (18.2 cm/d) during the period from 20 May to 21 July 2010. The discrepancy between observed and calculated data is interpreted as a slip along a basal surface of the slide. These results indicate that 70% of the displacement rate occurred between 7 m and 11 m depth, and highlight the deformation at the base of the sliding layer, already shown by the relative velocity changes derived from surface waves. The 2010 landslide interpretation is that the gravitational stress locally increased in the accumulation zone and exceeded the yield stress, generating a decrease in the material rigidity, as observed by the ambient noise measurements.

5. Discussion and Conclusions

[26] The Pont Bourquin landslide is a composite active wet earthslide-earthflow composed of clayey material with rock debris, continuously affected by numerous internal and superficial mass movements, as illustrated by the 2007 and 2010 events. From geophysical surveys, the depth of the main slip surface spatially ranges from a few m to about 11 m. Surface displacement monitoring has shown that the mass slides at mean velocities of about one to a few m/month and that a significant velocity increase in and above the accumulation zone was observed in July and August 2010, before slope failure. Due to continuous landslide activity, a bulge of remolded material (observed by Terrestrial Laser Scanning and Electronic Distance Meter) accumulated in the zone where the 2010 failure occurred. From ambient noise measurements and processing, a significant drop (7%) in Rayleigh wave velocity was observed a few days before the event, after an initial gentler decrease (2%). The frequency range (10–14 Hz) for which this drop occurred corresponds to a decrease in shear wave velocity in a 2 m thick layer located between 9 m and 11 m. This significant velocity decrease is interpreted as resulting from the

decay in clay mechanical property (rigidity) in the lower part of the layer in motion, precluding the rupture. This is in agreement with a yield stress viscoplastic behavior, for which the material flows once a critical yield stress has been exceeded. For the 2010 event, the gravitational stress was locally increased by the long-term accumulation of the displaced material.

[27] This study has shown that it is possible to detect mechanical behavior changes in the sliding material by monitoring ambient seismic noise, which offers new insights into the rheology of landslides. The observed significant drop in seismic velocity prior to slope failure suggests that time-dependent variation in this parameter could be a valuable precursor. This method could be applied to all clay-rich earthslides, particularly those regularly affected by earthflows and debris flows occurring in the same areas, i.e., at the boundary between the accumulation zone and a lower well-defined narrow track area [Malet *et al.*, 2005; Picarelli *et al.*, 2005]. For large earthslides, small-scale earthflows can be independently triggered all along the different scarps, and a more complex array of receivers would then be required. From a methodological point of view, the present method could be applied where the background seismic noise is excited at frequencies that are relevant to monitor the structure: from the order of 1 Hz for deep and thick edifices (100 m or more) to a few tens of Hz for shallower ones (a few meters depth). Three conditions are requested to apply the method: (1) at least some sources of ambient noise have to remain stable in position during the observation time (river, road, factories, wind or oceanic activity), (2) the subsurface in the area is not affected by other external changes than the landslide itself (large excavation works, mining), and (3) the receivers have a fixed and stable position and orientation.

[28] The method, which has proved to be efficient in a clay-rich landslide, could also be successfully applied in coarser material, including loose sandy soils, provided that a precursor rigidity change can be observed. In large-scale landslide experiments on loose sandy soils, rapid movements were triggered by rising pore water pressure [Iverson *et al.*, 2000]. During the precursory period, the wetting caused soil compaction and a decrease in porosity from 0.52 to 0.49 (6% variation). No V_s measurement was made during this experiment, but we can try to estimate the V_s change resulting from this porosity decrease. Fawad *et al.* [2011] performed V_s measurements during the compaction of sand samples and calibrated an effective law to relate V_s and the porosity for different stresses. Using this law, the porosity decay measured by Iverson *et al.* [2000] is expected to provoke a V_s increase of more than 10%, a value far over the 2% velocity change detected in the Pont Bourquin landslide. These results give hope that the application of ambient seismic noise monitoring could be extended to rapid mass movements in coarse soil. In rocks, ambient noise measurements were recently applied to study the evolution of the natural frequencies of a rock column until its fall [Lévy *et al.*, 2010]. The cross-correlation technique used in the present study could constitute an alternative to the resonance frequency determination for detecting and monitoring medium changes like fracturing in rock slopes. This issue has to be investigated in the future.

[29] **Acknowledgments.** This work was supported by the French ANR project SISCA, the European project “Mountain Risks” (Marie Curie program), and the Department of Isère (France) through the Pôle Grenoblois des Risques Naturels. E.L. acknowledges support from the ERC WHISPER grant. The seismic experiment was operated and maintained by A. Mariscal and L. Darras. The authors would like to thank L. Baron, A. Pedrazzini, A. Loye, M. Choffet, D. Carrea, T. Planes, L. Chaumond, G. Bacques, P. Bottelin, J. Letort, and V. Lebruc for their participation in the seismic measurements. The authors also thank the editor and three anonymous reviewers for their valuable comments.

References

- Angeli, M. G., A. Pasuto, and S. Silvano (2000), A critical review of landslide monitoring experiences, *Eng. Geol. Amsterdam*, 55, 133–147, doi:10.1016/S0013-7952(99)00122-2.
- Badoux, H., J. H. Gabus, and C. H. Mercanton (1990), Les Diablerets, in *Swiss Geological Atlas*, sheet 1285, scale 1:25000, Swiss Fed. Off. for Water and Geol., Wabern, Switzerland.
- Baltsavias, E. P. (1999), Airborne laser scanning: Basic relations and formulas, *ISPRS J. Photogramm. Remote Sens.*, 54, 199–214, doi:10.1016/S0924-2716(99)00015-5.
- Besl, P. J., and N. D. McKay (1992), A method for registration of 3-D shapes, *IEEE Trans. Pattern Anal. Mach. Intel.*, 14(2), 239–256, doi:10.1109/34.121791.
- Bièvre, G., U. Knies, D. Jongmans, E. Pathier, S. Schwartz, C. van Westen, T. Villemin, and V. Zumbo (2011), Paleotopographic control of landslides in lacustrine deposits (Trièves plateau, French western Alps), *Geomorphology*, 125, 214–224, doi:10.1016/j.geomorph.2010.09.018.
- Brenguier, F., N. M. Shapiro, M. Campillo, V. Ferrazzini, Z. Duputel, O. Coutant, and A. Nercessian (2008a), Towards forecasting volcanic eruptions using seismic noise, *Nat. Geosci.*, 1, 126–130, doi:10.1038/ngeo104.
- Brenguier, F., M. Campillo, C. Hadziioannou, N. M. Shapiro, R. M. Nadeau, and E. Larose (2008b), Postseismic relaxation along the San Andreas fault at Parkfield from continuous seismological observations, *Science*, 321, 1478–1481, doi:10.1126/science.1160943.
- Coe, J. A., W. L. Ellis, J. W. Godt, W. Z. Savage, J. E. Savage, J. A. Michael, J. D. Kibler, P. S. Powers, D. J. Lidke, and S. Debray (2003), Seasonal movement of the Slumgullion landslide determined from Global Positioning System surveys and field instrumentation, July 1998–March 2002, *Eng. Geol. Amsterdam*, 68, 67–101, doi:10.1016/S0013-7952(02)00199-0.
- Coussot, P. (1997), *Mudflow Rheology and Dynamics*, IAHM Monogr. Ser., 272 pp., Taylor and Francis, London.
- Crawford, C. B. (1968), Quick clays of eastern Canada, *Eng. Geol. Amsterdam*, 2, 239–265, doi:10.1016/0013-7952(68)90002-1.
- Crosta, G. B., and P. Frattini (2008), Rainfall-induced landslides and debris flows, *Hydrol. Processes*, 22, 473–477, doi:10.1002/hyp.6885.
- Cruden, D. M., and D. J. Varnes (1996), Landslide types and processes, in *Landslides, Investigation and Mitigation*, edited by A. K. Turner and R. L. Schuster, *Spec. Rep.—Natl. Res. Council., Transp. Res. Board*, 247, 36–75.
- Dahlin, T., and B. Zhou (2004), A numerical comparison of 2D resistivity imaging with 10 electrode arrays, *Geophys. Prospect.*, 52, 379–398, doi:10.1111/j.1365-2478.2004.00423.x.
- Dunkin, J. W. (1965), Computation of modal solutions in layered, elastic media at high frequencies, *Bull. Seismol. Soc. Am.*, 55, 335–358.
- Eilertsen, R. S., L. Hansen, T. H. Bargel, and I.-L. Solberg (2008), Clay slides in the Målselv valley, northern Norway: Characteristic occurrence, and triggering mechanisms, *Geomorphology*, 93, 548–562, doi:10.1016/j.geomorph.2007.03.013.
- Fawad, M., N. H. Mondol, J. Jahren, and K. Bjørlykke (2011), Mechanical compaction and ultrasonic velocity of sands with different texture and mineralogical composition, *Geophys. Prospect.*, 59, 697–720, doi:10.1111/j.1365-2478.2011.00951.x.
- Gili, J. A., J. Corominas, and J. Rius (2000), Using Global Positioning System techniques in landslide monitoring, *Eng. Geol. Amsterdam*, 55, 167–192, doi:10.1016/S0013-7952(99)00127-1.
- Hadziioannou, C., E. Larose, O. Coutant, P. Roux, and M. Campillo (2009), Stability of monitoring weak changes in multiply scattering media with ambient noise correlation: Laboratory experiments, *J. Acoust. Soc. Am.*, 125, 3688–3695, doi:10.1121/1.3125345.
- Huang, X., and M. H. García (1998), A Herschel-Bulkley model for mud flows down a slope, *J. Fluid Mech.*, 374, 305–333, doi:10.1017/S0022112098002845.
- Imran, J., P. Harff, and G. Parker (2001), A numerical model of submarine debris flow with graphical user interface, *Comput. Geosci.*, 27, 717–729, doi:10.1016/S0098-3004(00)00124-2.
- Iverson, R. M., M. E. Reid, and R. G. LaHusen (1997), Debris flow mobilization from landslides, *Annu. Rev. Earth Planet. Sci.*, 25, 85–138, doi:10.1146/annurev.earth.25.1.85.
- Iverson, R. M., M. E. Reid, N. R. Iverson, R. G. LaHusen, M. Logan, J. Mann, and D. L. Brien (2000), Acute sensitivity of landslide to initial soil porosity, *Science*, 290, 513–516, doi:10.1126/science.290.5491.513.
- Jaboyedoff, M., A. Pedrazzini, A. Loye, T. Opikof, I. Güell, M. Pons, and J. Locat (2009), Earth flow in a complex geological environment: The example of Pont Bourquin, Les Diablerets (Western Switzerland), in *Landslide Processes, From Geomorphologic Mapping to Dynamic Modelling*, edited by J. P. Malet, A. Remaitre, and T. Bogaard, pp. 131–137, CERG Ed., Strasbourg, France.
- Keefer, D. K., R. C. Wilson, R. K. Mark, E. E. Brabb, W. M. Brown, S. D. Ellen, E. L. Harp, G. F. Wicczorek, C. S. Alger, and R. S. Zarkin (1987), Real-time landslide warning during heavy rainfall, *Science*, 238, 921–925, doi:10.1126/science.238.4829.921.
- Lacoss, R. T., E. J. Kelly, and M. N. Toksoz (1969), Estimation of seismic noise structure using arrays, *Geophysics*, 34, 21–38, doi:10.1190/1.1439995.
- Larose, E., L. Margerin, A. Derode, B. van Tiggelen, M. Campillo, N. Shapiro, A. Paul, L. Stehly, and M. Tanter (2006), Correlation of random wave fields: An interdisciplinary review, *Geophysics*, 71, S111, doi:10.1190/1.2213356.
- Lee, K. T., and J. Y. Ho (2009), Prediction of landslide occurrence based on slope-instability analysis and hydrological model simulation, *J. Hydrol.*, 375, 489–497, doi:10.1016/j.jhydrol.2009.06.053.
- Lévy, C., L. Baillet, D. Jongmans, P. Mourou, and D. Hantz (2010), Dynamic response of the Chamousset rock column (western Alps, France), *J. Geophys. Res.*, 115, F04043, doi:10.1029/2009JF001606.
- Lichti, D. D., S. J. Gordon, and M. P. Stewart (2002), Ground-based laser scanners: Operation, systems and applications, *Geomatica*, 56, 21–33.
- Loke, M. H. (1998), RES2DINV, Rapid 2D resistivity and IP inversion using the least-squares method, user manual, 66 pp., Adv. Geosci., Inc., Austin, Tex.
- Malet, J. P., D. Laigle, A. Remaitre, and O. Maquaire (2005), Triggering conditions of debris-flows associated to complex earthflows, *Geomorphology*, 66, 215–235, doi:10.1016/j.geomorph.2004.09.014.
- Pacheco, C., and R. Snieder (2005), Time-lapse travel time change of multiply scattered acoustic waves, *J. Acoust. Soc. Am.*, 118, 1300–1310, doi:10.1121/1.2000827.
- Petley, D. N., F. Mantovani, M. H. Bulmer, and A. Zannoni (2005), The use of surface monitoring data for the interpretation of landslide movement patterns, *Geomorphology*, 66, 133–147, doi:10.1016/j.geomorph.2004.09.011.
- Picarelli, L., L. Urciuoli, G. Ramondini, and L. Comegna (2005), Main features of mudslides in tectonised highly fissured clay shales, *Landslides*, 2(1), 15–30, doi:10.1007/s10346-004-0040-2.
- Renalier, F., G. Bièvre, D. Jongmans, M. Campillo, and P.-Y. Bard (2010), Clayey landslide investigations using active and passive V_s measurements, in *Advances in Near-Surface Seismology and Ground-Penetrating Radar*, *Geophys. Dev. Ser.*, vol. 15, edited by R. D. Miller, J. H. Bradford, and K. Holliger, chap. 24, pp. 397–414, Soc. of Explor. Geophys., Tulsa, Okla.
- Reynolds, J. M. (1997), *An Introduction to Applied and Environmental Geophysics*, 796 pp., John Wiley, Chichester, U. K.
- Rivet, D., M. Campillo, N. M. Shapiro, V. Cruz-Atienza, M. Radiguet, N. Cotte, and V. Kostoglodov (2011), Seismic evidence of nonlinear crustal deformation during a large slow slip event in Mexico, *Geophys. Res. Lett.*, 38, L08308, doi:10.1029/2011GL047151.
- Rossetto, V., L. Margerin, T. Planes, and E. Larose (2011), Locating a weak change using diffuse waves: Theoretical approach and inversion procedure, *J. Appl. Phys.*, 109, 034903, doi:10.1063/1.3544503.
- Sens-Schönfelder, C., and U. Wegler (2006), Passive image interferometry and seasonal variations of seismic velocities at Merapi Volcano, Indonesia, *Geophys. Res. Lett.*, 33, L21302, doi:10.1029/2006GL027797.
- Shapiro, N. M., and M. Campillo (2004), Emergence of broadband Rayleigh waves from correlations of the ambient seismic noise, *Geophys. Res. Lett.*, 31, L07614, doi:10.1029/2004GL019491.
- Shapiro, N. M., M. Campillo, L. Stehly, and M. H. Ritzwoller (2005), High-resolution surface-wave tomography from ambient seismic noise, *Science*, 307, 1615–1618, doi:10.1126/science.1108339.
- U.S. Army Corps of Engineers (2003), NAVSTAR Global Positioning System surveying, *Eng. Manual EM 1110-1-1003*, 469 pp., U.S. Dept. of the Army, Washington, D. C.
- U.S. Army Corps of Engineers (2007), Control and topographic surveying, *Eng. Manual EM 1110-1-1005*, 498 pp., U.S. Dept. of the Army, Washington, D. C.

- van Asch, T. W. J., T. A. Van Beek, and L. P. H. Bogaard (2007), Problems in predicting the mobility of slow-moving landslides, *Eng. Geol. Amsterdam*, 91, 46–55, doi:10.1016/j.enggeo.2006.12.012.
- Wathelet, M. (2008), An improved neighborhood algorithm: Parameter conditions and dynamic scaling, *Geophys. Res. Lett.*, 35, L09301, doi:10.1029/2008GL033256.
- Weaver, R. L., and O. I. Lobkis (2001), Ultrasonics without a source: Thermal fluctuation correlations at MHz frequencies, *Phys. Rev. Lett.*, 87, 134301, doi:10.1103/PhysRevLett.87.134301.
- Weaver, R. L., C. Hadziioannou, E. Larose, and M. Campillo (2011), On the precision of noise correlation interferometry, *Geophys. J. Int.*, 185, 1384–1392, doi:10.1111/j.1365-246X.2011.05015.x.
-
- C. Brönnimann, GEOLEP, EPFL, Station 18, CH-1015 Lausanne, Switzerland.
- M. Jaboyedoff and C. Michoud, IGAR, University of Lausanne, Amphipôle 338, CH-1015 Lausanne, Switzerland.
- D. Jongmans, E. Larose, and G. Mainsant, ISTERre, CNRS, Université de Grenoble 1, BP 53, F-38041 Grenoble CEDEX 9, France. (eric.larose@ujf-grenoble.fr)

Annex A2

Cloutier C, Agliardi F, Crosta G, Frattini P, Froese C, Jaboyedoff M, Locat J, Michoud C and Marui H:
The First International Workshop on Warning Criteria for Active Slides: technical issues, problems and
solutions for managing early warning systems. Landslides 12, 205-2012, 2015

Landslides (2015) 12:205–212
 DOI 10.1007/s10346-014-0530-9
 Received: 2 June 2014
 Accepted: 15 October 2014
 Published online: 1 November 2014
 © Springer-Verlag Berlin Heidelberg 2014

Catherine Cloutier · Federico Agliardi · Giovanni Battista Crosta · Paolo Frattini ·
 Corey Froese · Michel Jaboyedoff · Jacques Locat · Clément Michoud · Hideaki Marui

The First International Workshop on Warning Criteria for Active Slides: technical issues, problems and solutions for managing early warning systems

Abstract Early warning systems (EWSs) rely on the capacity to forecast a dangerous event with a certain amount of advance by defining warning criteria on which the safety of the population will depend. Monitoring of landslides is facilitated by new technologies, decreasing prices and easier data processing. At the same time, predicting the onset of a rapid failure or the sudden transition from slow to rapid failure and subsequent collapse, and its consequences is challenging for scientists that must deal with uncertainties and have limited tools to do so. Furthermore, EWS and warning criteria are becoming more and more a subject of concern between technical experts, researchers, stakeholders and decision makers responsible for the activation, enforcement and approval of civil protection actions. EWSs imply also a sharing of responsibilities which is often averted by technical staff, managers of technical offices and governing institutions. We organized the *First International Workshop on Warning Criteria for Active Slides* (IWWCAS) to promote sharing and networking among members from specialized institutions and relevant experts of EWS. In this paper, we summarize the event to stimulate discussion and collaboration between organizations dealing with the complex task of managing hazard and risk related to active slides.

Keywords Warning criteria · Active landslide

Introduction

Background

Early warning is defined as “the set of capacities needed to generate and disseminate timely and meaningful warning information to enable individuals, communities and organizations threatened by a hazard to prepare and to act appropriately and in sufficient time to reduce the possibility of harm or loss” (UNISDR 2009). Effective early warning systems (EWSs) should encompass four main aspects: risk knowledge, monitoring and warning service, dissemination and communication and response capability (UNISDR 2009). A weakness or failure in any one aspect could result in failure of the whole system (UNISDR 2009). The first aspect regards the knowledge of the physical mechanisms that cause the hazard, and of the exposed elements at risk, with their level of vulnerability. The second aspect includes the technical capacity to continuously monitor the hazards and to develop evolutionary scenarios and to issue warnings. The third aspect regards the communication of these warnings. Finally, the last aspect includes the capacity to timely translate the predictions into a warning and action plan.

EWSs for landslides have been deployed since the 1970s in Hong Kong (Chan et al. 2003) and USA (Keefer et al. 1987), and more recently in other countries. However, these systems were mainly developed for the early warning of shallow landslides and

debris flows at regional scale, based on rainfall thresholds and meteorological monitoring systems (Aleotti 2004; Baum and Godt 2010; Jakob et al. 2012).

For large slides that are known to be active (herein called “active slides”), a local EWS needs to be deployed, based on a detailed knowledge of the landslide and on monitoring different parameters that can act as precursors, such as superficial and/or deep displacement rate, groundwater pressures and seismic noise (Angeli et al. 2000; Zan et al. 2002; Froese et al. 2006; Froese and Moreno 2014; Blikra 2008, 2012; Casagli et al. 2010; Yin et al. 2010; Intrieri et al. 2012; Michoud et al. 2013).

In this paper, we present the findings and recommendations of the First International Workshop on Warning Criteria for Active Slides (IWWCAS) that took place in Courmayeur, Italy, from June 10 to 12, 2013. The main idea of this paper, as well as the one of the workshop, is to stimulate discussion and collaboration between organizations dealing with the complex task of managing hazard and risk related to active slides. This report contributes to the activities supported by the International Consortium on Landslides (ICL).

Objective of the IWWCAS

The aim of this workshop was to provide a unique opportunity to share experiences about the challenges, problems and available tools to determine warning criteria. In particular, the main issues addressed by the workshop were on how to use available data, at different sites and stages of the studied problem, to choose indicators, to define threshold values and to update them with the evolution of the phenomenon in order to set up a reliable and shared EWS. Technological solutions were then considered as tools but not as a substantial aspect to the problem. The event schedule is presented in Table 1, including the titles and authors of the 22 talks that were given, and the participants are identified in Fig. 1. In addition, further details on the workshop organization are provided in Appendix.

Another objective was to find a venue that would provide an opportunity to visit at least one site where an active landslide is being investigated and ideally where an EWS is operating. Courmayeur was very suited for this purpose. The participants visited the Mont de La Saxe rockslide (Fig. 2), an active landslide under continuous monitoring since 2009 (Fig. 3) (Crosta et al. 2013). The rockslide monitoring data were used to run an exercise with involvement of all the contributors. The objective of this exercise was to walk as an expert group through all the steps leading from the planning to the design and management of a warning system, through the definition of shared scenarios. This exercise was tentatively steered on the basis of the information available at different stages since the beginning of the investigations and monitoring.

ICL/IPL Activities

Table 1 Talks given at the First International Workshop on Warning Criteria for Active Slides

Topic 1: Getting acquainted with our surroundings: introduction to slope hazard in Valle d'Aosta	
Davide Bertolo	Early warning and monitoring of large and evolutionary landslides in a densely populated alpine region. The Aosta Valley experience (Italian Western Alps)
Marco Vagliasindi ^a , Michèle Curtaz and Davide Bertolo	Glaciers-related risks: can warning criteria be applied?
Paola Dellavedova ^a and V. Segor	Local management of avalanche hazard on the Aosta Valley's roads
Luca Dei Cas ^a , Francesco Ferrarini and Francesco Giudes	The geological monitoring center of ARPA (Lombardy, Italy)
Topic 2: An overview of a variety of techniques for monitoring slides : the decision-making toolbox that can be used to provide the warning	
Clément Michoud ^a , Sara Bazin and Lars Harald Blikra	On the importance of landslide conceptual models by integrating and coupling different sources of data to set pertinent thresholds and proper EWS
Denis Jongmans ^a , Laurent Baillet, Eric Larose, Pierre Bottelin and Guénolé Mainsant	Use of seismic noise techniques for monitoring rapid landslides
Jean-Philippe Malet ^a , Julien Travelletti, Alexandre Mathieu and Patrice Ulrich	Rapid mudflows released from large landslides: early-warning criteria designed from geophysical monitoring, slope stability and runout modelling
Christian Zangerl ^a	Deep-seated slowly moving rock slides: the challenge of making reliable slope deformation and stability forecasts
André Stumpf ^a , Jean-Philippe Malet, Julien Travelletti and Julien Gance	On the possible integration of optical remote sensing in landslide early warning systems: status, limitations, and perspectives
Daniele Giordan ^a , Andrea Manconi, Paolo Allasia, Marco Baldo and Giorgio Lollino	RTS monitoring strategies on active slides: the influence of the elements at risk
Mario Lovisolo ^a , Mauro Battaglio and Thierry Rosset	A landslide geotechnical monitoring project for EW: the Acqui Terme example
Giovanni B. Crosta ^a , R. Castellanza, Paolo Frattini, Federico Agliardi, P. Cancelli and A. Tamburini	Investigation and monitoring of the Mt. de la Saxe landslide
Discussion led by Giovanni Crosta	
Topic 3: Theory applied. Overview of different forecasting models and application to case histories. Conceptual use of thresholds for warning.	
Pascal Horton ^a , Michel Jaboyedoff ^a , Antonio Abellan, Charles Oble and Clément Michoud	Using precipitation data and models for forecasting : Part 1: Nowcasting landslide displacements using precipitation data Part 2: Real-time statistical precipitation forecasting by means of the Analogue Method Part 3: Looking at thresholds for failure, conceptual models and tools for warnings
Hideaki Marui ^a , Chunxiang Wang, Hiroyuki Yoshimatsu and Eisaku Hamasaki	Warning criteria on the basis of creep theory and its practical application
Mauro Rossi ^a , Alessandro Cesare Mondini, Silvia Luciani, Dalia Kirschbaum, Daniela Valigi and Fausto Guzzetti	A new probabilistic clustering approach for predicting rainfall induced landslides
Discussion led by Michel Jaboyedoff	
Topic 4: Operational EWS: presentations from public organizations that manage operational EWS and the range of issues that are addressed.	
Jacques Locat ^a and Catherine Cloutier	The Gascons rockslide early warning system: preliminary considerations
Lars H. Blikra	Concepts and warning criteria for monitoring of large rockslides in Norway
Oldrich Hungr (in replacement of a no show)	
Carlo Troisi ^a and Nicoletta Negro	Managing of EW systems by public agencies: related problems
Discussion led by Lars H. Blikra	
Topic 5: Learnings from long term EWS, successes and failures	
Giovanni B. Crosta ^a , Federico Agliardi, Paolo Frattini, Carlo Rivolta and Luca Dei Cas	Long term real-time monitoring and early warning system for a large alpine rock slide
Corey Froese ^a	Turtle mountain: lessons learned from 10 years of operation of an early warning system
Carlo Rivolta ^a and Davide Leva	Some critical issues in monitoring natural hazards, selection of a modeling tool and defining warning criteria using data acquired by ground based synthetic aperture radars
Discussion led by Corey Froese	
Topic 6: Warning exercise	
Topic 7: Wrap-up discussion	
Day 3: Field trip at Monte de La Saxe	

^a The authors gave the talk



Fig. 1 Group picture. Seating down (*left to right*): Hideaki Marui, Marco Vagliasindi, Jacques Locat, Giovanni Crosta and Oldrich Hungr. First row standing up: Mario Lovisolo, Corey Froese, Nicoletta Negro, Denis Jongmans, Igor Bravo, Christian Zangerl, Paolo Fratinni, Carlo Troisi and Daniele Giordan. Second row standing up: Marc-Henri Derron, Jean-Philippe Mallet, Federico Agliardi, Michel Jaboyedoff, Lars Blikra. Last row: Clément Michoud, Carlo Rivolta, Catherine Cloutier, Mauro Rossi and André Stumpf

Findings and recommendations

The following presents various comments, conclusions and recommendations obtained from talks, discussions and from the exercise on the Mont de La Saxe rockslide. Most of the comments are presented as bullet points. It can be noticed that many questions are still open.

What are the concerns of scientists managing EWS?

- General concerns were evoked about the civil responsibility of the scientist/consultant designing EWSs, providing the

scenarios and defining the alert thresholds (Malone 2008; Jordan 2013; Alexander 2014). For example, the definition of warning criteria helps to reduce the responsibility of the person taking the decision of evacuation, because the decision is based on a pre-defined criterion. However, in cases of false alarm or if a slide happens without an alarm, what is the responsibility of the scientist/consultant who defined the threshold value? So, is it possible to define shared indicators and threshold values to share also the responsibilities? How uncertainty can be considered in the management of an EWS? Is it possible and advisable to communicate this uncertainty to



Fig. 2 View of the Mont de la Saxe and its rockslide. The village of Entrèves, where the participants were staying, is in the valley



Fig. 3 A visit of the Mont de la Saxe rockslide took place on the last day of the workshop. The village of Entrèves and the entrance to the Mont Blanc tunnel can be seen in the valley

the public? What are the differences involved in managing an EWS for landslides in natural or artificial environments?

- When studying an active landslide with potentially catastrophic consequences, the scientist/consultant might be working under psychological or political pressure. This kind of situation that threatens human life requires to quickly provide recommendations regarding safety measures once the landslide is recognized. The importance is to avoid an emotional decision that could be taken by the scientist/consultant or by the technical staff and to communicate properly the decision to the population, so to make it acceptable as much as possible.
- Uncertainty involves the limited knowledge relative to the immediate or future evolution of a landslide, or the change in its properties and consequently in the sensitivity to external perturbations of different sequence and intensity. How should we communicate the state of an active landslide and the related uncertainties to the authorities that do not have a robust understanding or scientific background? How can we convey the uncertainty to the public and to the managers or decision makers and stakeholders maintaining their confidence in the system and in the group of experts?
- Uncertainties are greater at the beginning of an investigation and should decrease with time and a better understanding. So, at the beginning of an investigation, should the scientist present all the scenarios to the authorities including the very pessimistic ones?
- Communication of threshold values and their successive readjustment can be of help or convey a feeling of inadequate knowledge and understanding. Is it reasonable to have multiple groups working independently at the same site and presenting different models explaining the landslide behaviour or diverse EWS solutions? At least for these last questions, we agree that a common understanding and set of threshold values and mitigation solutions should be reached and presented. In fact, any deficiency in sharing data and model

results or scenarios should be considered as the worst managing procedure when a collective understanding is required.

Are EWS suited for long term operation?

- EWS maintenance is expensive and requires time and effort to keep the system updated and a 100 % functional (e.g. Wilson 2004). The maintenance is complicated by quickly evolving technologies leading to incompatibility between older and newer systems. Keeping an EWS operational also implies conducting simulation exercises to train staff and update evacuation plans. Finally, a certain rotation within the personnel is recommended to avoid that know-how and system knowledge get lost when a key person is missing or more simply retire.
- The dilemma of calling or not an evacuation might come back year after year. This can be the consequence of different constraints which should be evaluated, and it is also related to the need for updating the threshold values adopted for alert and alarm phases. In fact, system managers often forget to consider a landslide as an evolving process, which change in properties and sensitivity and as such can present different response in time. For the same reason, it is important to make aware the stakeholders, population and administrators that a minimum monitoring time is requested for the experts to reach a consensus about the type of behaviour, expected evolution, possible scenarios as well as to reformulate them after each major reactivation.
- When a warning system has been in place for some time, and no acceleration periods were measured and an important maintenance is needed, should new money keep being invested or should a program of seasonal survey techniques be put in place instead? What criteria should come into play in the decision? Which kind of study or analysis should be completed? How this decision should be presented to the population and administrators? How can we communicate to

politicians and stakeholders that some EWS at specific study sites should be maintained active just to help improve our understanding and foresight in landslide behaviour?

- New technologies can be of help when the last series of questions arise. In fact, it is sometime possible to choose a monitoring system with lower or higher acquisition frequency that will save money and make sufficiently accurate monitoring to initiate pre-warning.

What should we think about when designing a warning system?

- A conceptual revisable model of the instability should be created before designing the EWS, as such a model is mandatory to choose the location of devices. At the same time, an EWS can grow by progressively implementing a monitoring network initially installed for the completion of a revisable conceptual model. In this way, the monitoring network and EWS can be improved in successive steps when understanding is also enhanced. The quality of the monitoring data depends on the knowledge of the instability geometry, failure mechanism and possible evolution in time and space, and as such will improve with time.
- From experience, the use of multiple redundant monitoring techniques is advantageous for landslide characterization. For example, it is helpful to ensure the relevance of displacement measurements used to interpret the kinematic behaviour and to remain operational also under critical weather conditions or very complex phases of evolution of the landslide.
- Active landslides with large cumulative displacements are extreme environments to be studied because the type of evolution causes short operational life for most of the monitoring equipment and especially for deep monitoring instrumentation. This is a major problem when aimed at the understanding of the role of some controlling factors such as groundwater recharge and pore pressure distribution, or displacements at depth. This is for example the case of the La Saxe rockslide (Crosta et al. 2013).
- Instruments, proper to conduct surveillance, should be installed from the beginning of the investigation, because they will be useful (1) to follow the slide more or less continuously in case the interpreted hazard level is preoccupying, (2) to improve the general safety (workers on site and other people at risk), as the evolution of the slide can be followed and (3) to evaluate the efficiency of countermeasures that could be installed following the analysis. This also requires the capability to interact with the system during the various phases of evolution so to adapt frequency of measurements, derived variables and type of indicators and threshold values.
- The remote location of some EWS limits their reliability as it hinders troubleshooting. For example, some agencies are now trying to rely less on private carrier (e.g. cellular network) and more on radio, because they can better control this type of communication channel maintaining operative also under critical conditions.
- Data processing was improved and simplified by research and application of monitoring techniques at an increasing number of sites. There is still room for improvement, for example to develop cheaper monitoring systems, or to optimize communication systems, data file size and transmission protocols.

- The analysis of monitored seismic noise showed that at some experimental site and in lab experiments the signal changes prior to an acceleration, so even before a minor displacement is captured by the monitoring system. Thus, seismic noise could be used to define threshold values for certain kinds of landslide (Mainsant et al. 2012). No operational warning system relies on this technique, yet but it could be a promising tool to experiment at sites involving different types of movement and affected materials.

How to determine warning criteria?

Discussion during the workshop emphasized the lack of tools to define warning criteria for active slides which could be established ahead of the collapse time and do not require continuous updating simultaneously to the event evolution. Here are some of the points that were raised by the participants:

- Most of the time, the threshold values are defined empirically, sometimes based only on literature values and at the very early stages of the investigations and monitoring. Nevertheless, it has been shown that the range of displacement rate typical of the pre-collapse phase can be quite broad.
- To define quantitative-physically based thresholds, we need a data set spanning over a long period of time and for which some of the most relevant variables are made available or collected. For systems close to collapse minimal changes in one of the controlling factors could bring to failure or catastrophic collapse, but following different evolutionary paths.
- The difficulties related to criteria definition are, in good part, due to our misunderstanding of mechanisms controlling rockslides.
- In the workshop talks, the factors accounted for warning criteria definition were (1) the landslide characteristics and dynamics (e.g. type of involved material), (2) the position of the element at risk in relation to the slide (on or below), (3) the previously monitored activity of the landslide and (4) the history of the slope (e.g. recently excavated or natural long term evolution). The definition of warning criteria is based on scenarios of failure and run out models. The participants insisted on the importance of creating rapidly a first geomechanic and kinematic model of the slide to confront our understanding to incoming data and subsequently improve the model.
- The participants discussed about the inverse velocity method as a prediction tool (Saito 1969; Fukuzono 1985, 1990; Crosta and Agliardi 2003; Rose and Hungr 2007; Federico et al. 2012) and successful applications of the technique were presented mainly for mine slopes. However, this technique is not totally safe from false alarm, as for a landslide undergoing seasonal variations, and its use is sometimes hampered by the availability only of superficial displacement data.
- Operational thresholds presented through the talks were, for the majority, velocity thresholds, sometime applied in conjunction with the inverse velocity method. Thus, most criteria for active slides are based on displacements data even though the triggering agent is recognized to be groundwater recharge (Michoud et al. 2013) associated to snow melting or intense rainfall. The role of water can be incorporated by studying slide sensitivity to groundwater

- recharge and by the use of precipitation thresholds. This approach is widely used for regional-scale EWS for shallow landslides and debris flows (Baum and Godt 2010). Crosta et al. (2013) discuss the evolution of the La Saxe slide sensitivity to groundwater recharge during the evolution of the slide itself, with the progressive change in hydraulic and mechanical properties accompanying the accumulation of large displacements, the opening of fractures and the localization of shear at depth.
- In the study cases presented at the workshop, the cumulative displacement was not a parameter directly used to define warning criteria. However, cumulative displacement has the advantage to be more stable than velocity, at least in most of the phases not immediately preceding the final collapse. The cumulative displacement has been sometime used to define warning criterion, for example, by fitting a curve to the evolution of displacements with time (Crosta and Agliardi 2002). It has been used also in the case of toppling failures (Zvelebil and Moser 2001).
 - It seems inadequate to fix warning levels based on a single criterion when coping with complex landslides especially in natural environments. The establishment of warning levels should take into account all parts of a system, such as displacement data, weather, season, consequences, groundwater recharge and other types of data. Data interpretation by an expert is often required prior to the initiation of emergency procedure and even more at the closure of the emergency phase.
 - During the exercise, the participants to the workshop did not reach a complete agreement on the type of thresholds to apply, neither on the values, nor the techniques on which to rely. This lack of general agreement points out to the need for EWS design guidelines and to the need of a longer and more informed discussion before the achievement of a consensus even within a community with a specific expertise on the subject. This can be surprising especially when considering that most of the participants recognized the level of knowledge and the relative abundance of monitoring data available for the La Saxe case study. Furthermore, this discussion emphasized the major difference between managing an EWS for natural slopes in highly populated areas and managing an EWS for slopes under artificial conditions and very specific type of occupancy, like mine slopes.
 - As groundwater pressures and precipitations appear to be driving factors for many active slides, there should be more work about the hydrogeology of active slides, considering also their progressive evolution from initial failure to collapse through a series of successive evolutionary steps.
 - Is the shear zone behaviour a key features for rapid failure? This has been suggested by many authors in the literature (Fukuoka et al. 2007; Pinyol and Alonso 2010; Kalenchuk et al. 2012), but its description and definition in many cases remains a difficult task which can require careful investigations and monitoring both in time and space.
 - Some new technologies must be more widely tested, such as seismic noise, in order to transfer these technologies from research to practice. More attention should be placed on data interpretation with respect to the simple acquisition by new technologies.
 - EWS should be limited to specific cases where countermeasures are not suitable.

A second workshop?

The main objective of the workshop was to focus on warning criteria definition, adoption and management. The workshop turned out to point out more to the problems related to their definition than to tools and solutions.

For a future second workshop, it is suggested to form small working groups prior to the event to gather suggestions and to make sure that the focus is on solutions. A few suggestions for working groups are proposed hereunder:

On what should focus future research?

- When possible, we should opt for monitoring techniques enabling characterization and monitoring at the same time, ensuring robustness and continuity in data acquisition
- There is a need for guidelines and for a tool box to help the scientists quickly provide answers to end-users (managers) (Intrieri et al. 2013).
- Guidelines for stakeholders, EWS managers, professionals, technical staff and scientists should be prepared to help steering the main steps of an EWS development and especially to steer the group towards a shared set of procedures, indicators and threshold values. This type of guidance should help in developing a participative system to support decisions and to share the responsibilities.
- A grouping of similar case studies to create some sort of classification chart, including types of scenario or run out, in order to have examples on which to rely for new designs of EWS.
- Guidelines for the application of different approaches such as the dated inverse velocity method on different types of landslide, including procedures, mathematical tools, precisions, types of landslide suited for the method, frequency of updating, etc.
- A review on the responsibilities, legally talking, of designers of a warning system in the case of false alarm or in the case of failure to predict an event causing consequences. For example, recently in Italy, scientists have been sued for false alarm because they are considered responsible for the economical losses resulting from a misplaced evacuation or for an underestimation of the level of risk. This is an important point, because in case of an EWS, it hampers its efficiency. This problem can be overpassed only by an informed and shared decisional process, where the final decision is the result of a common path done by all the stakeholders, experts and representative of the population.
- Define the requirements of land managers, in order to design warning systems that respond correctly to their needs and to those of the affected population and activities.
- To avoid the confusion between scenarios and thresholds. Scenarios refer for example to the expected volume and runout behaviour, whereas thresholds are values for specific indicators representative of an expected change in behaviour and which can be associated to a scenario. The same scenario can develop in a very short time or in a much longer one, according to some local or environmental constraints (e.g. rainfall,

snowmelt). Emergency or civil protection plans should consider this difference and evaluate the requirements for evacuation or activation of other emergency actions.

- Apart from displacement, velocity, acceleration, precipitation and groundwater recharge criteria, what are the other possibilities?
- When to choose EWS instead of active or other passive mitigation measures? Or when to combine them? By associating different probabilities of occurrence to the different scenarios?

Concluding remarks

The contained size of the *First International Workshop on Warning Criteria for Active Slides* (28 participants) enabled an open-minded discussion. This type of structure should be maintained. The venue, next to the active La Saxe rockslide, definitely immersed the participants into active landslides management and showed concretely the implications of EWS in terms of evacuation and repercussions on the population, as well as on the technical staff and the involved experts.

The participants shared their experience and issues related to the definition of warning criteria and to management of EWS. We realized that different organizations had common problems, especially in EWS management and maintenance. This observation leads to one of the conclusions of this workshop: EWSs are relatively new in natural hazard protection, and we are still learning how to make it right and the tools for warning criteria definition are limited. There are many benefits of landslide monitoring and surveillance; for example, it increases our understanding of the phenomenon and its possible changes and it shows the limited validity of some scenarios or the need for multiple scenarios both to decide about mitigations and to prepare suitable and alternative emergency plans.

Difficulties in forecasting the behaviour of a landslide are partly related to misunderstanding of complex active landslides physics. In fact, the group was constantly diverging towards a discussion about failure mechanism when trying to determine warning criteria.

The study cases presented at the workshop showed that, most of the time, characterization and surveillance of landslides are done synchronously and that for most of the cases, excepted for mining, the monitoring starts well after the beginning of the instability. It also showed that EWS requires regular analyses by an expert, or better an expert panel, to interpret the landslide behaviour, to detect any kind of evolution and to update the models.

Acknowledgments

The organizing committee wish to thank the Fondazione Montagna Sicura, the Courmayeur Municipality and the Regione Autonoma Valle d'Aosta for their support in the organization by hosting this workshop, for offering coffee breaks, to allow for the field trip on the landslide and to have overcome the last moment troubles due to the evacuation phase.

Appendix

Organization of the workshop

The convenors of the workshop were Giovanni Crosta (University of Milano-Bicocca, Italy), Corey Froese (Alberta Geological Survey, Canada), Michel Jaboyedoff (University of Lausanne, Switzerland)

and Jacques Locat (Université Laval, Canada). The convenors were helped by Federico Agliardi, Catherine Cloutier, Paolo Frattini and Clément Michoud for the organization of the event. The committee obtained support from La Montagna Sicura's staff (Regione Val d'Aosta): Michèle Curtaz and Marco Vagliasindi.

The workshop venue and schedule

The workshop took place from June 10 to 12, 2013, in Courmayeur (Western Italian Alps). The participants were staying in Entrèves, with a view on the Mont De La Saxe rockslide (Crosta et al. 2013) an active landslide under continuous monitoring since 2009. At the time of the workshop, the village of Entreves-La Palud was under a partial evacuation order from May 19 to June 24, 2013, due to the acceleration beyond the threshold values of the Mont de la Saxe rockslide displacement rates. Till the last minute, the workshop venue was uncertain due to this evacuation order, but it was also a great motivation to organize the event. In fact the presence of the workshop participants at the site during this stage was considered also an important communicative action with respect to the population and the personnel involved in the management of the civil protection plan.

To make sure that participants would contribute actively to the workshop, the organizing committee was seeking for experts that are, or were, in charge of EWS setting up or managing. An effort was made to gather experts from different parts of the world, still having in mind to limit the number of participants to create an open-discussion environment.

Twenty-eight participants attended the workshop: 15 from research institutions, six from regional offices and monitoring centres, five from private companies and three from the regional geological survey of Valle d'Aosta and the Montagna Sicura Foundation. The participants were asked to write an extended prior to the workshop and to give a 15-min talk.

References

- Aleotti P (2004) A warning system for rainfall-induced shallow failures. *Eng Geol* 73:247–265
- Alexander DE (2014) Communicating earthquake risk to the public: the trial of the “L'Aquila Seven”. *Nat Hazards* 72:1159–1173
- Angeli M-G, Pasuto A, Silvano S (2000) A critical review of landslide monitoring experiences. *Eng Geol* 55:133–147
- Baum RL, Godt JW (2010) Early warning of rainfall-induced shallow landslides and debris flows in the USA. *Landslides* 7:259–272. doi:10.1007/s10346-009-0177-0
- Blikra LH (2008) The Åknes rockslide: monitoring, threshold values and early-warning. In: *Landslides and engineering slopes: from the past to the future, proceedings of the 10th International Symposium on Landslides and Engineering Slopes*, Xi'an, China, 2008. Taylor & Francis Group, London, pp 1089–1094
- Blikra LH (2012) The Åknes rockslide, Norway. In: Clague JJ, Stead D (ed) *Landslides: types, mechanisms and modeling*. Cambridge, pp 323–335
- Casagli N, Catani F, Del Ventisette C, Luzi G (2010) Monitoring, prediction, and early warning using ground-based radar interferometry. *Landslides* 7(3):291–301
- Chan RKS, Pang PLR, Pun WK (2003) Recent developments in the landslip warning system in Hong Kong. In: *Proceedings of the 14th Southeast Asian Geotechnical Conference*. Balkema, Lisse, The Netherlands
- Crosta GB, Agliardi F (2002) How to obtain alert velocity thresholds for large rockslides. *Phys Chem Earth A/B/C* 27:1557–1565
- Crosta GB, Agliardi F (2003) Failure forecast for large rock slides by surface displacement measurements. *Can Geotech J* 40(1):176–191
- Crosta GB, di Prisco C, Frattini P, Frigerio G, Castellanza R, Agliardi F (2013). Chasing a complete understanding of the triggering mechanisms of a large rapidly evolving rockslide. *Landslides* 1–18. doi:10.1007/s10346-013-0433-1
- Federico A, Popescu M, Elia G, Fidelibus C, Internò G, Murianni A (2012) Prediction of time to slope failure: a general framework. *Environ Earth Sci* 66:245–256

- Froese CR, Moreno F (2014) Structure and components for the emergency response and warning system on Turtle Mountain, Alberta, Canada. *Nat Hazards* 70:1689–1712
- Froese CR, Carter G, Langenberg W, Moreno F (2006) Emergency response planning for a second catastrophic rock slide at Turtle Mountain, Alberta. In: First Specialty Conference on Disaster Mitigation, Calgary, Alberta, Canada, May 2006
- Fukuoka H, Sassa K, Wang G (2007) Shear behavior and shear structure of granular materials in naturally drained ring shear tests. In: Sassa K, Fukuoka H, Wang F, Wang G (eds) *Progress in landslide science*. Springer, 99–110
- Fukuzono T (1985) A new method for predicting the failure time of a slope. In: Fourth International Conference and Field Workshop on Landslides, Tokyo, Japan, 1985. pp 145–150
- Fukuzono T (1990) Recent studies on time prediction of slope failure. *Landslide News* 4:9–12
- Intrieri E, Gigli G, Mugnai F, Fanti R, Casagli N (2012) Design and implementation of a landslide early warning system. *Eng Geol* 147–148:124–136
- Intrieri E, Gigli G, Casagli N, Nadim F (2013) Landslide early warning system: toolbox and general concepts. *Nat Hazards Earth Syst Sci* 13(1):85–90
- Jakob M, Owen T, Simpson T (2012) A regional real-time debris-flow warning system for the District of North Vancouver, Canada. *Landslides* 9:165–178
- Jordan TH (2013) Lessons of L'Aquila for operational earthquake forecasting. *Seismol Res Lett* 84(1):4–7
- Kalenchuk K, Diederichs M, Hutchinson DJ (2012) Three-dimensional numerical simulations of the Downie Slide to test the influence of shear surface geometry and heterogeneous shear zone stiffness. *Comput Geosci* 16:21–38. doi:10.1007/s10596-011-9245-3
- Keefer DK, Wilson RC, Mark RK, Brabb EE, Brown WM III, Ellen SD, Harp EL, Wiecezorek GF, Alger CS, Zarkin RS (1987) Real-time landslide warning during heavy rainfall. *Science* 238(13):921–925
- Mainsant G, Larose E, Brönnimann C, Jongmans D, Michoud C, Jaboyedoff M (2012) Ambient seismic noise monitoring of a clay landslide: toward failure prediction. *J Geophys Res Earth Surf* 117, F01030. doi:10.1029/2011JF002159
- Malone S (2008) A warning about early warning. *Seismol Res Lett* 79(5):603–604
- Michoud C, Bazin S, Blikra LH, Derron M-H, Jaboyedoff M (2013) Experiences from site-specific landslide early warning systems. *Nat Hazards Earth Syst Sci* 13(10):2659–2673
- Pinyol NM, Alonso EE (2010) Fast planar slides: a closed-form thermo-hydro-mechanical solution. *Int J Numer Anal Methods Geomech* 34(1):27–52
- Rose ND, Hungr O (2007) Forecasting potential rock slope failure in open pit mines using the inverse-velocity method. *Int J Rock Mech Min Sci* 44(2):308–320
- Saito M (1969) Forecasting time of slope failure by tertiary creep. In: *Proceedings of the 7th International Conference on Soil Mechanics and Foundation Engineering*, Mexico City, Mexico, pp 677–683
- UNISDR (2009) *Terminology on disaster risk reduction*. United Nation International Strategy for Disaster Reduction, Geneva, 35 p. <http://www.unisdr.org>. Accessed 1 Jun 2014
- Wilson RC (2004) The rise and fall of a debris-flow warning system for the San Francisco Bay Region, California. In: Glade T, Anderson M, Crozier MJ (eds) *Landslide hazard and risk*. Wiley, New York, pp 493–516
- Yin Y, Wang H, Gao Y, Li X (2010) Real-time monitoring and early warning of landslides at relocated Wushan Town, the Three Gorges Reservoir, China. *Landslides* 7(3):339–349
- Zan L, Latini G, Piscina E, Polloni G, Baldelli P (2002) Landslides early warning monitoring system. In: *Geoscience and remote sensing symposium, 2002*. IEEE International 1:188–190
- Zvelebil J, Moser M (2001) Monitoring based time-prediction of rock falls: three case-histories. *Phys Chem Earth B* 26:159–167

Hideaki Marui is a member of ICL.

C. Cloutier (✉) · **J. Locat**

Laboratoire d'Études sur les Risques Naturels, Département de Géologie et de Génie Géologique, Université Laval, 1065 Avenue de la Médecine, Québec, QC G1V 0A6, Canada
e-mail: catherine.cloutier.2@ulaval.ca

F. Agliardi · **G. B. Crosta** · **P. Frattini**

Department of Earth and Environmental Sciences, Università degli Studi di Milano-Bicocca, Piazza della Scienza 4, 20126, Milan, Italy

C. Froese

Alberta Energy Regulator/Alberta Geological Survey, 4999-98 Ave NW, Edmonton, Alberta, Canada

M. Jaboyedoff · **C. Michoud**

Centre de Recherche sur l'Environnement Terrestre (CRET), Faculté des Géosciences et de l'Environnement, Université de Lausanne, UNIL-Mouline, Geopolis, 1015, Lausanne, Switzerland

H. Marui

Research Institute for Natural Hazards and Disaster Recovery, Division of Multi-Hazards, Section of Mechanical Analysis on Disasters, Niigata University, Niigata, Japan

Annex A3

Rouyet L, Kristensen L, Derron MH, Michoud C, Blikra LH, Jaboyedoff M and Lauknes TR: Evidence of rock slope breathing using GB-InSAR. Submitted to *Geomorphology*, 27 p, May 2015

EVIDENCE OF ROCK SLOPE BREATHING USING GROUND-BASED INSAR

Line Rouyet^{1,3}, Lene Kristensen², Marc-Henri Derron¹, Clément Michoud^{1,4}, Lars Harald Blikra², Michel Jaboyedoff¹ and Tom Rune Lauknes³

¹ Institute of Earth Sciences, Risk group, Géopolis, Quartier Mouline, University of Lausanne, 1015 Lausanne, Switzerland.

² Norwegian Water Resources and Energy Directorate (NVE), Ødegårdsvegen 176, 6200 Stranda, Norway.

³ Norut, P.O. Box 6434, Forskningsparken, 9294 Tromsø, Norway.

⁴ Terranum Ltd, 35bis rue de l'industrie, 1020 Bussigny, Switzerland.

E-mail addresses: L. Rouyet: line.rouyet@norut.no, L. Kristensen: lkr@nve.no, M.-H. Derron: marc-henri.derron@unil.ch, C. Michoud: clement.michoud@terranum.ch, L.H. Blikra: lab@nve.no, M. Jaboyedoff: michel.jaboyedoff@unil.ch. T.R. Lauknes: tom.rune.lauknes@norut.no

ABSTRACT

Ground-Based Interferometric Synthetic Aperture Radar (GB-InSAR) campaigns were performed in summer 2011 and 2012 in the Romsdalen valley (Møre & Romsdal county, western Norway) in order to assess displacements on Mannen/Børa rock slope. Located 1 km northwest, a second GB-InSAR system continuously monitors the large Mannen rockslide. The availability of two GB-InSAR positions creates a wide coverage of the rock slope, including a slight dataset overlap valuable for validation. A phenomenon of rock slope breathing is detected in a remote and hard-to-access area in mid-slope. Millimetric upward displacements are recorded in August 2011. Analysis of 2012 GB-InSAR campaign, combined with the large dataset from the continuous station, shows that the pattern is not homogenous in time and that inversions of movement have a seasonal recurrence. These seasonal changes are confirmed by satellite InSAR observations and can possibly be caused by hydrogeological variations. In addition, combination of GB-InSAR results, in situ measurements and satellite InSAR analyses contribute to a better overview of movement distribution over the whole area.

KEYWORDS: Rock slope, Stability, Rockslide, Ground-Based InSAR, SAR interferometry, Groundwater Effect.

1 INTRODUCTION

The detection, characterization and assessment of unstable slopes require a multidisciplinary approach, including mapping, field and laboratory measurements, modelling, etc. (i.a. Turner & McKuffey, 1996; Solheim, et al., 2005; Jaboyedoff, et al., 2005). The characterization of movement rate, distribution and evolution is a fundamental part in order to understand the behaviour of unstable slopes and forecast potential

33 collapse events (i.a. Angeli, et al., 2000; Crosta & Agliardi, 2003; Petley, et al., 2005; Blikra, 2008; Federico,
34 et al., 2012; Blikra & Kristensen, 2013; Froese & Moreno, 2014). Various tools and instrumentation are used
35 for this purpose. For the last decades, the development of remote sensing has had a major impact in this field
36 (i.a. Mantovani, et al., 1996; Metternicht, et al., 2005; Lillesand, et al., 2008; Michoud, et al., 2010; Stumpf,
37 et al., 2011; Derron, et al., 2011). It has proved being particularly valuable for operational reasons, due to its
38 large coverage capability, high resolution and accuracy, and the possibility to examine areas difficult to
39 access.

40 The contribution of active microwave remote sensing for detection, mapping and monitoring of ground
41 displacements using Synthetic Aperture Radar Interferometry (InSAR) has got an international scientific
42 recognition at the beginning of the nineties (Gabriel, et al., 1989; Massonnet, et al., 1993; Zebker, et al.,
43 1994). Firstly developed for spaceborne platforms, InSAR devices were then developed for ground-based
44 acquisitions (GB-InSAR) in the last decades. At the end of the nineties, a prototype of outdoor portable SAR
45 system LISA (LInear Synthetic Aperture radar) was available (Tarchi, et al., 1999; Luzi, 2010). Since then,
46 the use for mapping and monitoring of slope instabilities has quickly increased and numerous case studies
47 have been reported (i.a. Tarchi, et al., 2003; Noferini, et al., 2007; Herrera, et al., 2009; Gischig, et al., 2009;
48 Barla, et al., 2010; Casagli, et al., 2010; Del Ventisette, et al., 2011; Bozzano, et al., 2011; Herrera, et al.,
49 2011; Intrieri, et al., 2012; Monserrat, 2012; Schulz, et al., 2012; Agliardi, et al., 2013; Mazzanti, et al. 2015).

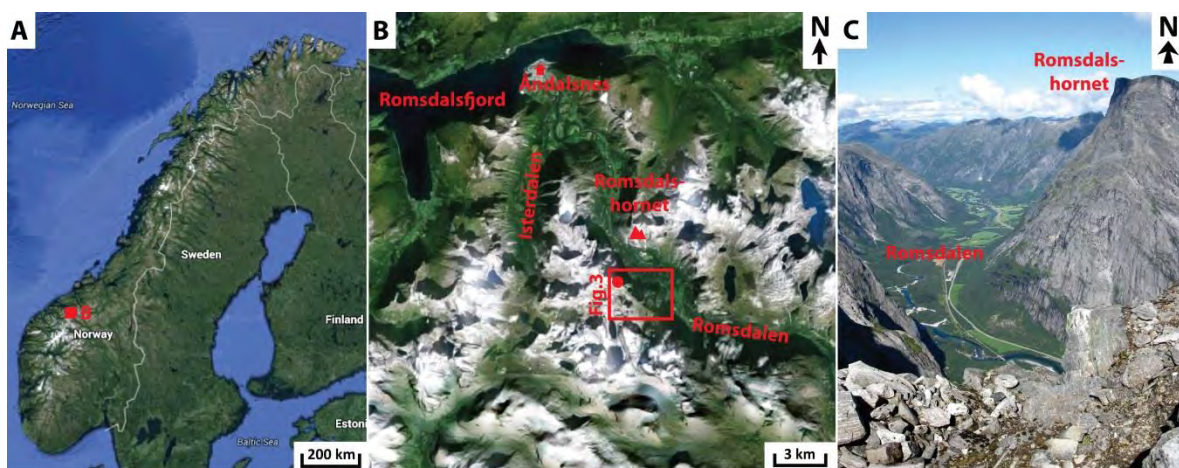
50 This paper provides an analysis of GB-InSAR measurements on Mannen/Børa rock slope, in western
51 Norway, where a large rockslide is continuously monitored using a wide multi-device network (Kristensen &
52 Blikra, 2013). Among these devices, two GB-InSAR systems are operating, one permanently and one during
53 intermittent campaigns. The presence of these two sensors makes possible a large coverage in unmonitored
54 and hard-to-access areas. Moreover, the areas imaged by the GB-InSAR systems are partially overlapping,
55 which allows the consistency of the measured displacements to be checked. In addition, GB-InSAR results
56 are complimented by in situ measurements and analysis of satellite InSAR. The results contribute to a better
57 overview of the movement distribution over the whole area. It especially highlights a peculiar seasonal
58 inversion of movement, hereby called rock slope breathing. This phenomenon is discussed thereafter in terms
59 of variations of groundwater pressure.

60 2 MANNEN/BØRA ROCK SLOPE

61 2.1 CONTEXT

62 The Mannen/Børa rock slope is located on the southwestern side of Romsdalen in Rauma Municipality in
 63 Møre & Romsdal county (western Norway) (Fig. 1, A–B). The glacially-shaped valley (Fig. 1, C) is
 64 characterized by extremely steep slopes and includes the highest vertical cliff in Europe (Trollveggen) with a
 65 drop of 1,700 m from the top to the bottom of the valley. Mannen is an active rockslide (Fig. 1, B red point;
 66 Fig. 2, top) and Børa is a large plateau located directly on the southeastern side of Mannen and showing
 67 extensive signs of instability (Fig. 2, bottom). The rock slope is north-east facing and has a mean slope of 40–
 68 50° in its upper part.

69 Geologically the area is included in the Western Gneiss Region, a large basement window of Precambrian
 70 crystalline rocks reworked during the Caledonian orogeny (Mosar, 2000; Smelror, et al., 2007). Mannen/Børa
 71 area is composed by metamorphic units, including dioritic-granitic gneiss, amphibolites and pegmatites
 72 (Saintot, et al., 2011a & 2012). The Romsdalen valley has been affected by various events of collapse and
 73 several other unstable areas were detected. This is due to a geological and geomorphological context
 74 unfavourable to slope stability, due to the role of the inherited structures of the ductile and brittle tectonic
 75 history, the steepness of the slopes along the U-shaped valley, as well as the post-glacial debuttressing of the
 76 valley flanks (Saintot, et al., 2011b).



77
 78 **Fig. 1 (2-column fitting, color version required):** A) Location of Mannen/Børa site in western Norway (map google - Landsat 2015).
 79 B) Location of Mannen/Børa in Romsdalen valley (map google - Landsat 2015). The red rectangle corresponds to the extent of Fig. 3. C)
 80 Picture from the top of Mannen rockslide (red point in B), toward the North, giving an overview of the U-shaped valley (Rouyet,
 81 11.08.2011).

82 **2.2 MANNEN ROCKSLIDE**

83 The main unstable area of Mannen rockslide is about 500 m wide and 600 m long. It is located between 1,290
84 and 600 m.a.s.l.; between 1,230 and 540 m above the valley bottom. It is delimited at the top by a steep
85 backscarp of about 25 m (Fig. 2).

86 The instability is known from the end of the nineties. Since this time, various studies have been carried out in
87 order to know its geometry and its activity. These include structural analyses (Henderson & Saintot, 2007;
88 Dahle, et al., 2008; Dahle, et al., 2010; Saintot, et al., 2011a, Saintot, et al., 2012), Terrestrial Laser Scanning
89 (TLS) (NGU, 2008 & 2010), boreholes (Saintot, et al., 2011a; Elvebakk, 2012), 2D resistivity survey
90 (Dalsegg & Rønning, 2012) and risk assessment (FylkesROS-fjellskred, 2011).

91 From field campaigns, it appears that the foliation has an average dip direction to S-SE and a penetrative
92 steep dip angle. However the area is located in a high-grade metamorphic unit intensively folded and is thus
93 affected by significant variations of the foliation (Saintot, et al., 2011a, Saintot, et al., 2012). The area is
94 highly fractured and includes several subvertical sets, as well as penetrative discontinuities that wedge-shape
95 the upper part of the instability (Henderson & Saintot, 2007; Dahle, et al., 2010; Saintot, et al., 2011a, Saintot,
96 et al., 2012). In addition to field measurements, structural analysis based on Terrestrial Laser Scanning (TLS,
97 point spacing: ≤ 7 cm) and Aerial Laser Scanning (ALS, DEM resolution: 1m) datasets has been performed
98 using the Coltop3D software (Terranum Ltd) designed to identify sets of discontinuities from point clouds
99 (Jaydoyedoff, et al., 2007). The results are shown as stereonet in Fig. 4. Comparing them to the field data, J3
100 can be identified as the foliation plane, J1/J1'-2' as main sets involved in the wedging and sliding processes
101 and J5/J6 as two major subvertical sets back-shaping the instability (Rouyet, 2013).

102 Based on these investigations, several possibly unstable volumes and corresponding collapse scenarios were
103 outlined (Dahle, et al., 2010). The instability A has a failure surface estimated at 40–80 m deep and a volume
104 of 2–4 Mm³, while the second instability (B) has an estimated 70–110 m deep failure surface and a volume of
105 15–25 Mm³. A third instability (C) includes a larger volume further southeast, estimated to 80–100 Mm³
106 (Saintot, et al., 2011a) (Fig.3).

107 Mannen is considered as a high risk rockslide (Blikra, et al., 2010), combining high probability of occurrence
108 and high potential casualties and damages (FylkesROS-fjellskred, 2011). It threatens houses, roads and a
109 railway track, either directly in the potential runout zone, or indirectly, in case of river damming and outburst.

110 Thus, since 2009, a continuous real-time monitoring network including differential GPS (DGPS), laser-
111 reflectors, extensometers, tiltmeters, a meteorological station and a GB-InSAR system (locations in Fig. 5)
112 has progressively been implemented (Blikra, et al., 2010; Kristensen & Blikra, 2013). The Norwegian Water
113 Resources and Energy Directorate (NVE) is in charge of the monitoring. In autumn 2014 and 2014 significant
114 acceleration in an area with a volume estimated to 120,000–180,000 m³ was recorded in the upper western
115 part of instability B, called Veslemannen. Inhabitants were evacuated and a high alarm level was maintained
116 several weeks before winter stabilization (Skrede, et al., 2015).

117 **2.3 BØRA PLATEAU**

118 Located at the southeastern edge of Mannen rockslide, Børa is an approximately 3 km long and 1 km wide
119 plateau located at 950–1,050 m.a.s.l., 890–990 m above the valley bottom. The largest outlined instability
120 corresponds to a volume estimated at 50–200 Mm³ (Braathen, et al., 2004), and even at 300 Mm³
121 (FylkesROS-fjellskred, 2011). Three smaller unstable parts were also highlighted (FylkesROS-fjellskred,
122 2011) (Fig. 2 and 3), but a revision and definitions of new scenarios are now in progress.

123 Structural analyses (Braathen, et al., 2004; Saintot, et al., 2011a; Saintot, et al., 2012), TLS (NGU, 2008), risk
124 assessment (FylkesROS-fjellskred, 2011), periodical DGPS measurements (Saintot, et al., 2012) and GB-
125 InSAR surveys were performed (locations in Fig. 5).

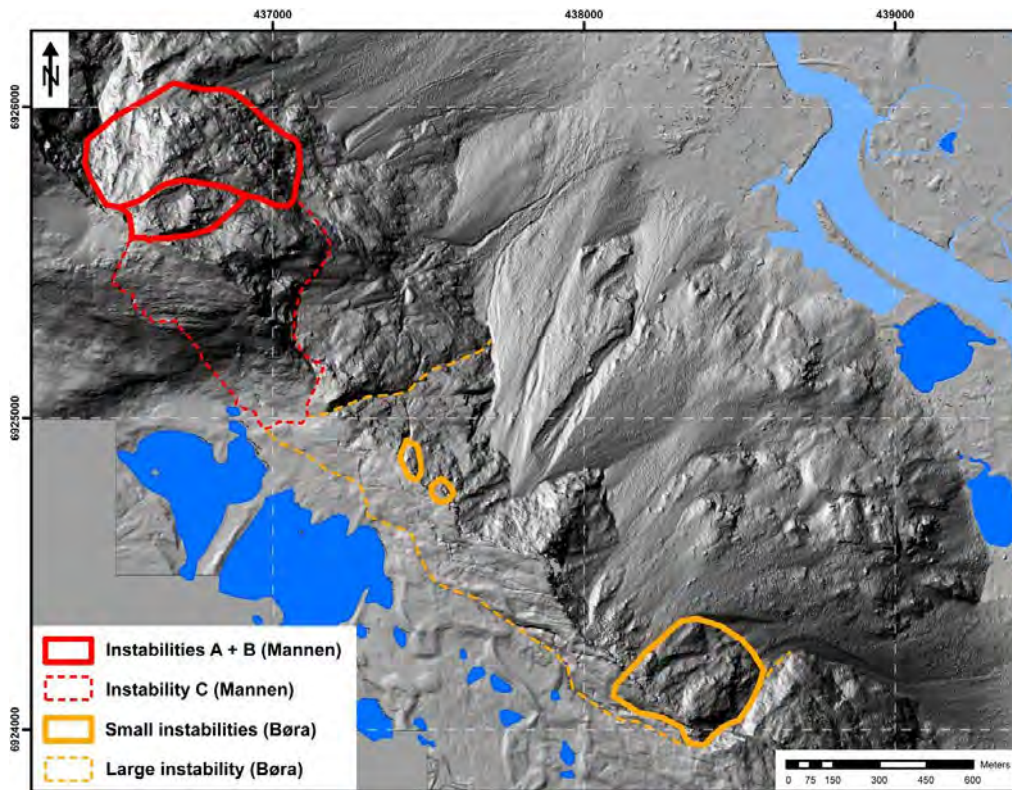
126 From the field campaigns, it appears that the plateau is affected by large subvertical fractures with dip
127 direction to N-NE/S-SW. A subvertical foliation with a dip direction to ENE/WSW highly contributes to
128 shape the edge of the plateau. A flat-lying joint is also identified and explained the development of the
129 instability by a sagging mechanism along flat-lying discontinuities and opening along the vertical sets
130 (Braathen, et al., 2004; Saintot, et al., 2011a, Saintot, et al., 2012). The results from the Coltop3D analysis
131 (Fig. 4, b) highlight overall the same elements, J6' corresponding most likely to the foliation plane and J1 as
132 flat-lying set. Results from 1m ALS DEM are also presented in Fig. 4 (c) and highlights overall the same sets
133 of discontinuities (with some variations of the dip angles as a probable effect of the lower spatial resolution)
134 (Rouyet, 2013).

135 Due to fewer signs of activity and lower estimated probability of failure than for Mannen, fewer
136 investigations were carried out on the plateau and no continuous monitoring is implemented.



137
138
139
140
141

Fig. 2 (2-column fitting, color version required): Top: Pictures of Mannen scarp corresponding to the upper edge of instability A (Rouyet, 11.08.2011). Bottom: Pictures of Børa plateau with edges of small (full lines) and large (dashed line) instabilities and networks of cracks (dotted lines) (Rouyet, 20.08.2012). Instabilities delineations according to Dahle, et al., 2010; Saintot, et al., 2011a; Braathen, et al., 2004; FylkesROS-fjellskred, 2011.



142
143
144

Fig. 3 (2-column fitting, color version required): Edges of Mannen and Børa instabilities according to Dahle, et al., 2010; Saintot, et al., 2011a; Braathen, et al., 2004; FylkesROS-fjellskred, 2011. Location in Fig. 1. Background: hillshade from 1m DEM.

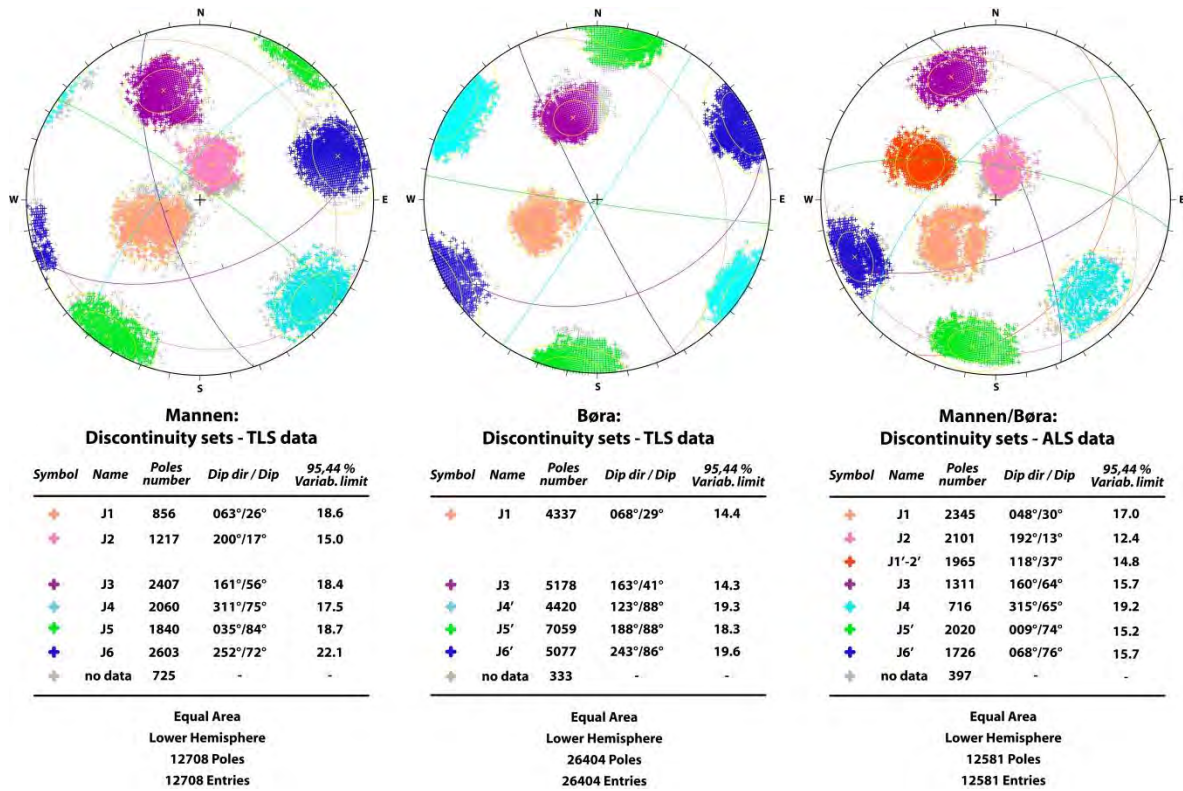


Fig. 4: Stereonets with the main discontinuity sets from Coltop3D analysis using TLS and ALS datasets (Rouyet, 2013)

145
146

147 3 DATA & METHODS

148 3.1 GB-INSAR

149 The current versions of GB-InSAR systems use generally a C, X or Ku frequency band. The measuring head
 150 including transmitting and receiving antennas moves along a 2–3 m long rail in order to synthesize the SAR
 151 images (Antonello et al., 2004; Luzi, 2010; Tofani, et al., 2010; Stumpf, et al., 2011). Details about the
 152 available systems and their characteristics are available in recent reviews (Montserrat, et al., 2014; Caduff, et
 153 al., 2014). The present research analysed data acquired by LiSALab GB-InSAR systems (Ellegi Ltd). It uses a
 154 Ku frequency band (central frequency: 17.2 GHz; wavelength: 17.44 mm). The range resolution (depending
 155 on the bandwidth) is between 0.5 and 3 m and the azimuth resolution (depending on the rail size and the
 156 range) can reach 1.5 m at 500 m. This system allows displacement rates from mm/year to a few m/day to be
 157 measured in near-real time, and up to 4 km away from the sensor. It has to be noted that only 1D
 158 displacements along the line-of-sight (LOS) can be detected. This leads to potential underestimation of the
 159 displacement if the LOS is oblique in respect to the real displacement vector.

160 In early 2010, a permanent GB-InSAR system was installed in the valley to continuously monitor Mannen
 161 rockslide (location: Fig. 5, red star A). The distance to the backscarp is about 2,100 m along the LOS. The
 162 LOS has a SW orientation and a mean view angle (between the beam and horizontal) of 35°.

163 In addition, a second station for intermittent GB-InSAR measurements of Børa area was built in summer
 164 2011 (location: Fig. 5, yellow star B). Two campaigns were carried out at the station B, during 15 days in
 165 August (10.08–24.08.2011) and 28 days in September–October (21.09–18.10.2011). In 2012, a new
 166 campaign was performed during 21 days (19.06–09.07.2012). The objective was to get information about
 167 displacements in Børa area and create a data overlap with the permanent GB-InSAR system in order to check
 168 the reliability of the results. The distance along the LOS to the top of the slope is about 2,000 m. The LOS has
 169 a SW orientation and a mean view angle of about 31°.

170 The main measurement parameters of the two GB-InSAR systems can be found in the Tab. 1. Pictures of the
 171 two stations and their measuring views are presented in Fig. 6 and the main coherent areas for the two sensors
 172 are displayed in Fig. 5. For sake of simplification, the two stations will be thereafter named station A
 173 (permanent GB-InSAR) and station B (intermittent GB-InSAR measurements). In 2014, two new radar
 174 positions were built to carry out periodic measurements, but will be not included in this paper.

175 **Tab. 1 (1.5-column fitting):** Summary of main GB-InSAR acquisitions parameters for the two available systems.

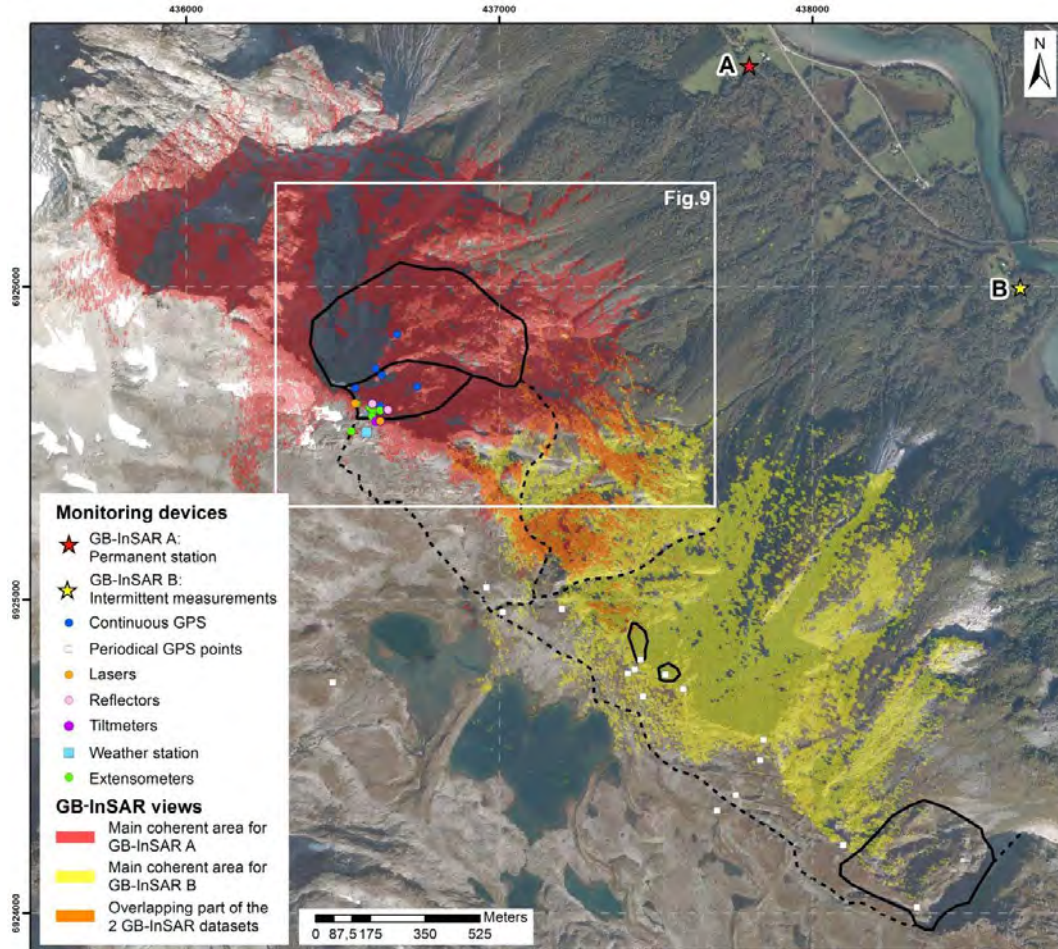
GB-InSAR parameters	Station A	Station B
Acquisition dates	02.2010–now (Continuous)	10.08–24.08.2011 21.09–18.10.2011* 19.06–09.07.2012
Maximum range	2,700 m	2,400 m
Range resolution	1.9 m	
Azimuth resolution	7.8 m at max. range 1.5 m at 500 m	6.9 m at max. range 1.5 m at 500 m
Azimuth width	2,200 m	2,400 m
Central frequency (wavelength)	17.2 GHz (17,44 mm)	
Bandwidth	80 MHz	
Number of freq. points	2001	
Synthetic aperture	3 m	
Number of steps inside the aperture	751	
Acquisition time	8 min	
Revisiting time	10 min	

176 * Campaign partly affected by snow.

177 Images acquired from station A were processed in order to get information about displacements over one year
178 in 2011–2012 (cf. Section 4.1.1). Because of the coherence loss during the winter season due to snowfall, the
179 reference periods were chosen in June. Datasets from the campaigns at the station B were also analysed. The
180 results presented in Section 4.1.2 correspond to the first 2011 campaign and the 2012 campaign. The second
181 2011 campaign did not highlight significant displacements and was partly affected by snowfall. Images
182 acquired from the station A at the same periods were also analysed and the results compared with those of the
183 station B. Using the large dataset acquired at the station A, time series at specific locations between February
184 2010 and December 2012 were extracted and are analyzed in Section 4.1.3.

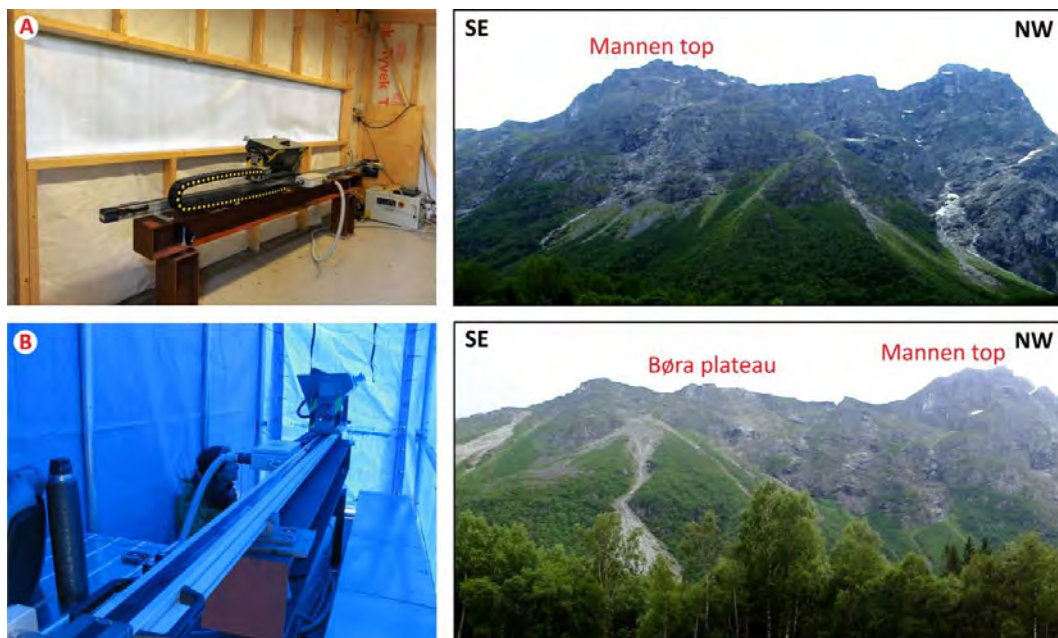
185 The GB-InSAR data were processed using LiSALab software (Ellegi srl.). The results are 3x3 multilooked
186 and analysed using a 0.7 coherence filter. A radar image is acquired every 10 minutes, but for comparisons
187 24h-averaged images were used. This kind of data requires a procedure to remove the atmospheric
188 component (i.a. Caduff, et al., 2014; Kristensen, et al., 2013). This has been performed by combining the 24h-
189 averaging and a supervised approach by manually selecting reference regions. The averaging contributes to
190 reduce significantly the noise and phase component related to turbulent atmosphere. The supervised approach
191 allows residual atmospheric disturbances to be corrected by selecting areas without any evidence of
192 significant ground deformation. Different areas have been tested by different operators and do not show
193 significant variations on the main areas of interest ($< 1\text{mm}$). In Mannen/Børa final results, the main moving
194 areas show clear spatially and temporally progressive trends. In the overlapping area, they are detected by
195 both GB-InSAR systems using two independent processing.

196 In Fig. 7–11 (cf. Section 4.1), negative values correspond to movements toward the sensor (distance
197 shortening along the LOS); positive values correspond to movements away from the sensor (distance
198 increasing along the LOS). For sake of simplification and reader convenience, they are expressed thereafter as
199 downward/upward displacements.



200
201
202

Fig. 5 (2-column fitting, color version required): Location of ground-based monitoring devices (in situ and GB-InSAR), coherent areas for GB-InSAR systems (here using 0.7 filter applied on 10-16.08.2011 interferogram). Background: 0.2m orthophoto 2006.

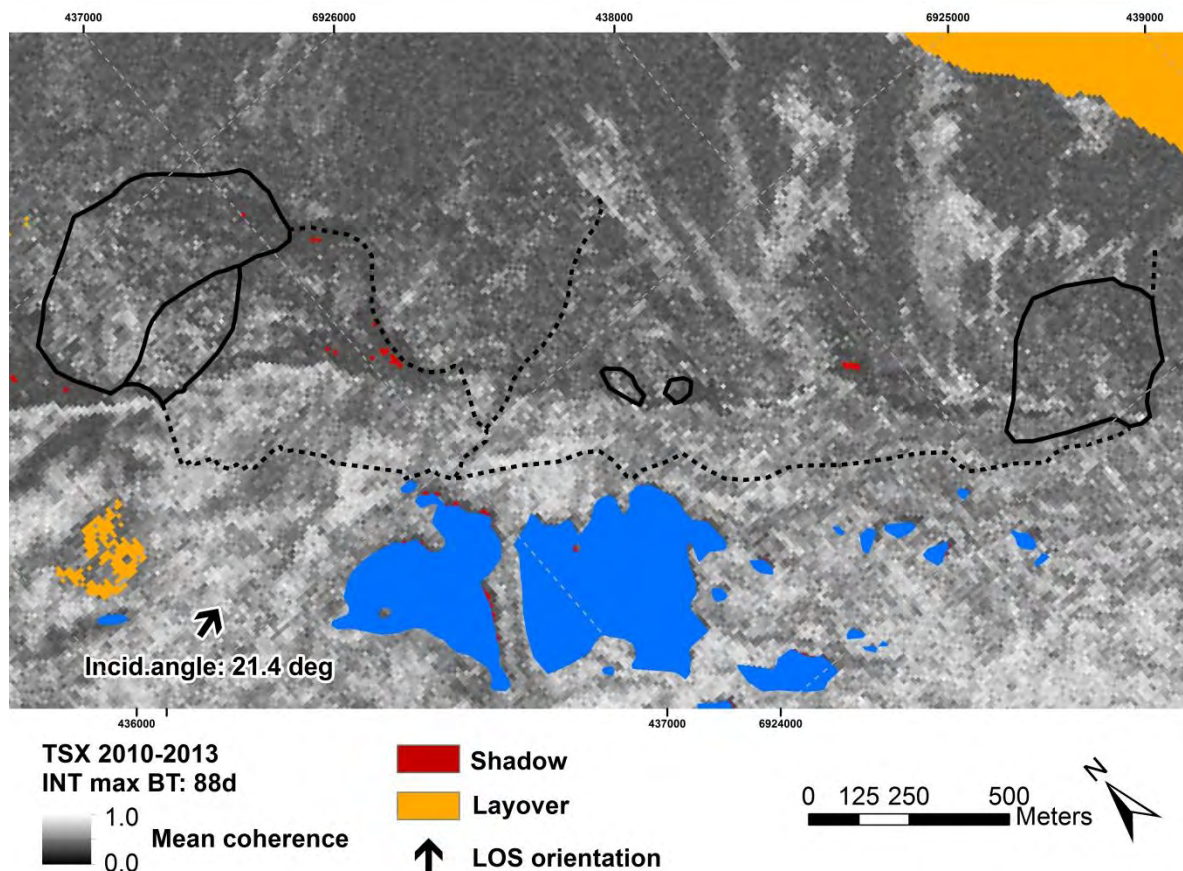


203
204
205
206

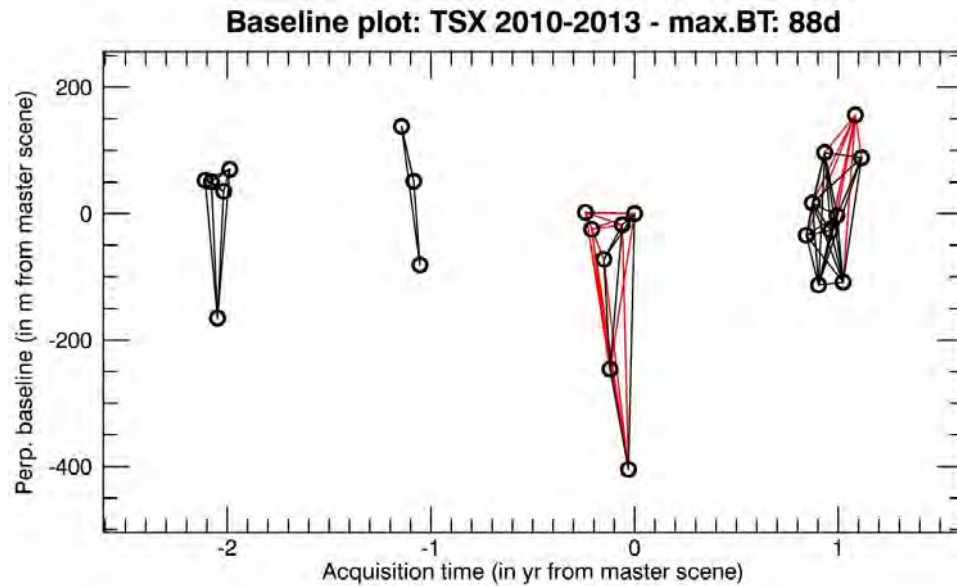
Fig.6 (2-column fitting, color version required): Left: Pictures of the two GB-InSAR stations. **A:** permanent GB-InSAR station, **B:** station for intermittent GB-InSAR measurements **Right:** Respective views from the stations (Rouyet/Derron, 20.08.2012). Acquisition parameters in Tab.1 and locations in Fig. 5.

207 **3.2 SATELLITE INSAR**

208 In addition to GB-InSAR data, satellite InSAR images acquired by TerraSAR-X/TanDEM-X (TSX/TDX)
 209 sensors (Airbus Defense & Space - Inforterra GmbH) were processed. The satellites use a X band (central
 210 frequency: 9.6 GHz; wavelength: 3.11 cm) and have a repeat-pass time interval of 11 days. The dataset was
 211 acquired with a StripMap mode and from an ascending orbit (LOS orientation: 75.2°N, incident angle: 21.4°)
 212 in order to get reduced geometrical distortions on east-facing slopes. The LOS and the land cover provide a
 213 good coverage of the plateau and the upper part of the slope. The bottom part of the slope is partly masked
 214 out due to vegetation inducing low coherence and layover effect from the other side of the valley (Fig. 7).
 215 Due to loss of coherence in case of snowfall, only 24 snow-free scenes between July 2010 and October 2013
 216 were used (Fig. 8). The satellite data characteristics are summarized in Tab. 2 (top).



217 **Fig. 7 (2-column fitting, color version required):** Satellite InSAR mean coherence map from Multi-year Stacking method using
 218 TSX/TDX satellite InSAR data from ascending geometry (geocoding resolution: 10m x 10m). Areas in orange and red are respectively
 219 affected by layover and shadow effects.
 220



221
 222 **Fig. 8 (1.5-column fitting, color version required):** Baseline plot (spatial baseline vs. acquisition time) with the 24 selected TSX/TDX
 223 ascending scenes (high density in summer, gaps in winter). Scenes: black circles, generated interferograms: lines (black: selected, red:
 224 removed).

225 The results presented thereafter as maps were obtained using a simple stacking of interferograms with small
 226 spatial (max. 600m) and temporal (max. 88d) baselines. This allows a large amount of interferograms from
 227 disconnected seasons to be processed together in order to reduce atmospheric effects and other noise sources
 228 (Zebker & Villasenor, 1992; Zebker, et al., 1997; Gabriel, et al., 1989). A second processing using only the
 229 interferograms from 2013 has been performed in order to get one connected set and be able to apply Small
 230 BAseline Subset (SBAS) method (Berardino, et al., 2012; Lauknes & Larsen, 2011). This allows the time
 231 series presented in Section 4.2 to be retrieved.

232 The processing was performed using the Norut developed GSAR software (Larsen et al., 2005), using the
 233 national 10m DEM (provided by Kartverket) to remove the topographic component. The InSAR processing
 234 parameters can be found in Tab. 2 (bottom). The numbers of generated interferograms depend on the chosen
 235 spatial/temporal baselines thresholds (column 4, InSAR processing parameters, Tab. 2) and a second manual
 236 selection is performed to remove interferograms affected by low coherence, significant atmospheric effects or
 237 obvious unwrapping errors (column 5, InSAR processing parameters, Tab. 2).

238 In Section 4.2 (Fig. 14–15), in order to have a straight-forward comparison with GB-InSAR results, signs
 239 convention is inverted from the LOS-logic: negative values correspond to movements away from the satellite
 240 and positive values correspond to movements toward the satellite.

241

Tab. 2 (2-column fitting): Summary of characteristics of satellite data and processing parameters

Satellite data characteristics							
Satellite	Band	Dataset	Time period	Repeat-pass interval	Number of images	Track angle (LOS orient.)	Incidence angle
TSX/TDX	X (λ : 3.11 cm)	StripMap Ascending	07.2010 – 10.2013	11 days	24	-14.81° (75,2°N)	21.4°

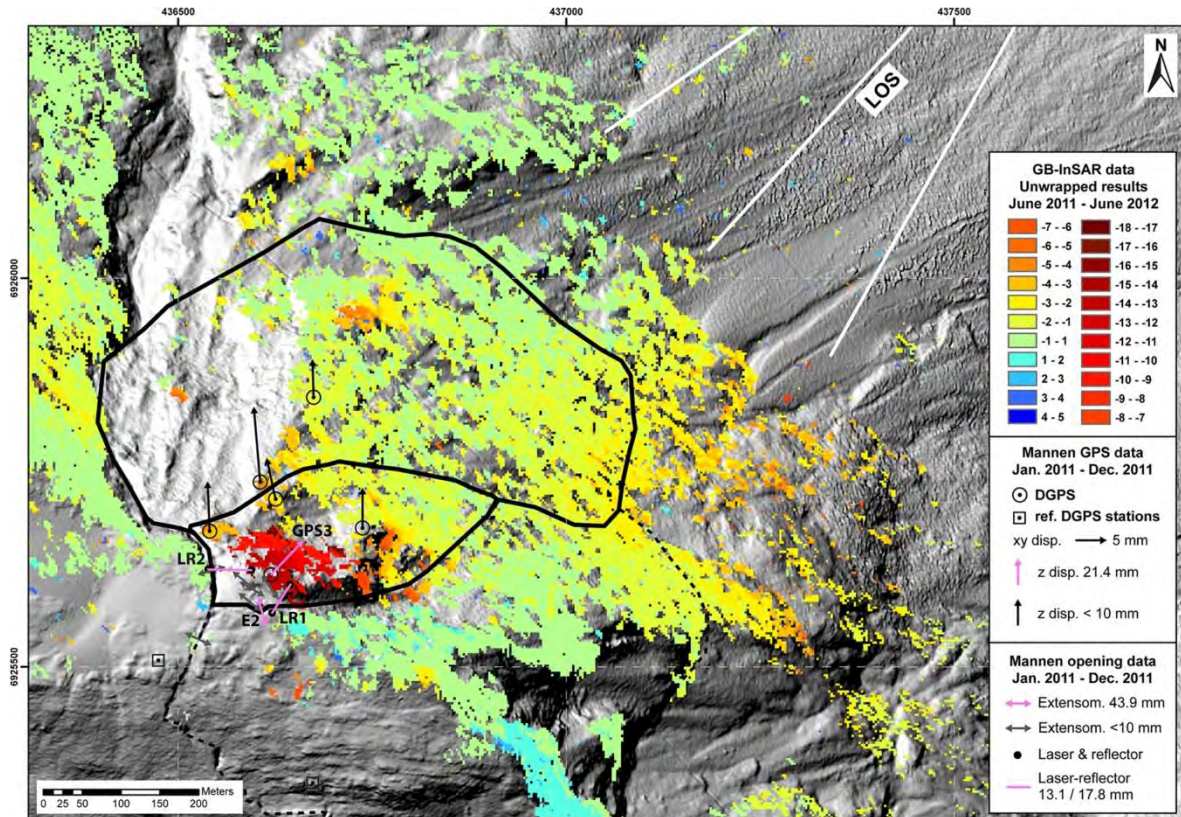
InSAR processing parameters							
Processing type	Multilooking (range x azimuth resolution)	Max. spatial & temporal baselines	Generated interfer.	Selected interfer.	SBAS spatial & temporal filters	Pixel selection (coh. & fraction of image thr.)	Calibration point (UTM 32N)
Multi-years Stacking	Factors: 3 x 4 (8.3 m x 8.3 m)	600 m / 88 d	69	49	-	0.4 & 0.6	6925508 436468
2013 SBAS			35	27	500 m / 44 d	0.4 & 0.6	(GPS 1 stable)

242 4 RESULTS

243 4.1 GB-INSAR RESULTS

244 4.1.1 ONE YEAR DISPLACEMENTS ON MANNEN ROCKSLIDE

245 The velocities recorded along the LOS between June 2011 and June 2012 reached 18 mm/year toward the
 246 GB-InSAR in the upper part of Mannen rockslide (Fig. 9). This is overall consistent with in situ data that
 247 show 23 mm/year with a main vertical component for DGPS3 and 18 mm/year for the laser-reflectors (Fig. 9,
 248 pink elements). A clear velocity contrast is noticeable between the upper southern part of the instability A and
 249 the rest of instabilities A and B. During this time interval, 7 mm toward the GB-InSAR is measured on the
 250 lower southeastern part. In the lower northern part, mainly horizontal displacements toward the north are
 251 recorded by DGPS. Due to an oblique LOS relatively to the displacement vectors, the GB-InSAR is not able
 252 to capture a significant part of the movement in this area. No information is available in the western part of
 253 instability B located in a shadow area. In order to overcome these problems, a new station for intermittent
 254 GB-InSAR campaigns was set up further northwest, and measurements started in September 2014 (Skrede, et
 255 al., 2015).



256
257
258
259
260

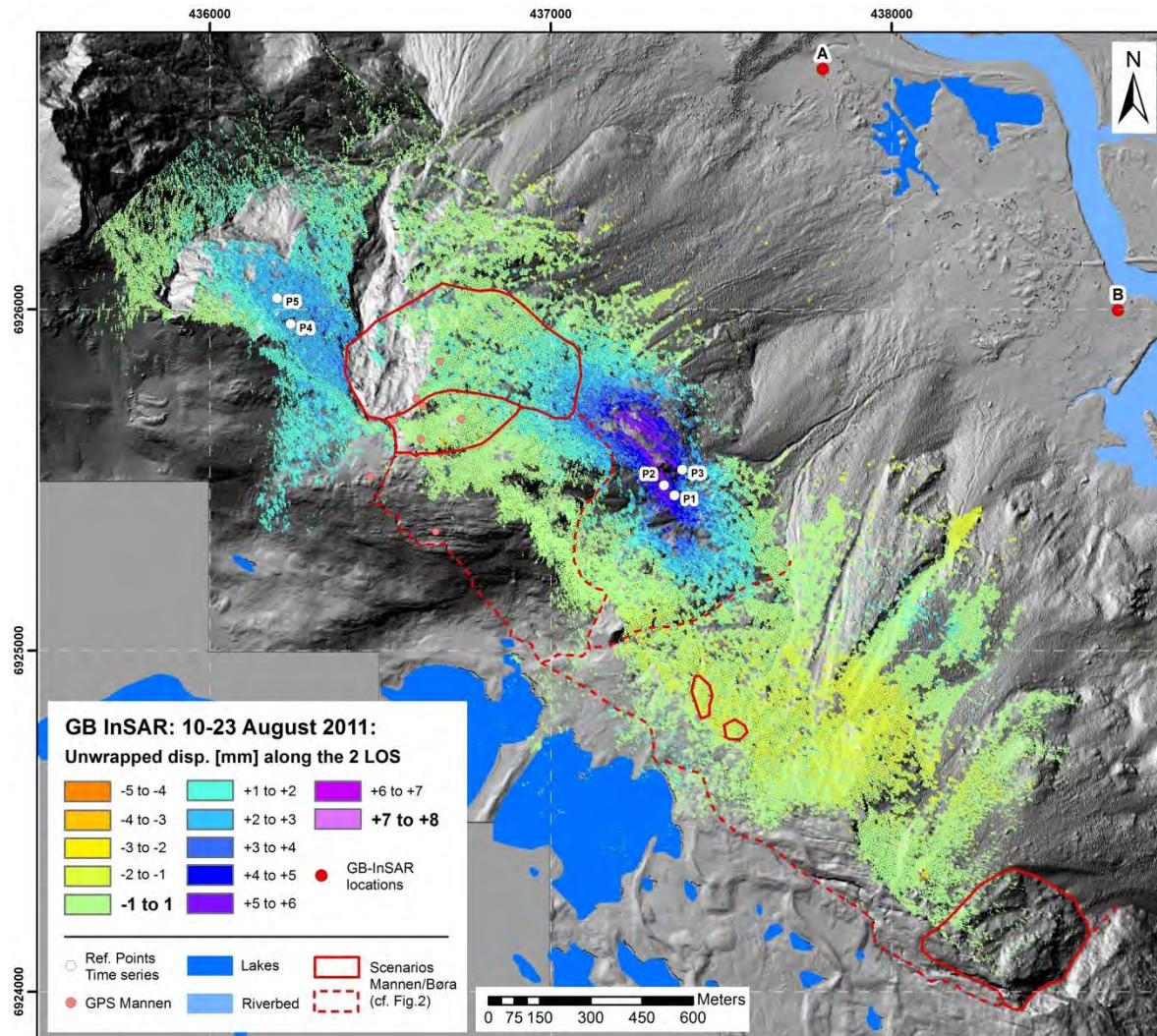
Fig. 9 (2-column fitting, color version required): 2011 monitoring data on Mannen rockslide: GB-InSAR displacements (station A) in mm between June 2011 and June 2012 (geocoding resolution: 3m x 3m) and in situ displacements in mm between January 2011 and December 2011 (in pink are displayed in situ results with most significant velocities). Location in Fig. 5. Background: hillshade from 1m DEM.

261 **4.1.2 INTERMITTENT BØRA CAMPAIGNS & CORRESPONDING MANNEN RESULTS**

262 During the first Børa campaign in August 2011, considering the interval 10.08–23.08.2011 (14 days), no
263 significant movement was detected on Mannen rockslide using GB-InSAR (station A). This is overall
264 consistent with the in situ data, which show that main periods of movements occurs during the thawing period
265 earlier in the season. On Børa, the results of the station B highlight a slight downward trend in the
266 northwestern upper part that can be ascribed to residual atmospheric effects, but several fast moving small
267 sectors are detected in active rockfall areas in the southeastern part of the dataset (Fig. 10). Displacements are
268 also detected in the lower part on debris cones affected by active torrential processes and significant
269 erosion/deposition cycles.

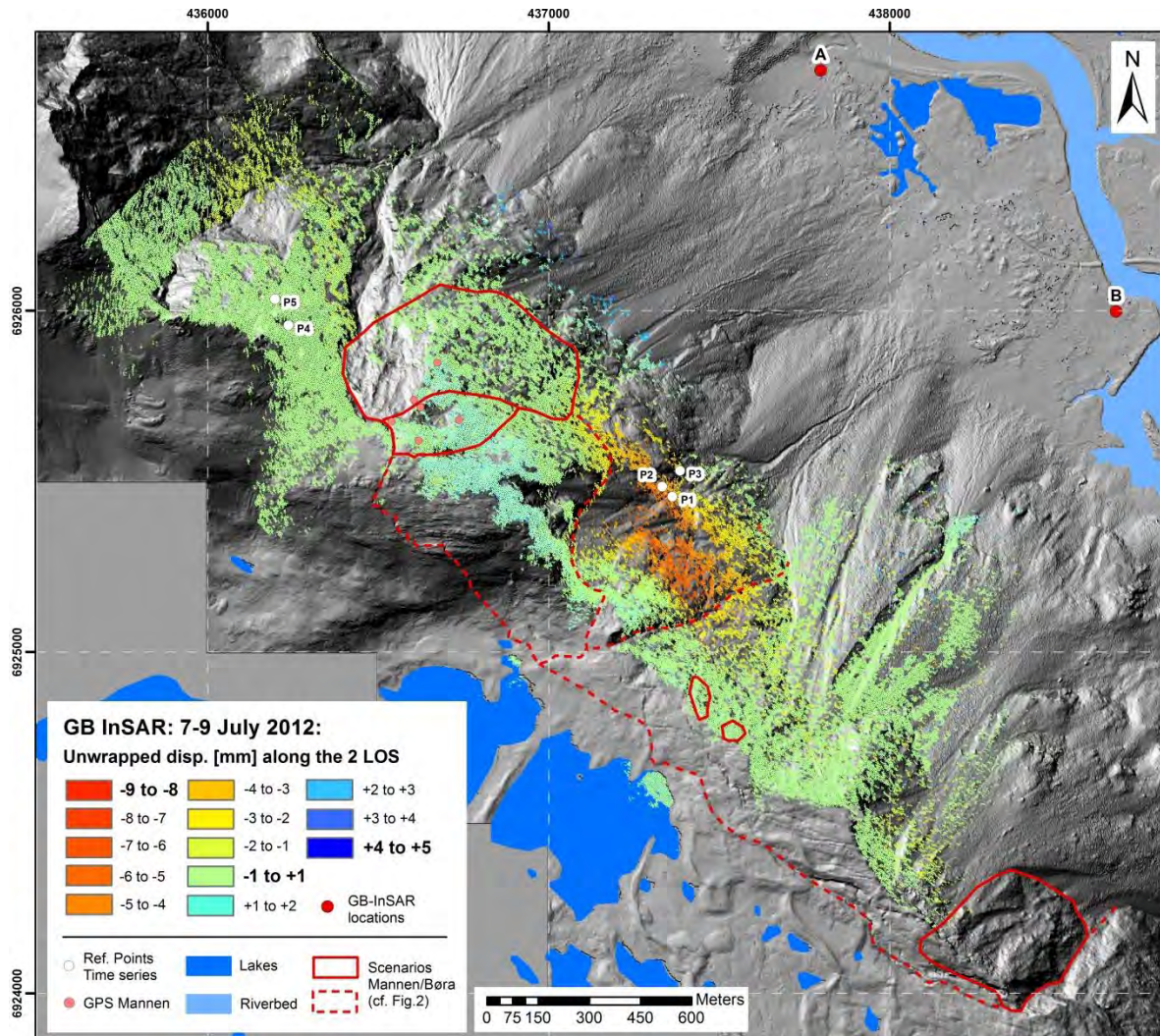
270 The main interesting element is located in the overlapping part of the two GB-InSAR datasets (cf. Fig. 5).
271 During August campaign in 2011 an increase of sensor-to-target distance is detected, corresponding to
272 upward displacements. The displacements exceed 8 mm in 13 days (Fig. 10). In July 2012, this moving part is
273 again clearly distinguishable, but this time the movements are inverted (shortening of sensor-to-target

274 distance, i.e. downward displacements). The highest displacement rate is reached during 07.09–09.07.2012
 275 interval (up to 8 mm in 2 days) (Fig. 11). For both campaigns at the station B (August 2011 and June–July
 276 2012), GB-InSAR results are consistent with station A in the overlapping part, and the georeferenced results
 277 show a good spatial fit of the two datasets (Fig. 10 and Fig. 11). The moving part is well delineated and
 278 affected an area of approximately 1x0.5 km².



279
 280
 281
 282
 283

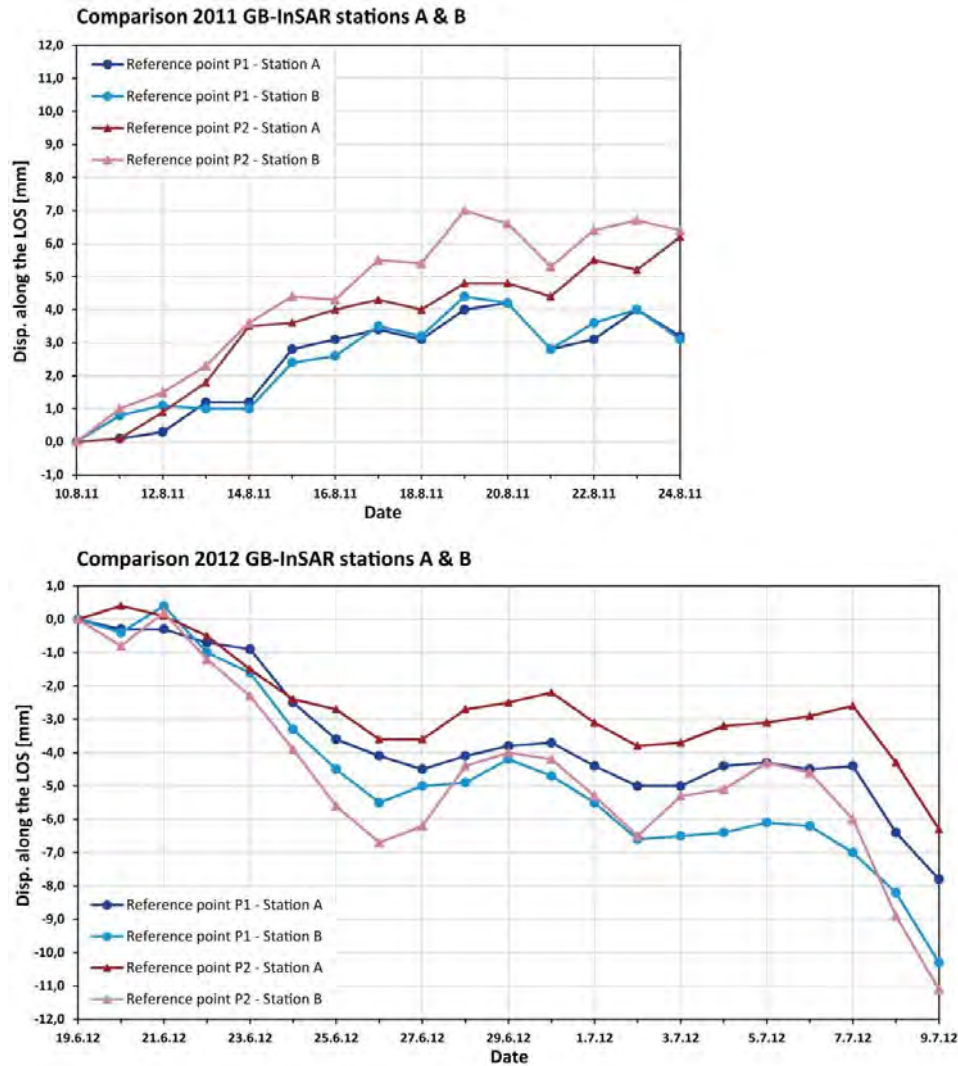
Fig. 10 (2-column fitting, color version required): Georeferenced and unwrapped GB-InSAR results (stations A and B) for the period 10.08–23.08.2011. Geocoding resolution: 2m x 2m. The GB-InSAR results are expressed along the respective LOS of the two systems. In overlapping part, when data are available for both devices, results from the station A are displayed. Background: hillshade from 1m DEM.



284
 285
 286
 287
 288

Fig. 11 (2-column fitting, color version required): Georeferenced and unwrapped GB-InSAR results (stations A and B) for the period 07.07–09.07.2012. Geocoding resolution: 2m x 2m. The GB-InSAR results are expressed along the respective LOS of the two systems. In overlapping part, when data are available for both devices, results from the station A are displayed. Background: hillshade from a DEM, resolution 1 m.

289 Time series are generated at two locations (P1 and P2) where coherent information is available for both GB-
 290 InSAR systems, in the overlapping part of the two datasets (Fig. 12, point locations in Fig. 10 and 11). The
 291 data are in the respective LOS for each GB-InSAR system. They confirm the upward trend in August 2011
 292 (Fig. 12, top). For both points, maximal displacements are reached after 9 days. The measurements show a
 293 relative stability the next 5 days. The two GB-InSAR systems provide measurements in good agreement
 294 (overall same rate of movement and variations). In June–July 2012, the time series confirm the movement
 295 inversion and the consistency of both datasets (Fig. 12, bottom). The time series show two main stages of
 296 acceleration during 21.06–26.06.2012 (7 mm in 5 days) and 06.07–09.07.2012 (7 mm in 3 days).



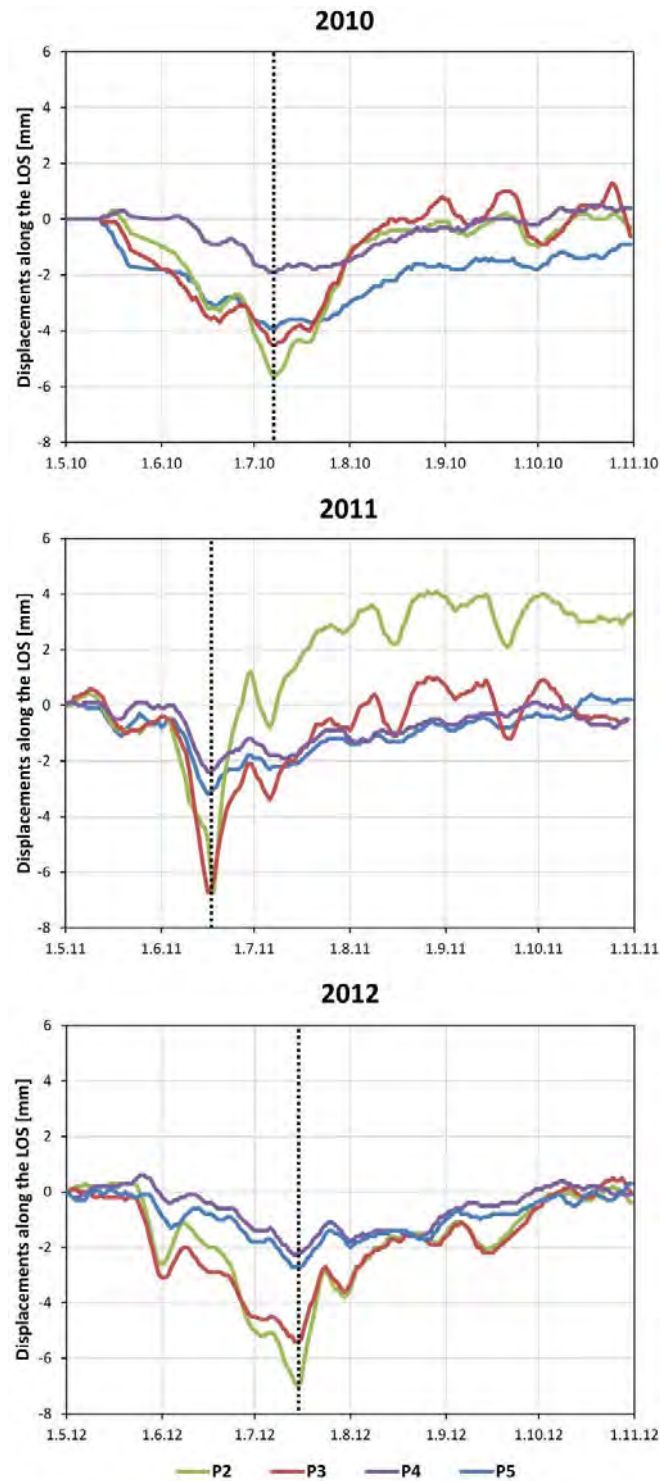
297
298
299

Fig. 12 (1.5-column fitting, color version required): Comparison of time series from GB-InSAR A & B at P1-P2 locations. **Top:** First campaign at the station B (10.08–23.08.2011). **Bottom:** 2012 campaign at the station B (19.06–9.07.2012) (points locations in Fig. 8–9)

300 **4.1.3 INTER-ANNUAL RESULTS**

301 Using the whole GB-InSAR dataset acquired at the station A since February 2010 to the end of 2012,
 302 significant variations are confirmed in the southeastern part (overlapping part with GB-InSAR B). Similar
 303 trends are visible in the northwestern part of the monitored area but with lower amplitude (P4–P5) (Fig. 13,
 304 point locations in Fig. 10–11). The movement cycles have a seasonal recurrence. In 2010, 2011 and 2012,
 305 movement inversions occur abruptly between June and July (from downward to upward displacements) and
 306 the fastest upward peaks occur afterwards every year between mid-June and August (dashed lines, Fig. 13).
 307 For P2, the upward displacement reaches 13 mm in 72 days in summer 2011. From the meteorological data
 308 (Fig. 13, graphs on the right. Station at the top of Mannen, cf. Fig. 5), it is possible to see that the downward
 309 trend is clearly related to the thawing period and its duration is affected by the abruptness of the transition

310 (short duration and sharp transition in 2011 vs longer duration and smoother transition in 2012). This
 311 inflation/deflation phenomenon, hereafter so called rock slope breathing, is discussed more into details in
 312 Section 5.2.



313
 314
 315

Fig. 13 (1-column fitting, color version required): Time series from GB-InSAR A at P2–P5 locations between May and October 2010, 2011 and 2012 (points locations in Fig. 10–11). Meteorological data from the top of Mannen (station location in Fig. 5)

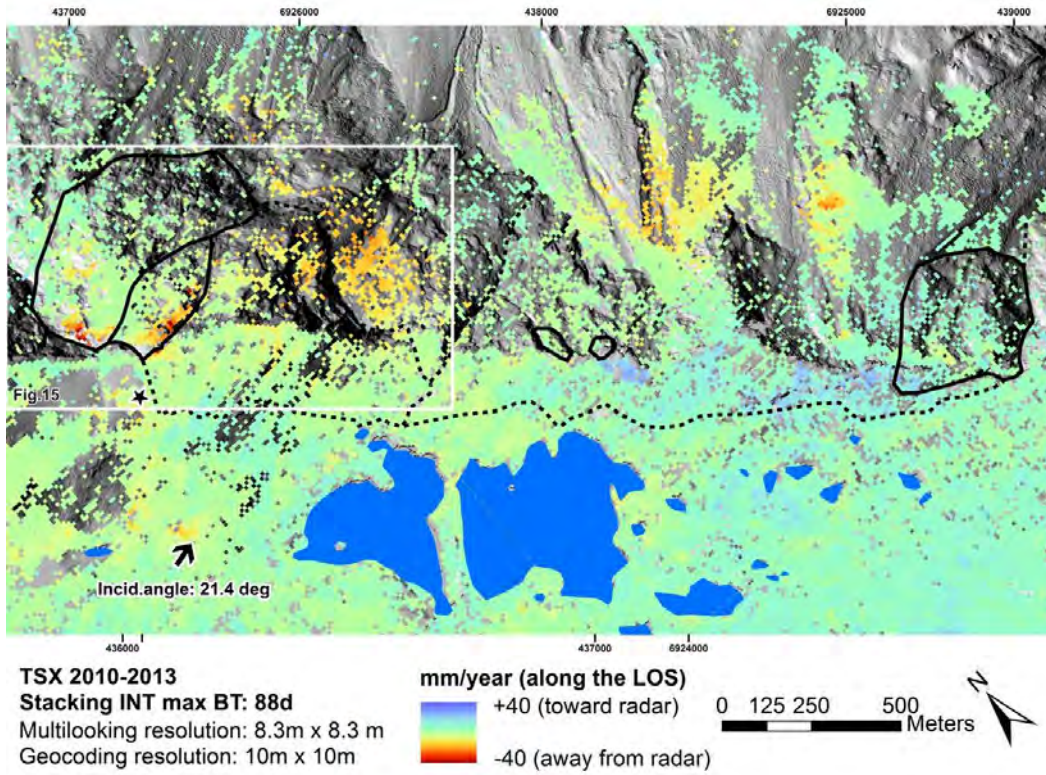
316 4.2 SATELLITE INSAR RESULTS

317 The TSX/TDX multi-years Stacking processing using maximal temporal baselines of 88 days (cf. Tab.2)
318 shows rate of movement up to 40 mm/year and 58 mm/year downward (distance increasing along the LOS)
319 recorded for some small sectors in the upper part of the instability A and B, while the main moving area has
320 values between 15 and 25 mm/year (Fig. 14–15). It has to be noted that the results expressed in annual mean
321 velocity correspond to an extrapolation of the snow-free seasons (no inter-annual interferogram). Large
322 displacements during these periods can thus lead to an overestimation of the values.

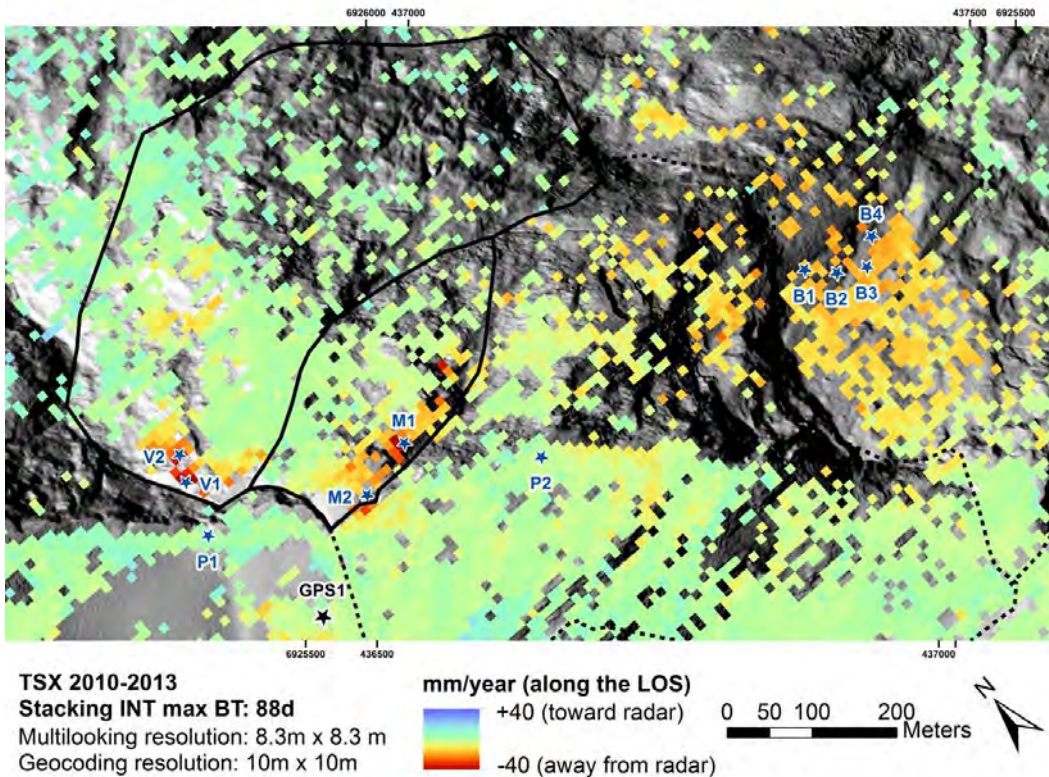
323 In the southwestern part of the instability B (Veslemannen), movements are detected. Previously this area was
324 not documented by ground-based instruments, but after significant movements and acceleration were
325 measured by GB-InSAR in September-October 2014, extensometers and geophones were installed at this
326 location and an automatic LiDAR system was put in the valley. The Veslemannen site is now closely
327 monitored (Skrede, et al., 2015).

328 On Børa some displacements are also detected, especially in the lower part (debris cones affected by
329 torrential processes and erosion/deposition cycles).

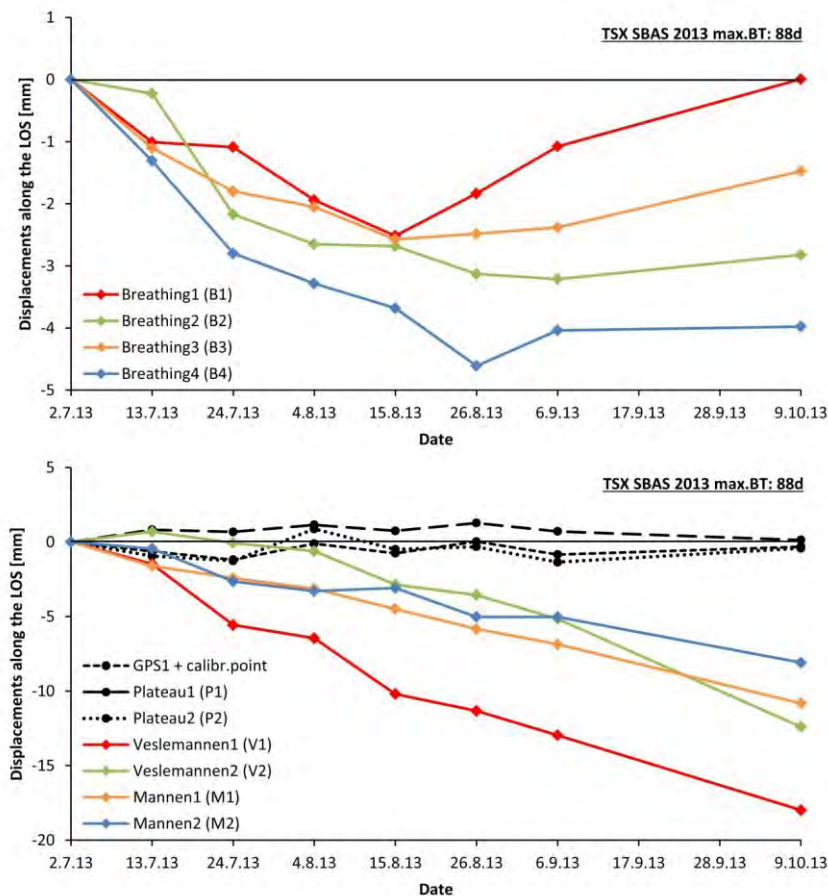
330 The area subjected to rock slope breathing in the overlap of the GB-InSAR systems is not totally well
331 documented by TSX/TDX satellites due to the lower coherence downslope. The LOS of the sensor can also
332 lead to potential misestimating of displacements in the area due to oblique or even perpendicular view in
333 respect to the real vectors. However, mean rates up to 28 mm/year downward are detected from the Multi-
334 year Stacking processing. Thanks to SBAS method using interferograms from 2013 it is also possible to
335 retrieve time series between July and October 2013. Results at different locations on the area affected by rock
336 slope breathing are presented in Fig.16 (top). For sake of comparison and reliability check, other time series
337 from the plateau (supposed as stable) and on Mannen rockslide can be seen in Fig. 16 (bottom). The locations
338 of the selected points are displayed on the map in Fig. 15. The results highlight three different clear trends: 1)
339 round zero displacements on the plateau, 2) quite linear displacements on the rockslide to 18mm in 3 months,
340 3) small displacements with inversions in August on the area affected by rock slope breathing, that confirm
341 the GB-InSAR results.



342
 343 **Fig. 14 (2-column fitting, color version required):** Multi-years Stacking results using 2010-2013 TSX/TDX satellite data from
 344 ascending geometry (geocoding resolution: 10m x 10m). Black arrow: LOS, black star: calibration point. Background: hillshade from 1m
 345 DEM.



346
 347 **Fig. 15 (2-column fitting, color version required):** Zoom on Mannen rockslide and area affected by rock slope breathing. Multi-years
 348 Stacking results using 2010-2013 TSX/TDX satellite data from ascending geometry (geocoding resolution: 10m x 10m). Black arrow:
 349 LOS, black star: calibration point, blue stars: location of SBAS time series. Location in Fig. 14. Background: hillshade from 1m DEM.



350

351
352

Fig. 16 (1.5-column fitting, color version required): SBAS time series in snow-free season 2013. **Top:** B1–4 on area affected by rock slope breathing. **Bottom:** Others examples of time series on the plateau and on Mannen rockslide. Note the difference of scale in y-axis.

353 5 DISCUSSION

354 This section is organized in two parts. In Section 5.1, the results from available measuring systems (GB-
355 InSAR, in situ and satellite InSAR) are summarized and main findings about the spatial distribution of
356 movement rate are described. As main focus of the article, the rock slope breathing phenomenon and the
357 current assumptions about the factors explaining this effect are discussed in Section 5.2.

358 5.1 MANNEN ROCKSLIDE & BØRA PLATEAU

359 The combined results of GB-InSAR, in situ and satellite InSAR contribute to have a good overview of the
360 Mannen rockslide behaviour and affine the extents of the different instabilities especially in the inaccessible
361 steep slopes. Overall the results are consistent and complementary. They allow the area to be divided in three
362 parts:

363 (1) A main active part in the upper southern part of the instabilities A. It is documented by DGPS 3 (23

364 mm/year in 2011), two lasers-reflectors (to 18 mm/year in 2011) and the extensometer 2 located in the
365 backcrack (44 mm/year in 2011), GB-InSAR data (to 18 mm/year between June 2010-2011) (Fig. 9) and
366 TSX/TDX satellite InSAR (to 40 mm/year) (Fig. 14-15). According to DGPS results, this moving area has a
367 main vertical component and a northeast horizontal orientation.

368 (2) A second active part in the upper western part of the instability B (Veslemannen), not documented by in
369 situ data but highlighted by satellite data (to 58 mm/year) (Fig.13), and recently by the new 2014 GB-InSAR
370 station (Skrede, et al., 2015).

371 (3) A slower part including the other in situ devices. The DGPS highlighted rates of displacement between 7
372 and 13 mm/year in 2011, the GB-InSAR data velocities to 6 mm/year (Fig. 9) and 10 mm/year for satellite
373 InSAR (Fig. 14–15). The especially low values recorded by GB-InSAR can be explained by an oblique LOS
374 orientation in respect to the movement orientation documented by the DGPS (main horizontal component
375 with a north orientation).

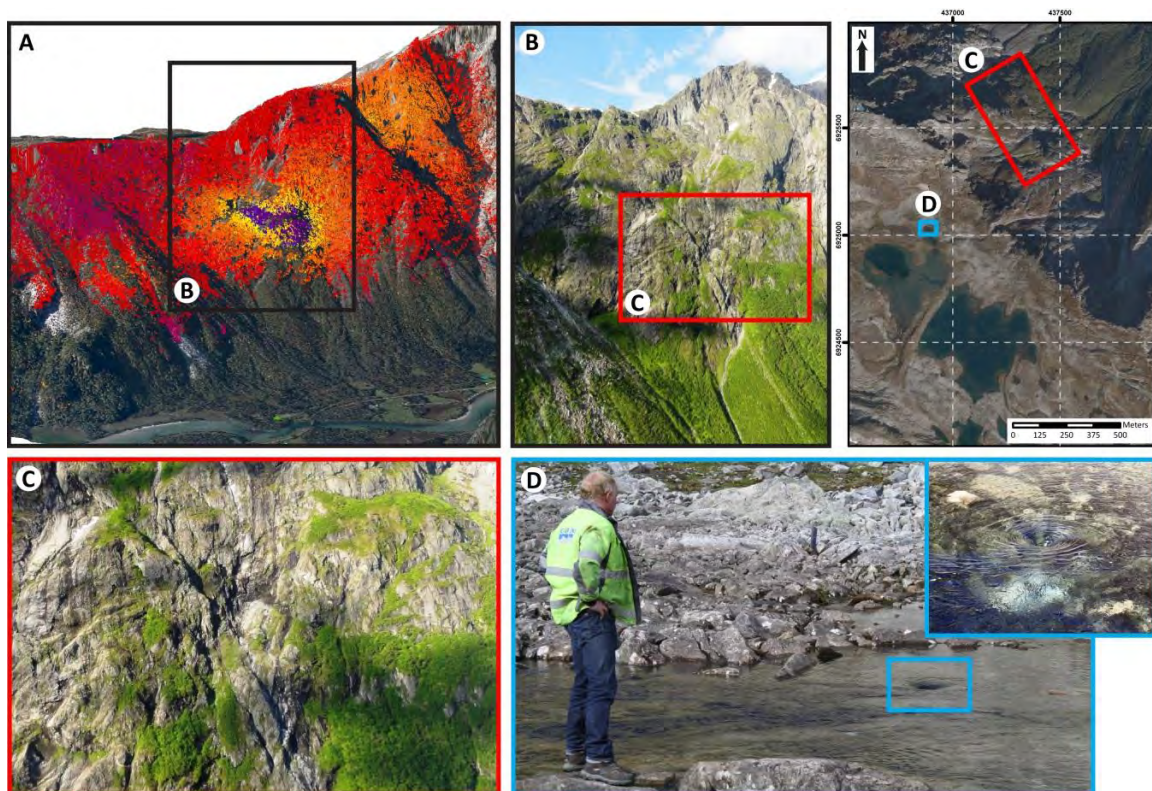
376 At Børa, GB-InSAR system did not highlight significant moving patterns during the intermittent campaigns,
377 except in the area discussed in Section 5.2. However, it detected some small hot spots along the upper part of
378 the slope and on debris cones downslope (Fig.10–12). This seems consistent with the satellite InSAR results
379 which highlight also some localized moving areas (Fig. 14–15).

380 **5.2 ROCK SLOPE BREATHING**

381 The GB-InSAR campaigns at station B highlighted the presence of an area subjected to variations of
382 movement in the overlapping part with the data from the continuous GB-InSAR system (station A). The
383 combination of the GB-InSAR datasets from two stations showed that the movements fluctuate in time and
384 has a seasonal recurrence (observed during three consecutive years of monitoring). SBAS time series from
385 TSX/TDX satellite data confirm these variations.

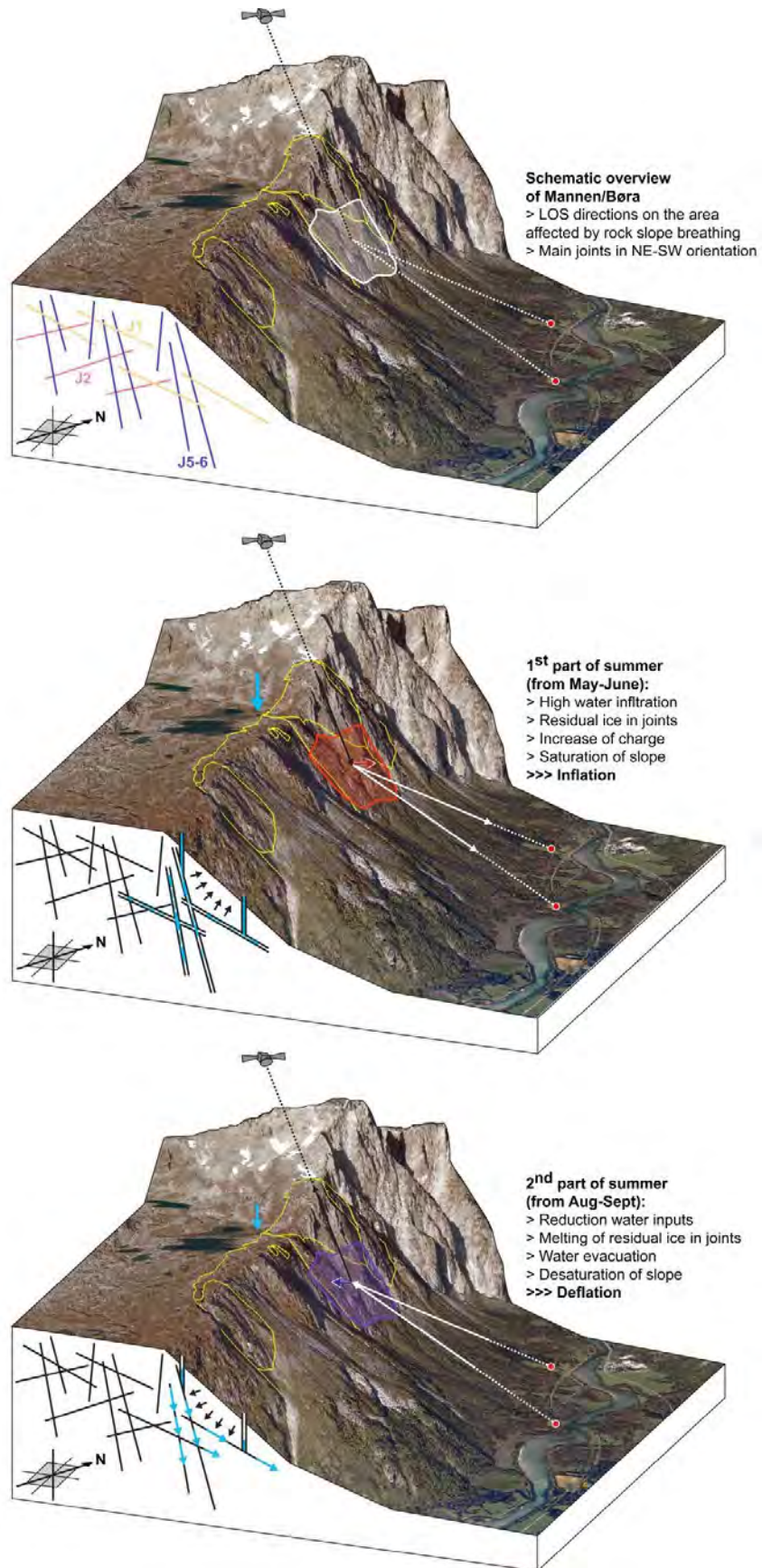
386 Looking at the location map (Fig. 17, top right), we can see that this part is located below the two
387 Kråkenesvatna lakes. These lakes have no visible outlets, but at their northern edge, a siphon phenomenon
388 can be observed during the summer (Fig. 17, D). This testifies a strong water infiltration in this area. Tracing
389 tests from Kråkenesvatna lakes were performed in October 2007 and concluded to a complex drainage system
390 involving multiple pathways of water in the rock mass. The measurements at 19 source locations in the valley

391 revealed indeed that the peaks of responses curves are multiple and vary between 3 and 10 days according to
 392 the location (Kvakland, 2009). Considering the time of transit through the rock mass the assumption of rock
 393 slope breathing caused by variations of groundwater charge is likely. The order of magnitude of 10 days fits
 394 well with the variations detected from GB-InSAR (Fig. 13). In Fig. 10–11, we can moreover see that the
 395 moving area is located just below and between the main delineated instabilities. It probably contributes to a
 396 convergence/concentration of groundwater from the large fractures at the basal and lateral edges of the
 397 unstable areas. Thus, the current assumption to explain the displacements measured by GB-InSAR is that the
 398 area is subjected to large variations in groundwater pressure. At the beginning of the thawing season, an
 399 increase of charge due to high water infiltration and possible presence of residual ice in fractures lead to
 400 millimetric inflation of the rock slope, and thus downward displacements. During the summer, the reduction
 401 of water inputs and complete melting of residual ice in fractures make possible a water evacuation and
 402 desaturation of the slope, which leads to a deflation, and thus upward displacements. The assumption is
 403 represented as simplified schemes in Fig. 18. The displayed structures are based on the approximate results of
 404 TLS/ALS analysis using Coltop3D software (Rouyet, 2013, cf. Fig. 4).



405
 406
 407
 408
 409

Fig.17 (2-column fitting, color version required): Focus on the area subjected to rock slope breathing. **A:** GB-InSAR results (here wrapped) of August 2011 campaign at station B and the corresponding results of station A. **B:** Picture of the slope (Rouyet, 20.08.2012). **C:** Zoom on sector subjected to rock slope breathing (Rouyet, 20.08.2012). **D:** Siphon phenomenon in Kråkenesvatna lakes (NVE, 09.09.2011).



410
 411
 412

Fig.18 (1.5-column fitting, color version required); Simplified 3D models of Mannen/Børa summarizing the geometries of the remote sensing systems, the main geological structures and discussing the rock slope breathing effect. Background: 0.2m orthophoto 2006.

413 To illustrate the impact of water variations, a calculation of elastic behaviour (Hooke’s law) can be performed
 414 considering a simplified theoretical case with isotropic and homogenous material, equal lateral stresses and
 415 no shear stresses (David & Selvadurai, 1996). By comparing the gravity stresses, considering dry and
 416 saturated cases, it is possible to calculate the differential vertical deformation due to water (see equations in
 417 Tab. 3).

418 **Tab. 3 (1.5-column fitting):** Equations applied for calculation of gravity stresses, resulting strain and deformation with and without
 419 water (David & Selvadurai, 1996, derived from Hooke’s law)

Case without water	Case with water
$\sigma_{zz}(z)(dry) = \int_0^z \rho_r(z)g dz$	$\sigma_{zz}(z)(saturated) = \int_0^z \rho_r(z)g - \rho_w(z)g dz$
$\sigma_{xx} = \sigma_{yy} = \frac{\nu}{1-\nu} \sigma_{zz}$	
$\varepsilon_{zz} = \frac{1}{E} [\sigma_{zz} - \nu(\sigma_{xx} + \sigma_{yy})] = \frac{1}{E} [\sigma_{zz} - 2\nu(\sigma_{xx})] = \frac{1}{E} \left[\sigma_{zz} - \frac{2\nu^2}{1-\nu} \sigma_{zz} \right]$	
$\varepsilon_{zz} = \frac{\Delta z}{z} \rightarrow \Delta z = \varepsilon_{zz} \cdot z \rightarrow \delta\Delta z = \Delta z(dry) - \Delta z(saturated)$	

420 Where σ_{zz} is the vertical stress [N/m²], σ_{xx}/σ_{yy} are the lateral stresses [N/m²], z is the height of the rock
 421 column [m], ρ_r is rock mass density [kg/m³], ρ_w is the water density [kg/m³], g is the acceleration of
 422 gravity [m/s²], ν is the poisson’s ratio [-], ε_{zz} is the extensional strain [-], E is the young’s modulus [N/m²],
 423 Δz is the deformation [m], $\delta\Delta z$ is the differential deformation [m].

424 In this way, applying accepted mean values for gneiss (0.25 for Poisson’s ratio, 50–70 GPa for Young
 425 modulus, Sivakugan, et al., 2013), a differential deformation between 10 and 15 mm in z component is found
 426 by using 300 m as height of rock column. In real cases the physics complexity is obviously much higher.
 427 However, this first estimation is relevant with the measured phenomenon at Mannen/Børa and highlights the
 428 need of further research in order to document and quantify this effect in different geological contexts.

429 In slope stability, role of groundwater variations is well known but usually analyzed in term of effective stress
 430 variations (i.a. Collins & Znidarcic, 2004; Johansson, 2014). Effects of water table level fluctuations inducing
 431 subsidence and uplift of rock mass were however studied to explain deformation related to tunnelling and
 432 hydroelectric infrastructure (i.a. Schneider, 1982; Zangerl, et al., 2008; Strozzi, et al., 2011). Using satellite
 433 InSAR, water loading fluctuations inducing land subsidence and uplift rebound were detected, but they are
 434 mainly related to cases of excess pumping of groundwater (i.a. Amelung, et al., 1999; Schmidt & Bürgmann,
 435 2003; Chen, et al., 2007; Galloway & Burbey, 2011). In case of rock instabilities, seasonal effects related to
 436 temperature, precipitations, snow-melting or permafrost have also been measured using conventional or/and

437 remote-sensing methods (i.a. Coe, et al., 2003; Nordvik, et al., 2010; Blikra & Christiansen, 2014). These
438 studies focus usually on the understanding of the triggers and controlling factors of the instabilities. The
439 elastic or semi-elastic behaviours of the rock mass associated to water or temperature variations and potential
440 fatigue mechanism related to cycles are still not well covered, although mentioned in several papers (i.a.
441 Jaboyedoff, et al., 2009; Mazzanti & Brunetti, 2010; Salvini, et al., 2015). In the way, our research provides
442 an interesting contribution to take into account small-scale movement fluctuations due to water pressure in
443 natural slopes. The rock slope breathing can indeed have a long-term impact on the rock slope structure by
444 progressive degradation and micro-fracturing due to differential deformation in the area affected by the
445 phenomenon.

446 **6 CONCLUSION & PROSPECT**

447 The Mannen/Børa rock slope is an interesting case study due to the availability of two GB-InSAR systems
448 imaging the same rock slope. They cover a large stretch of the slope and a slight data overlap allows the
449 reliability of the results to be checked. They have the advantage to provide information on the unmonitored
450 Børa plateau and in steep mid-slope where in situ devices are difficult to install. Thanks to GB-InSAR large
451 coverage, high temporal frequency, high resolution and accuracy, an approximately $1 \times 0.5 \text{ km}^2$ sector
452 subjected to millimetric variations and inversion of movement (inflation/deflation) has been highlighted.
453 Satellite InSAR time series from TSX/TDX data confirm these variations. Analysing the large GB-InSAR
454 dataset from the continuous station A, this rock slope breathing is proved to have a seasonal recurrence. The
455 phenomenon is ascribed to hydrogeological variations.

456 In addition and in order to overcome some limitations of GB-InSAR technique (1D measurements along the
457 LOS, intermittent campaigns, atmospheric effects removing, coherence loss, etc.), analyses of in situ
458 monitoring data and satellite InSAR were performed. The combination of in situ measurements, terrestrial
459 and spaceborne remote sensing provides a large amount of complementary information. In this way, the edge
460 and velocities of the main Mannen unstable areas can be better defined.

461 These preliminary results highlight the need for further research in this site, which can be summarized in two
462 parts. Firstly, further investigations are required to fully understand the hydrogeological processes and the
463 subsurface structures of the rock slope, especially to understand the rock slope breathing phenomenon and

464 confirm the assumption of the water pressure influence. This includes further investigations combining
465 surface and subground data to depict its complex geometry. In order to better understand and constrain the
466 behaviour of the rock masses in the area stress-strain numerical analysis should be performed and included in
467 further models. Secondly, a complete and systematic analysis of the large GB-InSAR dataset from station A,
468 as well as a more complete integration with the other GB-InSAR (intermittent measurements from station B
469 and new 2014 stations), in situ and satellite InSAR results would be valuable to provide information about
470 movement directions and contribute to confirm the likelihood of mechanisms. This could overcome the
471 intrinsic limitation of InSAR technique which provides only 1D deformation measurements along the LOS.

472 In addition to the elements of prospect related to Mannen/Børa rock slope, this work underlines the need of
473 research on the locations, amplitudes, causes and consequences of rock slope breathing in mountainous
474 regions. These small variations often ignored or undervalued in the analysis and monitoring of large
475 rockslides threatening population and infrastructure are indeed important to take into account for a complete
476 understanding of rock slope behaviour.

477 **ACKNOWLEDGMENTS**

478 The research would not have been possible without the great job of the team working at the NVE monitoring
479 center in Stranda. Thanks to the intensive work of each member of the crew, impressively huge and exciting
480 datasets from the performant monitoring network of Mannen/Børa are available for research. Many thanks
481 also to LiSALab team (Ellegi Ltd) and especially Carlo Rivolta for his support during GB-InSAR data
482 processing. The TerraSAR-X data has been provided by the German Aerospace Center (DLR) under the
483 TSX-AO project contract #GEO0764. We finally acknowledge the works of the landslide group of the
484 Geological Survey of Norway (NGU) that contribute to better understand geometry and behaviour of rock
485 instabilities in Romsdalen valley.

486 **REFERENCES**

- 487 Agliardi, F., Crosta, G., Sosio, R., Rivolta, C., & Mannucci, G. (2013). In situ and remote long term real-time monitoring of a large
488 alpine rock slide. In: Margottini, C., Canuti, P. & Sassa, K. (Eds.), *Landslide Science and Practice* (Vol.2, pp. 415–421).
489 Springer Berlin Heidelberg. DOI:10.1007/978-3-642-31445-2_54.
- 490 Amelung, F., Galloway, D. L., Bell, J. W., Zebker, H. A., & Lacznia, R. J. (1999). Sensing the ups and downs of Las Vegas: InSAR
491 reveals structural control of land subsidence and aquifer-system deformation. *Geology*, 27(6), pp. 483–486.
492 DOI:10.1130/0091-7613(1999)027<0483:STUADO>2.3.CO;2.
- 493 Angeli, M.-G., Pasuto, A., & Silviano, S. (2000). A critical review of landslide monitoring experiences. *Engineering Geology*, 55(3), pp.
494 133–147. DOI:10.1016/S0013-7952(99)00122-2.

- 495 Antonello, G., Casagli, N., Farina, P., Leva, D., Nico, G., Sieber, A., & Tarchi, D. (2004). Ground-based SAR interferometry for
496 monitoring mass movements. *Landslides*, 1, pp. 21–28. DOI:10.1007/s10346-003-0009-6.
- 497 Barla, G., Antolini, F., Barla, M., Mensi, E., & Piovano, G. (2010). Monitoring of the Beauregard landslide (Aosta Valley, Italy) using
498 advanced and conventional techniques. *Engineering Geology*, 116(3–4), pp. 218–235. DOI:10.1016/j.enggeo.2010.09.004.
- 499 Blikra, L. H. (2008). The Åknes rockslide; monitoring, threshold values and early warning. In: *Proceedings, 10th International*
500 *symposium on Landslides and Engineered Slopes* (Vol. 2, pp. 1089–1094). Xi'an, China.
- 501 Blikra, L. H., Kristensen, L., & Hole, J. (2010). *Mannen in Romsdalen: Monitoring and data analyses. Report 03/2013*. Stranda,
502 Norway: Åknes/Tafjord Beredskap.
- 503 Blikra, L. H., & Kristensen, L. (2013). Monitoring Concepts and Requirements for Large Rockslides in Norway. In: Margottini, C.,
504 Canuti, P. & Sassa, K. (Eds.), *Landslide Science and Practice* (Vol.2, pp. 193–200). Springer Berlin Heidelberg.
505 DOI:10.1007/978-3-642-31445-2_25.
- 506 Blikra, L. H., & Christiansen, H. H. (2014). A field-based model of permafrost-controlled rockslide deformation in northern Norway.
507 *Geomorphology*, 208, pp. 34–89. DOI:10.1016/j.geomorph.2013.11.014.
- 508 Berardino, P., Fornaro, G., Lanari, R., & Sansosti, E. (2002). A new algorithm for surface deformation monitoring based on small
509 baseline differential SAR interferograms. *IEEE Transactions on Geoscience and Remote Sensing*, 40(11), pp. 2375–2383.
- 510 Bozzano, F., Cipriani, I., Mazzanti, P., & Prestininzi, A. (2011). Displacement patterns of a landslide affected by human activities:
511 insights from ground-based InSAR monitoring. *Natural Hazards*, 59(3), pp. 1377–1396. DOI:10.1007/s11069-011-9840-6.
- 512 Braathen, A., Blikra, L., Berg, S. S., & Karlsen, F. (2004). Rock-slope failures in Norway; type, geometry, deformation mechanisms and
513 stability. *Norwegian Journal of Geology*, 84, pp. 67–88.
- 514 Caduff, R., Schlunegger, F., Kos, A., & Wiesmann, A. (2014). A review of terrestrial radar interferometry for measuring surface change
515 in the geosciences. *Earth Surface Processes and Landforms*, 40(2), pp. 208–228. DOI:10.1002/esp.3656.
- 516 Casagli, N., Catani, F., De Ventisette, C., & Luzi, G. (2010). Monitoring, prediction, and early warning using ground-based radar
517 interferometry. *Landslides*, 7(3), pp. 291–301. DOI:10.1007/s10346-010-0215-y.
- 518 Chen, C. T., Hu, J. C., Lu, C. Y., Lee, J. C., & Chan, Y. C. (2007). Thirty-year land elevation change from subsidence to uplift following
519 the termination of groundwater pumping and its geological implications in the Metropolitan Taipei Basin, Northern Taiwan.
520 *Engineering Geology*, 95(1), pp. 30–47. DOI:10.1016/j.enggeo.2007.09.001
- 521 Coe, J. A.; Ellis, W. L., Godt, J. W., Savage, W. Z., Savage, J. E., Michael, J. A., Kibler, J. D., Powers, P. S., Lidke, D.J., & Debray, S.
522 (2003). Seasonal movement of the Slumgullion landslide determined from Global Positioning System surveys and field
523 instrumentation, July 1998-March 2002. *Engineering Geology*, 68, pp.67–101.
- 524 Collins, B. D., & Znidarcic, D. (2004). Stability Analyses of Rainfall Induced Landslides. *Journal of Geotechnical and*
525 *Geoenvironmental Engineering*, 130(4), pp. 364–372. DOI:10.1061/(ASCE)1090-0241(2004)130:4(362).
- 526 Crosta, G. B., & Agliardi, F. (2003). Failure forecast for large rock slides by surface displacement measurements. *Canadian*
527 *Geotechnical Journal*, 40(1), pp. 171–191. DOI:10.1139/t02-085.
- 528 Dahle, H., Anda, E., Saintot, A., & Saetre, S. (2008). *Faren for fjellskred fra fjellet Mannen i Romsdalen. Report 2008.087* (in
529 *Norwegian*). Trondheim, Norway: Norges Geologiske Undersøkelse (NGU).
- 530 Dahle, H., Saintot, A., Blikra, L. H., & Anda, E. (2010). *Geofagleg oppfølging av ustabil fjellparti ved Mannen i Romsdalen. Report*
531 *2010.22* (in *Norwegian*). Trondheim, Norway: Norges Geologiske Undersøkelse (NGU).
- 532 Dalsegg, E., & Rønning, J. S. (2012). *Geofysiske målinger på Mannen i Rauma kommune, Møre og Romsdal. Report 2012.024* (in
533 *Norwegian*). Trondheim, Norway: Norges Geologiske Undersøkelse (NGU).
- 534 Davis, R. O., & Selvadurai, A. P. (1996). *Elasticity and Geomechanics*. New York: Cambridge University Press.
- 535 Del Ventisette, C., Intrieri, E., Luzi, G., Casagli, N., Fantì, R., & Leva, D. (2011). Using ground based interferometry during emergency:
536 the case of the A3 motorway (Calabria Region, Italy) threatened by a landslide. *Natural Hazards and Earth System Sciences*,
537 11, pp. 2483–2495. DOI:10.5194/nhess-11-2483-2011.
- 538 Derron, M.-H., Jaboyedoff, M., Pedrazzini, A., Michoud, C., & Villemin, T. (2011). Remote Sensing and Monitoring Techniques for the
539 Characterization of Rock Mass Deformation and Change Detection. In: Lambert, S. & Nicot, F. (Eds.), *Rockfall Engineering*
540 (pp. 39–65). ISTE and Wiley & Sons.
- 541 Elvebakk, H. (2012). *Borehullslogging med optisk televiuer, KH-02-11, Mannen, Rauma kommune, Møre og Romsdal. Report*
542 *2012.032* (in *Norwegian*). Trondheim, Norway: Norges Geologiske Undersøkelse (NGU).
- 543 Federico, A., Popescu, M., Elia, G., Fidelibus, C., Internò, G., & Murianni, A. (2012). Prediction of time to slope failure: a general
544 framework. *Environnemental Earth Sciences*, 66(1), pp. 245–256. DOI:10.1007/s12665-011-1231-5.
- 545 Froese, C. R., & Moreno, F. (2014). Structure and components for the emergency response and warning system on Turtle Mountain,
546 Alberta, Canada. *Natural Hazards*, 70(3), pp. 1689–1712. DOI:10.1007/s11069-011-9714-y.
- 547 FylkesROS-fjellskred. (2011). *Risiko- og sårbarhetsanalyse for fjellskred i Møre of Romsdal. Report* (in *Norwegian*). Norway:
548 Fylkesmannen i Møre og Romsdal, Møre og Romsdal fylkeskommune & Norges Geologiske Undersøkelse (NGU).
- 549 Gabriel, A. K., Goldstein, R. M., & Zebker, H. A. (1989). Mapping small elevation changes over large areas: Differential radar
550 interferometry. *Journal of Geophysical Research: Solid Earth*, 94(B7), pp. 9183–9191. DOI:10.1029/JB094iB07p09183.
- 551 Galloway, D. L., & Burbey, T. J. (2011). Review: Regional land subsidence accompanying groundwater extraction. *Hydrogeology*
552 *Journal*, 19(8), pp. 1459–1486. DOI:10.1007/s10040-011-0775-5.
- 553 Gischig, V. S., Loew, S., Kos, A., Moore, J. R., Raetzo, H., & Lemy, F. (2009). Identification of active release planes using Ground-
554 Based Differential InSAR at the Randa rock slope instability, Switzerland. *Natural Hazard and Earth System Sciences*, 9, pp.
555 2027–2038. DOI:10.5194/nhess-9-2027-2009.
- 556 Goldstein, R. M., Engelhardt, R., Kamp, B., & Frolich, R. M. (1993). Satellite radar interferometry for monitoring ice sheet motion:
557 Application to an Antarctic ice stream. *Science*, 262, pp. 1525–1530. DOI:10.1126/science.262.5139.1525.

- 558 Henderson, I. H., & Saintot, A. (2007). *Fjellskredundersøkelser i Møre og Romsdal. Report 2007.043 (in Norwegian)*. Trondheim,
559 Norway: Norges Geologiske Undersøkelse (NGU).
- 560 Herrera, G., Fernández-Merodo, F. A., Mulas, J., Pastor, M., Luzi, G., & Monserrat, O. (2009). A landslide forecasting model using
561 ground based SAR data: The Portalet case study. *Engineering Geology*, 105(3-4), pp. 220–230.
562 DOI:10.1016/j.enggeo.2009.02.009.
- 563 Herrera, G., Notti, D., García-Davalillo, J. C., O., M., Cooksley, G., Sánchez, M., Arnaud, A. & Crosetto, M. (2011). Analysis with C-
564 and X-band satellite SAR data of the Portalet landslide area. *Landslides*, 8(2), pp. 195–206. DOI:10.1007/s10346-010-0239-3
- 565 Intriери, E., Gigli, G., Mugnai, F., Fanti, R., & Casagli, N. (2012). Design and implementation of a landslide early warning system.
566 *Engineering Geology*, 147-148, pp. 124–136. DOI:10.1016/j.enggeo.2012.07.017.
- 567 Jaboyedoff, M., Baillifard, F., Derron, M.-H., Couture, R., Locat, J., & Locat, P. (2005). Modular and evolving rock slope hazard
568 assessment methods. In: Senneset, K., Flaate, K. & Larsen J. (Eds.), *Proceedings of the 11th International Conference and*
569 *Field Trip on Landslides (ICFL)*. Norway.
- 570 Jaboyedoff, M., Metzger, R., Oppikofer, T., Couture, R., Derron, M.-H., Locat, J. & Turmel, D. (2007). New insight techniques to
571 analyze rock-slope relief using DEM and 2D-imaging cloud-point: COLTOP-3D software. In: E. Eberhardt, D. Stead, & T.
572 Morrison (Eds.) *Rock mechanics: Meetings Society's Challenges and Demands* (Vol.1, pp. 61–68). Taylor & Francis.
- 573 Jaboyedoff, M., Couture, R. & Locat, P. (2009) Structural analysis of Turtle Mountain (Alberta) using digital elevation model: Toward a
574 progressive failure. *Geomorphology*, 103, pp. 5-16. DOI:10.1016/j.geomorph.2008.04.012.
- 575 Johansson, J. (2014). Impact of Water-Level Variations on Slope Stability. *Licentiate Thesis*. Division of Mining and Geotechnical
576 Engineering, Department of Civil, Environmental and Natural Resources Engineering, Luleå University of Technology.
- 577 Kristensen, L., & Blikra, L. H. (2013). Monitoring displacement on the Mannen rockslide in Western Norway. In: Margottini, C., Canuti,
578 P. & Sassa, K. (Eds.), *Landslide Science and Practice* (Vol.2, pp. 251–256). Springer Berlin Heidelberg. DOI:10.1007/978-3-
579 642-31445-2_32.
- 580 Kristensen, L., Rivolta, C., Dehls, J., Blikra, L. H. (2013). GB InSAR Measurement at the Åknes rockslide, Norway. *Italian Journal of*
581 *Engineering Geology and Environment - Book Series*, 6, pp. 336-228. DOI: 10.4408/IJEGE.2013-06.B-32
- 582 Kvakland, M. R. (2009). Drenering i fjell. Sporstoffstudier ved de to ustabile fjellsidene (in Norwegian). Åknes og Børa, Møre og
583 Romsdal. *Masteroppgave i Geografi*, Geografisk Institutt, NTNU, Trondheim, Norway.
- 584 Larsen, Y., Engen, G., Lauknes, T. R., Malnes, E., & Høgda, K.-A. (2005). A generic differential InSAR processing system, with
585 applications to land subsidence and SWE retrieval. *Proceedings ESA Fringe*, ESA ESRIN, Frascati, Italy, 28 November - 2
586 December 2005.
- 587 Lauknes, T. R. & Larsen, Y. (2011). InSAR Time Series using an L1-norm Small-Baseline Approach. *IEEE Transaction on Geoscience*
588 *and Remote Sensing*, 49(1), pp. 536–546.
- 589 Lillesand, T. M., Kiefer, R. W., & Chipman, J. W. (2008). *Remote Sensing and Image Interpretation* (6th ed.). Hoboken, U.S.A: John
590 Wiley & Sons.
- 591 Luzi, G. (2010). Ground based SAR interferometry a novel tool for Geoscience. In: Imperatore, P. & Riccio, D. *Geoscience and Remote*
592 *Sensing New Achievements*. INTECH Open Access Publisher.
- 593 Mantovani, F., Soeters, R., & Van Westen, C. J. (1996). Remote sensing techniques for landslide studies and hazard zonation in Europe.
594 *Geomorphology*, 15(3-4), pp. 213–225. DOI:10.1016/0169-555X(95)00071-C.
- 595 Massonnet, D., Rossi, M., Carmona, C., Adragna, F., Peltzer, G., Feigl, K., & Rabaute, T. (1993). The displacement field of Landers
596 earthquake mapped by radar interferometry. *Nature*, 364(8), pp. 138–142. DOI:10.1038/364138a0.
- 597 Mazzanti, P., Brunetti, A. (2010). Assessing rockfall susceptibility by Terrestrial SAR Interferometry. *Proceedings of the mountain risks*
598 *international conference*, Florence, Italy.
- 599 Mazzanti, P., Bozzano, F., Cipriani, I., & Prestininzi, A. (2015). New insights into the temporal prediction of landslides by terrestrial
600 SAR interferometry monitoring case study. *Landslides*, 12(1), pp. 55–68. DOI:10.1007/s10346-014-0469-x.
- 601 Metternicht, G., Hurni, L., & Gogu, R. (2005). Remote sensing of landslides: An analysis of the potential contribution to geo-spatial
602 systems for hazards assessment in mountainous environments. *Remote Sensing of Environment*, 98(2-3), pp. 284–303.
603 DOI:10.1016/j.rse.2005.08.004.
- 604 Michoud, C., Abellan, A., Derron, M.-H., & Jaboyedoff, M. (2010). *SafeLand Deliverable 4.1. Review of techniques for landslide*
605 *detection, fast characterization, rapid mapping and long-term monitoring*. Deliverable leader: IGAR-UNIL. 7th Framework
606 Programme. Cooperation Theme 6 Environment. Sub-Activity 6.1.3 Natural Hazard. Available at <http://www.safeland-fp7.eu>.
- 607 Monserrat, O. (2012). Deformation measurement and monitoring with Ground-Based SAR. *PhD. Dissertation*. Active Remote Sensing
608 Unit, Institute of Geomatics, Universitat Politècnica de Castelldefels, Spain.
- 609 Monserrat, O., Crosetto, M., & Luzi, G. (2014). A review of ground-based SAR interferometry for deformation measurement. *ISPRS*
610 *Journal of Photogrammetry and Remote Sensing*, 93, pp. 40–48. DOI:10.1016/j.isprsjprs.2014.04.001.
- 611 Mosar, J. (2000). Depth of extensional faulting on the Mid-Norway Atlantic passive margin. *Norge Geologiske Undersøkelse Bulletin*,
612 437, pp. 33–41.
- 613 Noferini, L., Pieraccini, M., Mecatti, D., Macaluso, G., Atzeni, C., Mantovani, M., Marcato, G., Pasuto, A., Silvano, S. & Tagliavini, F.
614 (2007). Using GB-SAR technique to monitor slow moving landslide. *Engineering Geology*, 95(3-4), pp. 88–98.
615 DOI:10.1016/j.enggeo.2007.09.002.
- 616 Petley, D. N., Mantovani, F., Bulmer, M. H., & Zannoni, A. (2005). The use of surface monitoring data for the interpretation of landslide
617 movement patterns. *Geomorphology*, 66(1-4), pp. 133–147. DOI:10.1016/j.geomorph.2004.09.011.
- 618 Rouyet, L. (2013). Monitoring and characterization of rock slope instabilities in Norway using GB-InSAR (Ground-based Interferometric
619 Synthetic Aperture Radar). *Master thesis*. Faculty of Geosciences and Environment, University of Lausanne, Switzerland.

- 620 Saintot, A., Elvebakk, H., Oppikofer, T., Ganerød, G., & Farsund, T. (2011a). *Mannen unstable rock slope (Møre & Romsdal): Logging*
 621 *of borhole and drill core KH-01-10, geomorphologic digital elevation model interpretation & displacement analysis by*
 622 *terrestrial laser scanning. Report 2011.026*. Trondheim, Norway: Norge Geologiske Undersøkelse (NGU).
- 623 Saintot, A., Henderson, I. H., & Derron, M.-H. (2011b). Inheritance of ductile and brittle structures in the development of large rock
 624 slope instabilities: examples from western Norway. *Geological Society, London, Special Publications*, 351(1), pp. 27–78.
 625 DOI:10.1144/SP351.3.
- 626 Saintot, A., Oppikofer, T., Derron, M.-H. & Henderson, I. (2012). Large gravitational rock slope deformation in Romsdalen valley
 627 (western Norway). *Revista de la Asociación Geológica Argentina*, 69(3), pp.354–371.
- 628 Salvini, R., Vanneschi, C., Ricucci, S., Francioni, M., Gulli, D. (2015). Application of an integrated geotechnical and topographic
 629 monitoring system in the Lorano marble quarry (Apuan Alps, Italy). *Geomorphology*, 241, pp. 209–223.
 630 DOI:10.1016/j.geomorph.2015.04.009.
- 631 Sivakugan, N., Shukla, S. K., Das, B. M. (2013). *Rock mechanics, an introduction*. Boca Raton, U.S.A.: CRC Press, Taylor & Francis.
- 632 Schmidt, D. A., & Bürgmann, R. (2003). Time-dependent land uplift and subsidence in the Santa Clara valley, California, from a large
 633 interferometric synthetic aperture radar data set. *Journal of Geophysical Research: Solid Earth*, 108(B9), pp. 1978–2012.
 634 DOI:10.1029/2002JB002267.
- 635 Schneider, T. R. (1982). Abnormal Behaviour of Zeuzier Arch-Dam (Switzerland), IV. Geological Aspects of the Extraordinary
 636 Behaviour of Zeuzier Arch Dam. *Wasser, Energie, Luft*, 74(3), pp. 81–94.
- 637 Schulz, W. H., Coe, J. A., Shurtleff, B. L., & Panosky, J. (2012). Kinematics of the Slumgullion landslide revealed by ground-based
 638 InSAR surveys. *Processings of Landslides and Engineered Slopes: Protecting Society through Improved Understanding - the*
 639 *11th International and 2nd North American Symposium on Landslides and Engineered Slope*, Banff, Canada.
- 640 Smelror, M., Dehls, J., Ebbing, J., Larsen, E., Lundin, E., Nordygulen, Ø., Osmundsen, P.T., Olesen, O., Ottesen, D., Pascal, C.,
 641 Redfield, T. F. & Rise, L. (2007). Towards a 4D topographic view of the Norwegian sea margin. *Global and Planetary*
 642 *Change*, 58(1), pp. 382–410.
- 643 Solheim, A., Bhasin, R., De Blasio, F. V., Blikra, L. H., Boyle, S., Braathen, A., Dehls, J., Elverhøi, A., Etzelmüller, B., Glimsdal, S.,
 644 Harbitz, C. B., Heyerdahl, H., Høydal, Ø. A., Iwe, H., Karlstud, K., Lacasse, S., Lecomte, I., Lindholm, C., Longva, O.,
 645 Lovholt, F., Nadim, F., Nordal, S., Romstad, B., Røed, J. K. & Strout, J. (2005). International Centre for Geohazards (ICG):
 646 Assessment, prevention and mitigation of geohazards. *Norwegian Journal of Geology*, 85(1-2), pp. 45–62.
- 647 Skrede, I., Kristensen, L., Hole, J. (2015). *Geologisk evaluering av Veslemannen – eit mindre fjellskred i utvikling. Rapport nr 41-2015*
 648 *(in Norwegian)*. Stranda, Norway: Norges vassdrags-og energidirektorat (NVE).
- 649 Stumpf, A., Kerle, N., & Malet, J.-P. (2011). *SafeLand Deliverable 4.4. Guidelines for the selection of appropriate remote sensing*
 650 *technologies for monitoring different types of landslides*. Deliverable Leader: ITC-University of Twente. 7th Framework
 651 Programme. Cooperation Theme 6 Environment. Sub-Activity 6.1.3 Natural Hazard. Available at <http://www.safeland-fp7.eu>.
- 652 Strozzi, T., Delaloye, R., Poffet, D., Hansmann, J., Loew, S. (2011). Surface subsidence and uplift above a headrace tunnel in
 653 metamorphic basement rocks of the Swiss Alps as detected by satellite SAR interferometry. *Remote Sensing and*
 654 *Environment*, 115(6), pp. 1353–1360. DOI:10.1016/j.rse.2011.02.001.
- 655 Tarchi, D., Rudolf, H., Luzi, G., Chiarantini, L., Coppo, P., & Siber, J. (1999). SAR Interferometry for Structural Changes Detection: a
 656 Demonstration Test on a Dam. In: *Geoscience and Remote Sensing Symposium. IGARSS'99 Proceedings, 28 June - 02 July*
 657 *(Vol.3, pp. 1522–1524)*, Hamburg, Germany. DOI:10.1109/IGARSS.1999.772006.
- 658 Tarchi, D., Casagli, N., Fanti, R., Leva, D. D., Luzi, G., Pasuto, A., Pieraccini, M. & Silvno, S. (2003). Landslide monitoring by using
 659 ground-based SAR interferometry: an example of application to the Tessina landslide in Italy. *Engineering Geology*, 68(1-2),
 660 pp. 15–30. DOI:10.1016/S0013-7952(02)00196-5.
- 661 Tofani, V., Gili, J., Luzi, G., & Catani, F. (2010). Ground-Based InSAR. In: Michoud, C., Abellán, A., Derron, M.-H. & Jaboyedoff, M.
 662 (Eds.), *SafeLand Deliverable 4.1. Review of techniques for landslide detection, fast characterization, rapid mapping and*
 663 *long-term monitoring*. 7th Framework Programme. Cooperation Theme 6 Environment. Sub-Activity 6.1.3 Natural Hazard.
 664 Available at <http://www.safeland-fp7.eu>.
- 665 Turner, A. K., & McKuffey, V. C. (1996). Organization of investigation process. In: Turner, A. K. & Schuster, L. R. (Eds.), *Landslides*
 666 *investigations and mitigation. Special report 247* (pp. 121–128). Washington, D.C.: National Academy Press.
- 667 Zangerl, C., Evans, K. F., Eberhardt, E. & Loew, S. (2008). Consolidation settlements above deep tunnels in fractured crystalline rock:
 668 Part 1 - Investigations above the Gotthard highway tunnel. *International Journal of Rock Mechanics & Mining Sciences*, 45,
 669 pp. 1195–1210. DOI:10.1016/j.ijrmms.2008.02.002.
- 670 Zebker, H. A., & Villasenor, J. (1992). Decorrelation in interferometric radar echoes. *IEEE Transactions on Geoscience and Remote*
 671 *Sensing*, 30(5), pp. 950–959. DOI:10.1109/36.175330.
- 672 Zebker, H. A., Rosen, P. A., Goldstein, R. M., Gabriel, A., & Werner, C. L. (1994). On the derivation of coseismic displacement fields
 673 using differential radar interferometry: The Landers earthquake. *Journal of Geophysical Research*, 99(B10), pp. 19617–
 674 19634. DOI:10.1029/94JB01179.
- 675 Zebker, H. A., Rosen, P. A., & Hensley, S., (1997). Atmospheric effects in interferometric synthetic aperture radar surface deformation
 676 and topographic maps. *Journal of Geophysical Research*, 102(B4), pp. 7547–7563. DOI:10.1029/96JB03804.

Annex B1

Michoud C, Derron MH Abellán A, Jaboyedoff M and Fornaro G: Radar Wave Principles, Interferometric Radar Distance-Meter and Differential SAR Interferometry. Deliverable 4.1 of the European project SAFELAND: Review of Techniques for Landslide Detection, Fast Characterization, Rapid Mapping and Long-Term Monitoring. Edited in 2010 by Michoud C, Abellán A, Derron MH and Jaboyedoff M, 105-125, 2010

1. RADAR WAVE PRINCIPLES

1.1. INTRODUCTION

Radar technologies have been developed since the beginning of the 20th century, first to remotely detect objects. The acronym Radar states for Radio Detection And Ranging. Radio-waves, or microwaves, are electromagnetic waves of wavelength from 1 mm to 1 m. Then radar methods have been used for accurate detection of movements and Earth surface imaging. The principles Radar technologies and applications are described in many publications, books and encyclopedias. About the radar imaging part used in environmental and Earth sciences, Massonnet and Feigl (1998), Hanssen (2001) and Woodhouse (2006) provide worthy introductions and overviews.

There are two kinds of Radar systems (Hanssen, 2001): bistatic radars use two different antennas, one for the emission and one for the reception of the electromagnetic wave; On the other hand, monostatic radars use only one antenna for both tasks. This last configuration is the most frequently applied technology for environmental purposes. A Radar transmitting antenna emits a wave by pulses with a predefined wavelength (Table 10) amplitude and phase. The Radar receiving antenna estimates the range (with the two-way travel time) and measures the amplitude and the phase of the backscattered pulses. The way the radar waves travel and are reflected to the antenna depend on several factors such as: pressure, temperature and partial water pressure of the environment, atmospheric layering, roughness and dielectric properties of the target (strongly influenced by the moisture and salt content) (Hanssen, 2001; Norland, 2006). In remote sensing, environmentalists usually describe a radar wave by its wavelength, because it gives some information about how the waves interact with the surface (roughness, interferences). Signal processing specialists prefer to work with frequencies as most of the computations are done in the frequency domain (convolution, filtering).

Table 10 : Main bands traditionally used by the Standard Radar Nomenclature (Woodhouse, 2006).

Band	Wavelength	Frequency
P	Decimetric (30 cm to ~ 1m)	0.3 – 1 GHz
L	Decimetric (~ 15 to 30 cm)	1 – 2 GHz
S	Decimetric (7.5 cm to ~ 15)	2 – 4 GHz
C	Centimetric (~ 3.75 to 7.5 cm)	4 – 8 GHz
X	Centimetric (~ 2.5 to 3.75 cm)	8 – 12 GHz

Compared to the optical and near infrared sensors, the radio waves are much less influenced and attenuated by the atmospheric conditions. As shown in the Figure 43, the attenuation of waves used by Radar systems is less than 0.1 decibel per kilometer (after Preissner, 1978). So data can be acquired even during heavy rainfalls (even though some significant interactions are reported for X-Band systems) or strong fog; however these are not the optimal conditions.

Moreover, as a radar is an active sensor (sending the initial signal), data can be acquired as well during the night than during the day.

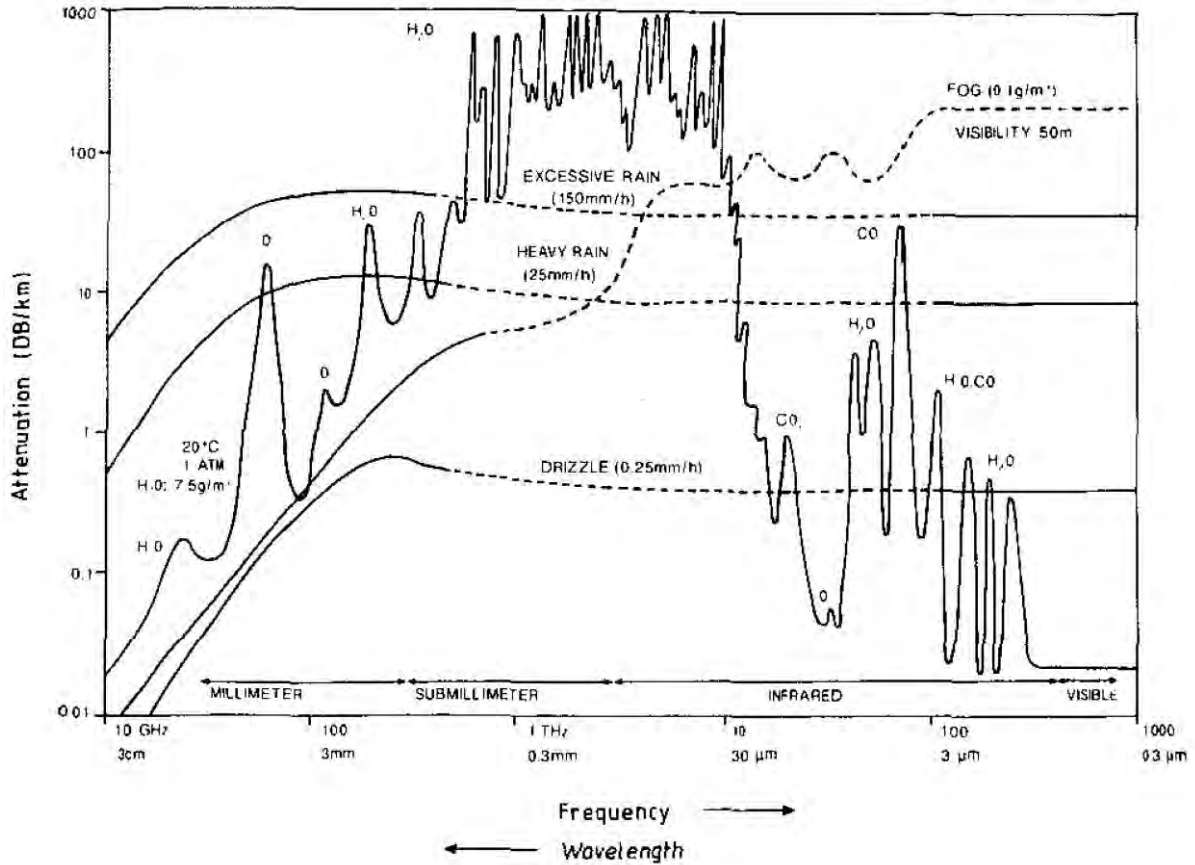


Figure 43 : attenuation of an electromagnetic wave by the atmosphere, depending of the wavelength for a clear weather, with shown for fog, heavy rain and drizzle. Contrary to the optical and near infrared, radio waves are only few attenuated by the atmospheric conditions (After Preissner 1978, cited in Peckham 1991 and Woodhouse 2006).

The choice of the frequencies used by the Radar sensors is regulated by the International Telecommunications Union. Usually, the space-borne sensors are transmitting radio waves in the bands X, C and L (Table 10). The longer the wavelength is, the worse the accuracy is both in terms of spatial resolution and measurement precision, but the better is the penetration capacity and the stability of the returned signal with respect to environmental changes..

1.2. RANGE AND PHASE SHIFT

Mathematically, the phase shift corresponds to:

$$\Phi = \frac{2\pi}{\lambda} \times \Delta R \quad \text{where } \Delta R = 2R$$

$$\Leftrightarrow \Phi = \frac{4\pi}{\lambda} \times R$$

In this formula, Φ is the phase shift in radians, λ the wavelength in meter and R the distance in meter from the sensor to the ground target.

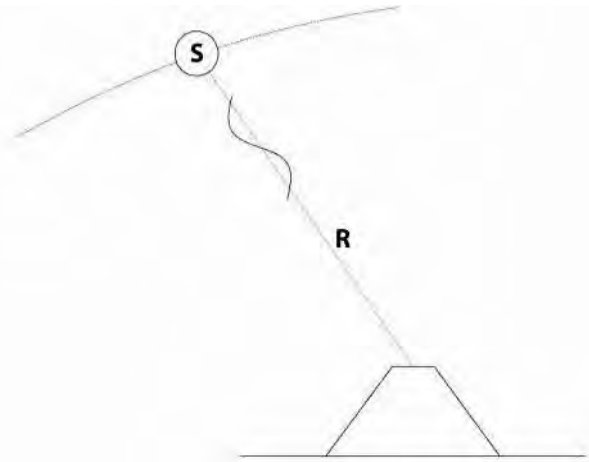


Figure 44 : representation of the Radar wave along the line of sight. The wave with a wavelength of λ is doing the 2-way of $2R$ from the sensor S to the ground target. As the sensor emitted the wave knowing the original phase, it can record the phase shift when the wave comes back.

So we can deduce in theory the distance R knowing the phase shift:

$$\Leftrightarrow R = \frac{\lambda}{4\pi} \times \Phi$$

2. INTERFEROMETRIC RADAR DISTANCE-METER

One direct application of the phase shift principle is the continuous monitoring of instabilities assessing the movements of punctual ground targets by Radar distance-meters. All the information including in this chapter comes from the case study of the Tafjorden instability in Norway (Norland, 2006).

As described before, the phase shift is function of the wavelength and the range:

$$\Leftrightarrow \Phi = \frac{4\pi}{\lambda} \times R$$

But practically, R is defined as

$$R = \frac{1}{n} \times \frac{C_0 \times t_{2way}}{2} \quad \text{where} \quad \begin{cases} C_0 = \text{velocity of light in vacuum} \\ t_{2way} = \text{travel time sensor} > \text{target} + \text{return} \\ n = \text{spatial and temporal index of refraction} \end{cases}$$

Indeed, even if the Radar amplitudes are only few influenced by atmospheric conditions (the attenuation of the signal is negligible in almost all used bandwidths), the phases are very sensitive (Figure 45 and chapter 3.3.3.2). In fact, the spatial and temporal index of refraction depends of the pressure, the temperature and of the partial water vapor pressure which can be estimated using the relative humidity of the atmosphere (Norland, 2006).

$$n = 77.6 \times \frac{p}{T} + 3.734 \cdot 10^5 \times \frac{e}{T^2} \quad \text{where} \quad \begin{cases} p = \text{pressure in mbar} \\ T = \text{temperature in } ^\circ\text{K} \\ e = \text{partial water vapor pressure in mbar} \end{cases}$$

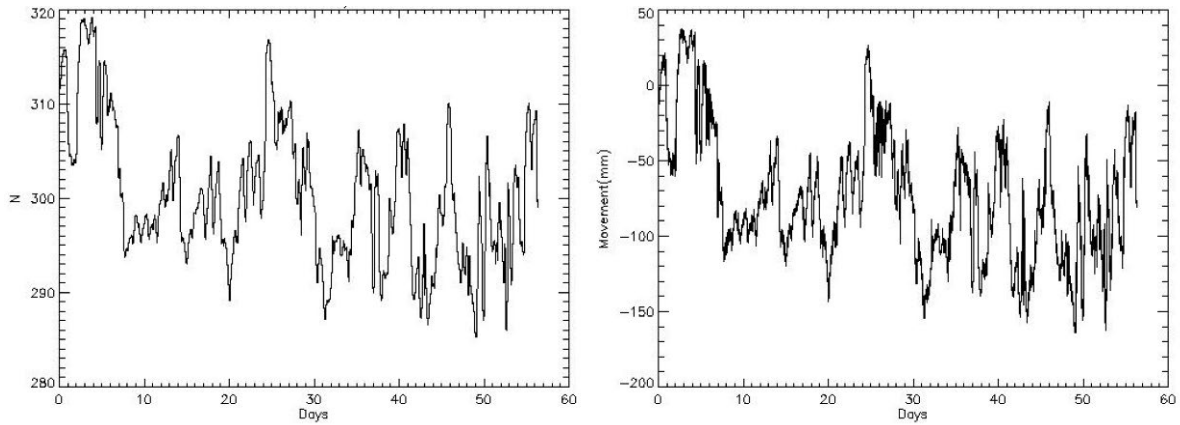


Figure 45 : strong correlations between the spatial and temporal index of refraction n (left) and the variation of range measured (right) (Norland, 2006; modified).

As shown in the figures above, there is a strong correlation between atmospherically conditions and displacement results. To separate the signal influenced by the atmosphere and the signal influenced by ground displacements, it is useful to introduce a second target on a stable part (Figure 46).

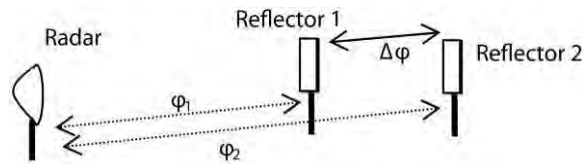


Figure 46 : theoretical arrangement for interferometric distance-meter (Norland, 2006).

So, assuming one reflector as fix, all variations of phase coming from the spatial and temporal index of refraction and not from the displacement can be filtered. Then, comparing phase results between the two reflectors by interferometry (phases differences), it is possible to assess the displacements of the second target (Norland, 2006).

$$\Delta\phi = \Phi_2 - \Phi_1 = \frac{4\pi}{\lambda} \times (R_2 - R_1)$$

$$\Rightarrow \Delta R = \frac{\lambda}{4\pi} \times \Delta\phi$$

So, in the case study of the Tafjorden instability, the reflectors are monitored with accuracy better than 0.1 mm at 2.9 km (Norland, 2006).

3. DIFFERENTIAL SAR INTERFEROMETRY

The main use of Differential Synthetic Aperture Radar Interferometry (DInSAR) is the detection of small deformations or movements at the surface, analyzing the phase differences

between two scenes acquired at different times. The Differential Synthetic Aperture Radar Interferometry is a combination of three main processing steps: first the Synthetic Aperture Radar (SAR), then the Interferometry (InSAR), and finally the Differential InSAR (DInSAR). These steps are described hereafter.

3.1. SYNTHETIC APERTURE RADAR

3.1.1. Radar imagery

In Radar imagery, a coherent and polarized wave is emitted by an antenna and the amplitude and the phase shift of each backscattered pulse are recorded in a complex number (Woodhouse, 2006):

$$\mathbf{z} = \mathbf{A} \cdot e^{i \cdot \Phi} \quad \text{where} \quad \begin{cases} z = \text{value for each cells} \\ A = \text{amplitude} \\ \Phi = \text{phase shift} \end{cases}$$

The amplitude of the backscattered signal is a function of the wave initial state, the environment crossed by the wave and the capacity of the target (reflectance, moisture) to reflect the wave (Figure 47). During the post-processing, it is easy to distinguish the emitted signal from the backscattered one. Moreover, airborne and satellite sensors are not looking vertically downwards but they are side-looking, avoiding the problem of knowing from which side of the nadir the pulse is backscattered.

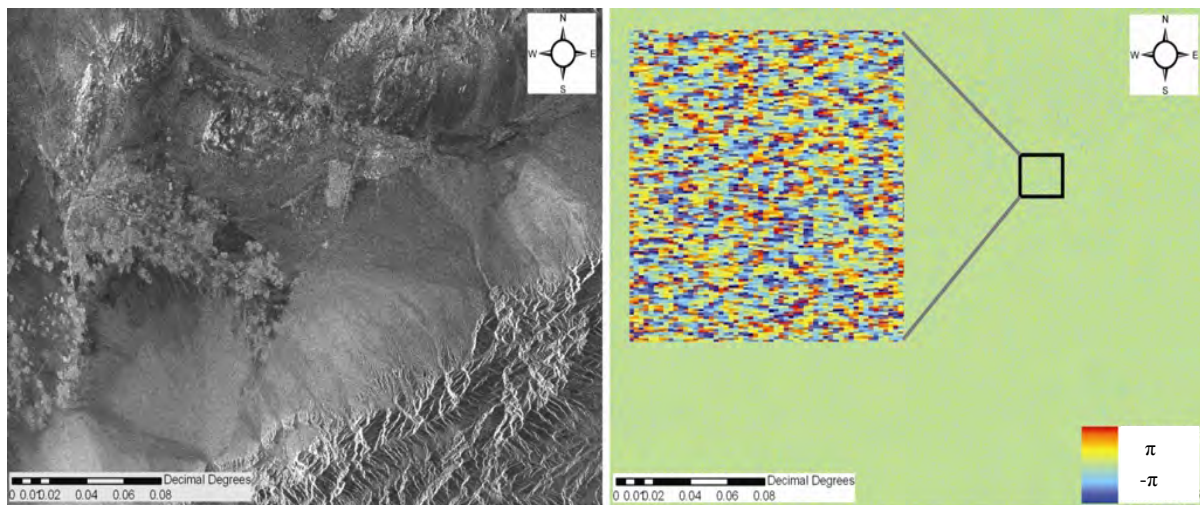


Figure 47 : Complex SAR image with the return amplitudes (left) and phases (right) of Bam area in Iran, December 2003 (Michoud et al., 2009).

In most cases, space borne Radar sensors are monostatic. So, the power of the return wave can be determined by the following formula detailed in the ESA Radar course III (website address in references):

$$P_r = P_t \times \frac{G^2 \cdot \lambda^2 \cdot \sigma}{(4\pi)^3 \cdot R^4} \quad \text{where} \quad \begin{cases} P_r = \text{Power received (W)} \\ P_t = \text{Power emitted (W)} \\ G = \text{Gain of the antenna} \\ \lambda = \text{Radar wavelength (m)} \\ \sigma = \text{radar scattering cross section (m}^2\text{)} \\ R = \text{distance antenna - target (m)} \end{cases}$$

But the effective area of the antenna is related to the gain by:

$$S = \frac{\lambda^2 \cdot G}{4\pi} \Rightarrow P_r = P_t \times \frac{S^2 \cdot \sigma}{4\pi \cdot \lambda^2 \cdot R^4}$$

The formula above gives the mean power per pixel in function of the size of the antenna. The bigger the antenna is, the higher the mean received power will be. And the higher the mean received power is, the better is the resolution. So one practical limit of the system is the maximal possible size of the antenna in space. It was demonstrated that to get a metric resolution from space borne sensor, a kilometer long antenna is needed (Prati, 2008).

To overcome this technical impossibility and obtain a reasonable ground resolution, a new acquisition method has been developed since the 50s (Wiley, 1954): the Synthetic Aperture Radar (SAR).

3.1.2. Synthetic Aperture Radar

Imagined in 1951 by Carl Wiley (Wiley, 1954; Hanssen, 2001), the Synthetic Aperture Radar principle wants to sum several echoes of the same target during the post-processing to improve the azimuthal resolution. Indeed, when the sensor transmits pulses along its track, the same ground target can reflect several times different echoes (Figure 48). Using the Doppler beam sharpening with the frequency information contained in the phase (Woodhouse, 2006), it is possible to differentiate two scatterers within the beam. So, the effective antenna aperture moving along the flight line is larger than in reality. In this way, the azimuthal resolution is improved (Figure 49). This process of synthesis can be compared to the multi-tracks processes in seismic geophysics.

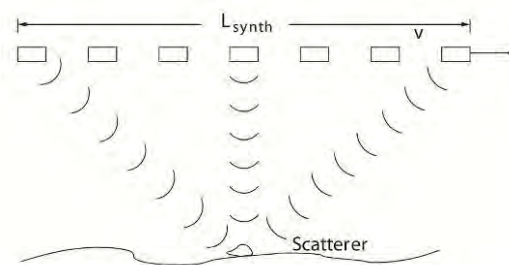


Figure 48 : Synthetic Aperture Radar principles. The same ground scatterer is shot from different points of view synthesizing an aperture much larger than the physical size of the real antenna, increasing the azimuth resolution (Lauknes, 2004).

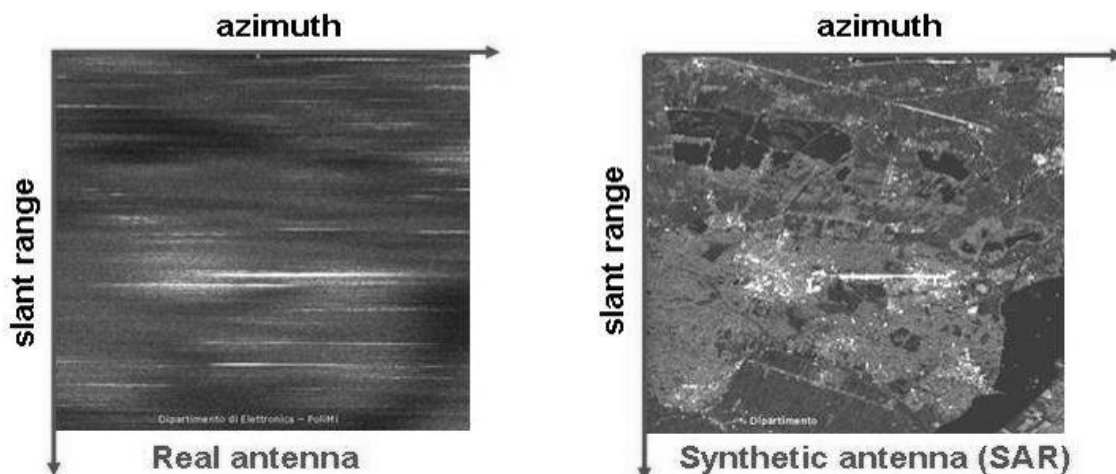


Figure 49 : Real Aperture Radar (left) and Synthetic Aperture Radar (right). The azimuth resolution is much better with SAR technology (Prati, 2008).

Once the azimuthal resolution has been improved by the SAR acquisition, it is also important to increase the range resolution. As explained in Woodhouse (2006), the shorter the pulse is, the better the range resolution is; but generating short pulses requires high peak power, actually not available on a satellite. In practice, a linear frequency modulated or chirped pulse (Figure 50) is used (Hanssen, 2001; Lauknes, 2004; Woodhouse, 2006). Thanks to a frequency post processing using the Fourier Transform, the echoes can be separated and re-attributed to their original ground target. Indeed, this technology allows to emit a chirped pulse of 40 μ s with a range resolution similar with a pulse of 60 ns (Woodhouse, 2006). However, to perform this technique, it has to be assumed that the fly is stable (reasonable in a satellite) and that the frequency variation law (modulation) is well known.

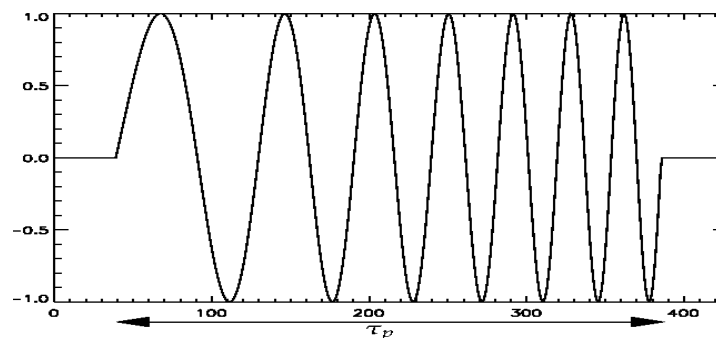


Figure 50 : linear chirp waveform – amplitude function of time (arbitrary units). Typical pulse durations for ERS and Envisat ASAR are between 30 and 40 micro seconds. (Lauknes, 2004).

3.1.3. Terminology and Space Resolution

The spaceborne acquisition of SAR images often uses specific terms which have to be defined or remembered in this section (to go further, see the website of the Canadian Center for Remote-Sensing).

- Ascending / Descending orbit: South-North / North-South trajectory of the platform.

- Azimuth: distance along the spaceborne flight direction. The azimuthal resolution can be performed by Synthetic Aperture Radar techniques.
- Complex signal: each pixel is registered by a complex number, keeping the information on the amplitude and the phase of the return signal. This is the raw data for an InSAR study.
- Ephemerides: satellite position and velocity vectors at any time t .
- Fringe: line of an interferogram corresponding of one color cycle.
- Ground range: distance along the perpendicular of the flight direction on the ground's surface. The range resolution can be performed emitting chirped pulses.
- Line of Sight: trajectory of the chirp between the radar antenna and the ground scatterers.
- Look angle θ : angle between the vertical and the LOS.
- Master / Slave images: reference / comparative images in interferometry.
- Nadir: projection on the Earth's surface of the platform's trajectory.
- Near / Far range: part of the image closest to / furthest from the Nadir.
- Resolution: size of the smallest object detectable by the sensor.
- Slant range: distance along the perpendicular of the azimuth on the SAR image. The slant range can be different of the ground range due to geometrical distortion, as explained in the following chapter.
- Track / Frame: Est-West / North-South limit of a SAR image.

Foreshortening may happen when a slope, with its normal vector looking towards the sensor, is less steep than the look angle. In this case, the surface will be smaller in the slant geometry than in reality (e.g. Figure 53). The layover may happen when the slope is steeper than the look angle. In this case, the backscattered pulse from the top of the slope will be collected by the sensor before the pulse reflected from the bottom of the slope (Figure 9). Then the top of the slope will be considered as closer in the slant range than the bottom, and the slope will look as reversed. The closer the slope is from the Nadir, the stronger the geometric distortions will be (Woodhouse, 2006). Indeed, the look angle is smaller close to the near range than to the far range and so more distortions are typically observed in the near range.

To correct both geometric distortions, foreshortening and layover, information on the real topography are used. By geocoding SAR images using a DEM, it is possible to rectify these distortions, as schematized in the Figure 54.

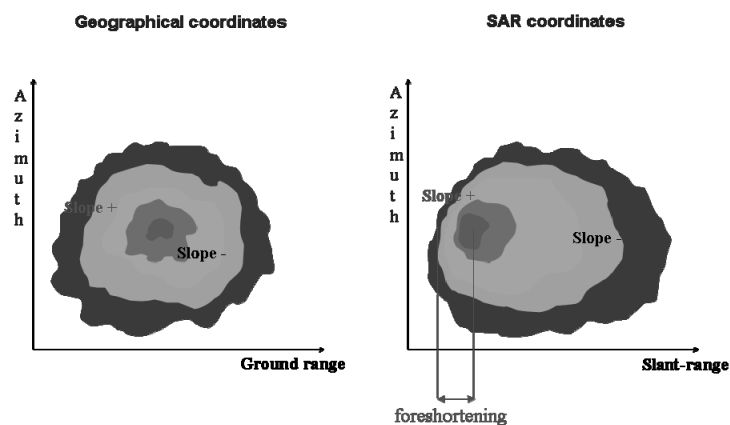


Figure 53 : schematic differences between ground range (left) and slant range (right), with a foreshortening slope (Prati, 2008).

The last distortion, shadowing, is a radiometric distortion that corresponds to an absence of signal (Figure 52). This distortion is the most restricting because the lost information is not recoverable. The only way to obtain additional data is to shoot from different positions, e.g. once in ascending orbit and the second time in descending orbit.

The last and facultative step of all processing is the geocoding, to transform and uniform the pixel sizes in a ground-coordinate system (Lauknes, 2004). For this process, Ground Control Points, DEM and precise orbit data are needed (ESA, Figure 54).

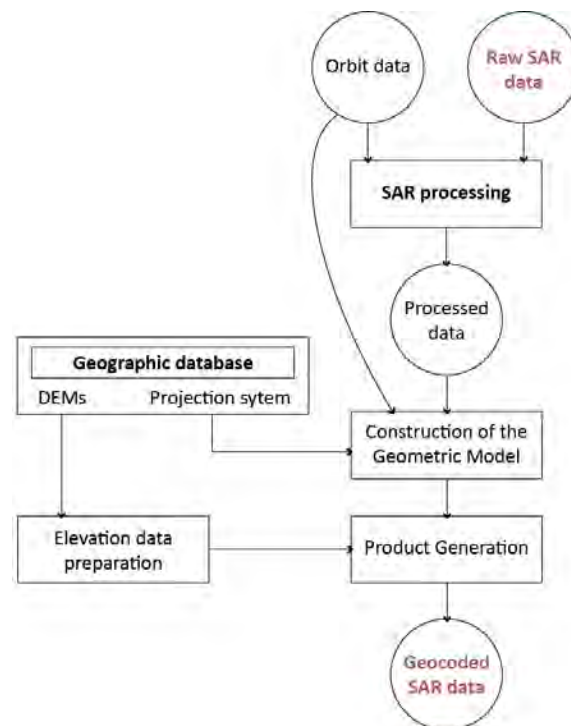


Figure 54 : Geocoding of SAR image (ESA document, 2008, modified)

3.2. SAR INTERFEROMETRY (INSAR)

Interferometric Synthetic Aperture Radar (InSAR) is a method to produce images of the interferometric phases of an area using images acquired from two different points of view. With SAR images as in optical stereoscopy, two images of an object from two distinct points of view allow seeing in relief and building Digital Elevation Models.

The interferograms shown as examples in the following chapters are processed using free ESA Envisat ASAR dataset of the Bam region (southeast Iran), where a strong earthquake occurred the 26th of December 2003.

Table 11 : raw input of Bam interferograms (free raw Envisat ASAR dataset provided by ESA).

Image	Sensor	Date	Normal Baseline
Sar1 (Slave)	ASAR Envisat	11 th of June 2003	475 m
Sar2 (Master)	''	3 rd of December 2003	0 m
Sar3 (Slave)	''	7 th of January 2004	520 m

3.2.1. Preparation of the dataset

3.2.1.1. Focusing

SAR is radar: similarly to surveillance radars, it therefore allows discriminating, i.e., resolving the targets in distance by measuring the delays of the transmitted pulses: the

narrower the pulse the higher the system range resolution. As already pointed out in a previous section, in order to limit the peak power and therefore to simplify the transmitter, usually chirp signal are used in transmission. These classes of pulses are characterized by large bandwidth duration products: to achieve short pulses the echoes that form the radar image must be correlated with the transmitted replica of the chirp signal. The received signal, i.e. the raw data, is therefore subject to a processing (range focusing) to achieve the maximum range resolution. Furthermore, SAR exploits the movement of the sensor to synthesize an antenna which is much larger, typically between 100 and 1000 times, the size of the real antenna mounted on-board the satellite (about 10m for the ERS and Envisat cases). Accordingly, the raw data must be further processed (azimuth focusing) along the azimuth direction to synthesize the large antenna and hence to achieve the highest azimuth resolution. Depending on the frequency and resolution, the azimuth focusing is generally more complex than the range focusing: it is intrinsically two-dimensional and space variant. However, thank to the research carried out in the last years, efficient focusing algorithms that make use of Fast Fourier Transform codes have been developed. In Bamler (1992) different focusing algorithms are compared.

It should be pointed out that to trade off between the coverage (swath width) and the resolution, SAR sensors may operate in different modes, see Fig 13. In the classical mode, referred to as stripmap mode, the antenna pointing is fixed: The movement of the sensor allows collecting the information from a ground strip. In the spotlight mode, the beam is steered backward in such a way to illuminate only a fixed portion (the ground spot): the size of the synthesized antenna and therefore the resolution is increased at the expense of the coverage. On the other hand by steering or better scanning the beam over different range swaths, SAR system may increase the range coverage at the expense of the azimuth resolution. Depending on the operational mode, the focusing operation must take into account the characteristics of the acquisition in order to properly process the signal and hence to achieve a full focusing. Most of the commercial packages allow focusing data for any acquisition mode. However, in case of beam steering the acquisition characteristics can impact also the subsequent interferometric processing steps: for instance spotlight and scansar interferometric acquisitions must be synchronized along the azimuth in such a way to limit the variability of the response of the scene as a function of the azimuth angle (aspect angle).

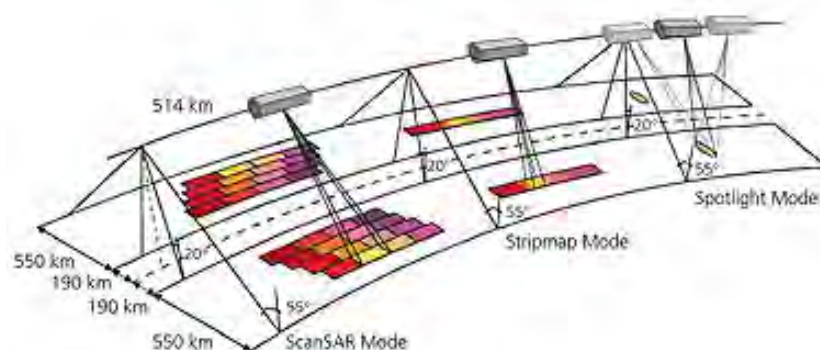


Figure 55 : different operational modes of SAR systems

3.2.1.2.Co-registration

Image registration is a process that aims to obtain a precise overlap between two or more images relative to the same object. Such images may be acquired from separated positions, by different sensors and/or at different times. For SAR interferometry, images need to be precisely aligned, with sub-pixel accuracy, to extract the phase interference relative to the same ground target, which is imaged at different positions in the two images due to distortion effects related to the different imaging geometry associated a) with a non zero orbit spatial separation, b) with the presence of orbit crossing. Incorrect alignments of the focused images, usually known as Single Look Complex (SLC) images, cause coherence losses in the interference operation, which, in turn, translate into inaccuracies in the final product.

Co-registration procedures for SAR images are based on the estimation of the so called azimuth and range warp-functions, i.e., the functions describing the transformation that maps the slave image onto the reference master image and that are subsequently used for resampling the slave image onto the reference master image grid. Warp functions are generally modeled in such a way to account for a few distortion effects: bilinear expansions are frequently used to account for rotation and scaling effects due to acquisition track crossing. Accordingly, warping functions are described in terms of few parameters that are estimated starting from control points. In the case of radar images, for the accuracy required in coherent data processing, such control points cannot be generally identified starting from features (road crossing, edges, etc.), because of the speckle noise. Ground corner reflectors could be exploited; however in practice matching measures of small image patches are employed to evaluate a sufficient number of tie points for the parameters estimate.

Standard image co-registration procedures based on polynomial expansion of the warp functions have been extensively used in the past to implement interferometry at small spatial baseline separation. However, accurate image registration of SAR data takes on a sub-pixel basis, where the passes span an orthogonal baseline interval of the order of few kilometers and the temporal intervals of several years (as it happen in interferometric stacking and persistent scatterers Interferometry for ground deformation monitoring) becomes a rather challenging step due to effects of topography and the presence of large temporal decorrelation which impair the accurate measurements of local distortions. Even more challenging is the registration of images for the latest high resolution SAR systems (i.e. TerraSAR-X and COSMO/SKYMED). To overcome the limitations of standard techniques, modern co-registration techniques make use of a geometrical computation of the warp functions starting from the orbital information and from an external (rough) DEM, (Sansosti 2006). This procedure allows easily achieving very accurate registration almost in all cases of interest for interferometrical application,

3.2.1.3.Filtering

In differential SAR Interferometry, angular imaging diversity is an unavoidable effect due to the impossibility to repeat exactly the same orbit: it also plays a positive role for the localization of the ground scatterers: In any case it is the source of noise that adds to the interferograms Besides the generation of image geometric distortions, which are usually compensated via a registration step, the interferometric phase associated with the topography plays a modulation role that causes, for a distributed scattering, the presence of incoherent components between the two images. For a planar surface this effect is known as spectral shift effect and it is shown schematically in the left part of Figure 14. The result is the introduction

of decorrelation noise on the interferometric fringes which is usually referred to as geometrical, spatial, or baseline decorrelation. Spatial decorrelation can be counteracted by proper filtered of the co-registered SLC images aimed at zeroing the unwanted components: the filtering is known as Common Band filtering and is schematically shown in the right part of Figure 14. Angular decorrelation is also present in the azimuth direction due to possible differences in the antenna beam pointing in the two acquisitions (Doppler centroid decorrelation). Common band filtering can be therefore beneficial also along the azimuth direction in the presence of large excursion of the Doppler Centroid. While in the azimuth direction the common band filtering is space invariant, the range filtering should be dependent on the local topography. In Fornaro and Monti Guarnieri 2002 it is discussed an efficient procedure for range space variant filtering. It should be pointed out that common band filtering should be performed only when the scattering is assumed to be distributed: this assumption is not verified in the case of strong scatterers and hence it is generally not implemented in permanent scatterers monitoring: Conversely it is usually performed in approaches like the low resolution monitoring via the Small BAseLine Subset approach.

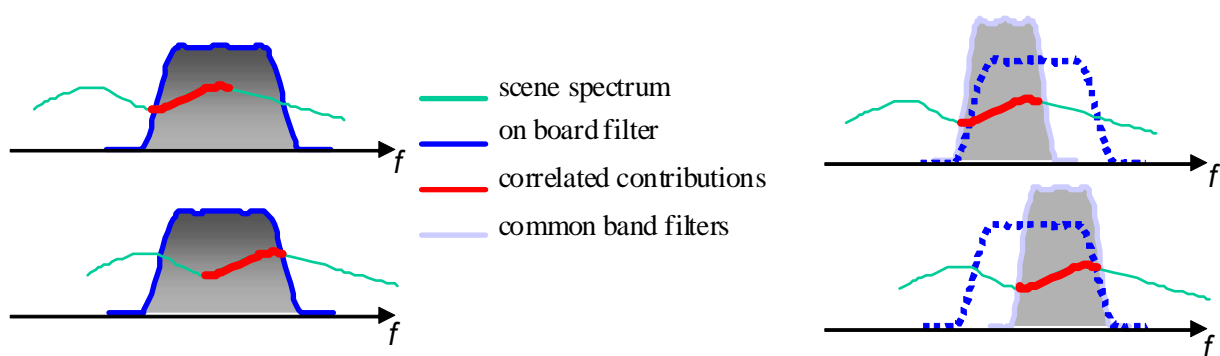


Figure 56 : the spectral shift effect (left) and the common band filtering (right)

3.2.2. Interferometric phase

Mathematically, the radar interferometry is defined by the difference of 2 phase shifts acquired by the sensor in two distinct times. So the formula 1 is the base of this method. More mathematical developments, which use the variables introduced in the Figure 57, are available on the following publications: Bamler & Hartl (1998), Massonnet and Feigl (1998), Hanssen (2001), Lauknes (2004), Catani et al. (2005), Colesanti & Wasowski (2006), Woodhouse (2006), Ferretti et al. (2007).

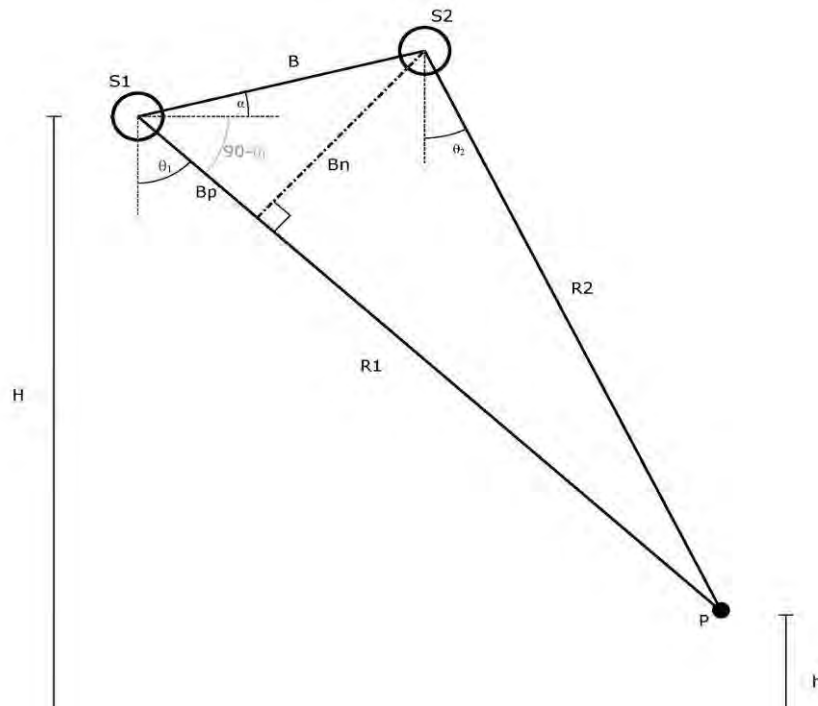


Figure 57 : InSAR acquisition parameters. S1 and S2 are the two antennas acquiring the image SAR 1 and SAR 2. S1 flight at the altitude H. P is a ground scatterer at the altitude h. R1 and R2 are the distances between P and S1 or S2. B is the distance between the two sensors (baseline), Bp and Bn being resp. the parallel and normal of B to R1. The angle between the vertical and R1 (resp. R2) is θ_1 (resp. θ_2). (Catani et al., 2005, modified)

Mathematical approach for one reflector acquired twice:

$$\varphi = \Phi_1 - \Phi_2$$

$$\Leftrightarrow \varphi = \frac{4\pi}{\lambda} \times R_1 - \frac{4\pi}{\lambda} \times R_2 = \frac{4\pi}{\lambda} \times (R_1 - R_2)$$

Due to the big distance considered, the approximation $B_p \approx R_1 - R_2$ can be admitted.

$$\Rightarrow \varphi \approx \frac{4\pi}{\lambda} \times B_p$$

$$\Rightarrow \varphi \approx \frac{4\pi}{\lambda} \times B_n \times \tan(\theta_1 - \alpha) \approx \frac{4\pi}{\lambda} \times B \times \sin(\theta_1 - \alpha)$$

Published with these two different forms, the formula 2 expresses the theoretical geometric relations of a raw interferogram (Figure 58).

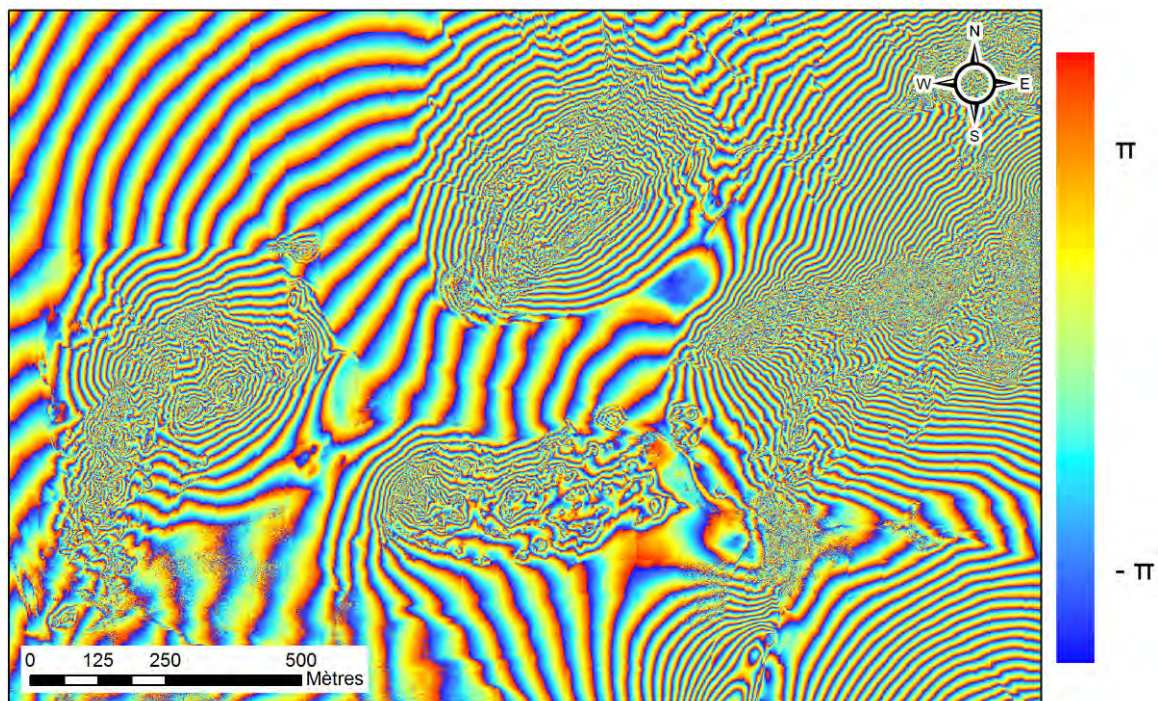


Figure 58 : interferogram using the images Sar2 and Sar3. One fringe is represented by one color cycle (from blue to yellow). (Michoud et al., 2009; processed with Erdas Imagine 9.2™)

3.2.3. Interferogram flattening

The topography is not the only contribution in an interferogram; there is also the flattening phase, which can be defined as “the phase variation proportional to the slant range displacement of the point target” (Ferretti et al., 2007). Removing this orbital contribution by an operation called interferogram flattening, it results fringes only influenced by the topography (and possibly the ground displacement) and proportional to it (Ferretti et al., 2007).

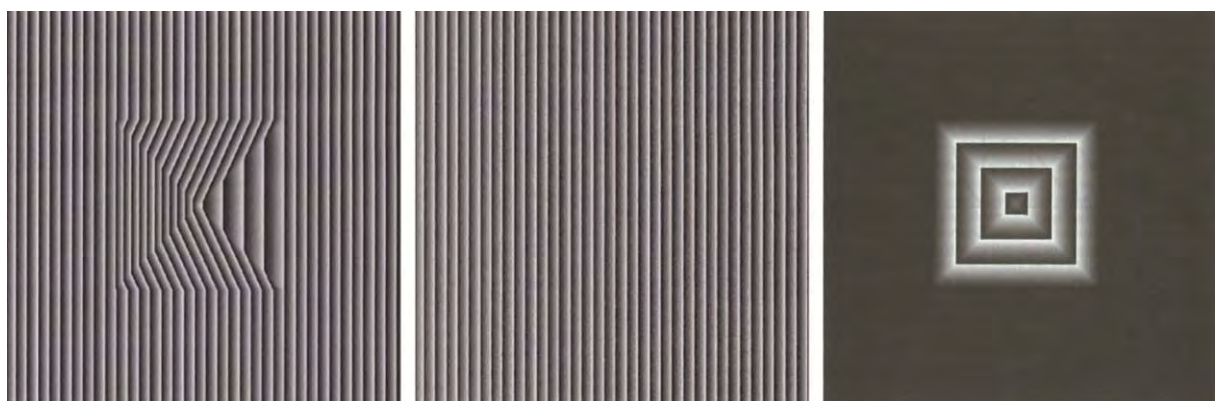


Figure 59 : theoretical interferogram simulating a pyramid. Left: raw interferogram – Center: flattening phase – Right: fringes proportional to the topography. (Woodhouse, 2006)

3.2.4. Altitude of ambiguity

The variation of the topography which creates an interferometric cycle of 2π is called altitude of ambiguity h_a (Massonnet and Feigl, 1998). In an interferogram, it corresponds to the altitude constituted by one complete fringe (from blue to red in the Figure 58).

$$\Delta\varphi = n \times 2\pi \quad , \quad \forall n \in \mathbf{IN}$$

$$h_a = \frac{\lambda}{4\pi} \times \frac{H \cdot \tan \theta_1}{B_n} \times 2\pi = \frac{\lambda}{2} \times \frac{H \cdot \tan \theta_1}{B_n} \quad \text{and for ERS} \quad h_a \approx \frac{9400}{B_n}$$

Considering the case of a normal baseline of 200 m, the altitude of ambiguity for ERS is 47 m. As shown later, the shorter the normal baseline is, the bigger the altitude of ambiguity is and the less accurate the altitude measurement is (Figure 64). But regarding to the geometrical loss of coherency, the normal baselines cannot be indefinitely long (cf.). To generate DEMs from ERS-satellite images, there is an optimum of the normal baseline at about 300-400 m (Ferretti et al., 1997).

3.2.5. Phase unwrapping

The fact that the interferometric phase is measured modulo 2π creates an ambiguity that must be removed by a course of phase unwrapping. This step converts each ambiguous 2π cycle to the absolute value of the interferometric phase (Figure 60 and Figure 61).

As suggested in the Figure 60, a certain continuity of phase values recorded is required to unwrap correctly the interferogram. Actually, several answers are acceptable for one initial wrapped interferogram (Ferretti et al., 2007). Actually, if the variation of the topography between two following scatterers is equal to the altitude of ambiguity (unwrapped phase 2 in the Figure 60), this gap is not considered in this processing step and the result will be without gap (unwrapped phase 1 in the Figure 60). Ferretti et al. (2007) emphasizes on the necessity to use “a-priori information to get the right solution”.

The other key point to assure a continuity of the values is to use only pixels which have a good coherence (cf. chapter 3.3.3), reducing the incoherent noise. Bernardino et al. (2003) advise to take only the pixels whose coherence is greater than 0.3.

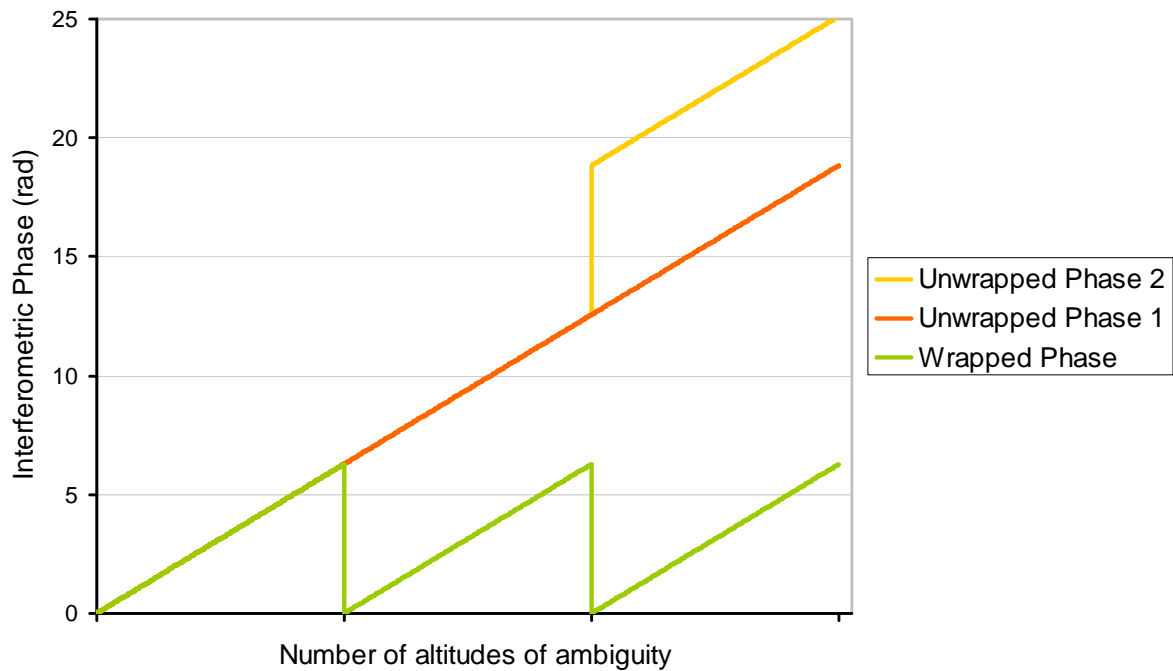


Figure 60 : difficulties of phase unwrapping. In fact, it exists several ways to unwrap correctly an interferogram. (Massonnet and Feigl, 1998, modified)

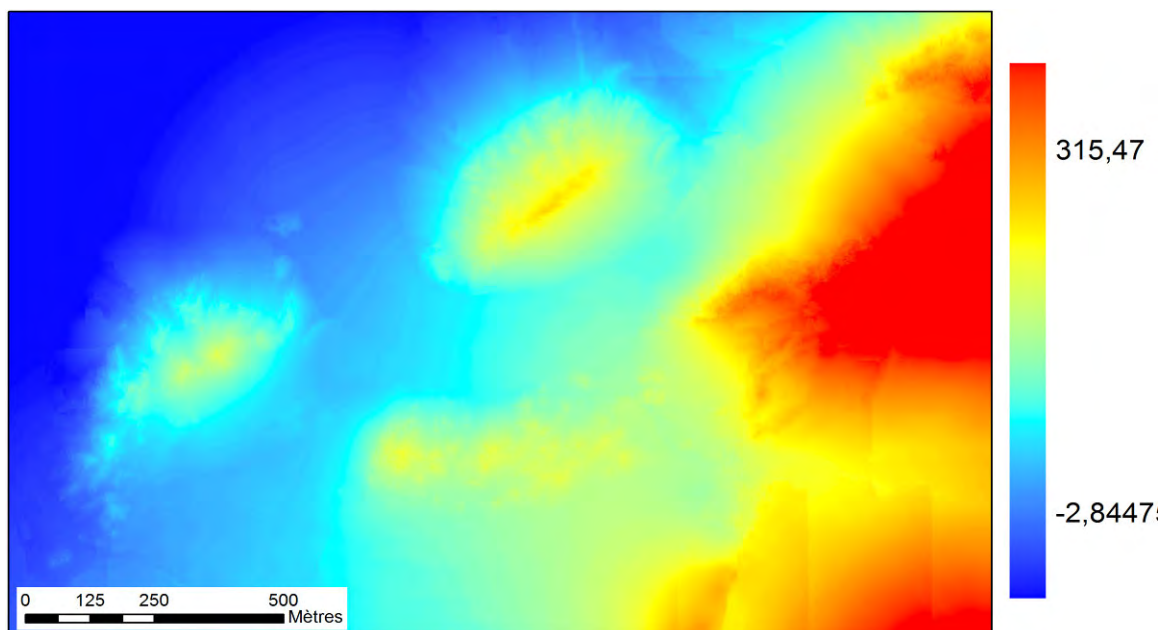


Figure 61 : unwrapped interferogram [Sar2/Sar3] of Bam area. (Michoud et al., 2009; processed with Erdas Imagine 9.2™)

3.2.6. DEM construction

The last step of the processing aims to construct numerically the DEM. The Figure 62 shows the helpful parameters needed to perform the model. The platform flying always at the same altitude, α is nil (cf. Figure 57). Moreover, the approximation $[S_1L] = [S_1P] = R_1$ is admitted.

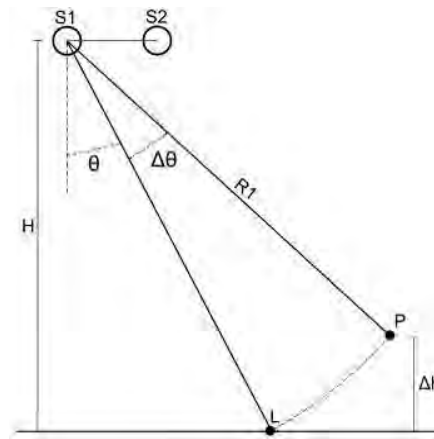


Figure 62 : parameters needed to calculate the altitude variations. (Michoud et al., 2009)

$$\begin{cases} \cos(\theta) = \frac{H}{R_1} \\ \cos(\theta + \Delta\theta) = \frac{(H - \Delta h)}{R_1} \end{cases} \Leftrightarrow \begin{cases} R_1 = \frac{H}{\cos(\theta)} \\ \Delta h = H - R_1 \times \cos(\theta + \Delta\theta) \end{cases}$$

Now, $\cos(\theta + \Delta\theta) = \cos\theta \times \cos\Delta\theta - \sin\theta \times \sin\Delta\theta$ and for $\Delta\theta$ small, $\begin{cases} \cos\Delta\theta \approx 1 \\ \sin\Delta\theta \approx \Delta\theta \end{cases}$

$$\Rightarrow \Delta h \approx H - R_1(\cos\theta - \Delta\theta \times \sin\theta)$$

$$\Rightarrow \Delta h \approx H - \frac{H}{\cos\theta}(\cos\theta - \Delta\theta \times \sin\theta)$$

$$\Rightarrow \Delta h \approx H \left(1 - \frac{\cos\theta}{\cos\theta} + \Delta\theta \times \frac{\sin\theta}{\cos\theta} \right)$$

$$\Rightarrow \Delta h \approx H \times \Delta\theta \times \tan\theta$$

Now, deriving φ in the formula 6 according to θ , we obtain $\frac{d\varphi}{d\theta} = \frac{4\pi}{\lambda} \times B \times \cos\theta$

As L and P are close, therefore we admit $\Delta\theta$ small and $\frac{d\varphi}{d\theta} = \frac{\Delta\varphi}{\Delta\theta}$

$$\Rightarrow \Delta\theta = \frac{1}{B} \times \frac{\lambda}{4\pi} \times \frac{\Delta\varphi}{\cos\theta}$$

$$\Rightarrow \Delta h \approx H \times \frac{1}{B} \times \frac{\lambda}{4\pi} \times \frac{\Delta\varphi}{\cos\theta} \times \tan\theta$$

$$\Rightarrow \Delta h \approx \frac{\lambda}{4\pi} \times \frac{H \cdot \tan \theta}{B_n} \times \Delta \varphi$$

Therefore, it is possible to obtain from the interferometric phase of two close scatterers the variation of altitude. Performing this method for all the pixels in the SAR images, it is possible to get a relative DEM of the area (Figure 63). Due to the initial ambiguity of 2π , the model cannot characterize the absolute altitudes, but only the variations of the topography. If the exact altitude of one pixel is known, it is then possible to shift the entire area to achieve a good DEM. To get a good DEM accuracy and to limit noise artifacts, it is advisable to process several SAR pairs and to average the results in order to decrease the signal to noise ratio (Ferretti et al., 2007).

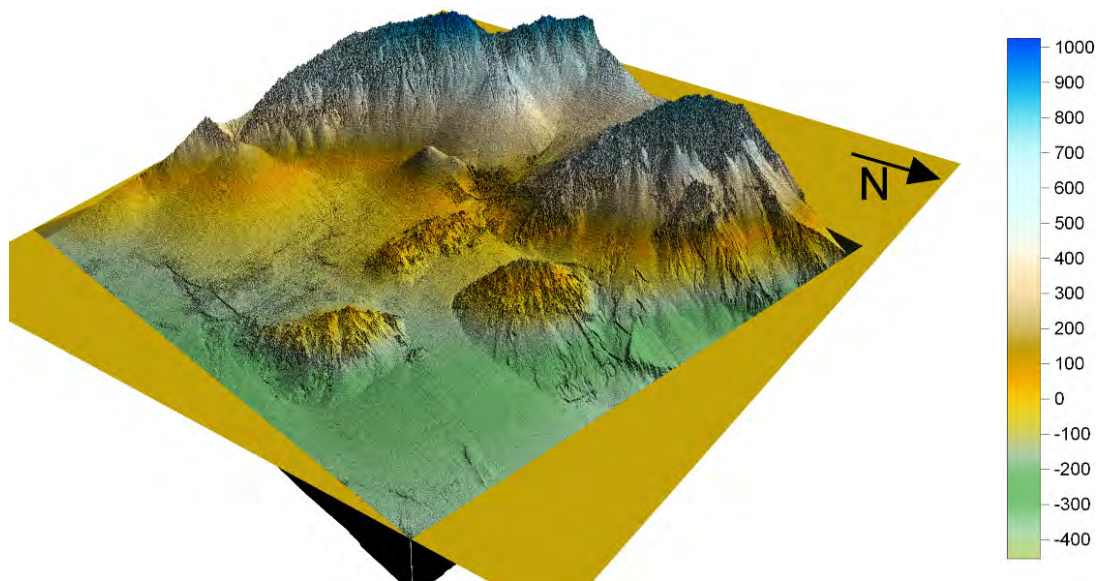


Figure 63 : Topography of BAM area, provided by the processing of the interferogram [Sar2|Sar3]. The model has a 20 m grid and a vertical accuracy of 1.5 m. (Michoud et al., 2009; processed with Surfer 8™)

The Shuttle Radar Topography Mission (SRTM), achieved in February 2000 by the NASA, scanned the Earth surface with two Radar antennas (C-band and X-band). Thanks to SRTM, it exists now a worldwide DEM at 90 m resolution (from 60°N to 56°S) and an American DEM at 30 m resolution (SRTM technical factsheet, JPL 2005).

For the data from the satellites ERS, the threshold of detection of a coherent signal regarding to the noise is $\pi/6$ (Catani et al., 2005). The following formulas show the importance of the normal baseline in the vertical accuracy (Δh) of a DEM (Figure 64). The longer the normal baseline is, the more accurate the DEM is.

$$\text{As } \Delta h \approx \frac{\lambda}{4\pi} \times \frac{H \cdot \tan \theta}{B_n} \times \Delta \varphi \text{ and } \Delta \varphi = \frac{\pi}{6}$$

$$\Rightarrow \Delta h = \frac{\lambda}{24} \times \frac{H \cdot \tan(\theta_1)}{B_n} \text{ and for ERS, } \Delta h \approx \frac{800}{B_n}$$

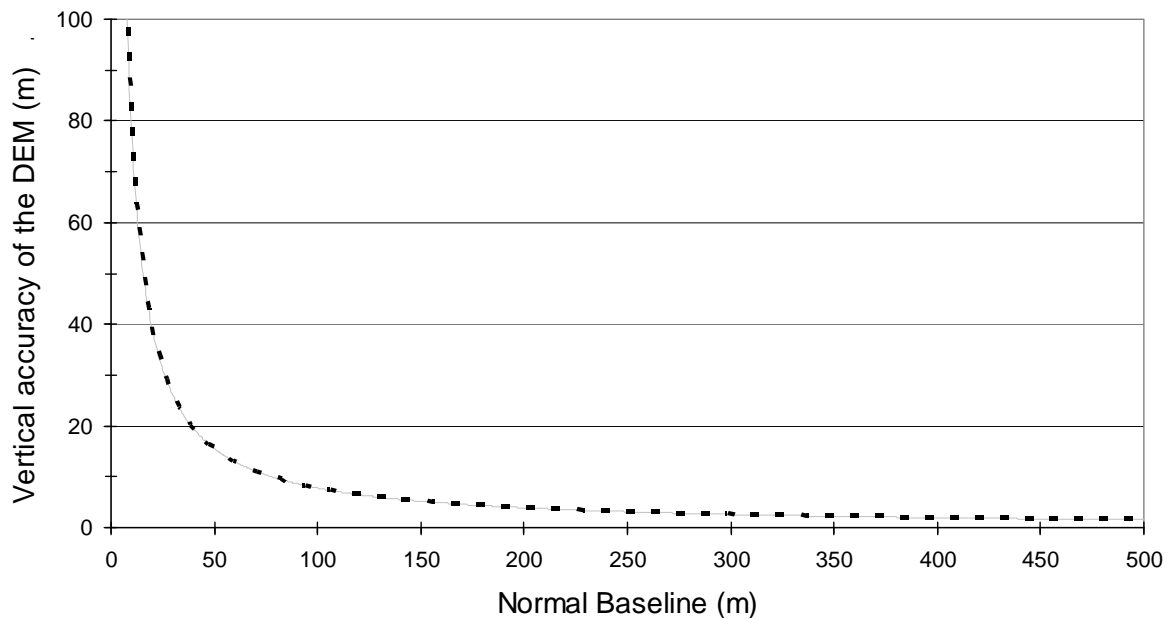


Figure 64 : vertical accuracy of a DEM regarding to the normal baseline of the interferometric pair. The function is calculated with the ERS parameters: $\lambda = 5.6 \text{ cm}$, $H = 785 \text{ km}$ and $\theta_1 = 23^\circ$. The longer the normal baseline is, the more accurate the DEM is.

3.3. DIFFERENTIAL SAR INTERFEROMETRY (DINSAR)

The main goal of differential InSAR (DInSAR) technique is to identify and quantify small ground deformations. Indeed, the phase difference is produced, provided by two contributions: the topography and the deformations (Figure 65). More information is available on Massonnet and Feigl (1998), Lauknes (2004), Catani et al. (2005), Colesanti and Wasowski (2006), Woodhouse (2006), Ferretti et al. (2007).

$$\Phi_{\text{way}} = \Phi_{\text{topography}} + \Phi_{\text{deformation}}$$

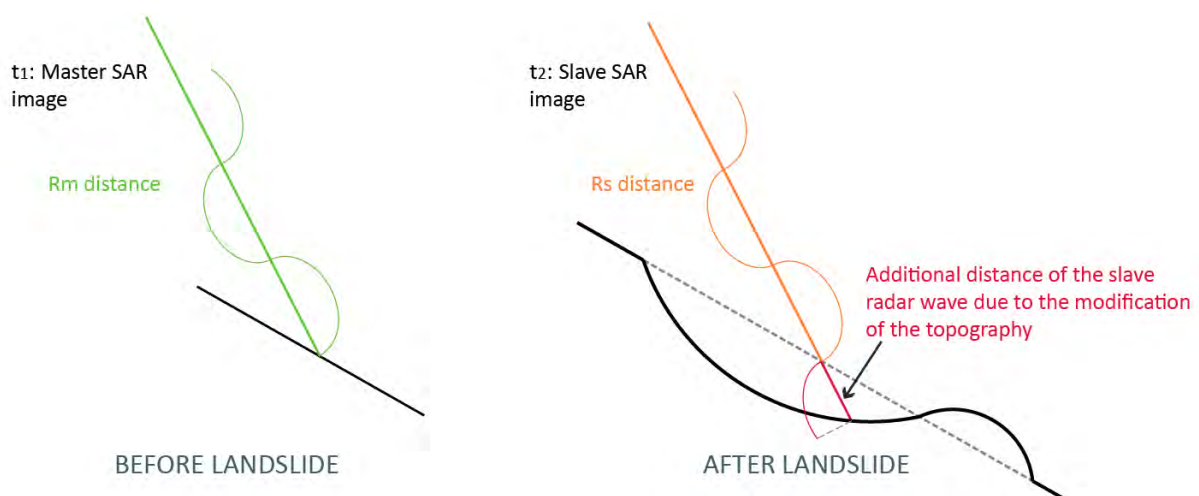


Figure 65 : Influences of a slope deformation on the phase decay. The way of the slave SAR image is longer than the way of the master SAR image, due to the rotational landslide (Michoud et al., 2009, modified).

3.3.1. Topographic phase

In DInSAR, the topographic phase is considered as an artifact. Indeed, the relief contribution scrambles the signal created by the ground deformations. The base of DInSAR techniques consists in using an ante-deformation DEM to perform a theoretical interferogram synthesizing the phase contribution of the topography. In this way, it is then possible to remove from the 2-way travel phase this topographical contribution to extract the deformation phase (Figure 66).

$$\Phi_{\text{deformation}} = \Phi_{\text{way}} - \Phi_{\text{topography}}$$

There are two methods to estimate the topographic contributions (Figure 66):

- Using an interferometric pair with the shortest temporal baseline as possible (e.g. from ERS Tandem). It is assumed that there is no ground deformation between the two acquisitions. Then the 2-way travel phase is equal to the topographic phase. But, this solution is not the best way to process due to recommendations made in the chapter 3.2.6 and for the unavoidable effects related to the propagation of the radiation through the atmosphere which typically varies between the two passes.
- Using an external DEM produced by another method (ALS, topographic maps, etc.). This way to process is the most powerful, because it uses one product independent of the SAR images. It allows to prevent errors due to bad SAR raw dataset.

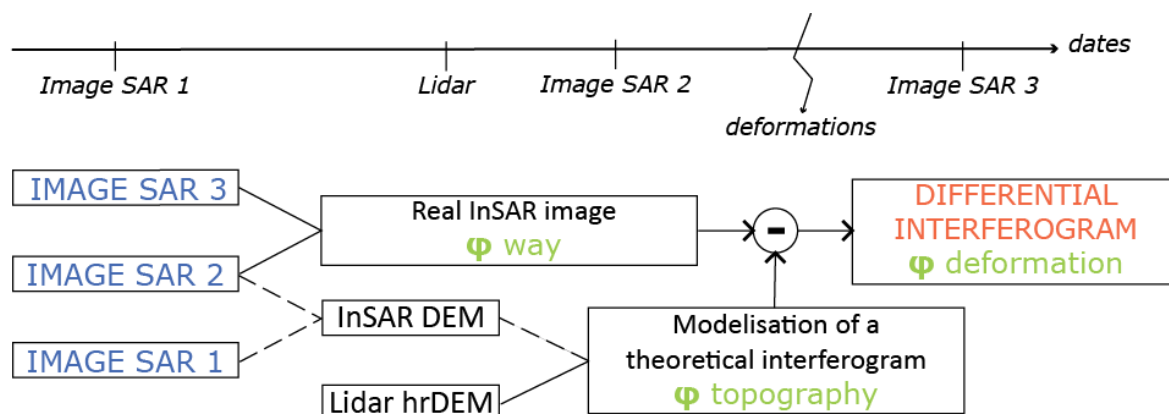


Figure 66 : creation of a Differential SAR Interferogram. The DEM injected provides a theoretical interferogram only influenced by the relief. The topographical phase is removed of the 2-way travel phase to isolate the deformation phase. (ESA, 2008, modified)

3.3.2. Deformation phase

Let consider the processing to be perfect and that all the contributions, the deformation phase excepted, are removed. The movements detected (Figure 68) by the formula shown below is in reality a projection of the deformations along the LOS (Figure 67) and not the 3D vector of displacement. The first publications on landslide monitoring with DInSAR techniques were published by Fruneau et al. (1996) and Carnec et al. (1996).

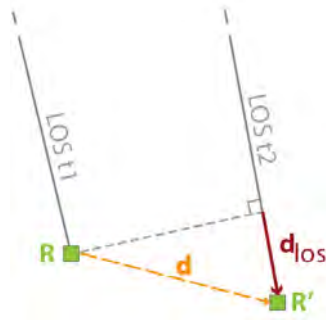


Figure 67 : projection of the displacements on the LOS. The red vector d_{los} is the projection of the real displacement (orange vector d) on the LOS. (Prati, 2008, modified)

Therefore, displacements perpendicular to the LOS are not detectable. In the following development, d represents the deformation and d_{los} is the projection on the real displacement on the LOS.

$$R_s = R_m + d$$

$$\Leftrightarrow \varphi_{def} = \frac{4\pi}{\lambda} \times d_{los}$$

$$\Leftrightarrow d_{los} = \frac{\lambda}{4\pi} \times \varphi_{def}$$

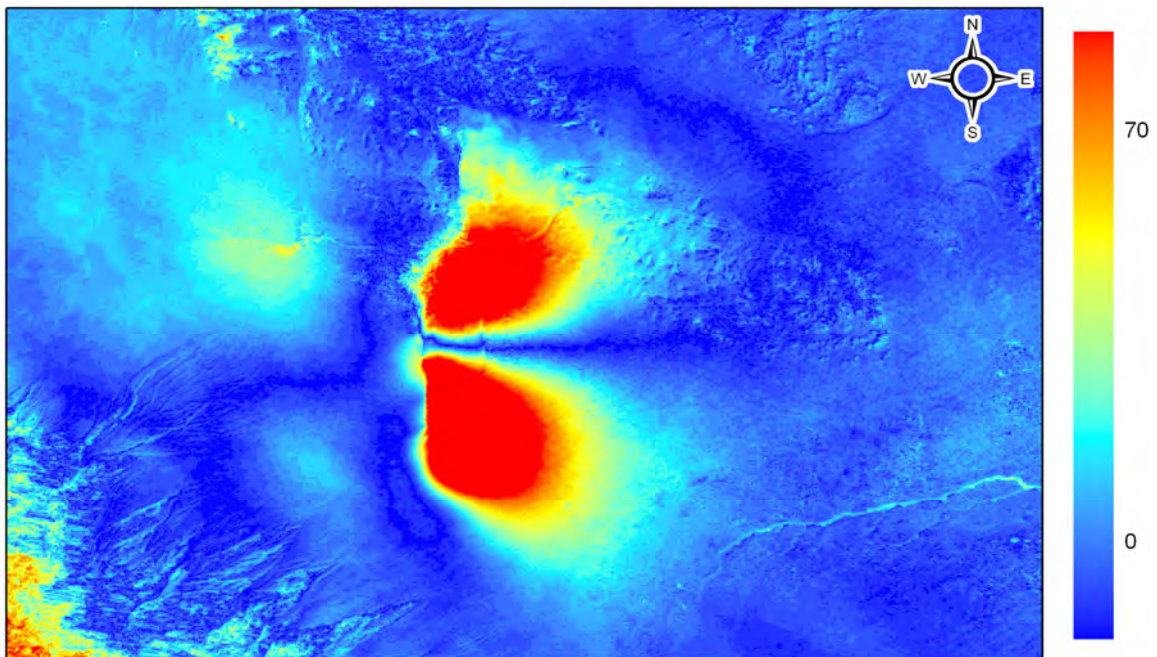


Figure 68 : unwrapped DInSAR [Sar2/Sar3] of Bam. (Michoud et al., 2009; processed with GSAR)

Finally, the accuracy of the detection depends on the Radar wavelength used and the threshold of detection of $\pi/6$ (chapter 3.2.6).

$$\text{As } \Delta\varphi_d = \frac{\pi}{6}, \quad \Delta d_{\text{los}} = \frac{\lambda}{4\pi} \times \Delta\varphi_d = \frac{\lambda}{4\pi} \times \frac{\pi}{6} = \frac{\lambda}{24}$$

Admitting a perfect processing, the accuracy expected can be subcentimetric; ERS and Envisat, which use C-band (5.6 cm), can reach an accuracy of 2.33 mm.

Unfortunately, all expressions and formulas shown above are available only for ideal conditions, and it is never the case on the Earth. Indeed, the SAR signal can be noised by atmospheric disturbances, orbital inaccuracy, etc. So it is very important to know all the contributions which can influence the radar signal, to process the data and interpret properly the results.

3.3.3. Limitations of conventional DInSAR

Several noise sources can influence the phase of the SAR signal. It is important to know all of them to be able to isolate only the interesting phases (Massonnet and Feigl, 1998; Lauknes, 2004; Hanssen, 2005; Colesanti and Wasowski, 2006; Ferretti et al., 2007).

$$\Phi_{\text{total}} = \Phi_{\text{decorrelation}} + \Phi_{\text{atmospheric}} + \Phi_{\text{orbital}} + \Phi_{\text{way}}$$

This section aims to explain those contributions.

3.3.3.1. Geometric and temporal decorrelation

Both temporal and spatial decorrelations contribute to a loss of coherence (2.3.4) between different SAR acquisitions.

The temporal decorrelation is due to changes of geometrical and electrical properties of the scatterer surface. Indeed, the evolutions of vegetation, morphology (erosion, rockfall, etc.), land use (farmed crops, fallow field, etc.) and soil moisture influence a lot the reflected signal. Now, those factors can change in time according to seasons and human activities. Therefore Massonnet and Feigl (1998) advise to use SAR images acquired always at the same period of the year to limit the temporal decorrelation. Usually, the best seasons are beginning of spring and end of fall, when trees have only few leaves and without snow covering the ground.

A too big difference of point of view (too long spatial baseline) between two SAR acquisitions creates the geometrical decorrelation. Bamler and Hartl (1998) indicate the existence of a critical baseline above which the interferometric signal is only composed by noise; this critical baseline is estimated at almost 1000 m for ERS dataset. It can be calculated thanks to the following formula (sarmap, 2008):

$$B_{n_{\text{critical}}} = \frac{\lambda \times R \times \tan\theta}{2 \times R_s}$$

where λ is the wavelength, R the range, θ the look-angle and R_s the pixel spacing (respectively 5.6 cm, 870 km, 23° and ~ 12.5 m for ERS).

3.3.3.2. Atmospheric artifacts

Even if the Radar wave amplitudes are not much attenuated by the atmosphere (Figure 1), the phase is sufficiently influenced by atmospheric conditions to perturb results. Atmospheric

conditions will change the velocity of propagation. Actually the variation in time and space of the partial water pressure in the troposphere is the main controlling factor (Zebker et al., 1997; Norland, 2006). Moreover, the variations of pressure and temperature can influence slightly the signal (Norland, 2006). Massonnet and Feigl (1998) advise to use SAR images acquired during night to limit the atmospheric artifact. As the atmosphere is colder and dryer than during the day, the Radar signal is less perturbed.

3.3.3.3. Orbital artifacts

It is very important to know the relative position of the platforms during the acquisitions. Indeed, as exposed in the formulas shown above, the values of the normal baselines are required by the interferometric equations. To limit the orbital artifacts due to bad positioning, precise orbits datafiles, called ephemerides (e.g. Delft or Doris precise orbits) are imported during the processing (Lauknes, 2004; Ferretti et al., 2007).

3.3.4. Coherence

To have an objective idea of the accuracy and the final reliability of an interferogram, the coherence index was created. Massonnet and Feigl (1998) define the coherence as “the degree of agreement between neighboring pixels in an interferogram”. The bigger the coherence is, the lower the artifacts are and the better the processing will be.

The coherence γ of an interferogram (Figure 69) processed with the complex SAR images S_1 and S_2 is calculated in this way:

$$\gamma = \frac{E[S_1 \cdot \overline{S_2}]}{\sqrt{E[|S_1|^2] \cdot E[|S_2|^2]}}$$

where E represents the statistical expectation and $\overline{S_2}$ the conjugated complex of S_2 . A coherence of 0 means that results are only composed by random phase noise and a coherence of 1 by very good signal with no noise (Prati, 2008). Colesanti and Wasowski (2006) explain that in practice, the coherence is computed “assuming ergodicity for the interferometric signal and, therefore, estimating $E[\#]$ using all pixels within a (e.g. rectangular) window centred in the image element”.

Hanssen (2005) advises to consider a-priori coherence expected in an area before ordering dataset to assess the feasibility and reliability of processed interferograms. Indeed, according to practical observations (Massonnet and Feigl, 1998; Berardino et al., 2003; Colesanti et al., 2004; Lauknes, 2004; Michoud et al., 2009), the coherence is better in arid or urban areas than in wooded counties where temporal decorrelations are stronger.

The following figure aims to compile all notes written before to optimize the coherence and the reliability of differential interferometric results.

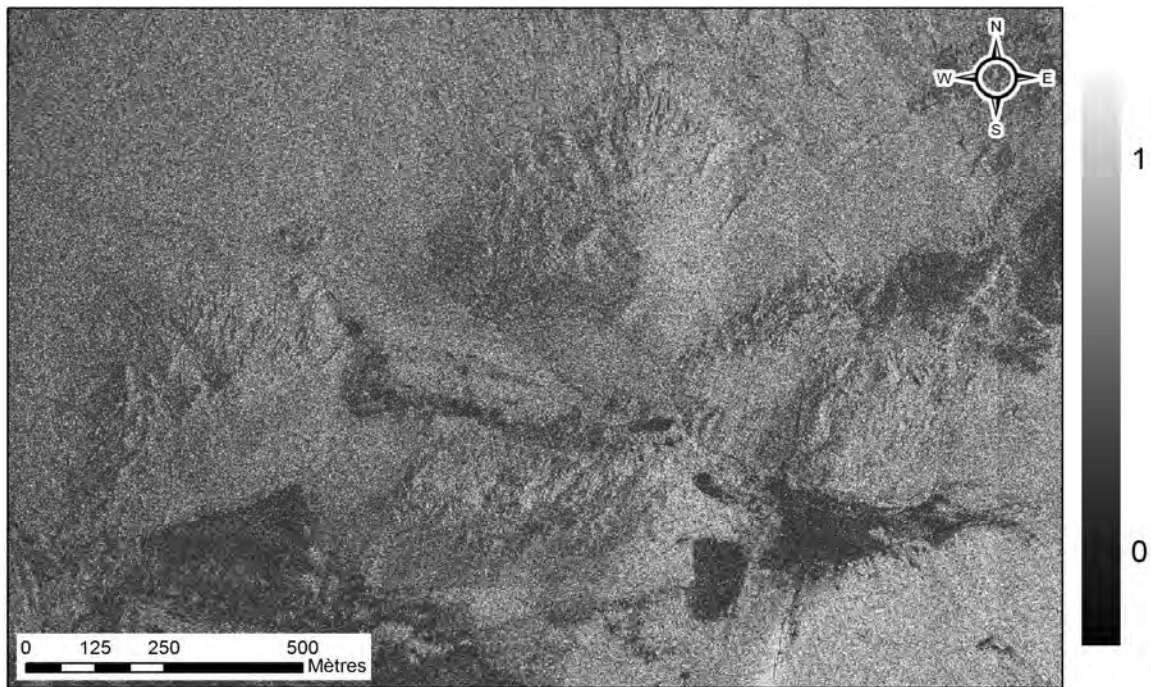


Figure 69 : coherences of the interferogram [Sar2|Sar3] of Bam. (Michoud et al., 2009; processed with Erdas Imagine 9.2™)

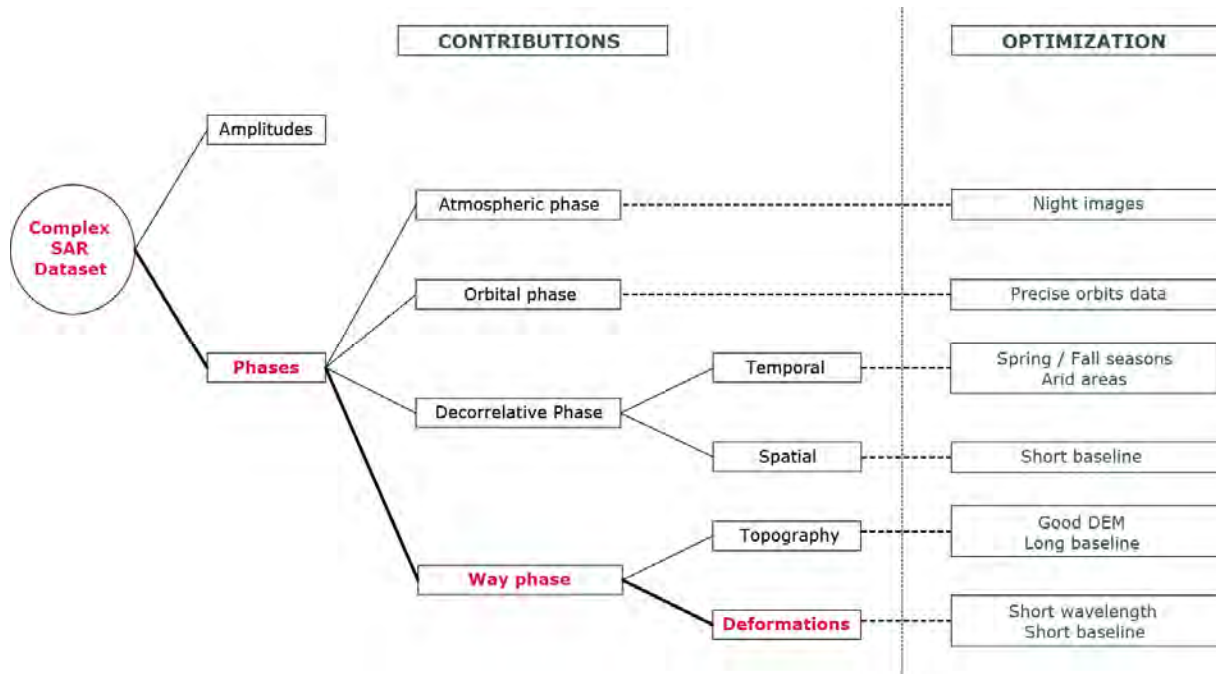


Figure 70 : optimization of the DInSAR processing. The best way to process dataset with good coherences and reliability is to choose night scenes from the beginning of spring or end of fall (snow and leaves free) with the shortest baselines as possible. (Michoud et al., 2009, modified)

Annex B2

Jaboyedoff M, Abellán A, Carrea D, Derron MH, Matasci B and Michoud C: LiDAR use for Mapping and Monitoring of Landslides, Accepted in Encyclopedia Natural Hazards, Taylor & Francis

LiDAR use for Mapping and Monitoring of Landslides

Michel Jaboyedoff, Antonio Abellán, Dario Carrea, Marc-Henri Derron, Battista Matasci and Clément Michoud.

Risk Analysis group, Institut des sciences de la Terre (ISTE) Faculty of Geosciences and Environment, University of Lausanne, Unil-Mouline, Geopolis, 1015 Lausanne, Switzerland.

Keywords: LiDAR, Laser scanner, landslide, mapping, monitoring, structural analysis.

Abstract

During the past 20 years, the fast development of several remote sensors (e.g. Optical imaging, LiDAR, RADAR, etc.) assembled on satellite, aerial or terrestrial platforms is changing our perception and analysis of the Earth's surface processes. Particularly, LiDAR technology is capable of acquiring faster, denser and more precise information about land terrain surface, allowing the 3D geometrical modelling of mountains, valleys and cliffs at different scales and with an unprecedented level of detail. Consequently, LiDAR applications on landslide mapping, characterization, monitoring and modelling are shedding a light into how landslides behave and evolve along space and time. Some examples include: (a) the precise landslide mapping through the identification of geomorphological features, (b) the accurate extraction of discontinuities characteristics that play a key role in slope stability, (c) the monitoring of landslides in order to analyse 3D displacements, (d) the magnitude/frequency quantification of fallen volumes along time in order to study erosion rates, (d) the improvement of rockfall hazard assessment, (e) the modelling of mass movements run-out, etc.

INTRODUCTION

During the last decade, the research on surface processes has taken profit from two main developments: (a) faster and more portable remote sensing devices and (b) more powerful computer processors and graphic capabilities. Since the beginning of the 21st century, one of these remote sensing techniques, the Light Detection And Ranging (LiDAR), also known as laser scanner, provides detailed and accurate topographic surveys (1). LiDAR allows to acquire more than 10.000 points per

second from fixed or moving positions, leading to huge sets of data in a three-dimensional Cartesian coordinate system (i.e. X, Y, Z coordinates), normally referred to as “point clouds”. This detailed and accurate representation of the terrain surface has been extensively used to characterize, monitor and model landslides **(2; 3; 4; 5; 6)**.

The two main categories of LiDAR for mapping and monitoring landslides are static and mobile devices. Static devices are commonly named such as Ground-Based LiDAR or Terrestrial Laser Scanners (TLS). Regarding mobile devices, the different instruments are normally classified depending on the platform configuration: either boats **(7)**, cars **(8)** or flying devices **(9)**. The latter, also known as Airborne Laser Scanners (ALS), include LiDAR assembled on airplanes, Unmanned Aerial Vehicles (UAV), and helicopters, and can be adjusted to the shooting direction **(10)**. Examples of point cloud density for TLS systems normally range from 100 to 500 pts./m² whereas ALS systems range from 0.5 to 50 pts./m².

Point clouds can be converted to surfaces through different surface reconstruction processes, usually involving Delaunay triangulation. For instance, the point cloud produced by ALS is normally transformed into Digital Elevation Models (DEM) or High Resolution DEM (HRDEM), which provides very detailed geomorphological information **(11; 12)**.

The main achievements on the application of the LiDAR technique to landslide investigations include: (a) the improvement of landslide mapping and inventories using HRDEM; (b) a complete characterization of the 3D slope deformation, allowing the forecasting of landslides failures **(13; 19; 21; 14)**; (c) a more accurate and detailed monitoring of rock failures **(15; 16; 17; 18; 19; 20; 21; 22)**; (d) the improvement in rock slope characterization in inaccessible areas thanks to the automatic extraction of discontinuity orientation **(23; 24; 25)**; and (e) the identification of geomorphic signatures of debris flows based on HRDEM and accurate erosion and deposit quantification **(26, 27)**.

Comparing LiDAR, with other 2D techniques, allows for the analysis of the surface features and real changes in 3D. Therefore, the main future challenges include: (a) the development of a software that may allow us to fully extract the 3D information from the point clouds; (b) coupling LiDAR with

other techniques such as InSAR or multi-spectral cameras. The accomplishment of these challenges will open new perspectives for a better understanding of the 3D behaviour of landslides, with significant implications on monitoring and early warning systems.

1. LiDAR AND LASER SCANNING TECHNIQUES

1.1 History

The history of LiDAR technology is directly linked to the LASER (Light Amplification by Stimulated Emission of Radiation) evolution. In 1957, the physicists Charles Townes and Arthur Shawlow at the Bell Labs investigated the development of optical MASER (Microwave Amplification by Stimulated Emission of Radiation), which later on became laser in 1959 (28). In May 1960, the first instrument which successfully produced a series of pulsed laser was designed (29). Less than one year later, the first LiDAR was manufactured for military purposes (28). Then in the Seventies, laser technologies became generalized for civilian applications such as surveying. Some examples include the use of Electronic Distance Meter (EDM) in quarries and tunnel environments (30; 31; 32).

At the same time, first ALS systems were able to measure the range of the emitted pulse with a precision of 1 m (33; 34), for altimetry and bathymetry purposes (35 and 36, respectively). Nevertheless, this technology was limited by the poor accuracy on the position and orientation of the airplane given by the Inertial Navigation Systems (INS). Afterwards, laser devices became more accurate, less heavy, less expensive and eye-safe. Moreover in the early nineties, the improvements on the navigation satellite constellations GPS-NAVSTAR (USA) and GLONASS (USSR) allowed for the overcoming of the limitations of former INS, considerably improving the ALS accuracy (37; 38). In the late nineties, theoretical and practical aspects of ALS techniques were well known and several important works were published (39; 40). Early applications of ALS consisted in the production of DEM (1; 41), the mapping of topographical changes of Greenland's ice sheet (42; 43), and the creation of a 3D model of an urban environment (44). The mapping and modelling of landslides from HRDEM at regional scale started at the beginning of the 21st century. 45; 46; 47; 48; 49).

During the last decade, the GLAS sensor (Geoscience Laser Altimeter System) illuminated the Earth with three lasers. One of these sensors was especially designed to monitor different environmental variables, such as polar ice sheet mass balances, vegetation canopy and land elevation with a vertical accuracy of 3 cm (50; 51; 52). One of the most relevant topographic products derived from the ICESat mission was the 500 m pixel resolution DEM of Antarctica (9; 53). Meanwhile, a spaceborne EDM device named MOLA (Mars Orbiter Laser Altimeter) was developed to observe Mars from 1999 to 2001 in order to survey its topography and atmosphere (54; 55). This sensor was measuring the surface of Mars during fifteen months, obtaining a DEM of Mars with a resolution of a few square kilometres and a vertical accuracy of 1 m (54).

At the same time, pioneering triangulation-based TLS systems were designed and used for archeological purposes (56). Later on, ground-based LiDAR sensors have been used for surveying and monitoring deformations of urban structures (57; 58). Geological applications of TLS are experiencing fast developments since 2002, including: (a) extraction of orientations and roughness of rock slope discontinuities (2; 59; 60; 61; 62; 63; 86; 117); (b) monitoring of volcanic activity (64); (c) litho-stratigraphic modelling (65; 66; 67); (d) rockfall detection (17; 18; 19; 21); and (e) landslide monitoring (16; 19; 68).

1.2 Instrument principle

(a) LiDAR functioning

A LiDAR device consists of a combination of a laser rangefinder and a scanning mechanism which allows for the precise measurement of a distance to a target and the orientation of the laser beam. The scanner device works through the internal rotation of one or two mirrors and/or the rotation of the whole device. Additional components normally include an electronic unit, an imaging device (e.g. digital camera) and specific software to control the whole system.

There are three main types of LiDAR, corresponding to three different ways of measuring the range, for instance the distance along the Line Of Sight (LOS) between the sensor and the terrain (see Fig.

1): (1) pulse LiDAR measures the Time-Of-Flight (TOF) of a laser pulse, (2) phase LiDAR uses phase shift between emitted and received signal and (3) triangulation LiDAR uses a camera to locate the laser spot on the scanned surface (69).

Pulse LiDAR is based on the measurement of the time delay (TOF) of a laser pulse travelling from the source (e.g. TLS) to a reflective target (e.g. ground surface) and back to the source, as follows:

$$d = \frac{1}{2} c \times \Delta t \text{ [Equation 1, 32]}$$

Where d is the range, c is the speed of light in the air (3×10^8 m/s) and Δt is the TOF. This technique allows for centimetre accuracy measurements at several kilometres distance. Phase LiDAR allows for more precise acquisition (some millimetres) but it only works for short ranges (less than 100m). Phase LiDAR uses a continuous amplitude or/and frequency modulated beam instead of pulses. The range is deduced from the phase shifts between emitted and backscattered signal for a couple of frequencies (32). Triangulation LiDAR estimates the range from two angles: the illumination angle of the laser beam and the observation angle of the camera (38). With a high accuracy (around 0.1 mm), triangulation LiDAR has very short ranges (less than 5 m). Pulse (or TOF) LiDAR is the main device used for landslide monitoring and mapping, since it is the only one that makes possible acquisitions for ranges longer than 100 m (up to a couple of kilometres for the most advanced sensors). There are few applications of phase and triangulation LiDAR for landslides, such as very detailed characterization of sliding surfaces or analogue modelling in the lab (70).

The footprint size depends on the range and on the width of the laser beam. The shape of the footprint on the surface depends on the local incidence angle, i.e. the angle between the LOS and the normal to the surface (Fig. 2). The range is measured at the peak of intensity of the backscattered pulse. If the surface is normal to the laser beam, it corresponds to the centre of the footprint (point P in Fig. 2). If the incidence angle is high (more than 70°) or the local relief is rough, the recorded point of location (point P' in Fig. 2) can lie anywhere within the spot (71; 72).

(b) Multiple echoes

Even if strongly collimated, laser beams of LiDAR are affected by divergence, i.e. the beam width increases with the range. Typical diameters of beam footprints are 30-50 cm for ALS at 1 km range, and 10 cm for TLS at 500 m range (71). As a result, the consequences are that several back-scattered pulses can correspond to a single emitted pulse (multiple echoes). For instance, when a pulse hits a tree part of the pulse can be reflected by the top of the canopy, another part by branches and the last one by the ground (see Fig. 2). This characteristic of the beam to “penetrate” the vegetation is a key advantage of LiDAR compared to photogrammetry, in order to get ground elevation models of vegetated areas. However, a dense forest may prevent the beam to reach the ground surface. Full wave LiDAR devices, usually ALS, provide a continuous record of the backscattered signal (full waveform). Most of TLS record only one or several discrete pulses. In landslide studies, the last pulse, (i.e. the pulse backscattered by the ground surface) is generally used. But it may be convenient to have other return pulses for vegetation removal purposes (32).

(c) Other parameters: Intensity + colour

In addition to 3D surface point locations, LiDAR devices measure the signal intensity of the backscattered laser signal. Intensity mainly depends on the type of material, orientation of the slope, range and laser wavelength. Additional external cameras can be coupled with LiDAR during acquisition, allowing the assignment of a colour attribute (i.e. RGB) to each point of the LiDAR point cloud. During ALS acquisitions, natural colours and/or infrared images are usually taken simultaneously. A SLR digital camera is frequently used to provide natural colours to TLS point clouds, but more advanced imaging devices such as hyperspectral cameras can be used too (73). Some of the main uses of intensity values or colour attributes for landslide studies include bedrock mapping, vegetation removal and interactive visualization of point clouds (74).

(d) ALS versus TLS

Aerial Laser Scanners are widely used, either by national topography agencies and private companies, to cover large areas for topographical surveying or forest management (9). The plane usually flies

1000 m above the ground and the ALS records 1-2 points by ground square-metre, with a position accuracy of 5-30 cm (37). Mobile techniques require a precise recording of the location and altitude of the scanning device during the acquisition, which is actually carried out by coupling the LiDAR with a GNSS (usually a differential GPS) and with an Inertial Measurement Unit (IMU). Then the location of each point of a scan is recalculated as a function of the LiDAR position and orientation during a post-processing stage. Due to its heavy logistics, ALS is operated by professional surveying companies. Other smaller mobile platforms are also occasionally used for laser scanning of landslides. For instance, LiDAR sensors can be assembled to helicopters, taking profit of its relatively low flying speed and flying heights close to terrain surface, which allows acquiring 3D information on cliffs from a an oblique view. It was used to scan a 2 km² area around the Åknes rock slide (Norway), providing 20 measurement points per m² with a position precision of 5 cm (75; 76). Also, offshore laser scanning from boat is used for coastal cliffs and river banks stability analysis, with a typical average point spacing of 10-20 cm (77). Finally, a fast growing technique is the set-up of laser scanners on cars or trains in order to acquire high resolution ground models along transport corridors. (8) This technique has been used to assess rock wall stability along roads and railways in Ontario (Canada) with an average point density of 100 points/m².

TLS is a fixed position scanning technique that only requires the device set-up on a tripod opposite the surface to scan within the maximum range limit. Because of this relatively easy implementation, TLS is usually operated directly by geoscientists in charge of the landslide investigation. With a high point density (up to 10000 points/ m²) and accuracy (about 1 cm), it is mostly limited by the availability of a good point of view, the maximum range of acquisition and the relatively small areas that can be covered in single acquisition due to a limited Field of View (FOV) angle (for instance, 40° in TLS Ilris3D). Usually, in order to cover the whole area of interest, several scans have to be acquired from different points of view.

(e) Spacing, accuracy, resolution and data types

The major differences between the two most commonly used techniques (i.e TLS and ALS) are: 1) average point spacing: metre scale for ALS and centimetre scale for TLS; 2) position and range accuracy: some tens of cm for ALS and about 1 cm for TLS; 3) point cloud geometry: as ALS is always shooting sub-vertically, it is very efficient in order to produce horizontally projected surface, such as gridded digital elevation models. But it only provides a poor representation of steep areas like rock cliffs. In addition to this, and opposite TLS devices, ALS is not able to have several ground surface elevation values of ground elevation (Z) for each horizontal position (X, Y), and thus it is unable to represent overhanging walls. Properly speaking, ALS products are 2.5 elevation surfaces and not full 3D representations of the terrain surface. As a result, most of ALS processing software is inefficient to work properly with point clouds from TLS acquisitions.

Measurement accuracy on single points depends on range, surface reflectivity and incident angle (**78; 79; 80; 71**). Inaccuracy of surface location and geometry is due not only to single measurement errors, but also to alignment and merging processes. This is particularly critical when several acquisitions are merged in one dataset. The quality of the final dataset must be carefully checked, as discussed in (**81**).

Point cloud resolution determines the level of detail that can be observed from a scanned point cloud (**82**), where the laser beam width plays an important role (**83**). However, TLS resolution and point spacing are normally mixed up. (**83**) It is recommended to place the optimal point spacing as 86% of the laser beam width at a given distance.

(f) Data acquisition issues: Occlusion and Biases

OCCLUSION: Due to relief roughness and natural variability, the acquisition of rock slope geometry from a single station is normally affected by the existence of shadow areas (also called occluded areas). In order to minimize occlusion issues, (**24**) different series of best practices and protocols are

proposed for survey planning. For instance, occlusion can be minimized using data acquisition from multiple locations (84; 85).

BIASES: Discontinuity characterization may be affected by biases depending on the intersection angle between discontinuity sets and the sensor's LOS (84; 86): the density of those families with normal vector parallel to the LiDAR's LOS may be overrepresented compared to the density of families with normal vector perpendicular to the LOS of the instrument. Indeed, this is a similar effect observed by (87), in which the density of families with direction parallel to the slope orientation may be over represented compared with those families perpendicular to the slope.

DATA QUALITY: the resolution of the datasets also plays an important role on the analysis of discontinuity orientation. As discussed in (86), low resolution datasets may lead to: (a) a truncation of non-persistent discontinuity sets due to a lack of information and (b) a shifting on discontinuity orientation due to a non-realistic smoothing of the surface geometry.

1.3 Data treatment

A series of pre-processing steps are necessary in order to transform the RAW LiDAR data (unfiltered point cloud both in ALS and TLS) into real terrain points, as follows (see Fig. 3):

(a) Full-waveform and automatic filtering

The first truly-operational Full-Waveform (FW) LiDAR systems for airborne applications appeared in 1999 (88). This new generation of instruments is able to capture not only the discrete signal return but also the entire waveform. The first experimental full-waveform LiDAR system was originally developed for forestry canopy and building segmentation. At the present time, full-waveform data are mainly used for ALS applications in order to discriminate the surface terrain from forestry, which is of great interest for vegetation removal and DEM generation. Current research on FW LiDAR data includes signal decomposition for object classification: terrain, vegetation, wires, buildings, etc.

(b) Non ground points filtering (including vegetation removal)

Non ground points (e.g. vegetation, cables, birds, dust, etc.) filtering is a time consuming task that is commonly performed manually. Although this approach may be straightforward when non ground points appear at small portions of the terrain, new semi-automatic methods aiming to classify ground points are being currently developed. These methods of classification, which are normally supervised by the user, are based on the identification of different values of the point cloud that allow to separate ground from non-ground points. For instance, while some methods use the colour coded value (RGB) or intensity of the laser return (e.g. 89; 90), other approaches include the study of some geometrical parameters as single point statistics (e.g. 91), local three dimensional point cloud statistics (e.g. 92), multi-scale dimensionality criterion (93) or using classifiers as Support Vector Machine (94), EM and/or Gaussian Mixture Models (95). Although these methods are highly promising, manual vegetation removal is still currently necessary in most of the cases.

(c) Co-registration and georeferencing

Georeferencing (also known as alignment) is the process of coordinates transformation from an internal referential system relative to the LiDAR device into a real world system of reference (e.g. UTM, lat/long, national grid coordinates, etc.). This process is typically a rigid-based body transformation consisting of a combination of translation and rotation (96). Two methods are often used for georeferencing: (a) target-based registration: the alignment of the TLS point cloud is classically carried out with Ground Control Points (GCPs) whose coordinates are previously acquired using dGPS, Total Station, etc. Complementarily, some modern techniques include the alignment of the 3D point cloud using co-registration of the scanned well-known geometries (i.e. cubes, spheres, cylinders, etc.) (97); (b) iterative closest points methods: aiming at minimizing the Euclidian distance between different point clouds, as proposed by (98) and (99). For a fast convergence of the alignment using this technique, an a priori alignment is normally carried out using either ground control point or already oriented and referenced commercial Digital Elevation Models (DEM).

Co-registration aims at: (a) reducing occlusion and shadow areas by merging multiple scans from the same epoch and different viewpoints into one single point cloud; (b) comparing different datasets and detecting changes on the topographical surface by aligning scans acquired sequentially, for instance by performing a multi-temporal TLS survey during a certain time lag in order to study slope evolution.

Co-registration errors mainly depend on instrumental accuracy, point spacing and percentage of overlapping area. Techniques for error propagation control must be performed when dealing with the overlapping of several scans, especially in long linear features, as when studying landslides along transportation corridors, marine cliffs, etc. (100). Although it is evident in classical surveying techniques, the points used for alignment must be restricted to stable areas, for instance the surroundings or the stable parts of a given landslide.

(d) Point cloud comparison

Point cloud comparison between sequential LiDAR datasets allows the detection of temporal differences in terrain morphology (17; 101). In order to make a comparison, several steps are required: (a) acquisition of a reference point cloud at initial time (t_0); (b) construction of a reference surface at t_0 ; (c) acquisition of successive data point cloud at different time lapses (t_1, t_2 , etc.); (d) co-registration between reference surface and successive data point clouds (c.f. previous paragraph, 98; 99); and, (e) change detection through the calculation of the differences for each period of comparison.

The single point distances between reference and successive point clouds are normally computed along a user defined vector in 1D. This vector can be defined both using a fixed orientation (17; 102) or using different local vectors defined perpendicular to the rock face at each section of the slope, as described in (93). Another method of comparison includes the use of the “shortest distance” between data point cloud and the reference model. Finally, the real 3D deformation of single blocks in terms of rotations and translations can be quantified by using the RT matrix technique as described in (19; 68)

Regarding sign criteria, a positive value is normally interpreted as an increase of material (e.g. deposition) or a displacement toward the external part of the slope (pre-failure deformation). Similarly, negative values are normally interpreted as a loss of material on a given period (e.g. soil erosion, rockfalls, etc.).

2. APPLICATIONS FOR LANDSLIDES

2.1 Landslides

Since the beginning of the 2000s, the ALS system has been widely used to produce HRDEM at regional scale (37). This technique quickly became an essential document of a regional landslide inventory map (3; 5). By creating hill shaded surface it is possible to highlight structures that cannot be seen from aerial photos or in field observation (e.g. 46; 48; 49; 103) either due to landslide scale (from metric to kilometric), or location (in inaccessible or densely vegetated areas) [Fig. 4]. Different approaches are usually employed for landslide mapping and identification, with various degrees of automation: (a) manual or expert-based approach, which focuses on the identification of landslides based on geomorphological evidences of crowns, main scarps, flanks, foot or toe and vegetation cover (104; 105; 106; 107; 108); (b) automatic geomorphological features recognition, which extracts different information derived from HRDEM, such as slope angle, curvature or roughness (109).

When several generations of ALS scans are available, then change detection between HRDEM can be used to characterize topographic changes. This technique has been employed to detect slope failures, soil erosion, slope displacements and terrain deformation (103; 110; 111; 112). Some examples of ALS for coastal cliff monitoring and erosion analysis are discussed in (113; 114). Furthermore, high resolution topography from airborne LiDAR can also be compared with less accurate historical aerial photographs, in order to analyse the kinematics of the landslide over a long-term period (115).

2.2 Rock slopes

(a) Structural analysis

The aim of the structural study is the detection and characterization of the main joint sets responsible for the fracturing of the rock mass. The analysis of the network of discontinuities is an essential step to study a rockfall scar or to assess the potential instable areas of a rock slope. The measurements of the orientation (Fig. 5), undulation, persistence, spacing, opening, roughness and water presence of the main joint sets are usually taken in the field with classical methods, such as photography, direct observations and compass measurements (116). TLS allows to perform most of these tasks faster, with a high accuracy, and even in inaccessible vertical areas (15; 25; **Erreur ! Signet non défini.**; 62; 84; 117; 118; 119; 86; 120). Georeferenced 3D TLS point clouds (see section 1.3c) allow us to extract the orientation of structures and to perform distance or volume measurements (96). Similar results can be obtained from HRDEM generated from aerial LiDAR, but with significant limitations imposed by the vertical shooting direction and by the size of the cells. The representation of structural features like planes or lines, which is classically done with stereoplots (116), can also be automatically extracted using modern algorithms. Early studies used a manually selected section of the point cloud and calculated the best-fitting plane (86; 96), which can be laborious and time-consuming. Later on, some authors proposed the construction of 2.5D surfaces such as Triangular Irregular Networks (TIN) for the automatic calculation of the discontinuity orientation (2; 24). More recently, techniques allow automatically computing local plane orientations directly from the point cloud (25; 62; 63; **Erreur ! Signet non défini.** 121). In order to facilitate structural interpretations, the orientation and inclination of each point of a TLS point cloud, or of a DEM cell, can be represented using a unique colour (61).

(b) Monitoring of fragmental rockfalls

Due to the steepness of rockslopes, terrestrial LiDAR is more extensively used than airborne LiDAR for the monitoring of fragmental rockfalls. Moreover, terrestrial LiDAR provides an unprecedented level of detail at site specific slope, both resolution and accuracy ranging from several mms to a few

cms. A pioneer approach for monitoring fragmental rockfalls along a section of marine cliffs in NE England was developed by (17; 18). Since then, TLS has become a widely used tool for automatic rockfall detection and volume calculation (21; 85; 122; 123; 124). Using the TLS technique, (125) detected a series of progressive rockfalls that occurred in exfoliated granitic rocks, analysing how a given fracture event initiated subsequent adjacent failures. A common application of TLS for rockfall monitoring includes the analysis of Magnitude-Frequency (MF) characterization of fragmental rock falls. Indeed, several authors have observed a scale-invariant pattern in a MF dimension under log-log scale (17; 101; 80; 126; 100; 127; Fig. 6), suggesting that a Self-Organized Criticality (SOC) may rule rockfall phenomena (128). Some other applications include the monitoring of several million cubic metres of rockslides (Fig. 7) in order to quantify deformation rates and failure mechanisms (19; 96; 129; 130), and the failure forecasting based on a given precursory indicator: either minor scale rockfalls or tertiary creep deformation (13; 21; 131).

(c) Rockfall susceptibility assessment

The simplest way to detect the potential rockfall source areas is by defining a slope angle threshold above which rockfalls are more susceptible to occur (132). This method can be optionally coupled with other criteria such as the presence of cliff areas (133). The slope threshold can be gathered from a detailed statistical analysis of slope angles, thus allowing to identify the cliff area (134; 135; 136, 137). A simple GIS approach developed by (138) allows identifying potential rockfall source areas along roads according to the presence or absence of four parameters: faults, scree slopes, rock cliffs, and steep slopes. A great improvement related to the use of DEMs for the detection of rockfall prone areas consists in the automatic realization of a kinematic analysis along the whole area (139; 140). This analysis allows detecting the topography areas where a discontinuity of a given orientation can lead to an instability. Using a standard classic stability criterion (141) together with a statistical analysis of the kinematic tests, (140) were able to produce probability maps of different failure mechanisms such as planar sliding, toppling and wedge sliding. More recently, the kinematic analysis criterion was applied to accurately detect the most unstable areas from TLS data (142). Spacing and persistence of the joint sets, which can be determined both in the field and on LiDAR point clouds

(86; 84), should also be taken into account in the stability calculations, as suggested by (143). According to these authors, the number of potential failures per cliff area can be calculated based on the spacing and on the trace length values, which considerably improves the rockfall susceptibility maps (144).

2.3 Debris flows

LiDAR is used for various tasks related to debris flows mapping, characterization and modelling. HRDEM from ALS are frequently used to identify and characterize initiation and propagation zones of debris flows (145; 146; 147; 148; 149), deposition fans (150), or to estimate the eroded and deposited volumes (151; 152; 153). Remarkably, (81) have used TLS to detect surface changes along a debris flow channel, and (26) have combined TLS and ALS to quantify sediment transport for debris flows events in the Austrian Alps, observing several metre changes between the two epochs (Fig. 8). ALS data are also used to estimate the volume of sediments that can be potentially entrained along the channels by a future event (154). Apart from geomorphic analysis, DEM from laser scanning is also used in debris flows propagation modelling. For instance, (155) have assessed the impact of HRDEM cell sizes (1, 4 and 25 m.) on modelled propagations, in particular the effect of resolution on debris flows confinement along recent channels.

2.4. Input for modelling

Mass movement modelling is the process of simulating its stability and/or its propagation across time. This analysis can be carried out using conventional representations of a terrain's surface, either DEM or HRDEM. Note: current models do not utilize real 3D point clouds but 2.5D projections of the topography.

One of the first applications of LiDAR topographic data for landslide modelling was presented by (156) using the SHALSTAB model. These authors showed that susceptibility mapping of shallow landslides can be considerably improved when using a HRDEM of 1m cell-size obtained from ALS. The results of this simulation demonstrated that the distribution of potentially unstable areas were

closer to the inventoried landslides than when using low resolution DEM. In addition, the total surface of affected terrain was smaller. The same trend has also been observed in other available models such as TRIGRS, which include more sophisticated infiltration models (157; 158).

The optimal accuracy and resolution of the DEM for modelling should be carefully considered. Although HRDEM usually improves the modelling of the phenomena, most of the conventional modelling packages do not necessarily require more than a 5 to 10 m DEM resolution (159). Modelling using a higher resolution DEM can even introduce artefacts and non-realistic noises that can mask the main terrain features (160). For instance, ALS derived DEM used for mapping debris flows kinematics have a strong dependency on lateral spreading on the DEM resolution (161; **155**). These authors observed how a too fine resolution also produced geometric artefacts degrading the quality of the modelling results. Similarly, the use of HRDEM for the simulation of rockfall propagation can lead to significant differences when compared with lower resolution DEMs (163; 162). For instance, the lateral dispersion of the trajectories and the kinetic energy vary with DEM resolution that controls the roughness of the terrain surface (163). According to (163), the maximum kinetic energy normally increases with the DEM resolution. However, the opposite result is presented in (164). This discrepancy may be explained by the fact that a higher resolution DEM has little impact on the accuracy of the results when other parameters (geology, vegetation, etc.) are poorly described (165). The resolutions of the LiDAR DEM are often too fine compared to the other required input data (166).

Erosion and hillslope evolution modelling has been greatly enhanced by using HRDEM (167). However, most of the current packages for landslide modelling are not able to make the best use of high resolution LiDAR data. The increasing power of computers will certainly lead to an extensive use of HRDEM as input for stability and run-out modelling. One can expect that the exploitation of full 3D data will be attained in the near future.

3. CONCLUSIONS and PERSPECTIVES

The current knowledge concerning the mapping and monitoring of landslides is now far beyond what was expected by the end of the nineties. This is mainly due to the recent advances in remote sensing techniques (including LiDAR) together with the exponential growth of computational capabilities. For instance, laser scanning has allowed for the development of new techniques to monitor slope changes and slope movements, providing innovative ways for hazard qualification and a better understanding of the surface processes such as rockfall failures.

Dense 3D data has become popular thanks to LiDAR. Nevertheless, one of the present-day key issues is the lack of software to extract all the landslide-relevant information from the LiDAR data, especially from full waveform data. At present, different modelling techniques benefit only partially from the full resolution of the LiDAR derived DEMs. This is linked to the fact that the density and the quality of the geometrical information are much higher than other parameters required for hazard assessment, such as geological maps. Despite this, the recent advances achieved on the study of rockfalls and rock slopes indicate that HRDEMs possess a great potential for the development of new methods and techniques for the analysis of landslide phenomena.

New applications and techniques are now emerging and will be used as a routine in a near future: (a) the development of new algorithms for the analysis of complex slope deformations in space and time; (b) the detection of slope movement in real-time and its integration on early warning systems (168); (c) the possibility to rapidly acquire accurate 3D data along transport corridors using mobile mappers (Fig. 9); (d) the improvement of TLS technical capabilities, including maximum range, accuracy and point density; (e) the acquisition of Earth surface topography by a new generation of satellite LiDAR (50; 53), such as ICESat-2 planned for 2017.

The integration of LiDAR derived 3D data with complementary information registered by other remote sensing methods is also in development. For instance, the coupling of LiDAR and InSAR data is a promising technique for displacement monitoring (169; 170; 171). Other spectral attributes

provided by multi-spectral imaging can also help improve interpretation and segmentation of 3D LiDAR data (73).

Summarizing, LiDAR is a tool that has completely revolutionized the landslide research and study concerning the characterization, mapping and monitoring of landslides. However, the scientific and engineer community still needs to develop innovative tools to rapidly extract Geo-hazard related information from LiDAR data.

Acknowledgments

The present work has been partially supported by the Swiss National Foundation project numbers 138015 (Understanding landslide precursory deformation from superficial 3D data), 127132 (Rockfall sources: toward accurate frequency estimation and detection) and 144040 (Characterizing and analyzing 3D temporal slope evolution).

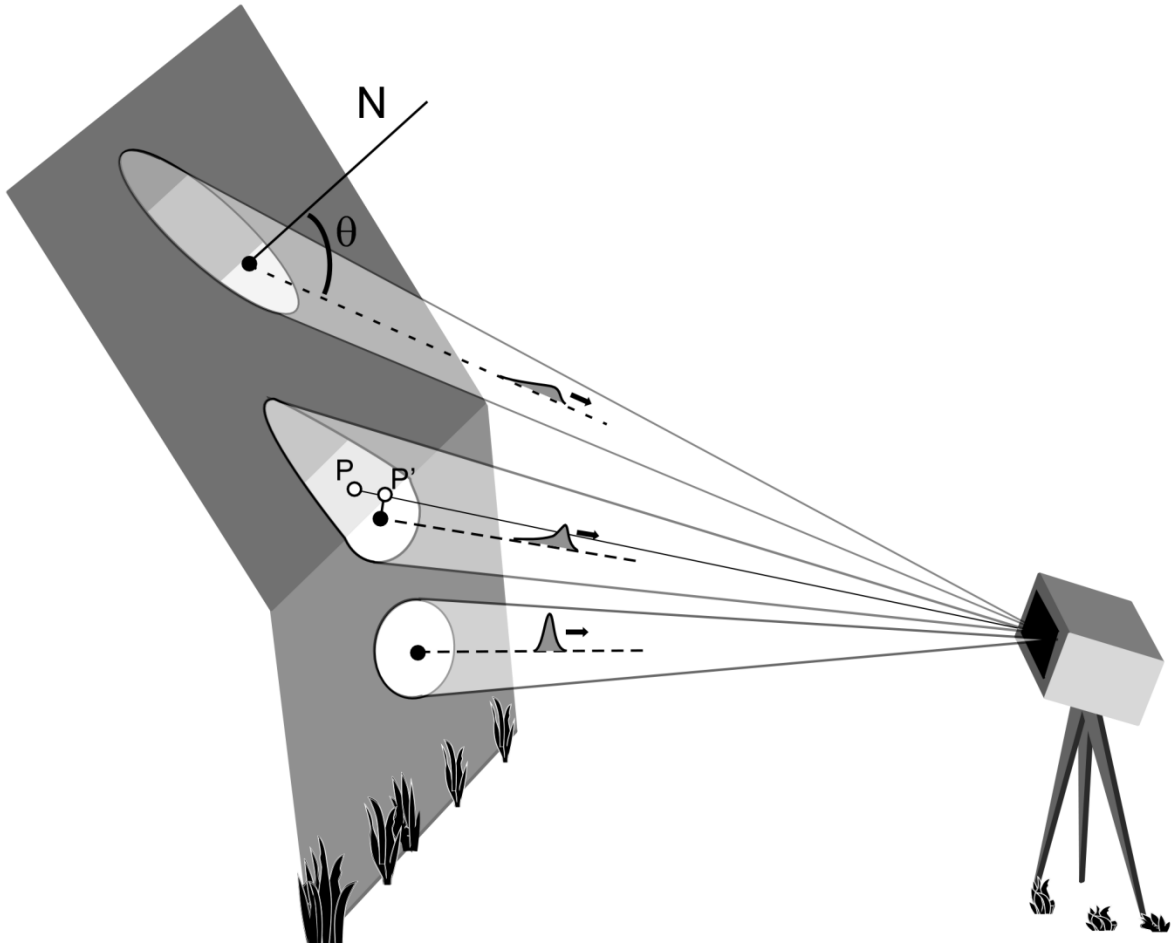


Figure 1: (a) Sketch of LiDAR functioning principle showing TLS device, Line of Sight and Spot Dimension; (b) Signal intensity vs. time of flight for two different methods of measurements: full wavelength method vs. pulse method.

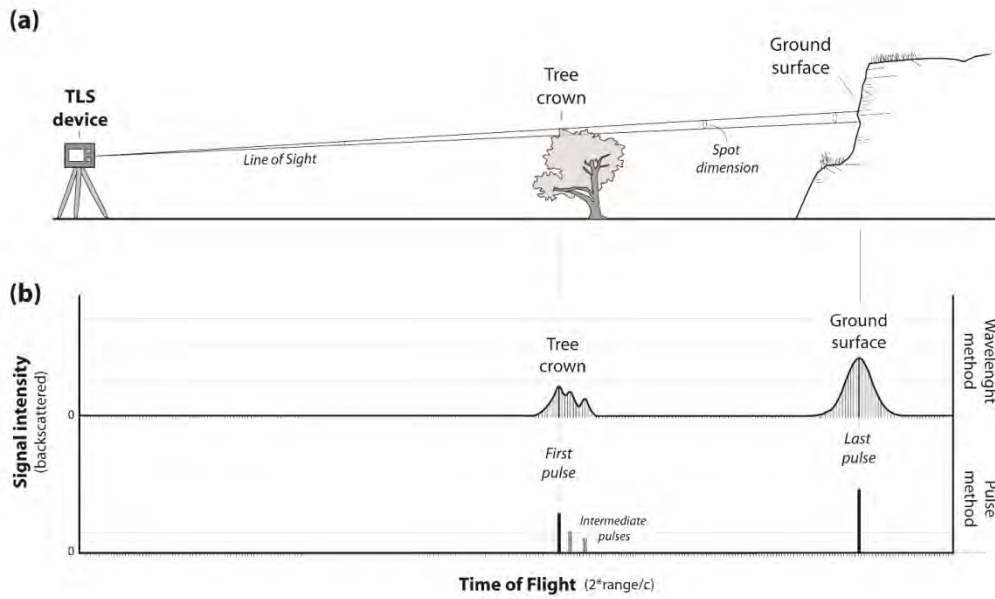


Figure 2. LiDAR footprint deformation (θ : incidence angle, N : normal to the surface). The point position is attributed to the centre of the beam (point P), but the range is measured at the maximum intensity of the backscattered pulse. Then, the actually measured point P' is located slightly before the rockface on the line of sight.

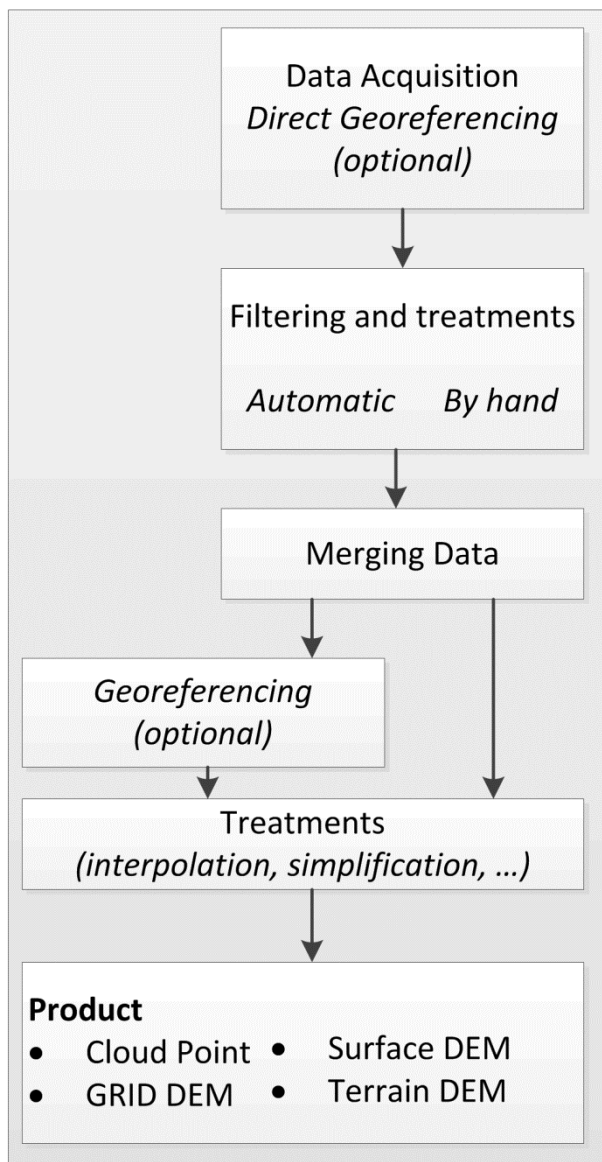


Figure 3. Workflow showing the main steps on data treatment.

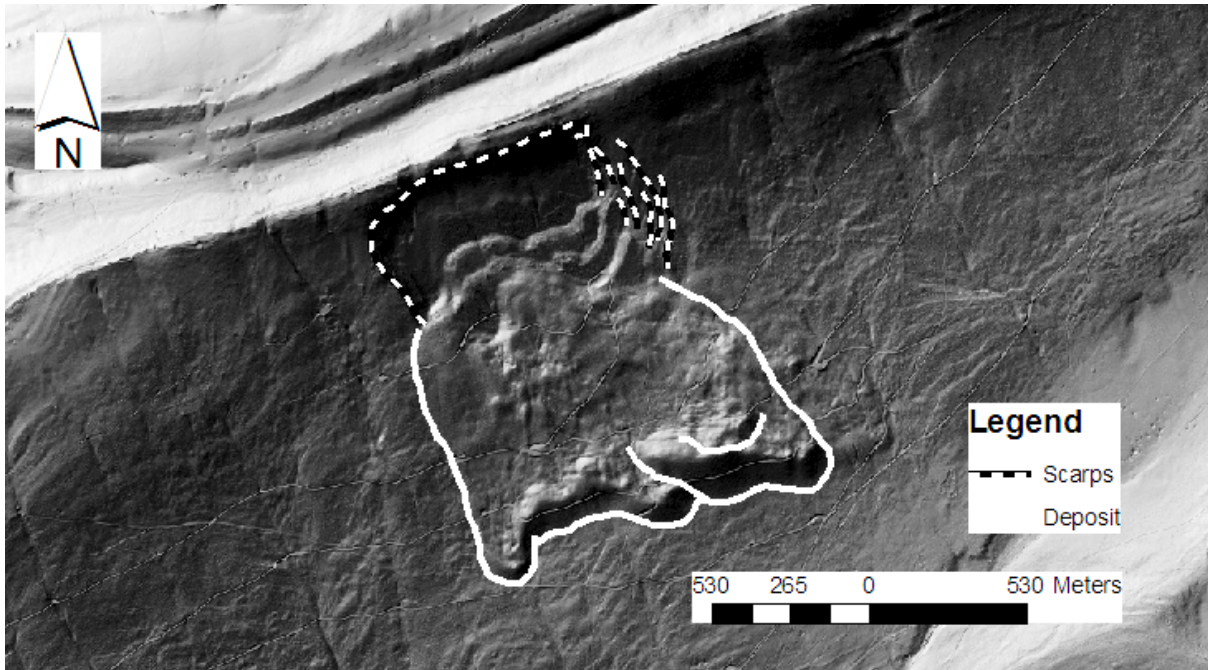


Figure 4. Mapping of a large scale landslide detected using a LiDAR based HRDEM. Bern canton, NW Switzerland (Data from Géodonnées © Swisstopo, DV084371)

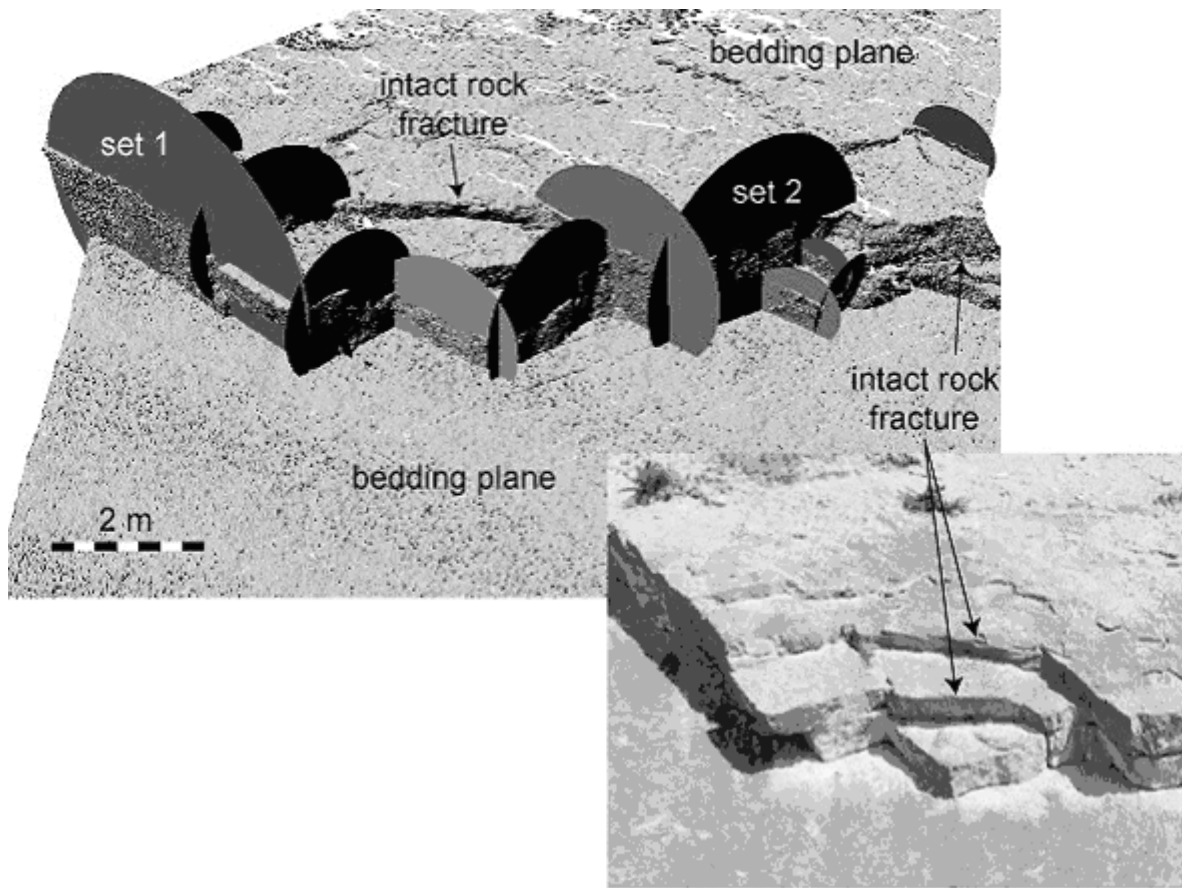


Figure. 5. Discontinuity mapping on a Terrestrial LiDAR point cloud, rendered using greyscale intensity values <Source: From Sturzenegger and Stead, 2009, with permission>.

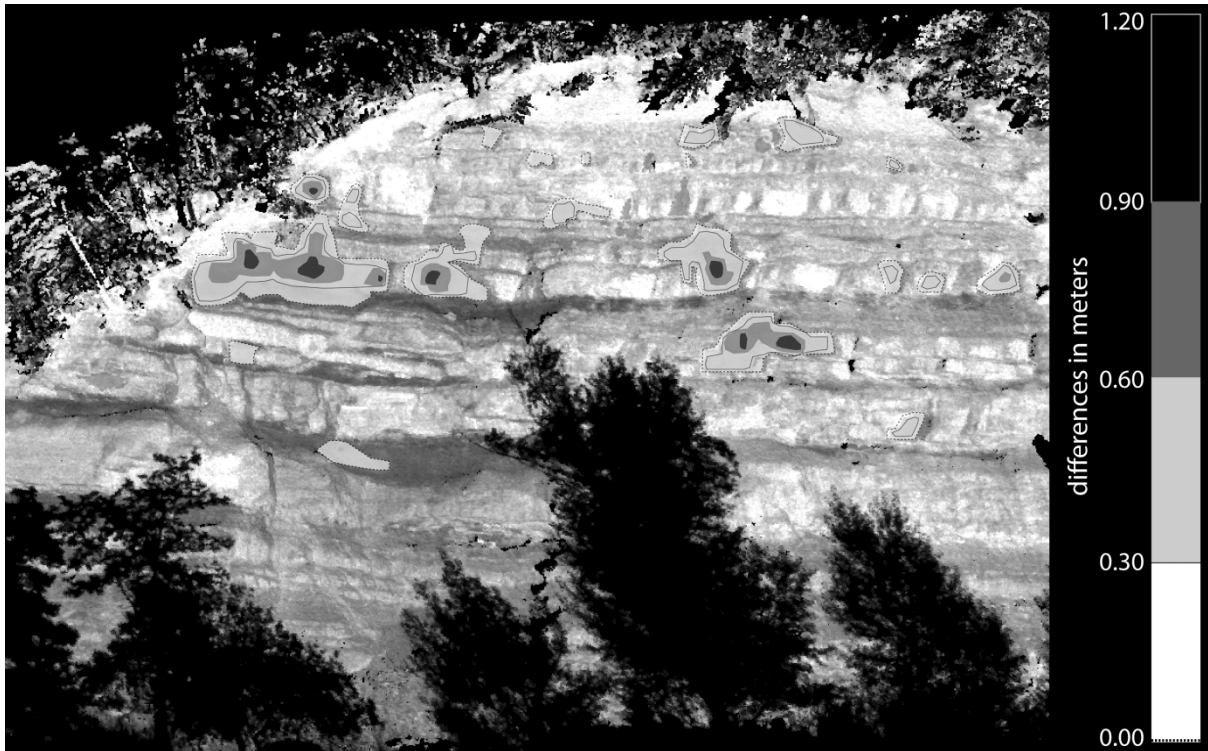


Figure 6. (a) Picture of La Cornalle study area (Vaud, Switzerland); (b) Model comparison showing the changes (i.e. rockfalls) along time.

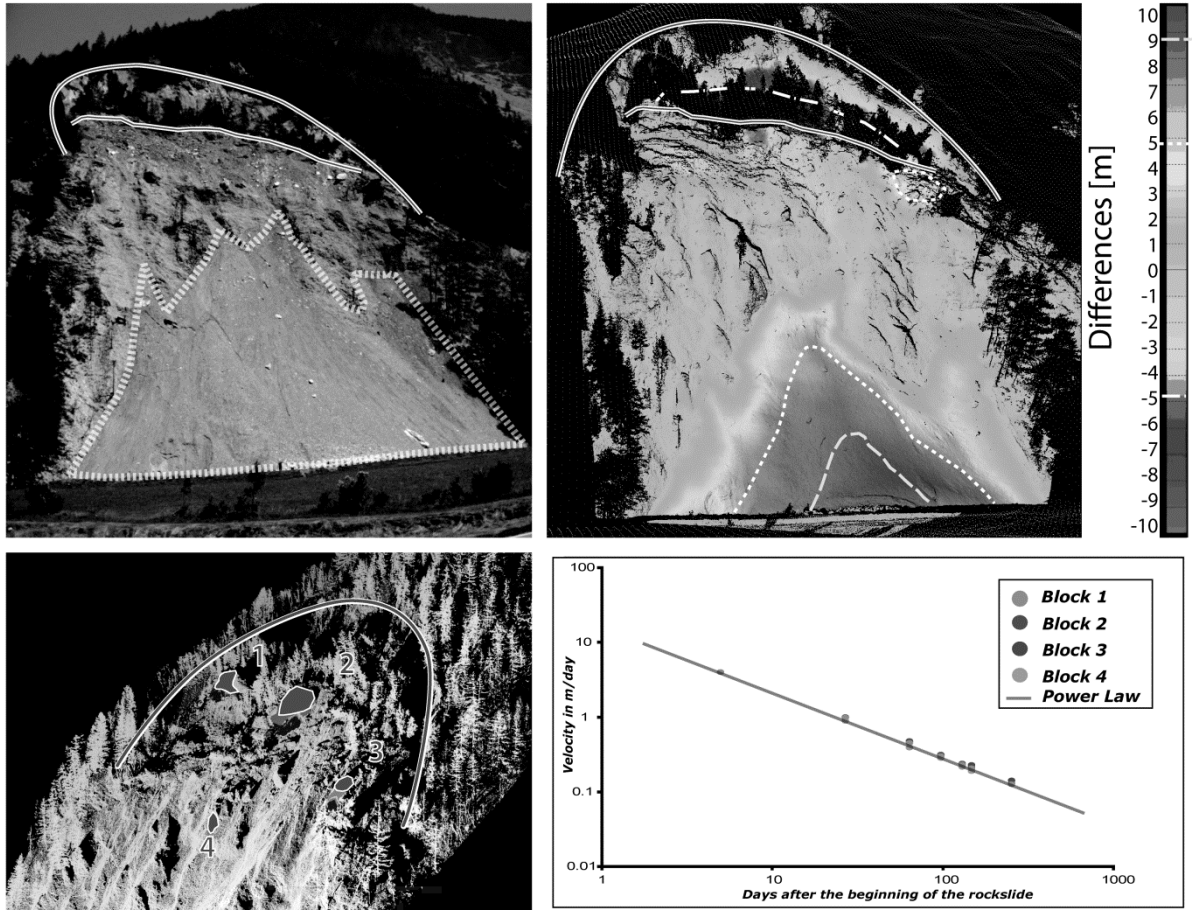


Figure 7. Different techniques for the quantification of a mass movement located on Montatuy mountain (Valais, Switzerland) using a ground-based LiDAR. (a) Picture of the study area; (b) filtered point cloud of the study area; each point is coloured according to the differences calculated between the 2009 ALS DEM and the TLS point cloud captured in April 2011; (c) rotated perspective of the LiDAR point cloud including the manual selection of different blocks for subsequent tracking; (d) velocity computation for each of the previously selected blocks; the straight line in log-log scale shows a progressive stabilization of the slope.

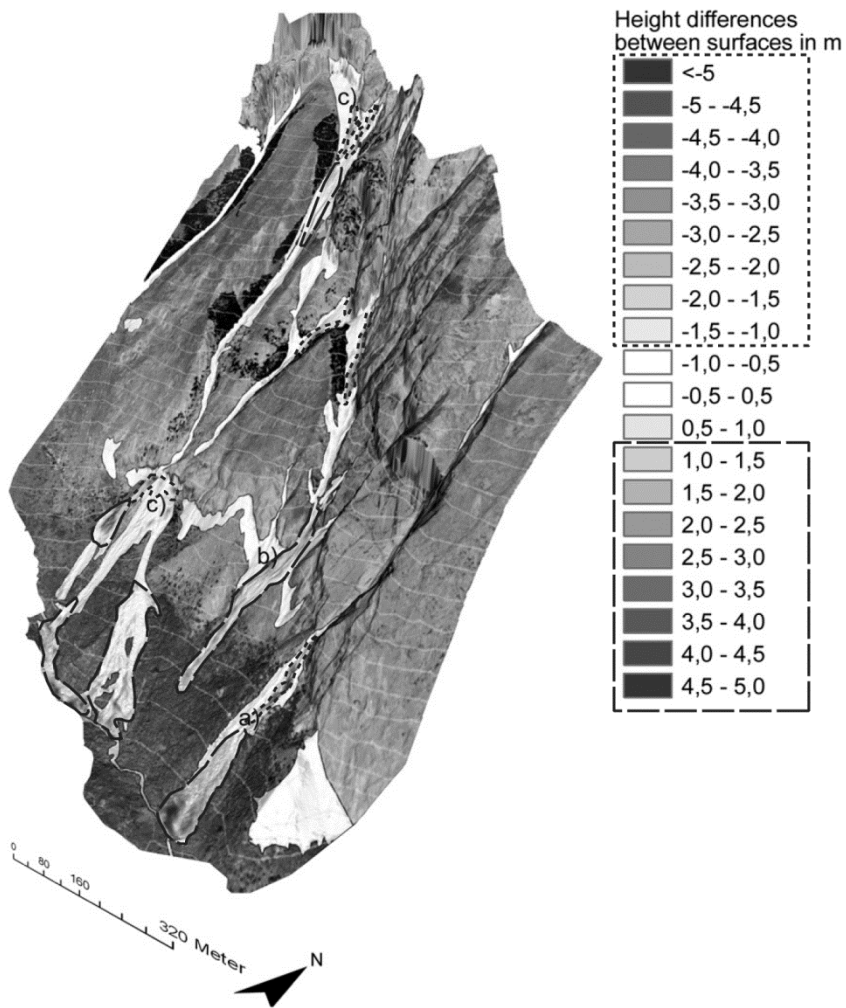


Figure 8. Surface differences between pre-event (ALS) and post-event (TLS) datasets (negative values for erosion) Source: <from Bremer and Sass 2012, with permission>.

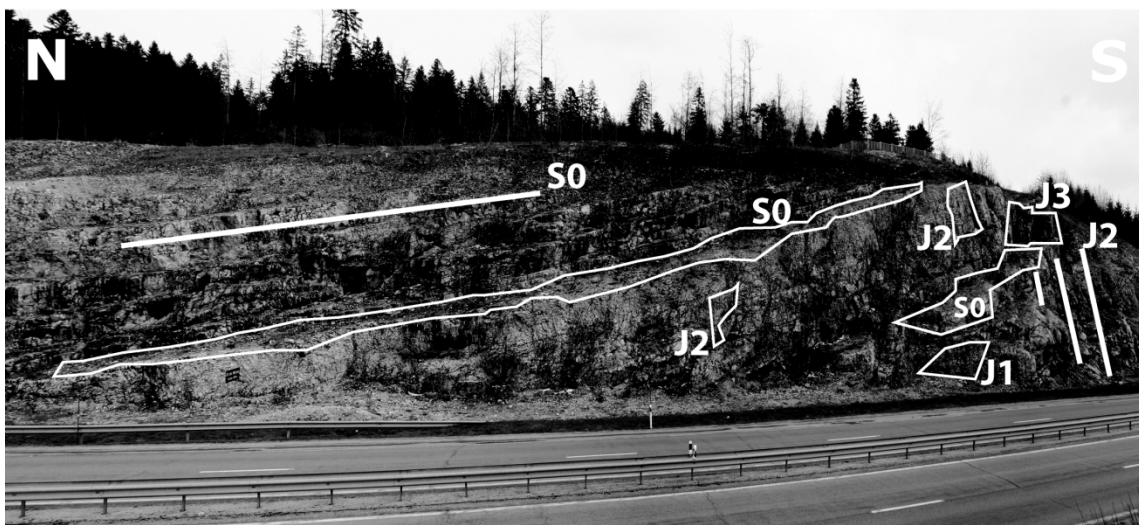
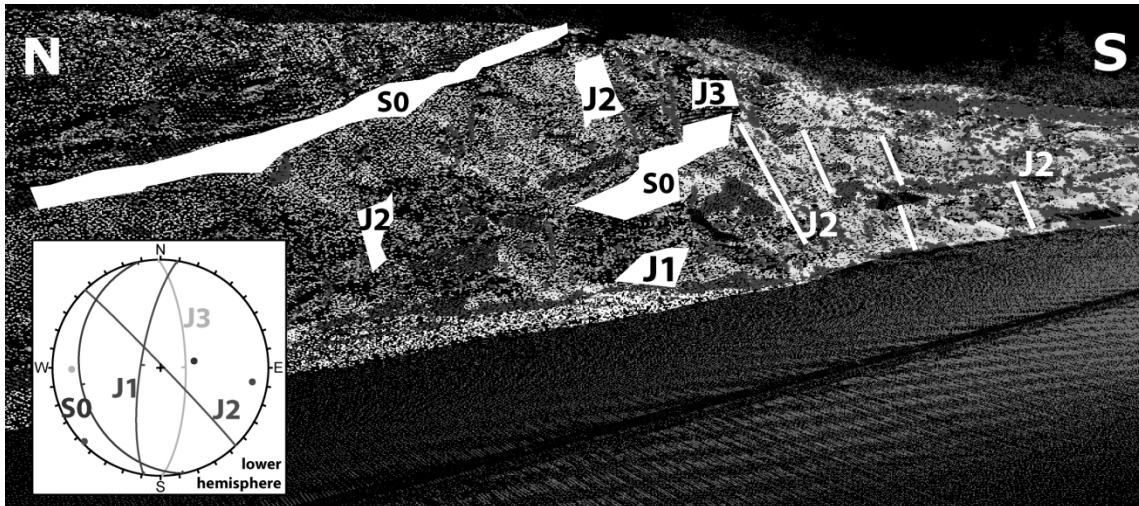


Figure 9. Example of discontinuities mapping along a highway at Pontarlier (East France) using an Optech Lynx Mobile Mapper LiDAR.

References

- 1 Carter, W.; Shrestha, R.; Tuell, G.; Bloomquist, D and Sartori, M. Airborne Laser Swath Mapping Shines New Light on Earth's Topography. *EOS* 2001, 82 (46), 549-564.
- 2 Slob, S.; Hack, R. and Keith, T. An approach to automate discontinuity measurements of rock faces using laser scanning techniques. In the Proceedings of the International Symposium on Rock Engineering for Mountainous Regions – Eurock 2002, Funchal, Portugal, November 25-28 2002; 87-94.
- 3 Mc Kean, J. and Roering, J. Objective landslide detection and surface morphology mapping using high-resolution airborne laser altimetry. *Geomorphology* 2004, 57, 331-351.
- 4 SafeLand Deliverable 4.1. Review of Techniques for Landslide Detection, Fast Characterization, Rapid Mapping and Long-Term Monitoring. Edited for the SafeLand European project by Michoud C., Abellán A., Derron M.-H. and Jaboyedoff M. (2010). Available at <http://www.safeland-fp7.eu>.
- 5 Jaboyedoff, M.; Oppikofer, T.; Abellan, A.; Derron, M.-H.; Loye, A.; Metzger, R.; Pedrazzini, A. Use of LiDAR in landslide investigations: a review, *Nat Hazards* 2012, 61:5–28, DOI 10.1007/s11069-010-9634-2.
- 6 Abellán, A.; Jaboyedoff, M.; Oppikofer, T.; Rosser, N.J.; Lim, M. and M. Lato. State of Science: Terrestrial Laser Scanner on rock slopes instabilities. *Earth surface proc. and landforms*. 2014, 39, 1, 80-97 . DOI: 10.1002/esp.3493
- 7 Alho P.; Kukko A.; Hyypä H.; Kaartinen H.; Hyypä J. and Jaakkola A.: Application of boat-based laser scanning for river survey, *Earth Surf. Process. Landforms*, 34, 1831-1838, 2009.
- 8 Lato, M.; Hutchinson, J.; Diederichs, M.; Ball, D. and Harrap, R. Engineering monitoring of rockfall hazards along transportation corridors: using mobile terrestrial LiDAR, *Nat. Hazards Earth Syst. Sci.*, 2009, 9, 935-946.
- 9 J. and Toth, K. Topographic laser ranging and scanning: principles and processing. CRC Press, Taylor & Francis Group 2008, LLC, UK.
- 10 Vallet, J. and Skaloud, J. Development and experiences with a fully-digital handheld mapping system operated from a helicopter. *Int Arch Photogramm Remote Sens.* 2004, 35(B5), 791–796.
- 11 Chigira, M.; Duan, F.; Yagi, H and Furuya, F. Using an airborne laser scanner for the identification of shallow landslides and susceptibility assessment in an area of ignimbrite overlain by permeable pyroclastics. *Landslides* 2004, 1, 203-209.
- 12 Ardizzone, F.; Cardinali, M. and Galli, M. Identification and mapping of recent rainfall-induced landslides using elevation data collected by airborne LiDAR. *Nat. Hazards Earth Syst. Sci.* 2007, 7, 637–650.
- 13 Rosser, N.J.; Lim, N.; Petley, D.N.; Dunning, S. and Allison, R.J. Patterns of precursory rockfall prior to slope failure. *Journal of Geophysical Research* 2007, 112, No. F4.
- 14 Pedrazzini, A.; Jaboyedoff, M.; Froese, C.R.; Langenberg, C.W. and Moreno F. Structural analysis of Turtle Mountain: origin and influence of fractures in the development of rock slope failures, *Geological Society, London, Special Publications* 2011, 351, 163–183
- 15 Slob, S. and Hack, R. 3-D Terrestrial Laser Scanning as a New Field Measurement and Monitoring Technique, in: *Engineering Geology for Infrastructure Planning in Europe, A European Perspective*, edited by: Hack, R., Azzam, R., and Charlier, R., *Lecture Notes in Earth Sciences*, Springer, Berlin/Heidelberg 2004, 104, 179–190.
- 16 Teza, G.; Galgaro, A.; Zaltron, N. and Genevois, R. Terrestrial laser scanner to detect landslide displacement fields: a new approach. *International Journal of Remote Sensing* 2007, 28 (16), 3425-3446.
- 17 Rosser, N.J.; Petley, D.N.; Lim, M.; Dunning S.A. and Allison, R.J. Terrestrial laser scanning for monitoring the process of hard rock coastal cliff erosion. *Quarterly Journal of Engineering Geology and Hydrogeology* 2005, 38, 363–375.
- 18 Lim, M., Petley, D.N., Rosser, N.J., Allison, R.J., Long, A. J., Pybus, D. Combined digital photogrammetry and time-of-flight laser scanning for monitoring cliff evolution. *Photogrammetric Record* 2005, 20(1), 109-129
- 19 Collins B. and Sitar N.: Processes of coastal bluff erosion in weakly lithified sands, Pacifica, California, USA, *Geomorphology*, 97, 483–501, 2008.
- 20 Oppikofer, T.; Jaboyedoff, M. and Keusen, H.R. Collapse at the eastern Eiger flank in the Swiss Alps. *Nature Geoscience* 2008, 1, 531-535.
- 21 Abellan A.; Vilaplana J.M.; Calvet J. and Blanchard J. Detection and spatial prediction of rockfalls by means of terrestrial laser scanning modelling. *Geomorphology* 2010, 119, 162-171.
- 22 Prokop, A. and Panholzer, H.: Assessing the capability of terrestrial laser scanning for monitoring slow moving landslides, *Nat. Hazards Earth Syst. Sci.*, 9, 1921-1928.
- 23 Bornaz, L.; Lingua, A. and Rinaudo, F. Engineering and environmental applications of laser scanner techniques. *Int. Arch. Photogramm. Remote Sens.* 2002, 34(3B):40–43.
- 24 Kemeny, J. and Turner, K. Ground-Based LiDAR: Rock Slope Mapping and Assessment. Federal Highway Administration report 2008, FHWA-CFL/TD-08-006. Available at <http://www.iaeg.info/portals/0/Content/Commissions/Comm19/GROUND-BASED LiDAR Rock Slope Mapping and Assessment.pdf>.

-
- 25 Gigli, G. and Casagli, N.: Semi-automatic extraction of rock mass structural data from high resolution LIDAR point clouds, *Int. J. Rock Mech. Min.*, 48, 187–198, 2011.
- 26 Cavalli, M. and Marchi, L. Characterisation of the surface morphology of an alpine alluvial fan using airborne LiDAR. *Nat. Hazards Earth Syst. Sci.* 2008, 8:323–333.
- 27 Bremer, M. and Sass, O. Combining airborne and terrestrial laser scanning for quantifying erosion and deposition by a debris flow event. *Geomorphology* 2012, 138, 1, 49-60.
- 28 Brooker, G. Introduction to sensing. *Introduction to Sensors for Ranging and Imaging*; SciTech Publishing Inc.: Raleigh, USA, 2009, 1-22.
- 29 Hecht, J. *Understanding Lasers: An Entry Level Guide*, 2nd Ed.; IEEE Press: New York, USA, 1994.
- 30 Dallaire, E.E., *Electronic distance measuring revolution well under way*, *Civil Engineering*, 1974, 44, 66-71.
- 31 Petri, G. Laser-based surveying instrumentation and methods. In *Engineering Surveying Technology*; Kennie, T.J.M., Petrie, G., Eds.; Blackie, Glasgow & London and Halsted Press, New York, USA, 1990, 48-83.
- 32 Petrie, G. and Toth, C. Introduction to Laser Ranging, Profiling, and Scanning. In *Topographic Laser Ranging and Scanning*; Shan, J., Toth, C.K., Eds.; CRC Press, Boca Raton, USA, 2009a, 1-27.
- 33 Miller, B. Laser altimeter may aid photo mapping, *Aviat Week Space Technol.* 1965, 88,60-64.
- 34 Krabill, W.B.; Collins, J.G.; Link, L.E.; Swift, R.N. and Butler, M.L. Airborne laser topographic mapping results, *Photogramm. Eng. Remote Sens.* 1984, 50, 685-694.
- 35 Sheperd, E.C. Laser to watch height, *New Scientist* 1965, 1, 33-37.
- 36 Hoge, F.E.; Swift, R.N. and Frederick, E.B. Water depth measurement using an airborne pulsed neon laser system, *Applied Optics* 1980, 19, 871-883.
- 37 Petrie, G. and Toth, C. Airborne and Spaceborne Laser Profilers and Scanners in *Topographic Laser Ranging and Scanning*; Shan, J., Toth, C.K., Eds.; CRC Press, Boca Raton USA 2009b, 29-85.
- 38 Beraldin, J.-A.; Blais, F. and Lohr, U. Laser Scanning Technology. In *Airborne and Terrestrial Laser Scanning*, Vosselman, G., Maas, H.-G., Eds.; Whittles Publishing 2010, Dunbeath, Scotland, 1-42.
- 39 Wehr, A. and Lohr, U. Airborne laser scanning – an introduction and overview. *ISPRS Journal of Photogrammetry & Remote Sensing* 1999, 54, 68-82.
- 40 Baltsavias, E.P. Airborne laser scanning: basic relations and formulas. *ISPRS Journal of Photogrammetry & Remote Sensing*, 1999a, 54, 199-214.
- 41 Baltsavias, E.P. A comparison between photogrammetry and laser scanning. *ISPRS Journal of Photogrammetry & Remote Sensing* 1999b, 54, 83-94.
- 42 Krabill, W.B.; Thomas, R.H.; Martin, C.F.; Swift, R.N. and Frederick, E.B. Accuracy of airborne laser altimetry over Greenland ice sheet, *Int. J. Remote Sens.* 1995, 16, 1211-1222.
- 43 Krabill, W.B.; Frederick, E.B.; Manizade, S.; Martin, C.F.; Sonntag, J.; Swift, R.N.; Thomas, R.; Wright, W.; Yungel and J. Rapid Thinning of Parts of the Southern Greenland Ice Sheet; *Science* 1999, 283, 1522-1524.
- 44 Haala, N. and Brenner, C. Extraction of buildings and trees in urban environments. *ISPRS Journal of Photogrammetry & Remote Sensing* 1999, 54, 130-137.
- 45 Haugerud, R.A.; Harding, D.J.; Johnson, S.Y.; Harless, J.L.; Weaver, C.S. and Sherrod, B.L. High-resolution lidar topography of the Puget Lowland, Washington—A Bonanza for earth science. *GSA Today* 2003, 13:4–10.
- 46 Schulz, W.H. Landslides mapped using LiDAR imagery, Seattle, Washington, U.S. Geological Survey Open-File Report 2004-1396; U.S. Department of the Interior: Seattle, USA, 2004, 1-11.
- 47 Schulz, W.H. Landslide susceptibility revealed by LIDAR imagery and historical records, Seattle, Washington. *Engineering Geology* 2007, 89, 67–87.
- 48 Van Den Eeckhaut, M.; Poesen, J.; Govers, G.; Verstraeten, G. and Demoulin, A. Characteristics of the size distribution of recent and historical landslides in a populated hilly region. *Earth and Planetary Science Letters* 2007, 256, 588–603.
- 49 Haneberg, W.C.; Cole, W.F. and Kasali, G. High-resolution LiDAR-based landslide hazard mapping and modeling, UCSF Parnassus Campus, San Francisco, USA. *Bull Eng Geol Environ* 2009, 68, 263–276.
- 50 Zwally, H.J.; Schutz, B.; Abdalati, W.; Abshire, J.; Bentley, C.; Brenner, A.; Bufton, J.; Dezio, J.; Hancock, D.; Harding, D.; Herring, T.; Minster, B.; Quinn, K.; Palm, S.; Spinhirne, J. and Thomas, R.; ICESat's laser measurements of polar ice, atmosphere, ocean, and land. *Journal of Geodynamics* 2002, 34,405–445.
- 51 Abshire, J.B.; Sun, X.; Riris, H.; Sirota, J.M.; McGarry, J.F.; Palm, S.; Yi, D.; Liiva, P. Geoscience Laser Altimeter System (GLAS) on the ICESat Mission: On-orbit measurement performance. *Geophysical Research Letters* 2005, Vol. 32.
- 52 Schutz, B. E.; Zwally, H. J.; Shuman, C. A.; Hancock, D.; DiMarzio, J. P. Overview of the ICESat Mission. *Geophysical Research Letters* 2005, Vol. 32.

-
- 53 DiMarzio, J. P. GLAS/ICESat 500 m Laser Altimetry Digital Elevation Model of Antarctica. Boulder, Colorado USA: National Snow and Ice Data Center, 2007.
- 54 Smith, D.E.; Muhleman, D.O.; Ivanov, A.B. Mars Orbiter Laser Altimeter: Experiment summary after the first year of global mapping of Mars, *Journal of Geophysical Research* 2001, Vol. 106, NO. E10, 23,689-23,722.
- 55 Neumann, G.A.; Smith, D.E.; Zuber, M.T. Two Mars years of clouds detected by the Mars Orbiter Laser Altimeter, *Journal of Geophysical Research*, 2003, Vol. 108, NO. E4, 5023, doi:10.1029/2002JE001849.
- 56 Beraldin, J.-A.; Blais, F.; Boulanger, P. Real world modelling through high resolution digital 3D imaging of objects and structures. *ISPRS Journal of Photogrammetry & Remote Sensing* 2000, 55, 230–250.
- 57 Gordon, S.; Litchi, D.; Stewart, M. Application of a High-Resolution, Ground-Based Laser Scanner for Deformation Measurements. In *New Techniques in Monitoring Surveys I*, Proceedings of the 10th FIG International Symposium on Deformation Measurements, Orange, USA, 2001, 23-32.
- 58 Litchi, D.; Gordon, S.; Stewart, M. Ground-Based Laser Scanners: Operation, Systems and Applications. *Geomatica* 2002, 56 (1), 21-33.
- 59 Fardin, N.; Feng, Q.; Stephansson, O. Application of a new in situ 3D laser scanner to study the scale effect on the rock joint surface roughness. *International Journal of Rock Mechanics & Mining Sciences* 2004, 41, 329–335.
- 60 Feng, Q.H.; Röschoff, K. In-situ mapping and documentation of rock faces using a full-coverage 3-D laser scanning technique. *International Journal of Rock Mechanics & Mining Sciences* 2004, 41 (3).
- 61 Jaboyedoff, M.; Metzger, R.; Oppikofer, T.; Couture, R.; Derron, M.-H.; Locat, J. and Turmel, D. New insight techniques to analyze rock-slope relief using DEM and 3D-imaging cloud points: COLTOP-3D software. In *Rock mechanics: Meeting Society's Challenges and Demands*, Proceedings of the 1st Canada-US Rock Mechanics Symposium, Vancouver, Canada, May 27–31 2007, 61-68.
- 62 Garcia-Selles D, Falivene O, Arbues P, Gratacos O, Tavani S, Munoz JA. 2011. Supervised identification and reconstruction of near-planar geological surfaces from terrestrial laser scanning. *Computers & Geosciences* 37 : 1584-1594. DOI: 10.1016/j.cageo.2011.03.007
- 63 Riquelme, A., Abellan, A., Tomás, R., Jaboyedoff, M (2014). A new approach for semi-automatic rock mass joints recognition from 3D point clouds. *Computers & Geosciences*, 68(0), pp.38–52. DOI: 10.1016/j.cageo.2014.03.014
- 64 Hunter, G.; Pinkerton, H.; Airey, R.; Calvari, S. The application of a long-range laser scanner for monitoring volcanic activity on Mount Etna. *Journal of Volcanology and Geothermal Research* 2003, 123, 203-210.
- 65 Bellian, J.A.; Kerans, C.; Jennette, D.C. Digital Outcrop Models: Applications of Terrestrial Scanning LiDAR Technology in Stratigraphic Modeling. *Journal of Sedimentary Research* 2005, 75 (2), 166-176.
- 66 Buckley, S.J.; Howell, J.A.; Enge, H.D.; Kurz, T.H. Terrestrial laser scanning in geology: data acquisition, processing and accuracy considerations. *Journal of the Geological Society* 2008, 165, 625-638.
- 67 Kurz, T.H.; Buckley, S.J.; Howell, J.A.; Schneider, D. Geological outcrop modeling and interpretation using ground based hyperspectral and laser scanning data fusion. In *WG VIII/12: Geological Mapping, Geomorphology and Geomorphometry*, Proceedings of the International Society for Photogrammetry and Remote Sensing Conference, Beijing, China, July 3-11 2008; 1229-1234.
- 68 Monserrat, O.; Crosetto, M. Deformation measurement using terrestrial laser scanning data and least squares 3D surface matching. *ISPRS Journal of Photogrammetry and Remote Sensing* 2008, 63(1), 142-154.
- 69 Vosselman, G. and Maas, H. *Airborne and terrestrial laser scanning*. CRC Press 2010, Boca Raton (USA), 318 pp. ISBN: 978-1904445-87-6.
- 70 Carrea, D.; Abellán, A.; Derron, M.H.; Gauvin, N.; Jaboyedoff, M. Using 3D surface datasets to understand landslide evolution: from analogue models to real case study. Proceedings of the 11th International Symposium on Landslides and 2nd North American Symposium on Landslides, June 2-8, 2012, Banff, Alberta, Canada.
- 71 Lichti, D.D. and Skaloud, J. Registration and Calibration. In *Airborne and Terrestrial Laser Scanning*, G. Vosselman and H.-G. Maas (Eds.). Whittles Publishing: Caithness 2010, UK, 83-133.
- 72 Schaer, P.; Skaloud, J.; Landtwinig, S.; Legat, K. Accuracy estimation for laser point cloud including scanning geometry, *ISPRS Archives – Volume XXXVI-5/C55*, 2007, WG I/5 et al., The 5th International Symposium on Mobile Mapping Technology, MMT '07, Padua, Italy, Editor(s): A. Vettore, N. El-Sheimy.
- 73 Kurz, T.; Buckley, S.; Howell, J.; Schneider, D. Integration of panoramic hyperspectral imaging with terrestrial LiDAR. *Photogrammetric Record* 2011, 26(134): 212-228.
- 74 Alba, M.; Barazzetti, L.; Roncoroni, F. and Scaioni, M. Filtering vegetation from terrestrial point clouds with low-cost near infrared cameras, *Italian Journal of Remote Sensing* 2011, pp.55-75.
- 75 Blikra, L.H.; Anda, E.; Belsby, S.; Jøgerud, K. and Klempe, Ø. (in Norwegian). Åknes/Tafjord prosjektet: Statusrapport for Arbeidsgruppe 1 (Undersøking og overvaking), Åknes/Tafjord project, Stranda, Norway 2006.
- 76 Jaboyedoff, M.; Oppikofer, T.; Derron, M.-H.; Blikra, L. H.; Böhme, M. and Saintot A. Complex landslide behaviour and structural control: a three-dimensional conceptual model of Åknes rockslide, Norway. *Geological Society, London, Special Publications* 2011, 351:147-161.
- 77 Alho, P.; Kukko, A.; Hyypä, H.; Kaartinen, H.; Hyypä, J. and Jaakkola, A. Application of boat-based laser scanning for river survey. *Earth Surf. Process. Landforms* 2009, 34, 1831–1838.

-
- 78 Ingensand, H. Metrological aspects in terrestrial laser-scanning technology. In Proceedings of the 3rd IAG/12th FIG Symposium 2006, Baden, Austria.
- 79 Lichti, D.D. Error modelling, calibration and analysis of an AM-CW terrestrial laser scanner system, *ISPRS Journal of Photogrammetry and Remote Sensing* 2007, 61 (5), 307–324.
- 80 Abellán, A.; Jaboyedoff, M.; Oppikofer, T. and Vilaplana, J.M. . Detection of millimetric deformation using a terrestrial laser scanner: experiment and application to a rockfall event. *Nat. Hazards Earth Syst. Sci.* 2009, 9, 365–372.
- 81 Schürch, P., Densmore, A., Rosse, N., Lim, M., McArdell, B.W. Detection of surface change in complex topography using terrestrial laser scanning: application to the Illgraben debris-flow channel. *Earth Surf. Process. Landforms* 2011, 36, 1847–1859.
- 82 Pesci A.; Teza, G.; Bonali, E. Terrestrial Laser Scanner Resolution: Numerical Simulations and Experiments on Spatial Sampling Optimization. *Remote Sensing* 2011, 3(1), 167-184.
- 83 Lichti, D.D. and Jamtsho, M. Angular resolution of terrestrial laser scanners. *Photogrammetric Record* 2006, 21(114), 141–160.
- 84 Lato, M. J.; Diederichs, M. S.; Hutchinson, D. J. Bias Correction for View-limited LiDAR Scanning of Rock Outcrops for Structural Characterization. *Rock Mech. Rock Eng.* 2010, 43 (5), 615-628. doi: 10.1007/s00603-010-0086-5.
- 85 Stock, G.M.; Bawden, G.W.; Green, J.K.; Hanson, E.; Downing, G.; Collins, B.D.; Bond, S. and Leslar, M. High-resolution three-dimensional imaging and analysis of rock falls in Yosemite Valley, California, *Geosphere* 2011, v. 7, no. 2 p. 573-581.
- 86 Sturzenegger, M. and Stead, D. Quantifying discontinuity orientation and persistence on high mountain rock slopes and large landslides using terrestrial remote sensing techniques, *Nat. Hazards Earth Syst. Sci.* 2009, 9, 267–287.
- 87 Terzaghi, K. Stability of slopes on hard unweathered rock. *Geotechnique* 1962, 12: 251-263.
- 88 1. Mallet C, Bretar F. Full-waveform topographic lidar: State-of-the-art. *ISPRS J. Photogramm. Remote Sens.* 2009; 64(1), 1–16.
- 89 Lichti, D. D. Spectral Filtering and Classification of Terrestrial Laser Scanner Point Clouds. *The Photogrammetric Record* 2005, 20, 218–240.
- 90 Franceschi, M.; Teza, G.; Preto, N.; Pesci, A.; Galgaro, A.; Girardi, S. Discrimination between marls and limestones using intensity data from terrestrial laser scanner. *ISPRS J. Photogramm.* 2009, 64(6), 522-528. doi:10.1016/j.isprsjprs.2009.03.003.
- 91 Huang, J.; Lee, A.; Mumford, D. Statistics of Range Images. Paper presented at the IEEE International Conference on Computer Vision and Pattern Recognition 2000 (CVPR'00), Los Alamitos, CA, USA.
- 92 Lalonde, J.-F.; Vandapel, N.; Huber, D.; and Hebert, M. Natural terrain classification using three-dimensional ladar data for ground robot mobility. *Journal of Field Robotics* 2006, 23(1):839-861.
- 93 Brodu, N.; Lague, D. 3D terrestrial LiDAR data classification of complex natural scenes using a multi-scale dimensionality criterion: Applications in geomorphology: *ISPRS Journal of Photogrammetry and Remote Sensing* 2012, v. 68.
- 94 Cristianini, N. and Shawe-Taylor J. *An Introduction to Support Vector Machines: And Other Kernel-Based Learning Methods.* Cambridge, England: Cambridge University Press 2000.
- 95 Xu, L.; Jordan, M.I. On Convergence Properties of the EM Algorithm for Gaussian Mixtures, *Neural Computation* 8 1996 (1): 129–151.
- 96 Oppikofer, T.; Jaboyedoff, M.; Blikra, L.; Derron, M.-H.; Metzger, R. Characterization and monitoring of the Aknes rockslide using terrestrial laser scanning, *Nat. Hazards Earth Syst. Sci.* 2009, 9, 1003–1019.
- 97 Rabbani, T.; Dijkman, S.; van den Heuvel, F. and Vosselman, G. An integrated approach for modelling and global registration of point clouds, *ISPRS Journal of Photogrammetry and Remote Sensing* 2007, 61(6), 355-370.
- 98 Besl, P.; McKay, N. A method for registration of 3-D shapes. *IEEE Transactions on Pattern Analysis and Machine Intelligence* 1992, 14:239-256.
- 99 Chen, Y.; Medioni, G. Object Modelling by Registration of Multiple Range Images. *Image and Vision Computing* 10 1992, 145–155.
- 100 Lim, M.; Rosser, N. J.; Allison, R. J. and Petley, D. N. Erosional processes in the hard rock coastal cliffs at Staithes, North Yorkshire. *Geomorphology* 2010, 114, 12-21.
- 101 Lim, M.; Petley, D.N.; Rosser, N.J.; Allison, R.J.; Long, A. J.; Pybus, D. Combined digital photogrammetry and time-of-flight laser scanning for monitoring cliff evolution. *Photogrammetric Record* 2005, 20(1), 109-129.
- 102 Girardeau-Montaut, D. Détection de changement sur des données géométriques tridimensionnelles. Doctorat Traitement du Signal et des Images, TSI/TII, ENST, 2006 <available at: <http://pastel.enst.fr/1745>>
- 103 Burns, W.J; Coe J.A.; Basak S.K; Lina M. Analysis of Elevation Changes Detected from Multi-Temporal LiDAR Surveys in Forested Landslide Terrain in Western Oregon. *Environmental & Engineering Geoscience* 2010, XVI(4), 315–341.
- 104 Zaruba, Q.; Mencl, V. *Landslides and Their Control.* Elsevier 1982, Amsterdam.
- 105 Cruden, D.M.; Varnes, D.J. Landslides investigation and mitigation, transportation research board. In: Turner AK, Schuster RL (eds) *Landslide types and process*, National Research Council, National Academy Press, Special Report 1996, 247:36–75.
- 106 Soeters, R.; Van Westen, C.J. Slope instability recognition, analysis, and zonation. In: Turner AK, Schuster RL (ed) *Landslides investigation and mitigation*, special report 247, Transportation research board, National research council. National Academy Press 1996, Washington, pp 129–177.

-
- 107 Agliardi, F.; Crosta, G.; Zanchi, A. Structural constraints on deep-seated slope deformation kinematics. *Engineering Geology* 2001, 59, 83–102.
- 108 Braathen, A.; Blikra, L.H.; Berg, S.S.; Karlsen, F. Rock-slope failures in Norway; type, geometry and hazard. *Norwegian Journal of Geology* 2004, 84, 67–88.
- 109 Glenn, N.F.; Streutker, D.R.; Chadwick, D.J.; Thackray, G.D.; Dorsch, S. J. Analysis of LiDAR-derived topographic information for characterizing and differentiating landslide morphology and activity. *Geomorphology* 2006, 73(1-2), 131-148.
- 110 DeLong, S.B.; Prentice, C.S.; Hilley, G.E.; Ebert, Y. Multitemporal ALSM change detection, sediment delivery, and process mapping at an active earthflow. *Earth Surf.Proc. Landf.* 2012, 37(3), 262-272.
- 111 DeLong SB, Prentice CS, Hilley GE, Ebert Y. Multitemporal ALSM change detection, sediment delivery, and process mapping at an active earthflow. *Earth Surf. Process. Landforms.* 2012; 37(3), 262–272. DOI: 10.1002/esp.2234.
- 112 Burns, W. J., Coe, J. A., Kaya, B. S., & Ma, L. Analysis of elevation changes detected from multi-temporal LiDAR surveys in forested landslide terrain in western Oregon. 2010. *Environmental & Engineering Geoscience*, 16 (4), 315-341.
- 113 Young AP, Ashford SA. Instability investigation of cantilevered seacliffs. *Earth Surf. Process. Landforms.* 2008; 33(11), 1661–1677. DOI: 10.1002/esp.1636.
- 114 Reineman BD, Lenain L, Castel D, Melville WK. A Portable Airborne Scanning Lidar System for Ocean and Coastal Applications. *J. Atmos. Ocean. Technol.* 2009; 26(12), 2626–2641.
- 115 Mackey BH, Roering JJ, McKean JA. Long-term kinematics and sediment flux of an active earthflow, Eel River, California. *Geol.* 2009; 37 (9): 803–806.
- 116 International Society for Rock Mechanics (ISRM), International Society for Rock Mechanics (ISRM), Suggested methods for the quantitative description of discontinuities in rock masses, *International Journal of Rock Mechanics and Mining Sciences & Geomechanics Abstracts* 1978, 15, pp. 319–368.
- 117 Kemeny, J. and Post, R. Estimating three-dimensional rock discontinuity orientation from digital images of fracture traces, *Computers & Geoscience* 2003, 29, pp. 65–77.
- 118 Jaboyedoff, M.; Couture, R.; Locat, P. Structural analysis of Turtle Mountain (Alberta) using digital elevation model: toward a progressive failure. *Geomorphology* 2009, 103, 5–16. DOI. 10.1016/j.geomorph.2008. 14.012.
- 119 Grenon, M.; Hadjigeorgiou, J. A design methodology for rock slopes susceptible to Wedge failure using fracture system modelling. *Engineering Geology* 2008, 98:78-93. doi:10.1016/j.enggeo.2007.10.002.
- 120 Longoni, L.; Arosio, D; Scaioni, M.; Papini, M.; Zanzi, L.; Roncella, R and Brambilla, D. Surface and subsurface non-invasive investigations to improve the characterization of a fractured rock mass, *J. Geophys. Eng.* 2012, 9, 5 461
- 121 Ferrero AM, Forlani G, Roncella R, Voyat HI. 2009. Advanced geostructural survey methods applied to rock mass characterization. *Rock Mechanics and Rock Engineering* 42(1): 631–665. DOI: 10.1007/s00603-008-0010-4
- 122 Collins, B.D. and Stock, G.M., 2012. Lidar-based rock-fall hazard characterization of cliffs, *ASCE Geotechnical Special Publication No. 225, Geotechnical Engineering State of the Art and Practice*, R.D. Hryciw, A. Athanasopoulos-Zekkos, and N. Yesiller, eds., pp. 3021-3030.
- 123 Tonini M, Abellan A. 2014. Rockfall detection from terrestrial LiDAR point clouds: A clustering approach using R, in *Journal of Spatial Information Science*, 8, 95-110. DOI: 5311/JOSIS.2014.8.123
- 124 Carrea, D., Abellán, A., M.-H., Derron, Jaboyedoff, M. (2014). Automatic rockfalls volume estimation based on Terrestrial Laser Scanning data, *International Association Engineering Geology Conference*, Sept 15-19, 2014 Torino (Italy).
- 125 STOCK, G.M., MARTEL, S.J., COLLINS, B.D., & HARP, E.L. (2012): Progressive failure of sheeted rock slopes: the 2009-2010 Rhombus Wall rock falls in Yo-semite Valley, California, USA. *Earth Surf. Process. Landforms*, 37: 546-561.
- 126 Dewez, T.; Gebrayel, D.; Lhomme, D.; Robin, Y. Quantifying morphological changes of sandy coasts by photogrammetry and cliff coasts by lasergrammetry. *La Houille Blanche* 2009, (1) 32-37 DOI: 10.1051/ lhb:2009002
- 127 Santana, D., Corominas, J., Mavrouli, O., & Garcia-Sellés, D. (2012). Magnitude–frequency relation for rockfall scars using a Terrestrial Laser Scanner. *Engineering Geology*, 145, 50-64.
- 128 Hergarten, S.: Landslides, sandpiles, and self-organized criticality, *Nat. Hazards Earth Syst. Sci.*, 3, 505-514, doi:10.5194/nhess-3-505-2003, 2003.
- 129 Ravanel, L.; Allignol, F.; Deline, P.; Gruber, S. and Ravello, M. Rock falls in the Mont-Blanc massif in 2007 and 2008, *Landslides* 2010, 7, 4, 493–501.
- 130 Avian, M.; Kellerer-Pirklbauer, A.; and Bauer, A. LiDAR for monitoring mass movements in permafrost environments at the cirque Hinteres Langtal, Austria, between 2000 and 2008, *Nat. Hazards Earth Syst. Sci.* 2009, 9, 1087-1094, doi:10.5194/nhess-9-1087-2009.
- 131 Royan M.J., Abellán, A., Jaboyedoff, M., Vilaplana, J.M., Calvet, J. (2013). Spatio-temporal analysis of rockfall pre-failure deformation using Terrestrial LiDAR. *Landslides* 1-13. DOI: 10.1007/s10346-013-0442-0
- 132 Guzzetti, F., Reichenbach, P., and Wieczorek, G. F.: Rockfall hazard and risk assessment in the Yosemite Valley, California, USA, *NHESS*, 3, 491–503, 2003.

-
- 133 Jaboyedoff, M. and Labiouse, V.: Preliminary assessment of rockfall hazard based on GIS data, in: 10th International Congress on Rock Mechanics ISRM 2003 – Technology roadmap for rock mechanics, South African Institute of Mining and Metallurgy, Johannesburg, South Africa, 575–578, 2003.
- 134 Strahler, A. N.: Quantitative geomorphology of erosional landscapes, *Compt. Rend. 19th Intern. Geol. Cong.*, Sec. 13, 341–354, 1954.
- 135 Baillifard, F., Jaboyedoff, M., Rouiller, J.-D., Couture, R., Locat, J., Robichaud, G., and Gamel, G.: Towards a GIS-based hazard assessment along the Quebec City Promontory, Quebec, Canada., in: *Landslides Evaluation and stabilization*, edited by Lacerda, W., Ehrlich, M., Fontoura, A., and Sayão, A. A., pp. 207 – 213, Balkema, 2004.
- 136 McKean, J. and Roering J.J.: Landslide detection and surface morphology mapping with airborne laser altimetry, *Geomorphology*, v. 57, p. 331-351. 2004.
- 137 Loye, A., Jaboyedoff, M., and Pedrazzini, A.: Identification of potential rockfall source areas at regional scale using a DEM-based quantitative geomorphometric analysis, *NHESS*, 9, 1643-1653, doi:10.5194/nhess-9-1643-2009, 2009.
- 138 Baillifard, F., Jaboyedoff, M., and Sartori, M.: Rockfall hazard mapping along a mountainous road in Switzerland using a GIS-based parameter rating approach, *NHESS*, 3, 435–442, 2003.
- 139 Wagner, A., Leite, E., and Olivier, R.: Rock and debris-slides risk mapping in Nepal – A user-friendly PC system for risk mapping, in: *Landslides, Proceedings of the 5th International Symposium on Landslides, Lausanne, Switzerland, 10–15 July 1988*, edited by Bonnard, C., A.A. Balkema, Rotterdam, 2, 1251–1258, 1988.
- 140 Gokceoglu, C., Sonmez, H., and Ercanoglu, M.: Discontinuity controlled probabilistic slope failure risk maps of the Altindag (settlement) region in Turkey, *Eng. Geol.*, 55, 277–296, 2000.
- 141 Norrish, N. and Wyllie, D.: *Landslides - Investigation and mitigation*, Transportation Research Board, special report 247, Rock slope stability analysis, p. 673, Turner, A.K. and Schuster, R.L. (Eds.), National Academy Press, Washington, DC, 1996.
- 142 Fanti R, Gigli G, Lombardi L, Tapete D, Canuti P (2012) Terrestrial laser scanning for rockfall stability analysis in the cultural heritage site of Pitigliano (Italy). *Landslides*. doi:10.1007/s10346-012-0329-5
- 143 Jaboyedoff, M., Baillifard, F., Philipposian, F. & Rouiller, J.-D.: Assessing the fracture occurrence using the "Weighted fracturing density": a step towards estimating rock instability hazard. *NHESS*, 4, 83-93. 2004.
- 144 Brideau M.A., Pedrazzini A., Stead D., Froese C., Jaboyedoff J., van Zeyl D., Three-dimensional slope stability analysis of South Peak, Crowsnest Pass, Alberta, Canada, *Landslides* (2011) 8:139–158, DOI 10.1007/s10346-010-0242-8.
- 145 Conway, S.J., Decaulne, A., Balme, M.R., Murray, J.B., Towner, M.C.. A new approach to estimating hazard posed by debris flows in the Westfjords of Iceland. *Geomorphology* 2010, 114, 4, 556-572.
- 146 Lancaster, S., Nolin, A., Copeland, E., Grant G. Periglacial debris-flow initiation and susceptibility and glacier recession from imagery, airborne LiDAR, and ground-based mapping. *Geosphere* 2012, 8, 417-430.
- 147 Lopez Saez, J., Corona, C., Stoffel, M., Gotteland, A., Berger, F., Liébault, F. Debris-flow activity in abandoned channels of the Manival torrent reconstructed with LiDAR and tree-ring data, *Nat. Hazards Earth Syst. Sci.* 2011, 5, 1247-1257.
- 148 Staley, D., Wasklewicz, T., Blaszczyński, J. Surficial patterns of debris flow deposition on alluvial fans in Death Valley, CA using airborne laser swath mapping data. *Geomorphology* 2006, 74, 1–4, 152-163.
- 149 Lancaster, S.T.; Nolin, A.W.; Copeland, E.A.; Grant, G.E. Periglacial debris-flow initiation and susceptibility and glacier recession from imagery, airborne LiDAR, and ground-based mapping. *Geosphere* 2012, 8(2), 417-430.
- 150 Staley, D.M.; Wasklewicz, T.A.; Blaszczyński, J.S. Surficial patterns of debris flow deposition on alluvial fans in Death Valley, CA using airborne laser swath mapping data. *Geomorphology* 2006, 74(1-4), 152-163.
- 151 Breien, H., De Blasio, F., Elverhøi, A., Høeg, K. Erosion and morphology of a debris flow caused by a glacial lake outburst flood, Western Norway, *Landslides* 2008, 5, 3, 271-280.
- 152 Bull, J.M.; Miller, H.; Gravley, D.M.; Costello, D.; Hikuroa, D.C.H.; Dix, J.K. Assessing debris flows using LIDAR differencing: 18 May 2005 Matata event, New Zealand, *Geomorphology* 2010, 124, 75–84.
- 153 Scheidl, C., Rickenmann, D., Chiari, M. The use of airborne LiDAR data for the analysis of debris flow events in Switzerland, *Nat. Hazards Earth Syst. Sci.* 2008, 5, 1113-1127.
- 154 Abancó, C., & Hürlimann, M. (2014). Estimate of the debris-flow entrainment using field and topographical data. *Natural Hazards*, 71(1), 363-383.
- 155 Stolz, A., Huggel, C. Debris flows in the Swiss National Park: the influence of different flow models and varying DEM grid size on modeling results, *Landslides* 2008, 5, 3, 311-319.
- 156 Dietrich, W.E.; Bellugi, D.; Real de Asua, R. Validation of the shallow landslide model, SHALSTAB, for forest management. In: Wigmosta MS, Burges SJ (eds) *Land use and watersheds: human influence on hydrology and geomorphology in urban and forest areas*, Water Science and Application 2001, 2, 195–227.
- 157 Godt, J.W., Baum, R.L., Savage, W.Z., Salciarini, D., Schulz, W.H., and Harp, E.L., 2008, Transient deterministic shallow landslide modeling—Requirements for susceptibility and hazard assessments in a GIS framework: *Engineering Geology*, v. 102, no. 3-4, *Landslide Susceptibility, Hazard and Risk Zoning for Land Use Planning*, p. 214-226, DOI: 10.1016/j.enggeo.2008.03.019.

-
- 158 Savage, W.Z.; Godt, J.W.; Baum, R.L. A model for spatially and temporal distributed shallow landslide initiation by rainfall infiltration. A model for spatially and temporally distributed shallow landslide initiation by rainfall infiltration In: Rickenmann D, Chen C (eds) Debris-flow hazards mitigation: mechanics, prediction, and assessment. Millpress 2003, Rotterdam.
- 159 Liao, Z.Hong, Y., Kirschbaum, D., Adler, R., Gourley, J.J. and Wooten, R. Evaluation of TRIGRS (transient rainfall infiltration and grid-based regional slope-stability analysis)'s predictive skill for hurricane-triggered landslides: a case study in Macon County, North Carolina. *Natural Hazards*, 2011,58, Issue 1, 325-339. dx.doi.org/10.1007/s11069-010-9670-y
- 160 Tarolli, P., and Tarboton, D.G. A New Method for Determination of Most Likely Landslide Initiation Points and the Evaluation of Digital Terrain Model Scale in Terrain Stability Mapping, *Hydrol. Earth Syst. Sci.*, 2006, 10, 663-677, ISSN: 1027-5606, doi:10.5194/hess-10-663-2006.
- 161 Horton, P.; Jaboyedoff, M.; Rudaz, B.; Zimmermann, M. Flow-R a model for susceptibility mapping of debris flows and other gravitational hazards at a regional scale. *NHESS in Press* 2013.
- 162 Janeras, M.; Navarro, M.; Arnó, G.; Ruiz, A.; Kornus, W.; Talaya, J.; Barberà, M.; López, F. Lidar applications to rock fall hazard assesment in Vall de Núria. *Proceeding of 4th ICA Mountain Cartography Workshop 2004*. Vall de Núria (SPA). pp. 1-14.
- 163 Agliardi, F. ; Crosta, G.B. High resolution three-dimensional numerical modelling of rockfalls. *Int. J. Rock Mecha. Mining Sci.* 2003, 40:455-471. doi:10.1016/S1365-1609(03)00021-2.
- 164 Jaboyedoff, M.; Giorgis, D.; Riedo, M. Apports des modèles numériques d'altitude pour la géologie et l'étude des mouvements de versant. *Bull. Soc. vaud. Sc. nat.* 2006, 90.1, 1-21.
- 165 1. Fuchs M, Torizin J, Kühn F. The effect of DEM resolution on the computation of the factor of safety using an infinite slope model. *Geomorphology*. 2014. DOI: 10.1016/j.geomorph.2014.07.015.
- 166 Brideau, M.-A., Pedrazzini, A., Stead, D., Froese, C., Jaboyedoff, M. and van Zeyl, D. Three-dimensional slope stability analysis of South Peak, Crowsnest Pass, Alberta, Canada. *Landslides*, 8, 2011, 139-158.
- 167 Roering, J.J., How well can hillslope evolution models 'explain' topography? *Simulating soil production and transport using high-resolution topographic data*, *Geological Society of America Bulletin*, 2008, 120, p. 1248-1262.
- 168 Olsen, J.M.; Butcher, S.; and Silvia, E.P. Real-time change and damage detection of landslides and other earth movements threatening public infrastructure, Final Report SR 500-500, OTREC-RR-11-23, Oregon Department of Transportation Research Section 2012, 62pp. Available at <http://www.oregon.gov/ODOT/TD/TP_RES/docs/Reports/2012/SR500_500_Landslides.pdf>
- 169 Farr, T.G.; Rignot, E.; Saatchi, S.; Simard, M. and Treuhaft, R. Lidar/InSAR Synergism for Earth Science Applications, *Synthetic Aperture Radar (EUSAR)*, 2008 7th European Conference on, pp.1-3, 2-5 June 2008.
- 170 Lingua, A.; Piatti, D. and Rinaudo, F. Remote Monitoring of a Landslide Using an Integration of GB-InSAR and LiDAR Techniques, In the *International Archives of the Photogrammetry, Remote Sensing and Spatial Information Sciences* 2008, Vol. XXXVII, Part B1, Beijing, 361-366.
- 171 Roering, J.J.; Stimely, L.L.; Mackey, B.H.; and Schmidt, D.A. Using DInSAR, airborne LiDAR, and archival air photos to quantify landsliding and sediment transport, *Geophysical Research Letters* 2009, Vol 36, L19402, doi:10.1029/2009GL040374.

Annex B3

Jaboyedoff M, Choffet M, Derron MH, Horton P, Loye A, Longchamp C, Mazotti B, Michoud C and Pedrazzini A: Preliminary slope mass movements susceptibility mapping using DEM and LiDAR DEM. In: Terrigenous Mass Movements, Pradhan and Buchroithner (Eds.), Springer-Verlag Berlin Heidelberg, 109-170, 2012.

Chapter 5

Preliminary Slope Mass Movement Susceptibility Mapping Using DEM and LiDAR DEM

M. Jaboyedoff, M. Choffet, M.-H. Derron, P. Horton,
A. Loye, C. Longchamp, B. Mazotti, C. Michoud
and A. Pedrazzini

Abstract Hazard mapping in mountainous areas at the regional scale has greatly changed since the 1990s thanks to improved digital elevation models (DEM). It is now possible to model slope mass movement and floods with a high level of detail in order to improve geomorphologic mapping. We present examples of regional multi-hazard susceptibility mapping through two Swiss case studies, including landslides, rockfall, debris flows, snow avalanches and floods, in addition to several original methods and software tools. The aim of these recent developments is to take advantage of the availability of high resolution DEM (HRDEM) for better mass movement modeling. Our results indicate a good correspondence between inventories of hazardous zones based on historical events and model predictions. This paper demonstrates that by adapting tools and methods issued from modern technologies, it is possible to obtain reliable documents for land planning purposes over large areas.

Keywords DEM · Lidar · Rockfall · Debris-flow · Floods · Snow avalanches · Regional hazard mapping · Models · Flow-R · RAS · Conefall · HISTOFIT

5.1 Introduction

Slope mass movement hazard mapping has been a major concern since the 1970s. In Varnes (1984), the authors made an overview of the principal mapping practices that were mainly linked to field investigations and aerial photo interpretations

M. Jaboyedoff (✉) · M. Choffet · M.-H. Derron · P. Horton ·
A. Loye · C. Longchamp · B. Mazotti · C. Michoud · A. Pedrazzini
Institute of Risk Analysis-University of Lausanne, Lausanne, Switzerland
e-mail: michel.jaboyedoff@unil.ch

(Cruden and Thomson 1987). Since the appraisal of geographical information systems (GIS) (Carrara and Guzzetti 1995) and the production of digital elevation models (DEM), hazard mapping of slope mass movements has increased significantly. In addition over the past decade, new techniques such as airborne laser scanning by Lidar (Light Detection and Ranging) provide to the earth sciences community high resolution DEM (HRDEM) with resolutions higher than 0.5 pts/m² (Shan and Toth 2008).

This computerization of hazard mapping has significantly supported susceptibility mapping at regional scale. This type of mapping is designed to provide a fast overview of area that is affected by potentially dangerous events. This is of primary importance for regional authorities and municipalities because of the responsibilities linked to risk management. The first step of a rational risk assessment is to have an overview of the area potentially endangered by slope movements such as deep-seated landslides, shallow landslides, debris flows, rockfall, flooding and erosion. This is most commonly done by producing preliminary susceptibility maps over the entire territory considered. According to Swiss guidelines, (Lateltin 1997; Loat and Petraschek 1997), this kind of maps is the first step of the process leading to detailed so-called “danger” maps used for local planning in communities.

However, such maps do not give any detailed information on the intensity or the frequency of occurrence of the slope movements. They only indicate the hazardous zones for instance at a 1:25,000 scale. The methods of mapping are various and numerous and some excellent recent overviews and recommendations published about landslides mapping can be found in Aleotti and Chowdhury 1999, Van Westen et al. 2006, Fell et al. 2008a, b, Cascini 2008. For floods, there is also a large variety of approaches (Merz et al. 2007). For snow avalanches, regional mapping was proposed by Toppe (1987) and more detailed mapping is also well established (Ancey et al. 2006; PPR 2011).

The present paper focuses on two examples in Western Switzerland of multi-hazards regional mapping. These examples show the variety of situations depending on the geological and geographical conditions but also on the number and types of data currently available. It is thus not possible to follow a unique method in all situations but it must be adapted to each circumstance (Jaboyedoff and Derron 2005). The proposed approach is based on deterministic simple modelling using DEM, interpretation of data produced from HRDEM like hillshades and fast field surveys. It demonstrates that up to a certain level, a simple relative hazard scale can be included in susceptibility maps. The use of all available modern documents HRDEM, vectorized topographic maps, orthophotos permits to obtain quite rapidly reliable results at regional scale. The limitations of such approach are usually: (1) the lack of data to calibrate the models, (2) the HRDEM permits to improve the quality of the results but they also induce some problems such as handling very large datasets or introducing some artefacts in the overly detailed topography.

5.2 Problem Identification/Conceptual Background

GIS has greatly improved the capacity of mass movement and flood hazard mapping and currently most such studies use a GIS framework (Carrara and Guzzetti 1995; Chacón et al. 2006). Hence, one of the principal improvements of these last ten years is the use of DEM and HRDEM, because it permits first to perform modeling and second to examine the details of the morphology. It must be observed that HRDEM often possess a resolution too high for modeling at regional scale, necessitating that its resolution be decreased. Therefore, regional scale mapping is now possible by relying on modeling, based only on geomorphologic approaches using HRDEM. Of course regional mapping benefits from old documents such as geological maps, which indicate some landslide locations, topographic maps, etc. However, the availability of new digital documents (vectorized geological maps, high resolution satellite images, series of orthophotos, etc.) is making it possible to improve all mapping methodologies, which have become highly dynamic. As a consequence, methods are no longer set permanently. This is an issue when working with regional/national authorities who would like to have a definitive methodology/product. It is possible that if the process of mapping takes a long time, the product is already outdated when it is issued, i.e., because a new HRDEM has been released in the mean time. Moreover at present, the coverage of regions by one type of document is frequently not homogeneous, which makes the creations of hazard maps more difficult.

One of the solutions for regional mapping purpose is to make cross validations of simple models using DEM with other documents and especially field investigations. Such an approach is one of the most efficient ways to obtain results making use of modeling and new documents. It is a heuristic type of approach mixed with a deterministic approach (Soeters and Van Westen 1996; Van Westen et al. 2006). The limits of such an approach are linked to the quality of data and the availability of inventories of events that are very important for calibrating the methods.

5.3 Review of Literature

Einstein (1988) presented one of the first reviews on landslide risk analysis including also the description of the maps needed for such purposes. Such risk approaches have underlined the necessity to use GIS to make further analysis for both mass movements, floods and erosion (Carrara and Guzzetti 1995; Consuegra et al. 1995). Nowadays publications on this topic abound and frequently papers related to GIS hazard assessments present several different methods. These methods have been classified by Soeters and Van Westen (1996), Van Westen et al. (2006) (see also Chacón et al. 2006) as:

1. Inventory based approach
2. Heuristic approach
3. Statistical and probabilistic approach
4. Deterministic approach.

The great difference between hazard assessment methods for landslides versus floods, erosion or snow avalanches is that the last three are mainly based on inventories, because the events are relatively frequent and repeated in an area (Marco 1994; Gilard and Gendreau 1998; PPR 2011). While landslide mapping is often based on poor inventories in numbers and as a consequence the potentialities of events are often difficult to locate precisely. Furthermore the prevention of floods and snow avalanches is more based on alerts and risk management (McClung and Schaerer 1993; Directive 2007/60/EC), versus landslides. Nevertheless the objectives of regional hazard maps are the same; they must point out the areas of conflict between hazardous zone and human activities (Lateltin 1997; Loat and Petraschek 1997).

Considering the amount of existing literature, we will focus this short summary on regional hazard mapping using DEM. For landslides, one of the first attempts to use GIS and DEM was proposed by Carrara et al. (1978, 1991) using the concept of slope units (Guzzetti et al. 1999); this approach is based on inventory and statistical methods. By multivariate analysis, using a map of known landslides, a detailed hazard zoning is then produced. Other statistical methods have been developed that are mainly based on several multivariate regressions (Chung et al. 1995). DEM are also used in a lot of new techniques for hazard mapping, referred to as neural networks, i.e., (Zeng-wang 2001; Pradhan and Lee 2010), fuzzy logic (Ercanoglu and Gokceoglu 2002, 2004; Chung and Fabbri 2008) and also logistic regression (Bai et al. 2009; Dominguez-Cuesta et al. 2009). However, these methods are mainly applied at a regional scale, but do not introduce expert knowledge in a simple way, except during the training step, within the method, which is based on inventories. More simple approaches use relative ratings of several parameters including those that derive from DEM (Gupta et al. 1999). Similar methods have been also applied to detect rockfall sources areas (Baillifard et al. 2003, 2004).

For flood hazard mapping and prediction, the main recent advance is TOPMODEL, which makes a simple and complete simulation of the hydrological processes that determines the discharge of rivers using a DEM (Beven and Kirkby 1979; Beven et al. 1995). Hazard assessments using TOPMODEL are closely linked to the return periods of high discharge, flood depth and velocity (Marco 1994; De Moel et al. 2009; Van Alphen et al. 2009; Loat and Petraschek 1997; PPR 1999). Flood depth can be modelled by shallow water approximation (Gilard and Gendreau 1998; De Moel et al. 2009), but the heuristic approach is recommended by both French and Swiss authorities (Loat and Petraschek 1997; PPR 1999), at least at the regional scale. USGS proposes a simplified physical model TrimR2D that uses Lidar-DEM (Jones 2004). Other models using HRDEM are based on stochastic approaches (Metzger 2003).

The philosophy of TOPMODEL (Beven and Kirkby 1979) led to the development of several deterministic (introducing random variables if necessary) models for shallow landslides using a “pixel” stability analysis: SHALSTAB (Montgomery and Dietrich 1994), SINMAP (Pack et al. 1998) and TRIGRS (Baum et al. 2002).

For modeling purposes rockfall, snow avalanches and debris flows have similar procedures; first we need to detect the source areas and second to estimate the propagations. At regional scale, the detection of source areas is often based on threshold angles: (1) for snow avalanches above 30° and less than 60° (McClung and Schaerer 1993; Salm 1983) and also on the slope orientation (McClung and Schaerer 1993); (2) for rockfall 37° was used as an example for a 10 m grid size DEM in Dolomites (Italy) (Frattini et al. 2008) and Guzzetti et al. (2003) used 60° with a 10 m grid size DEM in the special case of extreme glacial valley type of Yosemite (USA). For debris-flow, the zone of initiations is more complex to detect because it needs to estimate sediments availability, water input and slope gradient (Rickenmann and Zimmermann 1993; Takahashi 1981). The use of flow accumulation (Burrough and McDonnell 1998) permits to link slope angle and triggering conditions (Rickenmann and Zimmermann 1993; Heinimann et al. 1998).

The detection of rockfall sources can be refined using structural data that makes it possible to define the potential source areas that are affected by defined mechanisms by performing kinematic tests using the DEM (Willye and Mah 2004). This can be performed using a statistical approach (Jaboyedoff et al. 2004) that count the number of discontinuities per unit of topographic surface, or using stability analysis for each DEM pixel (Gokceoglu et al. 2000; Günther 2003; Günther et al. 2004). Fuzzy logic has also been tested mainly based on DEM deduced parameters (Aksoy and Ercanoglu 2006).

For snow avalanches and rockfall, Toppe (1987) used the simplest evaluation, based on the concept of shadow angle (Heim 1932; Lied 1977; Perla et al. 1980; Evans and Hungr 1993). This states that the propagations are most probably restricted to an area that is defined by the intersection of the DEM and a cone centred on the source possessing an angle ϕ° equivalent to a friction angle (Jaboyedoff and Labiouse 2003; Evans and Hungr 1993). For snow avalanches ϕ° can be adapted to the morphology of the valley flanks (Lied and Bakkehoi 1980).

More advanced techniques for rockfall are using 3D trajectory simulations that lead to regional assessment, but they require good information on the ground (Guzzetti et al. 2002, 2003; Agliardi and Crosta 2003; Dorren et al. 2003; Frattini et al. 2008). In order to obtain a continuous zoning Lan et al. (2007) interpolate the trajectories results using geostatistics.

Several applications for debris-flows propagation have been proposed but very few have been used at the regional scale (Van Westen et al. 2006). They are mostly based on multiple flow direction (Huggel et al. 2003; Heinimann et al. 1998) or on random walk (Gamma 2000). The runout distance of the debris-flow is either assessed using a friction model or using a limiting angle slope (Heinimann et al. 1998).

In addition, the geomorphologic analysis has been greatly improved in the past ten years by the introduction of airborne Lidar-DEM, because it permits to recognize in detail landslide features, and deep gravitational deformations (Crosta and Agliardi 2002). The limitations and the advantages of these mapping techniques are now well known, but has clearly shown its efficacy in creating and correcting inventories (Haugerud et al. 2003; Ardizzone et al. 2007; Schultz 2004, 2007). Some attempts have been made to automatically detect zones of landslides using roughness or dispersion of the orientation of the topography (McKean and Roering 2004; Roering et al. 2005; Glenn et al. 2006). Morphological characteristics can be also easily extracted from HRDEM (Chigira et al. 2004).

The potential information that can be extracted from HRDEM is probably not yet fully used, especially for flood geomorphic analysis. The above review shows that a combination of methods is the best way to fully use all the potentiality offered by new techniques and data.

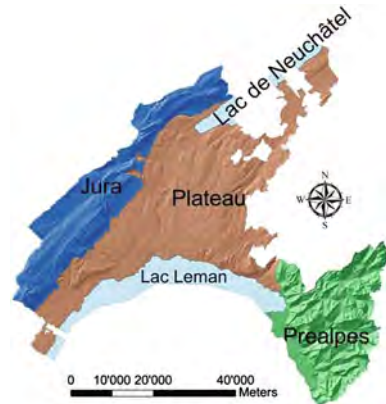
5.4 Study Area/Experimental Site

All the examples of susceptibility mapping presented in this paper has been taken from work conducted by the Institute of Geomatics and Risk Analysis of the University of Lausanne on two Swiss study areas: (1) the County of Vaud and (2) the Bagnes Valley. This chapter introduces the main relevant features for geohazards of these two areas.

5.4.1 *Vaud County*

The susceptibility mapping of potential slope movements (1:25,000) was performed on the entire territory of the county of Vaud (2800 km²), western Switzerland, for the following processes: rockfalls, shallow and deep seated landslides, mud and debris flows (Jaboyedoff et al. 2008). The geology of the county can be divided into three main regions (Trümpy 1980) (Fig. 5.1): (1) The northwestern region is located within the limestones of the Jura chain. Its elevation ranges from 400 m to approx. 2000 m a.s.l.. This area is composed of folded and thrust Mesozoic and Tertiary carbonates platform series, in a thin skin tectonic style. (2) The middle part of the Vaud county belongs to the Swiss Molasse Plateau. It corresponds to a foreland basin of Oligo-Miocene age. The rocks are mostly poorly consolidated sandstones with some layers of shales and conglomerates. The topography is gently hilly with few cliffs made of competent sandstones and some steep slopes resulting from fluvial erosion. (3) The southeast area belongs to the Prealpine units of the Alps. Here the steep and rugged topography ranges from 400 to more than 3000 m. The main rocks are: massive limestone, dolomites, marls, evaporites and shales of Mesozoic and Cenozoic ages.

Fig. 5.1 The canton Vaud could be divided in three distinct geological areas, characterized by a different lithology and a different tectonic history (hillshade, swisstopo© 2005 SIT)



The morphology of the valleys has been strongly shaped by glacial erosion and then reworked by fluvial erosion and slope mass movements. This third domain is by the far the most susceptible to mass movements.

5.4.2 Bagnes Valley

The Bagnes Valley (Valais county, Switzerland) has an area of 300 km² with an elevation between 600 m and 4200 m a.s.l. The development of the valley is rapid because of the fast growing ski resort of Verbier. Susceptibility maps at 1:25,000 have been provided to the local authorities for the following processes: landslides, shallow landslides, rockfall, debris flows, snow avalanches, flooding and river overflowing. Similar methods as for the County of Vaud were used. In addition, as the area is smaller, some methods were improved, historical event were included, field checks were conducted and feedback from local geologists and specialists was considered.

The Bagnes Valley is one of the only alpine valleys where the three main paleogeographical domains of the Alps are present, i.e. Helvetic, Penninic and Austro-Alpine (Trümpy 1980). An extremely wide variety of rocks is then present, from some Cambrian polycyclic basements to Mesozoic-Cenozoic sedimentary covers (Sartori et al. 2006). In the lower part of the valley (Fig. 5.2), the Helvetic domain is mainly composed of massive limestone that can form high fractured cliffs. The Lower Penninic unit is dominated by various schists, as on the catchment area of the Merdenson where the quantity of mobilizable fine material mobilized by debris-flow is very important (Jaboyedoff et al. 2010).

The Middle Penninic unit is mainly constituted of a complex succession of many different types of silicate rocks, from the old polymetamorphic basements to Permo-Trias sediments. It includes quartzites, quartzitic micaschists, various volcano-detritic sediments, granites and several felsic intrusions, meta-gabbro and

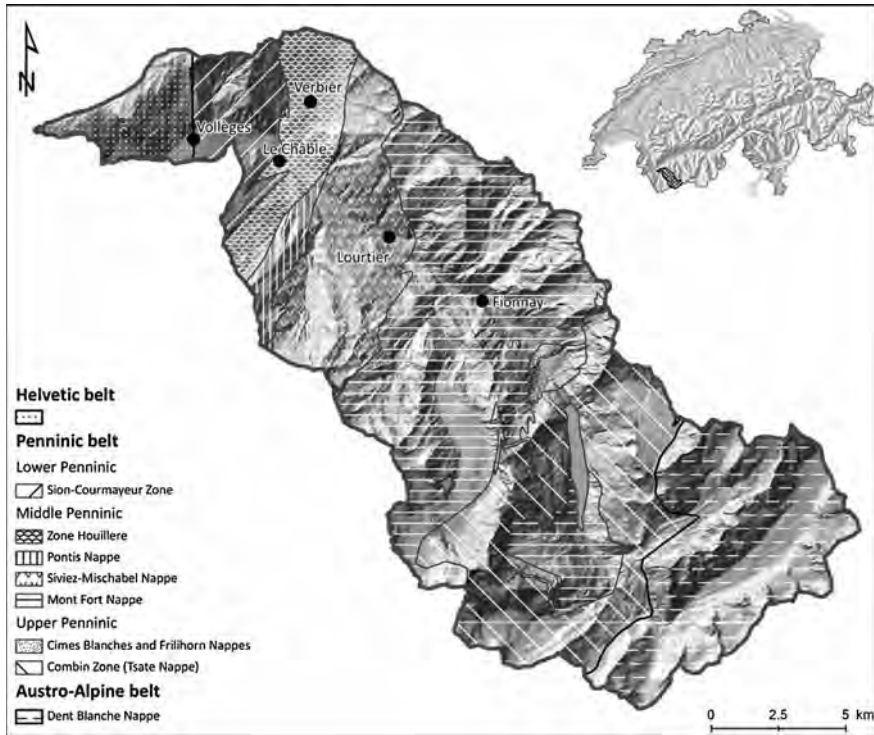


Fig. 5.2 Tectonic Units of the Val de Bagnes, from the geological national map. The valley cuts the three main belts of the Alps based on the Mesozoic paleogeography, the Helvetic, the Penninic and the Austro-Alpine belts. (modified from Thélin et al. 1994; geological national map and hillshade: ©swisstopo)

various types of amphibolitic gneisses. These lithologies are mainly outcropping between Le Châble and Mauvoisin and over all the width of the valley, it is the most important unit of the study area. All these rocks have been quite intensively deformed and metamorphised. Most of them are quite massive except some smicaschists and remnants gypsum and dolomites. It is in this tectonic unit that the most cases of rockfall occur along the road between Lourtier and Fionnay, or in Plamproz too (Jaboyedoff et al. 2010).

The Upper Penninic Unit in the Val de Bagnes is represented by a thick succession of calc-micaschists and metamorphised ophiolites. The Borne du Diable cliff, on the left shore of the Mauvoisin Lake, is mostly composed of schists and it concentrates in a small areas two debris flows channels, a major rockslide, several shallow landslides and repeated rockfalls (Jaboyedoff et al. 2010). Finally, the Dent Blanche Nappe from the Austro-Alpine domain is mainly composed by massive orthogneisses forming the highest peak of the area and abrupt cliffs at the Southern end of the valley.

5.5 Data and Tools

First we briefly introduce datasets used for the Vaud County and Valley of Bagnes projects. In addition, four original software programs were developed by the authors to draw these susceptibility maps. For three of them we only provide a short description of their principles and functionalities. The fourth one, the numerical model FLOW-R, is described more in detail as it has been extensively used in these projects, as well for debris flows, rockfall, snow avalanches and flooding.

5.5.1 Data

For the County of Vaud, a 1 m resolution digital elevation model (HRDEM) derived from aerial laser scanning was available. With a mean point density of 2 point per m², it has an altimetric accuracy of 30 cm, with ± 5 cm corresponding to one standard deviation. According to Van Den Eeckhaut et al. (2007), two different hillshade maps were created from this DEM, one with a sun elevation angle of 30° and a sun azimuth angle of 315° and another with a sun elevation angle of 30° and a sun azimuth angle of 45°. High resolution orthophotos with a ground resolution of 0.25 or 0.5 m were also used to complete and verify the DEM observations. National topographic maps 1:25,000 (Swisstopo), in both vector and raster format were been used to characterize the present-day land use.

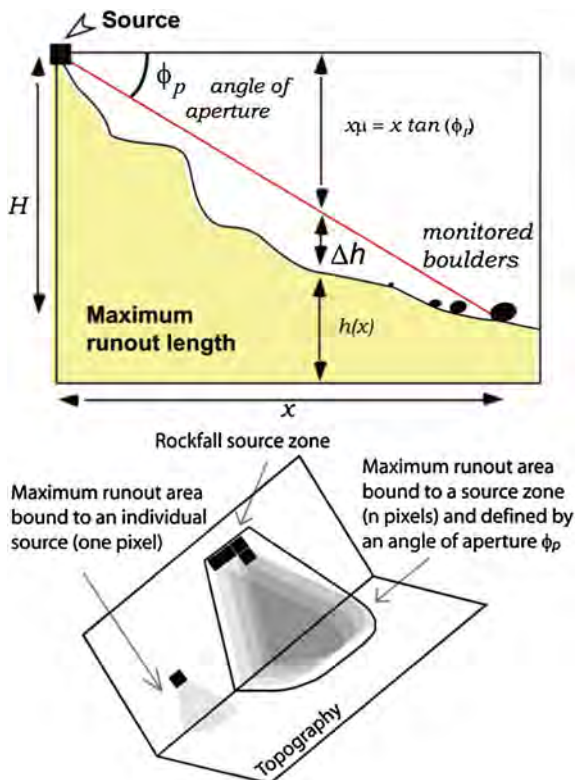
For the Bagnes Valley, a 2 m resolution DEM performed by aerial laser scanning was used for the altitudes lower than 2000 m. As for the County of Vaud dataset, the elevation accuracy is 30 ± 5 cm (Swisstopo 2005). For the altitudes higher than 2000 m, a 25 m DEM (MNT25, swisstopo) derived from the national maps at 1:25,000 (CN25, swisstopo) was used. The altimetric accuracy is between 2 and 5 m in the study area, with a horizontal accuracy from 2.5 to 7.5 m (Swisstopo 2004). National topographic maps 1:25,000 (Swisstopo), in both vector and raster format were also used to characterize the present-day land use, in addition to maps of the geological atlas of Switzerland at 1:25,000 in the raster format (edited by Swisstopo), as well as geological and tectonic vector maps at 1:500,000. Finally, the whole Val de Bagnes is covered by orthophotos (0.5 m resolution) taken in 1999 from Swisstopo.

5.5.2 Tools

5.5.2.1 HISTOFIT

HISTOFIT is an Excel©-based application that computes the most-likely Gaussian curves in an iterative way, so that the sum of those gaussian curves fits the slope angle frequency distribution of a topography. The fitting process is done by

Fig. 5.3 **a** Longitudinal cross-section of the idealized shadow angle method showing the relationship between ϕ_π and the maximum runout distance (modified from Jaboyedoff 2003). **b** Scheme of the shadow angle method in 3D implemented in the GIS-based freeware CONEFALL (modified from Jaboyedoff and Labiouse 2003)



minimizing the standard error using optimisation procedures of the Excel solver. This tool enables to fit the sum of up to 5 gaussian curves to a target function represented here by a slope angle histogram. HISTOFIT is a freeware available at www.unil.ch/igar.

5.5.2.2 CONEFALL

CONEFALL is a freeware that enables to model the runout area of rock fall. The method used to simulate rockfall runout surface generalizes the shadow angle (Fahrböschung) theory (Heim 1932; Scheidegger 1973; Evans and Hungr 1993) in a 3D GIS environment. Using this approach, rockfall is considered as a sliding and rolling process going down a slope with a certain average friction angle. The model considers thus that an individual block can reach any place in the area situated inside a cone of given aperture $90^\circ - \varphi_\pi$ (Fig. 5.3). The shadow angle method is empirical and does not require detailed input parameters, such as coefficient of friction and restitution coefficients.

The program requires a DEM and sources areas in a grid format. Beside the computation and display of the runout areas, the program can compute amongst other elements the number of contributing source pixels, the velocities of the blocs and their kinematic energy. CONEFALL can be downloaded from www.quanterra.org (Jaboyedoff 2003; Jaboyedoff and Labiouse 2011).

5.5.2.3 RAS

RAS is a software in development (previously at the Geological Survey of Norway and now at the University of Lausanne) to obtain a rapid assessment of snow avalanches and rockfall propagations over very large areas (up to more than one billion cells DEM). It uses the same shadow angle principle than Conefall, except that the angle of propagation is not kept constant. The angle of propagation is estimated for each source cell in function of the topography using the alpha/beta method of Lied and Bakkehoi (1980); (see also McClung and Schaerer 1993; Ancey et al. 2006). RAS has been used to map the snow avalanches potential propagation in the Bagnes Valley.

5.5.2.4 FLOW-R

The numerical model FLOW-R (Flow assessment at a Regional scale) has been developed for regional susceptibility mapping of gravitational processes (Horton et al. 2008). One of its strengths is to propose a choice of algorithms and an easy customization of the method in a graphical user interface (Fig. 5.4). The model, originally developed for debris flows, has proved to be relevant for other processes (rockfall, floodings and avalanches).

The procedure used has two steps. First, the sources are identified on the basis of various layers of data (e.g. DEM, land use map), and then these sources are propagated using a probabilistic and energetic approach (Horton et al. 2008). The volumes of the phenomena (debris-flow, rockfall etc.) are not taken into account in this model. Both the sources identification and the propagation area assessment are based on a regularly gridded DEM.

Source Area Identification

The source area identification is processed by combining various layers of data. In each layer, the cells are classified according to user-defined criteria into three possible values: possible source—excluded—ignored. The possible source option means that according to the selected criterion, the cell is a potential source area. The ignored option means that there is no evidence if the cell is a source or not, so no decision is fixed. The excluded option means that the cell cannot be a source area. In combining the grids established for the different criteria, a cell is selected

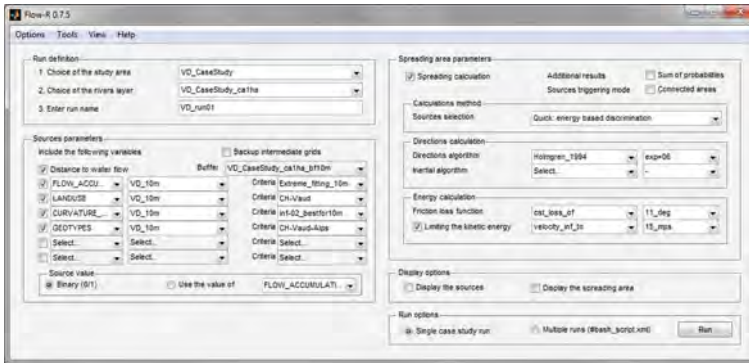


Fig. 5.4 Graphical user interface of the Flow-R model

as a source area if it was at least once identified as a possible source but never classified as excluded (Horton et al. 2008). Data can be either of a continuous or a discrete nature. In the first case, the selection is based on ranges, and in the second, on values.

Spreading Area Assessment

The spreading can be mathematically estimated by two types of algorithms: the first ones are called flow direction algorithms and determine the path that the debris flow will follow; the second ones determine mainly the runout distance (Horton et al. 2008). The propagation is calculated from each source cell. To calculate the propagation, only a grid with the source cells and a DEM are required.

1. Flow direction algorithms

First the flow direction algorithm apportions the flow from one cell to its eight neighbours in a way that there is always at least one cell in which the flow can run. The probability of spreading is a function of the slope angle and the persistence, which is a weighting of the directions according to the previous direction, allowing an integration of the notion of inertia (Gamma 2000). It is, however, not a probability in a strict mathematical sense, but it has to be interpreted in a qualitative way (Huggel et al. 2003).

The slope has a leading effect on the debris flow path. Various flow direction algorithms have been integrated and evaluated. All these algorithms are implemented in FLOW-R (Horton et al. 2008):

- D8: assigns the flow to only one adjacent cell. It is limited to directions of 45° and is very sensitive to small errors (Desmet and Govers 1996; Tarboton 1997; Erskine et al. 2006; Huggel et al. 2003; Endreny and Wood 2003).
- D_∞ : assigns the flow to one or two adjacent cells (Tarboton 1997).

- ρ_8 : stochastic method which gives a probability to every cell having an altitude inferior to the central cell. The path is randomly determined afterwards, producing a single flow direction (Fairfield and Leymarie 1991).
- Multiple flow direction: based on the previous method and considers the spreading over every non-zero cell in a continuous, and not random, way (Quinn et al. 1991).
- Multiple flow direction modified: an exponent of 1.1 was added by Freeman (1991).
- Parametric flow direction: a variable exponent was added to control the spreading (Holmgren 1994). The higher is the exponent, the more convergent the flow becomes (Eq. 5.1).

$$f_{si} = \frac{(\tan \beta_i)^x}{\sum_{j=1}^8 (\tan \beta_j)^x} \quad \text{for all } \tan \beta > 0 \quad (5.1)$$

where $i, j =$ flow directions (1 to 8), f_{si} = flow proportion in direction i , $\tan \beta_i$ = slope gradient indirection as defined above and x = variable exponent.

A weighting of the directions is included to take into account the persistence of the debris flow. Based on Gamma (2000), the weight is a function of the change in angle from the last flow direction (Eq. 5.2).

$$\begin{cases} f_{pi} = W_0 & \text{if } \alpha_i = 0^\circ \\ f_{pi} = W_{45} & \text{if } \alpha_i = 45^\circ \\ f_{pi} = W_{90} & \text{if } \alpha_i = 90^\circ \\ f_{pi} = W_{135} & \text{if } \alpha_i = 135^\circ \\ f_{pi} = 0 & \text{if } \alpha_i = 180^\circ \end{cases} \quad (5.2)$$

where $i =$ flow directions (1 to 8), f_{pi} = flow proportion in direction i , α_i = angle between the previous direction and the direction from the central cell to cell i , $w_{0,45,90,135}$ = weights for the corresponding change in direction.

Resulting probabilities are the combination of the slope-related algorithm and the persistence (Eq. 5.3).

$$f_i = \frac{f_{si} \cdot f_{pi}}{\sum_{j=1}^8 f_{sj} \cdot f_{pj}} \cdot f_0 \quad (5.3)$$

where $i, j =$ flow directions (1 to 8), f_i = total flow proportion in direction i , f_{si} = flow proportion from the slope-related algorithm, f_{pi} = flow proportion from the persistence, f_0 = previously determined flow proportion of the central cell.

Each cell with a probability more than a minimal threshold is then included in the path. For the spreading assessment of a source cell, the calculation thus integrates different paths or divergences in one run (Fig. 5.5). There is no need for random multiple runs as the field of all probabilities is covered (Horton et al. 2008).

1.0																				
	1.0	0.2	0.2	0.1	0.1									0.4	0.4					
		0.8	0.6	0.7	0.6	0.7	0.6	0.3	0.2	1.0			0.4	0.4		0.4				
			0.2	0.2	0.2	0.2	0.3	0.6	0.7	0.9	1.0	1.0					0.4			
				0.1	0.1	0.1	0.1	0.1					0.6		0.2	0.2	0.6	1.0	1.0	1.0
														0.6	0.6	0.4	0.4			

Fig. 5.5 Illustration of the conservative spreading. After Horton et al. (2008)

2. Runout distance calculation

The runout distance algorithms are energy-based calculations that define if a part of the flow can potentially reach the next cell of the DEM. Thus, they control the distance reached by the debris flow and in addition reduce the divergence. Therefore, the energy-based algorithms also influence the flow direction, as each cell that cannot be reached has a probability set to zero.

In a first regional assessment, the source mass is unknown. Thus, runout distance calculation is based on a unit energy balance (Eq. 5.4), a loss function and eventually a maximum threshold. This approach does not aim to represent exact physical processes, but to remain realistic (Horton et al. 2008).

$$E_{kin}^i = E_{kin}^{i-1} + \Delta E_{pot}^i - E_{loss}^i \tag{5.4}$$

where i = time step, E_{kin} = kinetic energy, ΔE_{pot} = change in potential energy and E_{loss} = loss.

The energy loss can be of two different kinds. The first case is a two parameters friction model (Perla et al. 1980) and the second is a constant loss characterized by an average slope angle along the path. The maximum threshold aims to limit the energy to reasonable values, mostly for the constant loss approach (Horton et al. 2008).

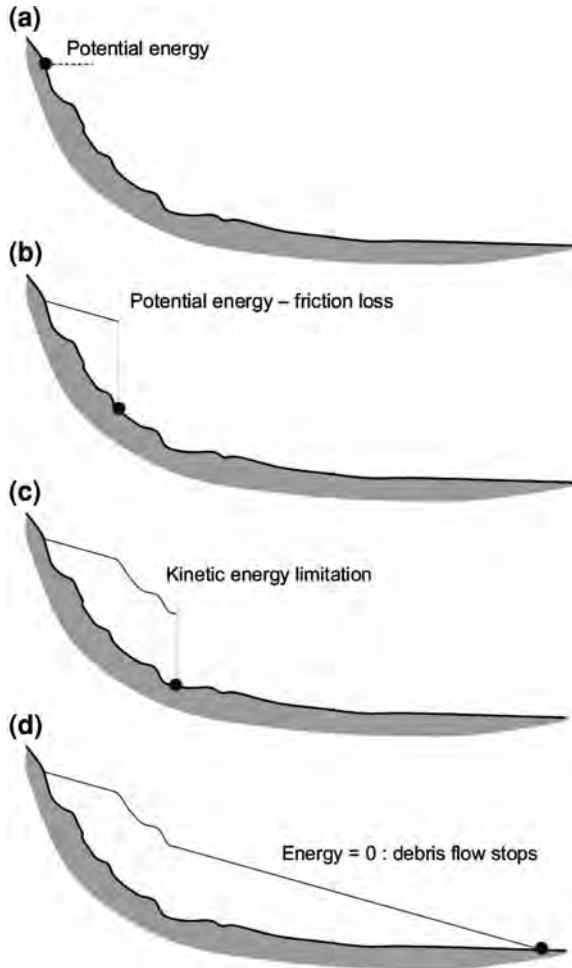
Figure 5.6 illustrates the runout distance calculation principles.

- (a) At the start, a source has a certain unit of potential energy (without considering the volume) regarding its adjacent cells downhill
- (b) During propagation, part of this energy is lost in friction
- (c) The kinetic energy is increasing and may reach the maximum threshold, leading to an energy line having the same shape as the terrain
- (d) The debris flow stops when the energy becomes null.

Results

The spreading areas of all sources are combined by keeping the maximum or the sum of the probability values. There are three outputs of the model: the sources, the propagation probabilities and the propagation kinetic energy (Fig. 5.7).

Fig. 5.6 Illustration of the runout distance calculation principles. After Horton et al. (2008)



5.6 Methodology

5.6.1 Landslide Inventory and Susceptibility

A landslide inventory is frequently the first step in landslide hazard identification. Several authors have outlined the importance of a uniform and well documented database to better define the potential unstable areas (Guzzetti et al. 2000; Malamud et al. 2004; Galli et al. 2008). Nowadays, the availability of high resolution digital data such as Aerial Laser Scanning digital elevation model, orthophotos and land use maps has made detailed mapping of geomorphological features possible (Chigira et al. 2004; Van Den Eeckhaut et al. 2007; Kasai et al. 2009).

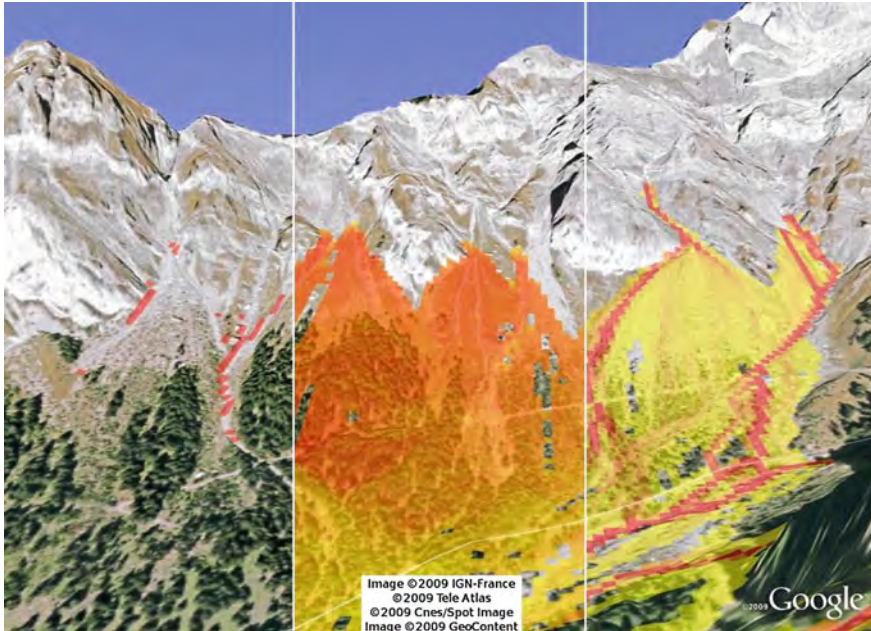


Fig. 5.7 Model outputs illustrations: sources, kinetic energy and probabilities (photos from GoogleEarth™)

5.6.1.1 Method

In both cases, Vaud County and Bagnes valley, the following method (Fig. 5.8) has been used to develop landslide (shallow and deep) inventories:

- (1) A visual analysis of high resolution DEM (hillshade and 3D viewing) and orthophotos to provide the main relevant geomorphological features (trench, scars, slope deposits, undulation, etc.)
- (2) An analysis of the 1:25,000 geological maps (www.swisstopo.ch) to include the sensitivity of lithologies to landslide and structural elements such as fault systems and tectonic lines
- (3) An analysis of the slope angle map to identify active erosion areas, morphological changes and assess the activity of some mass movements
- (4) The integration of registered historical events and fieldwork observations.

All the information related to the landslide inventory was stored in a GIS database. In order to improve the objectivity of the methodology, the database includes geomorphological criteria that have allowed the identification of the unstable area. The database contains five main attributes describing the characteristic of each detected landslide area:

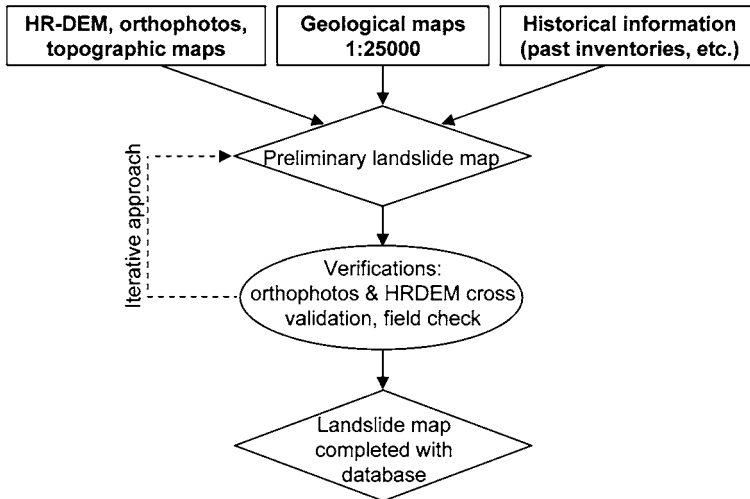


Fig. 5.8 Flowchart of the landslide inventory map creation

- (1) The document(s) used for its detection
- (2) Relevant geomorphological features
- (3) Main processes leading to the instability (pure gravity-driven, fluvial erosion of the toe, etc.)
- (4) Relative age (“old” when the geomorphological feature is smoothed and “recent” where the geomorphological feature of the landslide could be clearly differentiated compared of the surrounding topography)
- (5) Depth (shallow: 0–4 m, medium: 4–10 m, deep >10 m or unknown).

The uncertainty about the real extension and the present-day activity was also qualitatively assessed using descriptive terms (verified, probable and undetermined). When at least two geomorphological evidences are detected and reliable (landslide scar and deposit or landslide scar and morphological depression, etc.) the landslide polygon is considered as “verified or proved”. When morphological evidences are less distinct, with blur limits, the landslide polygon is considered as “probable or suspected”. If the landslide area has been delimited in previous inventory maps or in the geological map but the HRDEM and the orthophoto observations do not point out any geomorphological evidence, the attribute “undetermined” was employed.

The limiting factor in interpreting HRDEM hillshade 2D and its 3D visualization depends principally on the data artefacts and the application of intense human reworked areas. Artefacts are mostly related to the occurrence of locally very dense vegetation cover or occurrence of clouds during the data acquisition as well as some steep rugged topography that truncates the laser signal during the data acquisition. Human activities (urban areas, roads or agricultures) disturb the original surface and

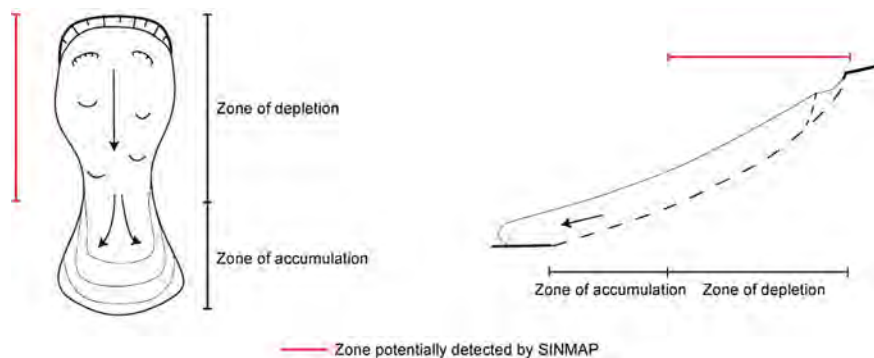


Fig. 5.9 Schematic representation of areas detected by the model SINMAP. Only the initiation zones are identified, while zones of accumulations are not detected (modified after Jaboyedoff et al. 2008)

remove the typical features associated with landsliding, in particular in case of ancient or dormant landslide. For these reasons, the landslide detection in strongly human–modified area needs to be supported by direct field investigations.

5.6.2 Shallow Landslides

The inventory provides information only on landslides that already occurred. To assess the potential extension of shallow instabilities and detect critical areas without any entry in the inventory, the SINMAP model (Pack et al. 1998) was used. This GIS-based approach allows a rapid and objective slope stability evaluation through a large territory based on relatively coarse information. SINMAP is limited to the detection of “starting zones” of shallow landslides (Fig. 5.9). It does not compute any runout. However, it is possible to couple with the propagation part of the models FLOW-R (Horton et al. 2008).

5.6.2.1 Methodology

The SINMAP (Stability INDEX MAPPING) methodology is based on the infinite slope stability model (Montgomery and Dietrich 1994) coupled with a steady state hydrological model, where the computed depth of saturated soil must be sufficient to sustain a lateral discharge proportional to the specific catchment area (Pack et al. 1998). The topographic wetness index used in SINMAP is a simplified version of the classical hydrological model as TOPMODEL (Beven and Kirby 1979). The main difference is that SINMAP does not account for a decreasing of the hydraulic conductivity with depth but assumes a uniform conductivity of the soil mantle (Pack et al. 1998). The factor of safety formulation became the following:

$$FS = \frac{C' + \cos^2 \theta [1 - wr] \tan \phi}{\sin \theta \cos \theta} \quad (5.5)$$

Where C' = dimensionless cohesion coefficient (integrating both soil and root cohesion and independent of soil thickness), θ = slope angle, ϕ = friction angle, r = water to soil density ratio and w = wetness index.

In Eq. 5.5 the wetness index defined for a given specific catchment area is represented by the ratio between the steady state recharge R [m/hr] and the soil transmissivity [m^2/hr], and is always equal or less than 1:

$$w = \text{Min} \left(\frac{Ra}{T \sin \theta}, 1 \right) \quad (5.6)$$

Where a = Specific catchment area and θ = slope angle

SINMAP allows entering variables uncertainties through the specification of lower and upper bounds for hydrological and geotechnical parameters adopting uniform distribution. These introduce a probabilistic approach in the calculation of the factor of safety that allows proposing different possible scenarios. The derived dimensionless susceptibility index (SI) is given by Pack et al. (1998):

$$SI = \frac{C' + \cos \theta [1 - \min(\frac{Ra}{T \sin \theta}, 1) r] \tan \phi}{\sin \theta} \quad (5.7)$$

Where C' = dimensionless cohesion coefficient, θ = slope angle, ϕ = friction angle, r = water to soil density ratio, a = specific catchment area, R/T = ratio corresponding to the steady state recharge relative to the effective rainfall quantity and the soil transmissivity.

The worst scenario is defined when $\tan \phi$, C parameters are close of the lower bound and R/T ratio close the upper bound (complete saturation). Areas under this worst case scenario, where FS is greater than 1, could be defined as unconditionally stable ($SI > 1$). Inversely, the best scenario is defined when the values for the parameters $\tan \phi$, C are close to the upper bounds and for the ratio R/T are minimal. Areas under this best case scenario, where FS is lower than 1, could be defined as unconditionally unstable ($SI = 0$). In between, different intermediate classes can be defined. Following Pack et al. (1998), six susceptibility classes are defined (Fig. 5.10).

5.6.2.2 Application of the SINMAP Model

The input data set for SINMAP consists of the DEM, the cohesion and the friction angle for the mechanical proprieties of the soil and the ratio R/T describing the hydrological conditions. The geomechanical parameter introduced in the model mainly emanate from the literature (Morrisey et al. 2001; Lan 2004; Salciarini et al. 2006) and from punctual in situ analyses (CPT and VAN test). The R (Recharge) parameter is more difficult to calculate. Hence, in our study, it was assumed to be the effective precipitation for 24 h rainfall with a return period of

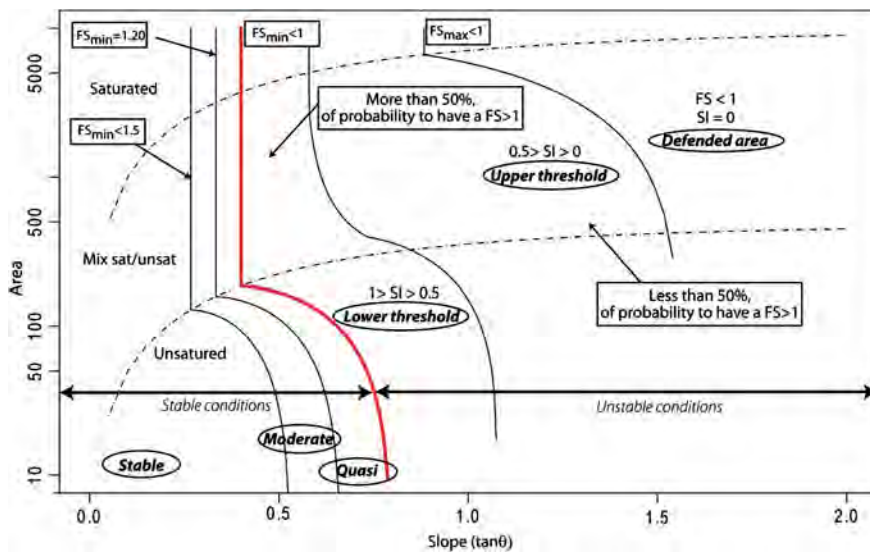


Fig. 5.10 Representation of the stability index in an Area-Slope space defining the different stability classes (modified after Pack et al. 1998)

100 years. The T (Transmissivity) parameter was derived from the hydraulic conductivity (minimal and maximal) of the different lithologies. These values have been chosen in order to give a maximal extension of the potential unstable area for rare event situations (Fig. 5.11).

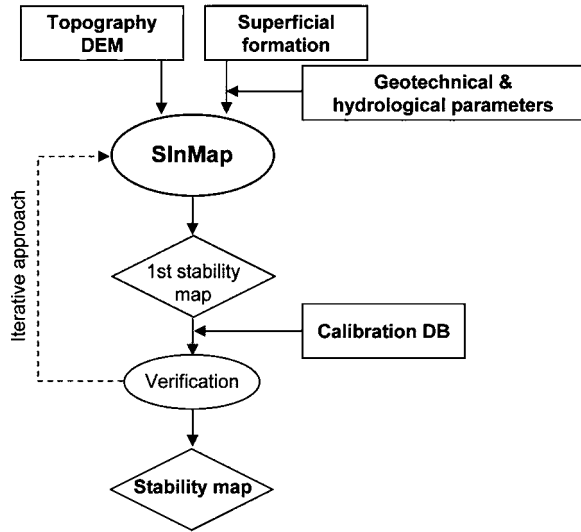
The final stability map was compiled following an iterative approach (Fig. 5.11). In the first step of the calculation, the applied geomechanical and hydrological parameters were deduced based on the available literature and adapted to the geological and land use conditions. A first susceptibility map was created and compared to the location of the well-know shallow instability. In a second step, the geomechanical parameters were adjusted for each lithology until the stability fit the know landslide areas. During this adjustment process, all the parameters remained in the range of values suggested in the literature.

5.6.3 Debris Flows

5.6.3.1 Introduction

Physical modelling of debris flows in the framework of regional mapping is difficult because of their complexity and the variability of controlling factors. GIS-based approaches associating an automatic detection of the source areas to a simple estimation of the debris flow propagation provide a substantial basis for a preliminary

Fig. 5.11 Flow chart describing the input data and the iterative procedure used for construction of the final susceptibility map



susceptibility assessment at regional scale. Figure 5.12 illustrates the principles of the methods used in both case studies, the Vaud County and the Bagnes Valley.

5.6.3.2 Source Areas Identification

According to Rickenmann and Zimmermann (1993) and Takahashi (1981), three criteria in a critical combination are relevant for a debris flow initiation: sediment availability, water input and slope gradient. As not all the lithologies produce the same amount of sediments, a detailed study of the area was conducted by means of a geological or lithological map. The upslope contributing area can account for water input. The slope gradient is a determining factor in triggering of debris flows (Takahashi 1981). Most debris flows occur from terrain with a slope higher than 15° (Rickenmann and Zimmermann 1993; Takahashi 1981). Some initiation thresholds of other factors can be expressed as a relation with the slope angle, as for the contributive area. Such a relationship was first defined by Heinimann et al. (1998), and a second one was assessed on the basis of the 1987 observations of debris flows made by Rickenmann and Zimmermann (1993) after the extreme rainstorms of 1987. The 1987 events in Switzerland could be considered as extraordinary, so it may be advisable to distinguish the obtained limits as an approximation for different probabilities of occurrence (Horton et al. 2008). Thus, two new limiting curves were established: the first one for rare events, based on the Heinimann et al. (1998) limit, and the second one for extreme events, based on Rickenmann and Zimmermann (1993) observations (Fig. 5.13). Both curves are bounded by the theoretical 15° limit gradient. Every point above a curve is considered as critical. The new limit for extreme events is given by Eq. 5.8:

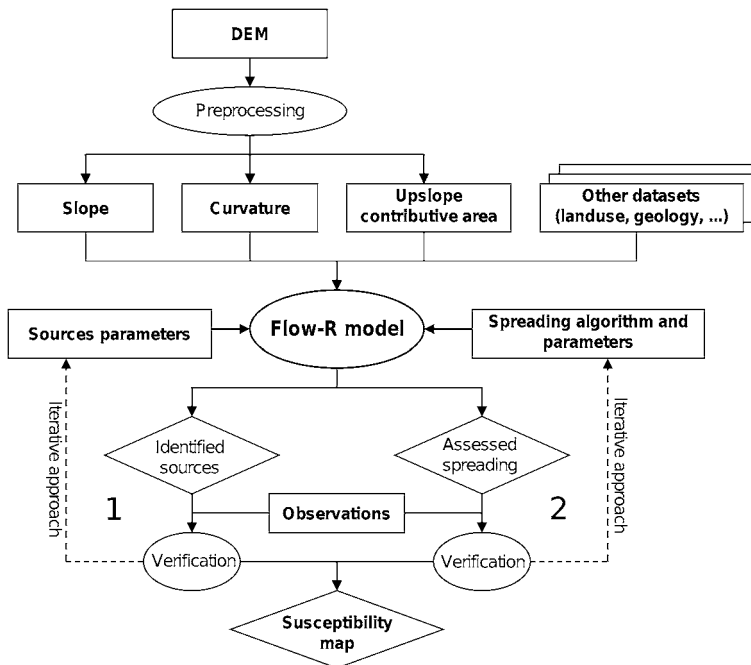


Fig. 5.12 Flow chart describing the input data and the iterative procedure used for construction of the final susceptibility map

$$\begin{cases} \tan \beta_{\text{lim}} = 0.31 \cdot S_{\text{UA}}^{-0.15} & \text{if } S_{\text{UA}} < 2.5 \text{ km}^2 \\ \tan \beta_{\text{lim}} = 0.26 & \text{if } S_{\text{UA}} \geq 2.5 \text{ km}^2 \end{cases} \quad (5.8)$$

where $\tan \beta_{\text{lim}}$ = slope gradient, S_{UA} = surface of the upslope contributing area.

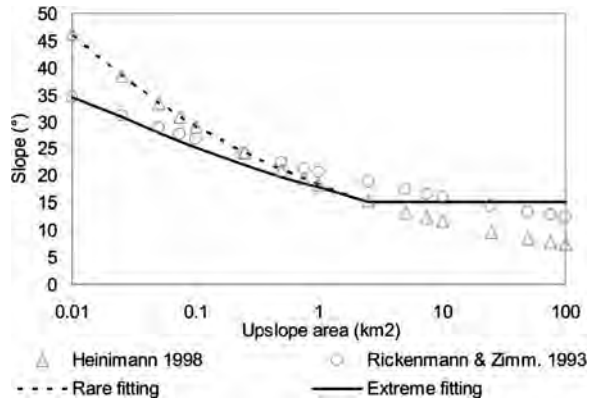
Another potential morphological characteristic is the curvature, as debris flows are found where the slope is concave (Delmonaco et al. 2003; Wieczorek et al. 1997). To allow an identification of gullies, the plan curvature, which is perpendicular to the steepest slope, was considered. The contributing area, the slope and the curvature are morphological data processed on the DEM.

Other data can be added to improve the source area accuracy, like a geological map or a landuse map. Those layers help identifying the sources previously selected that are not accurate due to another criterion that is not morphological.

5.6.3.3 Spreading Area Assessment

In FLOW-R, several spreading algorithms and parameters can be selected for debris flows to characterize the flow direction. Holmgren's algorithm was used in both applications because it is a good compromise between highly dispersive and overly channelised flows.

Fig. 5.13 Built gradient thresholds with regard to the upslope area for rare and extreme events. After Heinimann et al. (1998), Rickenmann and Zimmermann (1993), Horton et al. (2008)



For the energetic part of the propagation both the two parameters friction model and the constant loss function can be used for debris flow spreading.

5.6.4 Rockfall

A major issue in mapping rockfall hazard at regional scale is the identification of potential rockfall sources. Nowadays, high resolution topographic data (aerial/airborne LiDAR) can account for realistic landscape details even at a regional scale. For the preliminary assessment of rockfall runout areas, the integration of empirical or process-based methods in GIS environment have shown very promising results (Van Dijke and Van Westen 1990).

5.6.4.1 Identification of Potential Rockfall Source Areas

Potential rockfall initiation areas are identified by analysing the slope angle distribution (SAD) of the topography. A main factor required for the detachment of boulders is a slope greater than the frictional angle of the rock mass, hence, a steep slope (Heim 1932). According to Strahler (1950), the slope angle frequency distribution of a morphological unit (MU) of the relief varies randomly around its mean slope angle. The SAD expresses a range of slope angle values that are characteristic for a given morphology and rock type. The SAD can therefore be decomposed into several Gaussian slope angle frequency distributions that are characteristic of a specific morphological unit (GDMU) (Fig. 5.14a). In an Alpine topography for example, at least four morphological units (MUs) can be encountered:

- a. Low slope angles units corresponding to the plains formed by fluvio-glacial deposits.
- b. Mid/gentle slope angles units featuring the lower part of the hillslope, called here 'footslopes', and characterized by alluvial fans (debris flow) and landslides deposits.
- c. Steep slope angles units corresponding to the valley flanks covered with till deposits or consisted of rock outcrops lightly covered with vegetation
- d. Very steep slope angle units representing the cliff faces, outcropping areas and bare rock surfaces.

The sum of those Gaussian distribution must reproduce the SAD. The standard error can be minimized by using best-fitting methods, such as HISTOFIT (cf. Chapter Tools). Initial parameters can be defined according to the shape of the SAD, where the unsteadiness in the distribution tends to reveal a MU.

5.6.4.2 GDMU Interpretation

The slope angle distribution of each Gaussian curve in the SAD analysis can be seen as typical of the topography under consideration. Their mode can be considered as an average apparent slope angle of stability of their corresponding MU. Therefore, the SAD analysis and its decomposition in GDMU can be interpreted as follows (Fig. 5.14b):

1. A threshold angle is set at the intersection (noted A) between the two steepest MUs: the GDMUs "Steep slopes" and "Cliffs" (Rouiller et al. 1998). Above this slope angle, the cliffs MU become dominant over the steep slopes MU and can be potentially considered as rockfall sources. This is done independently of the local lithology and the land cover and includes therefore rocky slope surface lightly covered with vegetation.
2. There are some cases where the GDMU cliffs are missing within the SAD analysis. The highest GDMU is thus referred to the rocky steep slopes MU.
3. In very rugged landscape, such as the Alpine topography, the SAD analysis can reveal two GDMU cliffs. In this case, the lower value GDMU cliff is used to assess the threshold slope angle (see point 1).
4. When geo-thematic information (e.g. cliffs map, rocky outcrop map) is available, the SAD analysis can provide a second threshold angle taken at the mode of the GDMU steep slopes. Hence, cliffs zones and rocky outcropping areas lying above this threshold slope angle can be assumed as being above the average, often close to 35°, that is therefore more prone to be considered as potential rockfall source areas because these slopes will tend to readjust toward the average.

The SAD analysis provides finally two criteria to identify potential rockfall sources according to the morphology of the area under study. More details about this approach can be found in Loye et al. (2009).

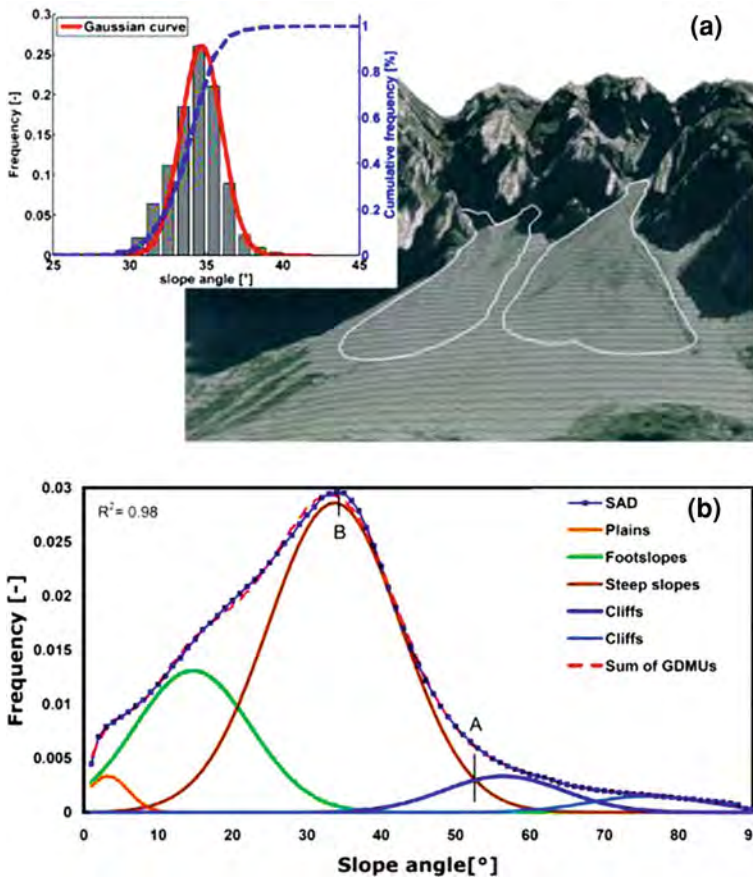


Fig. 5.14 **a** Example of the slope angle distribution of an undisturbed scree slope (delineated in white); The SAD shows that the slope angle values follow a normal distribution around an average close to 35° (orthophoto, swisstopo© 2005 SIT). **b** Example of the SAD of an alpine Valley featuring GDMU decomposition; **a** indicates the threshold angle above which the slope belongs dominantly to the cliffs and are therefore considered as potential rockfall source area; **b** indicates the mode of GDMU steep slopes. The two cliffs units represent two families of bare rock cliff faces lithologically distinct (Modified after Loye et al. 2009)

5.6.4.3 Assessment of the Maximum Runout Length

The maximum rockfall runout zones are estimated by a simple approach inspired from the shadow angle (Fahrböschung) method (Heim 1932) and generalized in 3D under the form of a cone. This model considers that an individual falling rock slides and rolls down the slope with a certain average friction angle ϕ_p (Scheidegger 1973; Evans and Hungr 1993). The angle of aperture ODF of the cone $90^\circ - \phi_p$ then determines the runout and is estimated as follows:

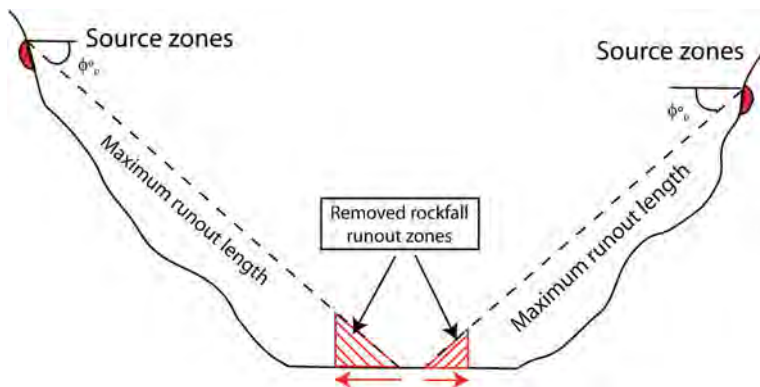


Fig. 5.15 Reduction of the length of the Fahrböschung line according to the rapid change of slope when boulders reach the bottom of the valley

$$\phi_p = \arctan\left(\frac{H_b}{X_b}\right) \quad (5.9)$$

where H_b is the height difference between the source area and the furthest runout reach and X_b the maximum runout length defined horizontally. The angle of aperture is defined empirically based on different aspects, such as information contained in the literature (Toppe 1987; Jaboyedoff and Labiouse 2003), comparison with known rockfall events taken from aerial photos and historical records or fieldwork. The results of several studies give an angle ϕ_p ranging between 28.5° and 35° (Crosta et al. 2001). For the lateral dispersion of the rockfall runout area, experience has shown that rockfall trajectories can be restricted to 15° from one side to the other of the greater slope gradient (Crosta and Agliardi 2003). As this approach doesn't require specific input parameters, such as coefficient of friction and bounding velocity, but is based exclusively on the topography (DEM), the cone angle method implemented in a 3D GIS environment is very convenient to be applied for large scale runout assessment. The runout area is then given as the maximum propagation zones that a boulder can reach. This first estimation can be further corrected for specific topography. For instance, source zones located high in steep mountain cliffs that overhang alluvial plains tend to model a maximum runout length that goes too far compared to field observations. Indeed, boulders reaching flat zones tend to greatly reduce their energy when the talus slope gets flat. Correction for valley-bottom can be then added to the previous consideration for particular topographical configuration (Fig. 5.15).

5.6.5 Snow Avalanches

To assess the susceptibility to snow avalanche, a two steps method was used: (1) Detection of the sources areas, (2) assessment of propagation zones. These avalanche susceptibility maps aim to provide a first overview of existing or

potential danger without any information on the intensity or the probability of occurrence of the phenomenon.

5.6.5.1 Source Areas Identification

For the detection of the sources areas, three criteria are used: (1) the slope, (2) the elevation, (3) the landuse, (4) source surface area. The slope is the most important factor to define avalanches source areas. In fact, 90% of the avalanches take place in slopes between 30° and 50° (Salm 1983; McClung and Schaerer 1993; Lied and Kristensen 2003). Depending of the region, there is a lower elevation that provide a lower limit to the occurrence of source areas. This limit is located at 1'100 meters above sea-level for the Swiss Alps (Gruber and Bartelt 2007). A landuse digital cover is available for the whole Swiss territory. For snow avalanches, we are interested in forest areas which influence their triggering. Depending on the goal of the study, source areas in the forested zones may or may not be ignored. The DEM resolution is another important limiting factor that defines the minimum area that can be detected for the avalanche sources. If the DEM has a high resolution, than this minimum area may be too small to be significant; a filter must then be applied to ignore these areas. In our case study in the Bagnes Valley, a morphological filter (opening) was applied.

5.6.5.2 Propagation Zones Assessment

Two models were used to estimate the avalanches propagation areas. One is based on a alpha-beta method (RAS, Sect. 5.5.2.3) and the other one on a Perla multiple-flows model (FLOW-R, Sect. 5.5.2.4).

RAS (Alpha-Beta Methodology)

The propagation is defined by a cone angle of propagation, alpha, using the software RAS. Alpha is automatically calculated for each source cell of the DEM using the alpha-beta method of Lied and Bakkehoi (1980). To estimate the propagation area, the alpha-beta relationship (Eq. 5.10) must be calibrated using an inventory of events (using the maximum propagations of avalanches).

$$\alpha = m \times \beta + n \quad (5.10)$$

Several sets of empirical coefficients were tested and the differences in the final results were negligible. Finally the coefficients of Adjel (1996) for snow avalanches in the Haute-Tarentaise (French Alps) were used because of the geographical proximity with our area and the large number of observations utilized ($\alpha = 0.82 \times \beta + 2.82$; $N = 168$). A minimum angle for alpha of 18° was used to avoid unrealistic long propagations.

Table 5.1 Susceptibility area classification methodology for snow avalanches

Susceptibility type	Propagation area		Known event
1. Probable	Flow-R and RAS	Or	Yes
2. Potential	Flow-R or RAS	And	No
3. Not susceptible	No one	and	No

FLOW-R

The details of FLOW-R, a multiple flow model with an energetic component, are described in Sect. 5.5.2.4. The main difference with the model RAS is that FLOW-R is much more sensitive to the topography. This has advantages, i.e. avoiding some overestimated lateral spreading, and some drawbacks, i.e. flat bottom valleys where it does not spread enough. Both models were used in the Bagnes Valley; both are very rough compared to the complexity of a snow avalanche and none of them allows the estimation of dynamic pressures, but they can be applied to large regions.

5.6.5.3 Avalanche Susceptibility Mapping

The susceptibility map of the Bagnes Valley was drawn combining the results of the two models: FLOW-R and RAS. The FLOW-R model tends to simulate the common avalanches (with a short return period) and the RAS model the extreme propagations. We chose to classify the susceptibility mapping in two categories, probable and potential. The Table 5.1 shows how we classify those two categories.

5.6.6 Flooding and Erosion

The goal of this chapter is to clarify the methods used to develop an indicative mapping of flood hazards on the territory of an Alpine valley. The study focuses on the main waterway and tributary streams crossing the valley and its purpose is to identify the areas subject to flooding. The proposed method is based on five distinct stages summarized in Fig. 5.16.

The five stages allow to identify the potential sources of overflow and the model FLOW-R allows to simulate the propagation of those.

5.6.6.1 GIS Analysis

The analysis of geographical documents allows the characterization of the alluvial geomorphology of the waterways present in the studied area. GIS is extremely useful for support, which can improve the detection of possible source of

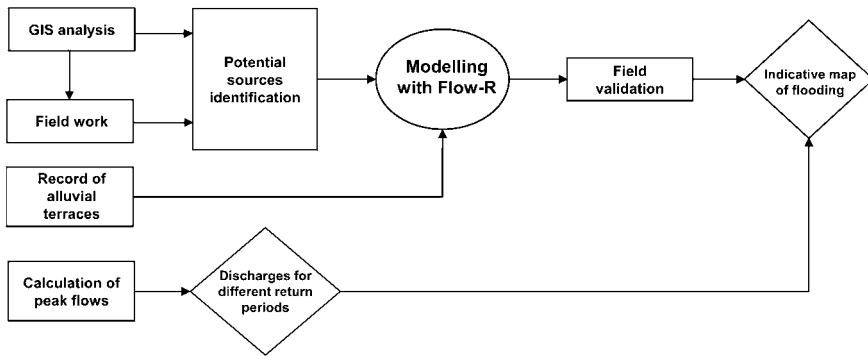


Fig. 5.16 Stages contributing to the development of the analysis

overflows. A high-resolution Digital Elevation Model allows the calculation of the flow direction, which helps to identify all the waterways that must be investigated next steps of the analysis. Using aerial photography observations, it is possible to identify eroded areas that may provide material which can dam the river. The geological maps are also an important indicator of potential erosion areas. A field survey is necessary to complete and validate the preliminary observations. Different factors could be extracted from the GIS analysis:

- alluvial plains and the different levels of alluvial terraces which correspond to different levels that can be reached by potential outburst;
- an assessment of bridge capacity is conducted.
- identify areas of bank erosion representing potentially mobilized material and areas of possible collapse;
- known elements, (i.e.: geological map, student works, and cadastre of events). The inventory of past events can improve the mapping and must be considered in the analysis. In fact, historical information is usually a good indicator for mapping hazard areas. It provides additional information on possible events and improves the evaluation of hazard.

5.6.6.2 Field Work

Field work is a necessary step to confirm or disprove the observations made during the GIS analysis. Moreover, it helps identifying pathologies of the hydrographical network, such as erosion banks, mobilizable material (trees with an eroded base, bank erosion, landslides along the waterway, important sediments deposits, etc.) or indices of past floods. These elements are used to calibrate the model FLOW-R described below.

5.6.6.3 FLOW-R Modelling

The model FLOW-R (Horton et al. 2008) is adapted to hydrological flows without material. It allows evaluating the propagation of flood. The location of sources of potential overflows areas is given according to two criteria:

- at the top of the channel for tributary streams and for the main river
- along the streams for simulation of dams.

Regarding the identification of the source areas of potential overflows, various criteria are chosen:

- the presence of a low bridge;
- the narrowing of the waterway;
- an obstacle to the flow;
- banks with a low level;
- the visual presence of past overflows;
- mobilized materials in abundance obstructing the waterway or threatening to obstruct it.

The algorithm used for spreading the water is the multiple flow direction algorithm, which makes possible to limit the lateral spreading by the topography only. Regarding the energy algorithm, the chosen approach is a linear decrease of the spreading energy.

5.6.6.4 Calculation of Maximum Discharge

The model Hydriff (OFEG 2003) of the Swiss Confederation is used to estimate the maximum discharge. It estimates the discharge based on the size of the watershed, the length of the hydrographical network and a growth factor, depending the considered return period and the catchment area deduced using standard GIS functions. This method is derived from multi-scale methods and it is applied for watersheds of medium size (1–500 km²).

5.6.6.5 Record of Alluvial Traces

A geomorphological analysis of the alluvial terraces is necessary in order to assess the historic levels of the river is taken into account in hazard mapping as, infrastructures present in the major and minor stream bed can be potentially threatened by rising waters. A distinction is made between the three following levels: sedimentary deposits from the river, lower terraces (representing the first terrace level above the river) and the upper terraces (representing the second terrace level above the river). The data used for this analysis are aerial photos and geological maps. The result of the analysis is integrated in the susceptibility map.

5.6.6.6 Classes and Scenarios

To provide a focused analysis, two classes for the assessing hazard are defined. The first class is related to the propagation resulting from a simulation in the channel. The second class is related to the propagation simulated using a chosen source outside the channel, simulating a jam.

The methods described in this chapter are applied to four distinct geographical sections (Table 5.2), namely:

- tributary streams
- the threat of jams in tributary streams;
- the main river
- the threat of jams in the main river.

5.7 Results

5.7.1 Landslide Inventory Map

5.7.1.1 County of Vaud

In the county of Vaud, a former instability database was created in the 1990s by aerial photo analysis and field investigation (Noverraz 1995). This database contains 6455 landslides differentiated according to their depth (shallow, medium and deep landslides) and their activity (geomorphological evidences). The first step of the inventory updating was to check and redraw landslide perimeters based on the high-resolution DEM (HRDEM) and digital orthophotos. The second step was to identify and redraws instabilities indicated by the geological maps (Geological Atlas of Switzerland 1:25,000; www.swisstopo.ch) on the HRDEM. Finally, the HRDEM of the entire county was re-examined in order to identify new instabilities.

Finally the new database contains 8501 slope instabilities. The mapped instabilities cover around the 8% of the study area which is close to the 6% obtained for the whole Switzerland by Lateltin et al. (1997). 2718 landslides were identified as not correctly delimited on the previous inventory and they were redrawn based on the new HRDEM. For 608 landslides described in the former inventories, the HRDEM analysis could not provide any valuable delimitation (Fig. 5.17). This was usually the case for landslides in human-modified slopes or near urban centres. For these landslides, a distinctive specification in the attribute table has been introduced. The analysis of the available geological maps has made possible to identify 909 new instabilities. Most of these instabilities, identified during fieldwork, affect only small areas (<10,000 m²) along river banks. During the

Table 5.2 Different scenarios analyzed and their characteristics for floods and erosion

Type of area	Tributary stream	Jam in a tributary stream	Main river	Jam in the main river
Type evaluation	Flow-R modelling and geodata analysis, Field work	Field work Flow-R to model the spread	Flow-R modelling and geodata analysis, Field work	Field work Flow-R to model the spread
Documents and support Criteria	Geographical data, geological map	Geographical material, geological map, existing hazard map Bridges, shrinkage, accumulation of material in the stream, barriers to the flow, low banks	Geographical data, geological map	Geographical material, geological map, existing hazard map Bridges, shrinkage, accumulation of material in the stream, barriers to the flow, low banks
Source areas	Source of the river, in the drainage channel	Overflow over the top of the bank	Source of the river	Overflow over the top of the bank
Class	Probable	Potential	Probable	Potential

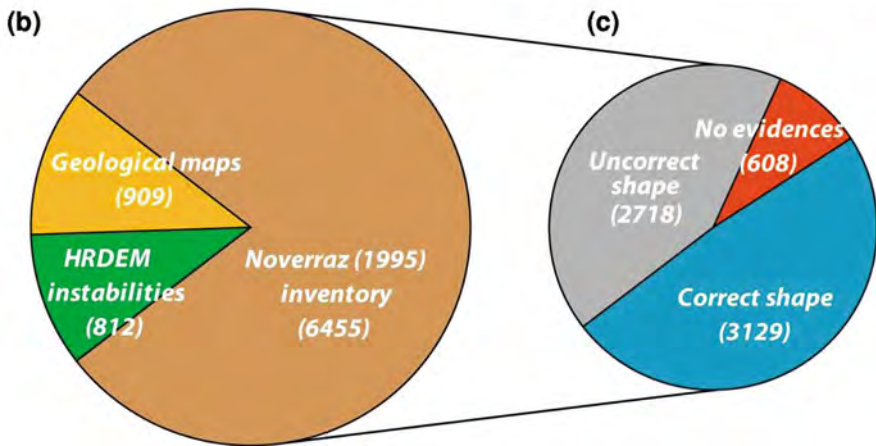
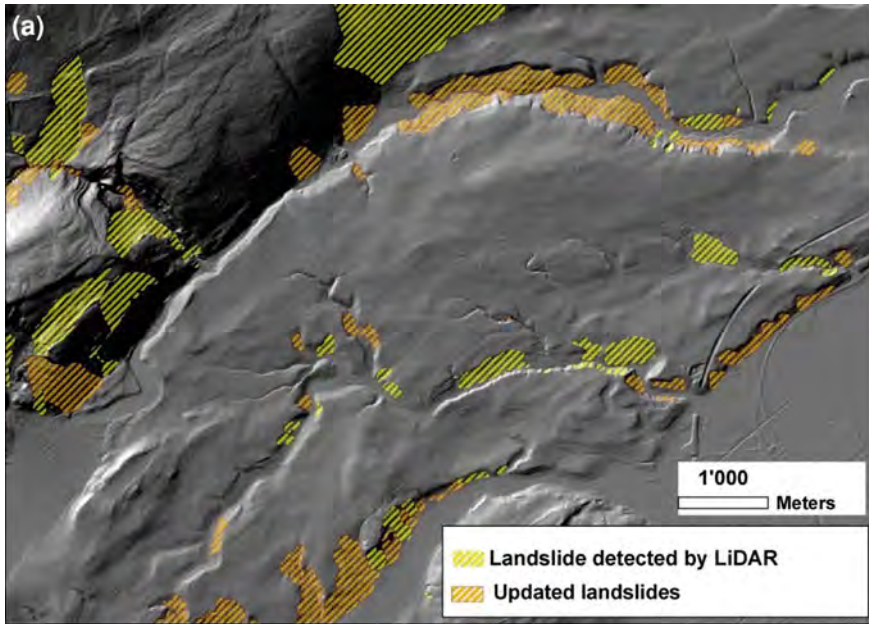


Fig. 5.17 Summary of the main results of the updating the landslide inventory map. **a** Origin of the different landslides listed in the database (hillshade, swisstopo© 2005 SIT). **b** Results of the revision of the Noverraz (1995) inventory

reanalysis of the entire Vaud County, 812 new instabilities were identified only using the HRDEM and the orthophotos. Most of these new detected instabilities were identified in the Plateau area (457 new instabilities) and in the Jura regions (183 new instabilities).

5.7.1.2 Valley of Bagnes

Contrary to the County of Vaud, no pre-existing landslide database was available for this region. The landslide inventory map of the Val de Bagnes was thus created based on the Geological Atlas of Switzerland 1:25,000 (www.swisstopo.ch), the HRDEM, the DEM25 and orthophotos. As the area is relatively small (300 km²), some fieldwork was conducted to check this inventory.

Based on the geological maps, 13 shallow landslides and 132 medium landslides were inventoried, representing almost 40% of the total number of landslides. Among them, 42 cannot be confirmed by geomorphological evidences on DEM or field investigations.

By comparing HRDEM, DEM25 and orthophotos, 21 new shallow landslides and 98 new medium landslides were detected (34% of the total). 67% of the landslides detected on the geological maps were updated based on these other documents. The 15 deep-seated slope gravitational deformations (DSGSD) were inventoried only based on DEM analysis.

Field investigations were consequently performed in order to verify the document analysis and to complete the inventory. At the end, each landslide was classed as “proved” or “suspected”, according to the criteria explained in the Sect. 5.6.1.1.

Finally, 15 DSGSD, 245 medium and 102 shallow landslides were identified in the Val de Bagnes.

5.7.2 Susceptibility Map of Shallow Landslides

5.7.2.1 Vaud County

The input dataset of SINMAP consists of the DEM and a few parameters quantifying the hydrological and geotechnical conditions. Due to the large area to be mapped, the LiDAR DEM was re-sampled into a grid of 15 x 15 m cell size. The study area was divided into three main zones corresponding to the 3 main tectonic subdivisions (Jura, Plateau and Alps). The lithology variation was introduced by the mean of the “Geotype maps” covering the entire Vaud area (Turberg et al. 2008). The Geotype map is a kind of lithological—genetic map in which the formations with similar rock or soil proprieties are merged together.

For the hydrological parameters, the effective precipitation for 24 h rainfall with a return period of 100 years was estimated for the different region based on the Hydrological Atlas of Switzerland (2006). The model calibration was performed based on pre-existing inventory maps (Noverraz 1995) and orthophoto interpretations. SINMAP model was originally developed to model translational landslides in a hilly topography. Its direct application to a more rugged topography like the Alps is not perfect. In fact, for steep mountain slope the SI will be very low even if the effective soil thickness is too thin to develop a landslide-type

instability. To avoid this problem, all the bedrock outcrops were delimited with the 1:25,000 topographic vector map and the source area identified during the rock susceptibility map. In these zones the geomechanical parameter, the transmissivity and the recharge parameters were adapted to keep the SI high. The final raster map was cleaned and smoothed of small scale artefacts using a majority filter (ArcGIS®) based on four contiguous neighbourhoods.

According to the goal of the susceptibility mapping project, the results of the SINMAP analysis were reclassified in two different ways (Fig. 5.18):

A map containing a single susceptibility class for the pixels where the Stability index is lower than 1.

A map containing three susceptibility classes corresponding to a SI between 1 and 0.5, (lower threshold) between 0.5 and 0 (upper threshold) and equal to 0 (defended).

5.7.2.2 Bagnes Valley

As for the application to the Canton of Vaud, the input dataset for SINMAP consisted of a HRDEM degraded to a 10 m cell size grid below 2000 m a.s.l. and the DEM25 above 2000 m. a.s.l. However for this area, there was no numerical document which distinguishes the type of substratum such as the Geotypes of the Vaud County. The first step of the processing was then to identify the superficial formations. To perform this classification, the information of two documents was used: the land use occupation indicated by the Vector25 and the 1:500,000 vectorized geological maps. As shown in the Fig. 5.19, twelve classes of soil with distinct geotechnical parameters have been extracted: alluvium, breccia, bedrock, dense forest, flysch, high altitude soils, moraine, reworked soils, schist, scree deposits, sparse forest and sparse shrubs.

The geotechnical and hydrological parameters assigned to each class were taken from Morrisey et al. (2001), Lan (2004), Salciarini et al. (2006), Hydrological Atlas of Switzerland (2006). To calibrate the model, 67 shallow landslides that occurred during summer 2009 were inventoried in various types of superficial formations (Fig. 5.20).

The results of the SINMAP analysis were provided in one map containing six susceptibility classes corresponding to:

- Class 1: $0 < SI < 0.001$ Defended area
- Class 2: $0.001 < SI < 0.5$ Upper threshold
- Class 3: $0.5 < SI < 1$ Lower threshold
- Class 4: $1 < SI < 1.25$ Quasi-Stable
- Class 5: $1.25 < SI < 1.5$ Moderate Stable
- Class 6: $1.5 < SI$ Stable

Finally, 46% (almost 140 km²) of the Bagnes Valley has a stability index lower than 1. The major part (52%) of the susceptibility areas ($SI < 1$) are in the class 3 “Upper threshold”.

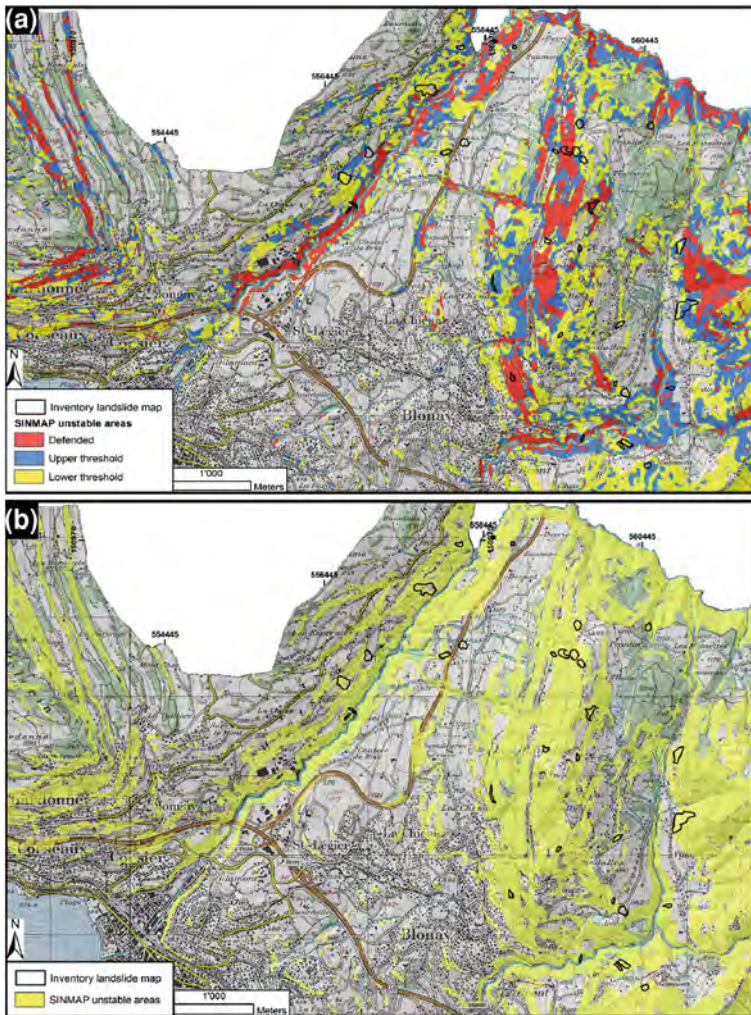


Fig. 5.18 Close up of the shallow landslide susceptibility map, showing the good agreement with the inventoried shallow landslide. **a** 3 classes map and **b** single class map (hillshade and topographic map, swisstopo© 2005 SIT)

5.7.3 Debris Flows

5.7.3.1 Vaud County

The DEM available for the Canton de Vaud territory is a laser DEM with a resolution of 1 meter. In order to reduce the processing time and to be more consistent with the phenomenon scale, it was degraded to a 10 m cell grid.

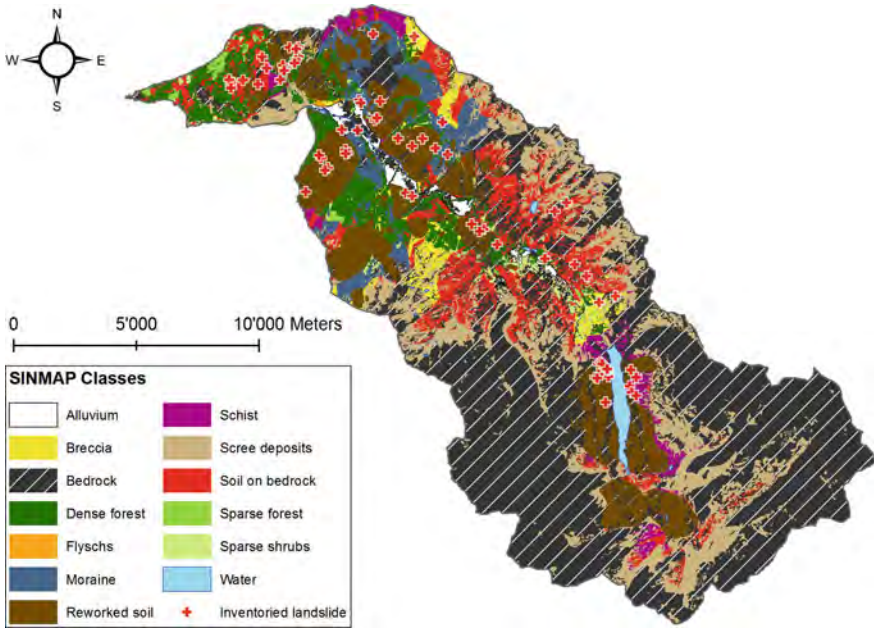


Fig. 5.19 Representation of the classified superficial formations issued from the Vector25 and the 1:500,000 geological atlas of Switzerland

Several types of processes were addressed in the study of this region: debris flows, deposits remobilization, mud flows and hyperconcentrated flows. Only the debris flows are presented hereafter.

Source Areas Identification

Although the curvature is often used to recognize the gullies, there is no admitted threshold. A limit had to be established on the basis of aerial photographs and the analysis of the 10 m DEM. For this study area, a curvature of $-2/100 \text{ m}^{-1}$ was found as optimal on the basis of the analysis of orthophotographs (Horton et al. 2008).

The minimum flow accumulation threshold chosen was of 1 ha, after calibration on observed debris flows. The extreme threshold was selected in accordance with the work objective which is to make an indicative map, supposed to cover the worst case scenario (Horton et al. 2008).

The lithology was taken into account by means of a “geotypes” map (Perret 2007; Turberg et al. 2008), which contains uniform and complete information about surface formations for the whole study area. The selected lithologies are debris flow prone rocks (marl, slate, siltstone) and slope deposits.

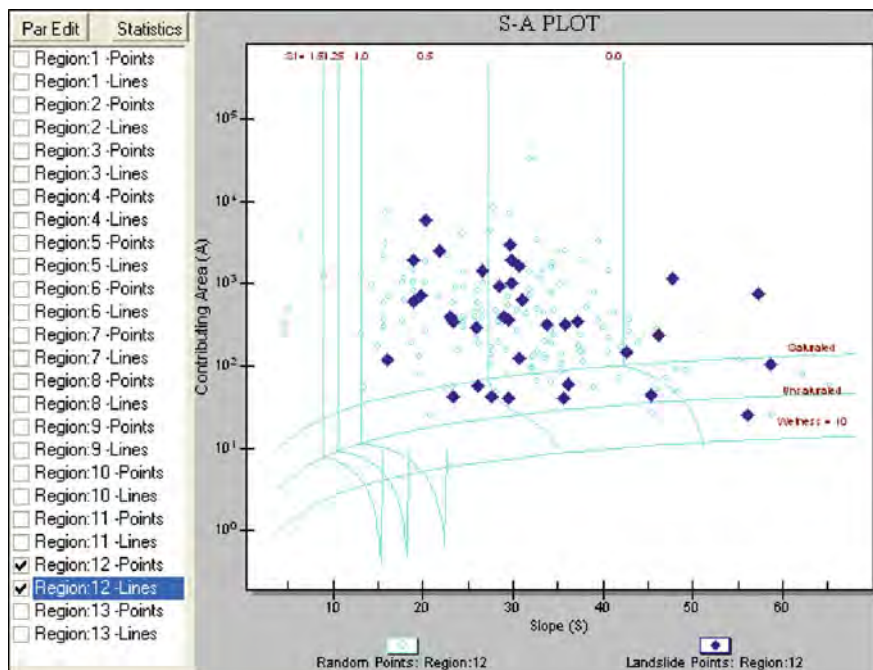


Fig. 5.20 S-A plot within SINMAP allowing the calibration of geotechnical and hydrological parameters for reworked soils according to shallow landslides inventoried

Landuse maps helped to detect certain inaccurate sources, located in developed areas or due to man-made infrastructures. Outcropping or suboutcropping rocks were also excluded from potential sources (Fig. 5.21).

Spreading Area Assessment

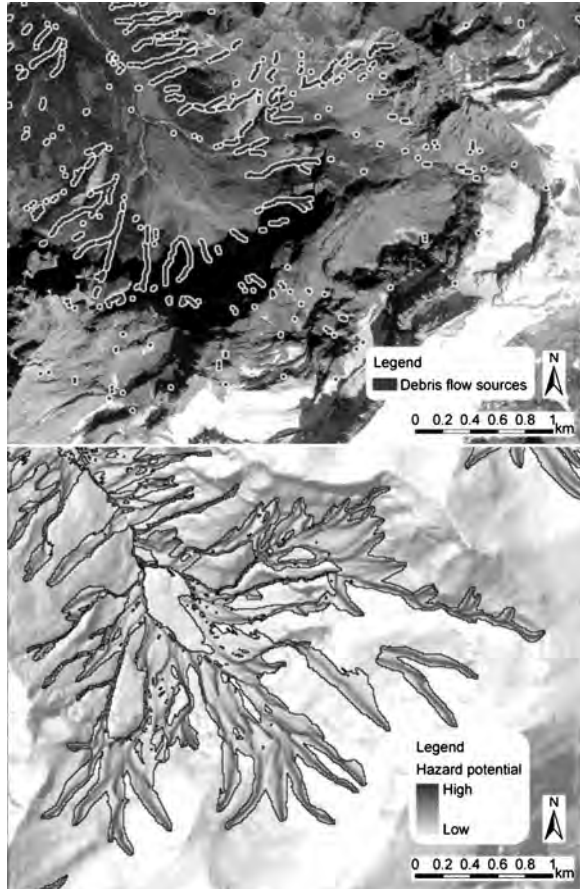
The Holmgren's algorithm was chosen because it best fits the events that can be observed on orthophotographs. Its exponent was set to 4, as proposed by Claessens et al. (2005) on the basis of field and laboratory measurements.

The probable maximum runout is characterized by an average slope gradient of 11° (Huggel et al. 2002). The chosen energy threshold was set to a maximum velocity of $15 \text{ m}\cdot\text{s}^{-1}$. The observed maximum velocity among various debris flows events in Switzerland is 13 to $14 \text{ m}\cdot\text{s}^{-1}$ (Rickenmann and Zimmermann 1993).

5.7.3.2 Bagnes Valley

The main difference between this case study and the County of Vaud is that source areas were divided in two classes: proved and potential. In addition field investigation was carried out in order to evaluate the real debris flows susceptibility.

Fig. 5.21 Identified debris flows sources and corresponding spreading in the Diablerets region (hillshade, swisstopo© 2005 SIT)



The FLOW-R model was applied, and four test sites in the valley were chosen to calibrate the model parameters for the source areas detection and the propagation. The datasets used in this case are: a 10 m resolution DEM, the 25 m land-use map (Vector25), the topographic maps, the orthophotos and the local inventory of historical debris flows events.

Source Areas Detection

As describe in [Chap. 6.3.2](#), at least the slope, the curvature (Delmonaco et al. 2003) and the water input (Rickenmann and Zimmermann 1993; Horton et al. 2008; Jaboyedoff et al. 2008) are needed to detect the debris flow sources. The criteria used are described in [Table 5.3](#):

In the case of Val de Bagnes, the landuse and the geological information were also taken into account in order to suppress source areas detected on bedrock or

Table 5.3 Debris flows source detection criteria

Criteria	Slope	Curvature	Water input
Parameters	>15°	-2/100 m ⁻¹	1 ha

Table 5.4 Sources classification methodology

Source types	Past event	Phenomena evidences	Debris
Proved source area	Recorded	Recent evidences of debris flow activities	Debris stock sufficient for debris flow triggering
Potential source area	No	record	Fossil evidences of debris flow activities or suspected activities
Debris stock sufficient for debris flow triggering			
Incorrect detection	No	record	No activity evidences
Not enough debris stock for debris flow triggering			

Table 5.5 Spreading parameters

Criteria	Inertia	Flow direction algorithms	Runout distance calculation	
			μ	M/D
Parameters	Default mode	Holmgren exp. 6	0.09	30

man-made structures. The source areas classification is a crucial step in the creation of the debris flows susceptibility map. In this case, a distinction between proved, potential and incorrect detected source area has been made. The Table 5.4 presents the different parameters for the different kind of sources.

Propagation Area Assessment

Field observations and numerical data analysis (orthophotos, DEM, topographic maps) were used to calibrate the model parameters (Table 5.5). After several tests, the 2-parameters friction model (Perla et al. 1980) was chosen because it provides the best results comparing with the archived events.

The propagation area classification depends on the sources area classification. For example, if a source area is classified as “probable”, the spreading area will be “probable” too. For the *probable* propagations, a distinction was made between the probabilities that are under 2% (*probable danger*) and higher than 2% (*strong probable danger*) (FLOW-R, Sect. 5.5.2.4).

In two watersheds, historical debris flow propagations are longer than expected within a normal parameterization of the model. This is due to the high amount of loose material that can be mobilized, their important size or hydrological characteristics. For these special cases, the method was adapted to obtain the known maximum runout distances. An average propagation slope angle of 5° with an energy threshold of 15 m/s (the other parameters are the same) were chosen.

Detection and Propagation: Example of the Merdenson

The Fig. 5.22 shows the result of the source detection and debris flow propagation simulation for one watershed of the Bagnes valley. This region contains active debris flows gullies and a main road is often affected by events (numbers 1 and 2 in Fig. 5.22). In this example, the sources detected by the model correspond well with the field observations, confirming a good correlation between the model's simulated propagation and field investigations (Figs. 5.22, 5.23), picture taken from the point 3, 4 and 5). Point 5 in Figs. 5.22 and 5.23 represents the debris flow triggering area and the black arrows shows the most probable propagation path.

5.7.4 Rockfall Susceptibility Map

5.7.4.1 Vaud Territory

The decomposition of the slope angle distribution in Gaussian populations was performed with the 1 m cell size DEM of the Vaud County (2800 km²). The potential source zones were aggregated to a cell size of 25 m and the run-out model was run with a DEM of same cell size. The runout areas were computed with CONEFALL. The territory was divided into 5 five distinct zones: the Alpine part is composed of the Helvetic, Ultrahelvetic and Prealpines Nappes; the Jura Mountains and the molassic Plateau are the last two zones. The slope angle distribution decomposition in Gaussian distribution was performed with HISTOFIT. Results of the threshold slopes angle are summarized in Table 5.6.

Therefore, potential rockfall sources were defined by all slopes belonging to the units cliffs defined according to the slope angle histogram decomposition. Moreover, all rocky outcrops and cliffs available from the 1:25,000 topographic vector map where their slope angle is steeper than the mode of the unit steep slopes were added to the map of potential rockfall sources. Finally, a minimum size of 10 m² was set in order to consider a surface as rockfall source zones. This had the advantage of filtering out possible artefacts contained in the DEM without removing any essential information.

For the runout area assessment, CONEFALL was applied to each potential source defined previously. The angle of aperture $\phi_p = 33^\circ$ was the best compromise with all the information collected through the available documents Fig. 5.24. Furthermore, an angle of 33° has the advantage of including a potential

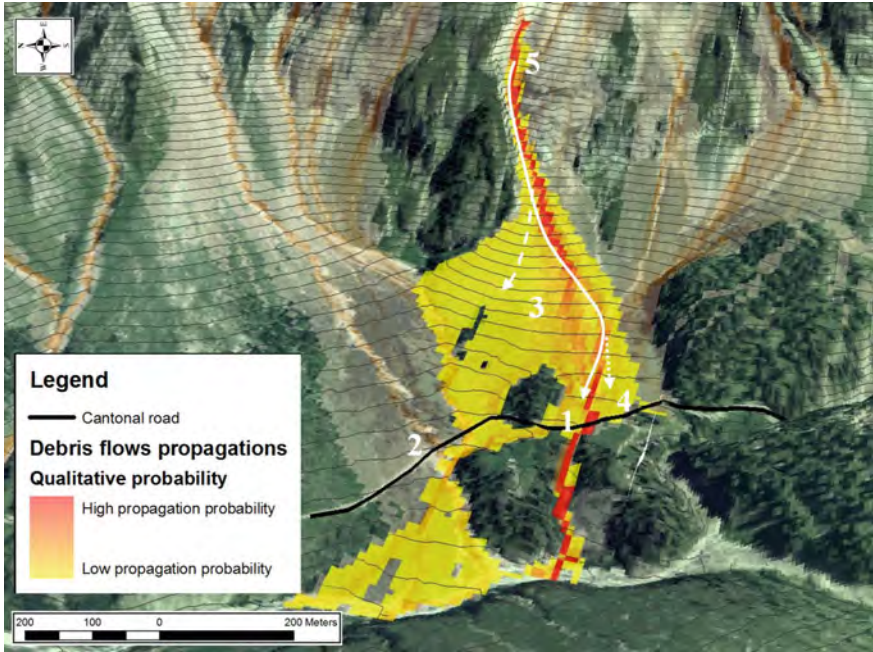


Fig. 5.22 Example of spreading assessment in the Mauvoisin region (orthophoto and isolines: ©swisstopo)



Fig. 5.23 Field investigation. Correspondences with the spreading assessment in Fig. 5.22

Table 5.6 Threshold slope angles above which rockfall source areas are potentially considered

Location	HMA	Threshold angles for	
		A. Minimum threshold angle for the unit cliffs	B. mode of the unit steep slopes
Alps	Helvetic	54°	36°
	Préalpes Médiannes	53°	34°
	Ultraschweizer	49°	33°
Plateau	Molassic Plateau	46°	30°
Jura	Jura Mountains	46°	32°

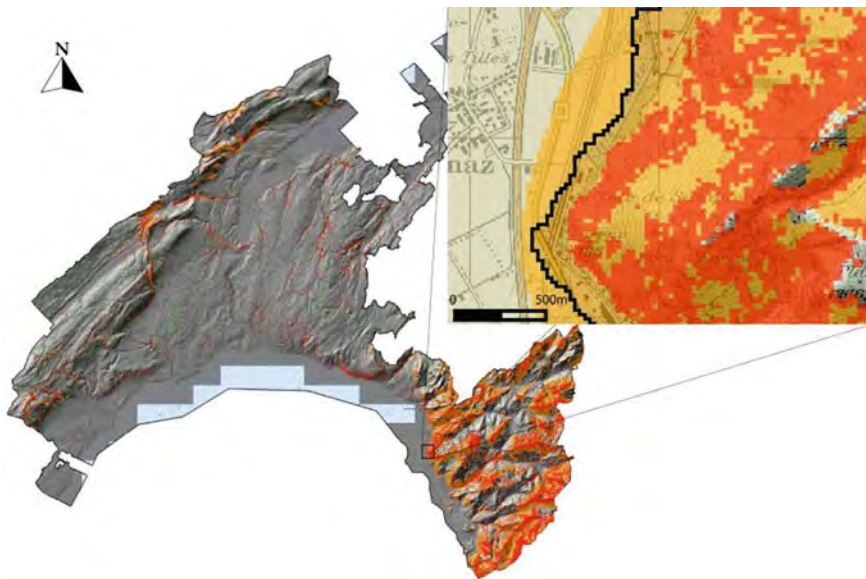


Fig. 5.24 (Left) Susceptibility rockfall hazard map for the canton of Vaud (Switzerland). Rockfall sources zones are drawn in red and the runout perimeters in brown. (Right) Correction for the Valley-bottom performed on the maximum runout area, limiting the very unlikely propagation of boulders far into the flat lands (light beige) (hillshade and topographic map, swisstopo© 2005 SIT)

remobilization of the screes located beneath the rockfall sources area, which usually have a mean slope angle of 35° (Loye et al. 2009).

The correction for the flat bottom valleys was performed when a surface bigger than 2.5 km² has a mean slope gradient lower than 11°. Based on orthophotos analyses of scree deposits along flat zones, maximum runout length of boulder reaching those plains was limited to 60 m for tributaries valley-bottom. This limit was expanded to 100 m in the alluvial plain of the Rhône Valley due to its higher falling velocities resulting from the greater size of its valley flanks (Fig. 5.24).

Table 5.7 Threshold slope angles above which rockfall source areas are potentially considered in the Val de Bagne

HMA	HRDEM	DEM25		
	A. Minimum threshold angle for the unit cliffs	B. mode of the unit steep slopes	A. Minimum threshold angle for the unit cliffs	B. mode of the unit steep slopes
Acid rocks	47°	36°	46°	35°
Basic rocks	Not present	48°	32°	
Conglomerate	52°	34°	45°	32°
Flysch	52°	36°	47°	35°
Limestone	52°	37°	46°	36°
Moraine	51°	30°	38°	30°
Marble and breccia	50°	35°	46°	33°
Schists	49°	35°	48°	32°

5.7.4.2 Bagnes Territory

To identify to potential rockfall source areas, the homogeneous morphometric areas HMA were extracted from the 1:500,000 vectorised geological Atlas of Switzerland. Then the Slope Angle Distribution for each HMA area was extracted on the HRDEM for altitudes lower than 2000 m and on the DEM25 for the entire study area.

The SAD decomposition in Gaussian distributions was performed with the tool HISTOFIT. As for the Canton of Vaud, the potential rockfall source areas resulted from a combination of two sources defined by minimum threshold angles (Table 5.7): Areas which have a slope angle higher than the threshold angle of slopes belonging to the population cliffs;

Areas of the Vector25 mapped as crops which have a slope angle higher than the mode of the population steep slopes.

The differences of threshold slope angles detected with the HRDEM and the DEM25 were expected. As shown in Loye et al. (2009), the bigger the resolution, the lower the threshold angle for the same cliff. Source areas less than 10 m² were filtered out to avoid artefacts due to potential local errors of the DEM.

Two propagation simulations were performed in order to estimate two susceptibility classes, one with CONEFALL and one with FLOW-R (Fig. 5.25). Both computations were performed on the DEM25 to ensure continuous and homogeneous results. According to previous detailed works on the valley of Bagnes and the experience of the county of Vaud, the propagation angle used was 33°. Even if FLOW-R is based on constant friction loss which relates this model to the shallow angle method, the algorithms simulates far fewer propagations than pure geometrical models as CONEFALL. Furthermore, the multiple flow direction algorithm (Holmgren 1994) used in FLOW-R calculates more channelized runouts.

The final results were presented in two classes: (1) Probable propagation areas, corresponding to runout assessed by FLOW-R with higher susceptibility, (2) potential propagation areas, corresponding to runout assessed only by CONEFALL with lower susceptibility.

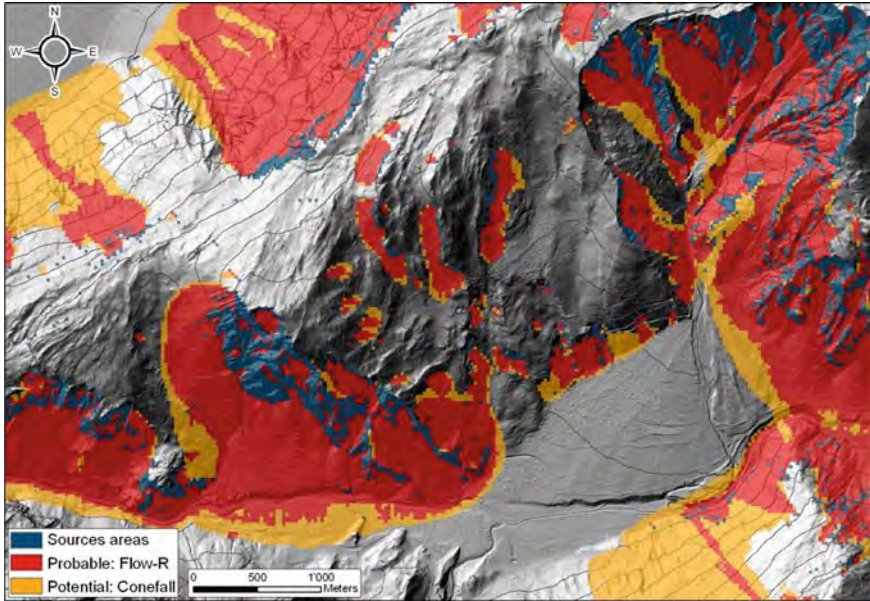


Fig. 5.25 Rockfall susceptibility map. The runout was separated in two classes: probable susceptibility, which belongs to FLOW-R processing, and potential susceptibility, which belongs to CONEFALL processing (hillshade and isolines: ©swisstopo)

5.7.5 Snow Avalanches

5.7.5.1 Bagnes Valley

The data upon which this case is based consist of a 2 m resolution DEM under 2000 m elevation and the DEM25 above 2000 m, the 1:25,000 landuse map (Vector25), the topographic maps and the inventory of historical avalanches propagations. The used resolution extracted from the 2 m DEM was 10 m for the entire study area in order with the phenomenon scale and to reduce the processing time (24 h of processing with this resolution). Moreover, we conducted a smoothing operation on the DEM to better simulate the inertia of this phenomenon (smoothing of the topographic irregularities).

Source Ares Identification

The Table 5.8 shows the parameters used for this analysis case for the four detection criteria:

Table 5.8 Avalanche source detection parameters

Detection criteria	Parameters
Slope	30° to 50°
Altitude	>1,000 meters high
Landuse	Outside of forest area
Minimum surface of avalanches triggering	Sources area >900 m ²

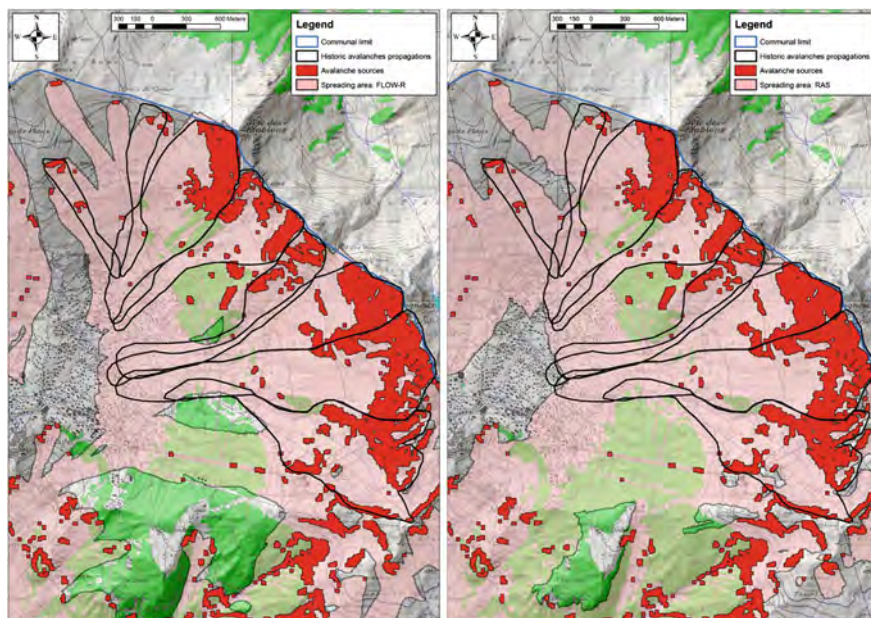


Fig. 5.26 Example of propagations. At left: Flow-R propagations. At right: RAS propagations. The dark lines are the maximum avalanche propagations recorded in the archives (hillshade and topographic map: ©swisstopo)

Spreading Area Assessment

To use the model RAS (Fig. 5.26, right), we first had to calibrate the relationship between α and β . After some tests, we decided to use the coefficients determined by Adjel (1996) in Haute-Tarentaise in the French Alps (Table 5.9). In the Bagnes valley itself, only 5 to 10 sectors have good inventories; this is not enough sufficient for making good calibrations.

For the model FLOW-R (Fig. 5.26, left), (as explained in Sect. 5.5.2.4), we must calibrate the inertia, energy and direction algorithms on past, well archived, propagation events. We selected four test areas homogeneously distributed in the study area and we chose to use the following propagation parameters (Table 5.10):

Table 5.9 Law alpha–beta used for the avalanche spreading assessments with the RAS model

Location	Number of event	Alpha–beta relationship	r	σ
Haute-Tarentaise	168	$\alpha = 0.82 * \beta + 2.82^\circ$	0.81	2.6

Table 5.10 Spreading parameters used with the FLOW-R model

Flow direction algorithm	Runout distance calculation (Perla et al. 1980)	
	μ	M/D
Holmgren exp. 4	0.28	2,500

Detection and Spreading, Example of the Folorsi

To illustrate our choices and the ability of our method to create an avalanche susceptibility map, we now present the case of the Folorsi corridor (Fig. 5.27). This corridor is marked by annual avalanches cutting the forest roads (3 and 5). In this example we can see that there is a good correspondence with the detection of the triggering areas (1, 2 and 4), the spreading area and the event shown in the picture on the left. In addition we can observe that an avalanche with a large volume has the potential to flow beyond the point 5, down to the valley bottom.

5.7.6 Flooding

5.7.6.1 Bagnes Territory

The methodology presented in the Chap. 6.6 was applied to create the indicative map of flood hazard in Val de Bagnes (Valais, Switzerland). The Val de Bagnes has a particular hydrological context because of the presence of glaciers in the watershed and the strong human impact on rivers. For example, the Mauvoisin dam, with a retention capacity of over 210 million m³, plays an important role in flood control for the valley. Many conducts redirecting water of various watersheds have an impact on discharges.

For this study, it was decided to take into account the ‘natural’ watersheds, which correspond to the boundaries of an extreme event in case of flooding. In-depth field work was conducted to identify potential overflow areas feeding the model FLOW-R. These include the various weakness of the hydrographical system such as shrinkage, bridges, debris that could create a jam or other obstructions to the watercourse (Fig. 5.28). The indicative map of danger does not take into account the intensity of the phenomenon.

The final map shows that the main danger comes from tributary streams (Fig. 5.29). Indeed, the watersheds composing the valley are large and present relatively strait outlets, resulting in many opportunities for overflows. Moreover,

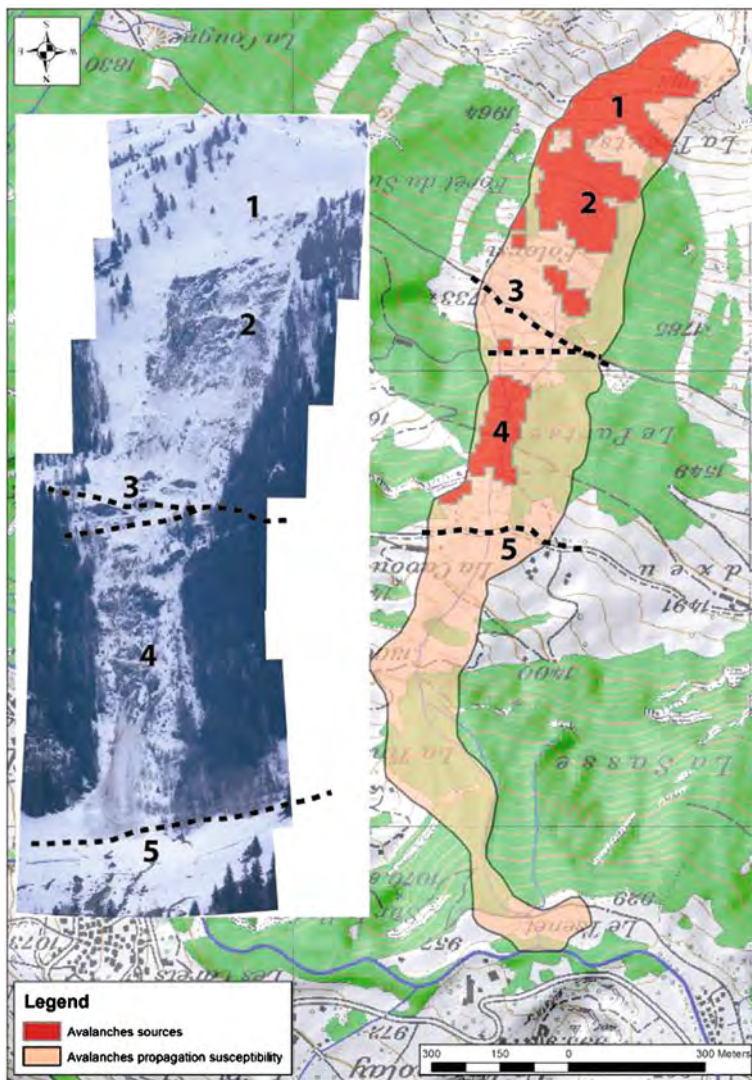


Fig. 5.27 Correspondence between the sources detected, the spreading area assess and the reality (Folorsi sector), the numbers indicate the same location on the picture and the map (hillshade and topographic map: ©swisstopo)

the human impact on rivers has led to a change in their natural course, creating an additional danger. Propagations performed with the software FLOW-R highlight those areas to be considered in a subsequent study of risk.



Fig. 5.28 An example of a potential source of overflow and its corresponding modeled spreading (orthophoto: ©swisstopo)

5.8 Discussion

The above-described multi hazard susceptibility assessment is based on quite simple models, but they are cross-checked with field observations and inspections of other sources of information such as orthophotos, partial inventories, and feedback from local people in charge of natural hazards. This point makes this approach quite flexible. One of the major advantages is the fact the parameters used in the model are few, except for SINMAP, and are tangible. Yet this approach has its own limits and does not reflect the local controlling factors and specific conditions. The specific conditions have to be integrated in more detailed studies when the scale of study is more precise than 1:2,500; this scale corresponds for instance to the “danger maps” in Switzerland, contrasting with the present approach that correspond to the “indicative danger map” (Lateltin 1997; Loat and Petraschek 1997). Nevertheless, the proposed method demonstrates the efficiency of such a simplified approach, with results in good agreements with the observations. It must be noticed also that the original results of the models are usually kept, but a relative rating of the “plausibility” of these results is assigned, creating a susceptibility scale.

Because the models are mainly based on DEM, the DEM is the source of any issues that may arise. For instance, DEM generated topography is sometimes too detailed; source areas containing bridges or ditches do not permit to assess the potential area of propagation of debris-flows or floods, because the flow is channelized and thus to simulate flooding or debris-flow propagation the bridges or ditches must be artificially broken, which must be performed manually.

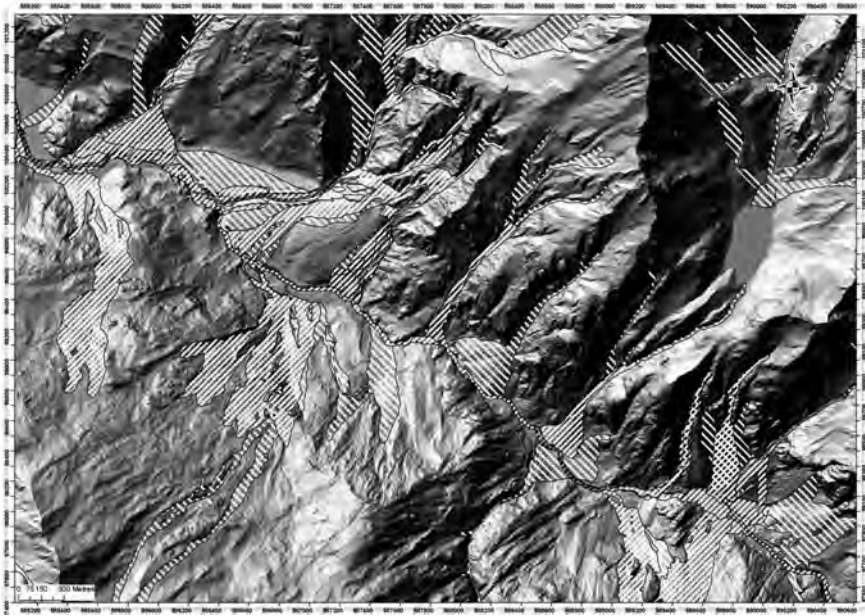


Fig. 5.29 Lots of tributary streams could be a danger for infrastructure. The final map illustrates the propagation of possible overflows (hillshade: ©swisstopo)

5.8.1 Landslide Inventory Maps and Shallow Landslides

Both examples coming from Vaud and Bagnes show different situations. In the first case, an existing inventory was available (DUTI 1985) and 1:25,000 geological maps were available in addition to orthophotos and vectorized topographic maps. In the second case, no inventory was available, only a partial cover of geological maps, but the local knowledge was used. This discrepancy shows the problem of data collection and treatment. The large area did not permit to make a detailed field check but the available inventory was the base of the investigations. The main issue was to link the former inventory based on relief interpretation at 1:25,000 (DUTI inventory + info from geological maps) to the Lidar-DEM hillshade with a resolution of 1 m. As shown by Ardizzone et al. (2007), this creates a problem of merging information without losing information. As the time allocated for this work was short it was not possible to create a completely new inventory; instead rules were used to obtain a scale of “plausibility”. This problem occurred also in Bagnes to a lesser extent as little information existed from previous studies. However it was possible to validate the inventory according to local geologists’ knowledge because of the relatively small size of the concerned area. According to the local experts, the landslide inventory map created for the Val de Bagnes was quite reliable. Nevertheless, this study has demonstrated the necessity to use a

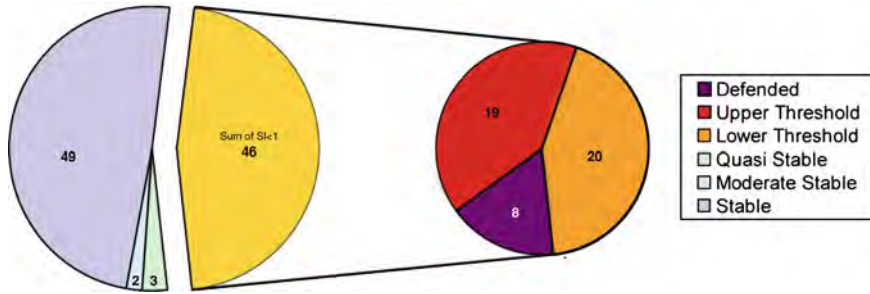


Fig. 5.30 Percentage of the total Val de Bagnes territory classed according to the different stability classes

HRDEM in order to identify landslides. Another issue linked to the data is that above 2000 m, mapping is based on the DEM25, because the Lidar-DEM does not exist. The use of orthophotos and aerial photo observations were the only way to check the results.

Shallow landslide modeling is one the most standard and used assessment method. Nevertheless it faces the usual problems: lack of information on soil and hydrological parameters and also limitations as the model only considers a constant soil thickness. Nonetheless, on average the results are valuable and reliable if they are connected with other information.

In the County of Vaud the comparison between the SINMAP results and the inventory landslide map shows that 78% of the inventoried landslides are contained in the predicted unstable zone. In general, 85% of inventoried landslides are found in a buffer of 50 m around the predicted unstable areas. The main differences between SINMAP results and the inventory map are found in the Jura region where the particular hydrological system (mainly karstic) makes the application of SINMAP model more difficult. Compared to the total surface of the study area, the SINMAP analysis shows that 18% (576 km²) of the County of Vaud can be potentially affected by shallow landslides. The most susceptible region is the alpine region where the susceptible area increases to 55% of the overall surface. For the Val de Bagnes area 46% (almost 140 km²) of the territory shows a stability index lower than 1. The main portion of the detected unstable areas have been classified in the susceptibility classes 2 and 3 respectively “Lower” and “Upper threshold” (Fig. 5.30). If only surface areas below 2000 m a.s.l. are considered for statistics, the area showing a stability index lower than 1 increases to 71% (Fig. 5.31). This is related to the presence of steep slopes glacier and rock-glacier surfaces above 2000 m a.s.l., where no shallow landslide can be initiated.

Some interesting points can be deduced form the relationship between shallow landslides, landslides and DSGD and other features:

- The DSGSD, which represent 13% of the Val de Bagnes territory (almost 40.5 of 300 km²), are destabilizing entire slopes and promoting the formation of

volume and the type of material of the various debris sources, requiring average data for large areas.

More generally, the propagation area modelling is strongly dependent on the quality of the DEM. In case of a wrong representation of the real topography, the propagation area will contain nonsense results. For example, a stream flowing under a high bridge will act as a dam; if the DEM is too detailed the channel can not be overtopped which can occur if the debris-flow erodes or if it is dammed promoting an outburst. These effects are not simulated by the model.

For the Bagnes Valley more than 50% of the sources detected by the model are confirmed by field observations, while 35% of the sources are classified “potential” (i.e. without evidence of past event) and 14% are classified as incorrect. This last “false” class is mainly due to the fact that the outcropping bedrock information was not of high quality. In this case, some actual bedrock areas were included in the source areas where no debris-flow triggering is possible as there is not any loose material (soil, moraine, debris, etc.).

The chosen methods show realistic results and allow a first fast assessment of debris-flow susceptibility over a large region, despite a limited knowledge of the local controlling factors. Again the results are contrasted:

1. For the Vaud County, both observations and the model are in good agreement, using a unique source of information, i.e., the DEM and regional geologic information.
2. The possibility to perform a qualitative classification of the source areas permits to obtain a good first overview of the debris-flow impacts in the communal territory of Bagnes Valley, which is directly useful for local authorities to prioritize remediation actions.
3. The propagation assessment based on probabilistic and basic energy calculations results in debris-flow susceptibility close to observed events.

This model has been applied with success also in Italy and France (Blahut et al. 2010; Lari et al. [in review](#); Kappes et al. 2011), using a similar approach.

5.8.3 Rockfall

The detection of source areas using the slope angle histogram decomposition by normal distributions is efficient, but it can be improved by additional data such as geological maps, vectorized topographic maps and orthophotos. The morphological units that are identified by decomposing the slope classes in cliff faces and steep slopes are significant for identifying the morphology (Strahler 1950; Loye et al. 2009). When using a Lidar-DEM the detection is very detailed even in the zone covered with vegetation.

The angle ϕ_p of the cone aperture was set to 33° for both studies performed here. The results show to be in good conformity with an orthophotos analysis and field work. Yet when using CONEFALL at regional scale, a valley-bottom

correction is required to consider local areas where such an angle of propagation would be too large. In addition, the unlimited lateral aperture of the cone does not seem to overestimate the lateral propagation of the rockfall runout. Using the Flow-R model, the runout length is taken into account. The multiple flow direction algorithm (Holmgren 1994) used for propagation in Flow-R takes into account channelized topography. The use of both models permits to create a classification of susceptibility with the result from Flow-R classified as probable and those from CONEFALL as potential.

Such a combined approach provides a fast and cost-effective way of identifying rockfall prone areas, without taking into account the structural setting and mechanical parameters in detail. This approach can be based on a DEM of poorer resolution as well, as demonstrated by Loye et al. (2009).

5.8.4 Snow Avalanches

Mapping snow avalanches is a tedious task especially at the regional scale, because in mountainous areas more or less all slopes from 30° to 60° are susceptible to snow avalanches, albeit sometimes with a very low frequency. Hazard assessments in the case of snow avalanches is mainly based on inventories and fine tuning modelling in specific sites (PPR 2011). This means that implicitly the frequency is taken into account in the choice of the sites, because snow avalanches are possible everywhere but in most cases only exceptionally.

Although the methodology used in this study to create an avalanche susceptibility map shows good correspondence between the archived events and the simulated one, some limitations should be noted. First there is a problem with the quantity of avalanche sources detected by the model. Indeed, the detection parameters are only topographic (slope, altitude) and for a steep alpine region this means that a lot of sources are detected. To solve this problem, first a reduction of the quantity of the sources detected according to the source sizes was tried. Then the spreading area was limited using the forest areas. Those tests were not conclusive because in both cases, there are some avalanche sources or propagation areas observed in reality that were ignored by the models. Further investigations still need to be conducted to decrease the number of potential sources in such steep valleys.

5.8.5 Floods in Bagnes Territory

In general, the application of the methods presented here has allowed covering the entire territory in a homogeneous and coherent way. Some remarks can be made about some specific points. The computation of discharge for important return periods must be applied to all locations where streams flow under bridges. An estimation of bridge capacity would give major information for the development

of a hazard map; this requires improving mapping procedures if implemented for regional susceptibility mapping. The human impact on hydrological network complicates the representation of reality. In the case of the susceptibility map of Val de Bagnes, the most critical situations were always considered. The analysis was particularly focused on the tributary streams of the Dranse Bagnes, where hazard is higher rather than on the main stream. In fact, it has never been adapted to raise the possibility of overflow.

In any case, the Laser-DEM geomorphic interpretation is an important input, but it still needs to be used in a more rigorous approach.

5.9 Conclusion

The possibility to treat large amount of data is mainly due to availability of powerful computers and GIS technology for hazard assessment at regional scale by mainly using DEM. In addition, more readily available digital documents such as topographic maps with attributes such as landuse, geological maps, orthophotos, etc. greatly improves the simple model used for such purposes. Models must be simple for two reasons: (1) it is still difficult to use complex models over a large area if the DEM is a HRDEM having a resolution higher than 1 m; (2) complex models often require several unknown parameters. In this sense, the usefulness of SINMAP is borderline when it is applied to large inhomogeneous areas.

Depending on the time available the proposed simple modelling can be improved, especially based on comparisons with field observations or inspecting other data. Yet this interaction between the different types of information is of primary importance to create reliable susceptibility maps. The susceptibility classification depends on the ability to mixed models with different inputs that are in accordance with different confidence levels of the input data.

The greatest problem is linked to updating former inventories. The information produced by Lidar-DEM is often far more detailed than what we can expect from field observations, especially in forested areas. As a result, ad hoc solutions must be found in order to maintain past information and to improve the final product.

Nowadays, the availability of Lidar-DEM is the major input that permits to obtain a rapid overview of potential unstable areas or to perform more detailed studies as well. It provides input for geomorphic studies as well as for modelling.

5.10 Summary/Futuristic Vision

As already indicated, the future is linked to the power of computers and to the availability of new types of mapping documents. We expect that Lidar-DEM will become available more or less everywhere around the world, and a standard

procedure for hazard mapping in the near future. At present, the method of regional hazard assessment is evolving very fast, because new techniques such as Interferometric Synthetic Aperture Radar (InSAR) are completely revolutionising the monitoring of mass movements, flood observations etc. Yet InSAR shows also a lot of limitations due to vegetation cover, slope orientations or mass movement directions. This example underlines the necessity for hazard assessment methods to always be validated by another one, which can be simply field investigations.

Thus the greatest current progress in hazard mapping arises from the Lidar technique, which gives high quality images of the ground even under dense vegetation. Lidar resolution and information content (full wave forms and intensities) are constantly improving, opening new fields of investigation. It seems that the geomorphology and soil and rock mechanics have not yet taken full advantage of the information that can be extracted from the high resolution Lidar-DEM, i.e., to characterize the mechanical properties of the ground or curvature of scars, which contain important information on failure mechanisms.

In addition, the modelling of natural hazards such as landslides, debris-flows, rockfall, snow avalanches, and floods has to take advantage of the fine resolution offered by new HRDEM, but as the data are huge and efforts must be made to find simpler models with few parameters that are suitable for modelling hazard on large areas.

Acknowledgments We are grateful to the authority of the Canton de Vaud for their permission to publish these results and for the helpful discussion we had with D. Moratel and P. Fouvy (SFFN), N. Christinet (DSE), C. Gerber (Cantonal geologist), D. Giorgis (OIT). We thank also the Bagnes municipality and his geologist Dr. F.J. Baillifard for allowing us to publish maps and results and for the useful discussions that make it possible to validate the models. We are also grateful to our colleagues K. Sudmeier for improving the English and to M. Charrière for the creation of the reference list. We are grateful to the National Swiss Foundation for Science project Number 200021-118105 and from the EU project Safeland.

References

- Adjel G (1996) Méthodes statistiques pour la détermination de la distance d'arrêt des avalanches. Ph.D. thesis, Université Joseph-Fourier, Grenoble, France
- Agliardi F, Crosta GB (2003) High resolution three-dimensional numerical modeling of rockfalls. *Int J Rock Mech Min Sci* 40:455–471
- Aksoy H, Ercanoglu M (2006) Determination of the rockfall source in an urban settlement area by using a rule-based fuzzy evaluation. *Nat Hazards Earth Syst Sci* 6:941–954
- Aleotti P, Chowdhury R (1999) Landslide hazard assessment: summary review and new perspectives. *Bull Eng Geol Environ* 58:21–44
- Ancy C, Bain V, Bardou E, Borrel G, Burnet R, Jarry F, Kölbl O, Meunier M (2006) Dynamique des avalanches. Presses polytechniques et universitaires romandes (Lausanne, Suisse) and Cemagref (Antony, France), p 338
- Ardizzone F, Cardinali M, Galli F, Guzzetti F, Reichenbach P (2007) Identification and mapping of recent rainfall-induced landslides using elevation data collected by airborne lidar. *Nat Hazards Earth Syst Sci* 7:637–650

- Bai B, Wang J, Pozdnoukhov A, Kanevski MF (2009) Validation of logistic regression models for landslide susceptibility maps, IEEE computer society. In: Proceedings of the 2009 WRI world congress on computer science and information engineering, vol 2. Washington, DC, pp 355–358
- Baillifard F, Jaboyedoff M, Sartori M (2003) Rockfall hazard mapping along a mountainous road in Switzerland using a GIS-based parameter rating approach. *Nat Hazards Earth Syst Sci* 3:435–442
- Baillifard F, Jaboyedoff M, Rouiller JD, Couture R, Locat J, Locat P, Robichaud G, Hamel G (2004) Towards a GIS-based hazard assessment along the Quebec city Promontory, Quebec, Canada. In: Lacerda WA, Ehrlich M, Fontoura AB, Sayao A (eds) *Landslides evaluation and stabilization*. Balkema, Rotterdam, pp 207–213
- Baum RL, Savage WZ, Godt JW (2002) TRIGRS—a fortran program for transient rainfall infiltration and grid-based regional slope stability. Open-file report 02-424, U.S. geological survey, p 61
- Beven KJ, Kirkby MJ (1979) A physically based variable contributing area model of basin hydrology. *Hydrol Sci Bull* 24:43–69
- Beven KJ, Lamb R, Quinn P, Romanowicz R, Freer J (1995) Topmodel. In: Singh VP (ed) *Computer models of watershed hydrology*. Water Resource Publications, Highlands Ranch, pp 627–668
- Blahut J, Horton P, Sterlacchini S, Jaboyedoff M (2010) Debris flow hazard modeling on medium scale: Valtellina di Tirano, Italy. *Nat Hazards Earth Syst Sci* 10:2379–2390
- Burrough P, McDonnell RA (1998) *Principles of geographical information systems*. Oxford University Press, Oxford, p 330
- Carrara A, Guzetti F (1995) *Geographical information systems in assessing natural hazards*. Kluwer Academic Publisher, Dordrecht, p 353
- Carrara A, Catalano E, Sorriso-Valvo M, Reali C, Osso I (1978) Digital terrain analysis for land evaluation. *Geologia Applicata e Idrogeologia* 13:69–127
- Carrara A, Cardinali M, Detti R, Guzetti F, Pasqui V, Reichenbach P (1991) GIS techniques and statistical models in evaluating landslide hazard. *Earth Surf Proc Land* 16:427–445
- Cascini L (2008) Applicability of landslide susceptibility and hazard zoning at different scales. *Eng Geol* 102:164–177
- Chacón J, Irigaray C, Fernández T, El Hamdouni R (2006) Engineering geology maps: landslides and geographical information systems. *Bull Eng Geol Environ* 65:341–411
- Chigira M, Duan F, Yagi H, Furuya T (2004) Using an airborne laser scanner for the identification of shallow landslides and susceptibility assessment in an area of ignimbrite overlain by permeable pyroclastics. *Landslides* 1:203–209
- Chung CJ, Fabbri AG (2008) Predicting landslide for risk analysis—spatial models tested by cross-validation technique. *Geomorphology* 94:438–452
- Chung CJ, Fabbri AG, Van Westen CJ (1995) Multivariate regression analysis for landslide hazard zonation. In: Carrara A, Guzetti F (ed) *Geographical information systems in assessing natural hazards*. In: Carrara A, Guzetti F (ed) Kluwer Academic Publisher, Dordrecht, pp 107–133
- Claessens L, Heuvelink GBM, Schoorl JM, Veldkamp A (2005) DEM resolution effects on shallow landslide hazard and soil redistribution modelling. *Earth Surf Proc Land* 30:461–477
- Consuegra D, Joerin F, Vitalini F (1995) Flood delineation and impact assessment in agricultural land using GIS technology. In: Carrara A, Guzetti F (eds) *Geographical information systems in assessing natural hazards*. Kluwer Academic Publisher, Dordrecht, pp 107–133
- Crosta GB, Agliardi F (2002) How to obtain alert velocity threshold for large rockslides. *Phys Chem Earth* 27:1557–1565
- Crosta GB, Agliardi F (2003) A methodology for physically based rockfall hazard assessment. *Nat Hazards Earth Syst Sci* 3:407–422
- Crosta GB, Frattini P, Sterlacchini S (2001) Valutazione e gestione del rischio da frana. Regione Lombardia, Milano, p 169
- Cruden DM, Thomson S (1987) *Exercises in terrain analysis*. The Pica Pica Press, The University of Alberta Press, Edmonton, Alberta, p 185

- De Moel H, Van Alphen J, Aerts JCJH (2009) Flood maps in Europe—methods, availability and use. *Nat Hazards Earth Syst Sci* 9:289–301
- Delmonaco G, Leoni G, Margottini C, Puglisi C, Spizzichino D (2003) Large scale debris-flow hazard assessment: a geotechnical approach and GIS modelling. *Nat Hazards Earth Syst Sci* 3:443–455
- Desmet PJJ, Govers G (1996) Comparison of routing algorithms for digital elevation models and their implications for predicting ephemeral gullies. *Geog Inf Syst* 10:311–331
- Directive 2007/60/EC of the European parliament and of the council of the 23 Oct 2007 on the assessment and management of flood risks, p 8
- Domínguez-Cuesta M, Montserrat JS, Colubi A, González-Rodríguez G (2009) Modelling shallow landslide susceptibility: a new approach in logistic regression by using favourability assessment. *Int J Earth Sci*. doi: [10.1007/s00531-008-0414-0](https://doi.org/10.1007/s00531-008-0414-0)
- Dorren LKA, Seijmonsbergen AC (2003) Comparison of three GIS-based models for predicting rockfall runoff zones at a regional scale. *Geomorphology* 56:49–64
- DUTI (1985) Détection et Utilisation des terrains instables—projet d'Ecole DUTI. Rapport final. Ecole Polytechnique Fédérale de Lausanne, Lausanne, Suisse, p 229
- Einstein HH (1988) Special lecture: landslide risk assessment procedure. In: Bonnard C (ed) *Proceedings of the 5th international symposium on landslides*, vol 2. Balkema, Lausanne, pp 1075–1090, 10–15 July 1988
- Endreny TA, Wood EF (2003) Maximizing spatial congruence of observed and DEM-delineated overland flow networks. *Int J Geog Inf Sci* 17:699–713
- Ercanoglu M, Gokceoglu C (2002) Assessment of landslide susceptibility for a landslide-prone area (north Yenice, NW Turkey) by fuzzy approach. *Env Geol* 41:720–730
- Ercanoglu M, Gokceoglu C (2004) Use of fuzzy relations to produce landslide susceptibility map of a landslide-prone area (west black sea region, Turkey). *Eng Geol* 75:229–250
- Erskine R, Green T, Ramirez J, MacDonald L (2006) Comparison of grid-based algorithms for computing upslope contributing area. *Water Res Res*, p 42
- Evans S, Hungr O (1993) The assessment of rockfall hazard at the base of talus slopes. *Can Geotech J* 30:620–636
- Fairfield J, Leymarie P (1991) Drainage networks from grid digital elevation models. *Water Resour Res* 27:709–717
- Fell R, Corominas J, Bonnard C, Cascini L, Leroi E, Savage WZ (2008a) Guidelines for landslide susceptibility, hazard and risk zoning for land-use planning. *Eng Geol* 102:85–98
- Fell R, Corominas J, Bonnard C, Cascini L, Leroi E, Savage WZ (2008b) Guidelines for landslide susceptibility, hazard and risk zoning for land-use planning—commentary. *Eng Geol* 102:99–111
- Frattini P, Crosta G, Carrara A, Agliardi F (2008) Assessment of rockfall susceptibility by integrating statistical and physicallybased approaches. *Geomorphology* 94:419–437
- Freeman TG (1991) Calculating catchment area with divergent flow based on a regular grid. *Comput Geosci* 17:413–422
- Galli M, Ardizzone F, Cardinali M, Guzzetti F, Reichenbach P (2008) Comparing landslide inventory maps. *Geomorphology* 94:268–289
- Gamma, P. (2000). *dfwalk-Ein Murgang-Simulationsprogramm zur Gefahrenzonierung*. Inaugural dissertation, Geographisches Institut der Universität Bern
- Gilard O, Gendreau N (1998) Inondabilité: une méthode de prevention raisonnable du risque d'inondation pour une gestion mieux intégrée des bassins versants. *Revue des Sci de l'Eau* 3:429–444
- Glenn NF, Streutker DR, Chadwick DJ, Thackray GD, Dorsch SJ (2006) Analysis of LIDAR-derived topographic information for characterizing and differentiating landslide morphology and activity. *Geomorphology* 73:131–148
- Gokceoglu C, Sonmez H, Ercanoglu M (2000) Discontinuity controlled probabilistic slope failure risk maps of the Altindag (settlement) region in Turkey. *Eng Geol* 55:277–296
- Gruber U, Bartelt P (2007) Snow avalanche hazard and modelling of large areas using shallow water numerical methods and GIS. *Environ Model Softw* 22:1472–1481

- Günther A (2003) SLOPEMAP: programs for automated mapping of geometrical and kinematical properties of hard rock hill slopes. *Comput Geosci* 29:865–875
- Günther A, Carstensen A, Pohl W (2004) Automated sliding susceptibility mapping of rock slopes. *Nat Hazards Earth Syst Sci* 4:95–102
- Gupta RP, Saha AK, Arora MK, Kumar A (1999) Landslide hazard zonation in part of the Bhagirathi valley, Garhwal mimalyas, using integrated remote sensing–GIS. *Himalayan Geol* 20:71–85
- Guzzetti F, Carrara A, Cardinali M, Reichenbach P (1999) Landslide hazard evaluation: a review of current techniques and their application in a multi-scale study, central Italy. *Geomorphology* 31:181–216
- Guzzetti F, Cardinali M, Reichenbach P, Carrara A (2000) Comparing landslide maps: a case study in the upper Tiber River Basin, Central Italy. *Environ Manage* 25:247–363
- Guzzetti F, Crosta G, Detti R, Agliardi F (2002) STONE: a computer program for the three-dimensional simulation of rock-falls. *Comput Geosci* 28:1079–1093
- Guzzetti F, Reichenbach P, Wieczorek GF (2003) Rockfall hazard and risk assessment in the Yosemite Valley, California, USA. *Nat Hazards Earth Syst Sci* 3:491–503
- Haugerud RA, Harding DJ, Johnson SY, Harless JL, Weaver CS (2003) High-resolution LIDAR topography of the Puget Lowland, Washington—a bonanza for earth science. *GSA Today* 13:4–10
- Heim A (1932) *Bergsturz und Menschenleben*. Fretz and Wasmuth Verlag, Zurich, p 218
- Heinimann HR, Hollenstein K, Kienholz H, Krummenacher B, Mani P (1998) *Methoden zur analyse und Bewertung von Naturgefahren*, Bundesamt für Umwelt, Wald und Landschaft (BUWAL), Bern
- Holmgren P (1994) Multiple flow direction algorithms for runoff modeling in grid based elevation models: an empirical evaluation. *Hydrol Process* 8:327–334
- Horton P, Jaboyedoff M, Bardou E (2008) Debris flow susceptibility mapping at a regional scale. In: Locat J, Perret D, Turmel D, Demers D, Leroueil S (ed) *Proceedings of the 4th canadian conference on Geohazards. From causes to management*. Presse de l'Université Laval, Québec, p 594
- Huggel C, Käab A, Haerberli W, Teyssie P, Paul F (2002) Remote sensing based assessment of hazards from glacier lake outbursts: a case study in the Swiss Alps. *Can Geotech J* 39:316–330
- Huggel C, Käab A, Haerberli W, Krummenacher B (2003) Regional-scale GIS-models for assessment of hazards from glacier lake outbursts: evaluation and application in the Swiss Alps. *Nat Hazards Earth Syst Sci* 3:647–662
- Hydrological Atlas of Switzerland (2006) Universität Bern and OFEV, Switzerland
- Jaboyedoff M (2003) CONEFALL 1.0: a program to estimate propagation zones of rockfall based on cone method. Quanterra, www.quanterra.ch
- Jaboyedoff M, Derron MH (2005) Integrated risk assessment process for landslides. In: Hungr O, Fell R, Couture RR, Eberhardt E (eds) *Landslide risk management*. On CD included in the book, A.A. Balkema, Leiden
- Jaboyedoff M, Labiouse V (2003) Preliminary assessment of rockfall hazard based on GIS data. ISRM 2003–technology roadmap for rock mechanics, symposium series—South African Institute of Mining and Metallurgy, vol 1. pp 575–578
- Jaboyedoff M, Baillifard F, Philipposian F, Rouiller JD (2004) Assessing the fracture occurrence using the “weighted fracturing density”: a step towards estimating rock instability hazard. *Nat Hazards Earth Syst Sci* 4:83–93
- Jaboyedoff M, Labiouse V (2011) Technical note: preliminary estimation of rockfall runoff zones. *Nat Hazards Earth Syst Sci* 11:819–828
- Jaboyedoff M, Pedrazzini A, Horton P, Loye A, Surace I (2008) Preliminary slope mass movements susceptibility mapping using LIDAR DEM. In: *Proceedings of the 61th Canadian geotechnical conference and 9th joint CGS/IAH-CNC Grounwater conference*. Edmonton, Canada, pp 419–426

- Jaboyedoff M, Michoud C, Mazotti B, Choffet M, Dubois J, Breguet A, Métraux V, Derron MH, Horton P, Loye A, Pedrazzini A (2010) Cartes Indicatives de dangers pour le Val de Bagnes et de Vollèges. Carnet méthodologique, p 89
- Jones JL (2004) Mapping a flood... before it happens. Fact sheet 2004–3060, U.S. geological survey, p 2
- Kappes M, Malet JP, Remaître A, Horton P, Jaboyedoff M (2011) Assessment of debris flow susceptibility at medium-scale in the Ubaye valley, France. *Nat Hazards Earth Syst Sci* 11:627–641
- Kasai M, Ikeda M, Asahina T, Fujisawa K (2009) LiDAR-derived DEM evaluation of deep-seated landslides in a steep and rocky region of Japan. *Geomorphology* 113:57–69
- Lan HX (2004) Landslide hazard spatial analysis and prediction using GIS in the xiaojiang watershed, Yunnan, China. *Eng Geol* 76:109–128
- Lan H, Martin CD, Lim CH (2007) RockFall analyst: a GIS extension for three-dimensional and spatially distributed rockfall hazard modeling. *Comput Geosci* 33:262–279
- Lateltin O (1997) Prise en compte des dangers dus aux mouvements de terrain dans le cadre des activités de l'aménagement du territoire. *Recommandations*, Office fédéral de l'Environnement, des forêts et du paysage
- Lari S, Frattini P, Crosta GB, Jaboyedoff M, Horton P (in review) Rockfall and debris flow societal and economic risk assessment at the regional scale. *Rendiconti Lincei Scienze Fisiche e Naturali*
- Lied K (1977) Rockfall problems in Norway. *Instituto sperimentale modelli e strutture* Publication 90:51–53
- Lied K, Bakkehøi S (1980) Empirical calculations of snow avalanche run-out distances based on topographic parameters. *J Glaciol* 26:165–177
- Lied K, Kristensen K (2003) Snøskred—Håndbook om snøskred. Vett and Viten AS, Nesbru, Norway, p 200
- Loat R, Pertrascheck A (1997) Prise en compte des dangers dus aux crues dans le cadre des activités de l'aménagement du territoire. *Recommandations, dangers naturels*. Office fédéral de l'économie des eaux, Office fédéral de l'aménagement du territoire, Office fédéral de l'environnement, des forêts et du paysage
- Loye A, Jaboyedoff M, Pedrazzini A (2009) Identification of potential rockfall source areas at a regional scale using a DEM-based geomorphometric analysis. *Nat Hazards Earth Syst Sci* 9:1643–1653
- Malamud BD, Turcotte DL, Guzzetti F, Reichenbach P (2004) Landslide inventories and their statistical properties. *Earth Surf Proc Land* 29:687–711
- Marco JB (1994) Flood risk mapping. In: Rossi G, Harmancioğlu N, Yevjevich V (ed) *Proceedings of the NATO advanced study institute on coping with floods*, vol 257. NATO applied sciences series, pp 353–374
- McClung DM, Schaerer PA (1993) *The avalanche handbook*. The Mountaineers, Seattle, p 271
- McKean J, Roering J (2004) Objective landslide detection and surface morphology mapping using high-resolution airborne laser altimetry. *Geomorphology* 57:331–351
- Merz B, Thieken AH, Gocht M (2007) Flood risk mapping at the local scale: concepts and challenges. In: Begum S, Stive MJF, Hall JW (eds) *Advanced in natural and technological hazards research*, vol 25. Springer Publication, New York, pp 231–251
- Metzger R (2003) *Modélisation des inondations par approches déterministe et stochastique avec prise en compte des incertitudes topographiques pour la gestion des risques liés aux crues*. Ph.D Thesis, Ecole Polytechnique de Lausanne, Lausanne, Suisse, p 167
- Montgomery DR, Dietrich WE (1994) A physically-based model for the topographic control on shallow landsliding. *Water Resour Res* 30:1153–1171
- Morrissey MM, Wiczorek GF, Morgan BA (2001) A comparative analysis of hazard models for predicting debris flows in Madison county, Virginia. *Open file report 01-0067*. Geological Survey, US
- Noverraz F (1995) *Carte des instabilités de terrain du Canton de Vaud*. Rapport conclusif et explicatif des travaux de levé de cartes. Ecole Polytechnique Fédérale de Lausanne, p 33

- OFEG (2003) Evaluation des crues dans les bassins versants de Suisse. Guide pratique. Rapport de l'OFEG, Série Eaux, 4. Berne, Suisse, p 114
- Pack R, Tarboton DG, Goodwill CN (1998) The SINMAP approach to terrain stability mapping. 8th congress of international association of engineering geology, Vancouver
- Perla RI, Cheng TT, McClung DM (1980) A two-parameter model of snow avalanche motion. *J Glaciol* 26:197–207
- Perret J (2007) Géotypes, une relecture, Tracés. Société des éditions des associations techniques universitaires
- PPR (1999) Plans de prévention des risques naturels—Risques d'inondation. Guide méthodologique. La documentation Française, Paris, France, p 123
- PPR (2011) Plans de prévention des risques d'avalanches. Guide méthodologique. <http://archives.prim.net>
- Pradhan B, Lee S (2010) Regional landslide susceptibility analysis using back-propagation neural network model at Cameron Highland, Malaysia. *Landslide* 7:13–30
- Quinn P, Beven K, Chevallier P, Planchon O (1991) The prediction of hillslope flow paths for distributed hydrological modelling using digital terrain models. *Hydrol Process* 5:59–79
- Rickenmann D, Zimmermann M (1993) The 1987 debris flows in Switzerland: documentation and analysis. *Geomorphology* 8:175–189
- Roering JJ, Kirchner JW, Dietrich WE (2005) Characterizing structural and lithologic controls on deep-seated landsliding: Implications for topographic relief and landscape evolution in the Oregon coast range, USA. *Geol Soc Am Bull* 117:654–668
- Rouiller JD, Jaboyedoff M, Marro C, Philipposian F, Mamin M (1998) Pentes instables dans le Pennique valaisan. Matterrock: une méthodologie d'auscultation des falaises et de détection des éboulements majeurs potentiels. Rapport final du PNR31. VDF Hochschulverlag AG, ETH Zürich, Switzerland, p 238
- Salciarini D, Godt JW, Savage WZ, Conversini P, Baum RL, Michael JA (2006) Modeling regional initiation of rainfall-induced shallow landslide the eastern Umbria region of central Italy. *Landslide* 3:181–194
- Salm B (1983) Guide pratique sur les avalanches. Club Alpin Suisse, Suisse, p 148
- Sartori M, Gouffon Y, Marthaler M (2006) Harmonisation et définition des unités lithostratigraphiques briançonnaises dans les nappes penniques du Valais. *Eclogae Geologicae Helvetiae* 99:363–407
- Scheidegger AE (1973) On the prediction of the reach and velocity of catastrophic landslides. *Rock Mech* 5:231–236
- Schulz WH (2004) Landslides mapped using LIDAR imagery, Seattle, Washington. Open-file report 04-1396. Geological survey, US, p 11
- Schulz WH (2007) Landslide susceptibility revealed by LIDAR imagery and historical records, Seattle, Washington. *Eng Geol* 89:67–87
- Shan J, Toth K (2008) Topographic laser ranging and scanning—principles and processing. CRC Press, LLC, p 590
- Soeters R, Van Westen CJ (1996) Slope instability recognition, analysis, and zonation. In: Turner AK, Schuster RL (ed) Landslides—investigation and mitigation—special report 247, Transportation research board, National research council. National Academy Press, Washington, pp 129–177
- Strahler AN (1950) Equilibrium theory of erosional slopes approached by frequency distribution analysis. *Am J Sci* 248(673–696):800–814
- Swisstopo (2004) MNT25—Le modèle numérique du terrain de la Suisse. Factsheet, Office fédéral de la topographie, p 15
- Swisstopo (2005) MNT-MO—Les géodonnées de la Suisse proposées par l'Office fédéral de la topographie pour une utilisation à caractère professionnel. Factsheet, Office fédéral de la topographie, p 3
- Takahashi T (1981) Estimation of potential debris flows and their hazardous zones: Soft countermeasures for a disaster. *Nat Disaster Sci* 3:57–89

- Tarboton DG (1997) A new method for the determination of flow directions and upslope areas in grid digital elevation models. *Water Resour Res* 33:309–319
- Thélin P, Gouffin Y, Allimann M (1994) Caractéristiques et métamorphisme des phyllosilicates dans la partie occidentale de la “super” nappe du Grand St-Bernard (Val d’Aoste et Valais). *Bulletin Géologique*, vol 327. Lausanne
- Toppe R (1987) Terrain models—a tool for natural hazard mapping. In: Salm B, Gubler H (eds) *Avalanche formation, movement and effects*, vol 162. IAHS Publication, Wallingford, pp 629–638
- Trümpy R (1980) *Geology of Switzerland—a guide book, part A: an outline of the geology of Switzerland*. Wepf & Co, Basel, p 104
- Turberg P, Parriaux A, Kalbermatten M, Golay F, Lance JM (2008) The geotype concept to develop GIS oriented analysis in engineering geology application. *Swiss Geoscience Meeting conference*, Lugano
- Van Alphen J, Martini F, Loat r, Slop m, Passchier R (2009) Flood risk mapping in Europe, experiences and best practices. *J Flood Risk Manage* 2:285–292
- Van Den Eeckhaut M, Poesen J, Verstraeten G, Vanacker V, Nyssen J, Moeyersons J, Van Beek LPH, Vandekerckhove L (2007) Use of LIDAR-derived images for mapping old landslides under forest. *Earth Surf Proc Land* 32:754–769
- Van Dijke JJ, van Westen CJ (1990) Rockfall hazard, a geomorphological application of neighbourhood analysis with ILWIS. *ITC J* 1:40–44
- Van Westen CJ, Van Asch TWJ, Soeters R (2006) Landslide hazard and risk zonation—why is it so difficult? *Bull Eng Geol Environ* 65:167–184
- Varnes DJ (1984) *Landslide hazard zonation: a review of principles and practice*. United Nations Educational, Scientific and Cultural Organization, Paris, p 63
- Wieczorek GF, Mandrone G, DeCola L (1997) The influence of hillslope shape on debris-flow initiation. In: ASCE (ed) *First international conference water resources engineering division*, San Francisco, CA, pp 21–31
- Wyllie DC, Mah CW (2004) *Rock slope engineering—civil and mining*, 4th edn. Spon Press, New York, p 431
- Zeng-Wang X (2001) GIS and ANN model for landslide susceptibility mapping. *J Geog Sci* 11:374–381

Annex B4

Jaboyedoff M, Horton P, Derron MH, Longchamp C and Michoud C: Monitoring Natural Hazards. In: Encyclopedia of Natural Hazards, Bobrowsky P.T. (Ed.), Springer Science+Business Media B.V., 12 p, 2012

M

2 MONITORING NATURAL HAZARDS

3 Michel Jaboyedoff, Pascal Horton, Marc-Henri Derron,
4 Céline Longchamp, Clément Michoud
5 University of Lausanne, Lausanne, Switzerland

6 Synonyms

7 [Observation](#); [Surveillance](#); [Watching](#)

8 Definition

9 The verb “to monitor” comes from the Latin “monere”
10 which means to warn. In geosciences, it means to watch
11 carefully at a hazardous situation and to observe its evolu-
12 tion and changes over a period of time. It is also used to
13 define the activity of a device that measures periodically
14 or continuously sensitive states and specific parameters.

15 Introduction

16 Hazard monitoring is based on the acquisition and the
17 interpretation of a signal indicating changes in behavior
18 or properties of a hazardous phenomenon or the occur-
19 rence of events. This ranges from acquiring basic
20 meteorological data to advanced ground movement mea-
21 surements. Hazards monitoring began sometime ago,
22 when the Babylonians first tried to forecast weather. When
23 Aristotle wrote his treatise *Meteorologica*, the Chinese
24 were also aware of weather observations (NASA,
25 2012a). Pliny the Elder studied in details the eruption of
26 the Vesuvius in August 79 AD, providing one of the first
27 scientific observations of a natural catastrophe. Presently,
28 the evolution and the precision of monitoring are closely
29 linked to the development of new technologies. A very
30 interesting example highlighting the importance of tech-
31 nological development is provided by hurricane statistics.
32 The number of hurricanes had often been underestimated
33 because of the lack of information prior to the appearance

of satellite imagery: many hurricanes that did not reach the 34
coasts were simply not registered (Landsea, 2007). Today, 35
the development of telecommunications and electronics 36
has made easier the adoption of monitoring systems. 37
In addition, satellite remote sensing has improved greatly 38
the detection of changes at Earth surface. Nevertheless, 39
monitoring remains a costly activity, implying that 40
actually only few hazard types and locations are 41
monitored. Moreover, as dangerous phenomena are 42
usually complex, several parameters have to be 43
monitored, and in most cases one single variable is not 44
a sufficient criterion to provide reliable warnings. 45

Monitoring can be either linked to an early warning 46
system, leading to act directly within the society, or used 47
to record hazardous events to provide data for hazard 48
assessment and a better understanding of the phenome- 49
non. Some of the monitoring results are public and acces- 50
sible at no cost, such as earthquake data, whereas 51
meteorological data are often sold because they are profit- 52
able due to their direct impact on society (such as agricul- 53
ture, air traffic, news, and tourism). In any case, with the 54
boom of Internet, more and more free data is accessible 55
in many countries. 56

In the following, we describe briefly the most common 57
sensor types used for monitoring several hazards and fur- 58
ther discuss monitoring aspects. 59

60 Instruments and measured variables

Originally, monitoring was mainly done by simple human 61
observations or with limited devices, and some were 62
performed manually, such as the first rain gauges. Now, 63
even if some monitoring is still based on observations, as 64
for snow avalanches, it is mainly instrumented, and many 65
sensors are also used for remote-sensing techniques. The 66
great advance in computer sciences and communication 67
technologies has increased the accessibility to instru- 68
ments, by improving technology and reducing costs. 69

70 Climatic variables are monitored by satellite and mete-
 71 orological stations. According to the World Meteorologi-
 72 cal Organization (WMO, 2012a), the global observing
 73 system (GOS) acquires “*meteorological, climatological,*
 74 *hydrological and marine and oceanographic data from*
 75 *more than 15 satellites, 100 moored buoys, 600 drifting*
 76 *buoys, 3,000 aircraft, 7,300 ships and some 10,000*
 77 *land-based stations.*”

78 Hazard monitoring consists primarily of treating
 79 a signal in order to obtain information about movement,
 80 moisture, temperature, pressure, or physical properties
 81 (Table 1). A monitoring sensor is local when it records
 82 properties at its own location (thermometer, rain gauge,
 83 etc.). Remote sensors are used to collect properties of
 84 distant objects. Remote-sensing techniques can be active
 85 (a signal is sent and received) or passive (only receiving).
 86 For instance, InSAR (interferometric synthetic aperture
 87 radar) is an active remote-sensing method to detect ground
 88 movement, whether Earth surface temperatures can be
 89 measured from satellites by passive remote sensing
 90 analyzing specific bands of the electromagnetic spectrum
 91 (Jensen, 2007). Currently, satellites using microwaves or
 92 bands in the visible and infrared spectra permit one to
 93 quantify environmental variables such as rainfall, CO₂,
 94 water vapor, cloud fraction, and land temperature (NASA,
 95 2012b).

96 Two important advances in the last 20 years now allow
 97 one to measure ground movements, one key factor for
 98 many natural hazards: (1) the GNSS (Global Navigation
 99 Satellite System), which allows measuring 3D
 100 displacements, and (2) the satellite and terrestrial InSAR
 101 techniques that permit one to map very accurate
 102 displacements using two successive radar images by
 103 comparing the phase signal. Of course, local direct
 104 measurements of displacements such as extensometers,
 105 tide float gauges, or inclinometers are still very much used
 106 and complement these recent techniques.

107 The final goal of hazard monitoring is to provide
 108 information about physical parameters directly or
 109 indirectly interpreted in order to evaluate the level of risk.
 110 The following presents some of the most current methods
 111 used to monitor the main hazards affecting human
 112 activities.

113 Meteorological monitoring

114 Monitoring meteorological variables is mainly dedicated
 115 to weather forecasting but also to the understanding of
 116 climate change. It covers phenomena from local to global
 117 scale. Spatial and temporal scales of the phenomena are
 118 linked. Local and extreme events, such as tornadoes, hail,
 119 or thunderstorms, last only a few minutes to hours, and
 120 their location and intensity cannot be forecasted in
 121 advance. These kind of events are the topics of short-range
 122 forecasting, or nowcasting, that rely on observations and
 123 measurements of the phenomena after its initiation, as,
 124 for instance, by means of satellite or ground-based radar
 125 data. Regional events, such as heavy precipitation

126 over a mountain range, strong winds over a country, or
 127 hurricanes, can usually be foreseen a few days in advance.
 128 These are forecasted at medium range by numerical
 129 weather forecast models that rely on the actual state of
 130 the atmosphere, assessed by radiosounding balloons,
 131 meteorological stations, or satellite images. The global
 132 scale is related to climate changes and is monitored by
 133 temperature measurements (Figure 1), sea level rise
 134 tracking, and various other indices.

135 Weather monitoring is thus dedicated to forecasting but
 136 also to increase the knowledge about the phenomena.
 137 Most of the data acquired during an event are then used
 138 by the scientific community for various applications, such
 139 as statistical analyses, improvement of the understanding
 140 of the processes, or development of more reliable models.

Monitoring of local extreme events

141 The short-range forecasting, often referred as nowcasting,
 142 focuses on the pending few hours and the local scale. It
 143 strongly relies on monitoring to anticipate the displace-
 144 ments of the occurring hazard.

145 Thunderstorms with intense precipitation or hail are
 146 usually tracked by means of ground-based precipitation
 147 radars. The returning radar pulses provide the spatial dis-
 148 tribution of the hydrometeors and so the intensity of the
 149 precipitation. The diameter of the raindrops or the hail
 150 may be approximated based on the reflectivity factor or
 151 the signal attenuation. The main advantage of radar mea-
 152 surements is that it provides real-time precipitation infor-
 153 mation on a large area, but there are several issues for
 154 precipitation estimation. The first one is that the drops
 155 are detected on a wide range of altitudes and the calculated
 156 intensity may not match ground observations due to wind
 157 or evaporation (Shuttleworth, 2012). Another issue is for
 158 mountainous regions, as mountain ranges are responsible
 159 for beam shielding (Germann et al., 2006). However, var-
 160 ious algorithms and correction methods exist to make the
 161 radar data valuable for nowcasting. The goal of such fore-
 162 casting is to assess the motion and the evolution of precip-
 163 itation patterns (Austin and Bellon, 1974). While it was
 164 initially just an extrapolation of the patterns, it is
 165 becoming more sophisticated by use of numerical
 166 forecasting models that are initialized with radar data
 167 (Wilson et al., 1998).

168 Tornado detection is possible using a Doppler radar,
 169 which uses the Doppler effect on the reflected pulse to
 170 assess the velocity of hydrometeors, according to the
 171 radial axis. By displaying the motion within a storm, it
 172 becomes possible to identify a tornado vortex signature
 173 (Donaldson, 1970; Brown et al., 1978), which is charac-
 174 terized by an intense and concentrated rotation. With this
 175 approach, the presence of tornado genesis can be identi-
 176 fied before a tornado touches the ground. The US govern-
 177 ment deployed a network of 158 Doppler radars for
 178 tornadoes monitoring between 1990 and 1997 (NOAA
 179 website).
 180

181 **Monitoring of regional meteorological variables**

182 Today's weather forecasts are mainly based on numerical
 183 weather prediction (NWP) models. However, these
 184 models rely on data assimilation, which is a statistical
 185 combination of observations and short-range forecasts,
 186 to adjust the initial conditions to the current state of the
 187 atmosphere (Daley, 1993; Kalnay, 2003). Data such as
 188 temperature, pressure, humidity, and wind are acquired
 189 by weather stations, or radiosounding balloons to get
 190 a profile of the troposphere (Malardel, 2005).

191 Air temperature, barometric pressure, wind speed, and
 192 direction are commonly measured at weather stations,
 193 but also with costal or drifting weather buoys. Some boats
 194 and aircrafts are also equipped with sensors acquiring var-
 195 ious atmospheric variables.

196 Rain gauge stations provide point precipitation mea-
 197 surement. It is the first and most common way to measure
 198 precipitation, and so it has the advantage that long time
 199 series exist. However, these are subject to systematic
 200 errors (values lower by about 5–10%) related to the wind
 201 and to the choice of the gauge site (over exposure to the
 202 wind in open area or shade effect from obstacles around)
 203 and gauge design (Shuttleworth, 2012). The height of
 204 the gauge is a defined parameter and balances the effect
 205 of the wind that decreases closer to the ground, and of
 206 the splash-in that increases nearer to the ground. The rain
 207 gauges evolved to reduce errors linked to the wind, to
 208 evaporation, and to condensation, and changed from man-
 209 ual measurements toward automatic recording.

210 Weather station networks are organized at a national or
 211 regional scale. In 1995, the World Meteorological Organi-
 212 zation proposed a resolution (Resolution 40) to "facilitate
 213 worldwide co-operation in the establishment of observing
 214 networks and to promote the exchange of meteorological
 215 and related information in the interest of all nations"
 216 (WMO, 2012b). This database contains time series from
 217 all over the world.

218 Precipitation assessment by remote sensing is not as
 219 accurate as ground-based measurements, but it provides
 220 information in area where no or few observations exist.
 221 It is likely to be the only way for precipitation measure-
 222 ment to be possible at a global scale (Shuttleworth,
 223 2012). The Tropical Rainfall Measuring Mission
 224 (TRMM) satellite with precipitation radar onboard allows
 225 measuring the vertical structure of precipitation (Iguchi
 226 et al., 2000; Kawanishi et al., 2000). Precipitation can also
 227 be derived from visible and infrared satellite data (Griffith
 228 et al., 1978; Vicente et al., 1998).

229 In addition, the meteorological satellites such as
 230 meteosat-9 (www.eumetsat.int) deliver images in visible
 231 or infrared spectra providing important data to the meteo-
 232 rologist. It is also a very important source of information
 233 in case of the development of severe hazards, such as
 234 hurricanes.

Monitoring of climate and climate change

235 Climate studies rely on long series of high-quality climate
 236 records (Figure 1). The most analyzed parameter is the air
 237 temperature. Scientists use data recorded at weather sta-
 238 tions over decades and employ different methods to recon-
 239 struct past data before the beginning of the measurements.
 240 Data reconstruction, rescue, and homogenization are still
 241 important topics today.

242 Some satellites have radiometers on board to monitor
 243 clouds and thermal emissions from the Earth and Sea Sur-
 244 face Temperature (SST) (NASA, 2012a). For instance,
 245 SST can be measured using the calibrated infrared Moder-
 246 ate Resolution Imaging Spectroradiometer (MODIS)
 247 installed on Observing System satellites Terra (Minnett
 248 et al., 2002). The sea level can be measured using
 249 a Radar altimeter of the Jason-2 satellite, which permits
 250 one to provide inputs for El Niño or hurricane monitoring.
 251 Sea level rise is mainly caused by climate change and is
 252 currently about 3.4 ± 0.4 mm/year (Nerem et al., 2010).
 253

Floods monitoring

254 Floods have several origins often linked to intense precip-
 255 itation, massive snowmelt, tsunamis, hurricanes, or storm
 256 surges, but several are related to other hazards like land-
 257 slides and rockfalls. The main instrumental setups to fore-
 258 cast floods are weather stations, with a particular emphasis
 259 on the rain gauge, weather radars, and meteorological
 260 models.

261 The direct monitoring of floods is done by measuring
 262 rivers discharge and/or lakes and sea level. The river dis-
 263 charge is linked to the measurement of the stage (or level),
 264 which is the water height above a defined elevation, by
 265 a stage-discharge relation. The stages of rivers or lakes
 266 are measured by float, ultrasonic, or pressure gauges
 267 (Olson and Norris, 2007; Shaw, 1994). The stage-
 268 discharge relation has to be updated frequently because
 269 of erosion and deposition problems. This relationship is
 270 established using current-meters based on rotor or acous-
 271 tic Doppler velocimeter which establishes the velocity
 272 contours of the river section (Olson and Norris, 2007;
 273 Shaw, 1994). Radars are also used and seem to be
 274 a promising way to obtain discharge (Costa et al., 2006),
 275 by using ground-penetrating radar (GPR; the echo of emit-
 276 ted microwave permit to get the river bed profile) coupled
 277 with a Doppler velocimeter in order to get the discharge
 278 estimation.
 279

280 In several lowland areas, flood monitoring includes the
 281 embankment monitoring that means stability analysis as
 282 for landslides. The survey of affected flood area is
 283 performed by man-made mapping, aerial photography,
 284 or satellite imaging when the flood area is wide, as in
 285 Bihar (India) in August 2008 (UNOSAT, 2012).

Earthquake monitoring

286 Earthquakes monitoring has two objectives: one to pro-
 287 vide data for hazard assessment and the other to develop
 288 some aspects for prediction. The main recent technologic
 289

290 advances are GNSS and InSAR techniques that allow one
291 to observe the deformation of the Earth's crust before
292 (interseismic), during (coseismic), and after (post-seismic)
293 an earthquake (Figure 2). This permits, for instance, to
294 expect large earthquakes like in the Cascadian area
295 (Hyndman and Wang, 1995), California, and Turkey
296 (Stein et al., 1997).

297 The displacements recorded by several seismometers
298 provide the necessary information to estimate the location
299 of an earthquake, its magnitude or the energy released.
300 The statistics of the magnitude for defined zones lead to
301 define the Guntherber-Richter law which may be used to
302 obtain the probability of occurrence for earthquakes of
303 a magnitude larger than a given value. In addition, fine
304 analysis using inversion methods of wave signal
305 provides information to characterize the surface of failure
306 (Ji et al., 2002).

307 The use of monitoring to predict events within a few
308 days or hours is not yet possible because of the variability
309 of geodynamical contexts. For example, a monitored vari-
310 able may display opposite signals depending on the con-
311 text, such as radon which can increase before earthquakes
312 as in Kobe in 1995 (Igarashi et al., 1995) but which can
313 also decrease (Kuo et al., 2006). The amplitude of the sig-
314 nal is thus not significant. The observation of an enhanced
315 activity close to a fault (foreshocks) can be used as signal,
316 but this activity increase does not necessarily lead to
317 earthquakes.

318 The forecast is still not accurate, but observed ground
319 deformations coupled with history of earthquakes permit
320 one to estimate the probability that large earthquakes
321 occur at a location within a period of time (Stein et al.,
322 1997). The two most promising methods are the follow-
323 ing: (1) The first is to characterize the ground mechanical
324 properties using ambient seismic noise. The post-seismic
325 period leads to significant seismic velocity changes
326 (Brennguier et al., 2008), indicating most probably stress
327 field modification, but it seems from recent results that it
328 can also be observed before the earthquake. (2) The sec-
329 ond is to analyze ionospheric anomalies of the total elec-
330 tron content that are detected before earthquakes by
331 GNSS systems (Heki, 2011).

332 Tsunamis monitoring

333 Tsunamis can have different origins including earth-
334 quakes, large volcanic eruptions, submarine landslides,
335 rock falling into water, etc. The indirect monitoring is
336 related to the triggering factors of the phenomenon, which
337 are mainly earthquakes or landslides. The Åknes rockslide
338 in Norway is an example of indirect monitoring applied to
339 mountainside instability of significant volume that can fall
340 into a fjord and generate a tsunami. The monitoring of the
341 instability is part of a full early warning system including
342 the evacuation of villages located on the coast within a few
343 minutes (Blikra, 2008).

344 The direct monitoring of tsunamis is the record of the
345 wave propagation and can be fundamental for different

346 reasons: a large earthquake does not lead necessarily to
347 a tsunami, then the alarm should be canceled if the closer
348 gauges do not indicate any wave (Joseph, 2011); the wave
349 can occur later than expected; the occurrence of landslides
350 (submarines or not) are not always detected. In addition to
351 tide gauges, several seafloor sensors (pressure) are located
352 near the coastal areas of continents and islands, but also in
353 the middle of the ocean (Joseph, 2011). The most
354 advanced monitoring system is the Deep-Ocean Assess-
355 ment and Reporting of Tsunamis (DART II), and it con-
356 sists in a surface buoy localized by GNSS and
357 communicating the pressure recorded at the bottom of
358 the ocean by a pressure sensor. The communication with
359 a satellite is bidirectional (Meinig et al., 2005). Such
360 devices are being deployed all over the world (NOAA,
361 2012) showing great results, like the satellite altimeters
362 that recorded accurately the 2004 Sumatra tsunami wave
363 all around the world (Smith et al., 2005).

364 Volcanoes monitoring

365 Volcanoes are one of the most spectacular natural hazards
366 on Earth and can be the most disastrous. As an example,
367 the eruption of the Krakatau (Indonesia) in 1883 killed
368 some 30,000 people, releasing a significant volume of
369 ash that briefly affected climate (Durant et al., 2010) and
370 generated a large tsunami wave (Gleckler et al., 2006).
371 As eruption types are so diverse, their monitoring is not
372 easy. Several activities can provide precursory signs,
373 linked to magma movements which change the properties
374 of the ground. The first activity signs that are usually mon-
375 itored by seismographs are tremors indicating stress
376 adjustments. These stress changes induce ground defor-
377 mations that can be observed by high precision tiltmeters,
378 indicating changes in slope of the surface. Currently,
379 GNSS are commonly used (Figure 3); they can provide
380 continuous 3D displacements and have partially replaced
381 the electronic distance meter (EDM) laser beam. In addi-
382 tion, since the early works of Massonnet et al. (1995),
383 the InSAR technique allows one to observe deformation
384 of volcanoes, providing information on their behaviors.
385 Any change in the ground can influence measurable
386 parameters such as gravity, temperature, and magnetic
387 field. All those variables can be monitored. The change
388 in gas composition in fumaroles is frequently reported,
389 especially an increase in CO₂ content or a change in the
390 ration F/Cl. Nevertheless, it is quite difficult to monitor
391 gases because they follow preferential paths up to the sur-
392 face that can change during a precursory period (McNutt
393 et al., 2000). At Etna volcano, ambient seismic noise sig-
394 nature has been recognized as a potential precursor that
395 can be monitored in order to forecast an eruption
396 (Brennguier et al., 2008).

397 The monitoring of volcanoes does not only involve the
398 volcano itself, but also ash that can disturb aerial traffic or
399 have an impact on the agriculture. Sulfur dioxide, ash, and
400 aerosols (sulfuric acid) are mostly monitored by satellite
401 imaging (ultraviolet and infrared sensors) which is not

402 designed directly for that purpose (Prata, 2009). As those
403 processes are closely linked to atmosphere movements,
404 many of the monitoring techniques of weather forecasting
405 are also used.

406 Landslides monitoring

407 Landslides are easily observed because they are moving
408 masses affecting and deforming the relief. As
409 a consequence, the main variables to monitor are the
410 movement and parameters that are modifying the stress
411 or the properties of the material that is under deformation
412 (SafeLand, 2010). Except in the case of earthquakes or
413 exceptional precipitation, the displacement is the main
414 parameter to monitor. In most of the cases, the failure is
415 preceded by an acceleration of movements. Depending
416 on the material geometry and the volume involved, the
417 failure may be forecasted (Crosta and Agliardi, 2003),
418 and this acceleration can sometime be directly correlated
419 with groundwater level using a mechanical model
420 (Corominas et al., 2005).

421 Two types of landslides must be distinguished: shallow
422 and deep-seated landslides. The first are too small and too
423 localized to be easily monitored, but today several
424 attempts are made to create early warnings for shallow
425 landslides (Sassa et al. 2009). The deep-seated failures
426 are usually sufficiently large to display significant move-
427 ments before catastrophic failure.

428 Large landslides monitoring

429 The main instruments used to monitor large landslides are
430 dedicated to movements. Physically, extensometers can be
431 used to measure displacements and crack meters can be
432 used to observe the opening of cracks. When boreholes
433 are available, manual inclinometer or permanent incli-
434 nometer columns may be used, providing the deformation
435 profiles and often the failure surface where most of the
436 deformation concentrates. These devices are often used
437 for early warning system, as for the site of Åknes (Nor-
438 way) (Blikra, 2008). As water plays an important role in
439 controlling movements of a landslide, boreholes can be
440 used to measure the level of the water table (manually or
441 by measuring the groundwater pressure).

442 Surface movements can be followed using targets and
443 total station (laser distance meter), but today, if the
444 required conditions of visibility are appropriate, perma-
445 nent GNSS can be used for a permanent monitoring of
446 the movements (Gili et al., 2000). The disadvantage of
447 these methods is that they are point measurements only.
448 By using advanced satellite InSAR techniques
449 (PS-InSAR, SBAS, etc.), a significant percentage of land-
450 slides can be imaged and monitored. In addition, time
451 series of displacement of ground reflectors can be
452 obtained. One of the last evolutions of the InSAR is the
453 SqueeSAR™ method that enhances significantly the
454 capability of tracking ground displacement (Ferretti
455 et al., 2011). Unfortunately, satellite InSAR is not suitable
456 for early warning because satellites take several days to

pass over an area a second time. If no appropriate reflec- 457
458 tive object exists on the monitored surface (for instance
459 due to forest cover), the InSAR method can be applied
460 only if corner reflectors are installed on the ground, pro-
461 viding movements on selected points only (Singhroy
462 et al., 2011). With ground-based InSAR (GB-InSAR), it
463 is possible to follow the movements of the surface of
464 a landslide or rockslide, when it is visible in the direction
465 of the line of sight. This is very useful to observe the
466 deformation evolution of the front of landslides
467 (Tarchi et al., 2003).

468 The Lidar technique provides full 3D point clouds in
469 the case of terrestrial Laser scanner (TLS), which allows
470 characterizing rock slopes and landslides (Safeland,
471 2010; Jaboyedoff et al., 2012). It permits one to monitor
472 and to follow the full evolution of a landslide surface that
473 is moving, to understand mechanisms of failure
474 (Oppikofer et al., 2008) and also to monitor rock fall
475 by comparison of successive acquisitions (Figure 4). The
476 airborne Laser scanner (ALS) is less accurate but permits
477 one to estimate differences between digital elevation
478 models.

479 For most landslides, several different sensors
480 are required to establish an early warning system
481 (Blikra, 2008; Froese and Moreno, 2011). Since a few
482 years ago, photogrammetry and image correlation have
483 developed, leading to very promising results (Travelletti
484 et al., 2012). Geophysics methods are also improving their
485 capabilities to image the underground. One of the most
486 interesting recent developments is ambient seismic
487 noise analysis. For a rock mass, it indicates a decrease of
488 the natural frequency before failures and for landslides,
489 a decrease of the surface wave velocity (Mainsant
490 et al., 2012).

491 Debris flow and shallow-landslides monitoring

492 Shallow landslides and debris flow landslides are mostly
493 dependent on precipitation. As a consequence, the main
494 monitored variables are precipitation intensity, and dura-
495 tion (Baum and Godt, 2010; Jakob et al., 2011). Satur-
496 ation, soil moisture, and antecedent precipitation are
497 variables that are also often monitored. In the case
498 of shallow landslides, the exact location cannot be
499 determined, thus the entire area is considered as hazardous
500 if some thresholds are exceeded. It must be noted that an
501 early warning system designed for rainfall-induced
502 landslides is operational in Hong Kong and has been
503 continuously improved since 1977 (Chan et al., 2003;
504 Sassa et al., 2009).

505 In the case of debris flows, sensitive catchments can be
506 equipped in order to issue warnings. The seismic sensors
507 and ultrasonic gauges permit one to deduce velocity and
508 peak discharge (Marchi et al., 2002).

509 Monitoring shallow landslides and debris flows is
510 still a topic of research under development because the
511 triggering and the localization of such phenomena are
512 not yet well understood.

513 **Snow avalanche monitoring**

514 Snow avalanches are seasonal events and depend
 515 strongly on climate variables such as previous precipita-
 516 tion, snowpack depth and strength, and temperatures. As
 517 a consequence, snow avalanches monitoring concentrates
 518 essentially on hazard level quantification. This is mainly
 519 performed using human observations (SLF, 2012)
 520 and weather stations equipped by ultrasonic snow depth
 521 sensors. Observed variables are strongly dependant on
 522 local physiographic conditions. In addition to monitored
 523 data, the observers perform snow hardness tests in order
 524 to detect the potential mechanical weakness in the snow-
 525 pack (Pielmeier and Schneebeili, 2002). The conditions
 526 for avalanches are so diverse (wet snow, large amount of
 527 fresh snow, etc.), that up to now, human intervention in
 528 the monitoring remains the main method to monitor and
 529 forecast this hazard.

530 **Other monitoring**

531 There are other hazards to monitor. Some require the
 532 integration of meteorological data in the monitoring
 533 design. For instance, a drought corresponds to a period
 534 of abnormally dry weather leading to a deficit of water
 535 in the hydrologic cycle and finally leading to problems
 536 (but the definition of drought is not unique). Forest fires
 537 are consequences of dryness, with origins that are often
 538 not natural, but anthropogenic. Hail storms are also haz-
 539 ardous phenomenon that can lead to serious damage; hail
 540 monitoring is mainly based on human observation and
 541 meteorological radar. Lightnings are monitored using an
 542 electromagnetic sensors network. All the sensors
 543 detecting one specific lightning provide the distance to
 544 it. The location is then deduced by searching the best
 545 agreement between all the detected distances to sensors.

546 **Future of monitoring as a demand of the society**

547 The monitoring of natural hazards is often a tedious task
 548 because if the physics well describes the single phenome-
 549 non, in natural environments, the occurrence of an event is
 550 controlled by several simultaneous phenomena. It implies
 551 that, for the analysis and prediction of events, a number of
 552 different variables are required to be able to describe all
 553 possible cases.

554 The power of computer science, communication
 555 technologies, and the improving quality of sensors,
 556 combined with decreasing prices, make the monitoring
 557 of environmental data more precise and easy. This leads
 558 to new understanding of natural hazards and also to the
 559 implementation of early warning systems that will permit
 560 one to manage territories in a safer way. In addition,
 561 nowcasting, as proposed by World Meteorological Orga-
 562 nization, is now an objective of this organization to pro-
 563 vide forecasts in less than 6 h. Such developments are
 564 mainly possible because of computer power available
 565 almost everywhere and a generalized ability to communi-
 566 cate rapidly by anybody with the “smartphone”
 567 technology.

Bibliography

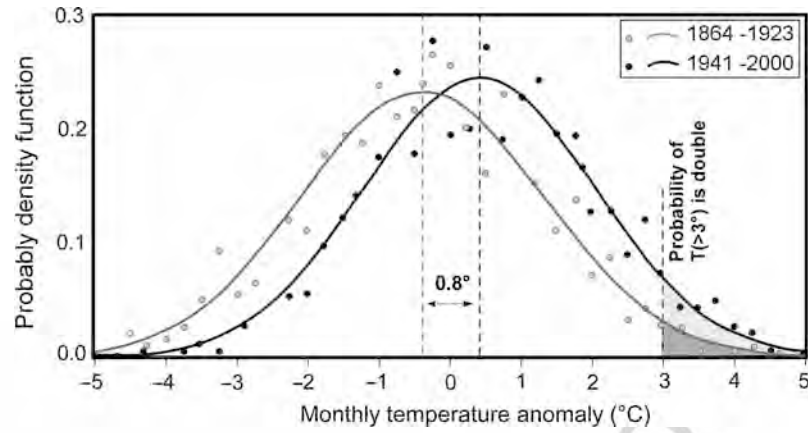
568 Austin, G. L., and Bellon, A., 1974. The use of digital weather radar
 569 records for short-term precipitation forecasting. *Quarterly Jour-
 570 nal of the Royal Meteorological Society*, **100**(426), 658–664. 571
 572 Baum, R. L., and Godt, J. W., 2010. Early warning of rainfall-
 573 induced shallow landslides and debris flows in the USA. *Land-
 574 slides*, **7**, 259–272, doi:10.1007/s10346. 574
 575 Blikra, L. H., 2008. The Åknes rockslide; monitoring, threshold
 576 values and early-warning. In Chen, Z., Zhang, J., Li, Z.,
 577 Wu, F., Ho, K. (eds.), *Landslides and Engineered Slopes, From
 578 Past to Future, Proceedings of the 10th International Sympo-
 579 sium on Landslides*. Taylor and Francis Group. pp. 1089–1094. 579
 580 Brenguier, F., Shapiro, N., Campillo, M., Ferrazzini, V., Duputel, Z.,
 581 Coutant, O., and Nercessian, A., 2008. Towards forecasting volca-
 582 nic eruptions using seismic noise. *Nature Geoscience*, **1**, 126–130. 582
 583 Brown, R., Lemon, L., and Burgess, D., 1978. Tornado detection by
 584 pulsed Doppler radar. *Monthly Weather Review*, **106**, 29–38. 584
 585 Chan, R. K. S., Pang, P. L. R., and Pun, W. K., 2003. Recent devel-
 586 opments in the landslips warning system in Hong Kong. In Ho,
 587 K. K. S., Li, K. S. (eds.) *Geotechnical engineering – meeting
 588 society’s needs, Proceedings of the 14th Southeast Asian Geo-
 589 technical Conference*. Hong Kong. Balkema, Rotterdam, pp.
 590 219–224. 590
 591 Corominas, J., Moya, J., Ledesma, A., Lloret, A., and Gili, J. A.,
 592 Prediction of ground displacements and velocities from
 593 groundwater level changes at the Vallcebre landslide (Eastern
 594 Pyrenees, Spain). *Landslides*, **2**, 83–96. 594
 595 Costa, J. E., Cheng, R. T., Haeni, F. P., Melcher, N., Spicer, K. R.,
 596 Hayes, E., Plant, W., Hayes, K., Teague, C., and Barrick, D.,
 597 2006. Use of radars to monitor stream discharge by noncontact
 598 methods. *Water Resources Research*, **42**, W07422,
 599 doi:10.1029/2005WR004430. 599
 600 Crosta, G., and Agliardi, F., 2003. Failure forecast for large rock
 601 slides by surface displacement measurements. *Canadian Geo-
 602 technical Journal*, **40**, 176–191. 602
 603 Daley, R., 1993. *Atmospheric Data Analysis*. Cambridge:
 604 Cambridge University Press. 604
 605 Donaldson, R. J., 1970. Vortex signature recognition by a Doppler
 606 radar. *Journal of Applied Meteorology*, **9**, 661–670. 606
 607 Durant, A. J., Bonadonna, C., and Horwell, C. J., 2010. Atmo-
 608 spheric and environmental impacts of volcanic particulates. *Ele-
 609 ments*, **6**, 235–240. 609
 610 Ferretti, A., Fumagalli, A., Novali, F., Prati, C., Rocca, F., and
 611 Rucci, A., 2011. A new algorithm for processing interferometric
 612 data-stacks: SqueeSAR. *IEEE Transactions on Geoscience and
 613 Remote Sensing*, **49**, 3460–3470. 613
 614 Froese, C. R., and Moreno, F., 2011. Structure and components for
 615 the emergency response and warning system on Turtle Moun-
 616 tain. *Natural Hazards*, doi:10.1007/s11069-011-9714-y. 616
 617 Germann, U., Galli, G., Boscacci, M., and Bolliger, M., 2006. Radar
 618 precipitation measurement in a mountainous region. *Quarterly
 619 Journal of the Royal Meteorological Society*, **132**, 1669–1692. 619
 620 Gili, J. A., Corominas, J., and Rius, J., 2000. Using global position-
 621 ing system techniques in landslide monitoring. *Engineering
 622 Geology*, **55**, 167–192. 622
 623 Gleckler, P. J., Wigley, T. M. L., Santer, B. D., Gregory, J. M.,
 624 AchutaRao, K., and Taylor, K. E., 2006. Volcanoes and climate:
 625 Krakatoa’s signature persists in the ocean. *Nature*, **439**, 675. 625
 626 Griffith, C., Woodley, W., Grube, P., Martin, D., Stout, J., and
 627 Sikdar, D., 1978. Rain estimation from geosynchronous satellite
 628 imagery-visible and infrared studies. *Monthly Weather Review*,
 629 **106**(8), 1153–1171. 629
 630 Heki, K., 2011. Ionospheric electron enhancement preceding the
 631 2011 Tohoku- Oki earthquake. *Geophysical Research Letters*,
 632 **38**, L17312. 632

- 633 Hyndman, R. D., and Wang, K., 1995. The rupture zone of Cascadia
 634 great earthquakes from current deformation and the
 635 thermal regime. *Journal of Geophysical Research*, **100**(B11),
 636 22133–22154.
- 637 Igarashi, G., Saeki, S., Takahata, N., Sumikawa, K., Tasaka, S.,
 638 Sasaki, Y., Takahashi, M., and Sano, Y., 1995. Ground-water
 639 radon anomaly before the Kobe earthquake in Japan. *Science*,
 640 **269**, 60–61.
- 641 Iguchi, T., Meneghini, R., Awaka, J., Kozu, T., and Okamoto, K.,
 642 2000. Rain profiling algorithm for TRMM precipitation radar
 643 data. *Advances in Space Research*, **25**(5), 973–976.
- 644 Jaboyedoff, M., Oppikofer, T., Abellán, A., Derron, M.-H., Loye, A.,
 645 Metzger, R., and Pedrazzini, A., 2012. Use of LIDAR in landslide
 646 investigations: a review. *Natural Hazards*, **61**, 5–28, doi:10.1007/
 647 s11069-010-9634-2.
- 648 Jakob, M., Owen, T., and Simpson, T., 2011. A regional real-time
 649 debris-flow warning system for the district of North Vancouver.
 650 Canada. *Landslides*, doi:10.1007/s10346-011-0282-8.
- 651 Jensen, J. R., 2007. *Remote Sensing of the Environment: An Earth*
 652 *Resource Perspective*, 2nd edn. Upper Saddle River, NJ:
 653 Prentice Hall.
- 654 Ji, C., Wald, D. J., and Helmberger, D. V., 2002. Source description
 655 of the 1999 Hector Mine, California, earthquake, part I: wavelet
 656 domain inversion theory and resolution analysis. *Bulletin of the*
 657 *Seismological Society of America*, **92**(4), 1192–1207.
- 658 Joseph, A., 2011. *Tsunamis: Detection, Monitoring, and*
 659 *Early-Warning Technologies*. Amsterdam: Academic.
- 660 Kalnay, E., 2003. *Atmospheric Modeling, Data Assimilation, and*
 661 *Predictability*. Cambridge: Cambridge University Press.
- 662 Kawanishi, T., Kuroiwa, H., Kojima, M., Oikawa, K., Kozu, T.,
 663 Kumagai, H., Okamoto, K., Okumura, M., Nakatsuka, H., and
 664 Nishikawa, K., 2000. TRMM precipitation radar. *Advances in*
 665 *Space Research*, **25**(5), 969–972.
- 666 Kuo, T., Fan, K., Kuochen, H., Han, Y., Chu, H., and Lee, Y., 2006.
 667 Anomalous decrease in groundwater radon before the Taiwan
 668 M6.8 Chengkung earthquake. *Journal of Environmental*
 669 *Radioactivity*, **88**, 101–106.
- 670 Landsea, C. W., 2007. Counting Atlantic tropical cyclones back to
 671 1900. *EOS Transactions, American Geophysical Union*,
 672 **88**(18), 197–202.
- 673 Mainsant, G., Larose, E., Brönnimann, C., Jongmans, D., Michoud,
 674 C., and Jaboyedoff, M., 2012. Ambient seismic noise monitoring
 675 of a clay landslide: toward failure prediction. *JGR-ES*, **117**,
 676 F01030, 12 pp, doi:10.1029/2011JF002159.
- 677 Malardel, S., 2005. *Fondamentaux de météorologie. À l'école du*
 678 *temps*, Toulouse: Cépaduès.
- 679 Marchi, L., Arattano, M., and Deganutti, A. M., 2002. Ten years of
 680 debris-flow monitoring in the Moscardo Torrent (Italian Alps).
 681 *Geomorphology*, **46**, 1–17.
- 682 Massonet, D., Briole, P., and Arnaud, A., 1995. Deflation of Mount
 683 Etna monitored by spaceborne radar interferometry. *Nature*, **375**,
 684 567–570.
- 685 McNutt, S. R., Rymer, H., and Stix, J., 2000. Synthesis of volcano
 686 monitoring, Chapter 8 of *Encyclopedia of Volcanoes*, San Diego:
 687 Academic Press, pp. 1165–1184
- 688 Meinig, C., Stalin, S. E., Nakamura, A. I., González, F., and
 689 Milburn, H. G., 2005. Technology developments in real-time
 690 tsunami measuring, monitoring and forecasting.
 691 In *Oceans 2005 MTS/IEEE, 19–23 September 2005*,
 692 Washington, DC.
- 693 Minnett, P. J., Evans, R. H., Kearns, E. J., and Brown, O. B., 2002.
 694 Sea-surface temperature measured by the Moderate Resolution
 695 Imaging Spectroradiometer (MODIS) Geoscience and Remote
 696 Sensing Symposium, 2002. IGARSS'02. 2002 IEEE, Vol. 2,
 697 pp. 1177–1179.
- NASA, 2012a. Temperature. *National Aeronautics and Space*
 698 *Administration*, [http://science.nasa.gov/earth-science/oceanog-](http://science.nasa.gov/earth-science/oceanography/physical-ocean/temperature)
 699 [raphy/physical-ocean/temperature](http://science.nasa.gov/earth-science/oceanography/physical-ocean/temperature), visited in Mai 2012. 700
- NASA, 2012b. <http://earthobservatory.nasa.gov/>, visited in Mai 701
 2012. 702
- Nerem, R. S., Chambers, D., Choe, C., and Mitchum, G. T., 2010. 703
 Estimating mean sea level change from the TOPEX and Jason 704
 Altimeter Missions. *Marine Geodesy*, **33**, 435–446. 705
- NOAA 2012. <http://www.ndbc.noaa.gov/dart.shtml>, visited in Mai 706
 2012. 707
- Olson, S. A., and Norris, J. M., 2007. U.S. Geological Survey 708
 Streamgaging. USGS-Fact Sheet 2005–3131. 709
- Oppikofer, T., Jaboyedoff, M., and Keusen, H.-R., 2008. Collapse 710
 of the eastern Eiger flank in the Swiss Alps. *Nature Geosciences*, 711
1, 531–535. 712
- Pedrazzini, A., Abellan, A., Jaboyedoff, M., and Oppikofer, T., 713
 2011. Monitoring and failure mechanism interpretation of an 714
 unstable slope in Southern Switzerland based on terrestrial laser 715
 scanner. *14th Pan-American Conference on Soil Mechanics and*
Geotechnical Engineering, Toronto. 716
 717
- Pielmeier, C., Schneebeli, M., 2002. Snow stratigraphy measured 718
 by snow hardness and compared to surface section images. In 719
Proceedings of the International Snow Science Workshop
 2002, Penticton, BC, Canada, pp. 345–352. 720
 721
- Prata, A. J., 2009. Satellite detection of hazardous volcanic clouds 722
 and the risk to global air traffic. *Natural Hazards*, **51**, 303–324. 723
- RCPEVE, 2012. The 2011 off the pacific coast of Tohoku Earth- 724
 quake (M9.0). *Research Center for Prediction of Earthquakes*
and Volcanic Eruptions, [http://www.aob.geophys.tohoku.ac.jp/](http://www.aob.geophys.tohoku.ac.jp/aob-e/info/topics/20110311_news/index.html)
[aob-e/info/topics/20110311_news/index.html](http://www.aob.geophys.tohoku.ac.jp/aob-e/info/topics/20110311_news/index.html), visited in Mai 725
 2012. 726
 727
- SafeLand, 2010. Deliverable 4.1 – Review of techniques for land- 728
 slide detection, fast characterization, rapid mapping and long- 729
 term monitoring. Edited for the SafeLand European project by 730
 Michoud, C., Abellán, A., Derron, M.-H., and Jaboyedoff, M. 731
 Available at <http://www.safeland-fp7.eu>. 732
 733
- Sassa, K., Picarelli, L., and Yueping, Y., 2009. Monitoring, 734
 prediction and early warning. In: Chapter 20 in Sassa, K., and 735
 Canuti, P. (eds.) *Landslides- disaster risk reduction*. Springer, 736
 pp. 351–375. 737
- Schär, C., Vidale, P. L., Lüthi, D., Frei, C., Häberli, C., Liniger, 738
 M. A., and Appenzeller, C., 2004. The role of increasing temper- 739
 ature variability in European summer heatwaves. *Nature*, 740
427(6972), 332–336. 741
- Shaw, E., 1994. *Hydrology in Practice*, 3rd edn. London: Chapman 742
 & Hall. 743
- Shuttleworth, W. J., 2012. *Terrestrial Hydrometeorology*. Chiches- 744
 ter: Wiley-Blackwell. 745
- Singhroy, V., Charbonneau, F., Froese, C., and Couture, R., 2011. 746
 Guidelines for InSAR Monitoring of Landslides in Canada. 747
14th Pan-American Conference on Soil Mechanics and
Geotechnical Engineering, Toronto. 748
 749
- SLF, 2012. [http://www.slf.ch/lawineninfo/zusatzinfos/howto/](http://www.slf.ch/lawineninfo/zusatzinfos/howto/index_EN)
[index_EN](http://www.slf.ch/lawineninfo/zusatzinfos/howto/index_EN), visited in Mai 2012. 750
 751
- Smith, W. H. F., Scharroo, R., Titov, V. V., Arcas, D., and Arbic, B. K., 752
 2005. Satellite altimeters measure tsunami. *Oceanography*, **18**, 753
 10–12. 754
- Stein, R. S., Barka, A. A., and Dieterich, J. H., 1997. Progressive 755
 failure on the North Anatolian fault since 1939 by 756
 earthquake stress triggering. *Geophysical Journal International*, 757
128, 594–604. 758
- Tarchi, D., Casagli, N., Fanti, R., Leva, D., Luzi, G., Pasuto, A., 759
 Pieraccini, M., and Silvano, S., 2003. Landslide monitoring by 760
 using ground-based SAR interferometry: an example of applica- 761
 tion to the Tessina landslide in Italy. *Engineering Geology*, **68**, 762
 15–30. 763

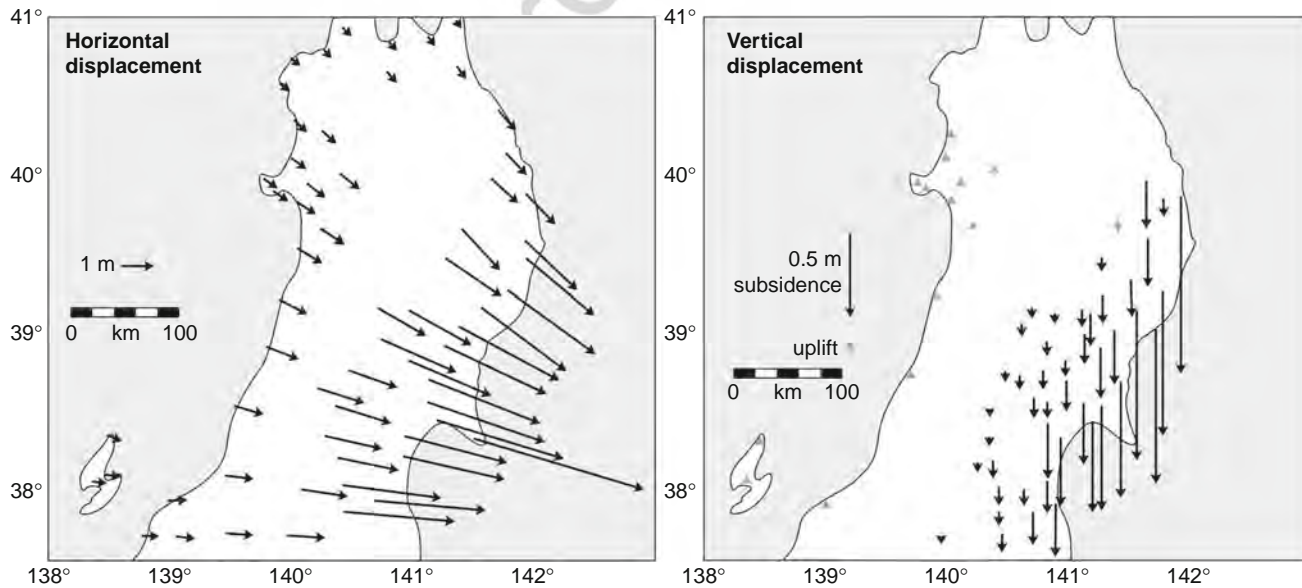
764	Travelletti, J., Delacourt, C., Allemand, P., Malet, J.-P., Schmittbuhl, J., Toussaint, R., and Bastard, M., 2012. Correlation of multi-temporal ground-based optical images for landslide monitoring: application, potential and limitations. <i>ISPRS Journal of Photogrammetry and Remote Sensing</i> , 70 , 39–55.	Climate change	790
765	UNOSAT, 2012. http://www.unitar.org/unosat/node/44/1259 , visited in Mai 2012.	Debris flow	791
766	Vicente, G., Scofield, R., and Menzel, W., 1998. The operational goes infrared rainfall estimation technique. <i>Bulletin of the American Meteorological Society</i> , 79 (9), 1883–1898.	Deep-seated gravitational slope deformations	792
767	Vilardo, G., Isaia, R., Ventura, G., De Martino, P., and Terranova, C., 2010. InSAR permanent scatterer analysis reveals fault re-activation during inflation and deflation episodes at Campi Flegrei caldera. <i>Remote Sensing of Environment</i> , 114 , 2373–2383.	Doppler weather radar	793
768	Wilson, J., Crook, N., Mueller, C., Sun, J., and Dixon, M., 1998. Nowcasting thunderstorms: a status report. <i>Bulletin of the American Meteorological Society</i> , 79 (10), 2079–2099.	Earthquake	794
769	WMO, 2012a. http://www.wmo.int/pages/themes/weather/index_en.html , visited in Mai 2012.	Earthquake prediction and forecasting	795
770	WMO, 2012b. http://www.wmo.int/pages/about/Resolution40_en.html , visited in Mai 2012.	El Niño/Southern oscillation	796
771		Eruption types (volcanic)	797
772		Flash flood	798
773		Flood hazard and disaster	799
774		Hurricane (cyclone, typhoon)	800
775		Hydrograph, flood	801
776		Inclinometer	802
777		North Anatolian fault	803
778		Piezometer	804
779		Pore-water pressure	805
780		Remote sensing of natural hazards and disasters	806
781		Rock avalanche	807
782		Rock fall	808
783		San Andreas fault	809
784		Santorini	810
785		Seismic gap	811
		Seismograph/seismometer	812
		Slope stability	813
786	Cross-references	Tiltmeters	814
787	Accelerometer	Tohoku, Japan, earthquake, tsunami and Fukushima accident (2011)	815
788	Aerial photography/satellite imagery	Tsunami	816
789	Avalanches		817

t1.1 **Monitoring Natural Hazards, Table 1** Description of the most common sensors used to monitor natural hazards

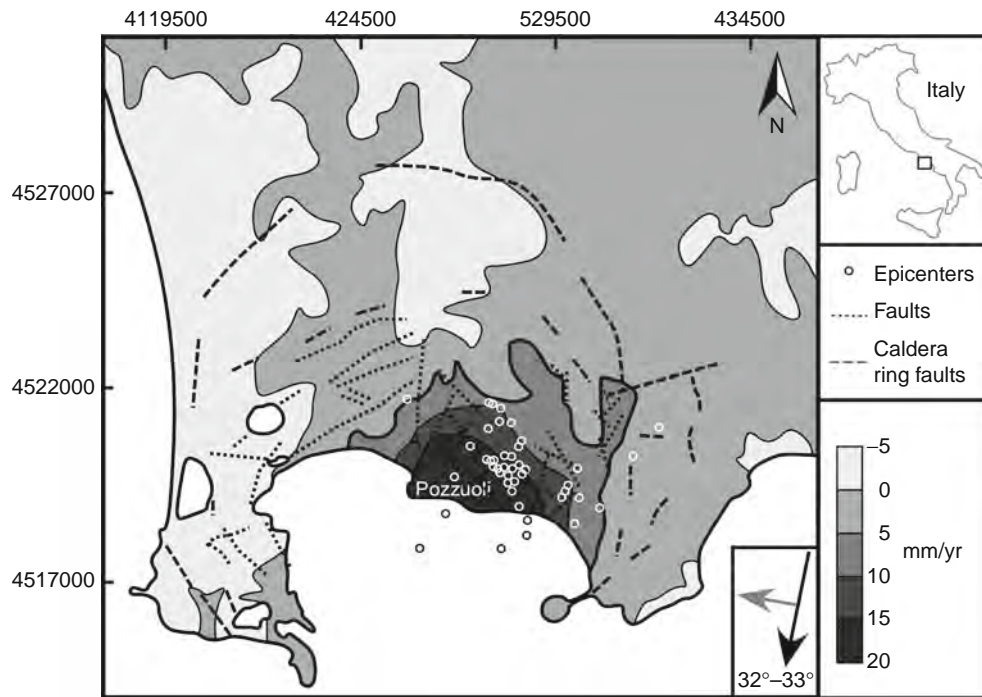
t1.2	Sensors	Monitored variables	Principles	Monitored phenomenon
t1.3	<i>Pressure measurement</i>	Pressure (air, water), in situ stress measurement	Barometer: used a height of fluid in vacuum to compensate the atmospheric pressure Pressure transducer: convert a material deformation electrical signal	Atmospheric circulation, water table, Earth crust deformations
t1.4	<i>Radar (Radio Detecting And Ranging)</i>	Distance to a hard object and velocity	Reflection of an emitted microwave by an object and received by an antenna. The Doppler effect permits to estimate the speed of an object	Precipitation imaging, river discharge (velocity), sea level rise, tornadoes
t1.5	<i>Laser (Light Amplification by Stimulated Emission of Radiation) and Lidar (Light Detection And Ranging)</i>	Distance to a surface and orientation	The Laser consists in amplifying coherent light by using the principle of stimulated emission, creating a narrow beam that can be reflected by surfaces. The Lidar uses the principle of range finder by evaluation of the distance by the time of flight or the phase comparison. The direction of the beam is recorder in order to obtain the 3D coordinates. Information on the reflectivity can be also obtained	Landslides movements and characterization, local atmospheric circulations
t1.6	<i>Thermometer</i>	Temperature	The measurement is realized using changes of the properties of materials under temperature variations such as volume (mercury), or the electric resistance such as thermistors or thermocouple which produce a current proportional to the temperature between two different materials	Climate, weather forecasts, volcano
t1.7	<i>Accelerometer and seismometer</i>	Acceleration, velocity, displacement	Measurement of ground acceleration using transforming movement into electrical signal	Earthquake, surface deformation (landslides)
t1.8	<i>Wind sensor</i>	Wind speed and direction	Anemometer is a rotating device entrained by wind such as cup. Anemometers usually use three half spheres like rotating along a vertical axe. The windvanes is a device which is orientated parallel to the wind. Measurement of ultrasonic wave by several sensors permits to obtain the wind velocity and direction	Weather, hurricanes, tornadoes
t1.9	<i>Rain gauge</i>	Amount of precipitation throughout time	The traditional rain gauges are tipping-bucket, like a container that is emptied each time the unitary volume that can be measured is reached. Precipitations can also be measured using rain drop impact counts	Weather, bad weather
t1.10	<i>InSAR (interferometric synthetic aperture radar)</i>	Topography, small surface displacement using radar	By using ground-based or satellite InSAR images, it is possible to extract a distance to the ground and a very accurate changes between two images down to millimeter resolution in the direction of line of site. This is based on microwave interference	Earth surface deformation: Earthquakes, volcanoes, landslides, subsidence
t1.11	<i>GNSS (Global Navigation Satellite System)</i>	Ground position	The principle is to acquire several highly precise travel times of microwaves from at least two satellites (with highly precise positions) and to compute the distance and location to calculate the best position (can be improved include the phase information). Highest accuracy is obtained by using differential GNSS method which computes difference with a well-known GNSS position. This remove several error such atmospheric and ionosphere one. The position resolution reaches a few millimeters	Earthquakes, volcanoes, landslides, subsidence
t1.12				



Monitoring Natural Hazards, Figure 1 Statistics of Swiss monthly temperature differences to the average over the whole period. This shows a shift of 0.8°C. The probability to get a monthly temperature 3°C greater than the average temperature is at least twice for the period 1941–2000 compare to 1864–1923 (Modified from Schär et al., 2004).

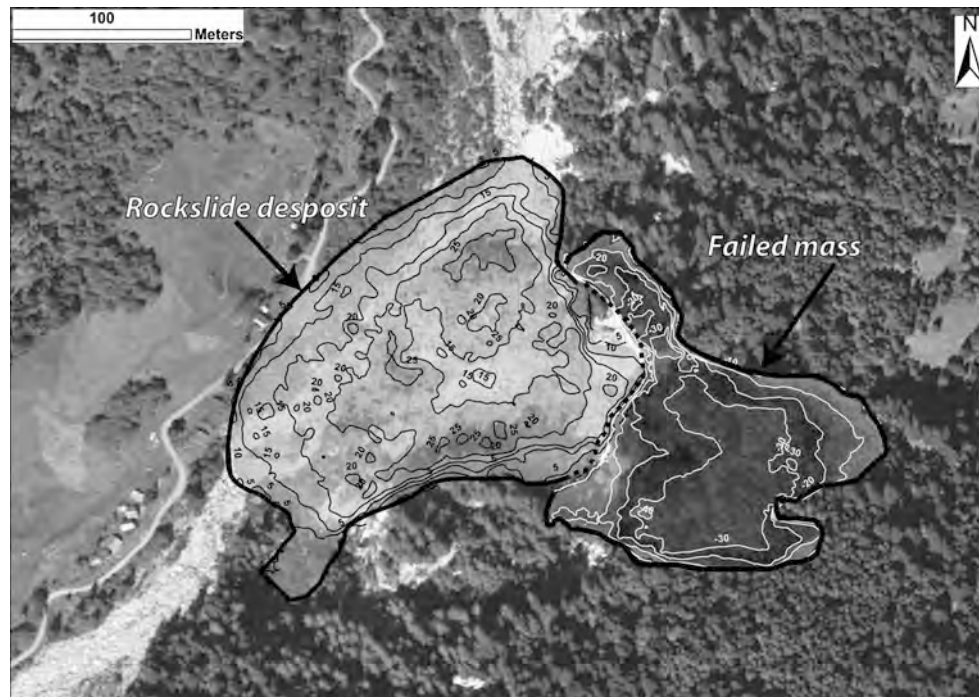


Monitoring Natural Hazards, Figure 2 Coseismic crustal deformation of the Tohoku Earthquake. Horizontal and vertical displacement. These displacements are defined by the difference between the positions on the day before the mainshock (March 10) and those after the mainshock, March 11 (Modified and simplified after RCPEVE, 2012).



Monitoring Natural Hazards, Figure 3 PS-InSAR™ showing uplift along the line of sight with data from descending orbit on October 2005–November 2006. Observe the correlation between uplifts, structures, and seismic activity (Modified and synthesized after Vilardo et al., 2010).

Uncorrected



Monitoring Natural Hazards, Figure 4 Map of the deposit and failed mass thickness of the of the Val Canaria rockslide (Ticino, Southern Swiss Alps). This map based on the comparison of the airborne and terrestrial Lidar digital elevation model taken before and after the 27.10.2009 rockslide event (modified after Pedrazzini et al., 2011; the aerial picture and airborne Lidar are provided by swisstopo).

Uncorrected

Annex B5

After Michoud C, Jaboyedoff M, Derron MH, Nadim F and Leroi E: Classification of landslide-inducing anthropogenic activities. 5th Canadian Conference on Geotechnique and Natural Hazards, Kelowna, Canada, 10 p., 2011



Classification of landslide-inducing anthropogenic activities

After Michoud C, Jaboyedoff M, Derron MH, Nadim F and Leroi E: Classification of landslide-inducing anthropogenic activities. 5th Canadian Conference on Geotechnique and Natural Hazards, Kelowna, Canada, 10 p., 2011.

Abstract

Although landslides are usually considered typical examples of natural hazards, they can be influenced by human activities. Many examples can be found in the literature about slope instabilities induced by anthropogenic activities, ranging from small superficial landslides to rock avalanches. Research on this topic is of primary importance for understanding and mitigation of landslide risk. Indeed, slope stabilities influenced by human actions contribute significantly to the risk level because, by definition, they are located where elements at risk and people are present. Within the framework of the European project SafeLand “Living with Landslide Risk in Europe”, we analyzed the landslides induced by anthropogenic factors in Europe and elsewhere. During the bibliographical research, it appeared that a complete and illustrated classification on human activities influencing slope stabilities does not yet exist. Therefore, a new classification is introduced about anthropogenic activities affecting slope stability conditions. This classification takes into account conceptual processes leading to landslides and the distinction between destabilization factors and triggering factors. The classification was tested and improved through fifty-eight well-documented case studies, such as Elm, Aberfan, Namsos or even Rissa landslides. Furthermore, the boundary between natural and “anthropogenic” landslide triggers (e.g. water run-off modified by new land-uses, creating landslides some km farther), and the time during which changes and reactions are to be considered as direct consequences of human activities were highlighted. Finally, anthropogenic influences can also be positive and examples of (non-voluntary) positive human impacts on slope stability are presented.

Keywords: Anthropogenic activities, Landslide-inducing, Classification.

1.1 Introduction

While often natural in origin, many landslides are triggered by anthropogenic activities, with reported sizes ranging from small shallow landslides, such as those observed in Gondo, Switzerland, to large rock avalanches such as Elm, Switzerland, or Frank slide, Canada. At each scale, landslides may present several levels of human implications. Within the framework of the SafeLand European project *Living with Landslide Risk in Europe*, the authors analyzed the landslides induced by

anthropogenic factors in Europe and elsewhere (Nadim et al. 2010). During the bibliographical research, it appeared that a complete and illustrated classification on human activities influencing slope stabilities does not yet exist. However, research on this topic is of primary importance. Slope stabilities influenced by human actions contribute significantly to the risk level because, by definition, they are located where elements at risk and people are present.

We propose to classify human activities influencing slope stabilities through internal parameters that affect the susceptibility, such as topography or geology, and external factors, such as freezing or infiltration (Jaboyedoff and Derron, 2005a). The most common factor is the modification of slope profile, usually caused by cuts and fills, that changes the slope factor of safety. Moreover, the effect of the modification of the ground water by a dam, a pipe leak or modification of overflow path can lead to changes in the behaviour of the material or changes in the water infiltration that again decrease the factor of safety.

In his famous paper *Mechanisms of Landslides*, Terzaghi (1950) highlighted the “internal” and “external” causes that can lead to landslides. Within the nineteen identified reasons, nine of them can be influenced or directly transformed by anthropogenic activities because of four physical agents:

- Weight of slope-forming material;
- Transported material;
- Water;
- High frequency vibration.

According to Vaunat et al. (1994) and Leroueil et al. (1996), landslides follow different stages of slope movements, i.e. the pre-failure, the onset of failure, the post-failure and the reactivation stages, which relate changing mechanical laws and parameters. Champetier de Ribes (1987) characterized landslide susceptibilities and activities according to:

1. Predispositions factors;
2. Aggravating factors;
3. Triggering factors.

Developing further Terzaghi's (1950) classification, we suggest taking into account conditions affecting the stability at different stages of slope movements described by Champetier de Ribes (1987), especially differentiating destabilizing and triggering actions. This new classification is illustrated by relevant case studies, such as Aberfan, Elm, Namsos or Vaiont landslides.

Furthermore, we want to highlight the boundary between natural and “anthropogenic” landslides (e.g. water run-off modified by new land-uses, creating landslides some km farther), and the time during which changes and reactions are to be considered as direct consequences of human activities.

Anthropogenic influences can also be positive. We will show examples of (non-voluntary) positive human impacts on slope stability.

1.2 Classification of anthropogenic activities inducing instabilities

1.2.1 Differences between destabilizing and triggering factors

Anthropogenic activities can affect slope stability by changing the strength or effective stresses, modifying the boundary conditions or inducing changes in material behaviour could influence the factor of safety (Terzaghi, 1950). After Champetier de Ribes' considerations (1987), we assume that human activities can affect predisposed internal parameters or external factors to destabilize stable slopes, as well as dormant and active landslides. Human activities can also create completely new instabilities (Figure 6.1).

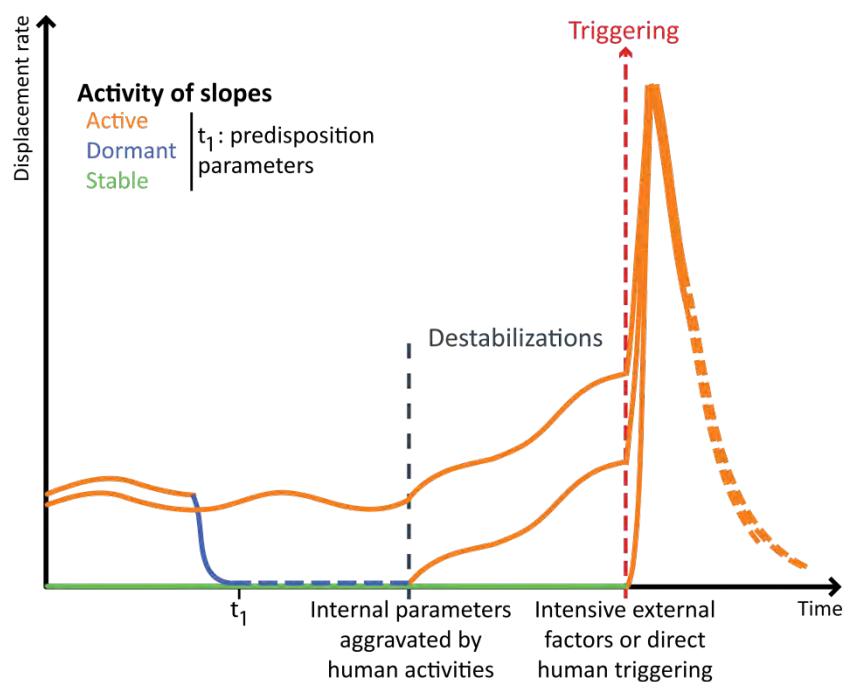


Figure 6.1: Anthropogenic activities can destabilize and trigger stable slopes, dormant or active landslides (modified after Vaunat et al. 1994, and Leroueil et al. 1996).

Then, taking into account the different stages of slope deformation (Leroueil et al. 1996, Vaunat et al. 1994), who stated that destabilization time durations as onset of failures and reactivations stages of slope movements, i.e. the time interval within which a continuous shear band is being formed or reactivated. Localized movements can affect some parts of the slope but the whole unstable area does not move entirely. Afterwards, the triggering happens when the whole slope is in movement or collapse. Terzaghi (1950) defined the destabilization time interval as a progressive decrease of the

Safety Factor (SF) of the entire unstable slope. The triggering of the whole sliding (or collapse) happens once the SF becomes lower than 1 (Figure 6.2).

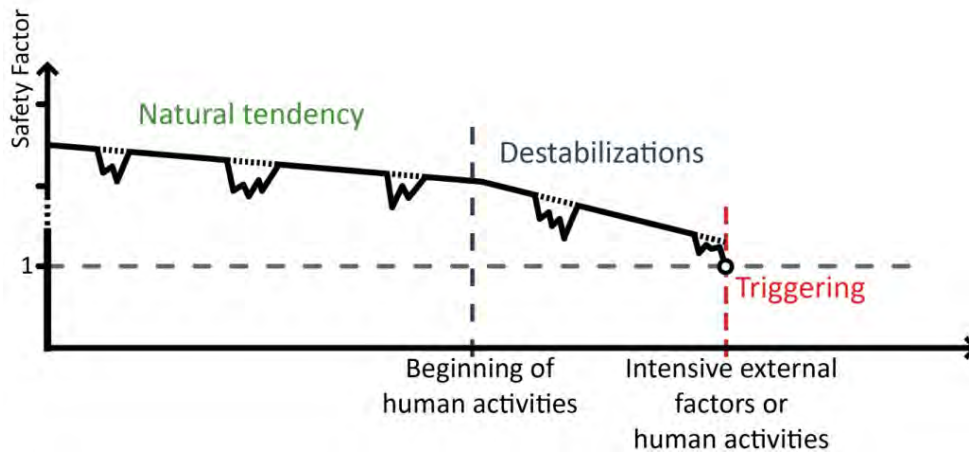


Figure 6.2: Evolution of the SF of Turtle Mountain before the Frank slide. The natural trend was a slow decreasing in stability conditions, due to bad geological settings, with seasonal worsening during melting of snow. Moreover, mining activities began to accelerate the aggravation of the SF. The 29 April 1903, the rock avalanche occurred and was probably triggered by freezing of melted snow inside joints, which drastically reduced the SF lower than 1 (modified after Terzaghi, 1950).

1.2.2 The Classification

To achieve the classification of all human activities influencing slope stability (Table 1), we first identified all physical actions (or non-actions) and their associated agents which can lead to instabilities, i.e.:

1. Modifications of slope profiles;
2. Modification of pore pressure;
3. Vibrations;
4. Degradation of artificial structures;
5. Head overcharges;
6. Foot slope destructions;
7. Rupture of artificial structures;
8. Explosives.

The physical effects of these actions on equilibrium conditions of slopes are described in Terzaghi (1950). Then, all anthropogenic activities which can affect natural slope regimes have been recognized and classified:

1. Embankments;
2. Tailing hills;
3. Fill slopes;

4. Cut slopes;
5. Pipe leaks;
6. Dam reservoirs;
7. Land-use changes;
8. Heavy traffic;
9. Filling of torrential check dams;
10. Weakening of terraced walls;
11. End of drainage systems;
12. Leaks in old canalization networks;
13. Construction work;
14. Excavation work;
15. Inappropriate retaining wall;
16. Pipe bursting;
17. Blasting.

The activities involved by this classification are explained in the next sections. Illustrated with 54 published case studies, the consequences of these influences are multiples: it can contribute and/or produce single or multiple landslide events within a confined or large area. This is relevant for rocks, debris and earth materials and for sliding and flowing movements (following the classification of Cruden and Varnes, 1996). Furthermore, within the synthesis of these case studies, it seems that there are three main human activities contexts leading to landslides, namely mining and quarry, agriculture and pastures, and civil engineering works.

Action	Agent	Human activities	Type	Famous and/or relevant examples
DESTABILIZATION	Weight of slope-forming material	Embankment	ES	Irbid-Amman Highway, Jordan (Al-Homoud et al., 1997)
			DF	Nice Harbour, France (Assier-Rzadkiewicz et al., 2000)
			RS>DS	Panama Canal, Panama (Van Hise et al., 1916 ; Alfaro, 1988)
	Tailing hill		DF	Aberfan, Wales (Bishop and Penman, 1968)
			DF	Vai di Stava, Italy (Alexander, 1986)
			DF	Blue Ridge Parkway, USA (Collins, 2008)
	Fill slope		DF	Gowan Creek, Canada (Collins, 2008)
			DS	Zefat, Israel (Katz and Crouvi, 2007)
			RS	Alesund, Norway (Befring, 2008)
	Modifications of slope profiles	Transported material	RS>RFa	Arvel, Switzerland (Choffat, 1929 ; Joboyedoff, 2003)
			ES	Belmont, Switzerland (Parioux, 2007)
			RS>RFa	Elm, Switzerland (Heim, 1882)
			RS	Eterpas, Switzerland (Baillifard et al., 2003)
			RS>RFa	Frank slide, Canada (Mc Connell and Brock, 1904 ; Benko and Stead, 1998)
			DT-DS	Luggar Bhatti, India (Sah and Mazari, 1998)
Pipe leak	Water	DS	Portalet, Spain (Herrera et al., 2010)	
		ES	Seattle, USA (Schulz, 2007)	
		DS	Sidi Rached Viaduct, Algeria (Guemache et al., accepted)	
		RS>DS	Caracas - La Guaira highway, Venezuela (Salcedo, 2009)	
		DF	Les Diablerets, Switzerland (Joboyedoff and Bonnard, 2007)	
		EF	Lutzenberg, Switzerland (Valley et al., 2004)	
		ES	Pays de Henve, Belgium (Preuth et al., 2010)	
		RS	Canelles, Spain (Pinyol and Alonso, 2008)	
		RS>DS	Quianjiaoping, 3 Gorges reservoir, China (Wang et al., 2004)	
		RS>DS	Shuping, 3 Gorges reservoir, China (Wang et al., 2005)	
Land-use change		RS>ES	Valont, Italy (Alonso and Pinyol, 2010)	
		ES	Caramanico Terme, Italy (Wasowski, 1998)	
		ES	Flemish Ardennes, Belgium (Van den Esckhaut et al., 2007)	
		ES	Hilly back countries, New-Zealand (Glade, 2003)	
		EF	Menton, France (Safel and deliverable 1.6, 2010)	
		EF	Northern back countries, Puerto Rico (Walker et al., 1996)	
		DS>DF	Northern Pakistan (Sudmeier-Rieux et al., 2007)	
		DF	Sarno, Italy (Cascini et al., 2008)	
		RS	Sihuas Valley, Peru (Hermanns et al., 2008)	
		DS	Californian roads, USA (McCauley et al., 1985 ; in Panteleidis, 2009)	
Heavy traffic		DS	Rio Mendoza Valley, Argentina (Moreiras, 2004)	
		DF	Siano Biato, Slovenia (Logar et al., 2000)	
		DF	Valtellina, Italy (Crosta et al., 2003)	
		RS>ES	Caramanico Terme, Italy (Wasowski, 1998)	
		ES	Vars, France (Martin, 1998)	
		DF	Fournière hill, France (Allix, 1930 ; Albenque, 1931)	
		ES	Rissa, Norway (Gregersen, 1981)	
		DS	Fornigal, Spain (Gonzales-Gallego et al., 2008)	
		ES	Mount Elgon, Uganda (Knapen et al., 2006)	
		RS>RFa	Panama Canal, Panama (Van Hise et al., 1916 ; Alfaro, 1988 ; Panama Canal Authority, 2001)	
Filling of torrential check dam		DF	Gondo, Switzerland (Rouillet and Joris, 2001)	
		EF	Ulu Klang, Malaysia (Gue See Sew and Tan Yean Chin, 2002)	
		DF	Cleuson-Divence dam gallery, Switzerland (Grande Dixence SA, 2005)	
		DF	Fully, Switzerland (Marquis, 2002)	
		DS	Sidi Rached Viaduct, Algeria (Guemache et al., accepted)	
		ES	Hawkesbury, Canada (Eden, 1956)	
		ES	Namsos, Norway (Nordal et al., 2009)	
		RFa	Sailion, Switzerland (Parioux, 2007)	
		RF	Yosemite National Park, USA (Wieczorek and Snyder, 2004)	
		TRIGGERING	Weight of slope-forming material	Construction works
DS	Fornigal, Spain (Gonzales-Gallego et al., 2008)			
RS>RFa	Panama Canal, Panama (Van Hise et al., 1916 ; Alfaro, 1988 ; Panama Canal Authority, 2001)			
Foot slope destruction	Transporting material		DF	Gondo, Switzerland (Rouillet and Joris, 2001)
			EF	Ulu Klang, Malaysia (Gue See Sew and Tan Yean Chin, 2002)
			DF	Cleuson-Divence dam gallery, Switzerland (Grande Dixence SA, 2005)
Rupture of artificial structures	Water		DF	Fully, Switzerland (Marquis, 2002)
			DS	Sidi Rached Viaduct, Algeria (Guemache et al., accepted)
			ES	Hawkesbury, Canada (Eden, 1956)
Explosives	High frequency vibration		ES	Namsos, Norway (Nordal et al., 2009)
		RFa	Sailion, Switzerland (Parioux, 2007)	
		RF	Yosemite National Park, USA (Wieczorek and Snyder, 2004)	
		RF	Yosemite National Park, USA (Wieczorek and Snyder, 2004)	

Table 6.1: New classification of anthropogenic activities affecting stability conditions. It takes into account processes leading to landslides and the distinction between destabilization factors and triggering factors. The classification has been tested and illustrated with fifty-eight relevant and/or famous published case studies. The initials within the "Type" column refer to the classification of Cruden and Varnes (1996): D- Debris, E- Earth, F- Flow, Fa- Fall, R- Rock, S- Slide, T- Topple.

1.3 Illustration of destabilizing activities

1.3.1 Modification of slope profile

Modifying slope profiles, there are two agents which influence slope stabilities: the weight of slope forming material and the transporting material. They essentially decrease material cohesions and increase shear strength (Terzaghi, 1950).

Classically the creation of artificial embankments for civil engineering works increases the weight of slope forming material; the associated landslides are mainly linked with new railway or road constructions, e.g. along the Irbid-Amman Highway in Jordan (Al-Homoud et al. 1997), and with coastal polders, as shown by the French Nice harbour (Assier-Rzadkiewicz et al. 2000). Such event occurs when dimensioning errors are performed.

Created by precarious anthropogenic deposits of non-consolidated mining and quarry debris, tailing hills are regularly badly designed. Thus, the material of these poorly stable slopes can become sources of debris flows after strong rainfall events, such as the 1966 Aberfan event (Bishop and Penman, 1968).

Fill slopes are essentially linked with civil engineering works and roads in hilly regions, involving the added material in rotational earth slides. Even if they usually affect small part of slopes, they can have a large impact by cutting important roads or railways (Collins, 2008). A second reason of destabilizations by filling is more historical, occurring in cities with long habitation histories. Katz and Crouvi (2007) introduced the case of Zefat, Israel. Buildings inside the old district are constructed directly on few meters of ballast, deposited during 2000 years of human presence. Thus, built on mechanically weak debris, the district is more susceptible to landslides and seismic-shaking.

Cut slopes are one of the major anthropogenic activities that lead to landslides. Indeed, remove or erode toe slopes destabilize rocks, debris and soils materials. Cut slopes are mainly carried out for civil engineering works along corridors (Sah and Mazari, 1998; Baillifard et al. 2003; Parriaux, 2007; Herrera et al. 2011) or in cities (Schulz, 2007; Befring, 2008). They can even lead to catastrophic rock avalanches during mining and quarrying activities, such as the event of 1923 in Arvel illustrated in Figure 6.3 (Choffat, 1929; Jaboyedoff, 2003a).

Along corridors, slopes can be cut and filled. Both linked works are destabilizing, and landslides are usually triggered just after heavy rainfalls, especially in mountain areas as shown in Figure 6.4 (Barnard et al. 2001; Moreiras, 2004, Sudmeier-Rieux et al. 2009).



Figure 6.3: Picture of the deposits below the rock face, after the 1922 rock fall event (Choffat, 1929, in Jaboyedoff, 2003a).



Figure 6.4: Cut and filled slope led to rotational earth slide along a Nepalese road in 2008 (courtesy of A. Breguet and K. Sudmeier-Rieux).

1.3.2 Modification of pore pressure

Modifications of natural pore pressures are usually dealing with disturbance of water runoff and seepage conditions. However, adding water in the system involves a decrease frictional strength, and even can create spontaneous liquefaction phenomena (Terzaghi, 1950). Canalization networks are leaking up to 30% (Giret and Rathieuville, 1996). Therefore pipe leaks are an important issue. Even if usually resulting landslides are small (Figure 6.5), the proximity to houses make them dangerous, such as the Lutzenberg earth flow which killed 3 people. Moreover, this destabilization can affect large areas, due to several leaks along water galleries leading to quite a lot of landslides (Preuth et al. 2010).

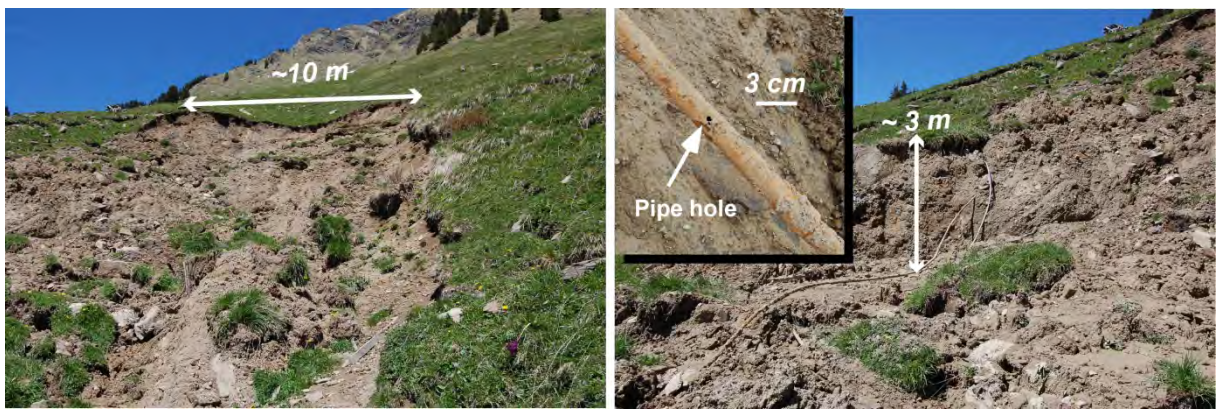


Figure 6.5: Earth flows occurred in 2007 in Les Diablerets, Switzerland, after a rainfall with a return period of 3 years. Previously, the water pipe leak aggravated the stability conditions, increasing the water pore pressure (modified from Jaboyedoff and Bonnard, 2007a).

The impacts of filling and drawdown dam reservoirs (Terzaghi, 1950) have been recently reinvestigated, in particular after several dramatic events. The 1963 Vaiont rock slide is one of the most famous and studied filling dam reservoir-induced landslides all over the world (Alonso and Pinyol, 2010). On the other hand, landslides can also be induced during reservoir drawdown (Terzaghi, 1950; Pinyol and Alonso, 2008). For now, China is doing great efforts in reservoir-induced instabilities to reduce fatalities from landslides along the world greatest reservoir of the Three Gorges dam, through the development of education means, site monitoring, early warning system and remediation measures (Wang et al. 2004; Wang et al. 2005).

Finally, land-use changes are the most important cause in modification of water pore pressure, because they relate to long-term and regional processes, such as deforestations (Glade, 2003; Remondo et al. 2006), urbanization (Wasowski, 1998; Cascini et al. 2008b) and irrigation works (Hermanns et al. 2008). They involved water seepages and run-off changes which can affect slopes some km farther than the human activities. After the past decades of fast urbanization without organization of superficial water collect, the numerous landslides of the November 2000 in the

Menton territory (France) is a relevant example of the possible distance between human-modified areas and sliding events, linked by water run-off (Nadim et al. 2010). New irrigation effort can lead to landslides too; indeed, the South American's largest irrigation project fertilizes progressively the deserted Sihuas plateau (Peru) for 25 years. As a consequence, new infiltrated waters increase severely the water pore pressure that is inducing few huge rockslides (Hermanns et al. 2008).

1.3.3 Vibrations

Vibrations due to heavy daily traffic along roads and highways can lead to increase shear stresses and to decrease the cohesion of materials (Terzaghi, 1950). Vibration-induced landslides are usually rare and small, but their impact can be high as they affect transportation ways. Along Californian highways, McCauley et al. (1985, in Pantelidis, 2009) counted 10 landslides destabilized by truck vibrations

1.3.4 Degradations of artificial structures

In the past, people who were living near potential instabilities built many structures which voluntarily (or not) acted as remediation systems. More recently, after many decades, population is leaving rural areas. As a consequence, some constructions useful for agricultural purposes, such as terraces and irrigations systems, are not maintained any more. Then, weakened terraced walls and irrigations systems do not play their roles of retaining and draining slopes, leading afterwards to landslides (Martin, 1998; Wasowski, 1998; Crosta et al. 2003a).

A second obvious reason of maintenance lacks is the falling into oblivions of old structures with the course of years, after wars and a series of political changes, like in Slovenia (Logar et al. 2000). For instance, historical abandoned canalization networks have oversaturated the sandy slopes filled with past debris of the Fourvière hill, in Lyon (France), for years. In November 1930, two dramatic debris flow occurred in the same night, killing 39 people (Allix, 1930; Albenque, 1931).

1.4 Illustration of Triggering factors

Anthropogenic-triggered landslides are usually caused by the same activities introduced before. Nevertheless, in these conditions, safety factors decreases compared below limit equilibrium during a shorter time lapse than the destabilizing period, inducing the sliding of the entire slope or the brutal activation of falls or flows.

In some cases, human activities release huge quantities of energy in the field, which affect a priori stable slopes with high safety factor. Indeed, the break of badly designed retaining walls poured tons of coarse materials on a building in 1993 in Malaysia (Gue See Saw and Tan Yean Chin, 2002).

Another example is the Cleuson-Dixence dam gallery, which suddenly burst the 12 December 2000 and triggered a massive debris flow, which killed three people. However, blasting operations are the most relevant examples of huge energy releases (Figure 1.6). They can trigger earth slides (Eden, 1956; Nordal et al. 2009) as well as large rock falls (Wieczorek and Snyder, 2004; Parriaux, 2007).

In another cases, human activities just trigger collapses of a priori unstable slopes with safety factors close to 1. Indeed, construction and excavation work can make heavy slope heads and severely cut toes. For instance, during the construction of the Panama's canal, recurrent events occurred in the Culebra's and Gaillard's cuts, even during dry seasons (Van Hise et al. 1916; Alfaro, 1988; Panama Canal Authority, 2001).

1.5 Discussions

In this section, we discuss the potential limits of this classification to draw attention to some open questions. We do not always offer unique answers to these questions, because some of these considerations are function of point of view.

1.5.1 Destabilization vs triggering

The temporal limit between destabilizing and triggering events is not yet well defined. As Wasowski (1998) highlighted, a one-hour intense tropical rainfall is considered as an evident triggering factor. Nevertheless, should we accept as trigger a three-day rainfall event? In the same way, the Fully's example illustrates this limit: after heavy rainfall, a water derivation pipe burst and carried water inside scree deposits and moraine debris 1500 m lower. After one night of discharge, a debris flow occurred (Marquis, 2002). In our point of view, events of one night could be reasonably considered as triggering factors. However, the temporal limit between destabilization and triggering is haziness, and some publications do not always allow to discriminate clearly both concepts.

Nevertheless it can be stated that the difference between destabilisation is the observations of three stages of deformations which possess very different time scale. The normal slope evolution can last hundreds to millions of years). The destabilizing period is the change in the mean behaviour of a normal slope deformation; while the triggering occurs in a shorter period compared to the previous one. This is not directly related to stages of deformation (Petley and Allison, 1997), this is indeed more related to the event that changed the behaviour during the time.

1.5.2 Successive events and real triggering

Landslides usually stem from several factors, and not from only one triggering action. We propose the terms of "successive events" for triggers initiating processes that lead rapidly to complete failure

of a slope. The destabilisation of a slope can be initiated in a small zone of the landslide by a human activity and propagate in a larger area like in Rissa (Gregersen, 1981) by successive retrogressive failures. Often rainfalls are considered as the major external parameter triggering instabilities. But in some cases of ruptures of artificial structures, meteorological events are not the direct trigger. For instance the water overpressure lead to break retaining walls, such as in Gondo (Rouiller and Joris, 2001), or to burst pipes, such as in Fully (Marquis, 2002). Thus, rainfalls are the cause but not the triggering, which is the massive and sudden carrying of material created by the rupture.

1.5.3 Human influences vs. natural causes

In some cases, the limits between human-induced and natural landslides can be unclear and hazy. The Caracas – La Guaira landslide (Salcedo, 2009) is a demonstrative example: the landslide reactivation was mainly due to the July 1967 Caracas earthquake; then the 19 March 2006 event was triggered by neotectonic movements. But Salcedo (2009) did not exclude that the increase of water pore pressure in urban areas due to inefficient drainages and limited sewages services acted as a second destabilization process. Nevertheless, no additional investigations were carried out and published to quantify the exact influences of anthropogenic effects compared to the seismic ones. Even if human effects can have only a minor role beside natural causes, they have to be always considered for detailed investigations.

1.5.4 Non-voluntary positive anthropogenic impacts

Finally, we introduce examples of anthropogenic activities which have non-voluntary positive impacts too on slope stabilities.

In the past, people in rural areas managed the territory carefully. Slope areas were terraced and water running off was considered a primordial resource (Nadim et al. 2010) that had to be collected in order to develop farming (Martin, 1998; Wasowski, 1998; Crosta et al. 2003a). Indirectly, they contributed to reduce the landslide onset probability.

More recently, the Puerto Rico island example is relevant as an example of non-voluntary reforestation. After economic changes, the industry-based economy became more active during the second half of the 20th century and human activities decreased in rural areas. In abandoned pastures and crops, the tropical forest begins to recover after 15 years post-abandonment (Aide et al. 1995). As a consequence, the natural reforestation contributes to stabilize slopes (Walker et al. 1996).

Another context: in the Swiss Alps, there are a lot of galleries which collect water from elevated springs for hydraulic power purposes. Thus, downstream torrents have less water. Consequently, debris flow hazard has decreased thanks to non-voluntary positive human impacts.

1.6 Conclusions

This paper proposes a classification of anthropogenic activities influencing slope stability. Taking into account the previous works of Terzaghi (1950), Vaunat et al. (1994) and Leroueil (1996), we classified landslide inducing human activities according to their destabilization or triggering ability, and then to their physical actions and agents involved. The initial conceptual classification was tested and improved through fifty-eight relevant and/or well known case studies.

Even if all issues are not yet solved, this classification furthers the investigations of human-induced landslides. It should help geologist and civil engineers to work together in order to prevent the foreseeable consequences of human activities and recommend remediation measures to improve the situation.

For example, in many urban areas, especially in Europe, infrastructures and water canalizations are quite old. Thus it is important that future studies focusing on landslide risk assessment in urban areas take into account the potential weakening and leaking of the oldest constructions. Thus, new assessment methods designed to consider the effects of ageing of the infrastructures have to be developed.

References

- Aide, T.M., Zimmerman, J.K, Herrera, L., Rosario, M. and Serrano, M. 1995. Forest recovery in abandoned tropical pastures in Puerto Rico, *Forest Ecology and Management*, 77: 77-86.
- Al-Homoud, A.S., Tal, A.B. and Teqieddin, S.A. 1997. A comparative study of slope stability methods and mitigative design of a highway embankment landslide with a potential for deep seated sliding, *Engineering Geology*, 47: 157-173.
- Albenque, A. 1931. L'éboulement de Lyon, *Annales de Géographie*, 40, 223: 105-106.
- Alexander, D. 1986. Northern Italian dam failure and mudflow, July 1985, *Disasters*, 10 (1): 3-7.
- Alfaro, L.D. 1988. The Risk of Landslide in the Gaillard Cut, Panama Canal Commission, Engineering Division, Geotechnical Branch : 78 p.
- Allix, A. 1930. L'éboulement de Fourvière (note préliminaire), *Les Etudes rhodaniennes*, 6, 4: 454-455.
- Alonso, E.E. and Pinyol, N.M. 2010. Criteria for rapid sliding 1. A review of Vaiont case, *Engineering Geology*, 114: 198-210.
- Assier-Rzadkiewicz, S., Heinrich, P., Sabatier, P.C., Savoye, B. and Bourillet, J.F. 2000. Numerical Modelling of a Landslide-generated Tsunami: The 1979 Nice Event, *Pure and Applied Geophysics*, 157: 1707-1727.
- Baillargé, C. 1893. The Quebec Land Slide of 1889, *The Canadian Society of Civil Engineers*, Vol. II Part I, 13p.
- Baillifard, F.J., Jaboyedoff, M. and Sartori, M. 2003. Rockfall hazard mapping along a mountainous road in Switzerland using a GIS-based parameter rating approach, *Natural Hazards and Earth System Sciences*, 3: 431-438.
- Barnard, P.L., Owen, L.A., Sharma, M.C. and Finkel, R.C. 2001. Natural and human-induced landsliding in the Garhwal Himalaya of northern India, *Geomorphology*, 40: 21-35.
- Bebring, O., Heggstad, M., Larsen, G.P., Andersen, F.M. and Blikra, L.H. 2008. Skredulykka i Ålesund: Rapport frå utvalet som har gjennomgått skredulykka i Ålesund 26 mars 2008, Public Technical Report for Authorities: 165p.
- Benko, B. and Stead, D. 1998. The Frank slide: a reexamination of the failure mechanism, *Canadian Geotechnical Journal*, 35: 299-311.

- Bishop, A.W. and Penman, A.D.M. 1968. The Aberfan disaster: technical aspects, British Geotechnical Society, Informal discussion, 13 November 1968: 317-318.
- Casini, L., Cuomo, S. and Guida, D. 2008. Typical source areas of May 1998 flow-like mass movements in the Campania region, Southern Italy, *Engineering Geology*, 96: 107-125.
- Choffat, Ph. 1929. L'écroulement d'Arvel (Villeneuve) de 1922. *Bull. SVSN*, 57: 5-28.
- Collins, T.K. 2008. Debris Flows caused by failure of fill slopes: early detection, warning, and loss prevention, *Landslides*, 5: 107-120.
- Crosta, G.B., Dal Negro, P. and Frattini, P. 2003. Soil slips and debris flows on terraced slopes, *Natural Hazards and Earth System Sciences*, 3: 31-42.
- Cruden, D. and Varnes, D. 1996. Landslides Types and Processes, in: *Landslides, Investigations and Mitigations*, Transportation Research Board, Turner, A., Schuster, R. (eds.): 36-75.
- Eden, W.J. 1956. The Hawkesbury Land Slide, National Research Council, Division of Building Research: 13 p.
- Giret, M. and Rathieuville, J. 1996. Optimizing the efficiency of the water networks, *L'Eau, l'industrie, les nuisances*, 188: 35-37.
- Glade, T. 2003. Landslide occurrence as a response to land use change: a review of evidence from New Zealand, *Catena*, 51: 297-314.
- González-Gallego, J., Moreno Robles, J., Carcía de la Oliva, J.L. and Pardo de Santayana, F. 2008. Stabilization of a large paleo-landslide reactivated because of the works to install a new ski lift in Formigal skiing resort, In: *Landslides and Engineered Slopes*, Proceedings of the 10th International Symposium on Landslides and Engineered Slopes, Xi'An, China, 30 June-4 July 2008: 1731-1736.
- Grande-Dixence SA. 2005. Historique d'EOS à Cleuson-Dixence en passant par Grande Dixence, available at: <http://www.grande-dixence.ch/energie/hydraulique/valais/historique.html>, last access: January 2011.
- Gregersen, O. 1981. The Quick Clay Landslide in Rissa, Norway. Proceedings of the X International Conference on Soil Mechanics and Foundation Engineering, Vol. 3, Stockholm, Sweden, 1981: 421-426.
- Gue See Sew and Tan Yean Chin. 2002. Mitigating the Risk of Landslide on Hill-Site Development in Malaysia, Proceedings of the 2nd World Engineering Congress, Sarawak, Malaysia, 22-25 July 2002: 1-10.
- Guemache, M.A., Chatelain, J.-L., Machane, D., Benahmed, S. and Djadia, L. Accepted. Failure of landslide destabilization measures: the Sidi Rached Viaduct case (Constantine, Algeria), *Journal of African Earth Sciences*, DOI: 10.1016/j.jafrearsci.2011.01.005.
- Hancox, G. 2002. The Abbotsford Landslide – its nature and causes, *TEPHRA*, June 2002: 9-13.
- Heim, A. 1882. Der Bergsturz von Elm, *Deutsche Geologische Gesellschaft*, 34: 74-115.
- Hermanns, R.L., Fauque, L., Small, L.F., Welkner, D., Folguera, A., Cazas, A. and Nuñez, H. 2008. Overview of Catastrophic Mega-Rockslide in the Andes of Argentina, Bolivia, Chile, Ecuador and Peru, *The First World Landslide Forum*, Tokyo, 2008: 255-258.
- Herrera, G., Notti, D., García-Davalillo, J.C., Mora, O., Cooksley, G., Sánchez, M., Arnaud, A. and Crosetto, M. 2010. Analysis with C- and X-band satellite SAR data of the Portalet landslide area, *Landslides*: 1-12
- Jaboyedoff, M. 2003. The rockslide of Arvel caused by human activity (Villeneuve, Switzerland): Summary, partial reinterpretation and comments of the work of Choffat, Ph. (1929): L'écroulement d'Arvel (Villeneuve) de 1922. *Quaternary open-file report*: 11p.
- Jaboyedoff, M. and Derron, M.-H. 2005. Integrated risk assessment process for landslides. In: *Landslide risk management*, Hungr, O., Fell, R., Couture, R. and Eberhardt, E. (eds.): 776 p.
- Jaboyedoff, M. and Bonnard, C. 2007. Report on Landslide Impacts and Practices in Switzerland: Need for New Risk Assessment Strategies, in: *The 2007 International Forum on Landslide Disaster Management*, Proceedings of the 2007 International Forum on Landslide Disaster Management, Ho, K and Li, V. (eds.), Hong Kong, 10-12 December 2007: 79-97.

- Katz, O. and Crouvi, O. 2007. The geotechnical effects of long human habitation (2000<years): Earthquake induced landslide hazard in the city of Zefat, northern Israel, *Engineering Geology*, 95: 57-78.
- Knapen, A., Kitutu, M.G., Poesen, J., Breugelmans, W., Deckers, J. and Muwanga, A. 2006. Landslides in a densely populated county at the footslopes of Mount Elgon (Uganda): Characteristics and causal factors, *Geomorphology*, 73: 149-165.
- Leroueil, S., Locat, J., Vaunat, J., Picarelli, L. Lee, H. and Faure, R. 1996. Geotechnical characterization of slope movements, *Landslides*, Senneset (ed.), 53-73.
- Logar, J., Fifer Bizjak, K., Kočevar, M., Mikoš, M., Ribičič, M. and Majes, B. History and present state of the Slano Blato landslide, *Natural Hazards and Earth System Sciences*, 5: 447–457.
- Marquis, F.-X. 2002. Le Bossay (commune de Fully). In: *Les crues 2000 – Analyse des événements / Cas exemplaires*, Rapport de l'OFEG, Série Eaux: 242-245.
- Martin, B. 1998. La rehabilitation d'un ancien réseau de drainage comme moyen de lutte contre les mouvements de terrain à Vars (Hautes-Alpes, France), *Revue de géographie alpine*, 86, 1: 59-65.
- McCauley, M.L., Works, B.W. and Naramore, S.A. 1985. Rockfall Mitigation – final report (FHWA/CA/TL-85/12), Washington, FHWA.
- McConnell, R.G. and Brock, R.W. 1904. Report on the great landslide at Frank, Alberta, Canada. Canadian Department of Interior, Annual Report, 1902-1903, Part 8.
- Moreiras, S.M. 2004. Landslide incidence zonation in the Rio Mendoza Valley, Mendoza Province, Argentina, *Earth Surface Processes and Landforms*, 29: 255-266.
- Nordal, S., Chalmers, C.A., Emdal, A., Jendeby, L., Sverige, V., Lyche, E. and Madshus, C. 2009. Skredet i Kattmarkvegen i Namsos 13 mars 2009, Rapport fra undersøkelsesgruppe satt ned av Samferdselsdepartementet : 86p.
- Panama Canal Authority. 2001. A History of the Panama Canal, French and American Construction Efforts, Available at: <http://www.pancanal.com/eng/history/history/>
- Pantelidis, L. 2009. Rock slope stability assessment through rock mass classification systems, *International Journal of Rock Mechanics & Mining Sciences*, 46: 315-325.
- Parriaux, A. 2007. Courses on Slope Stability, 2006-2007 edition, Notes of GEOLEP-EPFL.
- Petley, D.N., and Allison, R.J. 1997, The mechanics of deep-seated landslide, *Earth Surface Processes and Landforms*, 22: 747–758.
- Pinyol, N.M., Alonso, E.E. and Olivella, S. 2008. Rapid drawdown in slopes and embankments, *Water Resour. Res.*, 44, doi:10.1029/2007WR006525.
- Preuth, T., Glade, T. and Demoulin, A. 2010. Stability analysis of a human-induced landslide in eastern Belgium, *Geomorphology*, 120: 38-47.
- Remondo, J., Soto, J., González-Díez, A., Díaz de Terán, J.R. and Cendrero, A. 2005. Human impact on geomorphic processes and hazards in mountains areas in northern Spain, *Geomorphology*, 66: 69-84.
- Rouiller, J.-D. and Joris, C.-L. 2001. Intempéries d'octobre 2000 dans la région du Simplon: l'ovaille de Gondo, Technical Report of CREALP: 6p.
- SafeLand deliverable 1.6, 2010. Analysis of Landslides triggered by anthropogenic factors in Europe, SafeLand European Project Living with Landslide Risk in Europe: Assessment, Effects of Global Changes, and Risk Management Strategies, edited by Nadim, F., Høydal, Ø, Haugland, H. and McLean, A.: 81p.
- Sah, M.P. and Mazari, R.K. 1998. Anthropogenically accelerated mass movement, Kulu Valley, Himachal Pradesh, India, *Geomorphology*, 26: 123-138.
- Salcedo, D.A. 2009. Behavior of a landslide prior to inducing a viaduct failure, Caracas – La Guaira highway, Venezuela, *Engineering Geology*, 109: 16-30.
- Schulz, W.H. 2007. Landslide susceptibility revealed by LIDAR imagery and historical records, Seattle, Washington, *Engineering Geology*, 89: 67-87.

- Segoni, S., Mucci, A. and Casagli, N. 2010. The influence of lithology, land cover, road network and slope gradient in the landslides triggered during the period November 2008 – February 2009 in northern Tuscany (Italy), EGU General Assembly 2010, EGU2010-8528.
- Sudmeier-Rieux, K., Qureshi, R.A., Peduzzi, P., Nessi, J., Dubois, A., Jaboyedoff, M., Jaubert, R., Rietergen, S., Klaus, R. and Cheema, M.A. 2007. Disaster Risk, Livelihoods and Natural Barriers, Strengthening Decision-Making Tools for Disaster Risk Reduction, A Case Study from Northern Pakistan, A World Conservation Union Report: 53p.
- Sudmeier-Rieux, K., Breguet, A. and Dubois, J. 2009. Synthesis Report, Landslide Risk and Vulnerability, Eastern Nepal Study, September 2008, Technical Report of the Institute of Geomatics and Risk Analysis of the University of Lausanne: 53p.
- Terzaghi, K. 1950. Mechanism of Landslides, The Geological Society of America, Engineering Geology (Berkeley) Volume, 83-123.
- Valley B., Thuro K., Eberhardt E. and Raetz H. 2006. Geological and geotechnical investigation of a shallow translational slide along a weathered rock/soil contact for the purpose of model development and hazard assessment, Felsbau, 24: 68-74.
- Van Den Eeckhaut, M. Poesen, J., Govers, G., Verstraeten, G. and Demoulin, A. 2007. Characteristics of the size distribution of recent and historical landslides in a populated hilly region, Earth and Planetary Science Letters, 256: 588-603.
- Van Hise, C.R., Cross, W., Freeman, J.R., Abott, H.L., Carpenter, R.C., Hayford, J.F., Branner, J.C., Davis, A.P. and Reid, H.F. 1916. Preliminary Report Upon the Possibility of Controlling the Land Slides Adjacent to the Panama Canal, by the Committee of the National Academy of Sciences Appointed at the Request of the President of the United States, Proceedings of the National Academy of Sciences, 2 (4): 193-207.
- Vaunat, J., Leroueil, S. and Faure, R. 1994. Slope movements: a geotechnical perspective. Proc. 7th Int. Congress of Int. Association of Engineering Geology, Oliveira (ed.), 1637-1646.
- Walker, L.R., Zarin, D.J., Fetcher, N., Myster, R.W. and Johnson, A.H. 1996. Ecosystem Development and Plant Succession on Landslides in the Caribbean, Biotropica, 28 (4a): 566-576.
- Wang, F., Zhang, Y.-M., Huo, Z.-T., Matsumoto, T. and Huang, B.-L. 2004. The July 14, 2003, Quianjiangping landslide, Three Gorges Reservoir, China, China. Landslides, 1: 157-162.
- Wang, F., Wang, G., Sassa, K., Takeuchi, A., Araiba, K., Zhang, K. and Peng, X. 2005. Displacement Monitoring and Physical Exploration of the Shuping Landslide Reactivated by Impoundment of the Three Gorges Reservoir, China. In: Landslides, Risk Analysis and Sustainable Disaster Management, Proceedings of the first General Assembly of the International Consortium on Landslides: 313-319.
- Wasowski, J. 1998. Understanding rainfall-landslide relationships in man-modified environments: a case-history from Caramanico Terme, Italy, Environmental Geology, 35 (2-3): 197-209.
- Wieczorek, G.F. and Snyder, J.B. 2004. Historical Rock Falls in Yosemite National Park, California, U. S. Geological Survey Open-File Report 03-491: 11 p.